CARDIOVASCULAR IMAGING AND IMAGE ANALYSIS

Edited by

AYMAN EL-BAZ | JASJIT S. SURI

CRC Press
Taylor & Francis Group

Cardiovascular Imaging and Image Analysis

Taylor & Francis
Taylor & Francis Group
http://taylorandfrancis.com

Cardiovascular Imaging and Image Analysis

Edited by

Ayman El-Baz and Jasjit S. Suri

CRC Press
Taylor & Francis Group
Boca Raton London New York

CRC Press is an imprint of the
Taylor & Francis Group, an **informa** business

CRC Press
Taylor & Francis Group
6000 Broken Sound Parkway NW, Suite 300
Boca Raton, FL 33487-2742

Printed on acid-free paper

International Standard Book Number-13: 978-1-4987-9758-0 (Hardback)

Library of Congress Cataloging-in-Publication Data
Names: El-Baz, Ayman S., editor. | Suri, Jasjit S., editor.
Title: Cardiovascular imaging and image analysis / edited by Ayman El-Baz and Jasjit S. Suri.
Description: First edition. | Boca Raton : Taylor & Francis, [2019] |
Includes bibliographical references and index.
Identifiers: LCCN 2018022105 (print) | LCCN 2018022883 (ebook) | ISBN 9780429441493 (eBook General) | ISBN 9780429806223 (Adobe PDF) | ISBN 9780429806216 (ePUB) | ISBN 9780429806209 (Mobipocket) | ISBN 9781498797580 (hardback : acid-free paper)
Subjects: LCSH: Cardiovascular system--Diseases--Diagnosis. | Diagnostic imaging.
Classification: LCC RC670 (ebook) | LCC RC670 .C365 2019 (print) | DDC 616.1/075--dc23
LC record available at https://lccn.loc.gov/2018022105

Visit the Taylor & Francis Web site at
http://www.taylorandfrancis.com

and the CRC Press Web site at
http://www.crcpress.com

Dedication

With love and affection to my mother and father, whose loving spirit sustains me still

—Ayman El-Baz

To my late loving parents, immediate family, and children

—Jasjit S. Suri

Taylor & Francis
Taylor & Francis Group
http://taylorandfrancis.com

Contents

Preface

This book covers the novel strategy of the state-of-the-art approaches for automated non-invasive system for early cardiovascular disease diagnostics. Cardiovascular disease is the leading cause of death for people of most ethnicities in the United States, including African Americans, Hispanics, and whites. According to the American Heart Association, cardiovascular disease accounts annually for almost 801,000 deaths in the United States, which is about 1 of every 3 deaths. This means cardiovascular disease claims more lives each year than all forms of cancer. However, early detection of cardiovascular disease increases the chances of patients' survival.

Current non-invasive cardiovascular imaging includes ultrasound, computed tomography (CT), magnetic resonance imaging (MRI), magnetic resonance angiography (MRA), and computed tomography (CT). Today's CAD systems can analyze images from these different modalities for detecting cardiovascular disease and determining its aggressiveness. Generally, the CAD systems analyze the images in three steps: segmentation, description or feature extraction, and classification of the status.

The main aim of this book is to help advance scientific research within the broad field of early detection of cardiovascular disease. This book focuses on major trends and challenges in this area, and it presents work aimed at identifying new techniques and their use in biomedical image analysis.

Taylor & Francis
Taylor & Francis Group
http://taylorandfrancis.com

Acknowledgments

The completion of this book could not have been possible without the participation and assistance of so many people whose names cannot all be enumerated. Their contributions are sincerely appreciated and gratefully acknowledged. However, the editors would like to express their deep appreciation and indebtedness particularly to Dr. Ali H. Mahmoud for his endless support.

Taylor & Francis
Taylor & Francis Group
http://taylorandfrancis.com

About the Editors

Ayman El-Baz is a professor, university scholar, and chair of the Bioengineering Department at the University of Louisville. Dr. El-Baz earned his bachelor's and master's degrees in electrical engineering in 1997 and 2001, respectively. He earned his doctoral degree in electrical engineering from the University of Louisville in 2006. In 2009, Dr. El-Baz was named a Coulter Fellow for his contributions to the field of biomedical translational research. Dr. El-Baz has 15 years of hands-on experience in the fields of bio-imaging modeling and noninvasive computer-assisted diagnosis systems. He has authored or coauthored more than 450 technical articles (105 journals, 15 books, 50 book chapters, 175 refereed-conference papers, 100 abstracts, and 15 U.S. patents).

Jasjit S. Suri is an innovator, scientist, visionary, industrialist, and internationally known world leader in biomedical engineering. Dr. Suri has spent more than 25 years in the field of biomedical engineering/devices and its management. He received his doctorate from University of Washington, Seattle, and his MBA from the Weatherhead School of Management, Case Western Reserve University, Cleveland. Dr. Suri was awarded the President's Gold Medal in 1980 and became a Fellow of the American Institute of Medical and Biological Engineering for his outstanding contributions in 2004.

Taylor & Francis
Taylor & Francis Group
http://taylorandfrancis.com

Contributors

Yasmina Al Khalil received her B.Sc. and M.Sc. degrees in Electrical and Computer Engineering from Abu Dhabi University, Abu Dhabi, United Arab Emirates, in 2015 and 2017 respectively, where she has also been working as a teaching and research assistant in the Department of Electrical and Computer Engineering since 2015. During her time at ADU, she has received multiple awards, including the Abu Dhabi University Professional Achievement Award in 2017, as well as the Special Innovation Award of 1,000,000 AED from H.H. Sheikh Muhammad Bin Rashid Al Maktoum as part of the Best m-Government Service Award Competition during the Government Summit for the Al Najdah Mobile Application for accident detection in moving vehicles, and the award for the Lost and Found Mobile Application for the retrieval of lost personal objects. Among other awards, she has received the first place in the mGov Developer Jam hosted by the Telecommunications Regulatory Authority, the first place in the Digital Arabic Content Competition organized by United Nations Economic and Social Commission for Western Asia for an Iqraa mobile application, and the fourth place in the International Robotics for Good competition. Her research areas include artificial intelligence and machine learning, embedded and IOT systems, image and video processing, and mobile computing.

Mansour AlOmran is currently a Cardiac Surgery resident at McGill University, Montreal, Quebec, Canada. He is also pursuing a Master's degree in Experimental Surgery at the same university. He obtained his medical degree from King Saud University, Riyadh, Saudi Arabia.

Leiner Barba-J received his Bachelor degree in Electronic Engineering from the Universidad Popular del Cesar, Valledupar, Colombia (2005), where he is currently a lecturer and researcher. He received his Master (2012) and PhD (2017) degrees in Electrical Engineering from the Universidad Nacional Autónoma de México, México City. His current research interests include developing of image processing algorithms for medical applications using mathematical models, and analysis of cardiac images for evaluating the heart mechanical function.

Harish Bhaskar is an experienced data officer and an expert in Artificial Intelligence (AI)-powered data analytics with 15+ years' history of working in aerospace, telecommunication, automotive, security, geospatial and biomedical industries. He is the Director of Artificial Intelligence and Chief Scientist at the Linkay Technologies, Inc., group of companies headquartered in the USA. Prior to his current role, Harish was engaged on a consulting contract with The Sky Guys/Defiant Labs, Canada, as their Chief Data Scientist. Previously, he was a chief engineer at Samsung Electronics, India

and an assistant professor/lead at the Visual Signal Analysis and Processing (VSAP) research center at Khalifa University, UAE. Harish has also worked as a researcher, managing the Research and Development (R&D) of Ministry of Defense (MoD) UK and European Union (EU)-funded projects at Lancaster and Manchester Universities, UK. Harish has a Ph.D. in Computer Science and an M.Sc. in Autonomous Systems from Loughborough and Exeter Universities UK, respectively.

René M. Botnar received his PhD from the ETH Zurich. From 1996-97 he was a Research Associate in the Department of Radiology at the University Zurich. In 1997, he joined the Cardiac MR Center at the Beth Israel Deaconess Medical Center and Harvard Medical School.

In 2003, Dr. Botnar became the Scientific Director of the Cardiac MR Center at the Beth Israel Deaconess Medical Center and was appointed as Assistant Professor of Medicine at Harvard Medical School, Boston, MA. In 2005, Dr. Botnar accepted a Professorship of Biomedical Imaging at the Technische Universität München, where he setup a cardiac MR program with a special focus on preclinical and translational multimodality imaging. His work was funded by the German Ministry of Research and Education, by the German Excellence Program, and by industry. At the end of 2007, he joined the Division of Imaging Sciences and Biomedical Engineering at King's College London, where he is currently Chair of Cardiovascular Imaging and Interim Head of the Division of Imaging Sciences and Biomedical Engineering. Dr. Botnar is a Fellow of the International Society of Magnetic Resonance Imaging in Medicine and a member of the Society for Cardiovascular Magnetic Resonance; he was a board member of Society for Cardiovascular Magnetic Resonance from 2008-2011 and was on the scientific advisory board of the High Risk Plaque initiative. He is currently Associate Editor of the *Journal of Cardiac Magnetic Resonance* (JCMR) and has authored more than 210 peer-reviewed original papers, 30 review articles, and 25 book chapters in the field of CMR. He also holds 5 patents and is an editor of a CMR textbook on Cardiovascular Magnetic Resonance Imaging.

Erik Carbajal-Degante received his B.S. degree in Communication and Electronic Engineering from Instituto Politécnico Nacional, Mexico. He received a Master in Electrical Engineering from Universidad Nacional Autónoma de México (2017). He is currently pursuing a Ph.D. in Computer Science, and his research interests include bio-inspired models for image processing, with a special focus on texture.

Qi Dou received her B.E. degree in Biomedical Engineering from Beihang University, Beijing, in 2014. She is studying toward a Ph.D. degree in the Department of Computer Science and Engineering, The Chinese University of Hong Kong, Hong Kong. Her research interests include medical image analysis, deep learning, computer-aided detection, and image segmentation, among others.

Xiuquan Du was born in Chuzhou City, Anhui Province, China in August, 1982, and received his bachelor's degree and Ph.D. degree in computer science at Anhui University. His research interests include machine learning, medical image analysis, and bioinformatics.

Maryam El-Baz is a Magnet Science Technology student at duPont Manual High School. Her main interest is developing accurate methods for image segmentation.

Adel Elmaghraby, an IEEE Senior Member, is professor and chair of the Computer Engineering and Computer Science Department at the University of Louisville. He has also held appointments at Carnegie Mellon's Software Engineering Institute and the University of Wisconsin-Madison, and has advised over 60 master's graduates and 24 doctoral graduates. His research and publications span intelligent systems, neural networks, cyber-security, visualization, and simulation. The IEEE-Computer Society has recognized his work with multiple awards, including a Golden Core membership.

Alexander Emmott is a Ph.D. candidate at McGill University in the department of Chemical Engineering. Alex's research is focused on using both echocardiography and tensile analysis to better understand the mechanical properties of thoracic aortic aneurysms. Alex completed his BASc in Chemical Engineering at the University of British Columbia in 2009 and his MEng at McGill University in 2012.

Boris Escalante-Ramírez is a Professor at Universidad Nacional Autónoma de México. He received a PhD from the Technical University of Eindhoven (1992). His research areas include computational models for image processing.

Baowei Fei is Director of the Quantitative BioImaging Laboratory (www.fei-lab.org). He is a Full Professor in the Departments of Bioengineering and Computer Science at the Jonsson School of Engineering at the University of Texas at Dallas. He was an Associate Professor with tenure in the Department of Radiology and Imaging Sciences at Emory University School of Medicine and in the Joint Coulter Department of Biomedical Engineering at Emory University and Georgia Institute of Technology. He was also a faculty member in the Department of Mathematics and Computer Sciences at Emory University. Dr. Fei was a Georgia Research Alliance Distinguished Scientist.

Dr. Fei is a national leader in quantitative imaging and image-guided interventions. He serves as Conference Chair for the International Conference of SPIE Medical Imaging – Image-Guided Procedures, Robotics Interventions, and Modeling from 2017 to 2020. The SPIE Medical Imaging Conference is the internationally recognized premier forum for reporting state-of-the-art research and development in medical imaging. Dr. Fei serves as the Chair for the National Institutes of Health (NIH) Study Section ZRG1 SBIB-J (56) on Imaging and Image-guided Interventions and also co-Chair for multiple NIH and Department of Defense (DOD) Study Section Panels. He served as an Associate Editor for *Medical Physics*, an Editorial Board Member for five journals in the field of biomedical imaging, and a reviewer for more than 20 international journals in medical imaging. Dr. Fei has presented internationally and is widely published in the field of medical imaging.

Dr. Fei has received numerous national awards including the Academy of Radiology Research (ARR) Distinguished Investigator Award and the Society of Nuclear Medicine and Molecular Imaging (SNMMI) Young Investigator Award. He was a recipient of the Department of Defense Post-Doctoral Traineeship Award. His research on prostate cancer imaging and image-guided therapy was highlighted by the Department of Defense in 2003 and 2006. He also received multiple prestigious awards at the university and regional levels, including the Emory 1% Award and Georgia Cancer Coalition Distinguished Scholar Award.

Dr. Fei's NIH-supported research has emphasized applying multimodality imaging (PET/CT, MRI, ultrasound, and optical imaging) to the detection, diagnosis, and therapy of various diseases including cancers and heart diseases.

David Firmin: Prof. David Firmin is Professor of Biomedical Imaging at the National Heart and Lung Institute, Imperial College London, and the Physics Director of the Royal Brompton Hospitals Cardiovascular Research Centre. As the Director of Physics, he has led a number of pioneering advances in atheroma imaging, rapid and interactive cardiovascular MR, coronary angiography, myocardial perfusion imaging and tissue characterization. Prof. Firmin has more than 350 publications in cardiovascular MR imaging, including over 170 peer-reviewed academic journal papers.

Xiaohong W. Gao is a full professor in computer vision and imaging science. While her research focuses are on human vision, color appearance and medical imaging, she is currently working on the application of deep learning technique, in particular convolutional neural network and reinforcement learning, on a range of fields, including images and text documents.

Yitzhak Gebru received his B.S. and M.Eng. degrees in bioengineering from the University of Louisville in 2016 and 2017, respectively. His research interests include image processing, object detection, medical imaging, and analysis of MRA data. Currently, he is the CEO of 4th Dimension, LLC, a start-up company specializing in medical imaging analysis.

Mohammed Ghazal is a Senior Member of IEEE and a member of ACM and BMES. His research areas are bioengineering, image and video processing, and smart systems. He received his Ph.D. and M.A.Sc. in Electrical and Computer Engineering (ECE) from Concordia University in Montreal, Canada, in 2010 and 2006, respectively, and his B.Sc. in Computer Engineering from the American University of Sharjah (AUS) in 2004. He is now an Associate Professor and Chair of ECE at Abu Dhabi University and an adjunct Associate Professor of Bioengineering at the University of Louisville. He has received multiple awards, including the Distinguished Faculty Award of Abu Dhabi University in 2017 and 2014, a Special Innovation Award of AED 1,000,000 by the Office of Prime Minister of the UAE, NSERC's Alexander Graham Bell's Scholarship, AUS's President's Cup, and the Ministry of Education Shield for Creative Thinking. Dr. Ghazal has authored or co-authored over 40 publications in recognized international journals and conferences, including IEEE Transactions in Image Processing, IEEE Transactions in Circuits and Systems for Video Technology, IEEE Transactions in Consumer Electronics, Elsevier's Renewable Energy Reviews, and Springer's Multimedia Tools and Applications.

Giulia Ginami received her PhD from the University of Lausanne (CHUV-UNIL) in 2016, with a thesis titled "Advanced magnetic resonance imaging approaches for a non-invasive and comprehensive assessment of coronary artery disease progression." Subsequently, she became a postdoctoral Research Associate at the School of Biomedical Engineering and Imaging Sciences of the King's College London. Dr. Ginami has authored 11 peer-reviewed journal publications and more than 40 conference proceedings in the field of cardiovascular MRI. Her current research focuses on imaging different stages of coronary artery disease by developing novel multicontrast MRI acquisition strategies. Dr. Ginami is also interested in the development of efficient motion correction algorithms for improved visualization of the coronary arteries.

Guruprasad Giridharan received his B.Tech. in Chemical Engineering from the University of Madras, India, in 1998, and M.S. and Ph.D. degrees in Chemical Engineering from the University of Utah, Salt Lake City, UT, in 2002. He is currently the Associate Chair and Professor of Bioengineering at the University of Louisville. His research interests include cardiac and vascular mechanics, myocardial recovery, translational research, and biomedical device development.

Shouvik Haldar is a Consultant Cardiologist and Electrophysiologist at Royal Brompton & Harefield NHS Foundation Trust. His research expertise includes electrophysiology, cardiology, and applications in atrial fibrillation.

Pheng-Ann Heng is a professor at the Department of Computer Science and Engineering at The Chinese University of Hong Kong (CUHK). He has served as the Chairman of the department from 2014 to 2017 and as the Head of Graduate Division from 2005 to 2008 and also from 2011 to 2016. He has served as the Director of Virtual Reality, Visualization and Imaging Research Center at CUHK since 1999. He is also the Director of Center for Human-Computer Interaction at Shenzhen Institutes of Advanced Technology, Chinese Academy of Sciences, and has been appointed by the China Ministry of Education as a Cheung Kong Scholar Chair Professor in 2007. He is the author of over 400 peer-reviewed publications, including 160 international journal articles and 240 international conference papers. His research interests include AI and VR for medical applications, surgical simulation, visualization, graphics, and human-computer interaction.

Liqin Huang received his Ph.D. degree from Fuzhou University, Fuzhou, PR China. He is currently a professor at the School of Physics and Information Engineering, Fuzhou University, PR China. He is concerned with image processing, computer vision, and artificial intelligence.

Mario Guzmán Huerta is an M.D. from the U. Autónoma de Nayarit, México. He is specialist in Fetal Medicine, Neonatology and Gynecology and Obstetrics, and works at the Instituto Nacional de Perinatología in Mexico City.

Heba Kandil received her B.Sc. and M.S. degrees in Computer Science from Mansoura University, Mansoura, Egypt, in 2008 and 2012. In August 2016 she joined the BioImaging Laboratory at University of Louisville, Louisville, KY, USA, as a Ph.D. student in the Computer Science and Computer Engineering Department. Her current research is focused on developing new computer assisted diagnostic (CAD) system for diagnosing elevated blood pressure and correlated cerebrovascular changes from MRA images.

Jennifer Keegan: Dr Jenny Keegan is a principal physicist at the Royal Brompton & Harefield NHS Foundation Trust, and also an Honorary Senior Lecturer and Adjunct Reader at Imperial College London. Over the last 20 years, she has worked extensively in cardiac MRI techniques. Her current interests include respiratory motion compensation techniques, MR assessment of coronary artery flow, myocardial velocity mapping and high-resolution 3D imaging of late gadolinium enhancement.

Habib Khan: Dr. Habib Khan is a Cardiology Research Fellow and Cardiac Electrophysiologist at Royal Brompton & Harefield NHS Foundation Trust. He is interested in pursuing a career in clinical academia in cardiology. His objectives are to conduct good quality research and be able to translate that research into clinical practice.

Kevin Lachapelle obtained his medical degree from McGill University in 1988 and completed specialty training in General Surgery as well as Cardiothoracic Surgery at McGill University, followed by a fellowship under Professor Sir Magdi Yacoub. He is a practicing Cardiac Surgeon at the McGill University Health Centre specializing in Aortic Surgery and Percutaneous Valve Implantation. Dr Lachapelle is presently the Adair Chair of Surgical Education, the Vice–Chair of Surgery, and for 12 years, the Cardiac Surgery Program Director at McGill University.

Richard L. Leask received his B.A.Sc. and M.A.Sc. in Mechanical Engineering from the University of Waterloo in 1994 and 1996, respectively. In 2002, he completed his Ph.D. at the University of Toronto in Mechanical and Industrial Engineering as a member of the Institute for Biomedical Engineering. From 2001 to 2002 Prof. Leask worked at the Toronto General Hospital in Clinical and Surgical Pathology before joining the Department of Chemical Engineering at McGill. He is currently a Professor at McGill University and a Researcher at the Montreal Heart Institute. The Leask lab is internationally recognized for its pioneering work on endothelial cell mechanobiology and research into the biomechanics of thoracic aortic aneurysms and aortic dissections.

Lei Li is currently a PhD student at Shanghai Jiao Tong University. Her research interests are medical image analysis and computer-aided diagnosis.

Wei Li is a full lecturer in College of Physics and Electronic Information, Fuzhou University. Her research field is in motion tracking and medical image analysis. The current focus of her work is information mining of big data and the application of deep learning technique.

Zhongxing Liao is a full professor with tenure in Radiation Oncology specializing in thoracic malignancies, including cancer of the lung, esophagus, mesothelioma, and thymoma. She has a broad background in thoracic radiation oncology, with specific expertise in prospective comparative clinical trial and predictive models using radiation dosimetric metrics and biomarkers. She has pioneered the implementation of advanced radiation delivery technologies to enhance the therapeutic ratio by significantly reducing lung toxicity. She has extensive experience in addressing clinical questions in the setting of prospective clinical trials and has led a multi-institutional trial, “A Bayesian Randomized trial of Image-Guided Adaptive Conformal

Photon vs Proton Therapy, with Concurrent Chemotherapy, for Locally Advanced Non-Small Cell Lung Carcinoma: Treatment-Related Pneumonitis and Locoregional Recurrence." This is the first prospective randomized clinical protocol to compare proton and photon therapy for a "hard to treat" cancer. The completion of this trial is regarded as the most significant contribution to the field of modern radiation therapy. She is currently serving as the national PI on a phase III randomized trial comparing overall survival after protons and photons in lung cancer patients. Along with the development and conduct of these clinical trials, she has worked with medical physicists toward standardizing and automating the target and Organs-At-Risk delineation, and automation of radiation treatment planning.

Qiang Lin is a full professor in electronic information science. His research is focused on signal processing, biomedical engineering, and human vision. He is currently working on medical image consolidation and analysis, especially omni-directional echocardiogram system.

Martin Loomes is Pro-Vice Chancellor at Middlesex University, UK. His current research interests range from machine learning, computer logic simulation, and multicast routing to enhanced learning and teaching.

Yangkun Luo graduated from the Sichuan University and joined Sichuan Cancer Hospital and Institute in July 2006. Dr. Yangkun Luo was a visiting scientist at MD Anderson Cancer Center from 2015 to 2016. Dr. Yangkun Luo is an associate chief physician for Radiation Oncology. Dr. Yangkun Luo's clinical interests focus on radiation oncology of head and neck cancers, and thoracic and gynecologic cancers. His special interest is in precision radiotherapy for nasopharyngeal carcinoma, lung cancer, and cervical carcinoma. He is actively involved in laboratory research and focuses on basic and clinical research of radiation oncology.

Ali Mahmoud received his B.S. and M.S. degrees in electrical engineering from Alexandria University, Egypt, in 2005 and 2009, respectively. He received his Ph.D. degree in electrical engineering from the University of Louisville, Louisville, Kentucky, USA in 2014. He is currently working as a postdoctoral research associate in the Bioengineering Department at the University of Louisville. His research interests include computer vision and image processing, object detection and tracking, medical imaging, and facial biometrics.

Lisbeth Camargo Marín is a M.D. specialist in Fetal Medicine and Gynecology and Obstetrics. She works at the Instituto Nacional de Perinatología in Mexico City.

George Markousis-Mavrogenis has completed a bachelor's degree in medicine at the University of Groningen (Groningen, the Netherlands) with honors in science and is currently a student in the master's program in medicine at the same university. He has coauthored more than 30 publications in the field of cardiovascular magnetic resonance, with a focus on the applications of cardiovascular imaging in autoimmune rheumatic diseases.

Sophie I. Mavrogeni received her Diploma in Medicine in Greece (1985), where she was born. She has been a Specialist in Cardiology (Greek Board) since 1991. She completed her CMR training at Royal Brompton Hospital (London, 1991-1993), and undertook a CMR sabbatical at University of Alabama at Birmingham (1993). She is a member the AHA Cardiovascular Radiology Council (since 1996), SCMR (since 1998, founding member number 7), and ESC CMR WG (since 1999). She received her European Diploma in Cardiology in 2000, and is a Fellow of the European Society of Cardiology (FESC, 2000). She has achieved SCMR Credentialing (Level 3) by SCMR (2003) and CMR Credentialing (European exams) by EUROCMR (2003).

Dr. Mavrogeni has served as a reviewer for several journals, including *JCMR* (2001), *Stroke* (2003), *CAIM* (2005), *Eur Heart J* (2007), *JMRI* (2008), *JACC* (2007), *Circulation* (2007), *Arthritis Care and Research* (2008), and *Annals of Internal Medicine* (2008). She was the founder and first President of the Greek CMR Working Group (WG) (1999-2002) and of the Greek College of CMR Clinical Applications (2013). She has been a Nucleus member of the European Society of Cardiology CMR WG, responsible for CMR education topics (2004-2008), and she was elected Chair for the "Women in CMR" WG of SCMR in 2017.

Currently a cardiologist at Onassis Cardiac Surgery Center (Athens), Dr. Mavrogeni is in charge for CMR teaching, routine scans, and research activities. She serves as Organizer of the annual ATHENSCMR Level 1 course in Athens (since 2000), which is accredited by EBAC and endorsed by SCMR /EuroCMR. Her research interests include non-ischemic cardiomyopathy and specifically CMR in Internal Medicine (thalassemia, dystrophinopathies, myocarditis, and rheumatic diseases). She is also Director of the outpatient clinic for Rheumatic, Neuromuscular and Other Rare Diseases at Onassis Hospital (referral center of Greece).

Additionally, Dr. Mavrogeni is a Research consultant in the Pediatric Clinic of Kapodistrian University of Athens, and has published over 200 original articles and authored chapters in several books related to cardiovascular imaging and CMR.

Tim McGloughlin, following a period of 9 years in industry, has more than 25 years' experience in Higher Education at the University of Limerick, Ireland. He has published more than 120 refereed journal and conference papers in biomedical engineering, as well as two books and seven book chapters, and is a regular presenter at all of the major annual biomedical engineering meetings.

He pioneered the undergraduate B.Eng. (Biomedical Engineering) programme at the University of Limerick in 2002. In July 2012, he was appointed Head of the MABE Department, which has an undergraduate population of more than 500 students and more than 70 Master's and Ph.D. students. He served as External Examiner at Imperial College, London from 2010 to 2013.

Prof. McGloughlin was the Founding Director of the Centre for Applied Biomedical Engineering Research, a University Research Centre which has developed an international reputation in the field of vascular and cardiovascular fluid and solid mechanics and tissue engineering. He has supervised 17 PhD students to completion and has attracted in excess of €7m Euro in research funds. His international collaborators include the University of Pittsburgh, Georgia Institute of Technology, Duke University, Columbia University, Imperial College, London, and the University of Edinburgh. In 2010 he was conferred the University of Limerick Research Excellence Award for his outstanding contribution to research at the University of Limerick.

He is a member of the Executive Committee of the ASME Bioengineering Division, a member of the World Council for Biomechanics (elected), BMES and ESB. He is a Fellow of the Royal Academy of Medicine in Ireland (Bioengineering Section), a Fellow of Engineers Ireland, and a member of the Irish Medical Devices Association (IMDA).

Samineh Mesbah is a Ph.D. candidate at University of Louisville, Department of Electrical and Computer Engineering. She has a bachelor's degree in Electrical Engineering/Control Systems from Ferdowsi University, Mashhad, Iran, and a master's degree in Biomedical Engineering/Bioelectrics from Tehran Polytechnic University, Tehran, Iran. Her research in the Ph.D. program has been focused on automatic assessment of skeletal muscle response to the epidural electrical stimulation of the spinal cord in patients with severe spinal cord injuries. In her research, she has developed several computer software programs with state-of-the-art algorithms for signal and image processing to facilitate the efforts of understanding the neurophysiological response of human to the spinal cord epidural stimulation.

Raad Mohiaddin is Professor of Cardiovascular Imaging at the National Heart and Lung Institute Imperial College London and Royal Brompton & Harefield NHS Foundation Trust. His research interests include vascular imaging and assessment of the biophysical properties of the vascular wall, blood flow measurement and blood flow visualization, congenital heart disease, ischaemic and non-ischaemic heart disease, valvular disease, and the development of imaging techniques to guide electrophysiological and interventional procedures.

Eva Nyktari is a Locum Consultant and was previously a Cardiac MR Lead Clinical Fellow at Royal Brompton & Harefield Hospitals Charity. Dr. Nyktari's research focuses on cardiology, cardiovascular imaging, and echocardiography.

Jimena Olveres is a Professor at Universidad Nacional Autónoma de México (UNAM). She received her B.S. degree in Biomedical Engineering from Universidad Iberoamericana in Mexico City, a Master in Engineering, and a Ph.D. in Computer Science from UNAM. Her research areas include computational models for image processing, specializing in medical image analysis and cardiac imaging.

Giorgos Papanastasiou completed a B.Sc.Eng. degree in Material Science and Engineering (5-year degree), at the University of Ioannina, Greece. Giorgos has also received a M.Sc. degree in Biomedical Engineering from the National Technical University of Athens and University of Patras, Greece. During the second year of his M.Sc., he completed an internship and a master thesis at the University Medical Centre of Groningen, the Netherlands (Departments of Medical Physics and Medical Biology/Biomedical Engineering, respectively). He also completed a M.Sc.R. degree in Cardiovascular Biology from the School of Clinical Sciences of the University of Edinburgh, UK, during which he gained broad expertise in bioinformatics, bioengineering, biophysics, and biomathematics across different research projects. Further, Giorgos received a Ph.D. degree in Medical Physics and Mathematical modeling at the Clinical Research Imaging Centre and the British Heart Foundation-Centre for Cardiovascular Science of the University of Edinburgh, UK. Currently, he is a postdoctoral Research Fellow in Multimodality imaging working at the Image Analysis lab of the Edinburgh Imaging Facility in Queen's Medical Research Institute, of the University of Edinburgh. He participates in a number of research projects, and his research interests include multimodality imaging (including molecular imaging), signal and image processing, data analysis and development of mathematical modelling, as well as design and development of nanomaterials for biomedical imaging.

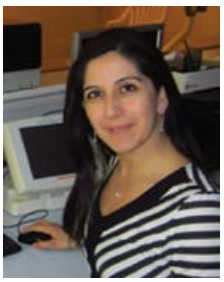

Claudia Prieto is a Senior Lecturer in the Biomedical Engineering Department at King's College London. Dr. Prieto received her Ph.D. from the Pontificia Universidad Catolica de Chile in 2007. She joined the Biomedical Engineering Department at King's College London in 2008 as Postdoctoral Research Associate and became Lecturer in Magnetic Resonance Imaging and Reconstruction in 2012. Dr. Prieto's research focuses on the development of novel reconstruction and motion correction techniques to accelerate the acquisition and improve the quality of cardiac MR and PET-MR imaging. She works closely with industrial partners to further promote clinical translation of her research. Dr. Prieto has published 45 peer-reviewed journal articles and more than 100 conference proceedings. Dr. Prieto and her group work on the development of novel pulse sequences, undersampled reconstruction and advanced motion correction techniques for free-breathing 3D whole-heart imaging of the coronary arteries (lumen and wall) and myocardial tissue characterization (black-blood LGE, quantitative T1/T2 mapping) for both cardiac MR and PET-MR images. More recently, her group is also developing methods to accelerate the acquisition of Magnetic Resonance Fingerprinting images.

Yu Qian has an educational background in electrical and electronics engineering and computer science, with bachelor's and master's degree from Hefei University of Technology, China, and a Ph.D. from the School of Computer Science of Middlesex University, UK. She is currently working in Cortexica as a senior research scientist. Her research interests focus on computer vision and machine learning, especially in visual feature representation for image retrieval.

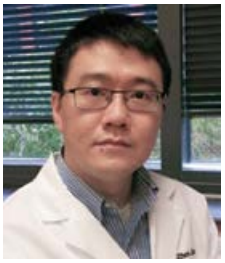

Zhen Qian is the Chief of Cardiovascular Imaging Research at the Piedmont Heart Institute, Atlanta, GA, USA. He received a B.S. degree in Electronic Engineering from the South China University of Technology (China). He received his M.S. degree in Computer Science and Ph.D. degree in Biomedical Engineering from Rutgers, the State University of New Jersey-New Brunswick, in 2007 and 2008, respectively. His research interests include medical image analysis, computer-aided intervention, 3D printing in medicine, and machine learning in biomedical applications. He is the author of over 70 refereed journal and conference papers in the aforementioned fields. Dr. Qian received the Best Abstract award, the Siemens Healthineers Outstanding Academic Research (SOAR) award finalist, and was named a Toshiba Young Investigator Award finalist (senior author) by the Society of Cardiovascular Computed Tomography in 2010, 2017 and 2017, respectively.

Jing Qin is an assistant professor in School of Nursing (SN), The Hong Kong (HK) Polytechnic University (PolyU). He is also a key member in the Centre for Smart Health, SN, PolyU, HK. He received his Ph.D. degree in Computer Science and Engineering from the Chinese University of Hong Kong in 2009. Dr. Qin's research interests include innovations for healthcare and medicine applications, medical image processing, deep learning, visualization and human-computer interaction and health informatics.

Xulei Qin is an Instructor in the Stanford Cardiovascular Institute, Stanford University School of Medicine. He received his bachelor degree in Biomedical Engineering and Ph.D. degree in Biophysics from Xi'an Jiaotong University. Afterwards, he conducted his postdoctoral training in cardiac imaging at Emory University and in molecular imaging and cardiac regenerative therapy at Stanford University, respectively. His current research focuses on imaging-based early detection and regenerative therapy for heart failure, which has led to more than 20 related publications in peer-review journals and book chapters. He is a member of the IEEE EMBS and the AHA, and a recipient of several early career awards from NHLBI, AHA, and Stanford University.

Imran Rashid is a Cardiologist with subspecialty training in cardiovascular magnetic resonance imaging. He completed a combined M.B.B.S./Ph.D. degree in 2010 at the University of Sydney, Australia, where his research focused on basic mechanisms of diabetic atherosclerosis. He then undertook specialist training in Clinical Cardiology at Royal Prince Alfred Hospital (Sydney, Australia), followed by a fellowship in clinical cardiovascular magnetic resonance imaging. During this time, he conducted postdoctoral research at the Victor Chang Cardiac Research Institute (Sydney, Australia),

which focused on the utility of molecular magnetic resonance imaging of myeloperoxidase (an inflammatory enzyme) activity for the identification of high-risk atherosclerotic plaque. He is currently based at King's College London, where he is undertaking studies to assess the clinical utility of novel magnetic resonance angiography sequences and contrast agents for the assessment of coronary artery disease.

Safa Salahat is an M.Sc. student who obtained her bachelor's degree in Computer Engineering from Khalifa University of Science and Technology in 2015, and master by Research in Engineering degree from the same university in 2017. She is a starting researcher who has authored or coauthored a number of publications, and acquired advanced places in multiple competitions. Her main research interests include artificial intelligence, computer vision, and medical imaging.

Ahmed Shalaby received his B.S. and M.S. degrees in electrical engineering from Alexandria University, Egypt, in 2003 and 2009, respectively. In addition, he received his Ph.D. degree in electrical engineering from the University of Louisville, Louisville, Kentucky, in 2014. He is currently working as a postdoctoral research associate at the bioengineering department at the University of Louisville. His research interests include computer vision and image processing, object detection and tracking, medical imaging, and facial biometrics.

Greg Slabaugh is a Senior Lecturer in the Department of Computer Science at City University of London. Dr. Slabaugh has a broad background in computer vision and medical image analysis. He has coauthored over 100 peer-reviewed papers and has been granted 36 patents for his work in image analysis and shape modeling.

Ahmed Soliman received his B.Sc. and M.S. degrees in Computer Engineering from Mansoura University, Mansoura, Egypt. In December 2011 he joined the BioImaging Laboratory at University of Louisville, Louisville, Kentuky, as a research assistant. He has actively been working on Design of Computer Aided-Diagnostic Systems for Lung Segmentation and Early Detection of Lung Nodules.

Dawn Sosnin received her B.Sc. in Bioengineering from the University of Louisville in Louisville, Kentucky, USA, in 2018. While there, she studied in the BioImaging Lab under Dr. Ayman El-Baz. She is planning to continue her studies to earn her Master's degree in Bioengineering at the University of Louisville.

Fatma Taher is assistant dean in the College of Technological Innovation at Zayed University, Dubai, UAE. Her research interests are in the areas of signal and image processing, pattern recognition, deep learning, machine learning, artificial intelligence, medical image analysis (especially the detection of cancerous cells), kidney transplants, autism, watermarking, remote sensing and satellite image research. She received her PhD from Khalifa University of Science, Technology and Research, UAE, in 2014. Dr. Fatma Taher has published more than 40 papers in international Journals and conferences. She has served as a member of the steering, organizing and technical program committees of many international conferences and on many editorial and reviewing boards of international journals and conferences. Dr. Fatma is the vice chair of IEEE UAE section and the chair of the Education Committee in British Society in UAE. Dr. Fatma has received many distinguished awards, such as the best paper award of the first prize in the PhD Forum of the 20th IEEE International Conference on Electronics, Circuits and Systems in 2013; the UAE Pioneers award as the first UAE citizen to create a computer-aided diagnosis system for early lung cancer detection based on the sputum color image analysis in 2015; and an innovation award at the 2016 Emirati Women Awards; and L'Oréal-UNESCO for Women in Science Middle East Fellowship in 2017.

Mani A Vannan is a pioneer in the field of Echocardiography and Cardiovascular Imaging and until recently Chief of CV Imaging at the Piedmont Heart Institute, Atlanta, Georgia, USA. He is currently Co-Chief of the Structural and Valvular Center of Excellence at the Piedmont Heart Institute. He has been a clinical cardiologist, educator, and investigator for over 15 years. He started his career graduating from medical school in India and then trained in the United Kingdom before pursuing further cardiology practice in the United States. He has been at the forefront of advanced imaging technologies, techniques and how these practices are applied in clinical practice. Dr. Vannan's passion is integrated cardiovascular imaging, in which a collaborative effort is made across different modalities to address questions for a given disease to aid in clinical-decision making and guide interventions and management.

Lorena Vargas-Quintero received the M.S. and Ph.D. degrees in electrical engineering from Universidad Nacional Autónoma de México, in 2012 and 2017, respectively. She is currently lecturer and researcher with Universidad Popular del Cesar, Valledupar, Colombia. Her areas of interest include signal and image processing, pattern recognition and medical image processing. She is currently working on analysis of fetal echocardiography sequences focused on segmentation and motion estimation.

Enrique Vallejo Venegas is an M.D. from Universidad Nacional Autónoma de México, specialist in Internal Medicine and Cardiology. He is mainly interested in the evaluation of the heart function using cardiac imaging.

Rick Wage is a Chief MRI Radiographer Electrophysiologist at Royal Brompton & Harefield NHS Foundation Trust.

Ben Wang is Gwaltney Chair in Manufacturing Systems and Professor in the School of Industrial and Systems Engineering at Georgia Tech, as well as Professor of Materials Science and Engineering. He is a Fellow of the Institute of Industrial Engineers (IIE), Society of Manufacturing Engineers (SME), and Society for the Advancement of Material and Process Engineering (SAMPE). His research interests are at the nexus of manufacturing, materials and biomedicine. He received a B.S. from Tunghai University (Taiwan) and M.S. and Ph.D. from the Pennsylvania State University, all in industrial engineering.

Kan Wang received the B.S. degree in theoretical and applied mechanics from Peking University, Beijing, China, in 2005, the M.S. degree in aircraft design from Beihang University, Beijing, in 2007, and the Ph.D. degree in industrial and manufacturing engineering from Florida State University, Tallahassee, Florida, USA, in 2013. He is currently a Research Engineer with the Georgia Tech Manufacturing Institute, Georgia Institute of Technology, Atlanta, GA, USA. His current research interests include nanomanufacturing, additive manufacturing, and printed electronics technologies and their applications in the biomedical field.

Lianyi Wang is a chief physician in First Hospital of Tsinghua University, Beijing. Her focuses are non-invasive diagnosis and treatment of cardiovascular disease, especially in the clinical application of new echocardiography techniques in evaluation of complex and congenital heart diseases.

Naoufel Werghi received a Ph.D. in Computer Vision from the University of Strasbourg, M.Sc. in Instrumentation and Control from the University of Rouen, France, and Principal Engineering Diploma in Electrical Engineering from the National School of Engineering of Monastir.

He has been a Research Fellow at the Division of Informatics in the University of Edinburgh, Lecturer at Department of Computer Sciences in the University of Glasgow, and Assistant Professor in the College of Information Technology of the University of Dubai, where he founded and headed the Intelligent Information System Research Group. He has been also a Visiting Professor in the Department of Electrical and Computer Engineering at the University of Louisville and Media Integration and Communication Centre at the University of Florence, Italy. Currently, he is Associate Professor at the Electrical and Computer Engineering Department in Khalifa University.

His main area of research is image analysis and interpretation, for which he has been leading several funded projects in the areas of biometrics, data analysis, medical imaging, geometrical reverse engineering, and intelligent systems. He received the Best Paper award at the International

Conference of Computer Vision, Theory and Applications 2011, and the University-Industry Research Award from the National Research Foundation, 2012. In 2012 he co-founded the Emirates Computational Intelligence & Vision Research Group.

He is senior IEEE member and Secretary/ Treasurer of the IEEE UAE section, and is a regular reviewer of several journals, including *Computer-Aided Design*, *IEEE Potential*, *Pattern Recognition Letters*, and *Optical Engineering*. He has been a committee member in many international conferences. He published more than 100 journal and conference papers.

Tom Wong is a Consultant Cardiologist and Electrophysiologist at the Royal Brompton & Harefield NHS Foundation Trust, and also a Reader in Cardiology at the National Heart and Lung Institute, Imperial College London. He has a special interest in the interventional aspect of arrhythmia management, including catheter ablation, device implantation, and management. Alongside the clinical practice, his research program is aimed at further characterizing atrial fibrillation in patients who have chronic heart failure, and atrial and ventricular tachyarrhytmias in patients who have adult congenital heart disease.

Guang Yang obtained his Ph.D. in medical image analysis from University College London. He is currently an Honorary Lecturer with the Neuroscience Research Centre, Cardiovascular and Cell Sciences Institute, St. George's, University of London. He is also an Image Processing Physicist and Honorary Senior Research Fellow working at Cardiovascular Research Centre, Royal Brompton Hospital, and is also affiliated with National Heart and Lung Institute, Imperial College London. He is interested in a wide range of medical image analysis and medical physics research topics.

Jinzhong Yang received his B.S. and M.S. degrees in Electrical Engineering from the University of Science and Technology of China, China, in 1998 and 2001 and his Ph.D. degree in Electrical Engineering from Lehigh University in 2006. In July 2008, Dr. Yang joined the University of Texas MD Anderson Cancer Center as a Senior Computational Scientist, and since January 2015 he has been an Assistant Professor of Radiation Physics. Dr. Yang is a board-certified medical physicist. His research interest focuses on deformable image registration and image segmentation for radiation treatment planning and image-guided adaptive radiotherapy, radiomics for radiation treatment outcome modeling and prediction, and novel imaging methodologies and applications in radiotherapy.

Xin Yang received his B.S. degree in biomedical engineering from South-Central University for Nationalities, Wuhan, China, in 2012. He received his M.S. degree in biomedical engineering from Shenzhen University, Shenzhen, China. He is currently working towards his Ph.D. degree in computer science and engineering at The Chinese University of Hong Kong, Shatin, Hong Kong. His research interests include deep learning, medical image computing, and computer vision.

Xujiong Ye is a reader in the school of Computer Science, University of Lincoln, UK. She has over 10 years' research and development experiences in medical imaging and processing from both academia and industry. Dr. Ye has over 40 publications in the fields of medical image processing, computer vision, and machine learning.

Chengjin Yu is a Ph.D. student in the school of computer science and technology, Anhui University. His research interests include deep learning and machine learning.

Lequan Yu received a B.S. degree in computer science and technology from Zhejiang University, Hangzhou, China, in 2015. He is currently working toward the Ph.D. degree in computer science and engineering at The Chinese University of Hong Kong, Shatin, Hong Kong. His research interests include deep learning, medical image computing, and computer vision.

Chuck Zhang is Professor in the H. Milton Stewart School of Industrial and Systems Engineering and an affiliated faculty member at Georgia Tech Manufacturing Institute at Georgia Institute of Technology. He is a Fellow of the Institute of Industrial and Systems Engineers (IISE). His current research interests include additive manufacturing (3D printing and printed electronics), cyber-physical systems, and advanced composite and nanocomposite materials manufacturing. He received a B.S. in Mechanical Engineering from Nanjing University of Aeronautics and Astronautics (China), M.S. in Industrial Engineering from State University of New York at Buffalo, and a Ph.D. in Industrial Engineering from the University of Iowa.

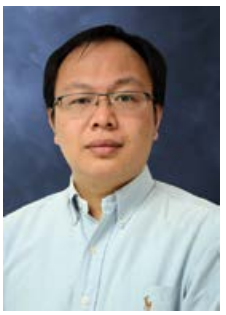

Heye Zhang received the B.S. and M.E. degrees from Tsinghua University, Beijing, China, in 2001 and 2003, respectively, and the Ph.D. degree from Hong Kong University of Science and Technology, Hong Kong, in 2007. He is currently an Associate Professor at the Institute of Biomedical and Health Engineering, Shenzhen Institutes of Advanced Technology, Chinese Academy of Sciences (CAS), ShenZhen, China. He is also with the Key Laboratory for Health Informatics of the Chinese Academy of Sciences (HICAS), China. His research interests include health information computing and medical image processing.

Yanping Zhang was born in 1962. She received her Ph.D. degree from Anhui University in 2003. She is a professor at Anhui University. Her research interests computational intelligence, quotient space theory, granular computing, and machine learning, among others.

Rongrong Zhou received her B.S. and M.S. degrees in Clinical Medicine from Central South University (Hunan Medical School) in 1993 and 2001, respectively. She received the M.D. and Ph.D degrees from Central South University in 2010 in the field of Clinical Oncology. She received her Postdoctoral Fellow training in the Department of Cancer Biology at MD Anderson Cancer Center from October 1999 to February 2002, supervised by Eugenie S. Kleinerman MD. Dr. Zhou is currently an associate professor and deputy director at the Department of Radiotherapy in Xiangya Hospital Central South University. Her primary interests are radiotherapy for thoracic malignancies through translational research.

Xiahai Zhuang is a Professor and Assistant Dean of the School of Data Science, Fudan University. Prof. Zhuang obtained his PhD from the Centre for Medical Image Computing, University College London. His research interests are medical image computing, medical data analysis, image processing, machine learning, cardiac modelling and translational software development.

1 Detection of Cerebrovascular Changes Using Magnetic Resonance Angiography

Yitzhak Gebru[1], Guruprasad Giridharan[1], Mohammed Ghazal[1,2], Ali Mahmoud[1], Ahmed Shalaby[1], Ayman El-Baz[1]
[1]University of Louisville
[2]Abu Dhabi University

CONTENTS

1.1 INTRODUCTION

High blood pressure (HBP) affects approximately one in three adults in the United States. HBP is the primary or contributing cause of mortality in 410,000 adults each year with associated health-care costs of $46 billion [1]. Chronic stress [2], high sodium intake [3], and renal dysfunction [4] are the primary causes for HBP and elevated cerebrovascular perfusion pressure (CPP). Chronically elevated CPP, which is directly related to HBP, changes the structure of cerebral blood vessels and disturbs cerebral vasoregulatory mechanisms. Significantly, high CPP induces hypertrophic and eutrophic remodeling in cerebral blood vessels [5]. In hypertrophic remodeling, elevated CPP increases the wall thickness and reduces the vessel lumen in cerebral blood vessels. For eutrophic remodeling, cells of smooth muscles undergo a rearrangement that results in reducing the vessel lumen without changing the total vascular mass or wall thickness. These cerebrovascular changes

are hypothesized to be a significant contributor to strokes, brain lesions, cerebral ischemic injury, dementia, and cognitive impairment [5–7].

Currently, HBP is diagnosed and medically managed when systemic BP measurements using a sphygmomanometer are greater than 140/90 mmHg. However, BP measurement via sphygmomanometer cannot quantify cerebrovascular structural changes that can increase the risk of cerebral adverse events. Importantly, some recent evidence suggests that cerebrovascular structural and CPP changes may precede elevation of systemic BP to clinical levels rather than cerebrovascular damage due to sustained exposure to HBP [8–11]. Thus, quantification of cerebrovascular changes may help identify and stratify patients at risk of cerebral adverse events, potentially enable medical treatment prior to the onset of systemic hypertension in conjunction with other cognitive tests, and optimize medical management of HBP patients.

Imaging techniques, which include Magnetic Resonance Imaging (MRI) and Magnetic Resonance Angiography (MRA) scans, have been traditionally used in the quantification of organ structural changes. In the literature, MRI scanning has been used for volumetric measurement of the ventricular cavities and myocardium [12] and to determine intravascular pressures from magnetic resonance (MR) velocity data in large vessels such as the aorta or pulmonary artery [13]. MRA scanning has been used to quantify measurements of the flow in the collateral arteries of patients that have occlusions in an internal carotid artery [14]. Neither MRA nor MRI has been utilized for the estimation of vascular pressure changes in the brain, to our knowledge. Detection of cerebrovascular or CPP changes using MRA analysis has not been accomplished due to the lack of accurate segmentation algorithms that can delineate the smaller blood vessels in the brain (in comparison to aorta or pulmonary arteries) from the surrounding soft tissue. Further, there are no methods to quantify cerebrovascular structural changes and to correlate them to changes in mean arterial pressure (MAP) from MRI/MRA imaging. This manuscript presents novel methodologies to delineate cerebral blood vessels from the surrounding tissue, quantify cerebrovascular structural changes, and correlate the cerebrovascular changes to MAP.

1.2 METHODS

The goal of this manuscript is to develop a new MRA-based framework for the detection of changes in cerebrovascular structure and to demonstrate proof-of-concept of correlation between cerebrovascular structural changes to MAP. Patient demographics, and details about the proposed methodology and data analysis, are presented next.

1.2.1 Patient Demographics

This work has been approved by the Institutional Review Board (IRB) at the University of Pittsburgh. MRA data and systemic BP measurements obtained from patients ($n = 15$, $M = 8$, $F = 7$, Age $= 49.2 \pm 7.3$) over a 700-day study period were retrospectively analyzed. The 15 subjects were selected to represent a range of blood pressure changes over the 700 days, and the imaging data were analyzed blinded to the patient BP. MRA imaging data were obtained using a 3T Trio TIM scanner using a 12-channel phased-array head coil. BP and MAP were determined from the arithmetic average of four sphygmomanometer readings taken during two visits immediately preceding the MRI scanning. The volume of scans was composed of 3D multi-slab high-resolution images with 160 slices, thickness of 0.5 mm, resolution of 384×448, a flip angle of 15 degrees, repetition time of 21 ms, and echo time of 3.8 ms.

The subjects had an average day 0 systolic pressure of 122 ± 6.9 mmHg, an average day 0 diastolic pressure of 82 ± 3.8 mmHg, an average day 700 systolic pressure of 118.9 ± 12.4 mmHg, and an average day 700 systolic pressure of 79.9 ± 11.0 mmHg (i.e., the mean systolic pressure remained comparable over time, though some individuals increased in pressure and some decreased or stayed the same).

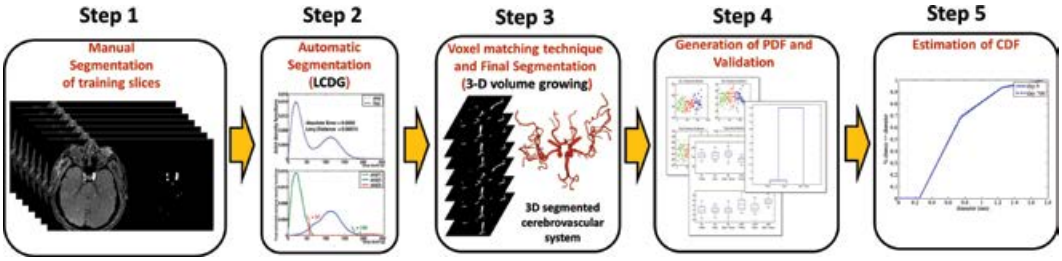

FIGURE 1.1 Framework of the data analysis for quantifying cerebrovascular changes from MRA imaging data.

1.2.2 Data Analysis

The analysis of patient MRA data consists of five key steps (Figure 1.1) consisting of: (1) manual segmentation of training slices to identify ground truth, (2) automatic segmentation for all slices to delineate the blood vessels from the surrounding soft tissue by combining the segmented ground truths with the Linear Combination of Discrete Gaussians (LCDG) models for gray level distribution, (3) voxel matching for obtaining temporal subtraction images to enhance the ability to see cerebrovascular change via a distance map created to quantify the change in patients between day 0 and day 700, (4) generation of a probability distribution function (PDF), which describes the distribution of pixel distances from vascular edges and is used to statistically correlate to BP, and (5) estimation of the cumulative distribution function (CDF) to observe the summated probability of cerebrovascular changes in the same patient from day 0 and day 700.

1.2.2.1 Manual Segmentation of Training Slices

MRA data from a patient consists of 160 MRA slices. Every tenth slice is manually segmented to extract the blood vessels from surrounding tissue using Adobe Photoshop. This methodology allows for delineation of the blood vessel from the surrounding tissue at a pixel level accuracy where the largest limitation is the resolution of the MRI machine itself. The manually segmented training binary (black for surrounding tissue and white for target vasculature) slices are referred to as ground truths (GT) as the images are correct and free from artifacts or noise (Figure 1.2). The manual

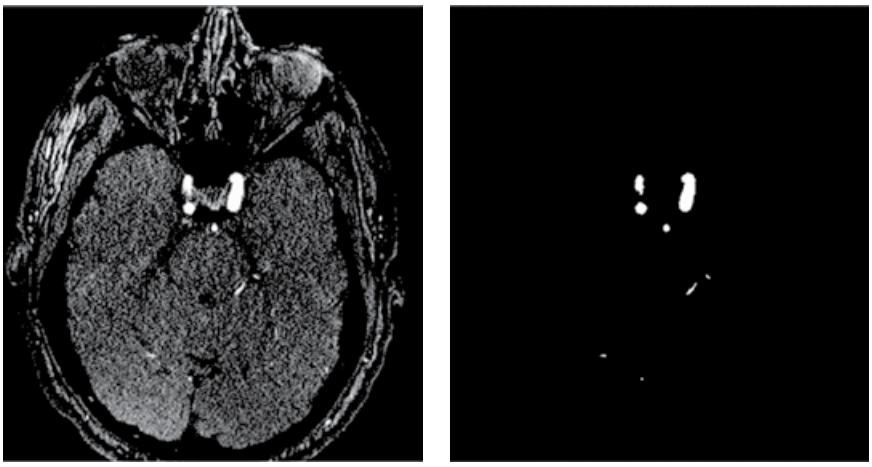

(a) (b)

FIGURE 1.2 (a) Original MRA image slice of sample patient at day 0. (b) Manually segmented ground truth (GT) image from image in (a).

segmentation of select slices is used for the initialization and optimization of the segmentation algorithm, which is subsequently used for segmenting all obtained slices.

1.2.2.2 Automatic Segmentation

One of the most challenging issues relating to common computer-assisted diagnostics is the segmentation of accurate 3D cerebrovascular system information from MRA images. Our approach is to rapidly and accurately extract the blood vessel data by defining the probability models for all regions of interest within the statistical approach and not predefining the probability models [15–17]. For each MRA slice, the empirical gray level distribution is closely approximated with an LCDG. Then, it is divided into three individual LCDGs, one for every region of interest associated with each of the following dominant modes: darker bones and fat, gray brain tissues, and bright blood vessels. The identified models specify an intensity threshold to extract blood vessels in that slice. A 3D connectivity filter is then applied on the extracted voxels (voxel = volume × element; a representation for a 3D pixel) to select the desired vascular tree. This method results in higher precision region models with higher segmentation accuracy compared to other methods [16].

Adapting the Expectation-Maximization (EM) based technique to the LCDG allows for precise identification of the LCDG model, which included the number of its components (positive and negative) [18], and for identification of a continuous LCDG model that contains the probability distribution.

An expected log-likelihood is used as a criterion for model identification [16]. Consider $\mathbf{X} = (\mathbf{X}_s : s = 1, \ldots, S)$ to be denoting a 3D MRA image that contains S co-registered 2D slices $\mathbf{X}_s = (X_s(i, j) : (i, j) \in R;\ X_s(i, j) \in Q)$. $\mathbf{R}$ and $\mathbf{Q} = \{0,1, \ldots, Q-1\}$ represent a rectangular arithmetic lattice that supports the 3D image and a finite set of Q-ary intensities (gray levels), respectively. Consider $\mathbf{F}_s = f_s(q) : q \in \mathbf{Q}; \Sigma_{q \in \mathbf{Q}}\ fs(q) = 1$, where q is the gray level, to be an empirical marginal probability distribution for gray levels of the MRA slice $\mathbf{X}_s$.

According to [18], each slice is considered a *K*-modal image with a known number *K* of the dominant modes related to the regions of interest. For the segmentation of the slice by modes separating, an estimation of the individual probability distributions of the signals associating each mode from $\mathbf{F}_s$ is necessary. $\mathbf{F}_s$ is closely approximated with LCDG opposing conventional mixture of Gaussians, one per region, or slightly more flexible mixtures involving other simple distributions, one per region. The image LCDG is then divided into submodels that are related to each dominant mode [19–21].

A discrete Gaussian distribution is defined on the set of integers (gray levels) $\mathbf{Q} = \{0,1, \ldots, Q-1\}$ by the probability mass function

$$\psi\left(q|\theta\right) = \begin{cases} \Phi(0.5), & q = 0 \\ \Phi(q + 0.5) - \Phi(q - 0.5), & 1 \le q < Q - 1 \\ 1 - \Phi(q - 0.5), & q = Q - 1, \end{cases}$$

where the parameter $\theta = (\mu, \sigma)$, and Φ is the CDF of a normal distribution with mean μ and variance σ^2. Then the LCDG with C_p positive components and C_n negative components, such that $C_p \ge K$, has the probability mass function

$$p_{w,Q}(q) = \sum_{r=1}^{C_p} w_{p,r} \psi\left(q|\theta_{p,r}\right) - \sum_{l=1}^{C_n} w_{n,l} \psi\left(q|\theta_{n,l}\right) \tag{1.1}$$

The weights $\mathbf{w} = (w_{p,1}, \ldots, w_{p,Cp}, w_{n,1}, \ldots, w_{n,Cn})$ are restricted to be all nonnegative and to satisfy

$$\sum_{r=1}^{C_p} w_{p,r} - \sum_{l=1}^{C_n} w_{n,l} = 1 \tag{1.2}$$

In general, valid probabilities are nonnegative: $p_{\mathbf{w},\Theta}(q) \geq 0$ for all $q \in \mathbf{Q}$. This implies that the probability distributions only make use of a valid subset of all the LCDGs in (1.1), which can have negative components $p_{\mathbf{w},\Theta}(q) < 0$ for some $q \in \mathbf{Q}$.

Our aim is finding a *K*-modal probability model that approximates closely the unknown marginal distribution of gray level. Consider $\mathbf{F}_s$, its Bayesian estimate $\mathbf{F}$ is as follows [22]: $f(q) = (|\mathbf{R}| f_s(q) + 1)/(|\mathbf{R}| + Q)$, and the intended model should maximize the expected log-likelihood of the statistically independent empirical data with the parameters of the model:

$$L(\mathbf{w}, \Theta) = \sum_{q \in \mathbf{Q}} f(q) \log p_{\mathbf{w},\Theta}(q) \tag{1.3}$$

The entire segmentation algorithm is as follows [16].

1. For each slice $\mathbf{X}_s$, $s = 1, \ldots S$,
   a. First gather the marginal empirical probability distribution F_s of gray levels.
   b. Find a starting LCDG model that is nearing F_s by using the initialization algorithm to approximate the values of $C_p - K$, C_n, and the parameters **w, Θ** (weights, means, and variances) of the negative and positive discrete Gaussians (DG).
   c. Fixing C_p and C_n, refine the LCDG model with the modified EM algorithm by manipulating the other parameters.
   d. Separate the final LCDG model into K submodels. Each dominant mode has a corresponding submodel. This is done by minimizing the misclassification predicted errors and selecting the LCDG submodel that has the greatest average value (corresponding to the pixels with highest brightness) to be the model of the wanted vasculature.
   e. Use intensity threshold t to extract the voxels of the blood vessels in the MRA slice, which separates their LCDG submodel from the background.
2. Remove the artifacts from the extracted voxels whole set with a connection filter that chooses the greatest connected tree system built by a 3D growing algorithm [23]. Algorithm 1 summarizes the adopted segmentation approach.

The aim of this procedure is to decipher the threshold for each MRA slice that will enable the complete extraction of the bright blood vessels while removing the darker, unwanted tissue while also separating surrounding non-vasculature tissue that may be of similar brightness and along the same boundaries. Step 1b's initialization creates the LCDG with the non-negative starting probabilities $p_{w,\theta}(q)$. The refinement in 1c increases the likelihood, but the probabilities continue to be non-negative. The experiments presented in [16] show the opposite situations were never met.

The automatic segmentation's accuracy is evaluated by calculating total error compared to the ground truths. True positive (TP), true negative (TN), false positive (FP), and false negative (FN) segmentations are measured for evaluation.

ALGORITHM 1 MAIN STEPS OF THE SEGMENTATION APPROACH

For each slice $\mathbf{X}_s$, the following steps were completed:

1. **LCDG Initialization:**
   - Find the marginal empirical probability distribution of gray levels $\mathbf{F}_s$.
   - Estimate $C_p - K, C_n$, $\mathbf{W}$, and $\boldsymbol{\Theta}$ of the positive and negative DGs.
   - Find the initial LCDG model that approximates $\mathbf{F}_s$.
2. **LCDG Refinement:**
   - Fixing C_p and C_n, refine the LCDG model with the modified EM algorithm by manipulating other parameters.
3. **Initial Segmentation:**
   - Divide the final LCDG model into K submodels by minimizing the expected errors of misclassification.
   - Select the LCDG submodel that has the largest mean value to be the model of the wanted vasculature.
   - Use the intensity threshold t to extract the voxels of the blood vessels in the MRA slice, separating their LCDG submodel from the background.
4. **Final Segmentation:**
   - Remove the artifacts from the extracted voxels whole set with a connection filter that chooses the greatest connected tree system built by a 3D growing algorithm.

In Figure 1.3, if C is the segmented region, G is the ground truth, and R represents the entire image frame, then the $TP = |C \cap G|$, the $TN = |R - C \cup G|$, the $FP = |C - C \cap G|$, and the $FN = |G - C \cap G|$. The total error ε is given in [24] as $\varepsilon = (FN + FP)/(TP + FN) = (FN + FP)/G$.

1.2.2.3 Voxel Matching

Voxels are an array of volume elements that constitute a notional three-dimensional space. A 3D affine registration is used to handle the pose, orientation, and the data spacing changes and other scanning parameter changes between day 0 and day 700 [25]. In this step, the determined Euclidian radii are converted into diameter values. The output is then converted into a distance map.

1.2.2.4 Generation of Probability Distribution Function and Validation

The EM-based technique is adapted to the LCDG model, and the distribution of pixel distances is extracted from the distance map to calculate the probability distribution of the cerebrovascular changes. The PDF marks the distribution of white pixels as a true value, and black pixels are ignored for the data set. The diameters of the blood vessels are determined by estimating Euclidian center

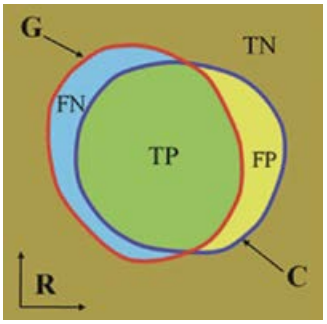

FIGURE 1.3 Illustration of segmentation accuracy and errors of the proposed automatic segmentation (C) by comparing to the ground truth (G) [5].

point distances from the edge of a vessel. The data points in the generated PDFs are then extracted and compared to the blood pressure data using statistical analysis.

1.2.2.5 Calculation of Cumulative Distribution Function

The integral of the PDF is used to generate the CDF (the CDF F_X of a random variable X is calculated from its PDF f_X using $F_X(x) = \int_{-\infty}^{x} f_X(t)dt$). The CDF shows the total summated probability that a blood vessel will take a value less than or equal to a diameter value, that represents an average blood vessel diameter in each slice. It shows the cumulative distribution of the PDF with an upper limit of 1. The more quickly the CDF line approaches 1, the more certain that the diameter of the blood vessel is smaller compared to a CDF that takes longer to approach 1. This is illustrated in the results section.

1.2.3 Statistical Analysis

Statistical analysis was performed using R software, version 3.3. A mixed effects linear model was used to test the relationship of MRA data with clinical BP measurements. Brain slices were separated into upper (above circle of Willis) and lower (below circle of Willis) compartments to determine correlation with clinical BP readings. The circle of Willis, near the brain base, is where the intracranial cerebral arteries take off from and give rise to progressively smaller vessels [5]. The BP measurements were combined into a single value, the estimated mean arterial pressure $MAP = (2 \times DBP + SBP)/3$, which was a covariate in the model. Also included in the model were patient age, gender, and a random intercept per patient. The dependent variable was the mean of the Euclidean distance map over the entire vascular tree within each compartment. (Two separate models were fit to the upper and lower compartments.) Statistical significance of fixed effects in the fitted models was determined using likelihood ratio chi-square tests.

1.2.4 3D Reconstruction of the Cerebral Vasculature

A growing tree model, which eliminates any unwanted segmented voxels by choosing the greatest connected vascular tree system, coupled with a smoothing algorithm, was used to generate a 3D model based on segmented slices [23]. An example of the resultant vascular system is visualized and illustrated in the results section.

1.3 RESULTS

Specificity and sensitivity values were obtained from the segmented images as shown in Table 1.1. The automatically segmented slices for all 15 patients were compared to the manually segmented GTs to determine accuracy of algorithm (Figure 1.4). The segmentation algorithm resulted in the cumulative sensitivity of 0.997 ± 0.008 (sensitivity range = 0.969 to 1) and the cumulative specificity of 0.9998 ± 0.0001 (specificity range = 0.9994 to 1).

TABLE 1.1
Sensitivity and specificity values for automatically segmented images at day 0, day 700, and cumulative sensitivity and specificity values.

Time	Sensitivity	Specificity
Day 0	0.997 ± 0.006	0.9998 ± 0.0001
Day 700	0.996 ± 0.008	0.9998 ± 0.0001
Cumulative	0.997 ± 0.008	0.9998 ± 0.0001

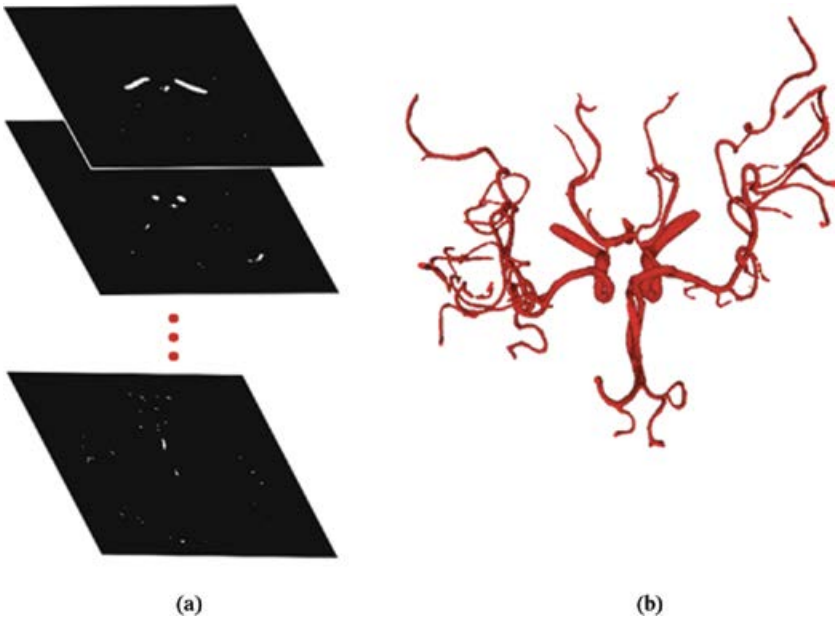

FIGURE 1.4 Example of segmentation algorithm output: (a) Sample image slices of a patient at day 0. The automatically segmented slices were compared to the manually segmented ground truths (GT) to determine the accuracy of the segmentation algorithm. (b) Sample 3D reconstruction of the segmented cerebrovascular system using a growing tree model.

The results of the linear mixed effects model analysis (Table 1.2) revealed an inverse relationship between MAP and the mean vessel diameter below the circle of Willis ($p = 0.0007$). The mean diameter of vessels below the circle of Willis was not found to vary significantly with the age of the patient or the gender of the patient. Above the circle of Willis, the mean diameter of vessels showed a statistically significant decrease with age ($p = 0.0005$).

TABLE 1.2

Mixed effects linear model statistical evaluation. *p*-values < 0.05 was considered statistically significant. Diameter denotes size of vasculature in segmentation images. Age, gender, and timepoints are clinically acquired data.

	Mean Diameter of Vessels below Circle of Willis		
	Effect	χ^2	***p*-value**
Age	3.2 µm/y	0.356	0.551
Gender	F > M by 12.8 µm	0.026	0.872
Mean Arterial Pressure	–5.3 µm/mmHg	11.63	0.0007
	Mean Diameter of Vessels above Circle of Willis		
	Effect	χ^2	***p*-value**
Age	–16.5 µm/y	12.29	0.0005
Gender	F > M by 16.0 µm	0.199	0.655
Mean Arterial Pressure	1.6 µm/mmHg	0.402	0.525

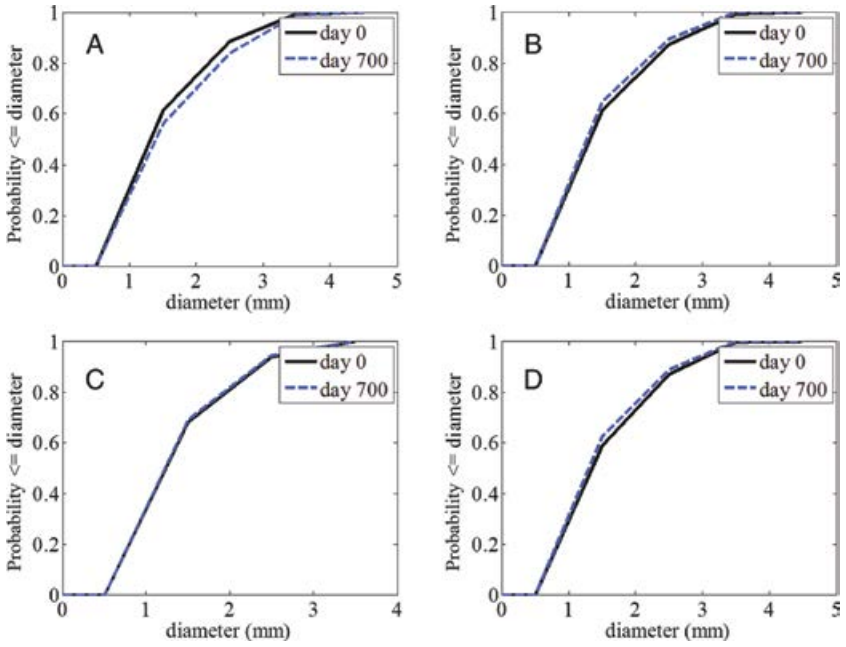

FIGURE 1.5 Sample patient CDFs demonstrating the temporal changes from day 0 to 700. The graphs indicate the probability that blood vessels may be of a certain diameter or less.

In the analysis, 13 out of 15 patients showed significant correlation between MAP and the diameters indicated via CDF. Out of the 13 patients that showed CDF correlation with MAP, two example patients (A and B) are shown with the two patients (C and D) where the correlation between CDF and MAP was not found (Figure 1.5). Patient C had a shift in CDF that was in opposition to the MAP change, and patient D had a larger shift in CDF compared to the MAP change (Figure 1.5c and 1.5d; Table 1.3). The 3D cerebrovascular model reconstruction of patients C and D indicated significant vascular changes between day 0 and day 700 (Figure 1.6).

1.4 DISCUSSION

The average cumulative segmentation algorithm had a sensitivity of 0.997 ± 0.008 and a specificity of 0.9998 ± 0.001. This high level of accuracy demonstrates the benefit of using a manual input to initialize automatic segmentation. Using manual segmentation alone would be too time intensive to be used in a practical healthcare setting, while utilizing only an automatic segmentation approach

TABLE 1.3
BP measurements of patients A, B, C, and D.

	Day 0			Day 700		
Patient	Systolic BP	Diastolic BP	MAP	Systolic BP	Diastolic BP	MAP
A	120	80.5	93.7	103.5	66.5	78.8
B	130.5	83	98.8	143.5	94	110.5
C	118	80.5	93	105.3	69	81.1
D	114	84.5	94.3	120	88	98.7

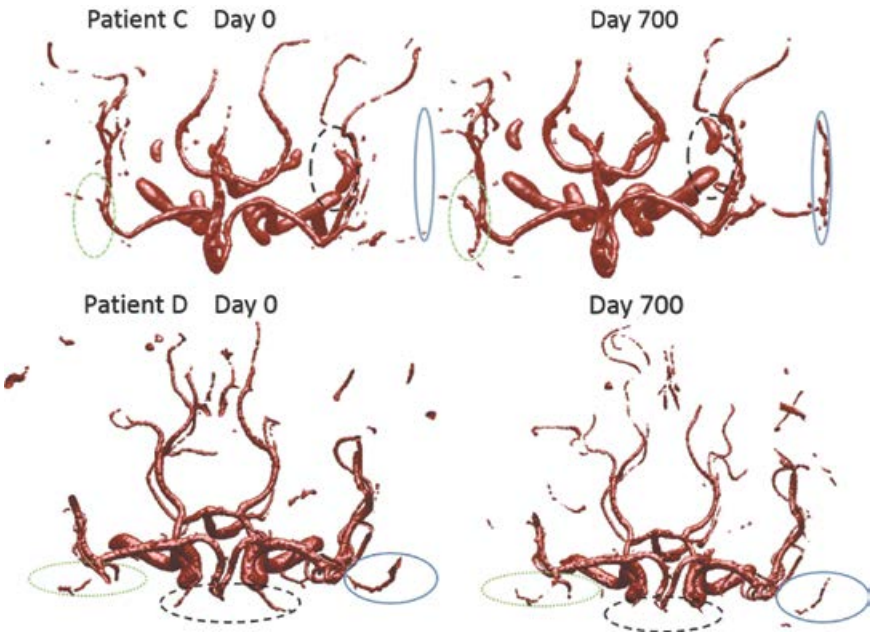

FIGURE 1.6 Applying a 3D growing algorithm to the volume of binary segmented images allows for visualization of the automatically segmented MRA data. Day 0 of patient C (top left). Day 700 of patient C (top right). Day 0 of patient D (bottom left). Day 700 of patient D (bottom right). These results demonstrate the temporal changes in cerebrovascular structure in these patients (circled).

would not provide sufficient segmentation accuracy to delineate and quantify the diameters of the smaller arteriolar (< 10 micrometers) cerebral blood vessels. The proposed segmentation algorithm combines the accuracy of manual segmentation with the benefit of an automated and less time-intensive approach and provides segmentation with a high degree of accuracy while also minimizing the required time and effort.

The high degree of sensitivity and specificity of our approach in accurately delineating blood vessels from surrounding brain tissue enables the quantification of cerebrovascular changes. The PDFs indicate the total blood vessel diameter change in time from day 0 and day 700. Below the circle of Willis, there is a statistical correlation between PDFs and systemic BP (p-value = 0.0007), demonstrating that increased MAP (and consequently CPP) are related to decreased average vessel diameter and PDF.

The BP and MAP measurements correlate well with most patients' non-invasive mean PDF diameter measurements below the circle of Willis. Since cerebral changes have been hypothesized to precede systemic hypertension [9,10,26], our methodology may present a tool for potentially initiating early treatment to prevent or optimize management of systemic HBP in conjunction with other approaches, such as cognitive testing.

This finding is important as it suggests that the remodeling of vessels due to increasing blood pressure occurs prior to the onset of diagnosed essential hypertension. Individuals in the current study were explicitly selected to have pre-hypertensive values of blood pressure. Of equal importance, the methodology can determine the relationship of cerebrovascular remodeling to cortical small vessel disease and lacunar lesions known to occur with advanced hypertensive disease and with implications for stroke and dementia [27,28]. The correlation of PDF to MAP was independent of patient gender. The difference in PDF of vessels above the circle of Willis was statistically significant with age, which indicates that older patients have constricted cerebral vessels, which may put them at a higher risk for strokes.

In some patients (C and D), the change in CDF did not correlate to changes in MAP, which may indicate impaired autoregulation of cerebral blood flow, potentially due to cerebrovascular remodeling [5,26]. The 3D cerebrovascular model reconstruction of these patients demonstrated significant vascular changes between day 0 and day 700. These results may indicate that drug therapies prescribed using systemic BP alone may not provide optimal medical management. Lack of correlation between CDF and MAP may indicate cerebrovascular changes and a higher risk of cerebrovascular adverse events, which necessitates more frequent monitoring and/or optimization of medical management, despite having normal systemic BP and MAP. Using a combination of BP and CDF changes may help minimize the occurrence of adverse events.

The segmentation algorithm and metrics for vascular and blood pressure changes (CDF, PDF) are not limited to cerebral vasculature. These methodologies may also be used to quantify vascular changes in other end organs that are sensitive to blood pressure (e.g., kidneys).

1.5 LIMITATIONS

While our segmentation algorithm significantly improves automatic segmentation methodologies, it is limited by the resolution limit of the MRI machine performing the MRA scanning. The CDF diameters (Figure 1.5) start at 0.5 mm because the distance map calculations determine radius from the edge of a blood vessel and a pixel in the MRA imaging represented 0.25 mm. Any value less than 0.5 mm would not be accurately represented due to the resolution limit. Subsequently, the accuracy of the statistical analysis decreases with decreasing blood vessel size (smaller blood vessels < 10 micrometers) above the circle of Willis.

Various over-the-counter medications and supplements were used by the subjects during the time period of this study; however, the BP changes caused by these medications should be minimal. Nonetheless, larger sample sizes are required to establish a definitive relationship with progression to HBP. While elevated CPP is hypothesized to precede systemic hypertension, essential hypertension remains likely due to a mosaic of causes that are not completely understood. Despite these limitations, our method is relevant to understanding brain pathology relevant to hypertension whether such pathology precedes or follows the establishment of clinical hypertension.

1.6 CONCLUSION

Changes in cerebral vasculature can be non-invasively obtained through MRA image analysis. Cerebrovascular changes are correlated to MAP below the circle of Willis. The improved segmentation algorithm coupled with the calculation of CDF and PDF can indicate cerebrovascular and cerebral perfusion pressure changes, which may be a useful tool for clinicians to optimize medical management of HBP. In addition to blood vessels [121,122,139,140], this work could also be applied to various other applications in medical imaging, such as the kidney, the heart, the prostate, the lung, and the retina. One application is renal transplant functional assessment. Chronic kidney disease (CKD) affects about 26 million people in the U.S. with 17,000 transplants being performed each year. In renal transplant patients, acute rejection is the leading cause of renal dysfunction. Given the limited number of donors, routine clinical post-transplantation evaluation is of immense importance to help clinicians initiate timely interventions with appropriate treatment and thus prevent the graft loss. In recent years an increased area of research has been dedicated to developing non-invasive CAD systems for renal transplant function assessment, utilizing different image modalities (e.g., ultrasound, computed tomography (CT), MRI, etc.). The accurate assessment of renal transplant function is critically important for graft survival. Although transplantation can improve a patient's well-being, there is a potential post-transplantation risk of kidney dysfunction that, if not treated in a timely manner, can lead to the loss of the entire graft, and even patient death. Thus, accurate assessment of renal transplant function is crucial for the identification of proper treatment.

In recent years, an increased area of research has been dedicated to developing non-invasive, image-based CAD systems for the assessment of renal transplant function. In particular, dynamic and diffusion MRI-based systems have been clinically used to assess transplanted kidneys with the advantage of providing information on each kidney separately. For more details about renal transplant functional assessment, please read [30–55].

The heart is also an important application to this work. The clinical assessment of myocardial perfusion plays a major role in the diagnosis, management, and prognosis of ischemic heart disease patients. Thus, there have been ongoing efforts to develop automated systems for the accurate analysis of myocardial perfusion using first-pass images [56–72]. Another application for this work could be the detection of retinal abnormalities. The majority of ophthalmologists depend on visual interpretation for the identification of disease types. However, inaccurate diagnosis will affect the treatment procedure, which may lead to fatal results. Hence, there is a crucial need for computer-automated diagnosis systems that yield highly accurate results. Optical coherence tomography (OCT) has become a powerful modality for the non-invasive diagnosis of various retinal abnormalities such as glaucoma, diabetic macular edema, and macular degeneration. The problem with diabetic retinopathy (DR) is that the patient is not aware of the disease until the changes in the retina have progressed to a level that treatment tends to be less effective. Therefore, automated early detection could limit the severity of the disease and assist ophthalmologists in investigating and treating it more efficiently [73,74].

Abnormalities of the lung could also be another promising area of research and a related application to this work. Radiation-induced lung injury is the main side effect of radiation therapy for lung cancer patients. Although higher radiation doses increase the radiation therapy effectiveness for tumor control, this can lead to lung injury as a greater quantity of normal lung tissues is included in the treated area. Almost one-third of patients who undergo radiation therapy develop lung injury following radiation treatment. The severity of radiation-induced lung injury ranges from ground-glass opacities and consolidation at the early phase to fibrosis and traction bronchiectasis in the late phase. Early detection of lung injury will thus help to improve management of the treatment [75–115].

This work can also be applied to other brain abnormalities, such as dyslexia and autism. Dyslexia is one of the most complicated developmental brain disorders that affect children's learning abilities. Dyslexia leads to the failure to develop age-appropriate reading skills in spite of normal intelligence levels and adequate reading instructions. Neuropathological studies have revealed an abnormal anatomy of some structures, such as the corpus callosum in dyslexic brains. There has been a lot of work in the literature that aims at developing CAD systems for diagnosing dyslexia and autism, along with other brain disorders [116–138].

Appendices

A. INITIALIZATION SEQUENTIALLY USING EM ALGORITHM

Consider **F** being the marginal distribution of gray level, EM algorithm [22,29] is used to initially build an LCDG model that approximates **F** as explained in the following steps:

1. A mixture $\mathbf{P}_K$ of dominant mode K positive discrete Gaussians (DG) is used to approximate **F**.
2. Subordinate components of the LCDG alternatingly approximate the deviations between **F** and $\mathbf{P}_K$ as follows:
   - Separating and scaling up the positive and the negative deviations to get the two probability distributions, $\mathbf{D}^p$ and $\mathbf{D}^n$.
   - Iteratively finding subordinate mixtures of positive and negative DGs using the same EM algorithm. These mixtures should best approximate $\mathbf{D}^p$ and $\mathbf{D}^n$. The mixtures sizes, $C_p - K$ and C_n, are found by sequentially minimizing the error between each distribution ($\mathbf{D}^p$ or $\mathbf{D}^n$) and its corresponding mixture model with the components number.
   - Scaling down the positive and negative subordinate mixtures and adding them to the dominant mixture, which gives the initial LCDG model whose size is $C = C_p + C_n$.

The initial LCDG has K dominant weights $w_{p,r}$, where $r = 1,2,\ldots,K$. The sum of these weights is equal to 1 ($\sum_{r=1}^{K} w_{p,r} = 1$). In addition, there are several lower valued subordinate weights that fulfil $\sum_{r=K+1}^{C_p} w_{p,r} - \sum_{l=1}^{C_n} w_{n,l} = 0$.

B. REFINING LCDGS USING MODIFIED EM ALGORITHM

Refining the initial LCDG is done by estimating the local maximum of the log-likelihood in (1.3) using the DGs adapted EM algorithm in [18], which extends the conventional EM algorithm in [22] [29] to handle the alternating components.

Consider $p_{w,\theta}^{[m]}(q) = \sum_{r-1}^{C_p} w_{p,r}^{[p]} \psi(q|\theta_{p,r}^{[m]}) - \sum_{l=1}^{C_n} w_{n,l}^{[m]} \psi(q|\theta_{n,l}^{[m]})$ to be the LCDG at the iteration m. Each signal $q \in Q$ contributes relatively to each positive and negative DG at iteration m as specified by the corresponding conditional weights

$$\pi_p^{[m]}(r|q) = \frac{w_{p,r}^{[m]} \psi\left(q|\theta_{p,r}^{[m]}\right)}{p_{\mathbf{w},\Theta}^{[m]}(q)};\ \pi_n^{[m]}(l|q) = \frac{w_{n,l}^{[m]} \psi\left(q|\theta_{n,l}^{[m]}\right)}{p_{w,\theta}^{[m]}(q)} \tag{1.4}$$

taking into consideration that the following constraints apply:

$$\sum_{r=1}^{C_p} \pi_p^{[m]}(r|q) - \sum_{l=1}^{C_n} \pi_n^{[m]}(l|q) = 1; q = 0,\ldots,Q-1 \tag{1.5}$$

Two main steps are repeated iteratively until the log-likelihood is maximized, the E-step[m] and the M-step[m], which are summarized as follows:

- E-step[m]: Fixing parameters $\mathbf{w}^{[m-1]}$, $\boldsymbol{\Theta}^{[m-1]}$, calculate the weights in (1.4) from the iteration $m-1$.
- M-step[m]: Maximize $L(\mathbf{w}, \boldsymbol{\Theta})$ fixing the weights of (1.4) to get the conditional maximum likelihood estimates (MLEs) $\mathbf{w}^{[m]}$, $\boldsymbol{\Theta}^{[m]}$.

The described process showed to be converging to a local log-likelihood maximum, using similar considerations as in [22] [29]. Moreover, it was demonstrated in [18] that this process is a block relaxation minimization-maximization.

Considering unit factor constraints in (1.5), the log-likelihood in (1.3) can be equivalently given as:

$$\mathrm{L}\left(\mathbf{w}^{[m]}, \boldsymbol{\Theta}^{[m]}\right) = \sum_{q=0}^{Q} f(q) \left[\sum_{r=1}^{C_p} \pi_p^{[m]}\left(r|q\right) \log p^{[m]}(q) - \sum_{l=1}^{C_n} \pi_n^{[m]}\left(l|q\right) \log p^{[m]}(q) \right] \tag{1.6}$$

Using (1.4), consider replacing $\log\, p^{[m]}(q)$ in the first summation with $\log \mathrm{w}_{p,r}^{[m]} + \log \psi(q|\theta_{p,r}^{[m]}) - \log \pi_p^{[m]}(r|q)$ and $\log\, p^{[m]}(q)$ in the second summation with $\log w_{n,l}^{[m]} + \log \psi(q|\theta_{n,l}^{[m]}) - \log \pi_n^{[m]}(l|q)$. During the E-step, the conditional Lagrange maximization of the log-likelihood of (1.6) under the restrictions of (1.5) yields the weights $\pi_p^{[m+1]}(r|q)$ and $\pi_n^{[m+1]}(l|q)$ of (1.4) for all $r = 1, \ldots, \mathrm{C}_p$; $l = 1, \ldots, \mathrm{C}_n$ and $q \in \mathrm{Q}$. During the M-step, the conditional Lagrange maximization of the log-likelihood in (1.6) under the restriction of (1.2) and the fixed conditional weights of (1.4) results in the DG weights $w_{p,r}^{[m+1]} = \sum_{q \in \mathrm{Q}} f(q) \pi_p^{[m+1]}(r|q)$ and $w_{n,l}^{[m+1]} = \sum_{q \in \mathrm{Q}} f(q) \pi_n^{[m+1]}(l|q)$. For each DG, the conventional MLEs of the parameters originating from maximizing the log-likelihood after each difference of the cumulative Gaussians can be approximated with the Gaussian density:

$$\mu_{c,r}^{[m+1]} = \frac{1}{w_{c,r}^{[m+1]}} \sum_{q \in \mathrm{Q}} q \cdot f(q) \pi_c^{[m+1]}\left(r|q\right)$$

$$\left(\sigma_{c,r}^{[m+1]}\right)^2 = \frac{1}{w_{c,r}^{[m+1]}} \sum_{q \in \mathrm{Q}} \left(q - \mu_{c,i}^{[m+1]}\right)^2 \cdot f(\mathrm{q}) \pi_c^{[m+1]}\left(r|q\right)$$

where c can be either p or n. The modified EM-algorithm is true till the weights w become strictly positive. The iterations must be ended if the log-likelihood of (1.3) becomes almost constant or starts decreasing resulting from rounding errors accumulation.

Associating the subordinate DGs with the dominant terms, the final mixed LCDG model p_C (q) is divided into the K LCDG submodels $P_{[K]} = [p(q|k) : q \in \mathbf{Q}]$, one per class $k = 1, \ldots, K$, and hence the misclassification rate becomes minimal.

References

1. About underlying cause of death, 1999–2015: (2015). http://wonder.cdc.gov/ucd-icd10.html.
2. Kulkarni, S., O'Farrell, I., Erasi, M., Kochar, M.: Stress and hypertension. *WMJ: Official Publication of the State Medical Society of Wisconsin* 97(11) (1998) 34–38.
3. Mohan, S., Campbell, N.R.: Salt and high blood pressure. *Clinical Science* 117(1) (2009) 1–11.

4. Sarnak, M.J., Levey, A.S., Schoolwerth, A.C., Coresh, J., Culleton, B., Hamm, L.L., McCullough, P.A., Kasiske, B.L., Kelepouris, E., Klag, M.J.: Kidney disease as a risk factor for development of cardiovascular disease. *Circulation* 108(17) (2003) 215–42169.
5. Iadecola, C., Davisson, R.L.: Hypertension and cerebrovascular dysfunction. *Cell Metabolism* 7(6) (2008) 476–484.
6. Van Dijk, E.J., Breteler, M.M., Schmidt, R., Berger, K., Nilsson, L-G., Oudkerk, M., Pajak, A., Sans, S., de Ridder, M., Dufouil, C.: The association between blood pressure, hypertension, and cerebral white matter lesions. *Hypertension* 44(5) (2004) 625–630.
7. Willmot, M., Leonardi-Bee, J., Bath, P.M.: High blood pressure in acute stroke and subsequent outcome. *Hypertension* 43(1) (2004) 18–24.
8. Barnes, J.N., Harvey, R.E., Zuk, S.M., Lundt, E.S., Lesnick, T.G., Gunter, J.L., Senjem, M.L., Shuster, L.T., Miller, V.M., Jack, C.R.: Aortic hemodynamics and white matter hyperintensities in normotensive postmenopausal women. *Journal of Neurology* 264(5) (2017) 938–945.
9. Jennings, J.R., Muldoon, M.F., Ryan, C., Gach, H.M., Heim, A., Sheu, L.K., Gianaros, P.J.: Prehypertensive blood pressures and regional cerebral blood flow independently relate to cognitive performance in midlife. *Journal of the American Heart Association* 6(3) (2017) e004856.
10. Jennings, J.R., Zanstra, Y.: Is the brain the essential in hypertension? *Neuroimage* 47(3) (2009) 914–921.
11. Launer, L.J., Lewis, C.E., Schreiner, P.J., Sidney, S., Battapady, H., Jacobs, D.R., Lim, K.O., D'Esposito, M., Zhang, Q., Reis, J.: Vascular factors and multiple measures of early brain health: CARDIA brain MRI study. *PloS one* 10(3) (2015) e0122138.
12. Van der Geest, R.J., Reiber, J.H.: Quantification in cardiac MRI. *Journal of Magnetic Resonance Imaging* 10(5) (1999) 602–608.
13. Amini, A.A., Chen, J., Wang, Y.: Imaging and analysis for determination of cardiovascular mechanics. *Abs* 692–695.
14. Van Everdingen, K., Klijn, C., Kappelle, L., Mali, W., Van der Grond, J.: MRA flow quantification in patients with a symptomatic internal carotid artery occlusion. *Stroke* 28(8) (1997) 1595–1600.
15. Chung, A.C., Noble, J.A.: Statistical 3D vessel segmentation using a Rician distribution. *Abs* 82–89.
16. El-Baz, A., Elnakib, A., Khalifa, F., El-Ghar, M.A., McClure, P., Soliman, A., Gimelrfarb, G.: Precise segmentation of 3D magnetic resonance angiography. *IEEE Transactions on Biomedical Engineering* 59(7) (2012) 2019–2029.
17. Wilson, D.L., Noble, J.A.: An adaptive segmentation algorithm for time-of-flight MRA data. *IEEE Transactions on Medical Imaging* 18(10) (1999) 938–945.
18. Gimel'farb, G., Farag, A.A., El-Baz, A.: Expectation-maximization for a linear combination of Gaussians. *Abs* 422–425.
19. Forkert, N.D., Säring, D., Illies, T., Fiehler, J., Ehrhardt, J., Handels, H., Schmidt-Richberg, A.: Direction-dependent level set segmentation of cerebrovascular structures. *Abs* 79623S-79623S-79628.
20. Holtzman-Gazit, M., Kimmel, R., Peled, N., Goldsher, D.: Segmentation of thin structures in volumetric medical images. *IEEE Transactions on Image Processing* 15(2) (2006) 354–363.
21. Xu, C., Prince, J.L.: Snakes, shapes, and gradient vector flow. *IEEE Transactions on Image Processing* 7(3) (1998) 359–369.
22. Webb, A.R.: *Statistical Pattern Recognition*. John Wiley & Sons (2003).
23. Sabry, M., Sites, C.B., Farag, A.A., Hushek, S., Moriarty, T.: A fast automatic method for 3D volume segmentation of the human cerebrovascular. In: *CARS 2002 Computer Assisted Radiology and Surgery*. Springer (2002) 382–387.
24. Suzuki, K.: Computerized segmentation of organs by means of geodesic active-contour level-set algorithm. In: *Multi Modality State-of-the-Art Medical Image Segmentation and Registration Methodologies*. Springer (2011) 103–128.
25. Itai, Y., Kim, H., Ishikawa, S., Katsuragawa, S., Doi, K.: Development of a voxel-matching technique for substantial reduction of subtraction artifacts in temporal subtraction images obtained from thoracic MDCT. *Journal of Digital Imaging* 23(1) (2010) 31–38.
26. Jennings, J.R., Heim, A.F.: From brain to behavior: Hypertension's modulation of cognition and affect. *International Journal of Hypertension* (2012).
27. Gorelick, P.B., Scuteri, A., Black, S.E., DeCarli, C., Greenberg, S.M., Iadecola, C., Launer, L.J., Laurent, S., Lopez, O.L., Nyenhuis, D.: Vascular contributions to cognitive impairment and dementia. *Stroke* 42(9) (2011) 2672–2713.
28. Iadecola, C., Yaffe, K., Biller, J., Bratzke, L.C., Faraci, F.M., Gorelick, P.B., Gulati, M., Kamel, H., Knopman, D.S., Launer, L.J.: Impact of hypertension on cognitive function: A scientific statement from the American Heart Association. *Hypertension* 68(6) (2016) e67–e94.

29. Friedman, J., Hastie, T., Tibshirani, R.: *The Elements of Statistical Learning*. 1. Springer series in statistics. Springer (2001).
30. Ali, A.M., Farag, A.A., El-Baz, A.: Graph cuts framework for kidney segmentation with prior shape constraints. In: *Proceedings of International Conference on Medical Image Computing and Computer-Assisted Intervention* (MICCAI'07). Volume 1. Brisbane, Australia, October 29–November 2 (2007) 384–392.
31. Chowdhury, A.S., Roy, R., Bose, S., Elnakib, F.K.A., El-Baz, A.: Non-rigid biomedical image registration using graph cuts with a novel data term. In: *Proceedings of IEEE International Symposium on Biomedical Imaging: From Nano to Macro* (ISBI'12). Barcelona, Spain, May 2–5 (2012) 446–449.
32. El-Baz, A., Farag, A.A., Yuksel, S.E., El-Ghar, M.E.A., Eldiasty, T.A., Ghoneim, M.A.: Application of deformable models for the detection of acute renal rejection. In Farag, A.A., Suri, J.S., eds.: *Deformable Models*. Volume 1. Springer (2007) 293–333.
33. El-Baz, A., Farag, A., Fahmi, R., Yuksel, S., El-Ghar, M.A., Eldiasty, T.: Image analysis of renal DCE MRI for the detection of acute renal rejection. In: *Proceedings of IAPR International Conference on Pattern Recognition* (ICPR'06). Hong Kong, August 20–24 (2006) 822–825.
34. El-Baz, A., Farag, A., Fahmi, R., Yuksel, S., Miller, W., El-Ghar, M.A., El-Diasty, T., Ghoneim, M.: A new CAD system for the evaluation of kidney diseases using DCE-MRI. In: *Proceedings of International Conference on Medical Image Computing and Computer-Assisted Intervention* (MICCAI'08). Copenhagen, Denmark, October 1–6 (2006) 446–453.
35. El-Baz, A., Gimel'farb, G., El-Ghar, M.A.: A novel image analysis approach for accurate identification of acute renal rejection. In: *Proceedings of IEEE International Conference on Image Processing* (ICIP'08). San Diego, California, USA, October 12–15 (2008) 1812–1815.
36. El-Baz, A., Gimel'farb, G., El-Ghar, M.A.: Image analysis approach for identification of renal transplant rejection. In: *Proceedings of IAPR International Conference on Pattern Recognition* (ICPR'08). Tampa, Florida, USA, December 8–11 (2008) 1–4.
37. El-Baz, A., Gimel'farb, G., El-Ghar, M.A.: New motion correction models for automatic identification of renal transplant rejection. In: *Proceedings of International Conference on Medical Image Computing and Computer-Assisted Intervention* (MICCAI'07). Brisbane, Australia, October 29–November 2 (2007) 235–243.
38. Farag, A., El-Baz, A., Yuksel, S., El-Ghar, M.A., Eldiasty, T.: A framework for the detection of acute rejection with Dynamic Contrast Enhanced Magnetic Resonance Imaging. In: *Proceedings of IEEE International Symposium on Biomedical Imaging: From Nano to Macro* (ISBI'06). Arlington, Virginia, USA, April 6–9 (2006) 418–421.
39. Khalifa, F., Beache, G.M., El-Ghar, M.A., El-Diasty, T., Gimel'farb, G., Kong, M., El-Baz, A.: Dynamic contrast-enhanced MRI-based early detection of acute renal transplant rejection. *IEEE Transactions on Medical Imaging* 32(10) (2013) 1910–1927.
40. Khalifa, F., El-Baz, A., Gimel'farb, G., El-Ghar, M.A.: Non-invasive image-based approach for early detection of acute renal rejection. In: *Proceedings of International Conference Medical Image Computing and Computer-Assisted Intervention* (MICCAI'10). Beijing, China, September 20–24 (2010) 10–18.
41. Khalifa, F., El-Baz, A., Gimel'farb, G., Ouseph, R., El-Ghar, M.A.: Shape-appearance guided level-set deformable model for image segmentation. In: *Proceedings of IAPR International Conference on Pattern Recognition* (ICPR'10). Istanbul, Turkey, August 23–26 (2010) 4581–4584.
42. Khalifa, F., El-Ghar, M.A., Abdollahi, B., Frieboes, H., El-Diasty, T., El-Baz, A.: A comprehensive non-invasive framework for automated evaluation of acute renal transplant rejection using DCE-MRI. *NMR in Biomedicine* 26(11) (2013) 1460–1470.
43. Khalifa, F., El-Ghar, M.A., Abdollahi, B., Frieboes, H.B., El-Diasty, T., El-Baz, A.: Dynamic contrast-enhanced MRI-based early detection of acute renal transplant rejection. In: *2014 Annual Scientific Meeting and Educational Course Brochure of the Society of Abdominal Radiology* (SAR'14). Boca Raton, Florida, March 23–28 (2014) CID: 1855912.
44. Khalifa, F., Elnakib, A., Beache, G.M., Gimel'farb, G., El-Ghar, M.A., Sokhadze, G., Manning, S., McClure, P., El-Baz, A.: 3D kidney segmentation from CT images using a level set approach guided by a novel stochastic speed function. In: *Proceedings of International Conference Medical Image Computing and Computer-Assisted Intervention* (MICCAI'11). Toronto, Canada, September 18–22 (2011) 587–594.
45. Khalifa, F., Gimel'farb, G., El-Ghar, M.A., Sokhadze, G., Manning, S., McClure, P., Ouseph, R., El-Baz, A.: A new deformable model-based segmentation approach for accurate extraction of the kidney from abdominal CT images. In: *Proceedings of IEEE International Conference on Image Processing* (ICIP'11). Brussels, Belgium, September 11–14 (2011) 3393–3396.

46. Mostapha, M., Khalifa, F., Alansary, A., Soliman, A., Suri, J., El-Baz, A.: Computer-aided diagnosis systems for acute renal transplant rejection: Challenges and methodologies. In El-Baz, A., Saba, J., Suri, L., eds.: *Abdomen and Thoracic Imaging.* Springer (2014) 1–35.
47. Shehata, M., Khalifa, F., Hollis, E., Soliman, A., Hosseini-Asl, E., El-Ghar, M.A., El-Baz, M., Dwyer, A.C., El-Baz, A., Keynton, R.: A new non-invasive approach for early classification of renal rejection types using diffusion-weighted MRI. *IEEE International Conference on Image Processing* (ICIP) (2016) 136–140.
48. Khalifa, F., Soliman, A., Takieldeen, A., Shehata, M., Mostapha, M., Shaffie, A., Ouseph, R., Elmaghraby, A., El-Baz, A.: Kidney segmentation from CT images using a 3D NMF-guided active contour model. *IEEE 13th International Symposium on Biomedical Imaging* (ISBI) (2016) 432–435.
49. Shehata, M., Khalifa, F., Soliman, A., Takieldeen, A., El-Ghar, M.A., Shaffie, A., Dwyer, A.C., Ouseph, R., El-Baz, A., Keynton, R.: 3D diffusion MRI-based CAD system for early diagnosis of acute renal rejection. *IEEE 13th International Symposium on Biomedical Imaging* (ISBI), (2016) 1177–1180.
50. Shehata, M., Khalifa, F., Soliman, A., Alrefai, R., El-Ghar, M.A., Dwyer, A.C., Ouseph, R., El-Baz, A.: A level set-based framework for 3D kidney segmentation from diffusion MR images. *IEEE International Conference on Image Processing* (ICIP) IEEE (2015) 4441–4445.
51. Shehata, M., Khalifa, F., Soliman, A., El-Ghar, M.A., Dwyer, A.C., Gimelfarb, G., Keynton, R., El-Baz, A., et al.: A promising non-invasive CAD system for kidney function assessment. *International Conference on Medical Image Computing and Computer-Assisted Intervention*. Springer (2016) 613–621.
52. Khalifa, F., Soliman, A., Elmaghraby, A., Gimelfarb, G., El-Baz, A.: 3D kidney segmentation from abdominal images using spatial-appearance models. *Computational and Mathematical Methods in Medicine* (2017).
53. Hollis, E., Shehata, M., Khalifa, F., El-Ghar, M.A., El-Diasty, T., El-Baz, A.: Towards non-invasive diagnostic techniques for early detection of acute renal transplant rejection: A review. *The Egyptian Journal of Radiology and Nuclear Medicine* 48(1) (2016) 257–269.
54. Shehata, M., Khalifa, F., Soliman, A., El-Ghar, M.A., Dwyer, A.C., El-Baz, A.: Assessment of renal transplant using image and clinical-based biomarkers. In: *Proceedings of 13th Annual Scientific Meeting of American Society for Diagnostics and Interventional Nephrology* (ASDIN'17). New Orleans, Louisiana, USA, February 10–12 (2017).
55. Shehata, M., Khalifa, F., Soliman, A., El-Ghar, M.A., Dwyer, A.C., El-Baz, A.: Early assessment of acute renal rejection. In: *Proceedings of 12th Annual Scientific Meeting of American Society for Diagnostics and Interventional Nephrology* (ASDIN'16). Phoenix, Arizona, USA, February 19–21 (2016).
56. Khalifa, F., Beache, G., El-Baz, A., Gimel'farb, G.: Deformable model guided by stochastic speed with application in cine images segmentation. In: *Proceedings of IEEE International Conference on Image Processing* (ICIP'10). Hong Kong, September 26–29 (2010) 1725–1728.
57. Khalifa, F., Beache, G.M., Elnakib, A., Sliman, H., Gimel'farb, G., Welch, K.C., El-Baz, A.: A new shape-based framework for the left ventricle wall segmentation from cardiac first-pass perfusion MRI. In: *Proceedings of IEEE International Symposium on Biomedical Imaging: From Nano to Macro* (ISBI'13). San Francisco, California, April 7–11 (2013) 41–44.
58. Khalifa, F., Beache, G.M., Elnakib, A., Sliman, H., Gimel'farb, G., Welch, K.C., El-Baz, A.: A new non-rigid registration framework for improved visualization of transmural perfusion gradients on cardiac first-pass perfusion MRI. In: *Proceedings of IEEE International Symposium on Biomedical Imaging: From Nano to Macro* (ISBI'12). Barcelona, Spain, May 2–5 (2012) 828–831.
59. Khalifa, F., Beache, G.M., Firjani, A., Welch, K.C., Gimel'farb, G., El-Baz, A.: A new nonrigid registration approach for motion correction of cardiac first-pass perfusion MRI. In: *Proceedings of IEEE International Conference on Image Processing* (ICIP'12). Lake Buena Vista, Florida, September 30–October 3 (2012) 1665–1668.
60. Khalifa, F., Beache, G.M., Gimel'farb, G., El-Baz, A.: A novel CAD system for analyzing cardiac first-pass MR images. In: *Proceedings of IAPR International Conference on Pattern Recognition* (ICPR'12). Tsukuba Science City, Japan, November 11–15 (2012) 77–80.
61. Khalifa, F., Beache, G.M., Gimel'farb, G., El-Baz, A.: A novel approach for accurate estimation of left ventricle global indexes from short-axis cine MRI. In: *Proceedings of IEEE International Conference on Image Processing* (ICIP'11). Brussels, Belgium, September 11–14 (2011) 2645–2649.
62. Khalifa, F., Beache, G.M., Gimel'farb, G., Giridharan, G.A., El-Baz, A.: A new image-based framework for analyzing cine images. In El-Baz, A., Acharya, U.R., Mirmedhdi, M., Suri, J.S., eds.: *Handbook of Multi Modality State-of-the-Art Medical Image Segmentation and Registration Methodologies*. Volume 2. Springer (2011) 69–98.
63. Khalifa, F., Beache, G.M., Gimel'farb, G., Giridharan, G.A., El-Baz, A.: Accurate automatic analysis of cardiac cine images. *IEEE Transactions on Biomedical Engineering* 59(2) (2012) 445–455.

64. Khalifa, F., Beache, G.M., Nitzken, M., Gimel'farb, G., Giridharan, G.A., El-Baz, A.: Automatic analysis of left ventricle wall thickness using short-axis cine CMR images. In: *Proceedings of IEEE International Symposium on Biomedical Imaging: From Nano to Macro* (ISBI'11). Chicago, Illinois, March 30–April 2 (2011) 1306–1309.
65. Nitzken, M., Beache, G., Elnakib, A., Khalifa, F., Gimel'farb, G., El-Baz, A.: Accurate modeling of tagged CMR 3D image appearance characteristics to improve cardiac cycle strain estimation. In: *19th IEEE International Conference on Image Processing* (ICIP). Orlando, Florida, USA, September (2012) 521–524.
66. Nitzken, M., Beache, G., Elnakib, A., Khalifa, F., Gimel'farb, G., El-Baz, A.: Improving full-cardiac cycle strain estimation from tagged CMR by accurate modeling of 3D image appearance characteristics. In: *9th IEEE International Symposium on Biomedical Imaging* (ISBI). Barcelona, Spain (2012) 462–465 (selected for oral presentation).
67. Nitzken, M.J., El-Baz, A.S., Beache, G.M.: Markov-Gibbs random field model for improved full-cardiac cycle strain estimation from tagged CMR. *Journal of Cardiovascular Magnetic Resonance* 14(1) (2012) 1–2.
68. Sliman, H., Elnakib, A., Beache, G., Elmaghraby, A., El-Baz, A.: Assessment of myocardial function from cine cardiac MRI using a novel 4D tracking approach. *J Comput Sci Syst Biol* 7 (2014) 169–173.
69. Sliman, H., Elnakib, A., Beache, G.M., Soliman, A., Khalifa, F., Gimel'farb, G., Elmaghraby, A., El-Baz, A.: A novel 4D PDE-based approach for accurate assessment of myocardium function using cine cardiac magnetic resonance images. In: *Proceedings of IEEE International Conference on Image Processing* (ICIP'14). Paris, France, October 27–30 (2014) 3537–3541.
70. Sliman, H., Khalifa, F., Elnakib, A., Beache, G.M., Elmaghraby, A., El-Baz, A.: A new segmentation-based tracking framework for extracting the left ventricle cavity from cine cardiac MRI. In: *Proceedings of IEEE International Conference on Image Processing* (ICIP'13). Melbourne, Australia, September 15–18 (2013) 685–689.
71. Sliman, H., Khalifa, F., Elnakib, A., Soliman, A., Beache, G.M., Elmaghraby, A., Gimel'farb, G., El-Baz, A.: Myocardial borders segmentation from cine MR images using bi-directional coupled parametric deformable models. *Medical Physics* (9) (2013) 1–13.
72. Sliman, H., Khalifa, F., Elnakib, A., Soliman, A., Beache, G.M., Gimel'farb, G., Emam, A., Elmaghraby, A., El-Baz, A.: Accurate segmentation framework for the left ventricle wall from cardiac cine MRI. In: *Proceedings of International Symposium on Computational Models for Life Science* (CMLS'13). Volume 1559, Sydney, Australia, November 27–29 (2013) 287–296.
73. Eladawi, N., Elmogy, M., et al.: Classification of retinal diseases based on OCT images. *Frontiers in Bioscience* 23 (2017) 247–264.
74. ElTanboly, A., Ismail, M., et al.: A computer aided diagnostic system for detecting diabetic retinopathy in optical coherence tomography images. *Medical Physics* 44(3) (2016) 914–923.
75. Abdollahi, B., Civelek, A.C., Li, X.F., Suri, J., El-Baz, A.: PET/CT nodule segmentation and diagnosis: A survey. In Saba, L., Suri, J.S., eds.: *Multi Detector CT Imaging*. Taylor, Francis (2014) 639–651.
76. Abdollahi, B., El-Baz, A., Amini, A.A.: A multi-scale non-linear vessel enhancement technique. In: *Engineering in Medicine and Biology Society, EMBC, 2011 Annual International Conference of the IEEE*. IEEE (2011) 3925–3929.
77. Abdollahi, B., Soliman, A., Civelek, A., Li, X.F., Gimel'farb, G., El-Baz, A.: A novel Gaussian scale space-based joint MGRF framework for precise lung segmentation. In: *Proceedings of IEEE International Conference on Image Processing* (ICIP'12). IEEE (2012) 2029–2032.
78. Abdollahi, B., Soliman, A., Civelek, A., Li, X.F., Gimelfarb, G., El-Baz, A.: A novel 3D joint MGRF framework for precise lung segmentation. In: *Machine Learning in Medical Imaging*. Springer (2012) 86–93.
79. Ali, A.M., El-Baz, A.S., Farag, A.A.: A novel framework for accurate lung segmentation using graph cuts. In: *Proceedings of IEEE International Symposium on Biomedical Imaging: From Nano to Macro* (ISBI'07). IEEE (2007) 908–911.
80. El-Baz, A., Beache, G.M., Gimel'farb, G., Suzuki, K., Okada, K.: Lung imaging data analysis. *International Journal of Biomedical Imaging* (2013).
81. El-Baz, A., Beache, G.M., Gimel'farb, G., Suzuki, K., Okada, K., Elnakib, A., Soliman, A., Abdollahi, B.: Computer-aided diagnosis systems for lung cancer: Challenges and methodologies. *International Journal of Biomedical Imaging* (2013).
82. El-Baz, A., Elnakib, A., Abou El-Ghar, M., Gimel'farb, G., Falk, R., Farag, A.: Automatic detection of 2D and 3D lung nodules in chest spiral CT scans. *International Journal of Biomedical Imaging* (2013).

83. El-Baz, A., Farag, A.A., Falk, R., La Rocca, R.: A unified approach for detection, visualization, and identification of lung abnormalities in chest spiral CT scans. In: *International Congress Series*. Volume 1256. Elsevier (2003) 998–1004.
84. El-Baz, A., Farag, A.A., Falk, R., La Rocca, R.: Detection, visualization and identification of lung abnormalities in chest spiral CT scan: Phase-I. In: *Proceedings of International Conference on Biomedical Engineering*. Cairo, Egypt. Volume 12 (2002).
85. El-Baz, A., Farag, A., Gimel'farb, G., Falk, R., El-Ghar, M.A., Eldiasty, T.: A framework for automatic segmentation of lung nodules from low dose chest CT scans. In: *Proceedings of International Conference on Pattern Recognition* (ICPR'06). Volume 3, IEEE (2006) 611–614.
86. El-Baz, A., Farag, A., Gimelfarb, G., Falk, R., El-Ghar, M.A.: A novel level set-based computer-aided detection system for automatic detection of lung nodules in low dose chest computed tomography scans. *Lung Imaging and Computer Aided Diagnosis* 10 (2011) 221–238.
87. El-Baz, A., Gimel'farb, G., Abou El-Ghar, M., Falk, R.: Appearance-based diagnostic system for early assessment of malignant lung nodules. In: *Proceedings of IEEE International Conference on Image Processing* (ICIP'12). IEEE (2012) 533–536.
88. El-Baz, A., Gimel'farb, G., Falk, R.: A novel 3D framework for automatic lung segmentation from low dose CT images. In El-Baz, A., Suri, J.S., eds.: *Lung Imaging and Computer Aided Diagnosis*. Taylor, Francis (2011) 1–16.
89. El-Baz, A., Gimel'farb, G., Falk, R., El-Ghar, M.: Appearance analysis for diagnosing malignant lung nodules. In: *Proceedings of IEEE International Symposium on Biomedical Imaging: From Nano to Macro* (ISBI'10). IEEE (2010) 193–196.
90. El-Baz, A., Gimel'farb, G., Falk, R., El-Ghar, M.A.: A novel level set-based CAD system for automatic detection of lung nodules in low dose chest CT scans. In El-Baz, A., Suri, J.S., eds.: *Lung Imaging and Computer Aided Diagnosis*. Volume 1. Taylor, Francis (2011) 221–238.
91. El-Baz, A., Gimel'farb, G., Falk, R., El-Ghar, M.A.: A new approach for automatic analysis of 3D low dose CT images for accurate monitoring the detected lung nodules. In: *Proceedings of International Conference on Pattern Recognition* (ICPR'08). IEEE (2008) 1–4.
92. El-Baz, A., Gimel'farb, G., Falk, R., El-Ghar, M.A.: A novel approach for automatic follow-up of detected lung nodules. In: *Proceedings of IEEE International Conference on Image Processing* (ICIP'07). Volume 5. IEEE (2007) V–501.
93. El-Baz, A., Gimel'farb, G., Falk, R., El-Ghar, M.A.: A new CAD system for early diagnosis of detected lung nodules. In: *IEEE International Conference on Image Processing*. Volume 2. IEEE (2007) II–461.
94. El-Baz, A., Gimel'farb, G., Falk, R., El-Ghar, M.A., Refaie, H.: Promising results for early diagnosis of lung cancer. In: *Proceedings of IEEE International Symposium on Biomedical Imaging: From Nano to Macro* (ISBI'08). IEEE (2008) 1151–1154.
95. El-Baz, A., Gimel'farb, G.L., Falk, R., Abou El-Ghar, M., Holland, T., Shaffer, T.: A new stochastic framework for accurate lung segmentation. In: *Proceedings of Medical Image Computing and Computer-Assisted Intervention* (MICCAI'08). (2008) 322–330.
96. El-Baz, A., Gimel'farb, G.L., Falk, R., Heredis, D., Abou El-Ghar, M.: A novel approach for accurate estimation of the growth rate of the detected lung nodules. In: *Proceedings of International Workshop on Pulmonary Image Analysis*. (2008) 33–42.
97. El-Baz, A., Gimel'farb, G.L., Falk, R., Holland, T., Shaffer, T.: A framework for unsupervised segmentation of lung tissues from low dose computed tomography images. In: *Proceedings of British Machine Vision* (BMVC'08). (2008) 1–10.
98. El-Baz, A., Gimelfarb, G., Falk, R., El-Ghar, M.A.: 3D MGRF-based appearance modeling for robust segmentation of pulmonary nodules in 3D LDCT chest images. In: *Lung Imaging and Computer Aided Diagnosis* (2011) 51–63.
99. El-Baz, A., Gimelfarb, G., Falk, R., El-Ghar, M.A.: Automatic analysis of 3D low dose CT images for early diagnosis of lung cancer. *Pattern Recognition* 42(6) (2009) 1041–1051.
100. El-Baz, A., Gimelfarb, G., Falk, R., El-Ghar, M.A., Rainey, S., Heredia, D., Shaffer, T.: Toward early diagnosis of lung cancer. In: *Proceedings of Medical Image Computing and Computer-Assisted Intervention* (MICCAI'09). Springer (2009) 682–689.
101. El-Baz, A., Gimelfarb, G., Falk, R., El-Ghar, M.A., Suri, J.: Appearance analysis for the early assessment of detected lung nodules. In: *Lung Imaging and Computer Aided Diagnosis* (2011) 395–404.
102. El-Baz, A., Khalifa, F., Elnakib, A., Nitkzen, M., Soliman, A., McClure, P., Gimel'farb, G., El-Ghar, M.A.: A novel approach for global lung registration using 3D Markov Gibbs appearance model. In: *Proceedings of International Conference Medical Image Computing and Computer-Assisted Intervention* (MICCAI' 12). Nice, France, October 1–5 (2012) 114–121.

103. El-Baz, A., Nitzken, M., Elnakib, A., Khalifa, F., Gimel'farb, G., Falk, R., El-Ghar, M.A.: 3D shape analysis for early diagnosis of malignant lung nodules. In: *Proceedings of International Conference Medical Image Computing and Computer-Assisted Intervention* (MICCAI'11). Toronto, Canada, September 18–22 (2011) 175–182.
104. El-Baz, A., Nitzken, M., Gimelfarb, G., Van Bogaert, E., Falk, R., El-Ghar, M.A., Suri, J.: Three-dimensional shape analysis using spherical harmonics for early assessment of detected lung nodules. In: *Lung Imaging and Computer Aided Diagnosis* (2011) 421–438.
105. El-Baz, A., Nitzken, M., Khalifa, F., Elnakib, A., Gimel'farb, G., Falk, R., El- Ghar, M.A.: 3D shape analysis for early diagnosis of malignant lung nodules. In: *Proceedings of International Conference on Information Processing in Medical Imaging* (IPMI'11). Monastery Irsee, Germany (Bavaria), July 3–8 (2011) 772– 783.
106. El-Baz, A., Nitzken, M., Vanbogaert, E., Gimel'farb, G., Falk, R., Abo El-Ghar, M.: A novel shape-based diagnostic approach for early diagnosis of lung nodules. In: *IEEE International Symposium on Biomedical Imaging: From Nano to Macro*. IEEE (2011) 137–140.
107. El-Baz, A., Sethu, P., Gimel'farb, G., Khalifa, F., Elnakib, A., Falk, R., El-Ghar, M.A.: Elastic phantoms generated by microfluidics technology: Validation of an imaged-based approach for accurate measurement of the growth rate of lung nodules. *Biotechnology Journal* 6(2) (2011) 195–203.
108. El-Baz, A., Sethu, P., Gimel'farb, G., Khalifa, F., Elnakib, A., Falk, R., El-Ghar, M.A.: A new validation approach for the growth rate measurement using elastic phantoms generated by state-of-the-art microfluidics technology. In: *Proceedings of IEEE International Conference on Image Processing* (ICIP'10). Hong Kong, September 26–29 (2010) 4381–4383.
109. El-Baz, A., Sethu, P., Gimel'farb, G., et al.: Validation of a new image-based approach for the accurate estimating of the growth rate of detected lung nodules using real CT images and elastic phantoms generated by state-of-the-art microfluidics technology. In El-Baz, A., Suri, J.S., eds.: *Handbook of Lung Imaging and Computer Aided Diagnosis*. Volume 1. Taylor, Francis (2011) 405–420.
110. El-Baz, A., Soliman, A., McClure, P., Gimel'farb, G., El-Ghar, M.A., Falk, R.: Early assessment of malignant lung nodules based on the spatial analysis of detected lung nodules. In: *Proceedings of IEEE International Symposium on Biomedical Imaging: From Nano to Macro* (ISBI'12). IEEE (2012) 1463–1466.
111. El-Baz, A., Yuksel, S.E., Elshazly, S., Farag, A.A.: Non-rigid registration techniques for automatic follow-up of lung nodules. In: *Proceedings of Computer Assisted Radiology and Surgery* (CARS'05). Volume 1281. Elsevier (2005) 1115–1120.
112. El-Baz, A.S., Suri, J.S.: *Lung Imaging and Computer Aided Diagnosis*. CRC Press (2011).
113. Soliman, A., Khalifa, F., Shaffie, A., Liu, N., Dunlap, N., Wang, B., Elmaghraby, A., Gimelfarb, G., El-Baz, A.: Image-based CAD system for accurate identification of lung injury. In: *Proceedings of IEEE International Conference on Image Processing* (ICIP'16). IEEE (2016) 121–125.
114. Soliman, A., Khalifa, F., Dunlap, N., Wang, B., El-Ghar, M., El-Baz, A.: An isosurfaces based local deformation handling framework of lung tissues. In: *IEEE 13th International Symposium on Biomedical Imaging* (ISBI). IEEE (2016) 1253–1259.
115. Soliman, A., Khalifa, F., Shaffie, A., Dunlap, N., Wang, B., Elmaghraby, A., El-Baz, A.: Detection of lung injury using 4D-CT chest images. In: *IEEE 13th International Symposium on Biomedical Imaging* (ISBI). IEEE (2016) 1274–1277.
116. Dombroski, B., Nitzken, M., Elnakib, A., Khalifa, F., El-Baz, A., Casanova, M.F.: Cortical surface complexity in a population-based normative sample. *Translational Neuroscience* 5(1) (2014) 17–24.
117. El-Baz, A., Casanova, M., Gimel'farb, G., Mott, M., Switala, A.: An MRI-based diagnostic framework for early diagnosis of dyslexia. *International Journal of Computer Assisted Radiology and Surgery* 3(3–4) (2008) 181–189.
118. El-Baz, A., Casanova, M., Gimel'farb, G., Mott, M., Switala, A., Vanbogaert, E., McCracken, R.: A new CAD system for early diagnosis of dyslexic brains. In: *Proceedings of the International Conference on Image Processing* (ICIP'2008). IEEE (2008) 1820–1823.
119. El-Baz, A., Casanova, M.F., Gimel'farb, G., Mott, M., Switwala, A.E.: A new image analysis approach for automatic classification of autistic brains. In: *Proceedings of the IEEE International Symposium on Biomedical Imaging: From Nano to Macro* (ISBI'2007). IEEE (2007) 352–355.
120. El-Baz, A., Elnakib, A., Khalifa, F., El-Ghar, M.A., McClure, P., Soliman, A., Gimel'farb, G.: Precise segmentation of 3-D magnetic resonance angiography. *IEEE Transactions on Biomedical Engineering* 59(7) (2012) 2019–2029.
121. El-Baz, A., Farag, A.A., Gimel'farb, G.L., El-Ghar, M.A., Eldiasty, T.: Probabilistic modeling of blood vessels for segmenting MRA images. *ICPR* (3) (2006) 917–920.

122. El-Baz, A., Farag, A.A., Gimelfarb, G., El-Ghar, M.A., Eldiasty, T.: A new adaptive probabilistic model of blood vessels for segmenting MRA images. In: *Medical Image Computing and Computer-Assisted Intervention* (MICCAI 2006). Volume 4191. Springer (2006) 799–806.
123. El-Baz, A., Farag, A.A., Gimelfarb, G., Hushek, S.G.: Automatic cerebrovascular segmentation by accurate probabilistic modeling of TOF-MRA images. In: *Medical Image Computing and Computer-Assisted Intervention* (MICCAI 2005). Springer (2005) 34–42.
124. El-Baz, A., Farag, A., Elnakib, A., Casanova, M.F., Gimel'farb, G., Switala, A.E., Jordan, D., Rainey, S.: Accurate automated detection of autism related corpus callosum abnormalities. *Journal of Medical Systems* 35(5) (2011) 929–939.
125. El-Baz, A., Farag, A., Gimelfarb, G.: Cerebrovascular segmentation by accurate probabilistic modeling of TOF-MRA images. In: *Image Analysis*. Volume 3540. Springer (2005) 1128–1137.
126. El-Baz, A., Gimelfarb, G., Falk, R., El-Ghar, M.A., Kumar, V., Heredia, D.: A novel 3D joint Markov-Gibbs model for extracting blood vessels from PC–MRA images. In: *Medical Image Computing and Computer-Assisted Intervention* (MICCAI 2009). Volume 5762. Springer (2009) 943–950.
127. Elnakib, A., El-Baz, A., Casanova, M.F., Gimel'farb, G., Switala, A.E.: Image-based detection of corpus callosum variability for more accurate discrimination between dyslexic and normal brains. In: *Proceedings of IEEE International Symposium on Biomedical Imaging: From Nano to Macro* (ISBI'2010). IEEE (2010) 109–112.
128. Elnakib, A., Casanova, M.F., Gimel'farb, G., Switala, A.E., El-Baz, A.: Autism diagnostics by centerline-based shape analysis of the corpus callosum. In: *Proceedings of IEEE International Symposium on Biomedical Imaging: From Nano to Macro* (ISBI'2011). IEEE (2011) 1843–1846.
129. Elnakib, A., Nitzken, M., Casanova, M., et al.: Quantification of age-related brain cortex change using 3D shape analysis. In: *21st International Conference on Pattern Recognition* (ICPR). IEEE (2012) 41–44.
130. Mostapha, M., Soliman, A., Khalifa, F., Elnakib, A., Alansary, A., Nitzken, M., Casanova, M.F., El-Baz, A.: A statistical framework for the classification of infant DT images. In: *IEEE International Conference on Image Processing* (ICIP). IEEE (2014) 2222–2226.
131. Nitzken, M., Casanova, M., Gimel'farb, G., Elnakib, A., Khalifa, F., Switala, A., El-Baz, A.: 3D shape analysis of the brain cortex with application to dyslexia. In: *18th IEEE International Conference on Image Processing* (ICIP). Brussels, Belgium, IEEE (September 2011) 2657–2660 (Selected for oral presentation. Oral acceptance rate is 10 percent and the overall acceptance rate is 35 percent.).
132. El-Gamal, F.E.Z.A., Elmogy, M., Ghazal, M., Atwan, A., Barnes, G., Casanova, M., Keynton, R., El-Baz, A.: A novel CAD system for local and global early diagnosis of Alzheimers disease based on PIB-PET scans. In: *IEEE International Conference on Image Processing* (ICIP). Beijing, China (2017).
133. Ismail, M., Soliman, A., Ghazal, M., et al.: A fast stochastic framework for automatic MR brain images segmentation. *PLoS one* (2017).
134. Ismail, M.M., Keynton, R.S., Mostapha, M.M., ElTanboly, A.H., Casanova, M.F., Gimel'farb, G.L., El-Baz, A.: Studying autism spectrum disorder with structural and diffusion Magnetic Resonance Imaging: a survey. *Frontiers in Human Neuroscience* 10 (2016).
135. Alansary, A., Ismail, M., Soliman, A., Khalifa, F., Nitzken, M., Elnakib, A., Mostapha, M., Black, A., Stinebruner, K., Casanova, M.F., et al.: Infant brain extraction in t1-weighted MR images using bet and refinement using LCDG and MGRF models. *IEEE Journal of Biomedical and Health Informatics* 20(3) (2016) 925–935.
136. Ismail, M., Barnes, G., Nitzken, M., et al.: A new deep-learning CAD system for early diagnosis of autism using structural MRI. *IEEE International Conference on Image Processing* (ICIP). Beijing, China (2017).
137. Ismail, M., Soliman, A., ElTanboly, A., Switala, A., Mahmoud, M., Khalifa, F., Gimel'farb, G., Casanova, M.F., Keynton, R., El-Baz, A.: Detection of white matter abnormalities in MR brain images for diagnosis of autism in children. *IEEE 13th International Symposium on Biomedical Imaging* (2016) 6–9.
138. Ismail, M., Mostapha, M., Soliman, A., Nitzken, M., Khalifa, F., Elnakib, A., Gimel'farb, G., Casanova, M., El-Baz, A.: Segmentation of infant brain MR images based on adaptive shape prior and higher-order MGRF (2015) 4327–4331.
139. Shalaby, A., Taher, F., El-Baz, M., Ghazal, V., Abou El-Ghar, M., Takieldeen, A., El-Baz, A.: Probabilistic modeling of blood vessels for segmenting magnetic resonance angiography images. In: *Medical Research Archive- MRA*. KEI (2017) 34–42.
140. Chowdhury, A.S., Rudra, A.K., Sen, M., Elnakib, A., El-Baz, A.: Cerebral white matter segmentation from MRI using probabilistic graph cuts and geometric shape priors. In: *ICIP* (2010) 3649–3652.

Taylor & Francis
Taylor & Francis Group
http://taylorandfrancis.com

2 Segmentation of Blood Vessels Using Magnetic Resonance Angiography Images

Ahmed Shalaby[1], *Ali Mahmoud*[1], *Mohammed Ghazal*[1,2], *Jasjit S. Suri*[3], *Ayman El-Baz*[1]
[1]University of Louisville
[2]Abu Dhabi University
[3]AtheroPoint, LLC

CONTENTS

2.1 INTRODUCTION

Accurate 3D cerebrovascular system segmentation from magnetic resonance angiography (MRA) images is one of the most important problems in practical computer-assisted medical diagnostics. Phase Contrast MRA (PC-MRA) provides good suppression of background signals and quantifies blood flow velocity vectors for each voxel. Time-of-flight MRA (TOF-MRA) is less quantitative, but it is fast and produces images with high contrast. The most popular techniques for extracting blood vessels from MRA data are scale-space filtering, centerline-based methods, deformable models, statistical models, and hybrid methods.

Multiscale filtering enhances curvilinear structures in 3D medical images by convolving an image with Gaussian filters at multiple scales [4–7]. Eigenvalues of the Hessian at each voxel are analyzed to determine the local shapes of 3D structures (by the eigenvalues, voxels from a linear structure, like a blood vessel, differ from those for a planar structure, speckle noise, or unstructured components). The multiscale filter output forms a new enhanced image such that the curvilinear structures become brighter, whereas other components become darker [4]. Such an image can be directly visualized, thresholded, and segmented using a deformable model. Alternatively, the obtained eigenvalues define a candidate set of voxels corresponding to the centerlines of the vessels [5]. Multiscale filter responses at each of the candidates determine the likelihood that a voxel belongs to a vessel of each particular diameter. The maximal response over all the diameters (scales) is assigned to each voxel, and a surface model of the entire vascular structure is reconstructed from the estimated centerlines and diameters. After segmenting the filtered MRA image using thresholding, anisotropic diffusion techniques are used to remove noise, while preserving small vessels [6]. Lacoste et al. [7] proposed a multiscale technique based on Markov marked point processes to extract coronary arteries from 2D X-ray angiograms. Coronary vessels are modeled locally as piece-wise linear segments

of varying locations, lengths, widths, and orientations. The vessels' centerlines are extracted using a Markov object process modeled by a uniform Poisson process. Process optimization was achieved via simulated annealing using a reversible Markov chain Monto Carlo algorithm.

Centerline minimal path-based techniques [8–10] formulate the two-point centerline extraction as the minimum cost integrated along the centerline path. Gülsün and Tek [8] used multiscale medialness filters to compute the cost of graph edges in a graph-based minimal path detection method to extract the vessels' centerlines. A post-processing step, based on the length and scale of vessel centerlines, was performed to extract the full vessel centerline tree. Pèchaud et al. [9] presented an automatic framework to extract tubular structures from 2D images by the use of shortest paths. Their framework combined multiscale and orientation optimization to propagate 4D (space + scale + orientation) paths on the 2D images. Li and Yezzi [10] represented the 3D vessel surface as a 4D curve, with an additional non-spatial dimension that described the radius (thickness) of the vessel. They applied a minimal path approach to find the minimum path between user-defined end points in the 4D space. The detected path simultaneously described the vessel centerline as well as its surface. To overcome the possible shortcut problem of minimal path techniques (i.e., track a false straight shortcut path instead of following the true curved path of the vessel), Zhu and Chung [11] used a minimum average-cost path model to segment the 3D coronary arteries from CT images. In their approach, the average edge cost is minimized along paths in the discrete 4D graph constructed by image voxels and associated radii.

Deformable model approaches to 3D vascular segmentation attempt to approximate the boundary surface of the blood vessels [12–17]. An initial boundary, called a snake [18], evolves in order to optimize a surface energy that depends on image gradients and surface smoothness. To increase the capture range of the evolving boundary, Xu and Prince [19] used a gradient vector flow (GVF) field as an additional force to drive snakes into object concavities, which was later used to segment the blood vessels from 3D MRA [12]. Geodesic active contours [20] implemented with level set techniques offer flexible topological adaptability to segment the MRA images [13], including more efficient adaptation to local geometric structures represented. Fast segmentation of blood vessel surfaces is obtained by inflating a 3D balloon with fast marching methods [14].

Holtzman-Gazit et al. [15] extracted blood vessels in computed tomography angiography (CTA) images based on variational principles. Their framework combined the Chan-Vese minimal variance model with a geometric edge alignment measure and the geodesic active surface model. Manniesing et al. [16] proposed a level set based vascular segmentation method for finding vessel boundaries in CTA images. The level set function is attracted to the vessel boundaries based on a dual object (vessels) and background intensity distributions, which are estimated from the intensity histogram. Recently, Forkert et al. [17] used a vesselness filter to guide the direction of a level set to extract vessels from TOF-MRA data. Compared to scale-space filtering, deformable models produce much better experimental results, but have a common drawback, namely, manual initialization. Also, both group approaches are slow when compared to statistical approaches.

Statistical extraction of a vascular tree is completely automatic, but its accuracy depends on the underlying probability models. The MRA images are multi-modal in that the signals (intensities, or gray levels) in each region of interest (e.g., blood vessels, brain tissues, etc.) are associated with a particular dominant mode of the total marginal probability distribution of signals. To the best of our knowledge, adaptive statistical approaches for extracting blood vessels from the MRA images have been proposed so far only by Wilson and Noble [21] for the TOF-MRA data and Chung and Noble [22] for the PC-MRA data. The former approach represents the marginal data distribution with a mixture of two Gaussians and one uniform component for the stationary cerebrospinal fluid (CSF), brain tissues, and arteries, respectively, whereas the latter approach replaces the Gaussians with the more adequate Rician distribution. To identify the mixture (i.e., estimate all its parameters), a conventional EM algorithm is used in both cases. It was called a "modified EM" [21], after replacing gray levels in individual pixels considered by their initial EM scheme with a marginal gray level distribution. Actually, such a modification returns to what has been in common use for decades for

density estimation (see e.g., [23]), while the individual pixels appeared in their initial scheme only as a verbatim replica of a general EM framework.

Different hybrid approaches have attempted to combine the aforementioned approaches. For instance, a region-based deformable contour for segmenting tubular structures is derived in [24] by combining signal statistics and shape information. Law and Chung [25] guided a deformable surface model with the second-order intensity statistics and surface geometry to segment blood vessels from TOF- and PC-MRA images. A combination of a Gaussian statistical model with the maximum intensity projection images acquired at three orthogonal directions [26] allows for extracting blood vessels iteratively from images acquired by rotational angiography. Alternatively, Hu et al. [27] extracted the object boundaries by combining an iterative thresholding approach with region growing and component label analysis.

Mille et al. [28] used a generalized cylinder (GC) region-based deformable model for the segmentation of the angiogram. The GC is modeled as a central planar curve, acting as a medial axis, and variable thickness. The GC is deformed by coupling the evolution of the curve and thickness using narrow band energy minimization. This energy was transformed and derived in order to allow implementation on a polygonal line deformed using a gradient descent approach. Tyrrell et al. [29] proposed a superellipsoid geometric model to extract the vessel boundaries from in-vivo optical slice data. Their approach predicted the direction of the centerline utilizing a statistical estimator. Chen and Metaxas [30] combined a prior Gibbs random field model, marching cubes, and deformable models. First, the Gibbs model is used to estimate object boundaries using region information from 2D slices. Then, the estimated boundaries and the marching cubes technique are used to construct a 3D mesh specifying the initial geometry of a deformable model. Finally, the deformable model fits the data under the 3D image gradient forces.

Recently, Shang et al. [31] developed an active contour framework to segment coronary artery and lung vessel trees from CT images. A region, competition-based active contour model is used to segment thick vessels based on a Gaussian mixture model of the gray-level distribution of the vessel region. Then, a multiscale vector field, derived from the Hessian matrix of the image intensity, is used to guide the active contour through thin vessels. Finally, the surface of the vessel is smoothed using a "vesselness" function that selects between a minimal principal curvature and a mean curvature criterion. Gao et al. [32] used a statistical model to find the main cerebrovascular structure from TOF-MRA. Then, an edge-strength function that incorporates statistical region distribution and gradient information is used to guide a 3D geometric deformable model to deal with the under-segmentation problem. Dufour et al. [33] proposed an interactive segmentation method that incorporates component-trees and example-based segmentation to extract the cerebrovascular tree from TOF-MRA data. Liao et al. [34] used a parametric intensity model to extract thick and most thin vessels from seven Tesla MRA images. To fill the remaining gaps, a generative Markov random field method was applied.

The previous overview shows the following limitations of the existing approaches:

1. Most of them presume only a single image type (e.g., TOF- or PC-MRA).
2. Most of them require user interaction to initialize a vessel of interest.
3. Some deformable models assume circular vessel cross-sections; this holds for healthy people, but not for patients with a stenosis or an aneurysm.
4. All but statistical approaches are computationally expensive.
5. Known statistical approaches use only predefined probability models that cannot fit all cases, because actual intensity distributions for blood vessels depend on the patient, scanner, and scanning parameters.

This chapter derives a more general probabilistic model of blood vessels on MRA images to account for normal and abnormal states of the vascular system, that is, for both laminar and turbulent blood flow without and with stenosis. To accurately separate blood vessels from other

regions-of-interest, the marginal distribution is precisely approximated with an adaptive linear combination of the derived model and a number of dominant and subordinate discrete Gaussians rather than with a mixture of only three pre-selected Gaussian and uniform or Rician components. Experiments show that our adaptive model results in significantly improved segmentation of MRA images. The rest of the chapter is organized as follows: in Sections 2.2 and 2.3, we discuss in detail the proposed probability model of vascular signals and the adaptive model of multi-modal MRA. Section 2.4 presents the experiments of proposed segmentation methodology of the blood vessels. Section 2.5 explains the validation, and compares our results with other alternatives. Finally, conclusions are drawn in Section 2.6.

2.2 PROBABILITY MODEL OF VASCULAR SIGNALS

Let q; $q \in \mathbf{Q} = \{0,1,\ldots,Q-1\}$, be the Q-ary signals (image intensity, or gray level). Conventional models of intensities for vessel voxels in [1], [21] assume laminar blood flow with parabolic velocity flow through a circular cross-section of the vessel [2]. Then the intensity profile for a vessel is $q_r = q_{\max}(1-\frac{r^2}{R^2})$ where q_r is the intensity at the distance r from the center of a vessel of radius R and the constant $q_{\max} \leq Q-1$ depends on the scanner. In this case the intensities over the circular cross-section are distributed uniformly with the probability density: $\varphi_{\text{lam}}(q) = \frac{1}{q_{\max}}$ in the range $[0, q_{\max}]$. Nonetheless, the laminar flow holds only for subjects with normal vascular systems [3].

Various diseases change either blood velocity or viscosity or both and cause the turbulent flow. Turbulence depends on the diameter of vessel and blood velocity and viscosity. For example, due to lower blood viscosity, anemia leads frequently to turbulence. Artery constrictions increasing blood velocity (see Figure 2.1) and vascular diseases such as thrombosis, embolism, thyrotoxicosis, atherosclerosis, and valvular heart diseases also result in turbulence [3].

Typically, the turbulence adds a uniform random factor ξ in the range $[-1,1]$ to the parabolic intensity profile [3]:

$$q_r = q_{\max}\left(1-\xi^2\frac{r^2}{R^2}\right) \tag{2.1}$$

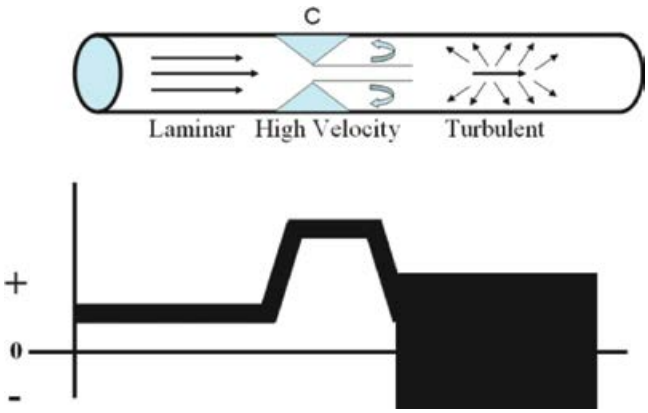

FIGURE 2.1 Influence of constriction (C) on the blood velocities in a vessel (arrows indicate flow directions) and ranges of velocities at each cross-section along the vessel [3].

To derive the probability density of the intensities in Eq. (2.1) over the vessel, let $a_r = \pi r^2$ and $a_{\max} = \pi R^2$ be a circular area of radius r and the maximum area for the circular vessel cross-section for radius R, respectively. Let $f(q|a_r)$, $\varphi_{\text{tur}}(q)$, and $\Phi_{\text{tur}}(x) = \Pr(q \le x) = \int_0^x \varphi_{\text{tur}}(q)dq$ denote the conditional density of intensities on the border of a_r, the unconditional density, and the probability of the intensities over the whole vessel, respectively.

The density of $y = \xi^2 \in [0,1]$ is $p(y) = (2\sqrt{y})^{-1}$ because $\Pr(y \le x) \equiv \Pr(-\sqrt{x} \le \xi \le \sqrt{x}) = 2\sqrt{x}$. In accord with Eq. (2.1), $y = \frac{a_{\max}}{a_r}(1 - \frac{q_r}{q_{\max}})$, and the intensities $q_r \in [q_{\max}(1 - \frac{a_r}{a_{\max}}), q_{\max}]$ have the conditional density $f(q|a_r) = \frac{1}{2}\sqrt{\frac{a_{\max}}{a_r q_{\max}}}\frac{1}{\sqrt{q_{\max} - q}}$. The probability distribution of the intensities over the vessel area is then:

$$\Phi_{\text{tur}}(x) = \frac{1}{a_{\max}} \int_0^{a_{max}} da_r \int_0^x f\left(q|a_r\right) dq = 2 - \frac{x}{q_{max}} - 2\sqrt{1 - \frac{x}{q_{max}}} \tag{2.2}$$

Therefore, the unconditional probability density is:

$$\varphi_{\text{tur}}(q) = \frac{1}{\sqrt{q_{\max}(q_{\max} - q)}} - \frac{1}{q_{max}} \tag{2.3}$$

Since the MRA may represent both normal and abnormal subjects, the model of vascular signals can be built as a mixture of the laminar and turbulent components:

$$\varphi(q) = (1-\beta)\varphi_{\text{lam}}(q) + \beta\varphi_{\text{tur}}(q) \equiv \frac{1-2\beta}{q_{\max}} + \frac{\beta}{\sqrt{q_{\max}(q_{\max} - q)}} \tag{2.4}$$

Probability densities for different mixing weights $\beta \in [0,1]$ in this model are presented in Figure 2.2.

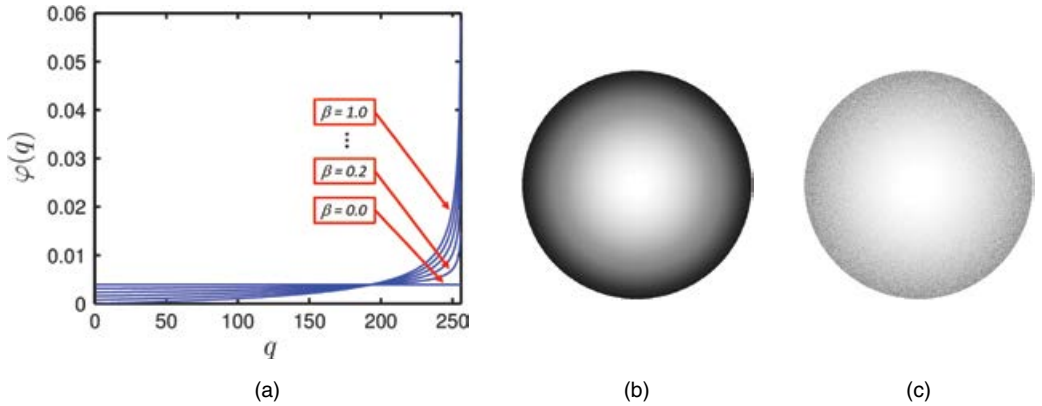

FIGURE 2.2 Probability densities for Eq. (2.4) with $\beta = 0.0, 0.2, 0.4, \ldots, 1.0$ and synthetic cross-section images of a blood vessel with laminar ($\beta = 0$, *b*) and turbulent ($\beta = 1$, *c*) flow.

2.3 ADAPTIVE MODEL OF MULTI-MODAL MRA

MRA images contain three regions-of-interest (signal classes): (*i*) darker CSF from bones and fat, (*ii*) brain tissues (gray matter and white mater), and (*iii*) brighter blood vessels. Marginal signal distributions for the first two classes are typically of intricate shape that differs greatly from the conventional individual Gaussians in [1], [21]. The model in Eq. (2.4) describes only circular vessels and should have additional terms changing its shape to account for variations of the blood flow due to stenosis. Generally, no predefined probability model can accurately describe all the signal variations due to changes in blood velocity and viscosity, vessel diameter, and scanner sensitivity.

Therefore, we propose an adaptive probability model to handle both normal and abnormal MRA images. It mixes three submodels representing the above-mentioned major image areas (abbreviated by "csf", "bt", and "bv", respectively):

$$p_{\mathrm{MRA}}(q) = \sum_{i \in \{\mathrm{bv,csf,bt}\}} \alpha_i \varphi_i(q) \tag{2.5}$$

where α_i are the mixing weights ($\alpha_1 + \alpha_2 + \alpha_3 = 1$). Each of the three submodels $\varphi_i(q)$ is a mixture of one dominant component with a linear combination of several sign-alternate subordinate components chosen to closely approximate corresponding parts of an empirical marginal signal distribution $F_{\mathrm{emp}} = (f_{\mathrm{emp}}(q) : q \in \mathbf{Q})$.

The dominant component for the blood vessels submodel is the discrete parametric distribution $\Psi_{\theta,\mathrm{bv}} = (\psi_{\mathrm{bv}}(q|\theta) : q = 0, \ldots, q_{\max})$ with a shorthand notation $\theta = (\beta, q_{\max})$ for its parameters. It is obtained by integrating the density in Eq. (2.4) over unit intervals corresponding to the integer values $q \in \mathbf{Q}$:

$$\psi_{\mathrm{bv}}(q|\theta) = \int_{q}^{q+1} \varphi_{\mathrm{bv}}(q)dq \equiv (1-\beta)\frac{1}{q_{\max}+1} + \beta\left(2\left(\sqrt{1-\frac{q}{q_{\max}+1}} - \sqrt{1-\frac{q+1}{q_{\max}+1}}\right) - \frac{1}{q_{\max}+1}\right)$$

Because typically $q_{\max} = Q-1$, this distribution has only a single parameter β.

Two other dominant components are discrete Gaussians (DGs) defined in [36] as a discrete probability distribution $\Psi_\theta = (\psi(q|\theta) : q \in \mathbf{Q})$ integrating a normal parametric density over unit intervals: $\psi(q|\theta) = \Phi_\theta(q+0.5) - \Phi_\theta(q-0.5)$ for $q = 1, \ldots, Q-2$, $\psi(0|\theta) = \Phi_\theta(0.5)$, $\psi(Q-1|\theta) = 1 - \Phi_\theta(Q-1.5)$ where $\Phi_\theta(q)$ is the cumulative Gaussian probability function with parameters $\theta = (\mu, \sigma^2)$, that is, the mean μ, and variance σ^2.

The subordinate part of each submodel $\varphi_i(q)$ is a linear combination of discrete Gaussians (LCDGs) with $C_{i,\mathrm{p}}$ positive and $C_{i,\mathrm{n}}$ negative components under obvious restrictions on their weights. To identify the three submodels (estimate parameters of their dominant components and numbers and parameters of the positive and negative subordinate components), we use the EM-based techniques introduced in [36]. The only difference here is in the non-analytical estimation of the parameter β on the M-steps using the gradient-based search for the global maximum of the goal likelihood function $G(\beta) = \sum_{q=0}^{q_{\max}} \pi(i = \mathrm{bv}|q) f_{\mathrm{emp}}(q) \ln \psi_{\mathrm{bv}}(q|\beta)$ where $\pi(i|q)$ is the responsibility of the submodel i for q [37].

2.4 SEGMENTATION OF BLOOD VESSELS

To justify the adaptive model of Eq. (2.5), Figure 2.3 shows how different scanners affect the measurements. These three TOF-MRA slices were acquired for a subject with anemia using a Picker 1.5T Edge MRI scanner with resolution of $512 \times 512 \times 93$, a subject with parietal lobe hemorrhage

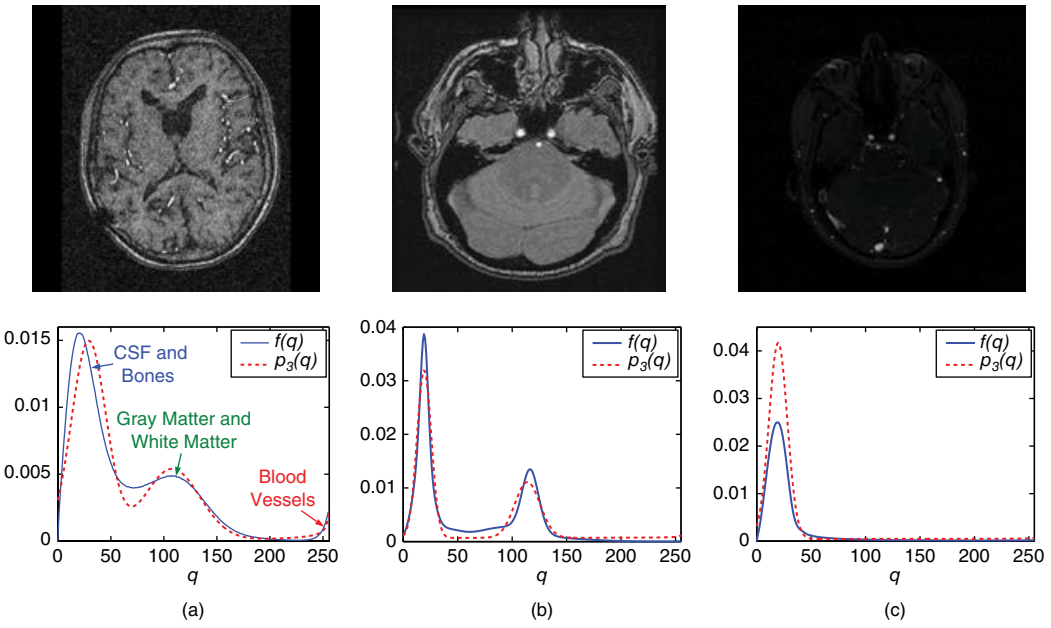

FIGURE 2.3 Three TOF-MRA slices with their empirical distributions $f_{\text{emp}}(q)$ overlaid with the dominant mixtures $p_3(q)$.

using a Signa Horizon GE 1.5T scanner with resolution $512 \times 512 \times 150$, and a normal subject using a state-of-the-art Siemens 3T scanner with resolution $512 \times 512 \times 125$, respectively. The slice thickness is 1 mm in all the cases.

The models of Eq. (2.5) were built with the EM-based approach (see [36] for detail). Figure 2.3 presents both the marginal empirical distributions F_{emp} and the initial three-component dominant mixtures for them containing the two Gaussian components and our model of blood vessels in Eq. (2.4). The estimated parameters β of the latter are 0.92, 0.18, and 0.038 for the slices A, B, and C in Figure 2.3, respectively, which reflects levels of blood turbulence expected from physics-based considerations.

Figure 2.4 illustrates basic stages of our EM-based initialization and final refinement of the whole model of Eq. (2.5) for the slice A. Given the dominant mixture $P_3 = (p_3(q) : q \in \mathbf{Q})$, the number and the parameters of the subordinate DGs are estimated from the absolute deviations $f_{\text{emp}}(q) - p_3(q)$ by minimizing the residual approximation error. In this case the eight DGs are added to the dominant mixture to obtain the best initial 3-class model. The final model is obtained using the EM-based refinement (here, the first nine refining iterations increase the log-likelihood of the model from -5.9 to -4.4. The final submodels of each class provide the best segmentation thresholds $t_1 = 64$ and $t_2 = 187$.

To highlight the advantages of our approach, Figure 2.5 shows results obtained with the model of Wilson and Noble [21] (the mixture of two Gaussians and $\varphi_{\text{lam}}(q)$). The quality is evaluated by the Levy distance [38] and the absolute error between the empirical distribution and the estimated 3-class model. In this example, the Wilson-Noble's and our approach result in the Levy distance of 0.14 and 0.0002 and the absolute error of 0.14 and 0.004, respectively. The lower Levy distance and absolute error suggest our approach yields the notably better approximation, ensuring more accurate separation of the blood vessels from their background. As shown later in Figure 2.8, the typically higher separation threshold of the Wilson-Noble's approach, e.g. $t_2 = 203$ versus our $t_2 = 187$ in this particular example, results in many missed blood vessels.

Figures 2.6 and 2.7 show our and Wilson-Noble's models estimated for the slices in Figure 2.3 B and C, respectively. In these examples, our models are more accurate. We compared both the approaches on 50 real MRA data sets, too. Results of the six tests in Figure 2.8 as well as other tests

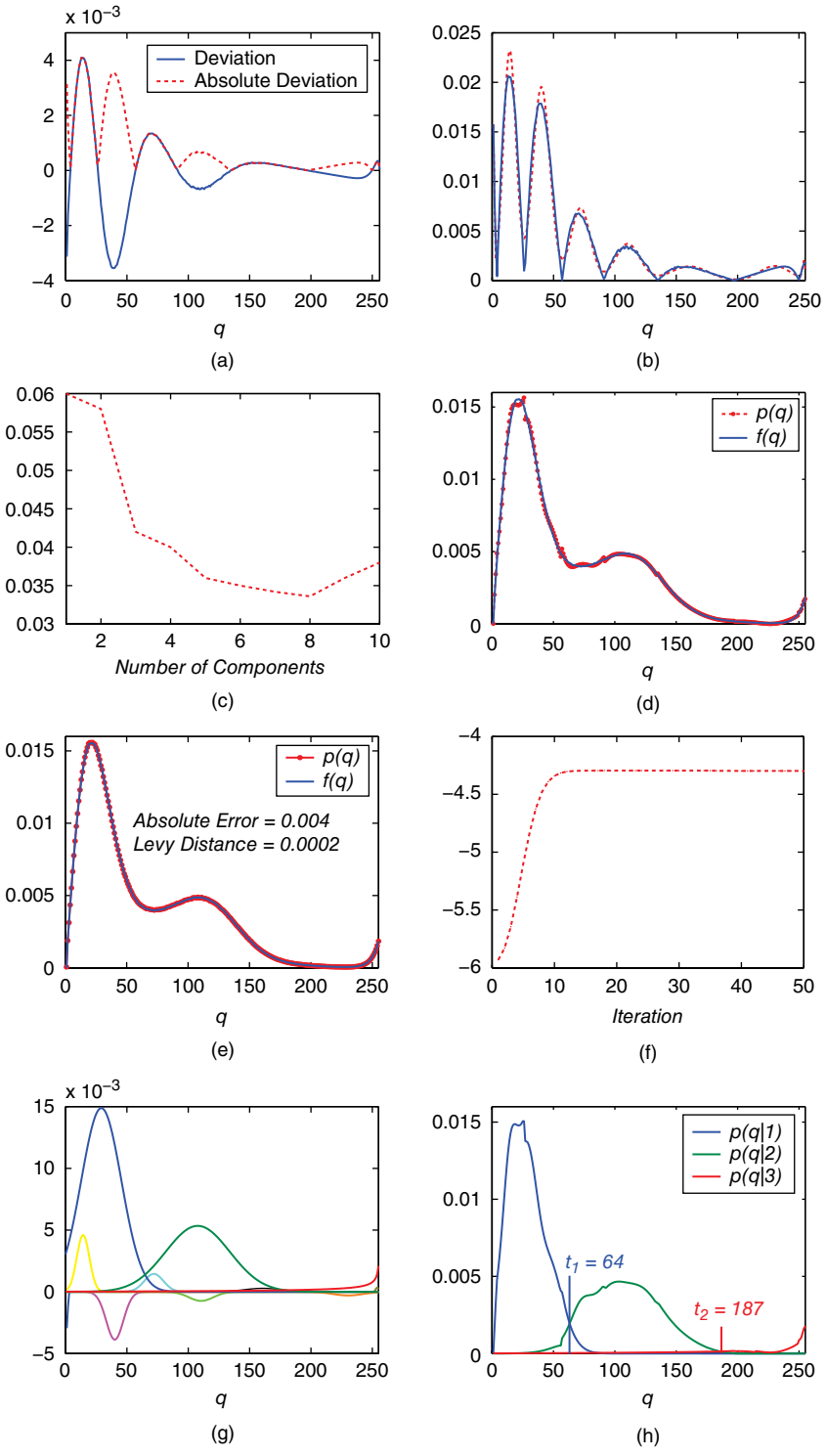

FIGURE 2.4 Deviations and absolute deviations $f_{\text{emp}}(q) - p_3(q)$ (a), the best mixture (b) to model the absolute deviations, the residual absolute error (c) in function of the number of DGs approximating the deviations, the initial (d) and final (e) 3-class model w.r.t. the empirical distribution, the log-likelihood dynamics (f) for the model refinement, the individual components (g), and the class submodels (h) for the refined model.

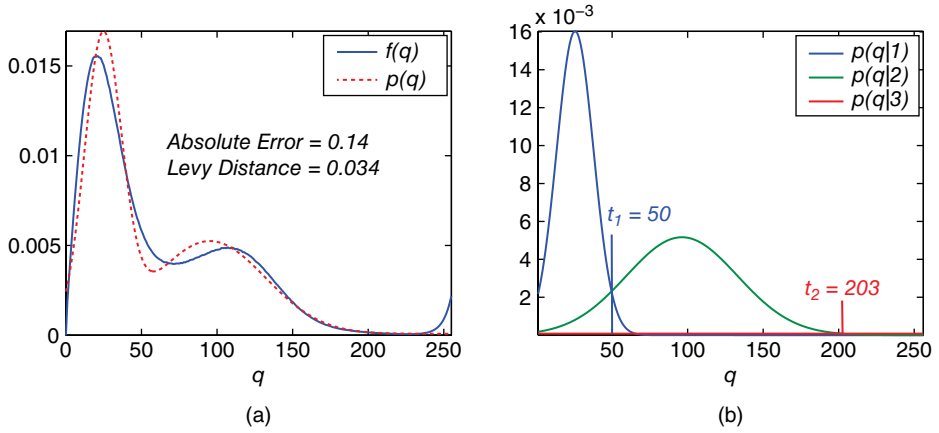

FIGURE 2.5 Estimated Wilson-Noble's model [21] (a) and its class submodels (b).

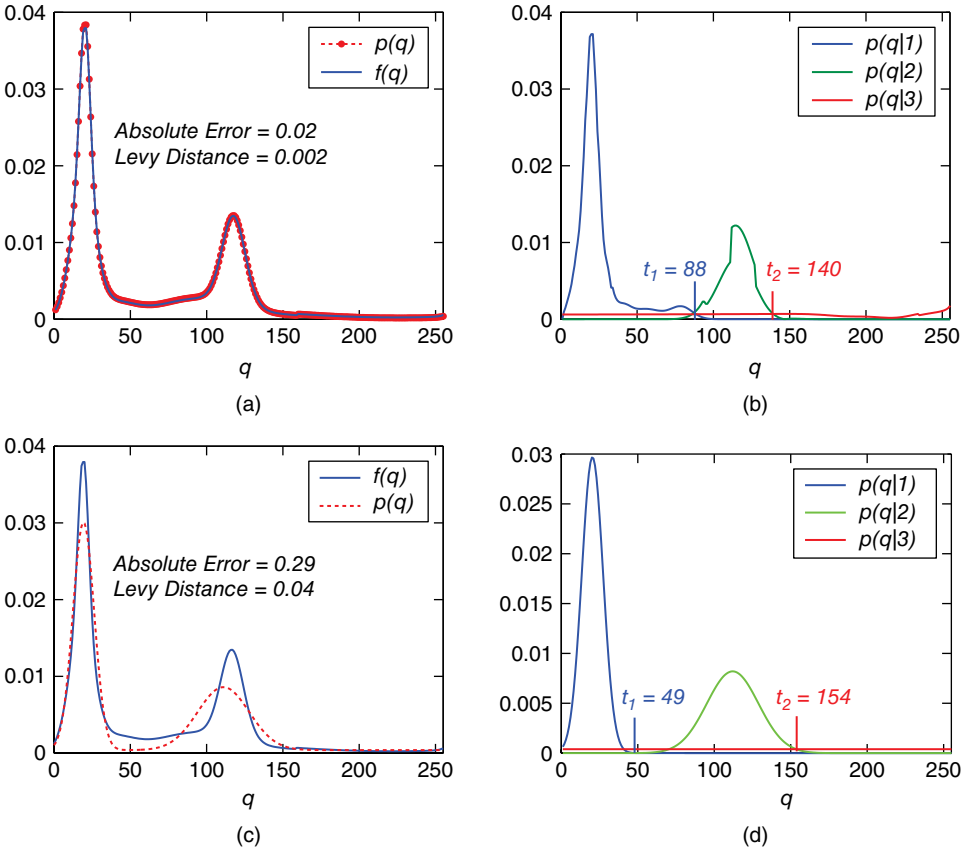

FIGURE 2.6 Slice in Figure 2.3,B: our final (a,b) and the Wilson-Noble's (c,d) 3-class model (a,c) with the individual class submodels (b,d).

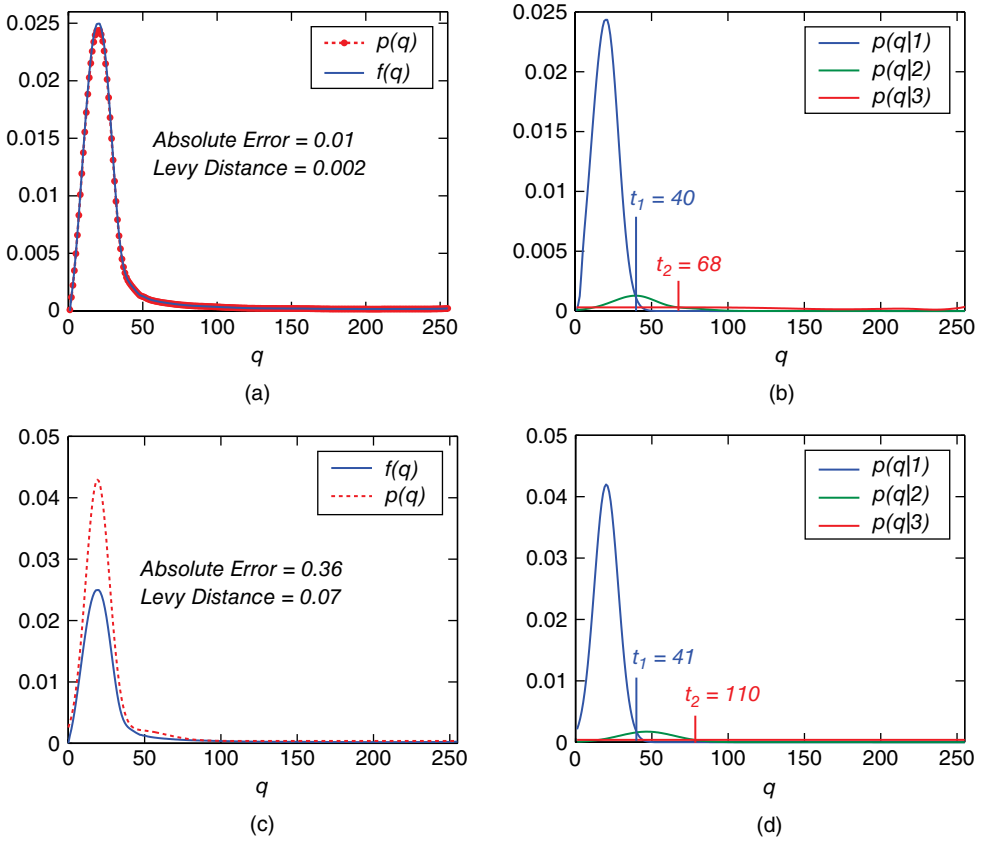

FIGURE 2.7 Slice in Figure 2.3,C: our final (a,b) and the Wilson-Noble's (c,d) 3-class model (a,c) with the individual class submodels (b,d).

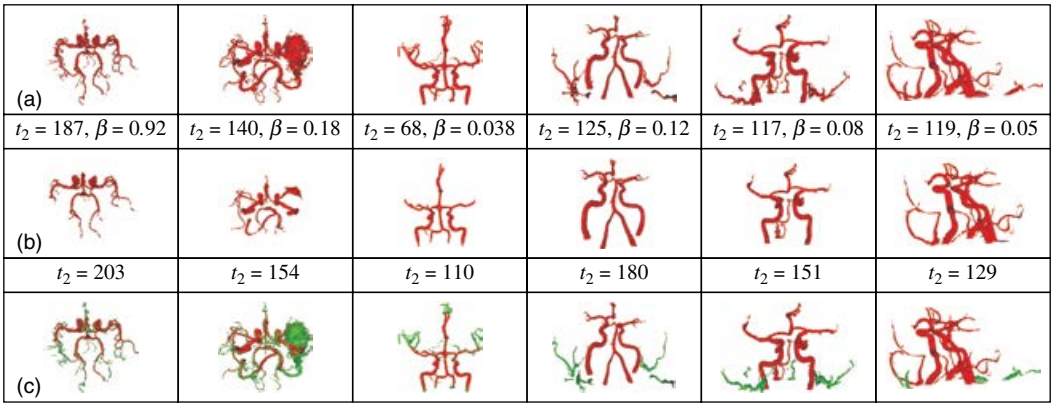

FIGURE 2.8 Each column relates to one patient: our (a) and the Wilson-Noble's (b) segmentation, and their differences (c): the red voxels are detected by the both approaches and the green ones are missed by the latter one.

confirm that the Wilson-Noble's approach fails to detect large fractions of vascular trees validated by an expert–radiologist. Our approach is more accurate in restoring detail of the brain vascular tree.

2.5 VALIDATION

It is very difficult to accurately get manually segmented **complete** vascular trees to validate our algorithm. To quantitatively evaluate its performance, we created three 3D phantoms in Figure 2.9 with geometrical shapes similar to blood vessels with known ground truth. These three phantoms mimic bifurcations, zero and high curvature existing in any vascular system, and their changing radii simulate both large and small blood vessels. To make the distributions of these three phantoms similar to MRA images, first we compute the empirical class distributions $p(q|\text{bv})$, $p(q|\text{csf})$, and $p(q|\text{bt})$ from the signals that represent blood vessels, CSF, and brain tissues from the MRA images segmented by a radiologist (we have selected 200 images from a data set of over 5,000 images of 50 subjects). Then, the phantoms signal are generated by using the inverse mapping methods. The resulting phantom's histograms are similar to those in Figure 2.4(e).

The total segmentation error is evaluated by a percentage of erroneous voxels with respect to the overall number of voxels in the ground truth 3D phantom. Figure 2.9 shows that, on average, our approach is 14 times more accurate than the Wilson-Noble approach. Table 2.1 gives error statistics for 440 synthetic slices segmented in the phantoms with both approaches and compares them to three other known segmentation algorithms.

Therefore, comparing to the more conventional probability model in [21], our adaptive model notably improves the accuracy of segmenting the MRA images acquired with different scanners. The conventional approaches either assume a purely laminar blood flow or pre-select a simple parametric distribution in attempts to take account of actual signal features. By contrast, our model is

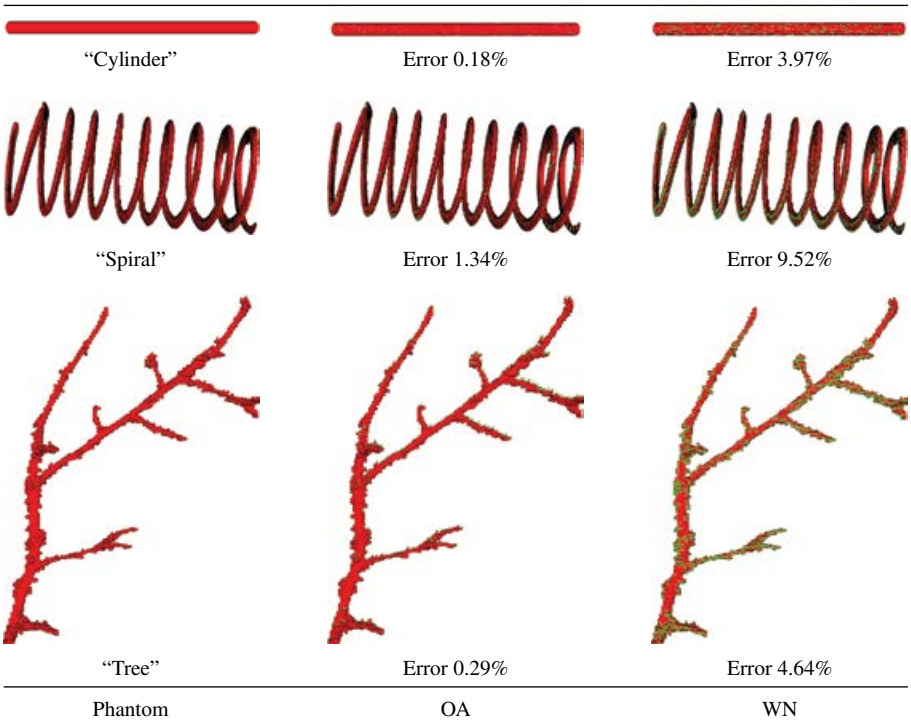

FIGURE 2.9 Segmentation of 3D phantoms with our (OA) and the Wilson-Noble's (WN) approaches (the same color code as in Figure 2.8).

TABLE 2.1

Minimum ε_n, maximum ε_x, and mean $\bar{\varepsilon}$ segmentation errors, and standard deviations σ of errors on the geometrical 3D TOF-MRA phantoms for our (OA) and the Wilson–Noble's (WN) approaches as well as for three other segmentation algorithms using iterative thresholding (IT) [27] and gradient based (DMG) [18] or gradient vector flow based (GVF) [19] deformable models.

	OA	WN	IT	DMG	GVF
$\varepsilon_n, \%$	**0.09**	0.10	4.81	10.1	2.45
$\varepsilon_x, \%$	**2.10**	12.1	33.1	21.8	13.6
$\bar{\varepsilon}, \%$	**0.61**	6.20	18.8	11.9	5.96
$\sigma, \%$	**0.93**	7.40	8.41	3.79	2.79

derived from the physical description of the blood flow and thus can accurately handle both normal and abnormal cases. Moreover, the estimated weights $\beta \in [0,1]$ in Eq. (2.4) provide a natural measure of the percentage of abnormality of the blood flow for a particular subject.

2.6 CONCLUSION

We presented a new physically justified adaptive probability model of blood vessels on magnetic resonance angiography (MRA) images. It accounts for laminar (normal subjects) and turbulent blood flow (abnormal cases like anemia or stenosis). Better accuracy of segmenting MRA images with our approach compared to more conventional algorithms is confirmed by experts-radiologists and also is validated using special 3D geometrical phantoms.

Our present C++ implementation of the algorithm on a single 2.4 GHz Pentium 4 CPU with 512 MB RAM takes about 49 sec to segment 93 TOF-MRA slices of size 512×512 pixels each.

The proposed model is suitable for segmenting both TOF-MRA and PC-MRA images. Experiments with the latter type was not included in this chapter due to space limitations. But the algorithm's code, sample data, and segmentation results for all the MRA images will be provided in our web page. This work could also be applied to various other applications in medical imaging, such as the kidney, the heart, the prostate, the lung, and the retina.

One application is renal transplant functional assessment. Chronic kidney disease (CKD) affects about 26 million people in the U.S. with 17,000 transplants being performed each year. In renal transplant patients, acute rejection is the leading cause of renal dysfunction. Given the limited number of donors, routine clinical post-transplantation evaluation is of immense importance to help clinicians initiate timely interventions with appropriate treatment and thus prevent the graft loss. In recent years an increased area of research has been dedicated to developing noninvasive CAD systems for renal transplant function assessment, utilizing different image modalities (e.g., ultrasound, computed tomography (CT), MRI, etc.). Accurate assessment of renal transplant function is critically important for graft survival. Although transplantation can improve a patient's well-being, there is a potential post-transplantation risk of kidney dysfunction that, if not treated in a timely manner, can lead to the loss of the entire graft, and even patient death. Thus, accurate assessment of renal transplant function is crucial for the identification of proper treatment. In recent years, an increased area of research has been dedicated to developing non-invasive image-based CAD systems for the assessment of renal transplant function. In particular, dynamic and diffusion MRI-based systems have been clinically used to assess transplanted kidneys with the advantage of providing information on each kidney separately. For more details about renal transplant functional assessment, please read [40]–[57], [57]–[65].

The heart is also an important application to this work. The clinical assessment of myocardial perfusion plays a major role in the diagnosis, management, and prognosis of ischemic heart disease patients. Thus, there have been ongoing efforts to develop automated systems for accurate analysis of myocardial perfusion using first-pass images [66]–[82].

Another application for this work could be the detection of retinal abnormalities. The majority of ophthalmologists depend on visual interpretation for the identification of disease types. However, inaccurate diagnosis will affect the treatment procedure, which may lead to fatal results. Hence, there is a crucial need for computer automated diagnosis systems that yield highly accurate results. Optical coherence tomography (OCT) has become a powerful modality for the non-invasive diagnosis of various retinal abnormalities such as glaucoma, diabetic macular edema, and macular degeneration. The problem with diabetic retinopathy (DR) is that the patient is not aware of the disease until the changes in the retina have progressed to a level that treatment tends to be less effective. Therefore, automated early detection could limit the severity of the disease and assist ophthalmologists in investigating and treating it more efficiently [83], [84].

Abnormalities of the lung could also be another promising area of research and a related application to this work. Radiation-induced lung injury is the main side effect of radiation therapy for lung cancer patients. Although higher radiation doses increase the radiation therapy effectiveness for tumor control, this can lead to lung injury as a greater quantity of normal lung tissues is included in the treated area. Almost 1/3 of patients who undergo radiation therapy develop lung injury following radiation treatment. The severity of radiation-induced lung injury ranges from ground-glass opacities and consolidation at the early phase to fibrosis and traction bronchiectasis in the late phase. Early detection of lung injury will thus help to improve management of the treatment [85]–[125].

This work can also be applied to other brain abnormalities, such as dyslexia and autism. Dyslexia is one of the most complicated developmental brain disorders that affect children's learning abilities. Dyslexia leads to the failure to develop age-appropriate reading skills in spite of a normal intelligence level and adequate reading instructions. Neuropathological studies have revealed an abnormal anatomy of some structures, such as the Corpus Callosum in dyslexic brains. There has been a lot of work in the literature that aims at developing CAD systems for diagnosing such disorders, along with other brain disorders [126]–[148].

References

1. A. Chung, J. A. Noble, and P. Summers, "Fusing speed and phase information for vascular segmentation of phase contrast MR angiograms," *Medical Image Analysis*, vol. 6, 2002, pp. 109–128.
2. C. G. Caro et al., *The Mechanics of the Circulation*, Oxford University Press, 1978.
3. W. F. Ganong, *Review of Medical Physiology*, McGraw-Hill, 15th edition, 1991.
4. Y. Sato, S. Nakajimaa, N. Shiragaa, H. Atsumia, S. Yoshidab, T. Kollerc, G. Gerigc, and R. Kikinisa, "Three-dimensional multi-scale line filter for segmentation and visualization of curvilinear structures in medical images," *Med. Image Anal.*, vol. 2, no. 2, 1998, pp. 143–168.
5. K. Krissian, G. Malandain, N. Ayache, R. Vaillant, and Y. Trousset, "Model based multiscale detection of 3D vessels," in *Proc. IEEE Conf. Comput. Vision and Pattern Recognition*, 1998, pp. 722–727.
6. F. Catté, P-L. Lions, J.-M. Morel, and T. Coll, "Image selective smoothing and edge detection by nonlinear diffusion," *SIAM J. Numerical Anal.*, vol. 29, no. 1, 1992, pp. 182–193.
7. C. Lacoste, G. Finet, and I. E. Magnin, "Coronary tree extraction from X-ray angiograms using marked point processes," in *Proc. IEEE Int. Symp. Biomed. Imaging*, 2006, pp. 157–160.
8. M. A. Gülsün and H. Tek, "Robust vessel tree modeling," in *Proc. Int. Conf. Med. Image Comput. Computer–Assisted Intervention*, 2008, pp. 602–611.
9. M. Pèchaud, R. Keriven, and G. Peyré, "Extraction of tubular structures over an orientation domain," in *Proc. IEEE Conf. Comput. Vision and Pattern Recognition*, 2009, pp. 336–342.
10. H. Li and A. Yezzi, "Vessels as 4-D curves: global minimal 4-D paths to extract 3-D tabular surfaces and centerlines," *IEEE Trans. Med. Imag.*, vol. 26, no. 9, 2007, pp. 1213–1223.
11. N. Zhu and A. C. Chung, "Minimum average-cost path for real time 3D coronary artery segmentation of CT images," in *Proc. Int. Conf. Med. Image Comput. Computer–Assisted Intervention*, 2011, pp. 436–444.

12. A. C. Jalba, M. H. Wilkinson, J. B. Roerdink, "CPM: a deformable model for shape recovery and segmentation based on charged particles," *IEEE Trans. Pattern Analysis and Machine Intell.*, vol. 26, 2004, pp. 1320–1335.
13. L. M. Lorigo, O. D. Faugeras, W. E. Grimson, R. Keriven, R. Kikinis, A. Nabavi, and C. F. Westin, "Curves: curve evolution for vessel segmentation," *Med. Image Anal.*, vol. 5, no. 3, 2001, pp. 195–206.
14. T. Deschamps and L. D. Cohen, "Fast extraction of tubular and tree 3D surfaces with front propoagation methods," in *Proc. IEEE Int. Conf. Pattern Recognition*, 2002, pp. 731–734.
15. M. Holtzman-Gazit, R. Kimmel, N. Peled, and D. Goldsher, "Segmentation of thin structures in volumetric medial images," *IEEE Trans. Image. Process.*, vol. 15, no. 3, 2006, pp. 354–363.
16. R. Manniesing, B. K. Velthuis, M. S. van Leeuwen, I. C. van der Schaaf, P. J. van Laar, and W. J. Niessen, "Level set based cerebral vasculature segmentation and diameter quantification in CT angiography," *Med. Image. Anal.*, vol. 10, no. 2, 2006, pp. 200–214.
17. N. D. Forkert, D. Säring, T. Illies, J. Fiehler, J. Ehrhardt, H. Handels, and A. Schmidt-Richberg, "Direction-dependent level set segmentation of cerebrovascular structures," in *Proc. SPIE'11, Image Processing: Medical Imaging*, 2011, vol. 7962, pp. 1–8.
18. M. Kass, A. Witkin, and D. Terzopoulos, "Snakes: active contour models," *Int. J. Comput. Vision*, vol. 1, 1988, pp. 321–331.
19. C. Xu and J. L. Prince, "Snakes, shapes, and gradient vector flow," *IEEE Trans. Image Process.*, vol. 7, no. 3, 1998, pp. 359–369.
20. V. Caselles, R. Kimmel, and G. Sapiro, "Geodesic active contours," *Int. J. Comput. Vision*, vol. 22, no. 1, 1997, pp. 61–79.
21. D. L. Wilson and J. A. Noble, "An adaptive segmentation algorithm for time-of-flight MRA data," *IEEE Trans. Med. Imaging*, vol. 18, no. 10, 1999, pp. 938–945.
22. A. C. S. Chung and J. A. Noble, "Statistical 3D vessel segmentation using a Rician distribution," in *Proc. Int. Conf. Med. Image Comput. Computer–Assisted Intervention*, 1999, pp. 82–89.
23. A. Webb, *Statistical Pattern Recognition*, J. Wiley & Sons, New York, 2002.
24. D. Nain, A. Yezzi, and G. Turk, "Vessels segmentation using a shape driven flow," in *Proc. Int. Conf. Med. Image Comput. Computer–Assisted Intervention*, 2004, pp. 51–59.
25. M. W. Law and A. C. Chung, "A deformable surface model for vascular segmentation," in *Proc. Int. Conf. Med. Image Comput. Computer–Assisted Intervention*, 2009, pp. 59–67.
26. R. Gan, A. C. Chung, C. K. Wong, and S. C. Yu, "Vascular segmentation in three-dimensional rotational angiography based on maximum intensity projections," in *Proc. IEEE Int. Symp. Biomed. Imaging*, 2004, pp. 133–136.
27. S. Hu and E. A. Hoffman, "Automatic lung segmentation for accurate quantization of volumetric X-ray CT images," *IEEE Trans. Med. Imag.*, vol. 20, no. 6, 2001, pp. 490–498.
28. J. Mille, R. Bonè, and L. D. Cohen, "Region-based 2D deformable generalized cylinder for narrow structures segmentation," in *Proc. Eur. Conf. Comput. Vision*, 2008, pp. 392–404.
29. J. Tyrrell, E. di Tomaso, D. Fuja, R. Tong, K. Kozak, R. K. Jain, and B. Roysam, "Robust 3-D modeling of vascuature imagery using superellipsoids," *IEEE Trans. Med. Imaging*, vol. 26, no. 2, 2007, pp. 223–237.
30. T. Chen and D. N. Metaxas, "Gibbs prior models, marching cubes, and deformable models: a hybrid framework for 3D medical image segmentation," in *Proc. Int. Conf. Med. Image Comput. Computer–Assisted Intervention*, 2003, pp. 703–710.
31. Y. Shang, R. Deklerck, E. Nyssen, A. Markova, J. de Mey, X. Yang, and K. Sun, "Vascular active contour for vessel tree segmentation," *IEEE Trans. Biomed. Eng.*, vol. 58, no. 4, 2011, pp. 1023–1032.
32. X. Gao, Y. Uchiyama, X. Zhou, T. Hara, T. Asano, and H. Fujita, "A fast and fully automatic method for cerebrovascular segmentation on time-of-flight (TOF) MRA image," *J. Digital Imaging*, vol. 24, no. 4, 2011, pp. 609–625.
33. A. Dufour, N. Passat, B. Naegel, and J. Baruthio, "Interactive 3D brain vessel segmentation from an example," in *Proc. IEEE Int. Symp. Biomed. Imaging*, 2011, pp. 1121–1124.
34. W. Liao, K. Rohr, C.-K. Kang, Z.-H. Cho, and S. Wörz, "A generative MRF approach for automatic 3D segmentation of cerebral vasculature from 7 Tesla MRA images," in *Proc. IEEE Int. Symp. Biomed. Imaging*, 2011, pp. 2041–2044.
35. G. Gimel'farb, A. A. Farag, and A. El-Baz, "Expectation-maximization for a linear combination of Gaussians," in *Proc. IEEE Int. Conf. Pattern Recognition*, 2004, vol. 3, pp. 422–425.
36. M. Sabry, C. B. Sites, A. A. Farag, S. Hushek, and T. Moriaty, "A fast automatic method for 3D volume segmentation of the human cerebrovascular," in *Proc. Computer–Assisted Radiology and Surgery*, 2002, pp. 382–387.

37. G. Gimelfarb, A. A. Farag, and A. El-Baz, "Expectation-maximization for a linear combination of Gaussians," in *Proc. IEEE Int. Conf. Pattern Recognit*, 2004, vol. 3, pp. 422–425.
38. J. W. Lamperti, *Probability*, J. Wiley & Sons, New York, 1996.
39. T. Hastie, R. Tibshirani, and J. Friedman, *The Elements of Statistical Learning*, Springer, New York, 2001.
40. A. M. Ali, A. A. Farag, and A. El-Baz, "Graph cuts framework for kidney segmentation with prior shape constraints," in *Proceedings of International Conference on Medical Image Computing and Computer-Assisted Intervention* (MICCAI'07), Brisbane, Australia, 2007, vol. 1, pp. 384–392.
41. A. S. Chowdhury, R. Roy, S. Bose, F. K. A. Elnakib, and A. El-Baz, "Non-rigid biomedical image registration using graph cuts with a novel data term," in *Proceedings of IEEE International Symposium on Biomedical Imaging: From Nano to Macro* (ISBI'12), Barcelona, Spain, 2012, pp. 446–449.
42. A. El-Baz, A. A. Farag, S. E. Yuksel, M. E. A. El-Ghar, T. A. Eldiasty, and M. A. Ghoneim, "Application of deformable models for the detection of acute renal rejection," in A. A. Farag, and J. S. Suri, eds., *Deformable Models*, vol. 1, 2007, pp. 293–333.
43. A. El-Baz, A. Farag, R. Fahmi, S. Yuksel, M. A. El-Ghar, and T. Eldiasty, "Image analysis of renal DCE MRI for the detection of acute renal rejection," in *Proceedings of IAPR International Conference on Pattern Recognition* (ICPR'06), Hong Kong, 2006, pp. 822–825.
44. A. El-Baz, A. Farag, R. Fahmi, S. Yuksel, W. Miller, M. A. El-Ghar, T. El-Diasty, and M. Ghoneim, "A new CAD system for the evaluation of kidney diseases using DCE-MRI," in *Proceedings of International Conference on Medical Image Computing and Computer-Assisted Intervention* (MICCAI'08), Copenhagen, Denmark, 2006, pp. 446–453.
45. A. El-Baz, G. Gimel'farb, and M. A. El-Ghar, "A novel image analysis approach for accurate identification of acute renal rejection," in *Proceedings of IEEE International Conference on Image Processing* (ICIP'08), San Diego, California, 2008, pp. 1812–1815.
46. A. El-Baz, G. Gimel'farb, and M. A. El-Ghar, "Image analysis approach for identification of renal transplant rejection," in *Proceedings of IAPR International Conference on Pattern Recognition* (ICPR'08), Tampa, Florida, 2008, pp. 1–4.
47. A. El-Baz, G. Gimel'farb, and M. A. El-Ghar, "New motion correction models for automatic identification of renal transplant rejection," in *Proceedings of International Conference on Medical Image Computing and Computer-Assisted Intervention* (MICCAI'07), Brisbane, Australia, 2007, pp. 235–243.
48. A. Farag, A. El-Baz, S. Yuksel, M. A. El-Ghar, and T. Eldiasty, "A framework for the detection of acute rejection with Dynamic Contrast Enhanced Magnetic Resonance Imaging," in *Proceedings of IEEE International Symposium on Biomedical Imaging: From Nano to Macro* (ISBI'06), Arlington, Virginia, 2006, pp. 418–421.
49. F. Khalifa, G. M. Beache, M. A. El-Ghar, T. El-Diasty, G. Gimel'farb, M. Kong, and A. El-Baz, "Dynamic contrast-enhanced MRI-based early detection of acute renal transplant rejection," *IEEE Transactions on Medical Imaging*, vol. 32, no. 10, 2013, pp. 1910–1927.
50. F. Khalifa, A. El-Baz, G. Gimel'farb, and M. A. El-Ghar, "Non-invasive image-based approach for early detection of acute renal rejection," in *Proceedings of International Conference Medical Image Computing and Computer-Assisted Intervention* (MICCAI'10), Beijing, China, 2010, pp. 10–18.
51. F. Khalifa, A. El-Baz, G. Gimel'farb, R. Ouseph, and M. A. El-Ghar, "Shape-appearance guided level-set deformable model for image segmentation," in *Proceedings of IAPR International Conference on Pattern Recognition* (ICPR'10), Istanbul, Turkey, 2010, pp. 4581–4584.
52. F. Khalifa, M. A. El-Ghar, B. Abdollahi, H. Frieboes, T. El-Diasty, A. El-Baz, "A comprehensive non-invasive framework for automated evaluation of acute renal transplant rejection using DCE-MRI," *NMR in Biomedicine*, vol. 26, no. 11, 2013, pp. 1460–1470.
53. F. Khalifa, M. A. El-Ghar, B. Abdollahi, H. B. Frieboes, T. El-Diasty, A. El-Baz, "Dynamic contrast-enhanced MRI-based early detection of acute renal transplant rejection," in *2014 Annual Scientific Meeting and Educational Course Brochure of the Society of Abdominal Radiology* (SAR'14), Boca Raton, Florida, 2014, CID: 1855912.
54. F. Khalifa, A. Elnakib, G. M. Beache, G. Gimel'farb, M. A. El-Ghar, G. Sokhadze, S. Manning, P. McClure, and A. El-Baz, "3D kidney segmentation from CT images using a level set approach guided by a novel stochastic speed function," in *Proceedings of International Conference Medical Image Computing and Computer-Assisted Intervention* (MICCAI'11), Toronto, Canada, 2011, pp. 587–594.
55. F. Khalifa, G. Gimel'farb, M. A. El-Ghar, G. Sokhadze, S. Manning, P. McClure, R. Ouseph, and A. El-Baz, "A new deformable model-based segmentation approach for accurate extraction of the kidney from abdominal CT images," in *Proceedings of IEEE International Conference on Image Processing* (ICIP'11), Brussels, Belgium, 2011, pp. 3393–3396.

56. M. Mostapha, F. Khalifa, A. Alansary, A. Soliman, J. Suri, and A. El-Baz, "Computer-aided diagnosis systems for acute renal transplant rejection: challenges and methodologies," in A. El-Baz, L. saba J. Suri, eds., *Abdomen and Thoracic Imaging*, Springer, 2014, pp. 1–35.
57. M. Shehata, F. Khalifa, E. Hollis, A. Soliman, E. Hosseini-Asl, M. A. El-Ghar, M. El-Baz, A. C. Dwyer, A. El-Baz, and R. Keynton, "A new non-invasive approach for early classification of renal rejection types using diffusion-weighted MRI," in *IEEE International Conference on Image Processing* (ICIP), IEEE, 2016, pp. 136–140.
58. F. Khalifa, A. Soliman, A. Takieldeen, M. Shehata, M. Mostapha, A. Shaffie, R. Ouseph, A. Elmaghraby, and A. El-Baz, "Kidney segmentation from CT images using a 3D NMF-guided active contour model," in *IEEE 13th International Symposium on Biomedical Imaging* (ISBI), IEEE, 2016, pp. 432–435.
59. M. Shehata, F. Khalifa, A. Soliman, A. Takieldeen, M. A. El-Ghar, A. Shaffie, A. C. Dwyer, R. Ouseph, A. El-Baz, and R. Keynton, "3d diffusion MRI-based CAD system for early diagnosis of acute renal rejection," in *2016 IEEE 13th International Symposium on Biomedical Imaging* (ISBI), IEEE, 2016, pp. 1177–1180.
60. M. Shehata, F. Khalifa, A. Soliman, R. Alrefai, M. A. El-Ghar, A. C. Dwyer, R. Ouseph, and A. El-Baz, "A level set-based framework for 3d kidney segmentation from diffusion MR images," in *IEEE International Conference on Image Processing* (ICIP), IEEE, 2015, pp. 4441–4445.
61. M. Shehata, F. Khalifa, A. Soliman, M. A. El-Ghar, A. C. Dwyer, G. Gimelfarb, R. Keynton, and A. El-Baz, "A promising non-invasive CAD system for kidney function assessment," in *International Conference on Medical Image Computing and Computer-Assisted Intervention*, Springer, 2016, pp. 613–621.
62. F. Khalifa, A. Soliman, A. Elmaghraby, G. Gimelfarb, and A. El-Baz, "3d kidney segmentation from abdominal images using spatial-appearance models," *Computational and Mathematical Methods in Medicine*, 2017.
63. E. Hollis, M. Shehata, F. Khalifa, M. A. El-Ghar, T. El-Diasty, and A. El-Baz, "Towards non-invasive diagnostic techniques for early detection of acute renal transplant rejection: a review," *The Egyptian Journal of Radiology and Nuclear Medicine*, vol. 48, no. 1, 2016, pp. 257–269.
64. M. Shehata, F. Khalifa, A. Soliman, M. A. El-Ghar, A. C. Dwyer, and A. El-Baz, "Assessment of renal transplant using image and clinical-based biomarkers," in *Proceedings of 13th Annual Scientific Meeting of American Society for Diagnostics and Interventional Nephrology* (ASDIN'17), New Orleans, Louisiana, 2017.
65. M. Shehata, F. Khalifa, A. Soliman, M. A. El-Ghar, A. C. Dwyer, and A. El-Baz, "Early assessment of acute renal rejection," in *Proceedings of 12th Annual Scientific Meeting of American Society for Diagnostics and Interventional Nephrology* (ASDIN'16), Phoenix, Arizona, 2016.
66. F. Khalifa, G. Beache, A. El-Baz, and G. Gimel'farb, "Deformable model guided by stochastic speed with application in cine images segmentation," in *Proceedings of IEEE International Conference on Image Processing* (ICIP'10), Hong Kong, 2010, pp. 1725–1728.
67. F. Khalifa, G. M. Beache, A. Elnakib, H. Sliman, G. Gimel'farb, K. C. Welch, and A. El-Baz, "A new shape-based framework for the left ventricle wall segmentation from cardiac first-pass perfusion MRI," in *Proceedings of IEEE International Symposium on Biomedical Imaging: From Nano to Macro* (ISBI'13), San Francisco, California, 2013, pp. 41–44.
68. F. Khalifa, G. M. Beache, A. Elnakib, H. Sliman, G. Gimel'farb, K. C. Welch, and A. El-Baz, "A new nonrigid registration framework for improved visualization of transmural perfusion gradients on cardiac first–pass perfusion MRI," in *Proceedings of IEEE International Symposium on Biomedical Imaging: From Nano to Macro* (ISBI'12), Barcelona, Spain, 2012, pp. 828–831.
69. F. Khalifa, G. M. Beache, A. Firjani, K. C. Welch, G. Gimel'farb, and A. El-Baz, "A new nonrigid registration approach for motion correction of cardiac first-pass perfusion MRI," in *Proceedings of IEEE International Conference on Image Processing* (ICIP'12), Lake Buena Vista, Florida, 2012, pp. 1665–1668.
70. F. Khalifa, G. M. Beache, G. Gimel'farb, and A. El-Baz, "A novel CAD system for analyzing cardiac first-pass MR images," in *Proceedings of IAPR International Conference on Pattern Recognition* (ICPR'12), Tsukuba Science City, Japan, 2012, pp. 77–80.
71. F. Khalifa, G. M. Beache, G. Gimel'farb, and A. El-Baz, "A novel approach for accurate estimation of left ventricle global indexes from short-axis cine MRI," in *Proceedings of IEEE International Conference on Image Processing* (ICIP'11), Brussels, Belgium, 2011, pp. 2645–2649.
72. F. Khalifa, G. M. Beache, G. Gimel'farb, G. A. Giridharan, and A. El-Baz, "A new image-based framework for analyzing cine images," in A. El-Baz, U. R. Acharya, M. Mirmedhdi, J. S. Suri, eds., *Handbook of Multi Modality State-of-the-Art Medical Image Segmentation and Registration Methodologies*, vol. 2., 2011, pp. 69–98.

73. F. Khalifa, G. M. Beache, G. Gimel'farb, G. A. Giridharan, and A. El-Baz, "Accurate automatic analysis of cardiac cine images," *IEEE Transactions on Biomedical Engineering*, vol. 59, no. 2, 2012, pp. 445–455.
74. F. Khalifa, G. M. Beache, M. Nitzken, G. Gimel'farb, G. A. Giridharan, and A. El-Baz, "Automatic analysis of left ventricle wall thickness using short-axis cine CMR images," in *Proceedings of IEEE International Symposium on Biomedical Imaging: From Nano to Macro* (ISBI'11), Chicago, Illinois, 2011, pp. 1306–1309.
75. M. Nitzken, G. Beache, A. Elnakib, F. Khalifa, G. Gimel'farb, and A. El-Baz, "Accurate modeling of tagged CMR 3D image appearance characteristics to improve cardiac cycle strain estimation," in *19th IEEE International Conference on Image Processing* (ICIP), Orlando, Florida, 2012, pp. 521–524.
76. M. Nitzken, G. Beache, A. Elnakib, F. Khalifa, G. Gimel'farb, and A. El-Baz, "Improving full-cardiac cycle strain estimation from tagged CMR by accurate modeling of 3D image appearance characteristics," in *9th IEEE International Symposium on Biomedical Imaging* (ISBI), Barcelona, Spain, 2012, pp. 462–465 (Selected for oral presentation).
77. M. J. Nitzken, A. S. El-Baz, and G. M. Beache, "Markov-Gibbs random field model for improved full-cardiac cycle strain estimation from tagged CMR," *Journal of Cardiovascular Magnetic Resonance*, vol. 14, no. 1, 2012, pp. 1–2.
78. H. Sliman, A. Elnakib, G. Beache, A. Elmaghraby, and A. El-Baz, "Assessment of myocardial function from cine cardiac MRI using a novel 4D tracking approach," *J Comput Sci Syst Biol*, vol. 7, 2014, pp. 169–173.
79. H. Sliman, A. Elnakib, G. M. Beache, A. Soliman, F. Khalifa, G. Gimel'farb, A. Elmaghraby, and A. El-Baz, "A novel 4D PDE-based approach for accurate assessment of myocardium function using cine cardiac magnetic resonance images," in *Proceedings of IEEE International Conference on Image Processing* (ICIP'14), Paris, France, 2014, pp. 3537–3541.
80. H. Sliman, F. Khalifa, A. Elnakib, G. M. Beache, A. Elmaghraby, and A. El-Baz, "A new segmentation-based tracking framework for extracting the left ventricle cavity from cine cardiac MRI," in *Proceedings of IEEE International Conference on Image Processing* (ICIP'13), Melbourne, Australia, 2013, pp. 685–689.
81. H. Sliman, F. Khalifa, A. Elnakib, A. Soliman, G. M. Beache, A. Elmaghraby, G. Gimel'farb, and A. El-Baz, "Myocardial borders segmentation from cine MR images using bi-directional coupled parametric deformable models," *Medical Physics* vol. 40, no. 9, 2013, pp. 1–13.
82. H. Sliman, F. Khalifa, A. Elnakib, A. Soliman, G. M. Beache, G. Gimel'farb, A. Emam, A. Elmaghraby, and A. El-Baz, "Accurate segmentation framework for the left ventricle wall from cardiac cine MRI," in *Proceedings of International Symposium on Computational Models for Life Science* (CMLS'13), Sydney, Australia, 2013, vol. 1559, pp. 287–296.
83. N. Eladawi, M. Elmogy, et al., "Classification of retinal diseases based on OCT images," *Frontiers in Bioscience Landmark Journal*, 2017.
84. A. ElTanboly, M. Ismail, et al., "A computer aided diagnostic system for detecting diabetic retinopathy in optical coherence tomography images," *Medical Physics*, 2016.
85. B. Abdollahi, A. C. Civelek, X. F. Li, J. Suri, and A. El-Baz, "PET/CT nodule segmentation and diagnosis: a survey, "in L. Saba, J. S. Suri, eds., *Multi Detector CT Imaging*, Taylor, Francis, 2014, pp. 639–651.
86. B. Abdollahi, A. El-Baz, and A. A. Amini, "A multi-scale non-linear vessel enhancement technique," in *Engineering in Medicine and Biology Society, EMBC, 2011 Annual International Conference of the IEEE*, 2011, pp. 3925–3929.
87. B. Abdollahi, A. Soliman, A. Civelek, X. F. Li, G. Gimel'farb, and A. El-Baz, "A novel Gaussian scale space-based joint MGRF framework for precise lung segmentation," in *Proceedings of IEEE International Conference on Image Processing* (ICIP'12), 2012, pp. 2029–2032.
88. B. Abdollahi, A. Soliman, A. Civelek, X. F. Li, G. Gimelfarb, and A. El-Baz, "A novel 3D joint MGRF framework for precise lung segmentation," in *Machine Learning in Medical Imaging*, Springer, 2012, pp. 86–93.
89. A. M. Ali, A. S. El-Baz, and A. A. Farag, "A novel framework for accurate lung segmentation using graph cuts," in *Proceedings of IEEE International Symposium on Biomedical Imaging: From Nano to Macro* (ISBI'07), 2007, pp. 908–911.
90. A. El-Baz, G. M. Beache, G. Gimel'farb, K. Suzuki, and K. Okada, "Lung imaging data analysis," *International Journal of Biomedical Imaging*, 2013.
91. A. El-Baz, G. M. Beache, G. Gimel'farb, K. Suzuki, K. Okada, A. Elnakib, A. Soliman, and B. Abdollahi, "Computer-aided diagnosis systems for lung cancer: challenges and methodologies," *International Journal of Biomedical Imaging*, 2013.
92. A. El-Baz, A. Elnakib, M. Abou El-Ghar, G. Gimel'farb, R. Falk, and A. Farag, "Automatic detection of 2D and 3D lung nodules in chest spiral CT scans," *International Journal of Biomedical Imaging*, 2013.

93. A. El-Baz, A. A. Farag, R. Falk, and R. La Rocca, "A unified approach for detection, visualization, and identification of lung abnormalities in chest spiral CT scans," in *International Congress Series*, vol. 1256, Elsevier, 2003, pp. 998–1004.
94. A. El-Baz, A. A. Farag, R. Falk, and R. La Rocca, "Detection, visualization and identification of lung abnormalities in chest spiral CT scan: Phase-I," in *Proceedings of International Conference on Biomedical Engineering*, Cairo, Egypt, 2002, vol. 12.
95. A. El-Baz, A. Farag, G. Gimel'farb, R. Falk, M. A. El-Ghar, and T. Eldiasty, "A framework for automatic segmentation of lung nodules from low dose chest CT scans," in *Proceedings of International Conference on Pattern Recognition* (ICPR'06), 2006, vol. 3, pp. 611–614.
96. A. El-Baz, A. Farag, G. Gimelfarb, R. Falk, and M. A. El-Ghar, "A novel level set-based computer-aided detection system for automatic detection of lung nodules in low dose chest computed tomography scans," *Lung Imaging and Computer Aided Diagnosis*, vol. 10, 2011, pp. 221–238.
97. A. El-Baz, G. Gimel'farb, M. Abou El-Ghar, and R. Falk, "Appearance-based diagnostic system for early assessment of malignant lung nodules," in *Proceedings of IEEE International Conference on Image Processing* (ICIP'12), 2012, pp. 533–536.
98. A. El-Baz, G. Gimel'farb, and R. Falk, "A novel 3D framework for automatic lung segmentation from low dose CT images," in A. El-Baz, J. S. Suri, eds., *Lung Imaging and Computer Aided Diagnosis*, Taylor, Francis, 2011, pp. 1–16.
99. A. El-Baz, G. Gimel'farb, R. Falk, and M. El-Ghar, "Appearance analysis for diagnosing malignant lung nodules," in *Proceedings of IEEE International Symposium on Biomedical Imaging: From Nano to Macro* (ISBI'10), 2010, pp. 193–196.
100. A. El-Baz, G. Gimel'farb, R. Falk, and M. A. El-Ghar, "A novel level set-based CAD system for automatic detection of lung nodules in low dose chest CT scans," in A. El-Baz, J. S. Suri, eds., *Lung Imaging and Computer Aided Diagnosis*, vol. 1, Taylor, Francis, 2011, pp. 221–238.
101. A. El-Baz, G. Gimel'farb, R. Falk, and M. A. El-Ghar, "A new approach for automatic analysis of 3D low dose CT images for accurate monitoring the detected lung nodules," in *Proceedings of International Conference on Pattern Recognition* (ICPR'08), 2008, pp. 1–4.
102. A. El-Baz, G. Gimel'farb, R. Falk, and M. A. El-Ghar, "A novel approach for automatic follow-up of detected lung nodules," in *Proceedings of IEEE International Conference on Image Processing* (ICIP'07), vol. 5, 2007, pp. v–501.
103. A. El-Baz, G. Gimel'farb, R. Falk, and M. A. El-Ghar, "A new CAD system for early diagnosis of detected lung nodules," in *IEEE International Conference on Image Processing*, vol. 2, IEEE, 2007, II–461.
104. A. El-Baz, G. Gimel'farb, R. Falk, M. A. El-Ghar, and H. Refaie, "Promising results for early diagnosis of lung cancer," in *Proceedings of IEEE International Symposium on Biomedical Imaging: From Nano to Macro* (ISBI'08), 2008, pp. 1151–1154.
105. A. El-Baz, G. L. Gimel'farb, R. Falk, M. Abou El-Ghar, T. Holland, and T. Shaffer, "A new stochastic framework for accurate lung segmentation," in *Proceedings of Medical Image Computing and Computer-Assisted Intervention* (MICCAI'08), 2008, pp. 322–330.
106. A. El-Baz, G. L. Gimel'farb, R. Falk, D. Heredis, and M. Abou El-Ghar, "A novel approach for accurate estimation of the growth rate of the detected lung nodules," in *Proceedings of International Workshop on Pulmonary Image Analysis*, 2008, pp. 33–42.
107. A. El-Baz, G. L. Gimel'farb, R. Falk, T. Holland, and T. Shaffer, "A framework for unsupervised segmentation of lung tissues from low dose computed tomography images," in *Proceedings of British Machine Vision* (BMVC'08), 2008, pp. 1–10.
108. A. El-Baz, G. Gimelfarb, R. Falk, and M. A. El-Ghar, "3D MGRF-based appearance modeling for robust segmentation of pulmonary nodules in 3D LDCT chest images," in *Lung Imaging and Computer Aided Diagnosis*, 2011, pp. 51–63.
109. A. El-Baz, G. Gimelfarb, R. Falk, and M. A. El-Ghar, "Automatic analysis of 3D low dose CT images for early diagnosis of lung cancer," *Pattern Recognition*, vol. 42, no. 6, 2009, pp. 1041–1051.
110. A. El-Baz, G. Gimelfarb, R. Falk, M. A. El-Ghar, S. Rainey, D. Heredia, and T. Shaffer, "Toward early diagnosis of lung cancer," in *Proceedings of Medical Image Computing and Computer-Assisted Intervention* (MICCAI'09), Springer, 2009, pp. 682–689.
111. A. El-Baz, G. Gimelfarb, R. Falk, M. A. El-Ghar, and J. Suri, "Appearance analysis for the early assessment of detected lung nodules," in *Lung Imaging and Computer Aided Diagnosis*, 2011, pp. 395–404.
112. A. El-Baz, F. Khalifa, A. Elnakib, M. Nitkzen, A. Soliman, P. McClure, G. Gimel'farb, and M. A. El-Ghar, "A novel approach for global lung registration using 3D Markov Gibbs appearance model," in *Proceedings of International Conference Medical Image Computing and Computer-Assisted Intervention* (MICCAI'12), Nice, France, 2012, pp. 114–121.

113. A. El-Baz, M. Nitzken, A. Elnakib, F. Khalifa, G. Gimel'farb, R. Falk, and M. A. El-Ghar, "3D shape analysis for early diagnosis of malignant lung nodules," in *Proceedings of International Conference Medical Image Computing and Computer-Assisted Intervention* (MICCAI'11), Toronto, Canada, 2011, pp. 175–182.
114. A. El-Baz, M. Nitzken, G. Gimelfarb, E. Van Bogaert, R. Falk, M. A. El-Ghar, and J. Suri, "Three-dimensional shape analysis using spherical harmonics for early assessment of detected lung nodules," in *Lung Imaging and Computer Aided Diagnosis*, 2011, pp. 421–438.
115. A. El-Baz, M. Nitzken, F. Khalifa, A. Elnakib, G. Gimel'farb, R. Falk, and M. A. El-Ghar, "3D shape analysis for early diagnosis of malignant lung nodules," in *Proceedings of International Conference on Information Processing in Medical Imaging* (IPMI'11), Monastery Irsee, Germany, 2011, pp. 772–783.
116. A. El-Baz, M. Nitzken, E. Vanbogaert, G. Gimel'Farb, R. Falk, and M. Abo El-Ghar, "A novel shape-based diagnostic approach for early diagnosis of lung nodules," in *International Symposium on Biomedical Imaging: From Nano to Macro*, IEEE, 2011, pp. 137–140.
117. A. El-Baz, P. Sethu, G. Gimel'farb, F. Khalifa, A. Elnakib, R. Falk, and M. A. El-Ghar, "Elastic phantoms generated by microfluidics technology: validation of an imaged-based approach for accurate measurement of the growth rate of lung nodules," *Biotechnology Journal*, vol. 6, no. 2, 2011, pp. 195–203.
118. A. El-Baz, P. Sethu, G. Gimel'farb, F. Khalifa, A. Elnakib, R. Falk, and M. A. El-Ghar, "A new validation approach for the growth rate measurement using elastic phantoms generated by state-of-the-art microfluidics technology," in *Proceedings of IEEE International Conference on Image Processing* (ICIP'10), Hong Kong, 2010, pp. 4381–4383.
119. A. El-Baz, P. Sethu, G. Gimel'farb, et al., "Validation of a new imaged-based approach for the accurate estimating of the growth rate of detected lung nodules using real CT images and elastic phantoms generated by state-of-the-art microfluidics technology," in A. El-Baz, J. S. Suri, eds., *Handbook of Lung Imaging and Computer Aided Diagnosis*, vol. 1, Taylor & Francis, New York, 2011, pp. 405–420.
120. A. El-Baz, A. Soliman, P. McClure, G. Gimel'farb, M. A. El-Ghar, and R. Falk, "Early assessment of malignant lung nodules based on the spatial analysis of detected lung nodules," in *Proceedings of IEEE International Symposium on Biomedical Imaging: From Nano to Macro* (ISBI'12), 2012, pp. 1463–1466.
121. A. El-Baz, S. E. Yuksel, S. Elshazly, and A. A. Farag, "Non-rigid registration techniques for automatic follow-up of lung nodules," in *Proceedings of Computer Assisted Radiology and Surgery* (CARS'05), vol. 1281, Elsevier, 2005, pp. 1115–1120.
122. A. S. El-Baz and J. S. Suri, *Lung Imaging and Computer Aided Diagnosis*, CRC Press, 2011.
123. A. Oliman, F. Khalifa, A. Shaffie, N. Liu, N. Dunlap, B. Wang, A. Elmaghraby, G. Gimelfarb, and A. El-Baz, "Image-based CAD system for accurate identification of lung injury," in *Proceedings of IEEE International Conference on Image Processing* (ICIP'16), 2016, pp. 121–125.
124. A. Soliman, F. Khalifa, N. Dunlap, B. Wang, M. El-Ghar, and A. El-Baz, "An iso-surfaces based local deformation handling framework of lung tissues," *13th International Symposium on Biomedical Imaging* (ISBI), IEEE, 2016, pp. 1253–1259.
125. A. Soliman, F. Khalifa, A. Shaffie, N. Dunlap, B. Wang, A. Elmaghraby, and A. El-Baz, "Detection of lung injury using 4d-CT chest images," in *13th International Symposium on Biomedical Imaging* (ISBI), IEEE, 2016, pp. 1274–1277.
126. B. Dombroski, M. Nitzken, A. Elnakib, F. Khalifa, A. El-Baz, and M. F. Casanova, "Cortical surface complexity in a population-based normative sample," *Translational Neuroscience*, vol. 5, no. 1, 2014, pp. 17–24.
127. A. El-Baz, M. Casanova, G. Gimel'farb, M. Mott, and A. Switala, "An MRI-based diagnostic framework for early diagnosis of dyslexia," *International Journal of Computer Assisted Radiology and Surgery*, vol. 3, no. 3–4, 2008, pp. 181–189.
128. A. El-Baz, M. Casanova, G. Gimel'farb, M. Mott, A. Switala, E. Vanbogaert, and R. McCracken, "A new CAD system for early diagnosis of dyslexic brains," in *Proc. International Conference on Image Processing* (ICIP'2008), IEEE, 2008, pp. 1820–1823.
129. A. El-Baz, M. F. Casanova, G. Gimel'farb, M. Mott, and A. E. Switwala, "A new image analysis approach for automatic classification of autistic brains," in *Proc. IEEE International Symposium on Biomedical Imaging: From Nano to Macro* (ISBI'2007), IEEE, 2007, pp. 352–355.
130. A. El-Baz, A. Elnakib, F. Khalifa, M. A. El-Ghar, P. McClure, A. Soliman, and G. Gimel'farb, "Precise segmentation of 3-D magnetic resonance angiography," *IEEE Transactions on Biomedical Engineering*, vol. 59, no. 7, 2012, pp. 2019–2029.
131. A. El-Baz, A. A. Farag, G. L. Gimel'farb, M. A. El-Ghar, and T. Eldiasty, "Probabilistic modeling of blood vessels for segmenting MRA images," in *ICPR*, vol. 3, 2006, pp. 917–920.

132. A. El-Baz, A. A. Farag, G. Gimelfarb, M. A. El-Ghar, and T. Eldiasty, "A new adaptive probabilistic model of blood vessels for segmenting MRA images," in *Medical Image Computing and Computer-Assisted Intervention* (MICCAI 2006), vol. 4191, Springer, 2006, pp. 799–806.
133. A. El-Baz, A. A. Farag, G. Gimelfarb, and S. G. Hushek, "Automatic cerebrovascular segmentation by accurate probabilistic modeling of tof-mra images," in *Medical Image Computing and Computer-Assisted Intervention* (MICCAI 2005), Springer, 2005, pp. 34–42.
134. A. El-Baz, A. Farag, A. Elnakib, M. F. Casanova, G. Gimel'farb, A. E. Switala, D. Jordan, and S. Rainey, "Accurate automated detection of autism related corpus callosum abnormalities," *Journal of Medical Systems*, vol. 35, no. 5, 2011, pp. 929–939.
135. A. El-Baz, A. Farag, and G. Gimelfarb, "Cerebrovascular segmentation by accurate probabilistic modeling of TOF-MRA images," in *Image Analysis*, vol. 3540, Springer, 2005, pp. 1128–1137.
136. A. El-Baz, G. Gimelfarb, R. Falk, M. A. El-Ghar, V. Kumar, and D. Heredia, "A novel 3D joint Markov-Gibbs model for extracting blood vessels from PC–MRA images," in *Medical Image Computing and Computer-Assisted Intervention* (MICCAI 2009), vol. 5762, Springer, 2009, pp. 943–950.
137. A. Elnakib, A. El-Baz, M. F. Casanova, G. Gimel'farb, and A. E. Switala, "Image-based detection of corpus callosum variability for more accurate discrimination between dyslexic and normal brains," in *Proc. IEEE International Symposium on Biomedical Imaging: From Nano to Macro* (ISBI'2010), IEEE, 2010, pp. 109–112.
138. A. Elnakib, M. F. Casanova, G. Gimel'farb, A. E. Switala, A. El-Baz, "Autism diagnostics by centerline-based shape analysis of the corpus callosum," in *Proc. IEEE International Symposium on Biomedical Imaging: From Nano to Macro* (ISBI'2011), IEEE, 2011, pp. 1843–1846.
139. A. Elnakib, M. Nitzken, M. Casanova, H. Park, G. Gimel'farb, and A. El-Baz, "Quantification of age-related brain cortex change using 3D shape analysis," in *21st International Conference on Pattern Recognition* (ICPR), IEEE, 2012, pp. 41–44.
140. M. Mostapha, A. Soliman, F. Khalifa, A. Elnakib, A. Alansary, M. Nitzken, M. F. Casanova, and A. El-Baz, "A statistical framework for the classification of infant DT images," in *2014 IEEE International Conference on Image Processing* (ICIP), IEEE, 2014, pp. 2222–2226.
141. M. Nitzken, M. Casanova, G. Gimel'farb, A. Elnakib, F. Khalifa, A. Switala, and A. El-Baz, "3D shape analysis of the brain cortex with application to dyslexia," in *18th IEEE International Conference on Image Processing* (ICIP), Brussels, Belgium, IEEE, 2011, pp. 2657–2660 (Selected for oral presentation. Oral acceptance rate is 10 percent and the overall acceptance rate is 35 percent).
142. F. E. Z. A. El-Gamal, M. Elmogy, M. Ghazal, A. Atwan, G. Barnes, M. Casanova, R. Keynton, and A. El-Baz, "A novel CAD system for local and global early diagnosis of Alzheimers disease based on pib-pet scans," in *2017 IEEE International Conference on Image Processing* (ICIP), Beijing, China, IEEE, 2017.
143. M. Ismail, A. Soliman, et al., "A fast stochastic framework for automatic MR brain images segmentation."
144. M. M. Ismail, R. S. Keynton, M. M. Mostapha, A. H. ElTanboly, M. F. Casanova, G. L. Gimel'farb, and A. El-Baz, "Studying autism spectrum disorder with structural and diffusion magnetic resonance imaging: a survey," *Frontiers in Human Neuroscience*, vol. 10, 2016.
145. A. Alansary, M. Ismail, A. Soliman, F. Khalifa, M. Nitzken, A. Elnakib, M. Mostapha, A. Black, K. Stinebruner, M. F. Casanova, et al., "Infant brain extraction in t1-weighted MR images using BET and refinement using LCDG and MGRF models," *IEEE Journal of Biomedical and Health Informatics*, vol. 20, no. 3, 2016, pp. 925–935.
146. M. Ismail, G. Barnes, et al., "A new deep-learning CAD system for early diagnosis of autism using structural MR."
147. M. Ismail, A. Soliman, A. ElTanboly, A. Switala, M. Mahmoud, F. Khalifa, G. Gimel'farb, M. F. Casanova, R. Keynton, and A. El-Baz, "Detection of white matter abnormalities in MR brain images for diagnosis of autism in children," 2016, pp. 6–9.
148. M. Ismail, M. Mostapha, A. Soliman, M. Nitzken, F. Khalifa, A. Elnakib, G. Gimel'farb, M. Casanova, and A. El-Baz, "Segmentation of infant brain MR images based on adaptive shape prior and higher-order MGRF," 2015, pp. 4327–4331.
149. A. Shalaby, F. Taher, M. El-Baz, V. Ghazal, M. Abou El-Ghar, A. Takieldeen, and A. El-Baz, "Probabilistic modeling of blood vessels for segmenting magnetic resonance angiography images," in *Medical Research Archive* (MRA), KEI, 2017, pp. 34–42.
150. A. S. Chowdhury, A. K. Rudra, M. Sen, A. Elnakib, and A. El-Baz, "Cerebral white matter segmentation from MRI using probabilistic graph cuts and geometric shape priors," in *ICIP*, 2010, pp. 3649–3652.

3 Vascular Tree Segmentation from Different Image Modalities

Ali Mahmoud[1], Ahmed Shalaby[1], Fatma Taher[2], Maryam El-Baz[1], Jasjit S. Suri[3], Ayman El-Baz[1]
[1]University of Louisville
[2]Zayed University
[3]AtheroPoint, LLC

CONTENTS

3.1 INTRODUCTION

The human cerebrovascular system is a complex three-dimensional (3D) anatomical structure. Serious types of vascular diseases such as carotid stenosis, aneurysm, and vascular malformation may lead to brain stroke, which is the third leading cause of death and the number one cause of disability [1]. An accurate model of the vascular system is needed to detect these diseases at an early stage and make invasive treatments unnecessary.

Increasingly, imaging is being applied in minimally invasive surgery to provide two-dimensional (2-D) and 3-D visualization of vascular structures to assist clinicians in pre-operation planning, real-time operating room decision making, and post-operation monitoring. One emerging area of interest is in quantitative image processing techniques that can aid in the development of new and safer methods of endovascular treatment for intracranial saccular aneurysms, whereby tiny platinum coils are used to prevent blood flow within cerebral aneurysms [2].

Magnetic resonance imaging has always been especially suited for vascular imaging [3], [4]. This was first made possible by the flow void phenomenon and later by special vascular sequences known as in-flow or TOF and phase-contrast imaging (PCA). This led to the term magnetic resonance angiography (MRA). The direct relationship between signal intensity and flow velocity allowed MRAs to be used for quantitative measurement, but MRAs also have inherent drawbacks in areas

of increased flow (stenosis) and reduced or complex flow (aneurysms). Ideally, MRA suppresses the signal from static tissue so that the signal comes exclusively from flowing blood and theoretically the vessel segmentation becomes very simple.

Segmentation and 3D rendering of vascular structures require sufficient vessel contrast. Computed tomographic angiography (CTA) is able to acquire this type of data and has been applied to arteriovenous malformations and cerebral aneurysms [5]. Helical CT acquires this data at a much higher speed than classic CT, and thus is capable of imaging a wide variety of vascular lesions while preserving bony morphology for anatomic reference.

X-ray angiography is used to image and diagnose diseases of the blood vessels of the body, including the brain and heart [6], [7]. Traditionally, angiography was used to diagnose pathology of these vessels such as blockage caused by plaque buildup. However in recent decades, radiologists, cardiologists, and vascular surgeons have used X-ray angiography to guide minimally invasive procedures of the blood vessels and arteries of the heart.

Medical image processing applications such as surgical planning and navigation benefit from segmentation of anatomical structures from medical images. For example, CT data segmentation of some structures can be performed simply using an intensity threshold. In general, however, segmentation is challenging and requires sophisticated algorithms and significant human input. The distribution of gray level values corresponding to one structure may vary throughout the structure and may also overlap those of another structure.

In many cases, the 3D segmentation is performed using deformable models. The mathematical foundation of such models represents the confluence of physics and geometry [10]. The latter represents an object shape and the former puts constraints on how the shape may vary over space and time. Deformable models have had great successes in imaging and computer graphics. In particular in [11], the deformable models recover the object's structure using some properties of its shape. The model evolves iteratively towards the steady state of energy minimization. But the disadvantage of this method is that the initial contour should be close to the final one. The model faces problems with topological changes of a complex structure.

Level set techniques of segmentation overcome problems of the classical deformable models [12]–[14]. A curve in 2D or a surface in 3D evolves in such a way as to cover a complex shape or structure. Its initialization is either manual or automatic, and it need not be close to the desired solution. But these methods depend on a large number of parameters to be tuned for the success of the process.

In [15], a more efficient 3D segmentation technique was proposed. In this approach, surface evolution is controlled by current probabilistic region information. Probability density functions for the regions are assumed to be Gaussian and their parameters are estimated iteratively. The level set model designed is based on these density functions.

Brain vessels extraction has attracted lots of attention from the computer vision community, with developments of very interesting dedicated level-sets implementations for thin tubular structure extraction. In this field, Lorigo et al. [16] have developed flows using the Hessian information [18], co-dimension 2 evolution schemes for the extraction of thin curves in 3D [17], with application to the brain vessels. The same target was followed in [19] where the authors use a flow based on the divergence of the gradient in the image. Both works achieve extraction of thin curves where even level-sets classical formulation cannot. However, the computing cost to achieve this result is too significant.

Choyke et al. [20] presented a method for reconstructing vessel surfaces from 3-D angiographic images that allows for objective measurement of vessel stenosis. The method is a deformable model that employs a tubular coordinate system. Vertex merging is used with the coordinate system to maintain even vertex spacing and to avoid problems of self-intersection of the surface.

Yim et al. [21] proposed a methodology for deforming the isosurface to conform to the boundaries of objects in the image with minimal a priori assumptions of object shape. As in conventional methods, external forces attract the surface toward edges in the image. However, smoothing is produced by a moment that aligns the normals of adjacent surface triangles. Notably, the moment produces no translational motion of surface triangles.

There is another class of techniques based on statistical approaches for extracting the vascular tree. Wilson et al. [8] proposed an adaptive statistical approach for the extraction of blood vessels from TOF-MRA data. This algorithm is based on a mixture of three components that model the intensity distribution of TOF-MRA data. The first component is uniformly distributed and represents the blood vessels. The other two components have Gaussian distributions and model the fat, bones, and brain tissues (white matter and gray matter). The parameter estimation of these three components is performed recursively on smaller and smaller subvolumes of data using the EM algorithm. In [9] they improved the model proposed in [8] by using the Rician distribution to model the background-noise to better match the empirical density distribution and the estimated distribution. In [22] they improved the model proposed in [8] by using a mixture of one Rayleigh and two normal distributions to model the histogram intensity of TOF-MRA data.

In this chapter we introduce a novel approach to extract the vascular tree in images from various modalities. This approach depends on combining the level set techniques with a precise statistical model for the intensity distribution of the given data. The proposed technique is considered to be a nonparametric level set approach that does not need any tuning of parameters. The statistical approach gives accurate estimates for the empirical density of the data using a linear combination of Gaussian with positive and negative components.

We propose an extension for our work in [15]. The adaptive Gaussian models are modified using an expectation-maximization algorithm that approximates an empirical probability density function of scalar data with a linear combination of Gaussians (LCG). Due to both positive and negative components, the LCG approximates interclass transitions more accurately than a conventional mixture of only positive Gaussians.

The initialization of level set functions is very important for the success of this segmentation process. An automatic seed initialization is used to accelerate the process and make it less sensitive to noise. The chosen initialization needs an accurate estimate of the density function of each class. Our modified EM algorithm is used to give initial estimates of class density. Our experiments in 3D segmentation of the vascular tree demonstrate the accuracy of the algorithm.

3.2 SURFACE MODELLING BY LEVEL SETS

Within the level set formalism [23], the evolving surface is a propagating front embedded as the zero level of a 4D scalar function $\phi(x, t)$. This hypersurface is usually defined as the signed distance function positive inside, negative outside, and zero on the boundary of a region. The continuous change of ϕ can be described by the partial differential equation:

$$\frac{\partial \phi(x,\ t)}{\partial t} + FF\left|\nabla \phi(x,\ t)\right| = 0, \tag{3.1}$$

where FF is a scalar velocity function depending on the local geometric properties (local curvature) of the front and on the external parameters related to the input data (e.g., image gradient). The hypersurface ϕ deforms iteratively according to FF, and the position of the 3D front is given at each iteration step by the equation $\phi(x,\ t) = 0$. Practically, instead of Eq. (3.1), the value $\phi(x,\ t_{n+1})$ at step $n+1$ is computed from $\phi(x, t_n)$ at step n by the relation:

$$\phi\left(x,\ t_{n+1}\right) = \phi\left(x,\ t_n\right) - \Delta t \cdot FF\left|\nabla \phi\left(x,\ t_n\right)\right|, \tag{3.2}$$

The design of the velocity function FF plays a major role in the evolutionary process. Among several formulations proposed in [24] and [25], we have chosen the following formulation:

$$FF = h(I)(\nu - \varepsilon k), \tag{3.3}$$

where $\nu = 1$ or -1 for the contracting or expanding front, respectively, ε is a smoothing coefficient always small with respect to 1, and k is the local curvature of the front defined in the 3D case as follows:

$$\begin{aligned} k = &\left(\left(\phi_{xx} + \phi_{yy}\right)\phi_z^2 + \left(\phi_{xx} + \phi_{zz}\right)\phi_y^2\right. \\ &+\left(\phi_{zz} + \phi_{yy}\right)\phi_x{}^2 - 2\phi_x\phi_y\phi_{xy} - 2\phi_x\phi_z\phi_{xz} \\ &\left.-2\phi_z\phi_y\phi_{zy}\right) / \left(2\left(\phi_x^2 + \phi_y^2 + \phi_z^2\right)^{3/2}\right), \end{aligned} \tag{3.4}$$

The latter parameter acts as a regularization term. The data consistency term $h(I)$ acts as a stopping criterion at the location of the desired boundaries; it is defined according to the intensity I of the input data.

With this representation a single level set either contracts until vanishing, or expands to cover all the space. To stop the evolution at the edge, FF can be multiplied by a value that is a function of the image gradient [26]. But if the edge is missed, the surface can not move back. So to depend only on the edge is not sufficient for accurate segmentation; thus other information from the image should be used.

The segmentation partitions the image into regions, each belonging to a certain class. In our approach, a separate level set function is defined for each class and the automatic seed initialization is used. Given the gray level density of each class, the volume is initially divided into equal non-overlapping sub-volumes. For each sub-volume, the average gray level is used to specify the most probable class with the given density estimated by the modified EM. Such initialization differs from that in [27] where only the distance to the class mean is used. Then a signed distance level set function for the associated class is initialized. The automatic seed initialization produces initially non-overlapped level set functions. The competition between level sets based on the probability density functions stops the evolution of each level set at the boundary of its class region.

3.3 STATISTICAL GRAY LEVEL DISTRIBUTION MODEL

In this chapter we introduce a new algorithm called a modified expectation-maximization algorithm that approximates an empirical probability density function of scalar data with a linear combination of Gaussians (LCG) with positive and negative components. Due to both positive and negative components, the LCG approximates interclass transitions more accurately than a conventional mixture of only positive Gaussians.

To most accurately identify the model, we approximate the marginal gray level probability density in each region with a LCG having $C_{\mathrm{p},i}$ positive and $C_{\mathrm{n},i}$ negative components [31], [32]:

$$p(q|i) = \sum_{r=1}^{C_{\mathrm{p},i}} w_{\mathrm{p},i,r}\varphi\left(q|\theta_{\mathrm{p},i,r}\right) - \sum_{l=1}^{C_{\mathrm{n},i}} w_{\mathrm{n},i,l}\varphi\left(q|\theta_{\mathrm{n},i,l}\right); \tag{3.5}$$

such that $\int_{-\infty}^{\infty} p(q|i)dq = 1$. Here, q is the gray level, and $\varphi(q|\theta)$ is a Gaussian density having a shorthand notation $\theta = (\mu, \sigma^2)$ for its mean, μ, and variance, σ^2. In contrast to more conventional normal mixture models, the components are now both positive and negative and have only one obvious restriction in line with Eq. (3.5): $\sum_{r=1}^{C_{\mathrm{p},i}} w_{\mathrm{p},i,r} - \sum_{l=1}^{C_{\mathrm{n},i}} w_{\mathrm{n},i,l} = 1$. These weights are not the prior probabilities, and the LCG of Eq. (3.5) is considered as a functional form of the approximation of a probability density depending on parameters (w, θ) of each component.

In the general case, the actual probability densities belong to a proper subset of the set of all possible LCGs of Eq. (3.5). In the subset, the weights and parameters of the Gaussians are limited to maintain non-negative values of the combined densities over the whole infinite signal range. The latter restriction would normally be considered impracticable because it results in strongly interdependent parameters. However, in our particular case the interdependence may be ignored. We use the LCG model to better approximate not only the main bodies but also the tails of the empirical distributions, to within a finite and relatively small actual signal range $[0,Q]$. Thus, the model behavior outside the range and the associated restrictions on the model parameters are of no concern. Moreover, the likelihood maximization is also directed toward keeping the probability densities positive at points where they approximate the empirical positive values.

The mixture of K LCGs, $p(q)=\sum_{i=1}^{K} w_i p(q|i)$, has the same form but a larger number of components, for example, $C_{\mathrm{p}}=\sum_{i=1}^{K} C_{\mathrm{p},i}$ and $C_{\mathrm{n}}=\sum_{i=1}^{K} C_{\mathrm{n},i}$ if all the values $\theta_{\mathrm{p},i,r}$ and $\theta_{\mathrm{n},i,l}$ differ for the individual models:

$$p(q)=\sum_{r=1}^{C_{\mathrm{p}}} w_{\mathrm{p},r}\varphi\left(q|\theta_{\mathrm{p},r}\right)-\sum_{l=1}^{C_{\mathrm{n}}} w_{\mathrm{n},l}\varphi\left(q|\theta_{\mathrm{n},l}\right) \tag{3.6}$$

To identify this model in the unsupervised mode, the mixed empirical distribution of gray levels over the image has to be first represented by a joint LCG of Eq. (3.6) and then partitioned into individual LCG-models for each class $i=1,\ldots,K$.

Under the fixed number of the positive and negative components, C, the model parameters $\mathbf{w}=\{w_c;c=1,\ldots,C\}$ and $\Theta=\{\theta_c:c=1,\ldots,C\}$ maximizing the image likelihood can be found using an EM algorithm introduced in Section 3.3.1. It modifies the conventional EM-scheme to take account of the components with alternating signs [33], [34].

The modified EM algorithm is sensitive to both its initial state specified by the numbers of positive and negative Gaussians, and the initial parameters (mean and variance) of each component. To find a close initial LCG-approximation of the empirical distribution, we develop in Section 3.3.2 a sequential initializing EM-based algorithm (see also [35]).

3.3.1 Modified EM Algorithm for LCGs

Let $\mathbf{F}=[f(q):q\in\mathbf{Q}]$ be an empirical relative frequency distribution representing an unknown probability density function $\psi(q)$ such that $\int_{-\infty}^{\infty}\psi(q)dq\equiv\sum_{q=0}^{Q} f(q)=1$. We assume that $\mathbf{F}$ is approximated by an LCG $\mathbf{P}_{C:\mathrm{W},\Theta}=[p_C(q):q\in\mathbf{Q}]$ with C_{p} positive and C_{n} negative components $\varphi(q|\theta)$:

$$p_{\mathbf{w},\Theta}(q)=\sum_{r=1}^{C_{\mathrm{p}}} w_{\mathrm{p},r}\varphi\left(q|\theta_{\mathrm{p},r}\right)-\sum_{l=1}^{C_{\mathrm{n}}} w_{\mathrm{n},l}\varphi\left(q|\theta_{\mathrm{n},l}\right) \tag{3.7}$$

In line with Eq. (3.7), the positive weights $\mathbf{w}$ are restricted as follows:

$$\sum_{r=1}^{C_{\mathrm{p}}} w_{\mathrm{p},r}-\sum_{l=1}^{C_{\mathrm{n}}} w_{\mathrm{n},l}=1 \tag{3.8}$$

We also assume here that the numbers C_{p} and C_{n} of the components of each type are known after the initialization in Section 3.3.2 and do not change during the EM process. The initialization provides also the starting parameter values $\mathbf{w}^{[0]}$ and $\Theta^{[0]}$.

The probability densities form a proper subset of the set of the LCGs due to the additional restriction $p_{\mathbf{w},\Theta}(q) \geq 0$, which holds automatically only for probability mixtures with no negative components. As was mentioned earlier, this special feature is ignored because our goal is to closely approximate the empirical data only to within the limited range $[0,Q]$. The approximating function of Eq. (3.7) is assumed strictly positive only in the points $q = 0,1,\ldots,Q$.

The LCG that provides a local maximum of the log-likelihood of the empirical data:

$$L(\mathbf{w},\Theta) = \sum_{q\in\mathbf{Q}} f(q)\log p_{\mathbf{W},\Theta}(q) \tag{3.9}$$

can be found using the iterative block relaxation process extending conventional EM schemes.

Let $p^{[m]}_{\mathbf{w},\Theta}(q) = \sum_{r=1}^{C_{\mathrm{p}}} w^{[m]}_{\mathrm{p},r}\varphi(q|\theta^{[m]}_{\mathrm{p},r}) - \sum_{l=1}^{C_{\mathrm{n}}} w^{[m]}_{\mathrm{n},l}\varphi(q|\theta^{[m]}_{\mathrm{n},l})$ be the LCG at step, or iteration m. Relative contributions of each data item $q = 0,\ldots,Q$ into each positive and negative Gaussian at the step m are specified by the following respective conditional weights

$$\begin{gathered}\pi^{[m]}_{\mathrm{p}}(r|q) = \frac{w^{[m]}_{\mathrm{p},r}\varphi\left(q|\theta^{[m]}_{\mathrm{p},r}\right)}{p^{[m]}_{\mathbf{w},\Theta}(q)};\ \pi_{\mathrm{n}}(l|q) = \frac{w^{[m]}_{\mathrm{n},l}\varphi\left(q|\theta^{[m]}_{\mathrm{n},l}\right)}{p^{[m]}_{\mathbf{w},\Theta}(q)} \\ \sum_{r=1}^{C_{\mathrm{p}}}\pi^{[m]}_{\mathrm{p}}(r|q) - \sum_{l=1}^{C_{\mathrm{n}}}\pi^{[m]}_{\mathrm{n}}(l|q) = 1; q = 0,\ldots,Q\end{gathered} \tag{3.10}$$

Using these weights, the log-likelihood of Eq. (3.9) can be rewritten in the equivalent form:

$$L\left(\mathbf{w}^{[m]},\Theta^{[m]}\right) = \sum_{q=0}^{Q} f(q)\left[\sum_{r=1}^{C_{\mathrm{p}}}\pi^{[m]}_{\mathrm{p}}(r|q)\log p^{[m]}_{\mathbf{w},\Theta}(q)\right] - \sum_{q=0}^{Q} f(q)\left[\sum_{l=1}^{C_{\mathrm{n}}}\pi^{[m]}_{\mathrm{n}}(l|q)\log p^{[m]}_{\mathbf{w},\Theta}(q)\right] \tag{3.11}$$

where $\log p^{[m]}_{\mathbf{w},\Theta}(q)$ in the first and the second brackets should be replaced with the equal terms: $\log w^{[m]}_{\mathrm{p},r} + \log\varphi(q|\theta^{[m]}_{\mathrm{p},r}) - \log\pi^{[m]}_{\mathrm{p}}(r|q)$ and $\log w^{[m]}_{\mathrm{n},l} + \log\varphi(q|\theta^{[m]}_{\mathrm{n},l}) - \log\pi^{[m]}_{\mathrm{n}}(l|q)$, respectively.

The block relaxation converging to a local maximum of the likelihood function in Eq. (3.11) repeats iteratively the following two steps:

1. E-step $[m+1]$: to find the parameters $\mathbf{w}^{[m+1]},\Theta^{[m+1]}$ by maximizing $L(\mathbf{w},\Theta)$ under the fixed conditional weights of Eq. (3.10) for the step m, and
2. M-step $[m+1]$: to find these latter weights by maximizing $L(\mathbf{w},\Theta)$ under the fixed parameters $\mathbf{w}^{[m+1]},\Theta^{[m+1]}$

until the changes of the log-likelihood and all the model parameters become small.

The E-step performs the conditional Lagrange maximization of the log-likelihood of Eq. (3.11) under the restriction of Eq. (3.8) to obtain the following estimates of the weights:

$$w^{[m+1]}_{\mathrm{p},r} = \sum_{q\in\mathbf{Q}} f(q)\pi^{[m]}_{\mathrm{p}}(r|q);\ w^{[m+1]}_{\mathrm{n},l} = \sum_{q\in\mathbf{Q}} f(q)\pi^{[m]}_{\mathrm{n}}(l|q)$$

Then the parameters of each Gaussian are obtained by the unconditional maximization just as in the conventional EM scheme (below "c" stands for "p" or "n," respectively):

$$\mu_{c,r}^{[m+1]} = \frac{1}{w_{c,r}^{[m+1]}} \sum_{q \in \mathbf{Q}} q \cdot f(q) \pi_c^{[m]}(r|q)$$
$$\left(\sigma_{c,r}^{[m+1]}\right)^2 = \frac{1}{w_{c,r}^{[m+1]}} \sum_{q \in \mathbf{Q}} \left(q - \mu_{c,i}^{[m+1]}\right)^2 \cdot f(q) \pi_c^{[m]}(r|q)$$

The M-step performs the conditional Lagrange maximization of the log-likelihood of Eq. (3.11) under the $Q+1$ restrictions of Eq. (3.10), and determines the conditional weights $\pi_p^{[m+1]}(r|q)$ and $\pi_n^{[m+1]}(l|q)$ of Eq. (3.10) for all $r = 1, \ldots, C_p; l = 1, \ldots, C_n$ and $q = 0, \ldots, Q$. The modified EM-algorithm is valid until these weights are strictly positive, and the initial LCG-approximation should comply to this limitation. The iterations have to be terminated when the log-likelihood of Eq. (3.11) begins to decrease. Generally, if the initialization is incorrect, this algorithm may diverge at the first iteration. Thus the initial LCG has to closely approximate the empirical distribution.

3.3.2 Sequential EM-Based Initialization

We assume that the number of dominant modes is equal to the given number of classes. To simplify the notation, let the empirical distribution have only two separate dominant modes representing the object and the background, respectively. The algorithm we present is easily extended to the general case of $K > 2$ dominant modes. We assume that each dominant mode is roughly approximated with a single Gaussian and the deviations of the empirical density from the two-component dominant Gaussian mixture are described by other components of the LCG in Eq. (3.6). Therefore the model has the two dominant positive weights, say, $w_{p,1}$ and $w_{p,2}$, such that $w_{p,1} + w_{p,2} = 1$, and a number of "subordinate" weights of smaller absolute values such that $\sum_{r=3}^{C_p} w_{p,r} - \sum_{l=1}^{C_n} w_{n,l} = 0$.

The following sequential algorithm allows for estimating both the weights and parameters of the individual Gaussians in the latter LCG model, including the number of the non-dominant components

1. Approximate a given empirical distribution $\mathbf{F}$, of gray levels in the image $\mathbf{Y}$, with a dominant mixture $\mathbf{P}_2$, of two Gaussians using the conventional EM-algorithm.
2. Find the deviations $\Delta = [\Delta(q) = f(q) - p_2(q) : q \in \mathbf{Q}]$ between $\mathbf{F}$ and P_2 and split them into the positive and negative parts such that $\delta(q) = \delta_p(q) - \delta_n(q)$:

$$\begin{aligned} \Delta_p &= [\delta_p(q) = \max\{\delta(q), 0\} : q \in \mathbf{Q}] \\ \Delta_n &= [\delta_n(q) = \max\{-\delta(q), 0\} : q \in \mathbf{Q}] \end{aligned} \tag{3.12}$$

3. Compute the scaling factor for the deviations: $s = \int_{-\infty}^{\infty} \delta_p(q) dq \equiv \int_{-\infty}^{\infty} \delta_n(q) dq$.
4. If the factor s is less than a given accuracy threshold, terminate and return the model $\mathbf{P}_C = \mathbf{P}_2$.
5. Otherwise consider the scaled-up absolute deviations $\frac{1}{s}\Delta_p$ and $\frac{1}{s}\Delta_n$ as two new "empirical densities" and iteratively the conventional EM-algorithm to find sizes C_p and C_n of the Gaussian mixtures, $\mathbf{P}_p$ and $\mathbf{P}_n$ respectively, approximating the scaled-up deviations.

a. The size of each mixture corresponds to the minimum of the integral absolute error between the scaled-up absolute deviation Δ_p (or Δ_n) and its model $\mathbf{P}_p$ (or $\mathbf{P}_n$). The number of the components is increasing sequentially by unit step, while the error is decreasing.
b. Due to multiple local maxima, such a search may be repeated several times with different initial parameter values in order to select the best approximation.

6. Scale down the subordinate models $\mathbf{P}_p$ and $\mathbf{P}_n$ (i.e., scale down the weights of their components) and add the scaled model $\mathbf{P}_p$ to and subtract the scaled model P_n from the dominant model $\mathbf{P}_2$ in order to form the desired model $\mathbf{P}_C$ of the size $C = 2 + C_p + C_n$.

Since the EM algorithm converges to a local maximum of the likelihood function, it may be repeated several times with different initial parameter values for choosing the model giving the best approximation. In principle, this process can be repeated iteratively in order to approximate more and more closely the residual absolute deviations between ($\mathbf{F}$) and $\mathbf{P}_C$. But because each Gaussian in the latter model impacts all the values $p(q)$, the iterations should be terminated when the approximation quality begins to decrease.

We use the Levy distance [30], $\rho(\mathbf{F},\mathbf{P})$, between the estimated model $\mathbf{P}$ and the empirical distribution $\mathbf{F}$ to evaluate the approximation quality. The distance is defined as the minimum positive value α such that the two-sided inequalities $p(q-\alpha)-\alpha \le f(q) \le p(q+\alpha)+\alpha$ hold for all $q \in \mathbf{Q}$:

$$\rho(\mathbf{F},\mathbf{P}) = \min_{\alpha>0}\{\alpha : p(q-\alpha)-\alpha \le f(q) \le p(q+\alpha)+\alpha \ \forall q \in \mathbf{Q}\} \tag{3.13}$$

It is proven [30] that the model $\mathbf{P}$ weakly converges to $\mathbf{F}$ when $\rho(\mathbf{F},\mathbf{P}) \to 0$. Our experiments in Section 3.6 show that the modified EM algorithm typically decreases an initially large Levy distance between the empirical distribution and its estimated model to a relatively small value.

3.3.3 Classification of the Model Components

The final mixed LCG-model P has to be split into K LCG-submodels, one per class, by associating each subordinate component with a particular dominant term in such a way as to minimize the expected misclassification rate. To illustrate the association principle, let us consider the bi-modal case with the two dominant Gaussians having the mean values μ_1 and μ_2; $0 < \mu_1 < \mu_2 < Q$. Let all the subordinate components be ordered by their mean values, too. Then let those with the mean values smaller than μ_1 and greater than μ_2 relate to the first and second class, respectively. The components having the mean values in the range $[\mu_1,\mu_2]$ are associated with the classes by simple thresholding such that the means below the threshold, t, belong to the components associated with the first class. The desired threshold minimizes the classification error $e(t)$:

$$e(t) = \int_{-\infty}^{t} p(q|2)\,dq + \int_{t}^{\infty} p(q|1)\,dq. \tag{3.14}$$

3.4 EVOLUTIONARY SURFACE MODEL

The term ($\nu = \pm 1$) in Eq. (3.3) specifies the direction of the front propagation. Several approaches were developed to make all fronts either contracting or expanding (see, e.g., [28]) in order to evolve in both directions and avoid overlaps between the regions. The problem can be reformulated as classification of each point at the evolving front. If the point belongs to the associated class, the front expands; otherwise, it contracts.

3.4.1 PDE System

The classification decision is based on Bayes' decision [29] at point x as follows:

$$i^*(x) = \arg\max_{i=1,\ldots,K} \left(p_i(I(x)) \right). \tag{3.15}$$

where $p_i(I(x))$ is the estimated density of class i calculated using the modified EM algorithm and K stands for the number of classes. The term (ν) for each point x is replaced by the function $\nu_i(x)$ so the velocity function is defined as:

$$FF_i(x) = h_i(I)(\nu_i(x) - \varepsilon \cdot k(x)), \ \forall \ i = 1 \ldots K. \tag{3.16}$$

where

$$\nu_i(x) = \begin{cases} -1 \text{ if } & i = i^*(x) \\ 1 & \text{otherwise} \end{cases} \tag{3.17}$$

If the pixel x belongs to the front of the class $i = i^*(x)$ associated to the level set function, the front will expand, otherwise it will contract. Now, we put the Eq. (3.1) in the general form using the derivative of the Heaviside step function ($\delta_\alpha(z)$) [27] as follows:

$$\frac{\partial \phi_i(x,t)}{\partial t} = \delta_\alpha(\phi_i(x,t))(\varepsilon \cdot k(x) - \nu_i(x))\left|\nabla \phi_i(x)\right| h_i(I). \tag{3.18}$$

The function $\delta_\alpha(z)$ selects the narrow band points around the front. Solution of the PDEs requires numerical processing at each point of the image or volume, which is a time-consuming process. Actually we are interested only in the changes of the front, so that the solution is important at the points near the front. Such narrow band points are selected in Eq. (3.18). Points outside the narrow band are given large positive or large negative values to be excluded from processing in order to accelerate the iterations. Also the equation contains the magnitude of the image gradient to make sure that the evolution will stop at the boundary.

3.4.2 Data Consistency Coefficient $h_i(I)$

The data consistency term was always a function of image gradient. But this is a disadvantage when we have images with high noise. Our approach is similar to the one described in [36]. We have related the stopping factor h_i to the posterior probability of having a transition between the $class_i$ and its background of the other classes. Let x be a voxel of the current interface, and λ be the estimated class of x. The posterior probability of x being a transition, given I and λ, is given by:

$$p_T\left(x \middle| I, \lambda\right) = \begin{cases} \sum_{s \neq i} p_s(I(x')) \text{ if } & \lambda \in class_i \\ p_i(I(x')) & \text{otherwise} \end{cases} \tag{3.19}$$

where x' is a neighbouring voxel of x located outside the volume defined by hypersurface ϕ_i. Thus if x is more likely to be inside the object to be segmented, then the posterior transition probability of x is the probability of x' to be located outside the object to be segmented.

The data consistency term $h_i(I)$ at point x belonging to the interface is defined as a decreasing function of $p_T(x|I,\lambda)$. Then h_i is defined to be a decreasing function as follows:

$$h_i(p_T) = 1 - H_{\zeta_i}(p_T), \tag{3.20}$$

where H_{ζ_i} is a smoothed version of the Heaviside step function parameterized by the prior probability estimate ζ_i [27]. This estimate can be calculated by using the following equation:

$$\zeta_i = \frac{\int_\Omega H_\alpha(\phi_i)dx}{\sum_{i=1}^{K}\int_\Omega H_\alpha(\phi_i)\,dx}. \tag{3.21}$$

Where ζ_i is considered as a class proportion and it is calculated by counting the pixels in the level set area of interest and dividing by the total number of pixels.

By this representation, the coefficient will be large if the voxel and its neighbor belong to the same class and vice versa.

3.5 EVALUATION OF THE SEGMENTATION APPROACH

It is not easy to find a method of validating the vascular tree segmentation. We can not have a shape model or an atlas for the vascular system, which differs from patient to patient. Also the expert radiologists differ in their evaluation [22]. Thus, to validate the accuracy of our method, we created a 3D phantom of blood vessels with a tree shape (Table 3.1). This phantom is a part of a real wood tree. We made a CT scan of that part in order to have digital image slices of the phantom, which is $1024 \times 1024 \times 125$ in size.

A gold standard model is extracted from the CT scan manually. The modalities used in our experiments are the computed tomography of the aorta and magnetic resonance angiography of the brain. Each modality has a specific intensity distribution. To validate the segmentation of these modalities, we need a phantom that has a similar intensity distribution. Noise is added to the gold standard data to give the desired intensity distribution using the inverse mapping technique.

A level set function is assigned to each class. These functions are initialized using the automatic seed initialization except for the vessels or tree class. The tree level set function is initialized manually as a set of balloons inside the tree as shown in Figure 3.1.

As a result of such initialization, the estimated prior probability will change because the small region of the initial balloons can not represent the whole tree. So the equation for the priors of the non-vessels class are modified as follows:

$$\zeta_i = \frac{\int_\Omega H_\alpha(\phi_i)\,dx}{\int_\Omega dx}. \tag{3.22}$$

TABLE 3.1
The validation table for the phantom segmentation.

Modality	Pixels			
	No. of Pixels in Tree	Error Pixels in Tree	No. of Pixels in Background	Error Pixels in Background
TOF	211656	1316	130860344	198
PC	211656	120	130860344	2223
CT	211656	3510	130860344	1170

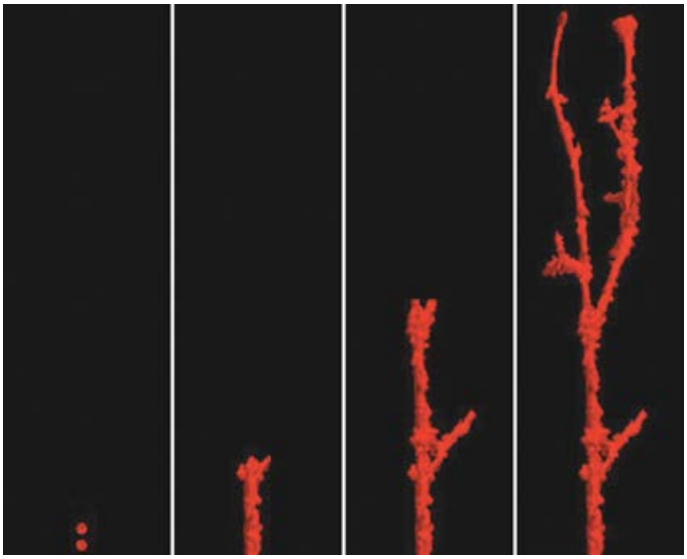

FIGURE 3.1 The visualization of the evolution of the level set function that represents the tree. The first image to the left shows the initialization of the balloons inside the tree.

Then the estimated prior probability of the tree (vessels) class is estimated by the following equation:

$$\zeta_{Vessels} = 1 - \sum \zeta_{non-Vessels}. \tag{3.23}$$

where the priors satisfy the obvious condition $\sum \zeta_i = 1$.

After these modifications, the initial balloons will evolve to cover the tree without overlapping the other regions.

3.6 EXPERIMENTAL RESULTS

To assess robustness and computational performance, the proposed segmentation techniques have been tested on three different types of medical images: MRA-TOF of the brain; MRA-PC of the brain; and CT of the aorta. The first two types were acquired with the Picker 1.5T Edge MRI scanner. The TOF-MRA slices are with a resolution of 512×512 and were 1 mm thick. The CT has the same in-plan size and resolution and was collected with 4 mm thick slabs reconstructed every 2 mm with a scanning pitch of 1.5 mm.

In our experiments, we used a Pentium III (1.8 GHZ) computer with 512 MB of RAM. Table 3.2 shows the average execution time per slice for each type of image modality with a different data set size. We demonstrate our experiments in detail in the following subsections.

TABLE 3.2

The average execution time per slice for different image modalities.

Modality	Data Set Size	Average Execution Time per Slice
TOF	$512 \times 512 \times 93$	3–5 mins
PC	$256 \times 256 \times 117$	1–2 mins
CT	$512 \times 512 \times 125$	3–5 mins

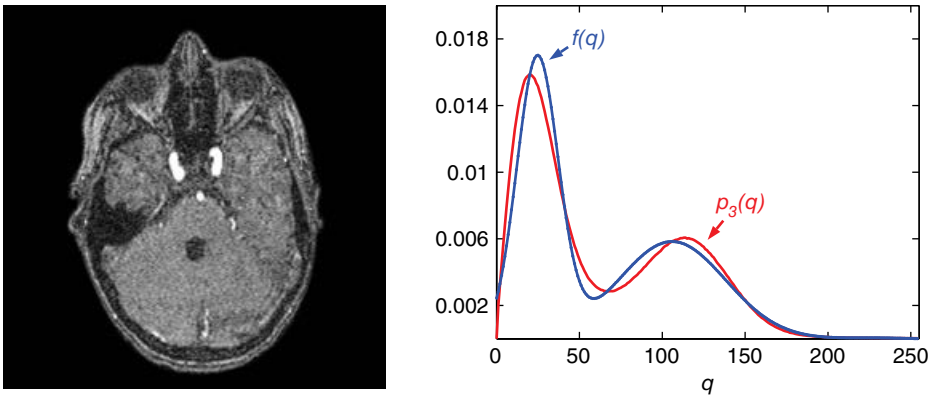

FIGURE 3.2 Typical TOF-MRA scan slice (a) and deviations between the empirical distribution and the dominant mixture (b).

3.6.1 Separation of Blood Vessels in MRA-TOF Images

The first application of the proposed algorithm is the extraction of blood vessels from MRA-TOF data. Figure 3.2 shows an MRA-TOF image and its tri-modal empirical gray level distribution approximated with the dominant three-component normal mixture. The three classes represent dark bones, brain tissues, and bright blood vessels, respectively. The goal is to separate the latter class in spite of its large intersection with the second class and very low prior probability. The initial parameters of the dominant mixture are given in Table 3.3, and the Levy distance of 0.08 indicates a significant mismatch between the mixture and the empirical distribution. Figure 3.3 shows the scaled deviations between these two distributions as well as the six estimated subordinate Gaussians giving the minimum approximation error.

Figure 3.4 shows the approximated absolute deviation and the initial LCG-model obtained after the subordinate LCG is combined with the dominant mixture. The minimum classification error of 0.01 on the intersecting distribution tails is obtained for the separation thresholds $t_1 = 57$ and $t_2 = 190$. In this case the subordinate components 1–3, 4–5, and 6 correspond to the first (bones), second (brain tissues), and third (blood vessels and fat) classes, respectively. The estimated LCG-submodels for each class are shown in Figure 3.5.

We apply the proposed approach on three data sets of MRA-TOF, and the results are shown in Figure 3.6. Figure 3.6(a) shows the segmentation using the proposed statistical approach only. Figure 3.6(b) shows the final segmentation using the combined level sets approach. The final

TABLE 3.3
Initial parameters of each dominant component of the LCG-model of the MRA image in Figure 3.2(a).

Parameters	Classes		
	Bones	Brain Tissues	Blood Vessels and Fat
Mean value	24.7	105.7	210.7
Variance	12.6	31.8	25.0
Weight (w)	0.518	0.456	0.026

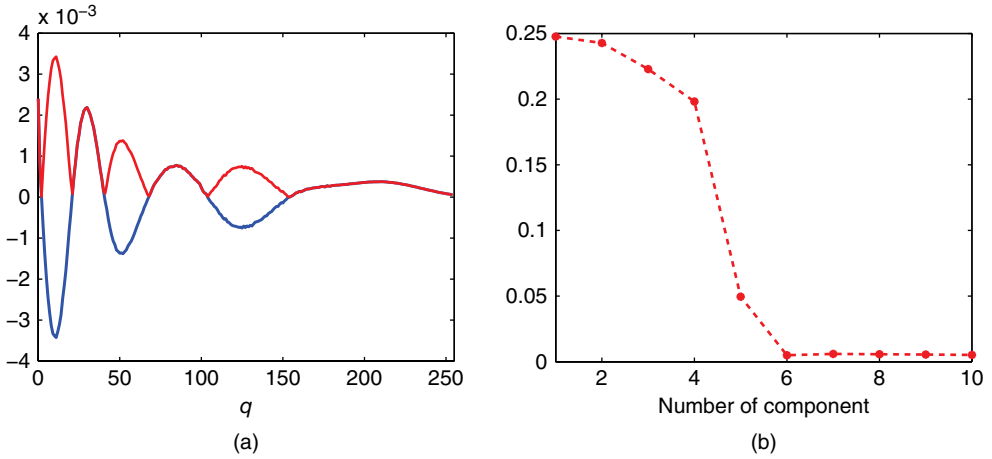

FIGURE 3.3 Estimated subordinate components of the absolute deviation (a) and the absolute error as a function of the number of Gaussians approximating the scaled absolute deviation in Figure 3.3(a).

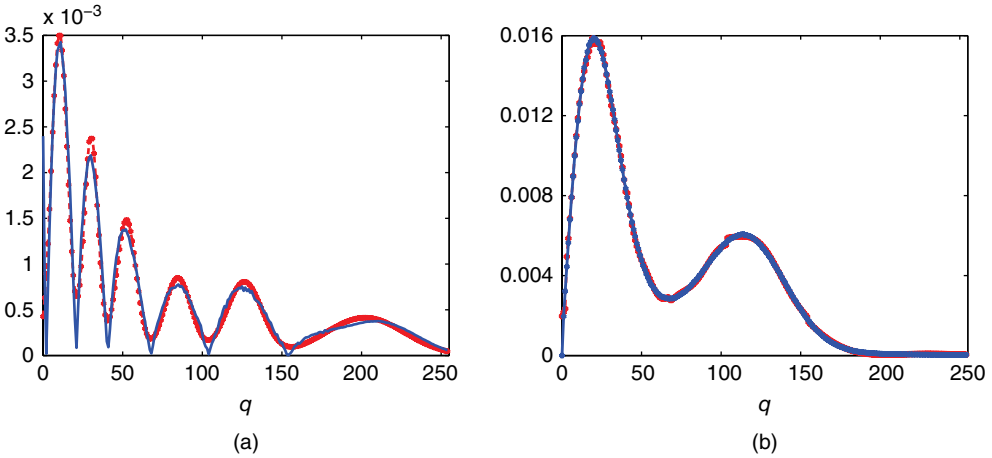

FIGURE 3.4 Subordinate mixture (a) estimated for the absolute deviation in Figure 3.3(a), and the empirical and estimated densities (b) for the MRA image in Figure 3.2(a).

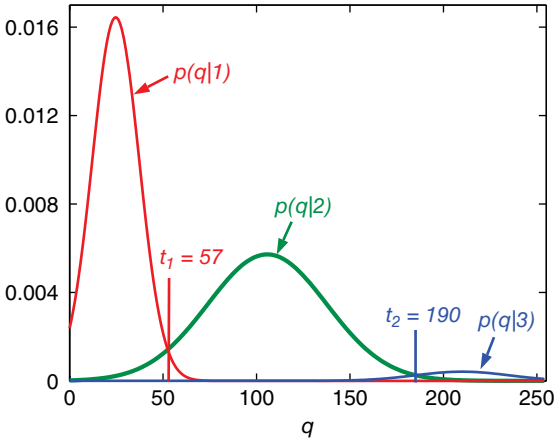

FIGURE 3.5 LCG-models of the classes "Bones," "Brain tissues," and "Blood vessels and fat."

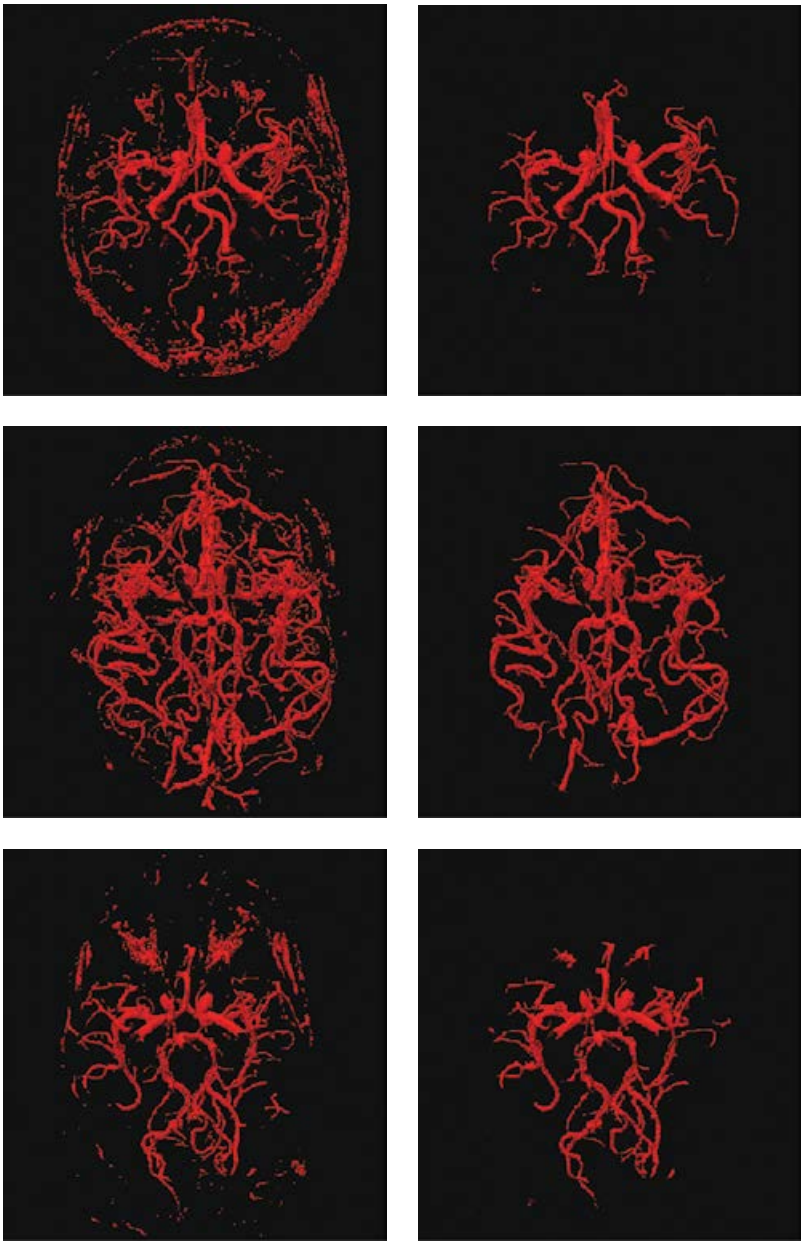

FIGURE 3.6 (a) Segmentation using the proposed statistical approach only. (b) Final segmentation after using the level sets approach.

parameters of the dominant mixture are given in Table 3.4. It is clear from Figure 3.6(a) if we use only the statistical model, the other tissues (e.g., fat, brain tissues, etc.) will appear around the blood vessels. Using the combined level set approach by initializing the level set function of the vessels inside those vessels with the largest cross-sections, we will get only the blood vessels as shown in Figure 3.6(b). The other tissues will be removed as they are not connected to the vessel tree.

TABLE 3.4
Final parameters of each dominant component of the LCG-model of the MRA image in Figure 3.2(a).

Parameters	Classes		
	Bones	Brain tissues	Blood vessels and fat
Mean value	23.2	101.5	208.9
Variance	9.9	32.9	27.0
Weight (w)	0.52	0.451	0.028

3.6.2 Extraction of Blood Vessels from Phase Contrast Images

The second application of the proposed algorithm is the extraction of blood vessels from MRA-PC data. Figure 3.7 shows an MRA-PC image and its tri-modal empirical gray level distribution approximated with the dominant three-component normal mixture. The three classes again represent dark bones, brain tissues, and bright blood vessels, respectively. The goal is to separate the latter class in spite of its large intersection with the second class and very low prior probability. As mentioned above, the first step in the proposed algorithm is to get an accurate density model for each class using LCG of positive and negative components. Figure 3.8(a) presents the final LCG-model obtained by the modified EM-algorithm. The resulting Levy distance of 0.02 indicates that the estimated distribution is very close to the empirical distribution. Successive changes of the log-likelihood at the refining iterations, the eight components of the final LCG-model, and the final LCG-models of each class for the refined separation thresholds $t_1 = 16$ and $t_2 = 71$ are shown in Figure 3.8(b)–(d), respectively. The first six iterations of the refining EM-algorithm increase the log-likelihood of Eq. (3.11) from –4.01 to –3.98. Then the refinement process is terminated since

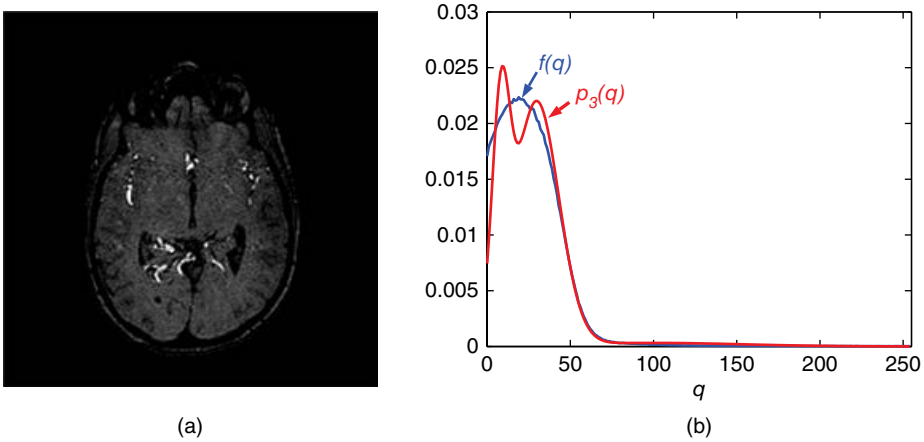

FIGURE 3.7 Typical TOF-PC scan slice (a) and deviations between the empirical distribution and the dominant mixture (b).

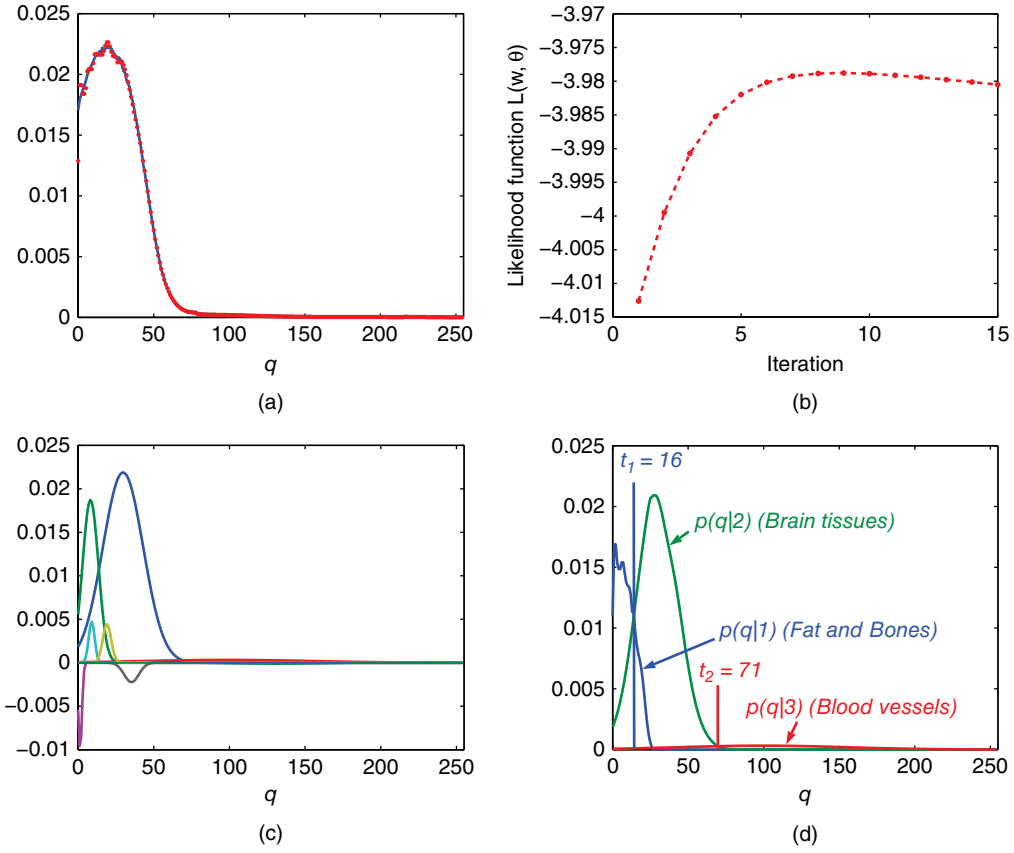

FIGURE 3.8 Final 3-class LCG-approximation of the mixed density (a), dynamics of the log-likelihood at the refining iterations (b), components of the final LCG (c), and the LCG-models of each class.

the log-likelihood in Eq. (3.11) begins to decrease. The results of the segmentation of blood vessels from MRA-PC using the combined level sets approach are shown in Figure 3.9.

3.6.3 Extraction of the Aorta from CTA Images

In this section we will use the proposed algorithm to extract the aorta and the major vessels from spiral CT angiograms in order to show that the proposed algorithm is general and can be used to extract the blood vessels from any medical imaging modality. Figure 3.10 shows a CTA image and its four-modal empirical gray level distribution approximated with the dominant four-component normal mixture. The four classes represent dark lung, liver, bright blood vessels, and heart, respectively. Figure 3.11(a) presents the final LCG-model obtained by the modified EM-algorithm. The resulting Levy distance of 0.011 indicates that the estimated distribution is very close to the empirical distribution. Successive changes of the log-likelihood at the refining iterations, the 13 components of the final LCG-model, and the final LCG-models of each class for the refined separation thresholds $t_1 = 51$, $t_2 = 161$ and $t_3 = 242$ are shown in Figure 3.11(b)–(d), respectively. The first five iterations of the refining EM-algorithm increase the log-likelihood of Eq. (3.11) from -5.0 to -4.2. Then the refinement process is terminated because the log-likelihood in Eq. (3.11) begins to decrease. The results of the segmentation of blood vessels from CT angiograms using the combined level sets approach are shown in Figure 3.12.

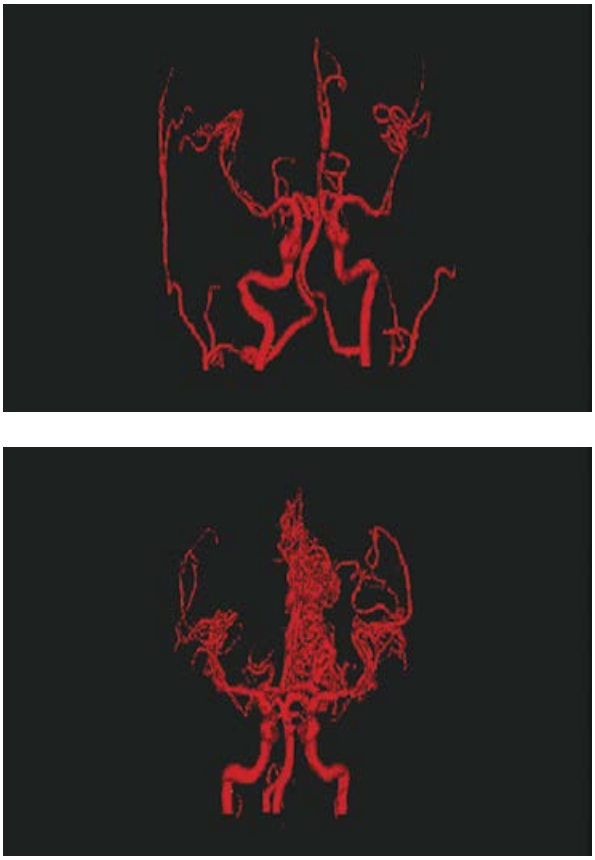

FIGURE 3.9 The visualization of two segmented PC data sets of size $256 \times 256 \times 117$.

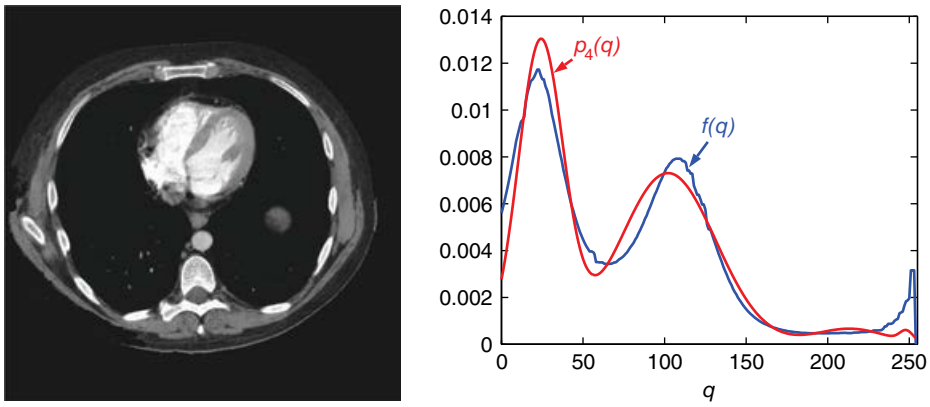

FIGURE 3.10 Typical CTA scan slice (a) and deviations between the empirical distribution and the dominant mixture (b).

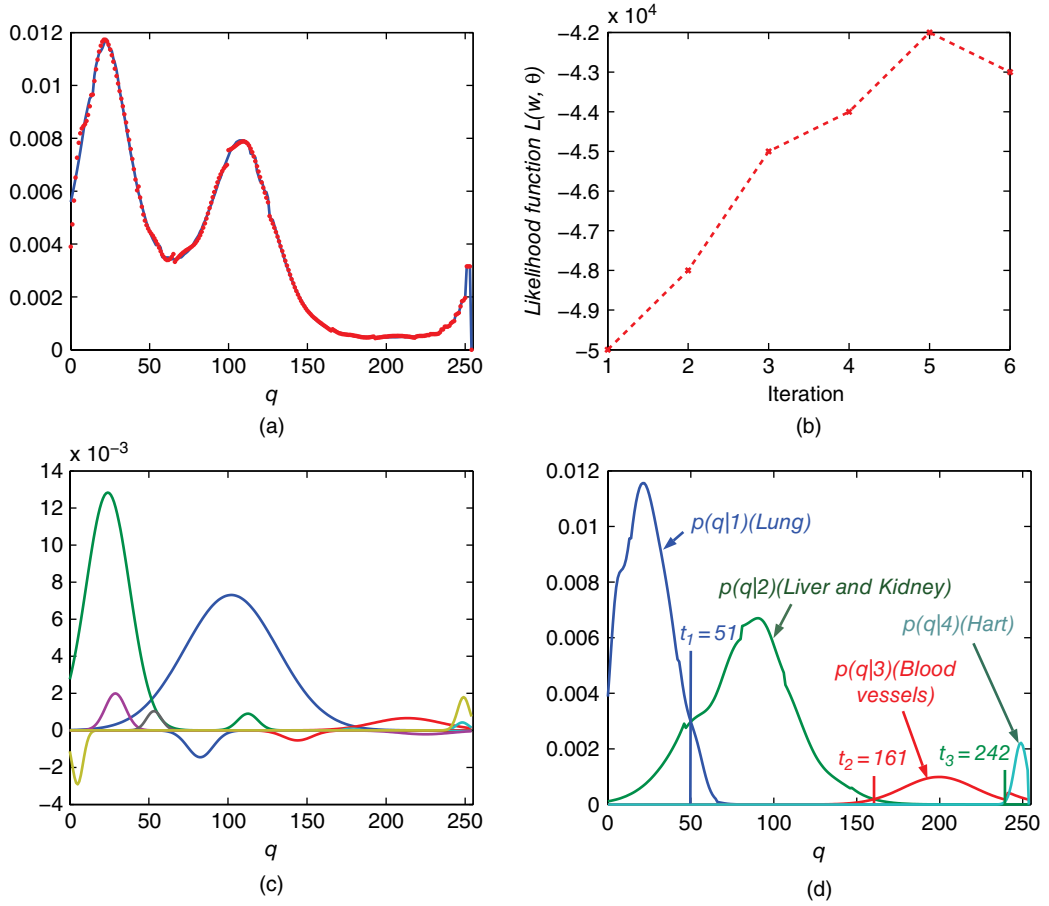

FIGURE 3.11 Final 3-class LCG-approximation of the mixed density (a), dynamics of the log-likelihood at the refining iterations (b), components of the final LCG (c), and the LCG-models of each class.

3.7 CONCLUSION AND FUTURE RESEARCH

We developed a simple and fast statistical evolutionary model based on the level set techniques. The model does not need fine tuning of weighting parameters, but the number of classes (regions) has to be known. Each class is assigned with a level set function, and our modified EM algorithm provides the probability density function of each class. These densities permit us to initialize the level sets near to the optimal solution in order to reduce considerably the number of iterations. Also the speed function of each level set depends on these densities.

We validated our approach using a tree phantom that is geometrically similar to the blood vessels. The segmentation results of the phantom in all cases show the accuracy of our approach (see Table 3.1).

Experiments with TOF, PC, and CTA 3D images confirm that the proposed method is robust and accurate. In future work, we are going to add some shape constraints to our model in order to increase the accuracy of the results.

This work could also be applied to various other applications in medical imaging, such as the kidney, the heart, the prostate, the lung, and the retina.

One application is renal transplant functional assessment. Chronic kidney disease (CKD) affects about 26 million people in the U.S. with 17,000 transplants being performed each year. In renal

FIGURE 3.12 The visualization of the segmented aorta from CT-angiogram data of size $512 \times 512 \times 125$.

transplant patients, acute rejection is the leading cause of renal dysfunction. Given the limited number of donors, routine clinical post-transplantation evaluation is of immense importance to help clinicians initiate timely interventions with appropriate treatment and thus prevent the graft loss. In recent years an increased area of research has been dedicated to developing noninvasive CAD systems for renal transplant function assessment, utilizing different image modalities (e.g., ultrasound, computed tomography (CT), MRI, etc.). Accurate assessment of renal transplant function is critically important for graft survival. Although transplantation can improve a patient's well-being, there is a potential post-transplantation risk of kidney dysfunction that, if not treated in a timely manner, can lead to the loss of the entire graft, and even patient death. Thus, accurate assessment of renal transplant function is crucial for the identification of proper treatment. In recent years, an increased area of research has been dedicated to developing non-invasive image-based CAD systems for the assessment of renal transplant function. In particular, dynamic and diffusion MRI-based systems have been clinically used to assess transplanted kidneys with the advantage of providing information on each kidney separately. For more details about renal transplant functional assessment, please read [37]–[54], [54]–[62].

The heart is also an important application to this work. The clinical assessment of myocardial perfusion plays a major role in the diagnosis, management, and prognosis of ischemic heart disease patients. Thus, there have been ongoing efforts to develop automated systems for accurate analysis of myocardial perfusion using first-pass images [63]–[79].

Another application for this work could be the detection of retinal abnormalities. The majority of ophthalmologists depend on a visual interpretation for the identification of disease types. However, inaccurate diagnosis will affect the treatment procedure, which may lead to fatal results. Hence, there is a crucial need for computer automated diagnosis systems that yield highly accurate results.

Optical coherence tomography (OCT) has become a powerful modality for the non-invasive diagnosis of various retinal abnormalities such as glaucoma, diabetic macular edema, and macular degeneration. The problem with diabetic retinopathy (DR) is that the patient is not aware of the disease until the changes in the retina have progressed to a level that treatment tends to be less effective. Therefore, automated early detection could limit the severity of the disease and assist ophthalmologists in investigating and treating it more efficiently [80], [81].

Abnormalities of the lung could also be another promising area of research and a related application to this work. Radiation-induced lung injury is the main side effect of radiation therapy for lung cancer patients. Although higher radiation doses increase the radiation therapy effectiveness for tumor control, this can lead to lung injury as a greater quantity of normal lung tissues is included in the treated area. Almost 1/3 of patients who undergo radiation therapy develop lung injury following radiation treatment. The severity of radiation-induced lung injury ranges from ground-glass opacities and consolidation at the early phase to fibrosis and traction bronchiectasis in the late phase. Early detection of lung injury will thus help to improve management of the treatment [82]–[122].

This work can also be applied to other brain abnormalities, such as dyslexia and autism. Dyslexia is one of the most complicated developmental brain disorders that affect children's learning abilities. Dyslexia leads to the failure to develop age-appropriate reading skills in spite of a normal intelligence level and adequate reading instructions. Neuropathological studies have revealed an abnormal anatomy of some structures, such as the Corpus Callosum in dyslexic brains. There has been a lot of work in the literature that aims at developing CAD systems for diagnosing such disorders, along with other brain disorders [123]–[145].

References

1. "Health Resources. Patient Resources," *Disorder of the Month. Cerebrovascular Disease. Neurosurgery:* On-Call [serial online], July 1999.
2. Guglielmi, G., Vinuela, F., Septka, I., and Macellar, V. "Electrothrombosis of saccular aneuryms via endovascular approach: electrochemical basis, technique and experimental," *J. Neurosurg.*, vol. 75, no. 1, pp. 1–7, 1991.
3. Valk, P.E., Hale, J.D., Kufman, L., Crooks, L.E., and Higgins, C.B., "MR imaging of the aorta with three dimensional vessel reconstruction: validation by angiography," *Radiology*, vol. 157, pp. 721–725, 1985.
4. Hale, J.D., Valk, P.E., Watts, J.C., Crooks, L.E., Higgins, C.B., and Deconick, F., "MR imaging of blood vessels using three dimensional reconstruction: methodology," *Radiology*, vol. 157, pp. 727–733, 1985.
5. Prokop, M., Schaefer, C., Doehring, W., Laas, J., Nischelsky, J., and Galanski, M., "Spiral CT for three-dimensional imaging of complex vascular anatomy," *Radiology*, vol. 181, no. P, p. 293, 1991.
6. Saint-Felix, D., Campagnolo, R., Crocci, S., le Masson, P., Picard, C., and Ponchut, C., "Three dimensional x-ray computerized angiography," *Eur Radiol*, supp ECR93, p. 159, 1993.
7. Bullitt, E., Aylward, S., Smith, K., Mukherji, S., Jiroutek, M., and Muller, K., "Symbolic description of intracerebral vessels segmented from magnetic resonance angiograms and evaluation by comparison with X-ray angiograms," *Medical Imag Analysis*, vol. 5, pp. 157–169, 2001.
8. Wilson, D.L., and Noble, J.A., "An adaptive segmentation algorithm for time-of-flight MRA data," *IEEE Trans. Med. Imaging*, vol. 18, no. 10, pp. 938–945, Oct. 1999.
9. Chung, A., and Noble, J., "Statistical 3D vessel segmentation using a Rician distribution," *MICCAI*, pp. 82–89, 1999.
10. Osher, S., and Paragios, N., *Geometric Level Set Methods in Imaging, Vision, and Graphics*, Springer, 2003.
11. Terzopoulos, D., "Regularization of inverse visual problems involving discontinuities," *IEEE Tr. on PAMI*, vol. 8, no. 2, pp. 413–424, 1986.
12. Caselles, V., Kimmel, R., and Sapiro, G., "Geodesic active contours," *IJCV*, vol. 22, pp. 61–79, 1997.
13. Zaho, H-K., Chan, T., Merriman, B., and Osher, S., "A variational level set approach to multiphase motion," *J. of Computational Physics*, vol. 127, pp. 179–195, 1996.
14. Goldenberg, R., Kimmel, R., Rivlin, E., and Rudzsky, M., "Cortex segmentation: a fast variational geometric approach," *IEEE Tr. on Medical Imaging*, vol. 21, no. 2, pp. 1544–1551, December 2002.

15. Farag, A., and Hassan, H., "Adaptive segmentation of multi-modal 3D data using robust level set techniques," *To Appear in MICCAI*, Rennes, France, September 2004.
16. Lorigo, L. M., Faugeras, O.D., Grimson, W.E.L., Keriven, R., Kikinis, R., Nabavi, A., and Westin, C.F., "CURVES: curve evolution for vessel segmentation," *Medical Image Analysis*, vol. 5, no. 3, pp. 195–206, September 2001.
17. Lorigo, L.M., Faugeras, O.D., Grimson, W.E.L., Keriven, R., Kikinis, R., Nabavi, A., and Westin, C.F., "Codimension-two geodesic active contours for the segmentation of tubular structures." In: *Proceedings of the IEEE Computer Society Conference on Computer Vision and Pattern Recognition (CVPR'00)*, vol. 1, pp. 444–451, 2000.
18. Lorigo, L.M., Faugeras, O.D., Grimson, W.E.L., Keriven, R., Kikinis, R., and Westin, C.F., "Co-dimension 2 geodesic active contours for MRA segmentation." In: *International Conference on Information Processing in Medical Imaging (IPMI'99)*, Visegrad, Hungary, June 1999.
19. Vasilevskiy, A., and Siddiqi, K., "Flux maximizing geometric flows." In: *Proceedings of the IEEE International Conference on Computer Vision (ICCV'01)*, vol. 1, Vancouver, Canada, pp. 149–154, 2001.
20. Yim, P.J., Cebral, J.J., Mullick, R., Marcos, H.B., and Choyke, P.L., "Vessel surface reconstruction with a tubular deformable model," *IEEE Transaction on Medical Imaging*, vol. 20, no. 12, pp. 875–881, December 2001.
21. Yim, P.J., Vasbinder, G.B.C., Ho, V.B., and Choyke, P.L., "Isosurfaces as deformable models for magnetic resonance angiography," *IEEE Transaction on Medical Imaging*, vol. 22, no. 7, pp. 875–881, July 2003.
22. Hassouna, M.S., Farag, A.A., Hushek, S., and Moriarty, T., "Statistical-based approach for extracting 3D blood vessels from TOF-MRA data." In: *Proc. International Conference on Medical Image Computing and Computer-Assisted Intervention (MICCAI'03)*, Montreal, Canada, pp. 680–687, Nov. 15–18, 2003.
23. Sethian, J.A., *Level Set Methods and Fast Marching Methods*, Cambridge University Press, USA, 1999.
24. Gomes, J., and Faugeras, O., "Reconciling distance functions and level-sets," *Technical Report 3666*, INRIA, April 1999.
25. Paragios, N., and Deriche, R., "Unifying boundary and region-based information for geodesic active tracking," *CVPR*, vol. 2, pp. 300–305, Fort Collins, Colorado, Jun. 1999.
26. Malladi, R., Sethian, J., and Vemuri, B., "Shape modeling with front propagation: A level set approach," *IEEE Tr. on PAMI*, vol. 17, no. 2, pp. 158–175, February 1995.
27. Samson, C., Blanc-Fraud, L., Aubert, G., and Zerubia, J., "Multiphase evolution and variational image classification," *Technical Report 3662*, INRIA, France, 1999.
28. Zeng, X., Staib, L.H., Schultz, R.T., Tagare, H., Win, L., and Duncan, J.S., "A new approach to 3D sulcal ribbon finding from MR images," *MICCAI*, pp. 148–157, Sep. 1999.
29. Duda, R., Hart, P., and Stork, D., *Pattern Classification*, Wiley, New York, 2001.
30. Lamperti, J.W., *Probability*, Wiley, New York, 1996.
31. Goshtasby, A., and O'Neill, W.D., "Curve fitting by a sum of Gaussians," *CVGIP: Graphical Models and Image Processing*, vol. 56, no. 4, pp. 281–288, 1999.
32. Poggio, T., and Girosi, F., "Networks for approximation and learning," *Proc. IEEE*, vol.78, no. 9, pp. 1481–1497, 1990.
33. Farag, A.A., El-Baz, A., and Gimel'farb, G., "Density estimation using modified expectation-maximization for a linear combination of Gaussians." In: *Proc. IEEE Int. Conf. Image Processing (ICIP 2004)*, Singapore, October 2004 [in print].
34. Gimel'farb, G., Farag, A.A., and El-Baz, A., "Expectation-maximization for a linear combination of Gaussians." In: *Proc. IAPR Int. Conf. Pattern Recognition (ICPR 2004)*, Cambridge, UK, August 2004 [in print].
35. Farag, A.A., El-Baz, A., and Gimel'farb, G., "Precise image segmentation by iterative EM-based approximation of empirical gray level distribution with linear combination of Gaussians." In: *Proc. IEEE Int. Workshop on Learning in Computer Vision and Pattern Recognition*, Washington, D.C., USA, June 2004.
36. Baillard, C., Barillot, C., and Bouthemy, P., "Robust adaptive segmentation of 3D medical images with level sets." In: *Technical Report*, INRIA, France, November 2000.
37. Ali, A.M., Farag, A.A., and El-Baz, A., "Graph cuts framework for kidney segmentation with prior shape constraints." In: *Proceedings of International Conference on Medical Image Computing and Computer-Assisted Intervention, (MICCAI'07).* volume 1, Brisbane, Australia, October 29–November 2 (2007) 384–392.
38. Chowdhury, A.S., Roy, R., Bose, S., Elnakib, F.K.A., and El-Baz, A., "Non-rigid biomedical image registration using graph cuts with a novel data term." In: *Proceedings of IEEE International Symposium on Biomedical Imaging: From Nano to Macro* (ISBI'12), Barcelona, Spain, May 2–5 (2012) 446–449.

39. El-Baz, A., Farag, A.A., Yuksel, S.E., El-Ghar, M.E.A., Eldiasty, T.A., and Ghoneim, M.A., "Application of deformable models for the detection of acute renal rejection." In: Farag, A.A., Suri, J.S., eds., *Deformable Models*. Volume 1. (2007) 293–333.
40. El-Baz, A., Farag, A., Fahmi, R., Yuksel, S., El-Ghar, M.A., and Eldiasty, T., "Image analysis of renal DCE MRI for the detection of acute renal rejection." In: *Proceedings of IAPR International Conference on Pattern Recognition* (ICPR'06), Hong Kong, August 20–24 (2006) 822–825.
41. El-Baz, A., Farag, A., Fahmi, R., Yuksel, S., Miller, W., El-Ghar, M.A., El-Diasty, T., and Ghoneim, M., "A new CAD system for the evaluation of kidney diseases using DCE-MRI." In: *Proceedings of International Conference on Medical Image Computing and Computer-Assisted Intervention* (MICCAI'08), Copenhagen, Denmark, October 1–6 (2006) 446–453.
42. El-Baz, A., Gimel'farb, G., and El-Ghar, M.A., "A novel image analysis approach for accurate identification of acute renal rejection." In: *Proceedings of IEEE International Conference on Image Processing* (ICIP'08), San Diego, California, October 12–15 (2008) 1812–1815.
43. El-Baz, A., Gimel'farb, G., and El-Ghar, M.A., "Image analysis approach for identification of renal transplant rejection." In: *Proceedings of IAPR International Conference on Pattern Recognition* (ICPR'08), Tampa, Florida, December 8–11 (2008) 1–4.
44. El-Baz, A., Gimel'farb, G., and El-Ghar, M.A., "New motion correction models for automatic identification of renal transplant rejection." In: *Proceedings of International Conference on Medical Image Computing and Computer-Assisted Intervention* (MICCAI'07), Brisbane, Australia, October 29–November 2 (2007) 235–243.
45. Farag, A., El-Baz, A., Yuksel, S., El-Ghar, M.A., and Eldiasty, T., "A framework for the detection of acute rejection with Dynamic Contrast Enhanced Magnetic Resonance Imaging." In: *Proceedings of IEEE International Symposium on Biomedical Imaging: From Nano to Macro* (ISBI'06), Arlington, Virginia, April 6–9 (2006) 418–421.
46. Khalifa, F., Beache, G.M., El-Ghar, M.A., El-Diasty, T., Gimel'farb, G., Kong, M., and El-Baz, A., "Dynamic contrast-enhanced MRI-based early detection of acute renal transplant rejection." *IEEE Transactions on Medical Imaging*, vol. 32, no. 10, pp. 1910–1927, 2013.
47. Khalifa, F., El-Baz, A., Gimel'farb, G., and El-Ghar, M.A., "Non-invasive image-based approach for early detection of acute renal rejection." In: *Proceedings of International Conference Medical Image Computing and Computer-Assisted Intervention* (MICCAI'10), Beijing, China, September 20–24 (2010) 10–18.
48. Khalifa, F., El-Baz, A., Gimel'farb, G., Ouseph, R., and El-Ghar, M.A., "Shape-appearance guided level-set deformable model for image segmentation." In: *Proceedings of IAPR International Conference on Pattern Recognition* (ICPR'10), Istanbul, Turkey, August 23–26 (2010) 4581–4584.
49. Khalifa, F., El-Ghar, M.A., Abdollahi, B., Frieboes, H., El-Diasty, T., and El-Baz, A., "A comprehensive non-invasive framework for automated evaluation of acute renal transplant rejection using DCE-MRI." *NMR in Biomedicine*, vol. 26, no. 11, pp. 1460–1470, 2013.
50. Khalifa, F., El-Ghar, M.A., Abdollahi, B., Frieboes, H.B., El-Diasty, T., and El-Baz, A., "Dynamic contrast-enhanced MRI-based early detection of acute renal transplant rejection." In: *2014 Annual Scientific Meeting and Educational Course Brochure of the Society of Abdominal Radiology* (SAR'14), Boca Raton, Florida, March 23–28 (2014) CID: 1855912.
51. Khalifa, F., Elnakib, A., Beache, G.M., Gimel'farb, G., El-Ghar, M.A., Sokhadze, G., Manning, S., McClure, P., and El-Baz, A., "3D kidney segmentation from CT images using a level set approach guided by a novel stochastic speed function." In: *Proceedings of International Conference Medical Image Computing and Computer-Assisted Intervention* (MICCAI'11), Toronto, Canada, September 18–22 (2011) 587–594.
52. Khalifa, F., Gimel'farb, G., El-Ghar, M.A., Sokhadze, G., Manning, S., McClure, P., Ouseph, R., and El-Baz, A., "A new deformable model-based segmentation approach for accurate extraction of the kidney from abdominal CT images." In: *Proceedings of IEEE International Conference on Image Processing* (ICIP'11), Brussels, Belgium, September 11–14 (2011) 3393–3396.
53. Mostapha, M., Khalifa, F., Alansary, A., Soliman, A., Suri, J., and El-Baz, A., "Computer-aided diagnosis systems for acute renal transplant rejection: Challenges and methodologies." In El-Baz, A., Suri, J., eds., *Abdomen and Thoracic Imaging*. Springer (2014) 1–35.
54. Shehata, M., Khalifa, F., Hollis, E., Soliman, A., Hosseini-Asl, E., El-Ghar, M.A., El-Baz, M., Dwyer, A.C., El-Baz, A., and Keynton, R., "A new non-invasive approach for early classification of renal rejection types using diffusion-weighted MRI." In: *IEEE International Conference on Image Processing* (ICIP), IEEE (2016) 136–140.

55. Khalifa, F., Soliman, A., Takieldeen, A., Shehata, M., Mostapha, M., Shaffie, A., Ouseph, R., Elmaghraby, A., and El-Baz, A., "Kidney segmentation from CT images using a 3D NMF-guided active contour model." In: *IEEE 13th International Symposium on Biomedical Imaging* (ISBI), IEEE (2016) 432–435.
56. Shehata, M., Khalifa, F., Soliman, A., Takieldeen, A., El-Ghar, M.A., Shaffie, A., Dwyer, A.C., Ouseph, R., El-Baz, A., and Keynton, R., "3d diffusion MRI-based CAD system for early diagnosis of acute renal rejection." In: *13th International Symposium on Biomedical Imaging (ISBI*), IEEE (2016) 1177–1180.
57. Shehata, M., Khalifa, F., Soliman, A., Alrefai, R., El-Ghar, M.A., Dwyer, A.C., Ouseph, R., and El-Baz, A., "A level set-based framework for 3d kidney segmentation from diffusion MR images." In: *IEEE International Conference on Image Processing* (ICIP), IEEE (2015) 4441–4445.
58. Shehata, M., Khalifa, F., Soliman, A., El-Ghar, M.A., Dwyer, A.C., Gimelfarb, G., Keynton, R., and El-Baz, A., "A promising non-invasive CAD system for kidney function assessment." In: *International Conference on Medical Image Computing and Computer-Assisted Intervention*, Springer (2016) 613–621.
59. Khalifa, F., Soliman, A., Elmaghraby, A., Gimelfarb, G., and El-Baz, A., "3d kidney segmentation from abdominal images using spatial-appearance models." *Computational and Mathematical Methods in Medicine* (2017).
60. Hollis, E., Shehata, M., Khalifa, F., El-Ghar, M.A., El-Diasty, T., and El-Baz, A., "Towards non-invasive diagnostic techniques for early detection of acute renal transplant rejection: a review." *The Egyptian Journal of Radiology and Nuclear Medicine*, vol. 48, no. 1, pp. 257–269, 2016.
61. Shehata, M., Khalifa, F., Soliman, A., El-Ghar, M.A., Dwyer, A.C., and El-Baz, A., "Assessment of renal transplant using image and clinical-based biomarkers." In: *Proceedings of 13th Annual Scientific Meeting of American Society for Diagnostics and Interventional Nephrology* (ASDIN'17), New Orleans, LA, February 10–12 (2017).
62. Shehata, M., Khalifa, F., Soliman, A., El-Ghar, M.A., Dwyer, A.C., and El-Baz, A., "Early assessment of acute renal rejection." In: *Proceedings of 12th Annual Scientific Meeting of American Society for Diagnostics and Interventional Nephrology* (ASDIN'16), Phoenix, Arizona, February 19–21 (2017).
63. Khalifa, F., Beache, G., El-Baz, A., and Gimel'farb, G., "Deformable model guided by stochastic speed with application in cine images segmentation." In: *Proceedings of IEEE International Conference on Image Processing* (ICIP'10), Hong Kong, September 26–29 (2010) 1725–1728.
64. Khalifa, F., Beache, G.M., Elnakib, A., Sliman, H., Gimel'farb, G., Welch, K.C., and El-Baz, A., "A new shape-based framework for the left ventricle wall segmentation from cardiac first-pass perfusion MRI." In: *Proceedings of IEEE International Symposium on Biomedical Imaging: From Nano to Macro* (ISBI'13), San Francisco, California, April 7–11 (2013) 41–44.
65. Khalifa, F., Beache, G.M., Elnakib, A., Sliman, H., Gimel'farb, G., Welch, K.C., and El-Baz, A., "A new nonrigid registration framework for improved visualization of transmural perfusion gradients on cardiac first–pass perfusion MRI." In: *Proceedings of IEEE International Symposium on Biomedical Imaging: From Nano to Macro* (ISBI'12), Barcelona, Spain, May 2–5 (2012) 828–831.
66. Khalifa, F., Beache, G.M., Firjani, A., Welch, K.C., Gimel'farb, G., and El-Baz, A., "A new nonrigid registration approach for motion correction of cardiac first-pass perfusion MRI." In: *Proceedings of IEEE International Conference on Image Processing* (ICIP'12), Lake Buena Vista, Florida, September 30–October 3 (2012) 1665–1668.
67. Khalifa, F., Beache, G.M., Gimel'farb, G., and El-Baz, A., "A novel CAD system for analyzing cardiac first-pass MR images." In: *Proceedings of IAPR International Conference on Pattern Recognition* (ICPR'12), Tsukuba Science City, Japan, November 11–15 (2012) 77–80.
68. Khalifa, F., Beache, G.M., Gimel'farb, G., and El-Baz, A., "A novel approach for accurate estimation of left ventricle global indexes from short-axis cine MRI." In: *Proceedings of IEEE International Conference on Image Processing* (ICIP'11), Brussels, Belgium, September 11–14 (2011) 2645–2649.
69. Khalifa, F., Beache, G.M., Gimel'farb, G., Giridharan, G.A., and El-Baz, A., "A new image-based framework for analyzing cine images." In: El-Baz, A., Acharya, U.R., Mirmedhdi, M., Suri, J.S., eds.: *Handbook of Multi Modality State-of-the-Art Medical Image Segmentation and Registration Methodologies*. Volume 2. Springer, New York (2011) 69–98.
70. Khalifa, F., Beache, G.M., Gimel'farb, G., Giridharan, G.A., and El-Baz, A., "Accurate automatic analysis of cardiac cine images." *IEEE Transactions on Biomedical Engineering*, vol. 59, no. 2, pp. 445–455, 2012.
71. Khalifa, F., Beache, G.M., Nitzken, M., Gimel'farb, G., Giridharan, G.A., and El-Baz, A., "Automatic analysis of left ventricle wall thickness using short-axis cine CMR images." In: *Proceedings of IEEE International Symposium on Biomedical Imaging: From Nano to Macro* (ISBI'11), Chicago, Illinois, March 30–April 2 (2011) 1306–1309.

72. Nitzken, M., Beache, G., Elnakib, A., Khalifa, F., Gimel'farb, G., and El-Baz, A., "Accurate modeling of tagged CMR 3D image appearance characteristics to improve cardiac cycle strain estimation." In: *IEEE International Conference on Image Processing* (ICIP), Orlando, Florida, IEEE (September 2012) 521–524.
73. Nitzken, M., Beache, G., Elnakib, A., Khalifa, F., Gimel'farb, G., and El-Baz, A., "Improving full-cardiac cycle strain estimation from tagged CMR by accurate modeling of 3D image appearance characteristics." In: *IEEE International Symposium on Biomedical Imaging* (ISBI), Barcelona, Spain, IEEE (May 2012) 462–465 (Selected for oral presentation).
74. Nitzken, M.J., El-Baz, A.S., and Beache, G.M., "Markov-Gibbs random field model for improved full-cardiac cycle strain estimation from tagged CMR." *Journal of Cardiovascular Magnetic Resonance*, vol. 14, no. 1, pp. 1–2, 2012.
75. Sliman, H., Elnakib, A., Beache, G., Elmaghraby, A., and El-Baz, A., "Assessment of myocardial function from cine cardiac MRI using a novel 4D tracking approach." *J Comput Sci Syst Biol*, vol. 7, pp. 169–173, 2014.
76. Sliman, H., Elnakib, A., Beache, G.M., Soliman, A., Khalifa, F., Gimel'farb, G., Elmaghraby, A., and El-Baz, A., "A novel 4D PDE-based approach for accurate assessment of myocardium function using cine cardiac magnetic resonance images." In: *Proceedings of IEEE International Conference on Image Processing* (ICIP'14), Paris, France, October 27–30 (2014) 3537–3541.
77. Sliman, H., Khalifa, F., Elnakib, A., Beache, G.M., Elmaghraby, A., and El-Baz, A., "A new segmentation-based tracking framework for extracting the left ventricle cavity from cine cardiac MRI." In: *Proceedings of IEEE International Conference on Image Processing* (ICIP'13), Melbourne, Australia, September 15–18 (2013) 685–689.
78. Sliman, H., Khalifa, F., Elnakib, A., Soliman, A., Beache, G.M., Elmaghraby, A., Gimel'farb, G., and El-Baz, A., "Myocardial borders segmentation from cine MR images using bi-directional coupled parametric deformable models." *Medical Physics*, vol. 40, no. 9, pp. 1–13, 2013.
79. Sliman, H., Khalifa, F., Elnakib, A., Soliman, A., Beache, G.M., Gimel'farb, G., Emam, A., Elmaghraby, A., and El-Baz, A., "Accurate segmentation framework for the left ventricle wall from cardiac cine MRI." In: *Proceedings of International Symposium on Computational Models for Life Science (CMLS'13).* Volume 1559, Sydney, Australia, November 27–29 (2013) 287–296.
80. Eladawi, N., Elmogy, M., et al., "Classification of retinal diseases based on OCT images." *Frontiers in Bioscience Landmark Journal* (2017).
81. ElTanboly, A., Ismail, M., et al., "A computer aided diagnostic system for detecting diabetic retinopathy in optical coherence tomography images." *Medical Physics* (2016).
82. Abdollahi, B., Civelek, A.C., Li, X.F., Suri, J., and El-Baz, A., "PET/CT nodule segmentation and diagnosis: A survey." In Saba, L., Suri, J., eds.: *Multi Detector CT Imaging*. Taylor, Francis (2014) 639–651.
83. Abdollahi, B., El-Baz, A., and Amini, A.A., "A multi-scale non-linear vessel enhancement technique." In: *2011 Annual International Conference of Engineering in Medicine and Biology Society* (EMBC), IEEE (2011) 3925–3929.
84. Abdollahi, B., Soliman, A., Civelek, A., Li, X.F., Gimel'farb, G., and El-Baz, A., "A novel Gaussian scale space-based joint MGRF framework for precise lung segmentation." In: *Proceedings of IEEE International Conference on Image Processing* (ICIP'12), IEEE (2012) 2029–2032.
85. Abdollahi, B., Soliman, A., Civelek, A., Li, X.F., Gimelfarb, G., and El-Baz, A., "A novel 3D joint MGRF framework for precise lung segmentation." In: *Machine Learning in Medical Imaging*. Springer (2012) 86–93.
86. Ali, A.M., El-Baz, A.S., and Farag, A.A., "A novel framework for accurate lung segmentation using graph cuts." In: *Proceedings of IEEE International Symposium on Biomedical Imaging: From Nano to Macro* (ISBI'07), IEEE (2007) 908–911.
87. El-Baz, A., Beache, G.M., Gimel'farb, G., Suzuki, K., and Okada, K., "Lung imaging data analysis." *International Journal of Biomedical Imaging* (2013).
88. El-Baz, A., Beache, G.M., Gimel'farb, G., Suzuki, K., Okada, K., Elnakib, A., Soliman, A., and Abdollahi, B., "Computer-aided diagnosis systems for lung cancer: Challenges and methodologies." *International Journal of Biomedical Imaging* (2013).
89. El-Baz, A., Elnakib, A., Abou El-Ghar, M., Gimel'farb, G., Falk, R., and Farag, A., "Automatic detection of 2D and 3D lung nodules in chest spiral CT scans." *International Journal of Biomedical Imaging* (2013).
90. El-Baz, A., Farag, A.A., Falk, R., and La Rocca, R., "A unified approach for detection, visualization, and identification of lung abnormalities in chest spiral CT scans." In: *International Congress Series*, Volume 1256, Elsevier (2003) 998–1004.

91. El-Baz, A., Farag, A.A., Falk, R., and La Rocca, R., "Detection, visualization and identification of lung abnormalities in chest spiral CT scan: Phase-I." In: *Proceedings of International Conference on Biomedical Engineering*, Cairo, Egypt. Volume 12. (2002).
92. El-Baz, A., Farag, A., Gimel'farb, G., Falk, R., El-Ghar, M.A., and Eldiasty, T., "A framework for automatic segmentation of lung nodules from low dose chest CT scans." In: *Proceedings of International Conference on Pattern Recognition (ICPR'06)*. Volume 3, IEEE (2006) 611–614.
93. El-Baz, A., Farag, A., Gimelfarb, G., Falk, R., and El-Ghar, M.A., "A novel level set-based computer-aided detection system for automatic detection of lung nodules in low dose chest computed tomography scans." *Lung Imaging and Computer Aided Diagnosis*, vol. 10, pp. 221–238, 2011.
94. El-Baz, A., Gimel'farb, G., Abou El-Ghar, M., and Falk, R., "Appearance-based diagnostic system for early assessment of malignant lung nodules." In: *Proceedings of IEEE International Conference on Image Processing* (ICIP'12), IEEE (2012) 533–536.
95. El-Baz, A., Gimel'farb, G., and Falk, R., "A novel 3D framework for automatic lung segmentation from low dose CT images." In El-Baz, A., Suri, J.S., eds.: *Lung Imaging and Computer Aided Diagnosis*. Taylor, Francis (2011) 1–16.
96. El-Baz, A., Gimel'farb, G., Falk, R., and El-Ghar, M., "Appearance analysis for diagnosing malignant lung nodules." In: *Proceedings of IEEE International Symposium on Biomedical Imaging: From Nano to Macro (ISBI'10)*, IEEE (2010) 193–196.
97. El-Baz, A., Gimel'farb, G., Falk, R., and El-Ghar, M.A., "A novel level set-based CAD system for automatic detection of lung nodules in low dose chest CT scans." In El-Baz, A., Suri, J.S., eds.: *Lung Imaging and Computer Aided Diagnosis*. Volume 1. Taylor, Francis (2011) 221–238.
98. El-Baz, A., Gimel'farb, G., Falk, R., and El-Ghar, M.A., "A new approach for automatic analysis of 3D low dose CT images for accurate monitoring the detected lung nodules." In: *Proceedings of International Conference on Pattern Recognition (ICPR'08)*, IEEE (2008) 1–4.
99. El-Baz, A., Gimel'farb, G., Falk, R., and El-Ghar, M.A., "A novel approach for automatic follow-up of detected lung nodules." In: *Proceedings of IEEE International Conference on Image Processing* (ICIP'07). Volume 5, IEEE (2007) V–501.
100. El-Baz, A., Gimel'farb, G., Falk, R., and El-Ghar, M.A., "A new CAD system for early diagnosis of detected lung nodules." In: *International Conference on Image Processing* (ICIP). Volume 2, IEEE (2007) II–461.
101. El-Baz, A., Gimel'farb, G., Falk, R., El-Ghar, M.A., and Refaie, H., "Promising results for early diagnosis of lung cancer." In: *Proceedings of IEEE International Symposium on Biomedical Imaging: From Nano to Macro (ISBI'08)*, IEEE (2008) 1151–1154.
102. El-Baz, A., Gimel'farb, G.L., Falk, R., Abou El-Ghar, M., Holland, T., and Shaffer, T., "A new stochastic framework for accurate lung segmentation." In: *Proceedings of Medical Image Computing and Computer-Assisted Intervention* (MICCAI'08), (2008) 322–330.
103. El-Baz, A., Gimel'farb, G.L., Falk, R., Heredis, D., and Abou El-Ghar, M., "A novel approach for accurate estimation of the growth rate of the detected lung nodules." In: *Proceedings of International Workshop on Pulmonary Image Analysis* (2008) 33–42.
104. El-Baz, A., Gimel'farb, G.L., Falk, R., Holland, T., and Shaffer, T., "A framework for unsupervised segmentation of lung tissues from low dose computed tomography images." In: *Proceedings of British Machine Vision* (BMVC'08), (2008) 1–10.
105. El-Baz, A., Gimelfarb, G., Falk, R., and El-Ghar, M.A., "3D MGRF-based appearance modeling for robust segmentation of pulmonary nodules in 3D LDCT chest images." In: *Lung Imaging and Computer Aided Diagnosis* (2011) 51–63.
106. El-Baz, A., Gimelfarb, G., Falk, R., and El-Ghar, M.A., "Automatic analysis of 3D low dose CT images for early diagnosis of lung cancer." *Pattern Recognition*, vol. 42, no. 6, pp. 1041–1051, 2009.
107. El-Baz, A., Gimelfarb, G., Falk, R., El-Ghar, M.A., Rainey, S., Heredia, D., and Shaffer, T., "Toward early diagnosis of lung cancer." In: *Proceedings of Medical Image Computing and Computer-Assisted Intervention (MICCAI'09)*, Springer (2009) 682–689.
108. El-Baz, A., Gimelfarb, G., Falk, R., El-Ghar, M.A., Suri, J., "Appearance analysis for the early assessment of detected lung nodules." In: *Lung Imaging and Computer Aided Diagnosis* (2011) 395–404.
109. El-Baz, A., Khalifa, F., Elnakib, A., Nitkzen, M., Soliman, A., McClure, P., Gimel'farb, G., El-Ghar, M.A., "A novel approach for global lung registration using 3D Markov Gibbs appearance model." In: *Proceedings of International Conference Medical Image Computing and Computer-Assisted Intervention* (MICCAI'12), Nice, France, October 1–5 (2012) 114–121.

110. El-Baz, A., Nitzken, M., Elnakib, A., Khalifa, F., Gimel'farb, G., Falk, R., and El-Ghar, M.A., "3D shape analysis for early diagnosis of malignant lung nodules." In: *Proceedings of International Conference Medical Image Computing and Computer-Assisted Intervention (MICCAI'11)*, Toronto, Canada, September 18–22 (2011) 175–182.
111. El-Baz, A., Nitzken, M., Gimelfarb, G., Van Bogaert, E., Falk, R., El-Ghar, M.A., and Suri, J., "Three-dimensional shape analysis using spherical harmonics for early assessment of detected lung nodules." In: *Lung Imaging and Computer Aided Diagnosis* (2011) 421–438.
112. El-Baz, A., Nitzken, M., Khalifa, F., Elnakib, A., Gimel'farb, G., Falk, R., and El-Ghar, M.A., "3D shape analysis for early diagnosis of malignant lung nodules." In: *Proceedings of International Conference on Information Processing in Medical Imaging* (IPMI'11), Monastery Irsee, Germany (Bavaria), July 3–8 (2011) 772–783.
113. El-Baz, A., Nitzken, M., Vanbogaert, E., Gimel'Farb, G., Falk, R., and Abo El-Ghar, M., "A novel shape-based diagnostic approach for early diagnosis of lung nodules." In: *IEEE International Symposium on Biomedical Imaging: From Nano to Macro* (2011) 137–140.
114. El-Baz, A., Sethu, P., Gimel'farb, G., Khalifa, F., Elnakib, A., Falk, R., and El-Ghar, M.A., "Elastic phantoms generated by microfluidics technology: validation of an imaged-based approach for accurate measurement of the growth rate of lung nodules." *Biotechnology Journal*, vol. 6, no. 2, pp. 195–203, 2011.
115. El-Baz, A., Sethu, P., Gimel'farb, G., Khalifa, F., Elnakib, A., Falk, R., and El-Ghar, M.A., "A new validation approach for the growth rate measurement using elastic phantoms generated by state-of-the-art microfluidics technology." In: *Proceedings of IEEE International Conference on Image Processing* (ICIP'10), Hong Kong, September 26–29 (2010) 4381–4383.
116. El-Baz, A., Sethu, P., Gimel'farb, G., et al., "Validation of a new imaged-based approach for the accurate estimating of the growth rate of detected lung nodules using real CT images and elastic phantoms generated by state-of-the-art microfluidics technology." In El-Baz, A., Suri, J.S., eds.: *Handbook of Lung Imaging and Computer Aided Diagnosis*. Volume 1. Taylor & Francis, New York (2011) 405–420.
117. El-Baz, A., Soliman, A., McClure, P., Gimel'farb, G., El-Ghar, M.A., and Falk, R., "Early assessment of malignant lung nodules based on the spatial analysis of detected lung nodules." In: *Proceedings of IEEE International Symposium on Biomedical Imaging: From Nano to Macro* (ISBI'12), IEEE (2012) 1463–1466.
118. El-Baz, A., Yuksel, S.E., Elshazly, S., and Farag, A.A., "Non-rigid registration techniques for automatic follow-up of lung nodules." In: *Proceedings of Computer Assisted Radiology and Surgery (CARS'05).* Volume 1281, Elsevier (2005) 1115–1120.
119. El-Baz, A.S., and Suri, J.S., *Lung Imaging and Computer Aided Diagnosis.* CRC Press (2011).
120. Soliman, A., Khalifa, F., Shaffie, A., Liu, N., Dunlap, N., Wang, B., Elmaghraby, A., Gimelfarb, G., and El-Baz, A., "Image-based CAD system for accurate identification of lung injury." In: *Proceedings of IEEE International Conference on Image Processing* (ICIP'16), IEEE (2016) 121–125.
121. Soliman, A., Khalifa, F., Dunlap, N., Wang, B., El-Ghar, M., and El-Baz, A., "An iso-surfaces based local deformation handling framework of lung tissues." In: *13th International Symposium on Biomedical Imaging* (ISBI), IEEE (2016) 1253–1259.
122. Soliman, A., Khalifa, F., Shaffie, A., Dunlap, N., Wang, B., Elmaghraby, A., and El-Baz, A., "Detection of lung injury using 4d-CT chest images." In: *13th International Symposium on Biomedical Imaging* (ISBI), IEEE (2016) 1274–1277.
123. Dombroski, B., Nitzken, M., Elnakib, A., Khalifa, F., El-Baz, A., and Casanova, M.F., "Cortical surface complexity in a population-based normative sample." *Translational Neuroscience*, vol. 5, no. 1, pp. 17–24, 2014.
124. El-Baz, A., Casanova, M., Gimel'farb, G., Mott, M., and Switala, A., "An MRI-based diagnostic framework for early diagnosis of dyslexia." *International Journal of Computer Assisted Radiology and Surgery*, vol. 3, no. 3–4, pp. 181–189, 2008.
125. El-Baz, A., Casanova, M., Gimel'farb, G., Mott, M., Switala, A., Vanbogaert, E., and McCracken, R., "A new CAD system for early diagnosis of dyslexic brains." In: *Proc. International Conference on Image Processing* (ICIP'2008), IEEE (2008) 1820–1823.
126. El-Baz, A., Casanova, M.F., Gimel'farb, G., Mott, M., and Switwala, A.E., "A new image analysis approach for automatic classification of autistic brains." In: *Proc. IEEE International Symposium on Biomedical Imaging: From Nano to Macro* (ISBI'2007), IEEE (2007) 352–355.
127. El-Baz, A., Elnakib, A., Khalifa, F., El-Ghar, M.A., McClure, P., Soliman, A., and Gimel'farb, G., "Precise segmentation of 3-D magnetic resonance angiography." *IEEE Transactions on Biomedical Engineering*, vol. 59, no. 7, pp. 2019–2029, 2012.
128. El-Baz, A., Farag, A.A., Gimel'farb, G.L., El-Ghar, M.A., and Eldiasty, T., "Probabilistic modeling of blood vessels for segmenting mra images." In: *ICPR* (3) (2006) 917–920.

129. El-Baz, A., Farag, A.A., Gimelfarb, G., El-Ghar, M.A., and Eldiasty, T., "A new adaptive probabilistic model of blood vessels for segmenting mra images." In: *Medical Image Computing and Computer-Assisted Intervention* (MICCAI 2006), Volume 4191, Springer (2006) 799–806.
130. El-Baz, A., Farag, A.A., Gimelfarb, G., and Hushek, S.G., "Automatic cerebrovascular segmentation by accurate probabilistic modeling of TOF-MRA images." In: *Medical Image Computing and Computer-Assisted Intervention* (MICCAI 2005) Springer (2005) 34–42.
131. El-Baz, A., Farag, A., Elnakib, A., Casanova, M.F., Gimel'farb, G., Switala, A.E., Jordan, D., and Rainey, S., "Accurate automated detection of autism related corpus callosum abnormalities." *Journal of Medical Systems*, vol. 35, no. 5, pp. 929–939, 2011.
132. El-Baz, A., Farag, A., and Gimelfarb, G., "Cerebrovascular segmentation by accurate probabilistic modeling of TOF-MRA images." In: *Image Analysis*. Volume 3540, Springer (2005) 1128–1137.
133. El-Baz, A., Gimelfarb, G., Falk, R., El-Ghar, M.A., Kumar, V., and Heredia, D., "A novel 3D joint Markov-Gibbs model for extracting blood vessels from PC–MRA images." In: *Medical Image Computing and Computer-Assisted Intervention* (MICCAI 2009), Volume 5762, Springer (2009) 943–950.
134. Elnakib, A., El-Baz, A., Casanova, M.F., Gimel'farb, G., and Switala, A.E., "Image-based detection of corpus callosum variability for more accurate discrimination between dyslexic and normal brains." In: *Proc. IEEE International Symposium on Biomedical Imaging: From Nano to Macro* (ISBI'2010), IEEE (2010) 109–112.
135. Elnakib, A., Casanova, M.F., Gimel'farb, G., Switala, A.E., and El-Baz, A., "Autism diagnostics by centerline-based shape analysis of the corpus callosum." In: *Proc. IEEE International Symposium on Biomedical Imaging: From Nano to Macro* (ISBI'2011), IEEE (2011) 1843–1846.
136. Elnakib, A., Nitzken, M., Casanova, M., Park, H., Gimel'farb, G., and El-Baz, A., "Quantification of age-related brain cortex change using 3D shape analysis." In: *International Conference on Pattern Recognition* (ICPR), IEEE (2012) 41–44.
137. Mostapha, M., Soliman, A., Khalifa, F., Elnakib, A., Alansary, A., Nitzken, M., Casanova, M.F., and El-Baz, A., "A statistical framework for the classification of infant DT images." In: *International Conference on Image Processing* (ICIP), IEEE (2014) 2222–2226.
138. Nitzken, M., Casanova, M., Gimel'farb, G., Elnakib, A., Khalifa, F., Switala, A., and El-Baz, A., "3D shape analysis of the brain cortex with application to dyslexia." In: *18th IEEE International Conference on Image Processing* (ICIP), Brussels, Belgium, IEEE (September 2011) 2657–2660 (Selected for oral presentation. Oral acceptance rate is 10 percent and the overall acceptance rate is 35 percent).
139. El-Gamal, F.E.Z.A., Elmogy, M., Ghazal, M., Atwan, A., Barnes, G., Casanova, M., Keynton, R., and El-Baz, A., "A novel CAD system for local and global early diagnosis of alzheimers disease based on pib-pet scans." In: *International Conference on Image Processing* (ICIP), Beijing, China, IEEE (2017).
140. Ismail, M., Soliman, A., et al., "A fast stochastic framework for automatic mr brain images segmentation".
141. Ismail, M.M., Keynton, R.S., Mostapha, M.M., ElTanboly, A.H., Casanova, M.F., Gimel'farb, G.L., and El-Baz, A., "Studying autism spectrum disorder with structural and diffusion magnetic resonance imaging: a survey." *Frontiers in Human Neuroscience*, vol. 10, 2016.
142. Alansary, A., Ismail, M., Soliman, A., Khalifa, F., Nitzken, M., Elnakib, A., Mostapha, M., Black, A., Stinebruner, K., Casanova, M.F., et al., "Infant brain extraction in t1-weighted MR images using BET and refinement using LCDG and MGRF models." *IEEE Journal of Biomedical and Health Informatics*, vol. 20, no. 3, pp. 925–935, 2016.
143. Ismail, M., Barnes, G., Nitzken, M., Switala, A., Shalaby, A., Hosseini-Asl, E., Casanova, M., Keynton, R., Khalil, A., and El-Baz, A., "A new deep-learning approach for early detection of shape variations in autism using structural MRI." In: *Proceedings of IEEE International Conference on Image Processing* (2017) 10571061.
144. Ismail, M., Soliman, A., ElTanboly, A., Switala, A., Mahmoud, M., Khalifa, F., Gimel'farb, G., Casanova, M. F., Keynton, R., and El-Baz, A., "Detection of white matter abnormalities in MR brain images for diagnosis of autism in children." In *International Symposium on Biomedical Imaging* (2016) 6–9.
145. Ismail, M., Mostapha, M., Soliman, A., Nitzken, M., Khalifa, F., Elnakib, A., Gimel'farb, G., Casanova, M., and El-Baz, A., "Segmentation of infant brain MR images based on adaptive shape prior and higher-order MGRF." In: *Proceedings of IEEE International Conference on Image Processing* (2015) 4327–4331.
146. Shalaby, A., Taher, F., El-Baz, M., Ghazal, V., Abou El-Ghar, M., Takieldeen, A., and El-Baz, A., "Probabilistic modeling of blood vessels for segmenting magnetic resonance angiography images." In: *Medical Research Archive* (MRA), KEI (2017) 34–42.
147. Chowdhury, A.S., Rudra, A.K., Sen, M., Elnakib, A., and El-Baz, A., "Cerebral white matter segmentation from MRI using probabilistic graph cuts and geometric shape priors." In: *ICIP* (2010) 3649–3652.

Taylor & Francis
Taylor & Francis Group
http://taylorandfrancis.com

4 Accurate Unsupervised 3D Segmentation of Blood Vessels Using Magnetic Resonance Angiography

Ahmed Shalaby[1], Ali Mahmoud[1], Samineh Mesbah[1], Maryam El-Baz[1], Jasjit S. Suri[2], Ayman El-Baz[1]
[1]University of Louisville
[2]AtheroPoint, LLC

CONTENTS

4.1 INTRODUCTION

Accurate segmentation of MRA images to extract a 3D cerebrovascular system is one of most important problems in practical computer-assisted medical diagnostics. PC-MRA provides good suppression of background signals and quantifies blood flow velocity vectors for each voxel. TOF-MRA is less quantitative, but it is fast and provides images with high contrast. The most popular present techniques for extracting blood vessels from the MRA data are scale-space filtering, deformable models, statistical models, and hybrid methods.

Multiscale filtering [1]–[6] enhances curvilinear structures in 3D medical images by convolving an image with Gaussian filters at multiple scales. Eigenvalues of the Hessian at each voxel are analyzed to determine the local shapes of 3D structures (by the eigenvalues, voxels from a linear structure like a blood vessel differ from those for a planar structure, speckle noise, or unstructured component). The multiscale filter output forms a new enhanced image such that the curvilinear structures become brighter, whereas other components (e.g., speckle noise and planar structures such as skin) are darker [1], [5], [6]. Such an image can be directly visualized [5], or thresholded [1], or segmented using a deformable model [6]. Alternatively, the obtained eigenvalues define a candidate set of voxels corresponding to centerlines of the vessels [2]–[4]. Multiscale filter responses at each of the candidates determine how likely that voxel belongs to a vessel of each particular diameter. The maximal response over all the diameters (scales) is assigned to each voxel, and a surface

model of the entire vascular structure is reconstructed from the estimated centerlines and diameters. After segmenting the filtered MRA image by thresholding, anisotropic diffusion techniques are used to remove noise but preserve small vessels [3], [7], [8].

An alternative medial axes based multiscale approach assumes the vessels centerlines are often the brightest and detects them as intensity ridges of the image [9]. The vessel's width is then determined by multiscale filter responses. This algorithm has been used in conjunction with 2D/3D registration to incorporate information from a pair of X-ray angiograms [10]. By involving differential geometry, the volumetric MRA image is treated as a hypersurface in a 4D space whose extrema of curvature correspond to the vessel centerlines [11].

Deformable model approaches to 3D vascular segmentation attempt to approximate the boundary surface of the blood vessels. An initial boundary is evolving in order to optimize a surface energy, which depends on image gradients and surface smoothness [12]. Topologically adaptable surfaces make classical deformable models more efficient for segmenting intracranial vasculature [13]. Geodesic active contours implemented with level set techniques offer flexible topological adaptability to segment the MRA images [14], including more efficient adaptation to local geometric structures represented (e.g., by tensor eigenvalues) [15]. Fast segmentation of blood vessel surfaces is obtained by inflating a 3D balloon with fast marching methods [16]. Two-step segmentation of a 3D vascular tree in [17] is first carried out locally in a small volume of interest. Then a global topology is estimated to initialize a new volume of interest. A multiscale geometrical flow is proposed in [18] to segment the vascular tree.

Comparing to the scale-space filtering, the deformable models produce much better experimental results but have a common drawback, namely, a manual initialization. Also both groups are slow compared to statistical approaches.

Statistical extraction of a vascular tree is completely automatic, but its accuracy depends on underlying probability models. The MRA images are multi-modal in that the signals (intensities, or gray levels) in each region-of-interest (e.g., blood vessels, brain tissues, etc.) are associated with a particular dominant mode of the total marginal probability distribution of signals. To the best of our knowledge, adaptive statistical approaches for extracting blood vessels from the MRA images have been proposed so far only by Wilson and Noble [19] for the TOF-MRA data and Chung and Noble [20] for the PC-MRA data. The former approach represents the marginal data distribution with a mixture of two Gaussians and one uniform component for the stationary CSF, brain tissues, and arteries, respectively, whereas the latter approach replaces the Gaussians with the more adequate Rician distributions. To identify the mixture (i.e., estimate all its parameters), a conventional EM algorithm is used in both cases. It was called a "modified EM" in [19], after replacing gray levels in individual pixels considered by their initial EM scheme with a marginal gray level distribution. Actually, such a modification simply returns to what is in common use for decades in probability density estimation (see, e.g., [21]), while the individual pixels appeared in their initial scheme only as an unduly verbatim replica of a general EM framework.

Different hybrid approaches attempt to combine the aforementioned three approaches. For instance, a region-based deformable contour for segmenting tubular structures is derived in [22] by combining signal statistics and shape information. A combination of a Gaussian statistical model with the maximum intensity projection (MIP) images acquired at three orthogonal directions [23] allows for extracting blood vessels iteratively from images acquired by rotational angiography. The MIP Z-buffer is segmented using a continuity criterion to generate candidate sets of "seed" voxels being then coupled with a global threshold to extract the whole tree using region growing techniques [24].

Cylinder matching [25], [26] detects vessels by minimizing the inertia moments of a cylinder and using prior knowledge about the intensity profiles in and at the edge of a vessel. A more generalized technique in [27] approximates the vessel's cross-section by a polygon. Continuity and orientation between the consecutive slices are used to calculate a locally optimal shape for the polygon with

good accuracy. An octree decomposition of a velocity field PC-MRA image is proposed in [28] to find an optimal tessellation. Each block of the octree contains at most one feature defined by gray levels and orientation vectors.

An alternative approach in [29] extracts an initial shape of vessels by image thresholding. Then a locally smooth surface is formed by region growing using binary morphological operations. A recursive hybrid segmentation framework in [30], [31] combines a prior Gibbs random field model, marching cubes, and deformable models. First, the Gibbs model is used to estimate object boundaries using region information from 2D slices. Then the estimated boundaries and the marching cubes technique are used to construct a 3D mesh specifying the initial geometry of a deformable model. Finally, the deformable model fits to the data under the 3D image gradient forces.

The preceding overview shows the following limitations of the existing approaches:

1. Most of them presume only a single type of image (e.g., TOF- or PC-MRA).
2. Most of them require user interaction to initialize a vessel of interest.
3. Some deformable models assume the circular vessels cross-sections; this holds for healthy people but not for patients with stenosis or aneurysm.
4. All but statistical approaches are computationally expensive.
5. Known statistical approaches use only predefined probability models that cannot fit all the cases because actual intensity distributions for blood vessels depend on the patient, scanner, and scanning parameters.

In the following, we show the fast and highly accurate statistical approach to extract blood vessels that can be obtained when the probability models of each region-of-interest in TOF- or PC-MRA images are precisely identified rather than predefined as in [19], [20]. In our approach, the empirical gray level distribution for each MRA slice is closely approximated with an LCDG. Then the latter is split into three individual LCDGs, one per region-of-interest. These regions associated with the three dominant modes relate to darker bones and fat, gray brain tissues, and bright blood vessels, respectively. The identified models specify an intensity threshold for extracting blood vessels in that slice. Finally, a 3D connectivity filter is applied to the extracted voxels to select the desired cerebrovascular system.

As our multiple experiments show, more precise region models result in significantly better segmentation accuracy compared to other methods.

4.2 SLICE-WISE SEGMENTATION WITH THE LCDG MODELS

We use the expected log-likelihood as a model identification criterion. Let $\mathbf{X} = (\mathbf{X}_s : s = 1,\ldots,S)$ denote a 3D MRA image containing S co-registered 2D slices $\mathbf{X}_s = (X_s(i,j) : (i,j) \in \mathbf{R}; X_s(i,j) \in \mathbf{Q})$. Here, $\mathbf{R}$ and $\mathbf{Q} = (0,1,\ldots,Q-1)$ are a rectangular arithmetic lattice supporting the 3D image and a finite set of Q-ary intensities (gray levels), respectively. Let $\mathbf{F}_s = (f_s(q) : q \in \mathbf{Q}; \sum_{q\in\mathbf{Q}} f_s(q) = 1$ where q denotes the gray level be an empirical marginal probability distribution of gray levels for the MRA slice $\mathbf{X}_s$.

In accord with [32], each such slice is considered as a K-modal image with a known number K of the dominant modes related to the regions of interest (in our particular case, $K = 3$). To segment the slice by separating the modes, we have to estimate from $\mathbf{F}_s$ individual probability distributions of signals associated with each mode. In contrast to a conventional mixture of Gaussians, one per region [21], or a slightly more flexible mixture involving other simple distributions, one per region, as for example in [19], [20], we will closely approximate $\mathbf{F}_s$ with a linear combination of discrete Gaussians (LCDG). Then the LCDG for the whole image is partitioned into the like submodels relating to each dominant mode.

The DG is defined as the probability distribution $\psi_\theta = (\psi(q|\theta) : q \in \mathbf{Q})$ on $\mathbf{Q}$ of gray levels such that each probability $\psi(q|\theta)$ relates to the cumulative Gaussian probability function $\Phi_\theta(q)$ as follows (here, θ is a shorthand notation $\theta = (\mu, \sigma^2)$ for the mean, μ, and variance, σ^2):

$$\psi\left(q|\theta\right) = \begin{cases} \Phi_\theta(0.5) & \text{for} \quad q = 0 \\ \Phi_\theta(q+0.5) - \Phi_\theta(q-0.5) & \text{for} \quad q = 1, \ldots, Q-2 \\ 1 - \Phi_\theta(Q-1.5) & \text{for} \quad q = Q-1 \end{cases}$$

The LCDG with C_p positive and C_n negative components such that $C_\mathrm{p} \geq K$:

$$p_{\mathbf{w},\Theta}(q) = \sum_{r=1}^{C_\mathrm{p}} w_{\mathrm{p},r}\, \psi\left(q|\theta_{\mathrm{p},r}\right) - \sum_{l=1}^{C_\mathrm{n}} w_{\mathrm{n},l}\, \psi\left(q|\theta_{\mathrm{n},l}\right) \tag{4.1}$$

has obvious restrictions on its weights $\mathbf{w} = [w_{p,\cdot}, w_{n,\cdot}]$, namely, all the weights are non-negative and

$$\sum_{r=1}^{C_\mathrm{p}} w_{\mathrm{p},r} - \sum_{l=1}^{C_\mathrm{n}} w_{\mathrm{n},l} = 1 \tag{4.2}$$

Generally, the true probabilities are non-negative: $p_{\mathbf{w},\Theta}(q) \geq 0$ for all $q \in \mathbf{Q}$. Therefore, the probability distributions comprise only a proper subset of all the LCDGs in Eq. (4.1), which may have negative components $p_{\mathbf{w},\Theta}(q) < 0$ for some $q \in \mathbf{Q}$.

Our goal is to find a K-modal probability model that closely approximates the unknown marginal gray level distribution. Given $\mathbf{F}_s$, the Bayesian estimate $\mathbf{F}$ of the latter is as follows [21]: $f(q) = (|\mathbf{R}|\, f_s(q) + 1) / (|\mathbf{R}| + Q)$, and the desired model has to maximize the expected log-likelihood of the statistically independent empirical data by the model parameters:

$$L(\mathbf{w}, \Theta) = \sum_{q \in \mathbf{Q}} f(q) \log p_{\mathbf{w},\Theta}(q) \tag{4.3}$$

For simplicity, we do not restrict the identification procedure to only the true probability distributions, but instead check the validity of the restrictions during the procedure itself. The Bayesian probability estimate $\mathbf{F}$ with no zero or unit values in Eq. (4.3) ensures that a sufficiently large vicinity of each component $f(q)$ complies to the restrictions.

To precisely identify the LCDG model including the numbers of its positive and negative components, we adapt to the LCDGs our EM-based techniques introduced in [32] for identification of a probability density with a continuous LCG-model. For completeness, the adapted algorithms are outlined in Appendix A.

The entire segmentation algorithm is as follows.

1. For each successive MRA slice $\mathbf{X}_s$, $s = 1, \ldots, S$,
   a. Collect the marginal empirical probability distribution $\mathbf{F}_s = (f_s(q) : q \in \mathbf{Q})$ of gray levels
   b. Find an initial LCDG model that closely approximates $\mathbf{F}_s$ by using an initializing algorithm in Appendix A to estimates the numbers $C_\mathrm{p} - K$, C_n and parameters $\mathbf{w}$, Θ (weights, means, and variances) of the positive and negative DGs.
   c. Refine the LCDG model with the fixed C_p and C_n by adjusting all other parameters with a modified EM algorithm in Appendix B.

d. Split the final LCDG model into K submodels, one per each dominant mode, by minimizing the expected errors of misclassification and select the LCDG submodel with the largest mean value (i.e., the submodel corresponding to the brightest pixels) as the model of the desired blood vessels.
e. Extract the blood vessels voxels in this MRA slice using the intensity threshold t separating best their LCDG submodel from the background ones.

2. Eliminate artefacts from the whole set of the extracted voxels using a connectivity filter that selects the largest connected tree structure built by a 3D volume growing algorithm [33].[1]

The main goal of the whole procedure is to find the threshold for each MRA slice that extracts the brighter blood vessels from their darker background in such a way that the vessels' boundaries are accurately separated from the surrounding structures with sometimes almost the same brightness along these boundaries.

The initialization at Step 1b always produces the LCDG with the non-negative starting probabilities $p_{\mathbf{w},\Theta}(q)$. While the refinement at Step 1c increases the likelihood, the probabilities continue to be non-negative. In our experiments as shown in the following, the opposite situations have never been met.

4.3 EXPERIMENTAL RESULTS

Experiments in extracting blood vessels have been conducted with the 3D TOF-MRA and PC-MRA images of the following spatial resolution and size acquired with the Picker 1.5T Edge MRI scanner:

	Resolution, mm	Size of each data set, voxels
TOF-MRA	$0.43 \times 0.43 \times 1.0$	$512 \times 512 \times 93$
PC-MRA	$0.86 \times 0.86 \times 1.0$	$256 \times 256 \times 123$

Both the image types are three-modal ($K = 3$) with the aforementioned signal classes of dark gray bones and fat, gray brain tissues, and light gray blood vessels. Typical 2D TOF- and PC-MRA slices and their 3-class dominant Gaussian mixtures $\mathbf{P}_3$ approximating the estimated marginal distributions $\mathbf{F}$ are shown in Figure 4.1.

4.3.1 Segmentation of Natural TOF- and PC-MRA Images

Figure 4.2 illustrates how Step 1b of our algorithm builds an initial LCDG model for the TOF- and PC-MRA images in Figure 4.1. Absolute deviations $|f(q) - p_3(q)|$ are scaled up to make the unit sums of the positive or absolute negative deviations for $q = 0,\ldots,Q-1$. The minimum approximation errors are obtained in both cases with the six-component Gaussian mixtures. Each initial LCDG model can be split, if necessary, into the three LCDG submodels for each signal class.

Figure 4.3 presents the final LCDG models after Step 1c of our algorithm and shows successive changes of the log-likelihood during the refining EM-process. For the TOF- and PC-MRA images, the first nine EM-iterations increase the log-likelihood from −5.7 to −5.2 and −5.5 to −4.4, respectively. The final LCDG submodels of each class (Step 1d) suggest that thresholds $t = 192$ and $t = 73$ separate blood vessels from the TOF- and PC-MRA images, respectively, with the minimum expected misclassification error.

To highlight the advantages of our approach, Figure 4.4 shows the approximation of the distributions $\mathbf{F}$ for the TOF- and PC-MRA images in Figure 4.1 with the three-component Wilson-Noble's [19]

[1] Step 2 is necessary due to MRA sensitivity to tissues with short T1 responses (e.g., subcutaneous fat) that may obscure the blood vessels in the segmented volume.

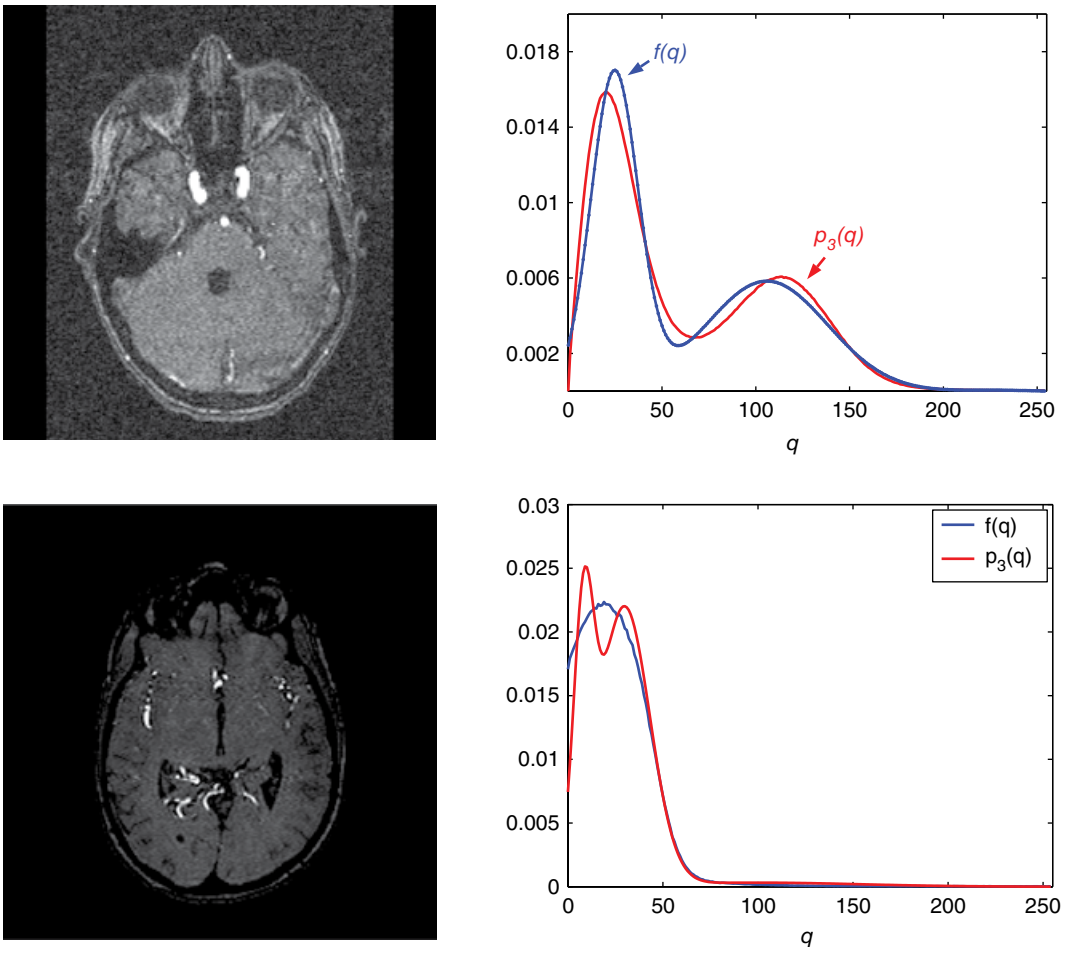

FIGURE 4.1 Typical TOF-MRA (top) and PC-MRA (bottom) slices with the dominant Gaussian mixtures $\mathbf{P}_3 = (p_3(q) : q \in \mathbf{Q})$ laid over the distributions $\mathbf{F} = (f(q) : q \in \mathbf{Q})$.

and Chung-Noble's [20] mixtures, respectively. Our approach provides considerably higher approximation quality in terms of the Levy inter-distribution distance [35] and the total absolute difference between two distributions:

		Levy distance	Absolute difference
TOF-MRA	Our approach	0.00013	0.00020
	Wilson-Noble [19]	0.110	0.123
PC-MRA	Our approach	0.0026	0.0085
	Chung-Noble [20]	0.110	0.093

Comparisons of the approaches on 50 natural TOF-MRA and 35 PC-MRA data sets confirm our more precise model yields much higher segmentation accuracy. Typically higher separation thresholds of the Wilson-Noble's or Chung-Noble's approaches (e.g., $t = 214$ versus our $t = 192$ for the TOF-MRA and $t = 97$ versus our $t = 73$ for the PC-MRA in the previous examples) miss some

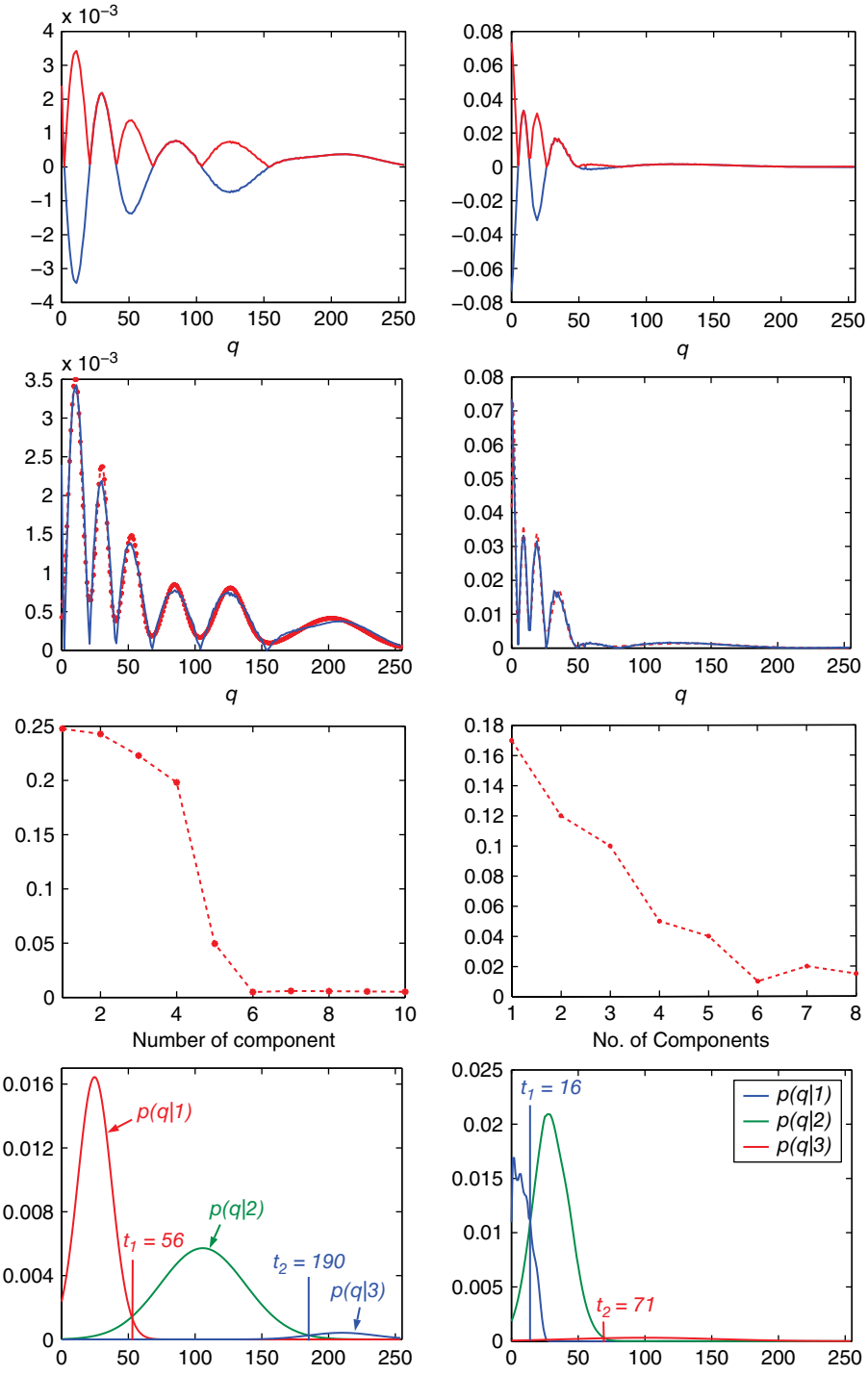

FIGURE 4.2 TOF- (the first column) and PC-MRA (the second column): from top to bottom – alternating and absolute deviations between $\mathbf{F}$ and $\mathbf{P}_3$; the mixture model of the absolute deviations; the absolute approximation error in function of the number of Gaussians approximating the scaled-up absolute deviations, and the initial LCDG submodels of each signal class.

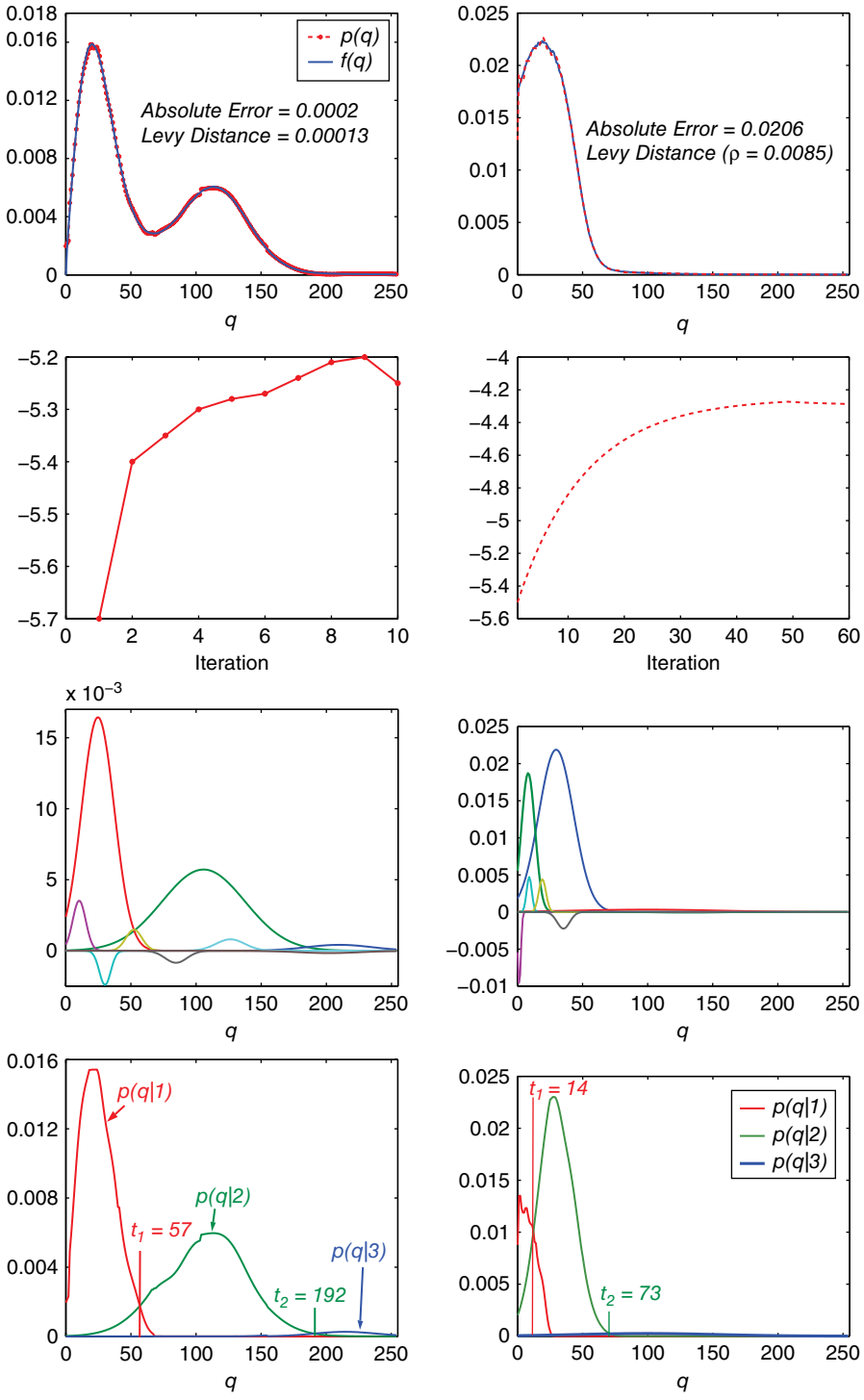

FIGURE 4.3 TOF- (the first column) and PC-MRA (the second column): from top to bottom – the final 3-class LCDG model laid over the distribution $\mathbf{F}$; the log-likelihood changes for the refining EM-iterations; the DGs for the final model, and the final LCDG submodels of each class.

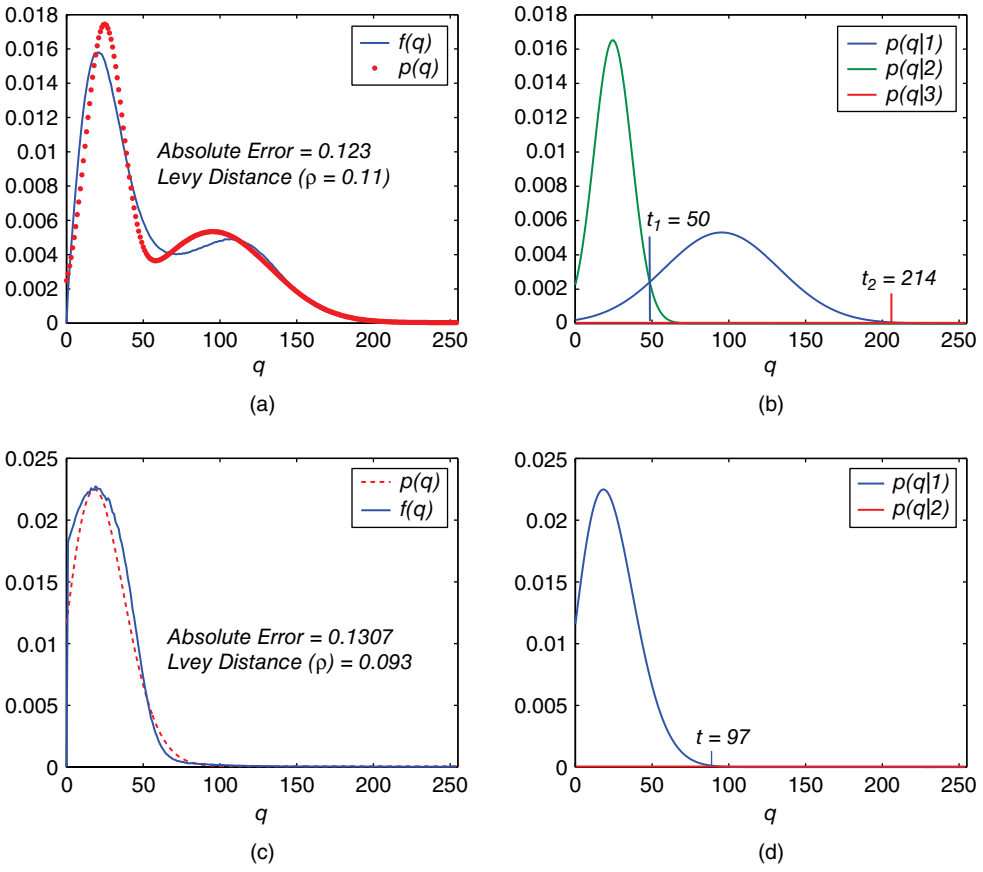

FIGURE 4.4 The Wilson-Noble's [19] (a,b) and Chung-Noble's [20] (c,d) models: the estimated distribution (a,c) and the class submodels (b,d).

blood vessels. For example, the test results in Figures 4.5 and 4.6 after applying the connectivity filter (Step 2) to our and Wilson-Noble's or Chung-Noble's segmentation, respectively, show these latter fail to detect sizeable parts of the brain vascular trees assigned by experts-radiologists to the actual trees and extracted by our approach. In the opposite cases, such as in the bottom row of Figure 4.6, the Chung-Noble's thresholding adds fat tissues to the vascular trees, whereas our approach correctly separates these.

4.3.2 Validating the Segmentation Accuracy with Special Phantoms

It is very difficult to get accurate "ground truth" data to evaluate the segmentation performance by manually segmenting complete vasculatures. Although qualitative visual analysis by experts-radiologists confirm the advantages of our approach, its quantitative validation is of prime importance. Thus we have constructed three wooden phantoms in Figure 4.7 to imitate geometric features of blood vessels typical for any vascular system including different sizes, bifurcations, and zero and high curvature. Each set of 2D slices obtained by scanning the phantoms with a CT scanner is manually segmented to produce "ground truth" region maps. Then synthetic TOF- or PC-MRA signals are generated with inverse mapping methods according to their marginal

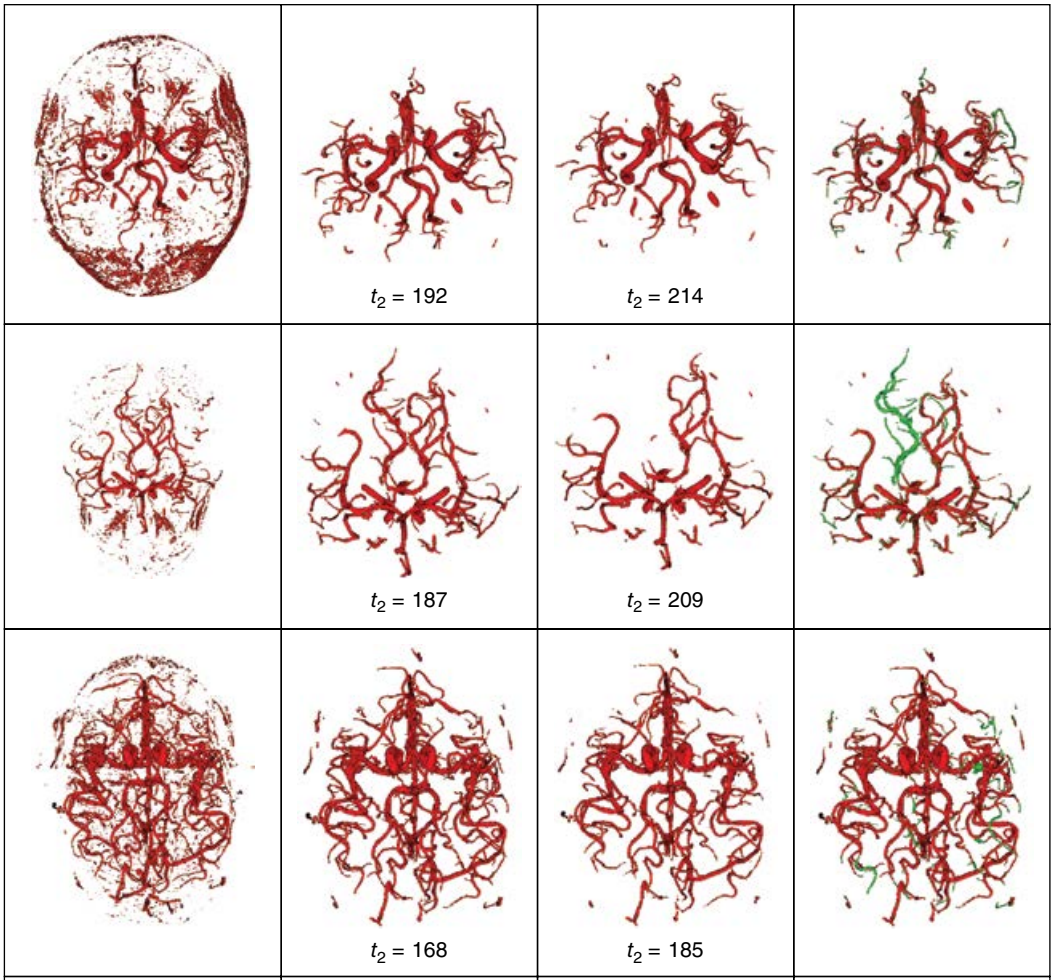

FIGURE 4.5 Each row relates to one patient: our segmentation before (a) and after (b) noise and small fat voxels are eliminated with the connectivity filter, the Wilson-Noble's segmentation (c) after the connectivity filter, and the differences (d) between both approaches highlighted in green.

probability distributions $p(q|3)$ ("blood vessels") and mixed $p(q|1)$, $p(q|2)$ ("background") in Figure 4.3(b,d), respectively. The resulting gray level distributions for each slice are similar to those in Figure 4.1(b and d).

Figure 4.7 compares results of our, the Wilson-Noble's, and the Chung-Noble's segmentation, the errors being in terms of the numbers of wrong (i.e., missed or extra) voxels relative to the total voxels number in the manually segmented 3D phantoms. In total, our approach produces 0.18–1.34% erroneous voxels compared to 3.97–9.52% for the Wilson-Noble's approach on the synthetic TOF-MRA data, and 0.14–0.79% of erroneous voxels compared to 2.12–4.01% for the Chung-Noble's approach on the synthetic PC-MRA data. The error constituents per each 2D slice of the three phantoms for all the approaches and data types are plotted in Figure 4.8.

Table 4.1 combines the error statistics for all the 440 synthetic TOF- or PC-MRA slices in these three phantoms segmented with our, the Wilson-Noble's or Chung-Noble's, and three other segmentation algorithms.

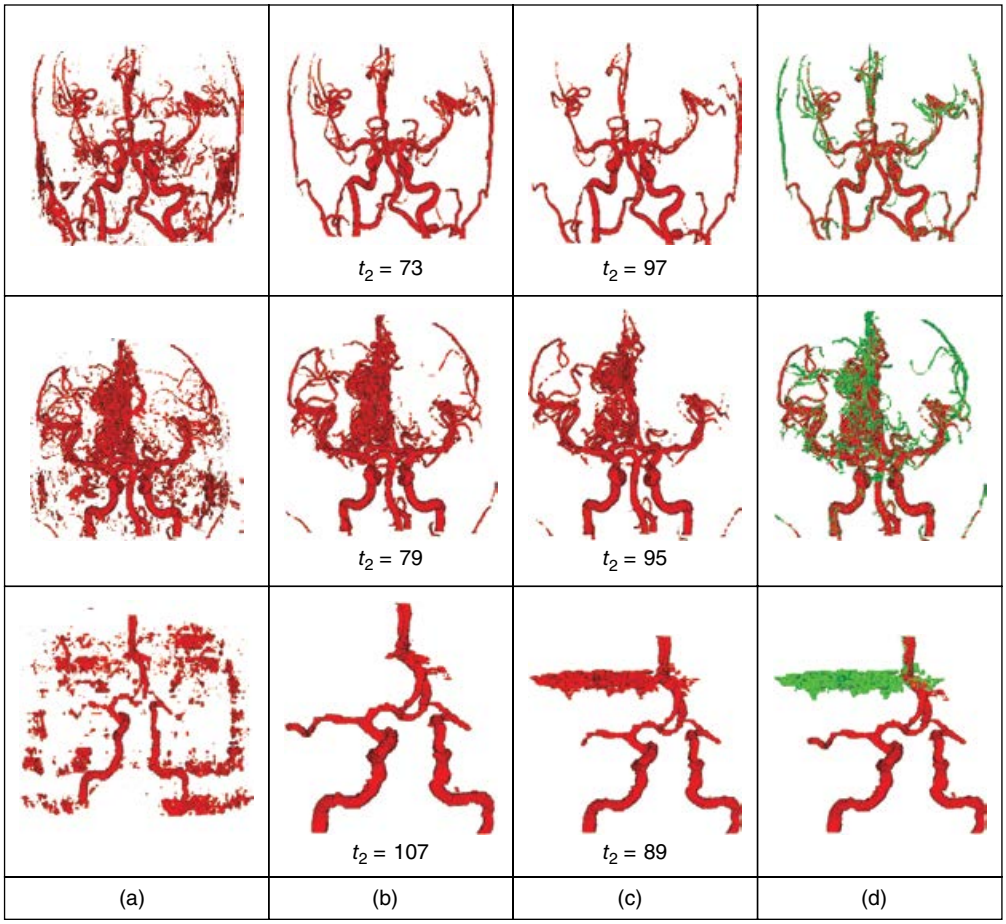

FIGURE 4.6 Each row relates to one patient: our segmentation before (a) and after (b) noise and small fat voxels are eliminated with the connectivity filter, the Chung-Noble's segmentation (c) after the connectivity filter, and the differences (d) between both approaches highlighted in green.

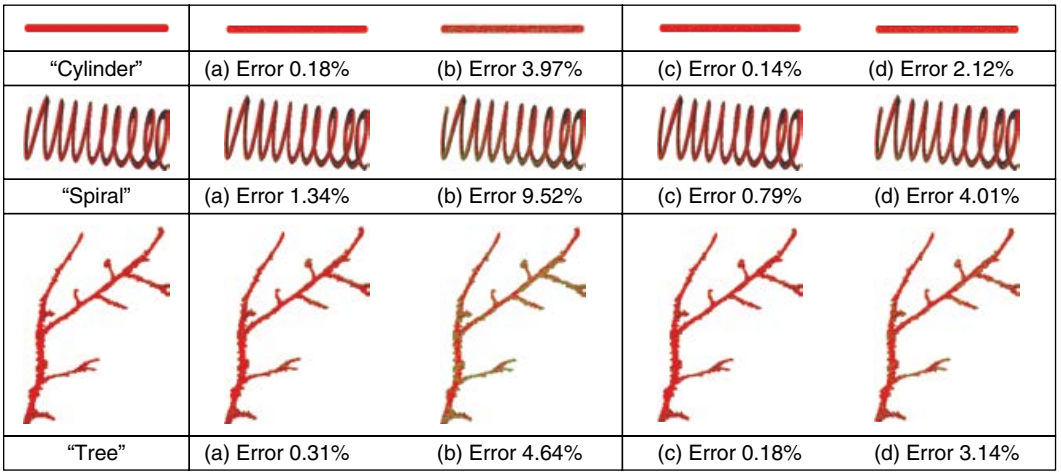

FIGURE 4.7 True 3D geometrical phantoms; our (a) and the Wilson-Noble's (b) segmentation of their synthetic TOF-MRA 3D images, and our (c) and Chung-Noble's (d) segmentation of their synthetic PC-MRA images.

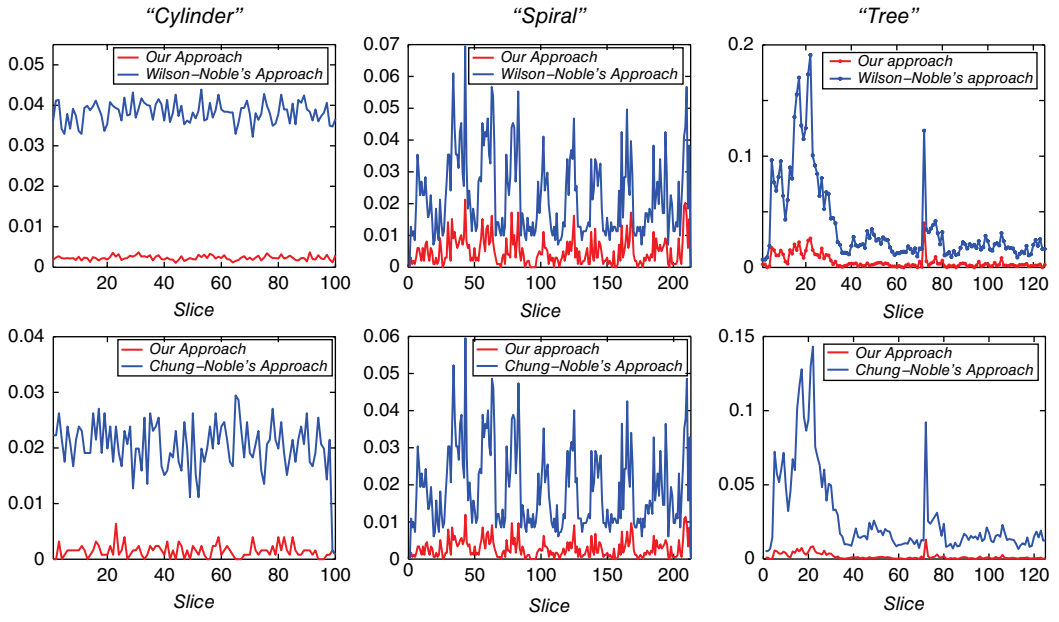

FIGURE 4.8 Total errors per slice in each 3D geometrical phantom for our and the Wilson-Noble's segmentation (top) and for our and the Chung-Noble's segmentation (bottom).

4.4 CONCLUSION

These and other experiments confirm high accuracy of the proposed LCDG-based extraction of blood vessels from the TOF- and PC-MRA images. Our present implementation on a single 2.4 GHZ Pentium 4 CPU with 512 MB RAM using C++ programming language takes about 49 sec for segmenting one TOF-MRA 3D data set with 93 2D slices of size 512×512 pixels each and 29 sec for one PC-MRA 3D data set with 123 2D slices of size 256×256 pixels each.

The proposed segmentation is not limited to only MRA; it could also be applied to various other applications in medical imaging, such as the kidney, the heart, the prostate, the lung, and the retina.

One application is renal transplant functional assessment. Chronic kidney disease (CKD) affects about 26 million people in the U.S. with 17,000 transplants being performed each year. In renal

TABLE 4.1

The minimum ε_n, maximum ε_x, mean $\bar{\varepsilon}$ segmentation error, and the standard deviation σ of errors on the TOF-MRA and PC-MRA phantoms for our approach (OA) and the Wilso-Noble's (WN) or Chung-Noble's (CN), respectively, as well as for the other algorithms using the iterative thresholding (IT) [36], the gradient-based deformable model (DMG) [37], and the deformable model based on the gradient vector flow (GVF) [38].

	TOF-MRA phantoms					PC-MRA phantoms				
	OA	WN	IT	DMG	GVF	OA	CN	IT	DMG	GVF
ε_n,%	**0.09**	0.10	4.81	10.1	2.45	**0.02**	0.08	3.71	9.80	1.96
ε_x,%	**2.10**	12.1	33.1	21.8	13.6	**1.25**	7.90	29.1	20.8	12.1
$\bar{\varepsilon}$,%	**0.61**	6.20	18.8	11.9	5.96	**0.37**	2.90	10.9	9.80	3.12
σ,%	**0.93**	7.40	8.41	3.79	2.79	**0.62**	4.30	6.22	2.10	2.06

transplant patients, acute rejection is the leading cause of renal dysfunction. Given the limited number of donors, routine clinical post-transplantation evaluation is of immense importance to help clinicians initiate timely interventions with appropriate treatment and thus prevent the graft loss. In recent years an increased area of research has been dedicated to developing noninvasive CAD systems for renal transplant function assessment, utilizing different image modalities (e.g., ultrasound, computed tomography (CT), MRI, etc.). Accurate assessment of renal transplant function is critically important for graft survival. Although transplantation can improve a patient's well-being, there is a potential post-transplantation risk of kidney dysfunction that, if not treated in a timely manner, can lead to the loss of the entire graft, and even patient death. Thus, accurate assessment of renal transplant function is crucial for the identification of proper treatment. In recent years, an increased area of research has been dedicated to developing noninvasive image-based CAD systems for the assessment of renal transplant function. In particular, dynamic and diffusion MRI-based systems have been clinically used to assess transplanted kidneys with the advantage of providing information on each kidney separately. For more detail about renal transplant functional assessment, please read [40]–[57], [57]–[65].

The heart is also an important application to this work. The clinical assessment of myocardial perfusion plays a major role in the diagnosis, management, and prognosis of ischemic heart disease. Thus, there have been ongoing efforts to develop automated systems for accurate analysis of myocardial perfusion using first-pass images [66]–[82].

Another application for this work could be the detection of retinal abnormalities. The majority of ophthalmologists depend on a visual interpretation for the identification of disease types. However, inaccurate diagnosis will affect the treatment procedure, which may lead to fatal results. Hence, there is a crucial need for computer automated diagnosis systems that yield highly accurate results. Optical coherence tomography (OCT) has become a powerful modality for the noninvasive diagnosis of various retinal abnormalities such as glaucoma, diabetic macular edema, and macular degeneration. The problem with diabetic retinopathy (DR) is that the patient is not aware of the disease until the changes in the retina have progressed to a level that treatment tends to be less effective. Therefore, automated early detection could limit the severity of the disease and assist ophthalmologists in investigating and treating it more efficiently [83], [84].

Abnormalities of the lung could also be another promising area of research and a related application to this work. Radiation-induced lung injury is the main side effect of radiation therapy for lung cancer patients. Although higher radiation doses increase the radiation therapy effectiveness for tumor control, this can lead to lung injury as a greater quantity of normal lung tissues is included in the treated area. Almost 1/3 of patients who undergo radiation therapy develop lung injury following radiation treatment. The severity of radiation-induced lung injury ranges from ground-glass opacities and consolidation at the early phase to fibrosis and traction bronchiectasis in the late phase. Early detection of lung injury will thus help to improve management of the treatment [85]–[125].

This work can also be applied to other brain abnormalities, such as dyslexia and autism. Dyslexia is one of the most complicated developmental brain disorders that affect children's learning abilities. Dyslexia leads to the failure to develop age-appropriate reading skills in spite of a normal intelligence level and adequate reading instruction. Neuropathological studies have revealed an abnormal anatomy of some structures, such as the Corpus Callosum in dyslexic brains. There has been a lot of work in the literature that aims at developing CAD systems for diagnosing such disorders, along with other brain disorders [126]–[148].

Appendices

A. SEQUENTIAL EM-BASED INITIALIZATION

The initial LCDG model closely approximating a given marginal gray level distribution **F** is built using the conventional EM-algorithm [21], [34], [39] adapted to the DGs. The approximation involves the following steps:

1. The distribution **F** is approximated with a mixture $\mathbf{P}_K$ of K positive DGs relating each to a dominant mode.
2. Deviations between **F** and $\mathbf{P}_K$ are approximated with the alternating "subordinate" components of the LCDG as follows.
   a. The positive and the negative deviations are separated and scaled up to form two seeming "probability distributions" $\mathbf{D}^{\mathrm{p}}$ and $\mathbf{D}^{\mathrm{n}}$.
   b. The same conventional EM algorithm is used iteratively to find a subordinate mixture of positive or negative DGs that approximates best $\mathbf{D}^{\mathrm{p}}$ or $\mathbf{D}^{\mathrm{n}}$, respectively (i.e., the sizes $C_{\mathrm{p}} - K$ and C_{n} of the mixtures are found by minimizing sequentially the total absolute error between each "distribution" $\mathbf{D}^{\mathrm{p}}$ or $\mathbf{D}^{\mathrm{n}}$ and its mixture model by the number of the components).
   c. The obtained positive and negative subordinate mixtures are scaled down and then added to the dominant mixture yielding the initial LCDG model of the size $C = C_{\mathrm{p}} + C_{\mathrm{n}}$.

The resulting initial LCDG has K dominant weights, say, $w_{\mathrm{p},1}, \ldots, w_{\mathrm{p},K}$ such that $\sum_{r=1}^{K} w_{\mathrm{p},r} = 1$, and a number of subordinate weights of smaller values such that $\sum_{r=K+1}^{C_{\mathrm{p}}} w_{\mathrm{p},r} - \sum_{l=1}^{C_{\mathrm{n}}} w_{\mathrm{n},l} = 0$.

B. MODIFIED EM ALGORITHM FOR REFINING LCDGs

The initial LCDG is refined by approaching the local maximum of the log-likelihood in Eq. (4.3) with the EM process adapting that in [32] to the DGs. The latter extends in turn the conventional EM-process in [34] onto the alternating components.

Let $p^{[m]}_{\mathbf{w},\Theta}(q) = \sum_{r=1}^{C_{\mathrm{p}}} w^{[m]}_{\mathrm{p},r}\, \psi(q|\theta^{[m]}_{\mathrm{p},r}) - \sum_{l=1}^{C_{\mathrm{n}}} w^{[m]}_{\mathrm{n},l}\, \psi(q|\theta^{[m]}_{\mathrm{n},l})$ denote the current LCDG at iteration m. Relative contributions of each signal $q \in \mathbf{Q}$ to each positive and negative DG at iteration m are specified by the respective conditional weights

$$\pi^{[m]}_{\mathrm{p}}(r|q) = \frac{w^{[m]}_{\mathrm{p},r}\, \psi\left(q|\theta^{[m]}_{\mathrm{p},r}\right)}{p^{[m]}_{\mathbf{w},\Theta}(q)}; \quad \pi^{[m]}_{\mathrm{n}}(l|q) = \frac{w^{[m]}_{\mathrm{n},l}\, \psi\left(q|\theta^{[m]}_{\mathrm{n},l}\right)}{p^{[m]}_{\mathbf{w},\Theta}(q)} \tag{4.4}$$

such that the following constraints hold:

$$\sum_{r=1}^{C_{\mathrm{p}}} \pi^{[m]}_{\mathrm{p}}(r|q) - \sum_{l=1}^{C_{\mathrm{n}}} \pi^{[m]}_{\mathrm{n}}(l|q) = 1; \quad q = 0, \ldots, Q-1 \tag{4.5}$$

The following two steps iterate until the log-likelihood increases and its changes become small:

> **E–step**$^{[m]}$: Find the weights of Eq. (4.4) under the fixed parameters $\mathbf{w}^{[m-1]}$, $\Theta^{[m-1]}$ from the previous iteration $m-1$, and
> **M–step**$^{[m]}$: Find conditional MLEs $\mathbf{w}^{[m]}$, $\Theta^{[m]}$ by maximizing $L(\mathbf{w},\Theta)$ under the fixed weights of Eq. (4.4).

Considerations closely similar to those in [21], [34], [39] show this process converges to a local log-likelihood maximum. The further evidence in [32] demonstrates it is actually a block relaxation MM-process (in a very general way, this is also shown in [39]). Let the log-likelihood of Eq. (4.3) be rewritten in the equivalent form with the constraints of Eq. (4.5) as unit factors:

$$L\left(w^{[m]},\Theta^{[m]}\right)=\sum_{q=0}^{Q}f(q)\left[\sum_{r=1}^{C_{\mathrm{p}}}\pi_{\mathrm{p}}^{[m]}\left(r\middle|q\right)\log p^{[m]}(q)-\sum_{l=1}^{C_{\mathrm{n}}}\pi_{\mathrm{n}}^{[m]}\left(l\middle|q\right)\log p^{[m]}(q)\right] \tag{4.6}$$

Let the terms $\log p^{[m]}(q)$ in the first and second brackets be replaced with the equal terms $\log w_{\mathrm{p},r}^{[m]}+\log\psi(q|\theta_{\mathrm{p},r}^{[m]})-\log\pi_{\mathrm{p}}^{[m]}(r|q)$ and $\log w_{\mathrm{n},l}^{[m]}+\log\psi(q|\theta_{\mathrm{n},l}^{[m]})-\log\pi_{\mathrm{n}}^{[m]}(l|q)$, respectively, which follow from Eq. (4.4). At the E-step, the conditional Lagrange maximization of the log-likelihood of Eq. (4.6) under the Q restrictions of Eq. (4.5) results just in the weights $\pi_{\mathrm{p}}^{[m+1]}(r|q)$ and $\pi_{\mathrm{n}}^{[m+1]}(l|q)$ of Eq. (4.4) for all $r=1,\ldots,C_{\mathrm{p}}$; $l=1,\ldots,C_{\mathrm{n}}$ and $q\in\mathbf{Q}$. At the M-step, the DG weights $w_{\mathrm{p},r}^{[m+1]}=\sum_{q\in Q}f(q)\pi_{\mathrm{p}}^{[m+1]}(r|q)$ and $w_{\mathrm{n},l}^{[m+1]}=\sum_{q\in\mathbf{Q}}f(q)\pi_{\mathrm{n}}^{[m+1]}(l|q)$ follow from the conditional Lagrange maximization of the log-likelihood in Eq. (4.6) under the restriction of Eq. (4.2) and the fixed conditional weights of Eq. (4.4). Under these latter, the conventional MLEs of the parameters of each DG stem from maximizing the log-likelihood after each difference of the cumulative Gaussians is replaced with its close approximation with the Gaussian density (in the following, "c" stands for "p" or "n," respectively):

$$\mu_{\mathrm{c},r}^{[m+1]}=\frac{1}{w_{\mathrm{c},r}^{[m+1]}}\sum_{q\in\mathbf{Q}}q\cdot f(q)\,\pi_{\mathrm{c}}^{[m+1]}\left(r\middle|q\right)$$

$$\left(\sigma_{\mathrm{c},r}^{[m+1]}\right)^2=\frac{1}{w_{\mathrm{c},r}^{[m+1]}}\sum_{q\in\mathbf{Q}}\left(q-\mu_{\mathrm{c},i}^{[m+1]}\right)^2\cdot f(q)\;\pi_{\mathrm{c}}^{[m+1]}\left(r\middle|q\right)$$

This modified EM-algorithm is valid until the weights $\mathbf{w}$ are strictly positive. The iterations should be terminated when the log-likelihood of Eq. (4.3) almost does not change or begins to decrease due to accumulation of rounding errors.

The final mixed LCDG model $p_C(q)$ is partitioned into the K LCDG submodels $\mathbf{P}_{[k]}=[p(q|k):q\in\mathbf{Q}]$, one per class $k=1,\ldots,K$, by associating the subordinate DGs with the dominant terms so that the misclassification rate is minimal.

References

1. Sato, Y., Nakajima, S., Shiraga, N., Atsumi, H., and Yoshida, S., "Three-dimensional multi-scale line filter for segmentation and visualization of curvilinear structures in medical images," *Medical Image Analysis*, vol. 2, no. 2, pp. 143–168, 1998.
2. Krissian, K., Malandain, G., and Ayache, N., "Model based detection of tubular structures in 3D images," *INRIA Technical Report* 373, INRIA, 1999.

3. Krissian, K., Malandain, G., and Ayache, N., "Directional anisotropic diffusion applied to segmentation of vessels in 3D images," *Proc. Int. Conf. Scale-Space Theory in Computer Vision*, Utrecht, The Netherlands, *Lecture Notes in Computer Science*, Springer Verlag, pp. 345–348, 1997.
4. Krissian, K., Malandain, G., Ayache, N., et al., "Model based multiscale detection of 3D vessels," *Proc. IEEE Int. Conf. Computer Vision Pattern Recognition*, Santa Barbara, California, pp. 722–727, 1998.
5. Frangi, A.F., Niessen, W.J., Vincken, K.L., and Viergever, M.A., "Multiscale vessel enhancement filtering," *Proc. Int. Conf. Medical Image Computing Computer-Assisted Intervention (MICCAI'98)*, Cambridge, MA, USA (*Lect. Notes Comp. Sci.* 1496), Springer, pp. 130–137, 1998.
6. Lorenz, C., Carlsen, I.-C., Buzug, T.M., et al., "A multi-scale line filter with automatic scale selection based on the Hessian matrix for medical image segmentation," *Proc. Int. Conf. Scale-Space Theories in Computer Vision*, Chalana, Kim (*Lect. Notes Comp. Sci.* 1252), Springer, pp. 152–163, 1997.
7. Perona, P., and Malik, J., "Scale-space and edge detection using anisotropic diffusion," *IEEE Trans. Pattern Analysis Machine Intell.*, vol. 12, pp. 629–639, 1990.
8. Catte, F., Coll, T., Lions, P.L., and Morel, J.M., "Image selective smoothing and edge detection by nonlinear diffusion," *SIAM J. Numer. Analysis*, vol. 29, pp. 182–193, 1992.
9. Aylward, S., Pizer, S.M., Bullitt, E., and Eberly, D., "Intensity ridge and widths for 3D object segmentation and description," *Proc. Workshop on Mathematical Methods in Biomedical Image Analysis (MMBIA '96)*, pp. 131–138, 1996.
10. Bullitt, E., Liu, A., Aylward, S., and Pizer, S.M., "Reconstruction of the intracerebral vasculature from MRA and a pair of projection views," *Proc. Int. Conf. Information Processing Medical Imaging*, Poultney, Vermont, USA (*Lect. Notes Comp. Sci.* 1230), Springer, pp. 537–542, 1997.
11. Prinet, V., Monga, O., Ge, C., et al., "Thin network extraction in 3D images: application to medical angiograms," *Proc. IAPR Int. Conf. Pattern Recognition*, Vienna, Austria, Aug. 1996, vol. 3, IEEE, pp. 386–390, 1996.
12. Caselles, V., Kimmel, R., and Sapiro, G., "Geodesic active contours," *Int. J. Computer Vision*, vol. 22, pp. 61–79, 1997.
13. McInerney, T., and Terzopoulos, D., "Medical image segmentation using topologically adaptable surface," *Proc. LNCS Series 1205 (CVRMED-MRCAS'97)*, pp. 23–32, 1997.
14. Lorigo, L.M., Faugeras, O.D., Grimson, W.E.L., and Keriven, R., "Curves: curve evolution for vessel segmentation," *Medical Image Analysis*, vol. 5, pp. 195–206, 2001.
15. Wink, O., Niessen, W.J., and Viergever, M.A., "Fast delineation and visualization of vessels in 3-D angiographic images," *IEEE Trans. Med. Imaging,* vol. 19, pp. 337–346, 2000.
16. Deschamps, T., and Cohen, L.D., "Fast extraction of tubular and tree 3D surfaces with front propagation methods," *Proc. 16th IAPR Int. Conf. Pattern Recognition*, Quebec City, Canada, Aug. 2002, vol. 1, IEEE, pp. 731–734, 2002.
17. Manniesing, R., and Niessen, W., "Local speed functions in level set based vessel segmentation," *Proc. Int. Conf. Medical Image Computing Computer-Assisted Intervention (MICCAI'04)*, Rennes, Saint-Malo, France, pp. 475–482, 2004.
18. Descotesux, M., Collins, L., and Siddiqi, K., "Geometric flows for segmenting vasulature in MRI: theory and validation," *Proc. Int. Conf. Medical Image Computing Computer-Assisted Intervention (MICCAI'04)*, Rennes, Saint-Malo, France, pp. 500–507, 2004.
19. Wilson, D.L., and Noble, J.A., "An adaptive segmentation algorithm for time-of-flight MRA data," *IEEE Trans. Med. Imaging*, vol. 18, pp. 938–945, 1999.
20. Chung, A.C.S., and Noble, J.A., "Statistical 3D vessel segmentation using a Rician distribution," *Proc. Int. Conf. Medical Image Computing Computer-Assisted Intervention (MICCAI'99)*, Cambridge, England, pp. 82–89, 1999.
21. Webb, A., *Statistical Pattern Recognition*, Wiley, New York, 2002.
22. Nain, D., Yezzi, A., and Turk, G., "Vessels segmentation using a shape driven flow," *Proc. Int. Conf. Medical Image Computing Computer-Assisted Intervention (MICCAI'04)*, Rennes, Saint-Malo, France, pp. 51–59, 2004.
23. Gan, R., Chung, A.C.S., Wong, W.C.K., and Yu, S.C.H., "Vascular segmentation in three-dimensional rotational angiography based on maximum intensity projections," *Proc. IEEE Int. Symposium on Biomedical Imaging (ISBI)*, pp. 133–136, 2004.
24. Dl, P., Be, C., Ja, R., and Al, A., "Enhanced image detail using continuity in the MIP Z-Buffer: applications to magnetic resonance angiography," *J. Magn. Reson. Imaging*, vol. 11, pp. 378–388, 2000.
25. Reuze, P., Coatrieux, J.L., Luo, L.M., and Dillenseger, J.L., "A 3-D moment based approach to blood vessels detection and quantification in MRA," *Technol. Health Care*, vol. 1, pp. 181–188, 2000.

26. Hernandez-Hoyos, M., Orkisz, M., Roux, J.P., and Douek, P., "Inertia based vessel axis extraction and stenosis quantification in 3D MRA images," *Comput. Assisted Radiol. Surg*., pp. 180–193, 1999.
27. Verdonck, B., Bloch, I., Maitre, H., et al., "A new system for blood vessel segmentation and visualization in 3D MR and spiral CT angiography," *Comput. Assisted Radiol. Surg*., pp. 177–182, 1999.
28. Summers, P.E., Bhalerao, A.H., and Hawkes, D.J., "Multiresolution, model-based segmentation of MR angiograms," *J. Magn. Reson. Imaging*, vol. 7, pp. 950–957, 1997.
29. Masutani, Y., Schiemann, T., Hhne, K.H., "Vascular shape segmentation and structure extraction using a shape-based region growing model," *Proc. Int. Conf. Medical Image Computing Computer-Assisted Intervention (MICCAI'98)*, Massachusetts Institute of Technology, Cambridge, MA, USA, pp. 1242–1249, 1998.
30. Chen, T., and Metaxas, D.N., "Image segmentation based on the integration of Markov random fields and deformable models," *Proc. Int. Conf. Medical Image Computing Computer-Assisted Intervention (MICCAI'2000)*, Pittsburgh, PA, USA, pp. 256–265, 2000.
31. Chen, T., and Metaxas, D.N., "Gibbs prior models, marching cubes, and deformable models: A hybrid framework for 3D medical image segmentation," *Proc. Int. Conf. Medical Image Computing Computer-Assisted Intervention (MICCAI'03)*, Montreal, Quebec, Canada, vol. 2, pp. 703–710, 2003.
32. Gimel'farb, G., Farag, A.A., and El-Baz, A., "Expectation-maximization for a linear combination of Gaussians," *Proc. 17th IAPR Int. Conf. Pattern Recognition*, Cambridge, UK, 23–26 Aug. 2004, vol. 3, IEEE, pp. 422–425, 2004.
33. Sabry, M., Sites, Ch.B., Farag, A.A., et al., "A fast automatic method for 3D volume segmentation of the human cerebrovascular," *Proc. 13th Int. Conf. Computer Assisted Radiology Surgery (CARS'02)*, Paris, France, 26–29 June 2002, pp. 382–387, 2002.
34. Schlesinger, M.I., and Hlavac, V., *Ten Lectures on Statistical and Structural Pattern Recognition*, Kluwer Academic, Dordrecht, 2002.
35. Lamperti, J.W., *Probability*, Wiley, New York, 1996.
36. Hu, S., and Hoffman, E.A., "Automatic lung segmentation for accurate quantization of volumetric X-ray CT images," *IEEE Trans. Medical Imaging*, vol. 20, pp. 490–498, 2001.
37. Kass, M., Witkin, A., and Terzopoulos, D., "Snakes: active contour models," *Int. J. Computer Vision*, vol. 1, pp. 321–331, 1987.
38. Xu, C., and Prince, J.L., "Snakes, shapes, and gradient vector flow," *IEEE Trans. Image Processing*, vol. 7, pp. 359–369, 1998.
39. Hastie, T., Tibshirani, R., and Friedman, J., *The Elements of Statistical Learning*, Springer, New York, 2001.
40. Ali, A.M., Farag, A.A., and El-Baz, A., "Graph cuts framework for kidney segmentation with prior shape constraints." In: *Proceedings of International Conference on Medical Image Computing and Computer-Assisted Intervention (MICCAI'07).* Brisbane, Australia, October 29–November 2 2007, vol. 1, pp. 384–392.
41. Chowdhury, A.S., Roy, R., Bose, S., Elnakib, F.K.A., and El-Baz, A., "Non-rigid biomedical image registration using graph cuts with a novel data term." In: *Proceedings of IEEE International Symposium on Biomedical Imaging: From Nano to Macro (ISBI'12)*, Barcelona, Spain, May 2–5 2012, pp. 446–449.
42. El-Baz, A., Farag, A.A., Yuksel, S.E., El-Ghar, M.E.A., Eldiasty, T.A., and Ghoneim, M.A., "Application of deformable models for the detection of acute renal rejection." In Farag, A.A., Suri, J.S., eds.: *Deformable Models*, vol. 1, pp. 293–333, 2007.
43. El-Baz, A., Farag, A., Fahmi, R., Yuksel, S., El-Ghar, M.A., and Eldiasty, T., "Image analysis of renal DCE MRI for the detection of acute renal rejection." In: *Proceedings of IAPR International Conference on Pattern Recognition (ICPR'06)*, Hong Kong, August 20–24 2006, pp. 822–825.
44. El-Baz, A., Farag, A., Fahmi, R., Yuksel, S., Miller, W., El-Ghar, M.A., El-Diasty, T., and Ghoneim, M., "A new CAD system for the evaluation of kidney diseases using DCE-MRI." In: *Proceedings of International Conference on Medical Image Computing and Computer-Assisted Intervention (MICCAI'08)*, Copenhagen, Denmark, October 1–6 2006, pp. 446–453.
45. El-Baz, A., Gimel'farb, G., and El-Ghar, M.A., "A novel image analysis approach for accurate identification of acute renal rejection." In: *Proceedings of IEEE International Conference on Image Processing (ICIP'08)*, San Diego, California, USA, October 12–15 2008, pp. 1812–1815.
46. El-Baz, A., Gimel'farb, G., and El-Ghar, M.A., "Image analysis approach for identification of renal transplant rejection." In: *Proceedings of IAPR International Conference on Pattern Recognition (ICPR'08)*, Tampa, Florida, USA, December 8–11 2008, pp. 1–4.

47. El-Baz, A., Gimel'farb, G., and El-Ghar, M.A., "New motion correction models for automatic identification of renal transplant rejection." In: *Proceedings of International Conference on Medical Image Computing and Computer-Assisted Intervention (MICCAI'07)*, Brisbane, Australia, October 29–November 2 2007, pp. 235–243.
48. Farag, A., El-Baz, A., Yuksel, S., El-Ghar, M.A., and Eldiasty, T., "A framework for the detection of acute rejection with Dynamic Contrast Enhanced Magnetic Resonance Imaging." In: *Proceedings of IEEE International Symposium on Biomedical Imaging: From Nano to Macro (ISBI'06)*, Arlington, Virginia, USA, April 6–9 2006, pp. 418–421.
49. Khalifa, F., Beache, G.M., El-Ghar, M.A., El-Diasty, T., Gimel'farb, G., Kong, M., and El-Baz, A., "Dynamic contrast-enhanced MRI-based early detection of acute renal transplant rejection." *IEEE Transactions on Medical Imaging*, vol. 32, no. 10, pp. 1910–1927, 2013.
50. Khalifa, F., El-Baz, A., Gimel'farb, G., and El-Ghar, M.A., "Non-invasive image-based approach for early detection of acute renal rejection." In: *Proceedings of International Conference Medical Image Computing and Computer-Assisted Intervention (MICCAI'10)*, Beijing, China, September 20–24 2010, pp. 10–18.
51. Khalifa, F., El-Baz, A., Gimel'farb, G., Ouseph, R., and El-Ghar, M.A., "Shape-appearance guided level-set deformable model for image segmentation." In: *Proceedings of IAPR International Conference on Pattern Recognition (ICPR'10)*, Istanbul, Turkey, August 23–26 2010, pp. 4581–4584.
52. Khalifa, F., El-Ghar, M.A., Abdollahi, B., Frieboes, H., El-Diasty, T., and El-Baz, A., "A comprehensive non-invasive framework for automated evaluation of acute renal transplant rejection using DCE-MRI." *NMR in Biomedicine*, vol. 26, no. 11, pp. 1460–1470, 2013.
53. Khalifa, F., El-Ghar, M.A., Abdollahi, B., Frieboes, H.B., El-Diasty, T., and El-Baz, A., "Dynamic contrast-enhanced MRI-based early detection of acute renal transplant rejection." In: *2014 Annual Scientific Meeting and Educational Course Brochure of the Society of Abdominal Radiology (SAR'14)*, Boca Raton, Florida, March 23–28 2014. CID: 1855912.
54. Khalifa, F., Elnakib, A., Beache, G.M., Gimel'farb, G., El-Ghar, M.A., Sokhadze, G., Manning, S., McClure, P., and El-Baz, A., "3D kidney segmentation from CT images using a level set approach guided by a novel stochastic speed function." In: *Proceedings of International Conference Medical Image Computing and Computer-Assisted Intervention (MICCAI'11)*, Toronto, Canada, September 18–22 2011, pp. 587–594.
55. Khalifa, F., Gimel'farb, G., El-Ghar, M.A., Sokhadze, G., Manning, S., McClure, P., Ouseph, R., and El-Baz, A., "A new deformable model-based segmentation approach for accurate extraction of the kidney from abdominal CT images." In: *Proceedings of IEEE International Conference on Image Processing (ICIP'11)*, Brussels, Belgium, September 11–14 2011, pp. 3393–3396.
56. Mostapha, M., Khalifa, F., Alansary, A., Soliman, A., Suri, J., and El-Baz, A., "Computer-aided diagnosis systems for acute renal transplant rejection: challenges and methodologies." In El-Baz, A., and Suri, J., eds.: *Abdomen and Thoracic Imaging.* Springer, pp. 1–35, 2014.
57. Shehata, M., Khalifa, F., Hollis, E., Soliman, A., Hosseini-Asl, E., El-Ghar, M.A., El-Baz, M., Dwyer, A.C., El-Baz, A., and Keynton, R., "A new non-invasive approach for early classification of renal rejection types using diffusion-weighted MRI." In: *IEEE International Conference on Image Processing (ICIP)*, IEEE, 2016, pp. 136–140.
58. Khalifa, F., Soliman, A., Takieldeen, A., Shehata, M., Mostapha, M., Shaffie, A., Ouseph, R., Elmaghraby, A., and El-Baz, A., "Kidney segmentation from CT images using a 3D NMF-guided active contour model." In: *13th International Symposium on Biomedical Imaging (ISBI)*, IEEE, 2016, pp. 432–435.
59. Shehata, M., Khalifa, F., Soliman, A., Takieldeen, A., El-Ghar, M.A., Shaffie, A., Dwyer, A.C., Ouseph, R., El-Baz, A., and Keynton, R., "3D diffusion MRI-based CAD system for early diagnosis of acute renal rejection." In: *13th International Symposium on Biomedical Imaging (ISBI)*, IEEE, 2016, pp. 1177–1180.
60. Shehata, M., Khalifa, F., Soliman, A., Alrefai, R., El-Ghar, M.A., Dwyer, A.C., Ouseph, R., and El-Baz, A., "A level set-based framework for 3d kidney segmentation from diffusion MR images." In: *International Conference on Image Processing (ICIP)*, IEEE, 2015, pp. 4441–4445.
61. Shehata, M., Khalifa, F., Soliman, A., El-Ghar, M.A., Dwyer, A.C., Gimelfarb, G., Keynton, R., and El-Baz, A., "A promising non-invasive CAD system for kidney function assessment." In: *International Conference on Medical Image Computing and Computer-Assisted Intervention*. Springer, pp. 613–621, 2016.
62. Khalifa, F., Soliman, A., Elmaghraby, A., Gimelfarb, G., and El-Baz, A., "3D kidney segmentation from abdominal images using spatial-appearance models." *Computational and Mathematical Methods in Medicine*, 2017.

63. Hollis, E., Shehata, M., Khalifa, F., El-Ghar, M.A., El-Diasty, T., and El-Baz, A., "Towards non-invasive diagnostic techniques for early detection of acute renal transplant rejection: A review." *The Egyptian Journal of Radiology and Nuclear Medicine*, vol. 48, no. 1, pp. 257–269, 2016.
64. Shehata, M., Khalifa, F., Soliman, A., El-Ghar, M.A., Dwyer, A.C., and El-Baz, A., "Assessment of renal transplant using image and clinical-based biomarkers." In: *Proceedings of 13th Annual Scientific Meeting of American Society for Diagnostics and Interventional Nephrology (ASDIN'17)*, New Orleans, LA, USA, February 10–12 2017.
65. Shehata, M., Khalifa, F., Soliman, A., El-Ghar, M.A., Dwyer, A.C., and El-Baz, A., "Early assessment of acute renal rejection." In: *Proceedings of 12th Annual Scientific Meeting of American Society for Diagnostics and Interventional Nephrology (ASDIN'16)*, Phoenix, Arizona, USA, February 19–21 2017.
66. Khalifa, F., Beache, G., El-Baz, A., and Gimel'farb, G., "Deformable model guided by stochastic speed with application in cine images segmentation." In: *Proceedings of IEEE International Conference on Image Processing (ICIP'10)*, Hong Kong, September 26–29 2010, pp. 1725–1728.
67. Khalifa, F., Beache, G.M., Elnakib, A., Sliman, H., Gimel'farb, G., Welch, K.C., and El-Baz, A., "A new shape-based framework for the left ventricle wall segmentation from cardiac first-pass perfusion MRI." In: *Proceedings of IEEE International Symposium on Biomedical Imaging: From Nano to Macro (ISBI'13)*, San Francisco, California, April 7–11 2013, pp. 41–44.
68. Khalifa, F., Beache, G.M., Elnakib, A., Sliman, H., Gimel'farb, G., Welch, K.C., and El-Baz, A., "A new nonrigid registration framework for improved visualization of transmural perfusion gradients on cardiac first–pass perfusion MRI." In: *Proceedings of IEEE International Symposium on Biomedical Imaging: From Nano to Macro (ISBI'12)*, Barcelona, Spain, May 2–5 2012, pp. 828–831.
69. Khalifa, F., Beache, G.M., Firjani, A., Welch, K.C., Gimel'farb, G., and El-Baz, A., "A new nonrigid registration approach for motion correction of cardiac first-pass perfusion MRI." In: *Proceedings of IEEE International Conference on Image Processing (ICIP'12)*, Lake Buena Vista, Florida, September 30–October 3 2012, pp. 1665–1668.
70. Khalifa, F., Beache, G.M., Gimel'farb, G., and El-Baz, A., "A novel CAD system for analyzing cardiac first-pass MR images." In: *Proceedings of IAPR International Conference on Pattern Recognition (ICPR'12)*, Tsukuba Science City, Japan, November 11–15 2012, pp. 77–80.
71. Khalifa, F., Beache, G.M., Gimel'farb, G., and El-Baz, A., "A novel approach for accurate estimation of left ventricle global indexes from short-axis cine MRI." In: *Proceedings of IEEE International Conference on Image Processing (ICIP'11)*, Brussels, Belgium, September 11–14 2011, pp. 2645–2649.
72. Khalifa, F., Beache, G.M., Gimel'farb, G., Giridharan, G.A., and El-Baz, A., "A new image-based framework for analyzing cine images." In El-Baz, A., Acharya, U.R., Mirmedhdi, M., Suri, J.S., eds.: *Handbook of Multi Modality State-of-the-Art Medical Image Segmentation and Registration Methodologies*, vol. 2. Springer, New York, pp. 69–98, 2011.
73. Khalifa, F., Beache, G.M., Gimel'farb, G., Giridharan, G.A., and El-Baz, A., "Accurate automatic analysis of cardiac cine images." *IEEE Transactions on Biomedical Engineering*, vol. 59, no. 2, pp. 445–455, 2012.
74. Khalifa, F., Beache, G.M., Nitzken, M., Gimel'farb, G., Giridharan, G.A., and El-Baz, A., "Automatic analysis of left ventricle wall thickness using short-axis cine CMR images." In: *Proceedings of IEEE International Symposium on Biomedical Imaging: From Nano to Macro (ISBI'11)*, Chicago, Illinois, March 30–April 2 2011, pp. 1306–1309.
75. Nitzken, M., Beache, G., Elnakib, A., Khalifa, F., Gimel'farb, G., and El-Baz, A., "Accurate modeling of tagged CMR 3D image appearance characteristics to improve cardiac cycle strain estimation." In: *International Conference on Image Processing (ICIP)*, Orlando, Florida, USA, September 2012, IEEE, pp. 521–524.
76. Nitzken, M., Beache, G., Elnakib, A., Khalifa, F., Gimel'farb, G., and El-Baz, A., "Improving full-cardiac cycle strain estimation from tagged CMR by accurate modeling of 3D image appearance characteristics." In: *International Symposium on Biomedical Imaging (ISBI)*, Barcelona, Spain, May 2012, IEEE, pp. 462–465 (Selected for oral presentation).
77. Nitzken, M.J., El-Baz, A.S., and Beache, G.M., "Markov-gibbs random field model for improved full-cardiac cycle strain estimation from tagged CMR." *Journal of Cardiovascular Magnetic Resonance*, vol. 14, no. 1, pp. 1–2, 2012.
78. Sliman, H., Elnakib, A., Beache, G., Elmaghraby, A., and El-Baz, A., "Assessment of myocardial function from cine cardiac MRI using a novel 4D tracking approach." *J Comput Sci Syst Biol*, vol. 7, pp. 169–173, 2014.

79. Sliman, H., Elnakib, A., Beache, G.M., Soliman, A., Khalifa, F., Gimel'farb, G., Elmaghraby, A., and El-Baz, A., "A novel 4D PDE-based approach for accurate assessment of myocardium function using cine cardiac magnetic resonance images." In: *Proceedings of IEEE International Conference on Image Processing (ICIP'14)*, Paris, France, October 27–30, 2014, pp. 3537–3541.
80. Sliman, H., Khalifa, F., Elnakib, A., Beache, G.M., Elmaghraby, A., and El-Baz, A., "A new segmentation-based tracking framework for extracting the left ventricle cavity from cine cardiac MRI." In: *Proceedings of IEEE International Conference on Image Processing (ICIP'13)*, Melbourne, Australia, September 15–18, 2013, pp. 685–689.
81. Sliman, H., Khalifa, F., Elnakib, A., Soliman, A., Beache, G.M., Elmaghraby, A., Gimel'farb, G., and El-Baz, A., "Myocardial borders segmentation from cine MR images using bi-directional coupled parametric deformable models," *Medical Physics*, vol. 40, no. 9, pp. 1–13, 2013.
82. Sliman, H., Khalifa, F., Elnakib, A., Soliman, A., Beache, G.M., Gimel'farb, G., Emam, A., Elmaghraby, A., and El-Baz, A., "Accurate segmentation framework for the left ventricle wall from cardiac cine MRI." In: *Proceedings of International Symposium on Computational Models for Life Science (CMLS'13)*, Sydney, Australia, November 27–29, 2013, vol. 1559, pp. 287–296.
83. Eladawi, N., Elmogy, M., et al., "Classification of retinal diseases based on OCT images." *Frontiers in Bioscience Landmark Journal*, 2017.
84. ElTanboly, A., Ismail, M., "A computer aided diagnostic system for detecting diabetic retinopathy in optical coherence tomography images," *Medical Physics*, 2016.
85. Abdollahi, B., Civelek, A.C., Li, X.F., Suri, J., and El-Baz, A., "PET/CT nodule segmentation and diagnosis: a survey." In Saba, L., Suri, J.S., eds.: *Multi Detector CT Imaging*. Taylor, Francis, pp. 639–651, 2014.
86. Abdollahi, B., El-Baz, A., and Amini, A.A., "A multi-scale non-linear vessel enhancement technique." In: *2011 Annual International Conference of the Engineering in Medicine and Biology Society (EMBC)*, IEEE, 2011, pp. 3925–3929.
87. Abdollahi, B., Soliman, A., Civelek, A., Li, X.F., Gimel'farb, G., and El-Baz, A., "A novel Gaussian scale space-based joint MGRF framework for precise lung segmentation." In: *Proceedings of IEEE International Conference on Image Processing (ICIP'12)*, IEEE, 2012, pp. 2029–2032.
88. Abdollahi, B., Soliman, A., Civelek, A., Li, X.F., Gimelfarb, G., and El-Baz, A., "A novel 3D joint MGRF framework for precise lung segmentation." In: *Machine Learning in Medical Imaging*. Springer, pp. 86–93, 2012.
89. Ali, A.M., El-Baz, A.S., and Farag, A.A., "A novel framework for accurate lung segmentation using graph cuts." In: *Proceedings of IEEE International Symposium on Biomedical Imaging: From Nano to Macro (ISBI'07)*, IEEE, 2007, pp. 908–911.
90. El-Baz, A., Beache, G.M., Gimel'farb, G., Suzuki, K., and Okada, K., "Lung imaging data analysis." *International Journal of Biomedical Imaging*, 2013.
91. El-Baz, A., Beache, G.M., Gimel'farb, G., Suzuki, K., Okada, K., Elnakib, A., Soliman, A., and Abdollahi, B., "Computer-aided diagnosis systems for lung cancer: challenges and methodologies." *International Journal of Biomedical Imaging*, 2013.
92. El-Baz, A., Elnakib, A., Abou El-Ghar, M., Gimel'farb, G., Falk, R., and Farag, A., "Automatic detection of 2D and 3D lung nodules in chest spiral CT scans." *International Journal of Biomedical Imaging*, 2013.
93. El-Baz, A., Farag, A.A., Falk, R., and La Rocca, R., "A unified approach for detection, visualization, and identification of lung abnormalities in chest spiral CT scans." In: *International Congress Series*, vol. 1256, Elsevier, pp. 998–1004, 2003.
94. El-Baz, A., Farag, A.A., Falk, R., and La Rocca, R., "Detection, visualization and identification of lung abnormalities in chest spiral CT scan: phase-I." In: *Proceedings of International Conference on Biomedical Engineering*, Cairo, Egypt, vol. 12, 2002.
95. El-Baz, A., Farag, A., Gimel'farb, G., Falk, R., El-Ghar, M.A., and Eldiasty, T., "A framework for automatic segmentation of lung nodules from low dose chest CT scans." In: *Proceedings of International Conference on Pattern Recognition (ICPR'06)*, vol. 3, IEEE, pp. 611–614, 2006.
96. El-Baz, A., Farag, A., Gimelfarb, G., Falk, R., and El-Ghar, M.A., "A novel level set-based computer-aided detection system for automatic detection of lung nodules in low dose chest computed tomography scans." *Lung Imaging and Computer Aided Diagnosis*, vol. 10, pp. 221–238, 2011.
97. El-Baz, A., Gimel'farb, G., Abou El-Ghar, M., and Falk, R., "Appearance-based diagnostic system for early assessment of malignant lung nodules." In: *Proceedings of IEEE International Conference on Image Processing (ICIP'12)*, IEEE, pp. 533–536, 2012.

98. El-Baz, A., Gimel'farb, G., and Falk, R., "A novel 3D framework for automatic lung segmentation from low dose CT images." In El-Baz, A., Suri, J.S., eds.: *Lung Imaging and Computer Aided Diagnosis*. Taylor, Francis, pp. 1–16, 2011.
99. El-Baz, A., Gimel'farb, G., Falk, R., and El-Ghar, M., "Appearance analysis for diagnosing malignant lung nodules." In: *Proceedings of IEEE International Symposium on Biomedical Imaging: From Nano to Macro (ISBI'10)*, IEEE, pp. 193–196, 2010.
100. El-Baz, A., Gimel'farb, G., Falk, R., and El-Ghar, M.A., "A novel level set-based CAD system for automatic detection of lung nodules in low dose chest CT scans." In El-Baz, A., Suri, J.S., eds.: *Lung Imaging and Computer Aided Diagnosis*, vol. 1. Taylor, Francis, pp. 221–238, 2011.
101. El-Baz, A., Gimel'farb, G., Falk, R., and El-Ghar, M.A., "A new approach for automatic analysis of 3D low dose CT images for accurate monitoring the detected lung nodules." In: *Proceedings of International Conference on Pattern Recognition (ICPR'08)*, IEEE, 1–4, 2008.
102. El-Baz, A., Gimel'farb, G., Falk, R., and El-Ghar, M.A., "A novel approach for automatic follow-up of detected lung nodules." In: *Proceedings of IEEE International Conference on Image Processing (ICIP'07)*, vol. 5, IEEE, V–501, 2007.
103. El-Baz, A., Gimel'farb, G., Falk, R., and El-Ghar, M.A., "A new CAD system for early diagnosis of detected lung nodules." In: *International Conference on Image Processing (ICIP 2007)*, vol. 2, IEEE, pp. II–461, 2007.
104. El-Baz, A., Gimel'farb, G., Falk, R., El-Ghar, M.A., and Refaie, H., "Promising results for early diagnosis of lung cancer." In: *Proceedings of IEEE International Symposium on Biomedical Imaging: From Nano to Macro (ISBI'08)*, IEEE, pp. 1151–1154, 2008.
105. El-Baz, A., Gimel'farb, G.L., Falk, R., Abou El-Ghar, M., Holland, T., and Shaffer, T., "A new stochastic framework for accurate lung segmentation." In: *Proceedings of Medical Image Computing and Computer-Assisted Intervention (MICCAI'08)*, IEEE, pp. 322–330, 2008.
106. El-Baz, A., Gimel'farb, G.L., Falk, R., Heredis, D., and Abou El-Ghar, M., "A novel approach for accurate estimation of the growth rate of the detected lung nodules." In: *Proceedings of International Workshop on Pulmonary Image Analysis*, pp. 33–42, 2008.
107. El-Baz, A., Gimel'farb, G.L., Falk, R., Holland, T., and Shaffer, T., "A framework for unsupervised segmentation of lung tissues from low dose computed tomography images." In: *Proceedings of British Machine Vision (BMVC'08)*, pp. 1–10, 2008.
108. El-Baz, A., Gimelfarb, G., Falk, R., and El-Ghar, M.A., "3D MGRF-based appearance modeling for robust segmentation of pulmonary nodules in 3D LDCT chest images." In: *Lung Imaging and Computer Aided Diagnosis*, pp. 51–63, 2011.
109. El-Baz, A., Gimelfarb, G., Falk, R., and El-Ghar, M.A., "Automatic analysis of 3D low dose CT images for early diagnosis of lung cancer." *Pattern Recognition*, vol. 42, no. 6, pp. 1041–1051, 2009.
110. El-Baz, A., Gimelfarb, G., Falk, R., El-Ghar, M.A., Rainey, S., Heredia, D., and Shaffer, T., "Toward early diagnosis of lung cancer." In: *Proceedings of Medical Image Computing and Computer-Assisted Intervention (MICCAI'09)*, Springer, pp. 682–689, 2009.
111. El-Baz, A., Gimelfarb, G., Falk, R., El-Ghar, M.A., and Suri, J., "Appearance analysis for the early assessment of detected lung nodules." In: *Lung Imaging and Computer Aided Diagnosis*, pp. 395–404, 2011.
112. El-Baz, A., Khalifa, F., Elnakib, A., Nitkzen, M., Soliman, A., McClure, P., Gimel'farb, G., and El-Ghar, M.A., "A novel approach for global lung registration using 3D Markov Gibbs appearance model." In: *Proceedings of International Conference Medical Image Computing and Computer-Assisted Intervention (MICCAI'12)*, Nice, France, October 1–5, 2012, pp. 114–121.
113. El-Baz, A., Nitzken, M., Elnakib, A., Khalifa, F., Gimel'farb, G., Falk, R., and El-Ghar, M.A., "3D shape analysis for early diagnosis of malignant lung nodules." In: *Proceedings of International Conference Medical Image Computing and Computer-Assisted Intervention (MICCAI'11)*, Toronto, Canada, September 18–22, 2011, pp. 175–182.
114. El-Baz, A., Nitzken, M., Gimelfarb, G., Van Bogaert, E., Falk, R., El-Ghar, M.A., Suri, J., "Three-dimensional shape analysis using spherical harmonics for early assessment of detected lung nodules." In: *Lung Imaging and Computer Aided Diagnosis*, pp. 421–438, 2011.
115. El-Baz, A., Nitzken, M., Khalifa, F., Elnakib, A., Gimel'farb, G., Falk, R., and El-Ghar, M.A., "3D shape analysis for early diagnosis of malignant lung nodules." In: *Proceedings of International Conference on Information Processing in Medical Imaging (IPMI'11)*, Monastery Irsee, Germany (Bavaria), July 3–8, 2011, pp. 772–783.

116. El-Baz, A., Nitzken, M., Vanbogaert, E., Gimel'farb, G., Falk, R., and Abo El-Ghar, M., "A novel shape-based diagnostic approach for early diagnosis of lung nodules." In: *International Symposium on Biomedical Imaging: From Nano to Macro*, IEEE, pp. 137–140, 2011.
117. El-Baz, A., Sethu, P., Gimel'farb, G., Khalifa, F., Elnakib, A., Falk, R., and El-Ghar, M.A., "Elastic phantoms generated by microfluidics technology: Validation of an imaged-based approach for accurate measurement of the growth rate of lung nodules." *Biotechnology Journal*, vol. 6, no. 2, pp. 195–203, 2011.
118. El-Baz, A., Sethu, P., Gimel'farb, G., Khalifa, F., Elnakib, A., Falk, R., and El-Ghar, M.A., "A new validation approach for the growth rate measurement using elastic phantoms generated by state-of-the-art microfluidics technology." In: *Proceedings of IEEE International Conference on Image Processing (ICIP'10)*, Hong Kong, September 26–29, 2010, pp. 4381–4383.
119. El-Baz, A., Sethu, P., Gimel'farb, G., Khalifa, F., Elnakib, A., Falk, R., et al., "Validation of a new imaged-based approach for the accurate estimating of the growth rate of detected lung nodules using real CT images and elastic phantoms generated by state-of-the-art microfluidics technology." In El-Baz, A., Suri, J.S., eds.: *Handbook of Lung Imaging and Computer Aided Diagnosis*, vol. 1. Taylor & Francis, New York, pp. 405–420, 2011.
120. El-Baz, A., Soliman, A., McClure, P., Gimel'farb, G., El-Ghar, M.A., Falk, R., "Early assessment of malignant lung nodules based on the spatial analysis of detected lung nodules." In: *Proceedings of IEEE International Symposium on Biomedical Imaging: From Nano to Macro (ISBI'12)*, IEEE, pp. 1463–1466, 2012.
121. El-Baz, A., Yuksel, S.E., Elshazly, S., and Farag, A.A., "Non-rigid registration techniques for automatic follow-up of lung nodules." In: *Proceedings of Computer Assisted Radiology and Surgery (CARS'05)*, vol. 1281, Elsevier, pp. 1115–1120, 2005.
122. El-Baz, A.S., and Suri, J.S., *Lung Imaging and Computer Aided Diagnosis*. CRC Press, 2011.
123. Soliman, A., Khalifa, F., Shaffie, A., Liu, N., Dunlap, N., Wang, B., Elmaghraby, A., Gimelfarb, G., and El-Baz, A., "Image-based CAD system for accurate identification of lung injury." In: *Proceedings of IEEE International Conference on Image Processing (ICIP'16)*, IEEE, pp. 121–125, 2016.
124. Soliman, A., Khalifa, F., Dunlap, N., Wang, B., El-Ghar, M., and El-Baz, A., "An iso-surfaces based local deformation handling framework of lung tissues." In: *International Symposium on Biomedical Imaging (ISBI)*, IEEE, pp. 1253–1259, 2016.
125. Soliman, A., Khalifa, F., Shaffie, A., Dunlap, N., Wang, B., Elmaghraby, A., and El-Baz, A., "Detection of lung injury using 4d-CT chest images." In: *International Symposium on Biomedical Imaging (ISBI)*, IEEE, pp. 1274–1277, 2016.
126. Dombroski, B., Nitzken, M., Elnakib, A., Khalifa, F., El-Baz, A., and Casanova, M.F., "Cortical surface complexity in a population-based normative sample." *Translational Neuroscience*, vol. 5, no. 1, pp. 17–24, 2014.
127. El-Baz, A., Casanova, M., Gimel'farb, G., Mott, M., and Switala, A., "An MRI-based diagnostic framework for early diagnosis of dyslexia." *International Journal of Computer Assisted Radiology and Surgery*, vol. 3, no. 3–4, pp. 181–189, 2008.
128. El-Baz, A., Casanova, M., Gimel'farb, G., Mott, M., Switala, A., Vanbogaert, E., and McCracken, R., "A new CAD system for early diagnosis of dyslexic brains." In: *Proc. International Conference on Image Processing (ICIP'2008)*, IEEE, pp. 1820–1823, 2008.
129. El-Baz, A., Casanova, M.F., Gimel'farb, G., Mott, M., and Switwala, A.E., "A new image analysis approach for automatic classification of autistic brains." In: *Proc. IEEE International Symposium on Biomedical Imaging: From Nano to Macro (ISBI'2007)*, IEEE, pp. 352–355, 2007.
130. El-Baz, A., Elnakib, A., Khalifa, F., El-Ghar, M.A., McClure, P., Soliman, A., and Gimel'farb, G., "Precise segmentation of 3-D magnetic resonance angiography." *IEEE Transactions on Biomedical Engineering*, vol. 59, no. 7, pp. 2019–2029, 2012.
131. El-Baz, A., Farag, A.A., Gimel'farb, G.L., El-Ghar, M.A., and Eldiasty, T., "Probabilistic modeling of blood vessels for segmenting MRA images." In: *ICPR*, vol. 3, pp. 917–920, 2006.
132. El-Baz, A., Farag, A.A., Gimelfarb, G., El-Ghar, M.A., and Eldiasty, T., "A new adaptive probabilistic model of blood vessels for segmenting MRA images." In: *Medical Image Computing and Computer-Assisted Intervention (MICCAI 2006)*, vol. 4191, Springer, pp. 799–806, 2006.
133. El-Baz, A., Farag, A.A., Gimelfarb, G., and Hushek, S.G., "Automatic cerebrovascular segmentation by accurate probabilistic modeling of TOF-MRA images." In: *Medical Image Computing and Computer-Assisted Intervention (MICCAI 2005)*, Springer, pp. 34–42, 2005.
134. El-Baz, A., Farag, A., Elnakib, A., Casanova, M.F., Gimel'farb, G., Switala, A.E., Jordan, D., and Rainey, S., "Accurate automated detection of autism related corpus callosum abnormalities." *Journal of Medical Systems*, vol. 35, no. 5, pp. 929–939, 2011.

135. El-Baz, A., Farag, A., and Gimelfarb, G., "Cerebrovascular segmentation by accurate probabilistic modeling of TOF-MRA images." In: *Image Analysis*, vol. 3540, Springer, pp. 1128–1137, 2005.
136. El-Baz, A., Gimelfarb, G., Falk, R., El-Ghar, M.A., Kumar, V., and Heredia, D., "A novel 3D joint Markov-Gibbs model for extracting blood vessels from PC–MRA images." In: *Medical Image Computing and Computer-Assisted Intervention (MICCAI 2009)*, vol. 5762, Springer, pp. 943–950, 2009.
137. Elnakib, A., El-Baz, A., Casanova, M.F., Gimel'farb, G., and Switala, A.E., "Image-based detection of corpus callosum variability for more accurate discrimination between dyslexic and normal brains." In: *Proc. IEEE International Symposium on Biomedical Imaging: From Nano to Macro (ISBI'2010)*, IEEE, pp. 109–112, 2010.
138. Elnakib, A., Casanova, M.F., Gimel'farb, G., Switala, A.E., and El-Baz, A., "Autism diagnostics by centerline-based shape analysis of the corpus callosum." In: *Proc. IEEE International Symposium on Biomedical Imaging: From Nano to Macro (ISBI'2011)*, IEEE, pp. 1843–1846, 2011.
139. Elnakib, A., Nitzken, M., Casanova, M., Park, H., Gimel'farb, G., and El-Baz, A., "Quantification of age-related brain cortex change using 3D shape analysis." In: *21st International Conference on Pattern Recognition (ICPR)*, IEEE, pp. 41–44, 2012.
140. Mostapha, M., Soliman, A., Khalifa, F., Elnakib, A., Alansary, A., Nitzken, M., Casanova, M.F., El-Baz, A., "A statistical framework for the classification of infant DT images." In: *2014 IEEE International Conference on Image Processing (ICIP)*, IEEE, pp. 2222–2226, 2014.
141. Nitzken, M., Casanova, M., Gimel'farb, G., Elnakib, A., Khalifa, F., Switala, A., and El-Baz, A., "3D shape analysis of the brain cortex with application to dyslexia." In: *2011 18th IEEE International Conference on Image Processing (ICIP)*, Brussels, Belgium, September 2011, IEEE, pp. 2657–2660. (Selected for oral presentation. Oral acceptance rate is 10 percent and the overall acceptance rate is 35 percent.)
142. El-Gamal, F.E.Z.A., Elmogy, M., Ghazal, M., Atwan, A., Barnes, G., Casanova, M., Keynton, R., and El-Baz, A., "A novel CAD system for local and global early diagnosis of alzheimers disease based on pib-pet scans." In: *2017 IEEE International Conference on Image Processing (ICIP)*, Beijing, China, IEEE, 2017.
143. Ismail, M., Soliman, A., et al., "A fast stochastic framework for automatic MR brain images segmentation."
144. Ismail, M.M., Keynton, R.S., Mostapha, M.M., ElTanboly, A.H., Casanova, M.F., Gimel'farb, G.L., and El-Baz, A., "Studying autism spectrum disorder with structural and diffusion magnetic resonance imaging: a survey." *Frontiers in Human Neuroscience*, vol. 10, 2016.
145. Alansary, A., Ismail, M., Soliman, A., Khalifa, F., Nitzken, M., Elnakib, A., Mostapha, M., Black, A., Stinebruner, K., Casanova, M.F., et al., "Infant brain extraction in t1-weighted MR images using bet and refinement using LCDG and MGRF models." *IEEE Journal of Biomedical and Health Informatics*, vol. 20 no. 3, pp. 925–935, 2016.
146. Ismail, M., Barnes, G., et al., "A new deep-learning CAD system for early diagnosis of autism using structural MR."
147. Ismail, M., Soliman, A., ElTanboly, A., Switala, A., Mahmoud, M., Khalifa, F., Gimel'farb, G., Casanova, M.F., Keynton, R., and El-Baz, A., "Detection of white matter abnormalities in MR brain images for diagnosis of autism in children," pp. 6–9, 2016.
148. Ismail, M., Mostapha, M., Soliman, A., Nitzken, M., Khalifa, F., Elnakib, A., Gimel'farb, G., Casanova, M., and El-Baz, A., "Segmentation of infant brain MR images based on adaptive shape prior and higher-order MGRF," pp. 4327–4331, 2015.
149. Shalaby, A., Taher, F., El-Baz, M., Ghazal, V., Abou El-Ghar, M., Takieldeen, A., and El-Baz, A., "Probabilistic modeling of blood vessels for segmenting magnetic resonance angiography images." In: *Medical Research Archive* (MRA), KEI, pp. 34–42, 2017.
150. Chowdhury, A.S., Rudra, A.K., Sen, M., Elnakib, A., and El-Baz, A., "Cerebral white matter segmentation from MRI using probabilistic graph cuts and geometric shape priors." In: *ICIP*, pp. 3649–3652, 2010.

Taylor & Francis
Taylor & Francis Group
http://taylorandfrancis.com

5 An Unsupervised Parametric Mixture Model for Automatic Cerebrovascular Segmentation

Mohammed Ghazal[1,2], *Yasmina Al Khalil*[2], *Ayman El-Baz*[1]
[1]University of Louisville
[2]Abu Dhabi University

CONTENTS

5.1 INTRODUCTION

Cerebrovascular diseases represent one of the most frequent reasons for neurological emergencies and constitute a leading cause of many serious long-term disabilities [1]. About 75 percent of patients affected by cerebrovascular diseases have lost the ability to work by a certain degree and almost 40 percent of them are severely physically disabled [2]. Despite the advances in treatment throughout recent years, almost 30 percent of strokes result in death within a month, while 70–80 percent cause significant long-term disabilities. Thus, early diagnosis and detection of potential stroke risk factors and threats is critical for preventing permanent neurological damage, complications, and death [3], [4].

A stroke is defined as rapid disturbance in the cerebral blood flow, resulting in a short-term or permanent change in cerebral function [5]. Based on its pathological background, stroke can be classified as either ischemic or hemorrhagic. Ischemic stroke is the most frequent type, caused by a brief interruption of the blood supply to a certain part of the brain. Ischemic strokes can further be classified as thrombotic and embolic. Thrombotic strokes are characterized by a blood clot (thrombus) blocking an artery to the brain, hence interrupting regular blood flow. Embolic strokes are a result of a thrombus travelling from its original location such that it blocks an artery downstream. The damage occurred by an embolic stroke depends on the depth of the blockage manifestation in the artery [6]. In most cases, arteries affected by thrombotic or embolic strokes are not entirely blocked, enabling a small stream of blood to the brain. However, reduced blood flow decreases the amount of nutrients coming to the cells, which quickly affects their functionality, leading to symptoms of stroke occurring [7]. To treat ischemic strokes, the obstruction blocking the blood flow needs to be removed to restore the functionality of the cells and affected brain regions. A common treatment is a tissue plasminogen activator (tPA), which must be applied within a maximum of

three hours from the occurrence of symptoms. However, only 3–5 percent of patients are able to reach the hospital in time for the treatment to be administered. Moreover, the tPA treatment increases the risk for intracranial hemorrhage. Other treatment options include intra-arterial thrombolysis with drugs or mechanical devices, carotid endarterectomy, and stenting of the cervical and intracranial vessels [8]. A hemorrhagic stroke can occur due to hypertension, fracture of an aneurysm or vascular deformity, as well as a consequence of anticoagulation medications. Two types of hemorrhage exist, an intracerebral hemorrhage and subarachnoid hemorrhage. An intracerebral hemorrhage occurs as a result of direct bleeding into the brain tissue, which further causes a lump within the brain. When bleeding expands into the cerebrospinal fluid areas around the brain, we refer to subarachnoid hemorrhage [1]. Due to intracranial pressure caused by bleeding, hemorrhagic stroke requires surgical treatment to prevent further damage and additional strokes. Stroke treatment additionally involves recovery and rehabilitation.

A frequent cause of ischemic strokes and attacks is carotid stenosis, which is defined as a severe blockage of internal carotid arteries by fat and cholesterol accumulation [9]. Symptoms of carotid stenosis usually first appear with transient ischemic attacks, caused by temporary interruption of blood flow to the brain. These last for a small period of time, for a couple of minutes, after which the symptoms disappear. Symptoms of transient ischemic attacks include weakness or numbness in an arm or leg, difficulty speaking, a drooping face, vision problems, or paralysis affecting one side of the body. Carotid stenosis is diagnosed by either a Doppler ultrasound of the neck, a computed tomography angiogram (CTA) of the neck, magnetic resonance angiography (MRA), or a cerebral angiogram [10]. An additional common cause of strokes is a cerebral aneurysm, defined by the area in the brain where the blood vessel weakens, resulting in expanding beyond the vessel wall. Aneurysms generally occur at the points where a blood vessel branches, as these regions are structurally weaker and exhibit higher vulnerability [11]. Unruptured cerebral aneurysms can be identified by noninvasive techniques, such as MRA or by a carotid angiogram. In case of a rupture, aneurysms cause subarachnoid hemorrhage, as well as intracranial hematoma (clot) if bleeding occurs in the cerebrospinal fluid. Ruptures can be detected using a CT scan or lumbar puncture, followed by cerebral angiography.

Regardless of what type of stroke the patient has suffered, it is critical that patients receive emergency medical treatment as soon as possible for the best possible outcome. Moreover, it is of the utmost importance to accurately detect signs and symptoms of stroke and apply preventive treatment to avert from the actual stroke or attack occurring. Thus, being able to obtain an early diagnosis of the aforementioned cerebrovascular diseases, especially detecting carotid stenosis and the development of aneurysms in time for applying early treatment.

With the rapid development of medical imaging technology, medical imaging techniques have become critical factors in patient care and essential tools for doctors to identify stroke risk factors and diagnose cerebrovascular diseases. Such technology allows for the detection of serious vascular diseases including carotid stenosis, aneurysm, and vascular malformation, which could potentially lead to severe headaches, strokes, or a life-threatening coma if left untreated [12]. Thus, accurate cerebrovascular segmentation is of prime importance for cerebrovascular anatomy analysis and vessel stenosis detection, which in turn enables timely diagnosis and endovascular treatment. However, precise cerebrovascular segmentation has posed a challenge for many years as cerebral vessels are of a relatively complex structure, while at the same time the differences in intensity levels between the surrounding tissue and vessels is often too narrow [4].

Computed tomography (CT) and magnetic resonance imaging (MRI) have had a major influence on the study of the brain, due to their noninvasive nature and ability to evaluate the brain structure more accurately and infer causes of different cerebrovascular diseases. Many cerebrovascular segmentation methods have been proposed utilizing images collected by applying CT and MRI techniques. However, a considerable drawback of CT is the need for a high radiation dose. On the other hand, MRI is a more complicated technique, as well as more time-consuming [13]. For the purpose of pathology detection applications and functional characterization, where cellular

activity is studied, positron emission tomography is utilized. When integrated with CT or MRI, utilizing both functional and structural information results in a higher sensitivity and specificity compared to using either modality by itself. Nevertheless, PET cannot be used as a stand-alone modality for these applications, as anatomical information from CT or MRI are needed for proper interpretation [14]. Moreover, ultrasound has been widely utilized for detection and evaluation of cerebrovascular diseases. One of the most significant ultrasound methods is transcranial Doppler sonography, due to being noninvasive, non-ionising, portable, and safe. It is utilized for the assessment of intracerebral blood flow by employing a pulsed Doppler transducer, as well as for the detection of occlusion of intracranial arteries [15]. However, these techniques are highly operator dependent, inaccurate because of poor acoustic window, and require extensive skills and experience for proper interpretation.

Currently, MRI provides the best solution for noninvasive imaging of brain vasculature and its segmentation. Compared to other modalities, MRI has a much greater range of available soft tissue contrast, depicts anatomy in more detail, and is more sensitive to abnormalities within the brain. Furthermore, scanning using MRI can be done in any imaging plane, without a need to physically move the patient, its contrast agents are low-risk toward any allergic reactions, and it allows for the interpretation of structures potentially concealed by artifacts from bones in CT images [13].

In the following sections, we introduce detailed imaging techniques using MRI, as well as segmentation methods of MRI-collected images. This is followed by proposing a new approach toward cerebrovascular system segmentation, which incorporates a statistical mixture of Gaussian model with the spatial interaction model defined by Markov-Gibbs random field models. The proposed two-level segmentation is applied on Gaussian scale spaces obtained by employing two Gaussian kernels with different sizes. Finally, we present experimental results obtained by applying the proposed segmentation method, and conclude with a small discussion.

5.2 MAGNETIC RESONANCE IMAGING

Magnetic resonance imaging (MRI) has become one of the most versatile and widely used tools for clinical diagnosis of diseases over the last few decades. It has been considered essential for diagnosis of acute injuries, musculoskeletal diseases, brain pathologies, cancer detection, and cardiac imaging [16]. Being a noninvasive imaging modality, it is preferred over CT, especially in children and patients requiring multiple imaging examinations. Further advantages include superior intrinsic soft tissue contrast, unrestricted penetration depth, and high anatomical resolution [17]. Thus, MRI characterizes anatomy in greater detail, and is more sensitive to abnormalities within the studied tissues, compared to CT methods. Moreover, it allows for the evaluation of structures that may be ambiguous due to remaining artifacts from bone tissues in CT images [18]. However, for accurate estimation of intracranial vascular diseases through cerebrovascular segmentation, we require functional information about organ impairment during the infection, which is not available through structural MRI. Noninvasive magnetic resonance angiography (MRA) can accurately represent high-level information of the anatomy, function, and metabolism of the studied tissue. MRA is useful for detecting aneurysm, occlusions, and stenoses. Moreover, it has been extensively utilized in cases when the injection of contrast agents introduces high risk. As such, MRA allows for an accurate and noninvasive evaluation of blood flow and blood vessel morphology [19]. Two main MRA techniques commonly used for observing vascular structures are contrast-enhanced and non-contrast-enhanced MRA. While contrast-enhanced MRA utilizes a contrasting substance, such as intravenous gadolinium injection for blood flow detection, non-contrast-enhanced MRA methods rely on the effects of vascular flow as a fundamental contrast. The latter exploit mechanisms such as time-of-flight (TOF) and phase contrast angiography (PCA) [20].

PCA-based methods are useful for quantifying flow velocity vectors for each voxel in an MRA image. The signal representing a contrast between flowing and stationary nuclei is generated

by producing a phase shift proportional to the velocity of blood flow [21]. Thus, two data-sets with opposite phases for moving nuclei and identical phases for stationary nuclei are obtained, respectively. Having the net phase of zero, stationary nuclei are not represented in the final image, while flowing nuclei remain as a residual due to movement from one position in the field gradient to another between the first and the second sensitization times. When the two data-sets are subtracted, the signal contribution from stationary nuclei is eliminated and only signals representing flowing nuclei remain [22]. However, the accuracy of PCA-based methods depends on the precise choice of a velocity encoding factor (VENC), which usually corresponds to the maximum velocity through a certain region. Inaccurate selection of VENC can lead to errors, where most common side effects include flow aliasing. A disadvantage of the phase contrast MRI is the need for multiple acquisitions to encode a single velocity direction, which ensues long-duration scan times [23].

On the other hand, TOF-MRA uses short echo time and flow compensation to produce high contrast images with a significantly shorter acquisition time compared to other methods, including PCA methods [24]. A signal difference between blood and stationary tissues is achieved by applying rapid radiofrequency excitation pulses that saturate stationary tissue signals, while the flowing spins are subjected to only a few excitation pulses [25]. Consequently, in-flowing spins moving into the saturated tissue have a bright signal compared to the suppressed background containing stationary tissue, as the blood flows continuously during image acquisition, never experiencing enough excitation pulses to become saturated [26]. Thus, slow blood flow or stasis, retrograde filling, tortuous vessels, or vessels existing in the same plane as the image slice cause the blood flow to be saturated in the image volume, which is followed by poor vessel visualization.

5.3 CEREBROVASCULAR SEGMENTATION USING MAGNETIC RESONANCE IMAGING

5.3.1 Related Work on Cerebrovascular Segmentation

Various approaches for cerebrovascular segmentation from MRA data have been proposed, which can be generalized into two categories: skeleton-based and non-skeleton-based. Skeleton-based methods [27]–[29] segment and reconstruct vessels by extracting the centerlines of the vessels from the two-dimensional slices, thus having the ability to construct the vessel tree or a skeleton. These methods are referred to as indirect since they require pre-computation of the vessel cross-sections through approaches such as edge-based techniques, parametric-based models, and geometric-based models [30]. Non-skeleton-based methods compute vessels directly without estimating the vessel cross-sections. Most prominent non-skeleton-based techniques employed for vascular segmentation from MRA data can be divided into two general categories: deformable models and statistical-based methods. Deformable models rely on contour functions to adjust an originally defined boundary surface to blood vessels, based on optimization techniques that depend on image gradients and smoothness of the surface. Commonly used deformable models include topologically adaptable surfaces [31], geodesic active contours with level set techniques [32], multi-scale geometrical flows [33], and region-based deformable contours [34]. Despite good reported performance and experimental results, these methods suffer from the need for manual initialization, as well as inefficiency in terms of speed, which makes them slower than statistical-based methods [24].

Statistical methods have the ability to derive vascular trees in an automatic manner, but the accuracy of such techniques varies with the ability to correctly predict or define the probability model representing the data [35]. Data collected from MRA imaging techniques can be described as multi-modal, where signals correlated with each class, label, or region-of-interest can be represented by a particular marginal probability distribution. Thus, each mode of the marginal probability

distribution can serve as a segmentation basis for objects of interest in the MRA image (e.g., blood vessels, brain tissues, etc.). Moreover, a statistical model can also be represented by a linear combination of several probability distribution functions derived based on the properties of observed anatomical structures. The choice or combination of probability distribution functions largely depends on the utilized imaging modality. By estimating the parameters of the chosen statistical models, objects of interests can be separated from the background based on a variety of statistical techniques, such as Bayesian inference statistics and maximum a posteriori estimation [36]. One of the first statistical-based cerebrovascular segmentation methods was proposed in [37], where they utilize a mixture of two Gaussian probability distributions and one uniform distribution to represent stationary cerebrospinal fluid (CSF), brain tissue, and arteries, respectively. They find that the lowest intensity area corresponds mainly to CSF (surrounding the brain tissue), bone tissue, and the background air. The next lowest intensity region represents brain tissues (gray and white matter) and eyes. Finally, the highest intensity region include cerebral vessels.

Estimation of parameters for the mixture model presented is done by using the traditional expectation-maximization (EM) algorithm. A more adaptive approach for cerebrovascular segmentation has been proposed in [38]. The approach consists of deriving an adaptive number of dominant and subordinate discrete Gaussian distributions, instead of a certain number of predefined distributions, to approximate intensity distributions of voxels in MRA images. Moreover, a model consisting of one Rayleigh and two Gaussian distributions for modeling CSF and brain tissue has been proposed in [39].

Cerebrovascular segmentation can be performed on 2D images, sequences of 2D images, or 3D volumetric images. The majority of proposed methods have focused on 2D images, while data characterized in 3D space is segmented individually, followed by post-processing algorithms to combine segmented 2D slices into a 3D volume or surface. The drawback of such approaches is the omission of important anatomical information contained in the 3D space, which could lead to inconsistencies and uneven surfaces [40]. Therefore, there is a need for the development of 3D segmentation algorithms for handling volumetric data to achieve more accurate volumetric segmentation. Moreover, statistical models discussed previously often fail to handle image noise and other imaging artifacts, thus making first-order feature insufficient for accurate cerebrovascular MRA segmentation. Therefore, more effective second-order discriminative features are employed, which combine spatial interaction between intensities with the first-order intensity model. The most popular models for defining local spatial interactions between pixel/voxel intensities are represented by the Markov random field (MRF) theory, which allows for decreasing misclassification errors due to image noise and artifacts after initial segmentation based on first-order features.

In the following discussion, we propose a probability model for estimating brain blood vessels from 3D volumetric MRA images, whose parameters are approximated using expectation-maximization (EM) algorithm, followed by refinement using Gibbs-Markov random field model with higher order cliques.

5.3.2 Proposed Work

TOF-MRA images consist of three regions-of-interest or three distinct classes: darker cerebrospinal fluid (CSF) together with bones and fat, brain tissues (gray matter and white mater), and brighter in appearance blood vessels. Based on this, we can employ statistically based parametric models to classify the three classes by assuming that each class exhibits a Gaussian distribution of intensities. Thus, the global distribution of data can be defined as a linear combination of the distributions of the three classes, referred to as a Gaussian mixture model and expressed as

$$p(q) = \sum_{k=0}^{M} w_k \rho\left(q|\theta_k\right) \tag{5.1}$$

where $q; q \in Q = 0,1,\ldots,Q-1$, is the gray or intensity level, $p(q)$ is the global distribution over the intensities q, M, is the number of classes or Gaussian distributions, θ_k stands for the parameters of the Gaussian distribution for a particular class k ($\theta_k = (\mu_k, \sigma_k)$), $\rho(q|\theta_k)$ is the Gaussian intensity distribution of class k, and w_k is the probability, or the mixing weight representing the proportions of each class within the data. Thus, each class is represented by a Gaussian distribution with mean μ_k and standard deviation σ_k, such that

$$\rho\left(q|k\right) = \frac{1}{2\pi\sigma_k^2} e^{-\frac{1}{2}\left(\frac{q-\mu_k}{\sigma_k}\right)^2} \tag{5.2}$$

To estimate the parameters θ_k for each given class, we utilize the EM algorithm, which maximizes the likelihood of the distribution for a certain set of data [41]. The EM algorithm estimates the distribution parameters by updating initial parameter estimates iteratively, with the aim of minimizing the difference between log-likelihood of the mixture distribution. Initial parameter values are either found manually or by a separate initialization procedure. Given the number of distributions or classes M, relative contribution or responsibility of each intensity level q toward the Gaussian distribution for each iteration n is given by

$$\pi_k^{[n]}\left(\omega_k|q\right) = \frac{w_k^{[n]}\rho\left(q\left|\theta_k^{[n]}\right.\right)}{\sum_{l=1}^{M} w_l^{[n]}\rho\left(q\left|\theta_l^{[n]}\right.\right)} \tag{5.3}$$

Furthermore, we estimate the distribution parameters, as well as prior probability or mixing weights w_k for each iteration $n+1$ as follows:

$$w_k^{[n+1]} = \frac{\sum_{q\in Q}\pi_k^{[n]}\left(\omega_k|q\right)}{\sum_{l=1}^{M}\sum_{q\in Q}\pi_l^{[n]}\left(\omega_k|q\right)}, \mu_k^{[n+1]} = \frac{\sum_{q\in Q}\pi_k^n q}{\sum_{q\in Q}\pi_k^n}, \tag{5.4}$$

$$\left(\sigma_k^{[n+1]}\right)^2 = \frac{\sum_{q\in Q}\pi_k^n\left(q-\mu_1^{[n]}\right)^2}{\sum_{q\in Q}\pi_k^n} \tag{5.5}$$

The iterations of the EM algorithm for updating the model parameters should be terminated when a certain stopping criteria is satisfied, such as in the case of the log-likelihood of the mixture distribution not being changed, as described in [42]. However, it is important to notice that all of the equations listed previously for parameter estimation perform the calculations on the entire number of voxels contained in the data-set. For large data-sets such as in the case of 3D data, this can be computationally expensive and inefficient. Thus, the computations shown previously are performed over every possible intensity instead of each voxel separately, by utilizing the frequency with which each intensity occurs in the data.

Employing only the statistically based intensity model or Gaussian mixture model for segmentation leads to misclassification errors, evident by our experimental results shown in III-C. Thus, we refine the results by employing a spatial interaction model based on the Gibbs-Markov Random Field (GMRF) theory. We define the finite arithmetic grid $T = \{(i,j,z): 1 \le i \le I, 1 \le j \le J, 1 \le z \le Z\}$ for grayscale TOF-MRA images such that $g: R \to Q$ and region maps $m: R \to M$, where $Q = 0,\ldots,Q-1$ represent the set of gray levels or intensities and $M = 1,\ldots,M$ are the set of classes. Q is the number of gray levels or intensities, and M is the number of classes that the image needs to be separated

in after segmentation. To segment the images using the GMRF model, we look at the joint probability distribution of the images and the needed region maps, as $P(g,m) = P(m)P(g|m)$. $P(m)$ is an unconditional probability distribution of maps, representing the higher level of the two-level Gibbs segmentation model, while $P(g|m)$ is the conditional distribution of images g given a map m, or the lower level of the model. Thus, $P(g|m)$ is estimated using the previously discussed Gaussian mixture model, while $P(m)$ is obtained using the MGRF models. The Bayesian maximum a posteriori (MAP) estimate of the map m, given the image g is

$$m = \underset{m \in M}{\operatorname{argmax}} \quad L(m,g) \tag{5.6}$$

and maximizes the log-likelihood function given by

$$L(g,m) = logP\left(g|m\right) + logP(m). \tag{5.7}$$

The generic Markov-Gibbs model of region maps defines only pairwise interactions between each region label and its neighbors. Moreover, the interactions are restricted to the nearest voxels and are by symmetry independent of relative region orientation, are the same for all classes, and depend only on whether the pair of labels are equal or not. Thus, the model is similar to conventional auto-binomial models [43], with the difference of having the potentials independent of any predefined functions and having analytically obtained estimates.

The symmetric label interactions we consider, only up to a 26-neighborhood system, include the closest horizontal, vertical, and diagonal interactions in the current slice (c_{hvd}), the closest horizontal, vertical, and diagonal interactions in the upper slice (u_{hvd}), and the closest horizontal, vertical, and diagonal interactions in the lower slice (l_{hvd}). Potentials of each type are bi-valued as only coincidental or different labels are considered. Let $V_a(\nu,\eta) = V_{a,eq}$ if $\nu = \eta : \nu, \eta \in M$ and $V_a(\nu,\eta) = V_{a,neq}$ if $\nu \neq \eta : \nu, \eta \in M$ indicate bi-valued Gibbs potentials characterizing symmetric pairwise potentials between each label consisting of $a \in A = \{c_{hvd}, u_{hvd}, l_{hvd}\}$. If $N_{c_{hvd}} = \{(-1,-1,0),(0,-1,0),(1,-1,0),(1,0,0),(1,1,0),(0,1,0),(-1,1,0),(-1,0,0)\}$, $N_{u_{hvd}} = \{(0,0,1),(-1,-1,1),(0,-1,1),(1,-1,1),(1,0,1),(1,1,1),(0,1,1),(-1,1,1),(-1,0,1)\}$, and $N_{l_{hvd}} = \{(0,0,-1),(-1,-1,-1),(0,-1,-1),(1,-1,-1),(1,0,-1),(1,1,-1),(0,1,-1),(-1,1,-1),(-1,0,-1)\}$ are subsets of inter-voxel offsets for the utilized neighborhood system. Thus, the Gibbs probability distribution of region maps is defined as:

$$P(m) \propto exp\left(\sum_{(i,j,z)\in R} \sum_{a\in A} \sum_{(\iota,\xi,\zeta)\in N_a} V_a\left(m_{i,j,z}, m_{i+\iota,j+\xi,z+\zeta}\right) \right) \tag{5.8}$$

Determining the MGRF model described in Eq. (5.8) requires the estimation of Gibbs parameters using the analytical maximum likelihood estimation proposed in [5], as follows:

$$V_{a,eq} = \frac{M^2}{M-1}\left(f_a'(m) - \frac{1}{M} \right), \tag{5.9}$$

$$V_{a,neq} = \frac{M^2}{M-1}\left(f_a''(m) - 1 + \frac{1}{M} \right), \tag{5.10}$$

where $f_a'(m)$ and $f_a''(m)$ stand for the relative occurence of the equal and non-equal label pairs in all equivalent voxel pairs $\{((i,j,z),(i+\iota,j+\xi,z+\zeta)) : (i,j,z) \in R; (i+\iota,j+\xi,z+\zeta) \in R; (\iota,\xi,\zeta) \in N_a\}$. To reduce the inhomogeneity in the obtained TOF-MRA data, we utilize the Gaussian scale space theory and convolve the original data with two different scales of the 3D Gaussian

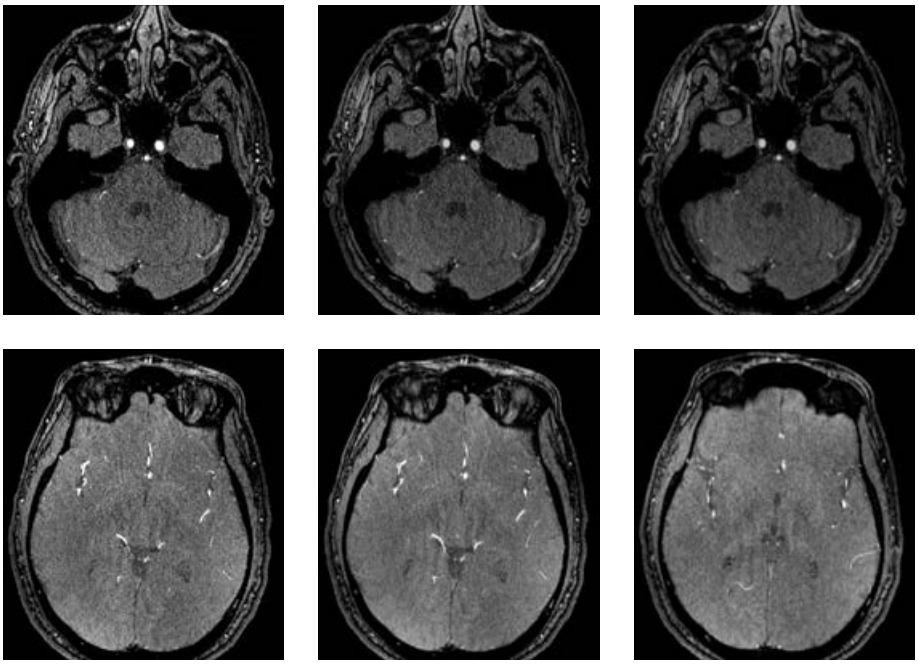

FIGURE 5.1 Original TOF-MRA images (a), smoothed TOF-MRA images by convolving the original images with the first 3D Gaussian kernel (first-scale) (b), and smoothed TOF-MRA images by convolving the original images with the second 3D Gaussian kernel (second-scale) (c).

kernels. Figure 5.1 provides an example of the original and smoothed TOF-MRA images using the 3D Gaussian kernels. Thus, the original image data and the generated Gaussian scale space data are segmented by the Gaussian mixture models, and iteratively refined by the MGRF model. Finally, the majority voting scheme is utilized to select the label of each voxel by selecting the label that most segmentations agree on. After the candidate vessel voxels have been determined, we apply the 3D connected component analysis to identify the vessels and discard the background containing CSF, bones, fat, and brain tissue. This further includes filling holes and removing any small noisy regions.

5.3.3 Experimental Results

Experiments were performed with the use of TOF-MRA images, containing 3D data-sets of size $696 \times 768 \times 161$. TOF-MRA images consist of three classes, darker bones and fat, brain tissue, and blood vessels that appear the brightest in the images. Typical TOF-MRA slices forming a 3D data-set, its empirical marginal gray level distribution $f(q)$, and the estimated Gaussian mixture model $p(q)$ are shown in Figure 5.2.

Using the final estimated parameters, data is segmented into different classes by labeling each voxel as belonging to the class k for which $w_k p(q|k) > w_j p(q|j)$ for all $k \neq j$. Figure 5.3 depicts the marginal gray level distribution $f(q)$ and the estimated Gaussian mixture model $p(q)$ for a different data-set, together with the Gaussian models for each of the three existing classes. Since we are interested in segmenting the voxels belonging to the blood vessels (depicted by $p(q|3)$ in Figure 5.3), we utilize the second threshold to discriminate between the voxels whose conditional probability of belonging to the third class is higher than the conditional probability of coming from either of the other two distributions, as these are the same voxels above the second intensity threshold.

Thus, we obtain the initial segmentation based on the intensity model described above, which can be observed in Figure 5.4 for different subjects from the 3D data-set. After refining the Gaussian mixture model or the intensity-based model using the MGRF model, we further employ

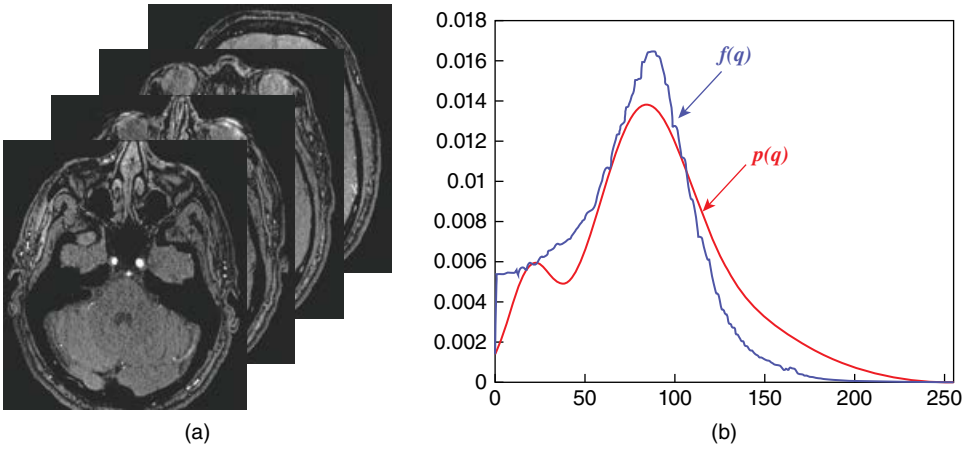

FIGURE 5.2 Typical TOF-MRA slices from the 3D data-set (a) and deviations between the empirical distribution $f(q)$ and the estimated Gaussian mixture model $p(q)$ (b).

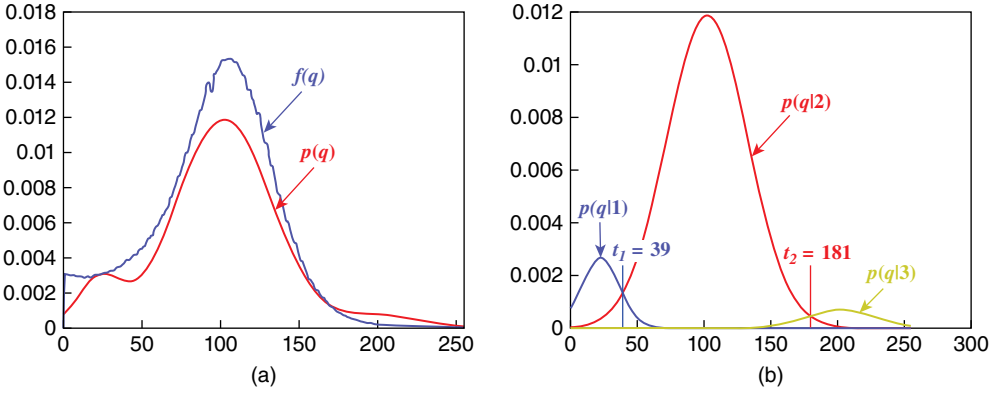

FIGURE 5.3 Deviations between the empirical distribution $f(q)$ and the estimated Gaussian mixture model $p(q)$ for a different data-set (a) and the estimated Gaussian models for each class (b).

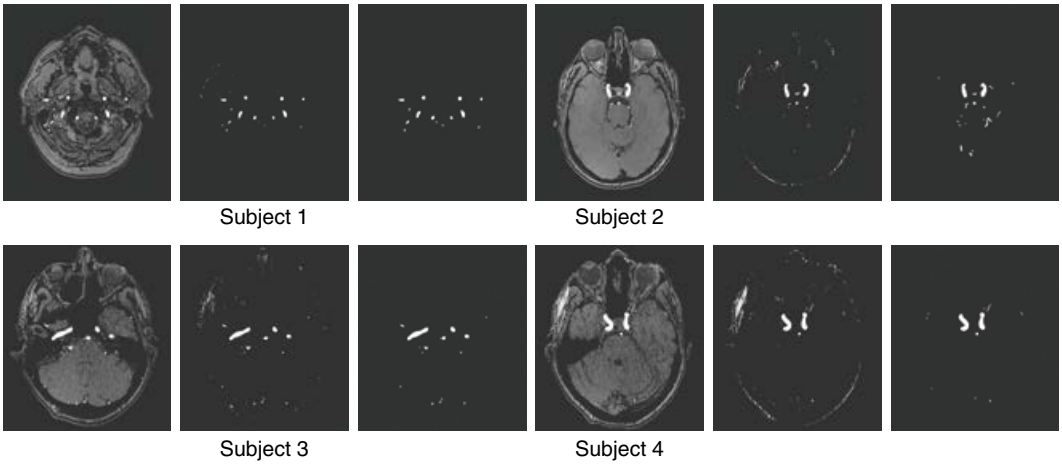

FIGURE 5.4 Original image from the TOF-MRA 3D data-set with the initial segmentation based on the intensity model and the ground truth for four different subjects.

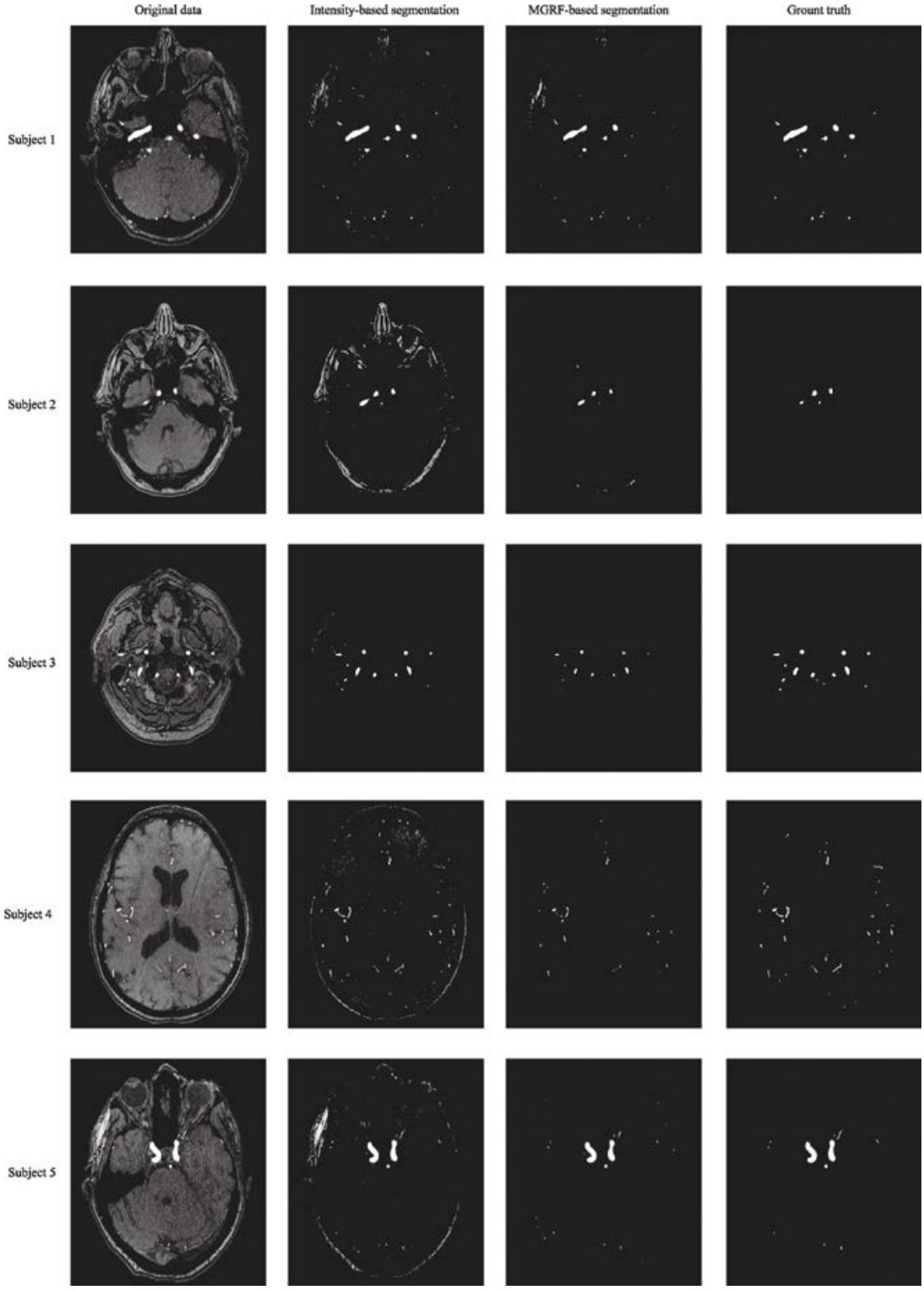

FIGURE 5.5 Two-level segmentation model applied to the original data w.r.t. the ground truth for five different patients in the TOF-MRA data-set.

majority voting on the refined original and generated Gaussian scale space data, to obtain the finalized segmentation. Figure 5.5 presents the initial and final segmentation of the vessels, at the same time comparing them to the expert's ground truth, for five different subjects in the TOF-MRA data-set. Figure 5.5 demonstrates the ability of the proposed two-level segmentation model to reduce misclassification errors and extract vessels with a significantly higher accuracy. TOF-MRA data tends to be sensitive to tissues such as subcutaneous fat, which can obscure the actual blood vessels in the segmented image or volume. Thus, to eliminate the unwanted tissue, the 3D volume is processed with a connectivity filter, which generates a 3D segmented volume by selecting the largest connected tree structures with the help of the 3D volume growing algorithm, presented in [45]. Final segmentation results visualized in 3D are presented in Figure 5.6. Figure 5.7 demonstrates the difference between the vascular trees obtained by the proposed two-level segmentation approach with respect to the vascular trees obtained by utilizing the ground truth data for two subjects.

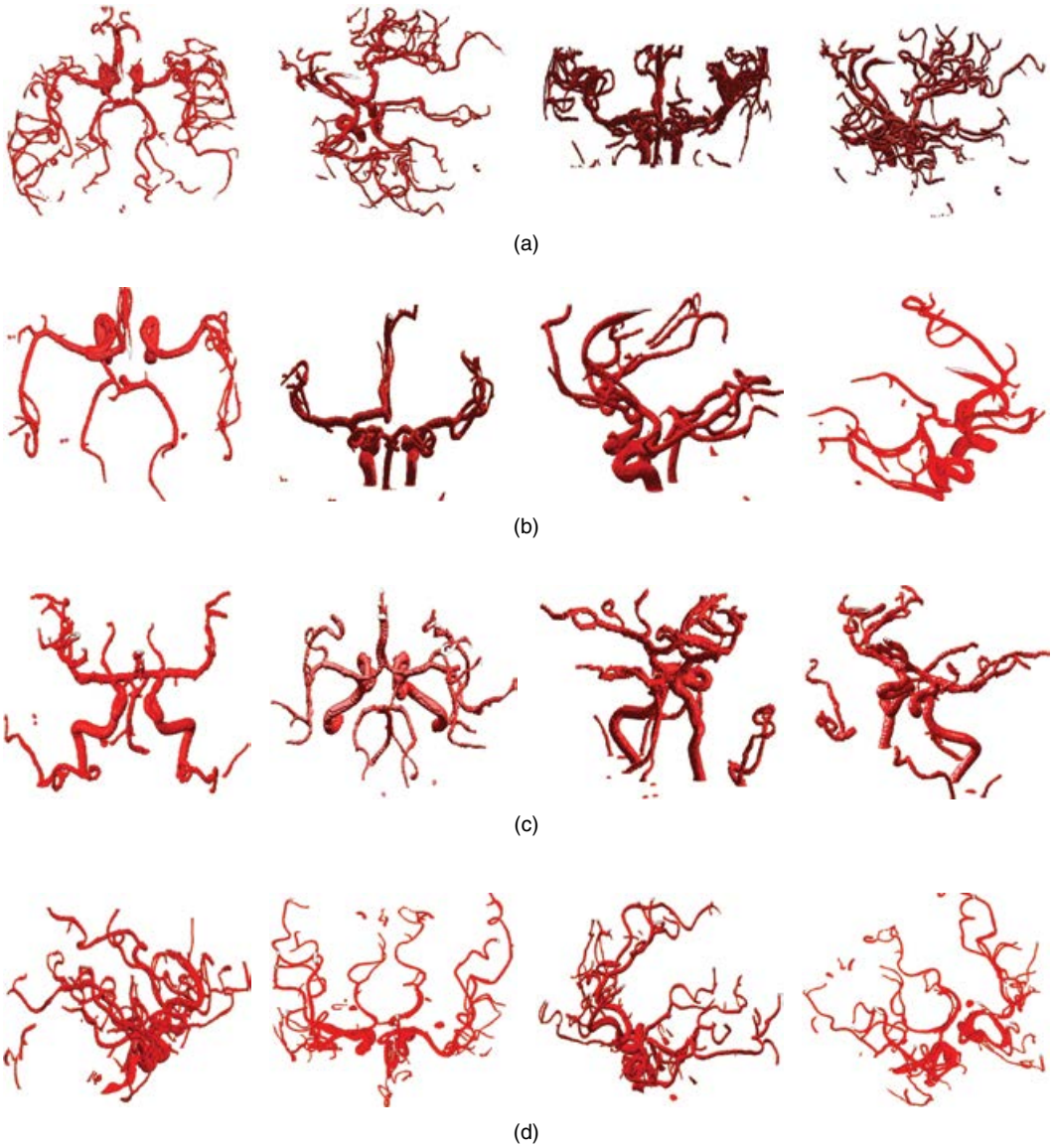

FIGURE 5.6 Segmented vascular trees obtained by the proposed approach, where each row relates to one patient.

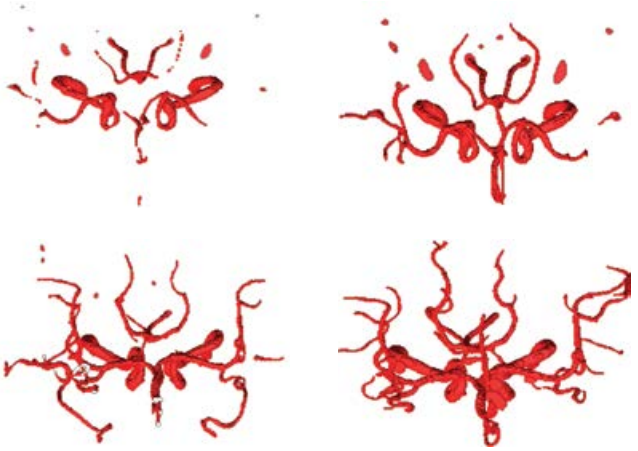

FIGURE 5.7 Deviations between segmented vascular trees using the TOF-MRA 3D data-set generated by the (a) proposed two-level segmentation approach (b) by the expert-generated ground truth for two different subjects.

5.4 CONCLUSION

Precise cerebrovascular segmentation is crucial for early diagnosis and timely endovascular treatment of intracranial vascular diseases. Magnetic resonance imaging has become the most powerful noninvasive tool for clinical diagnosis of diseases. It offers best soft tissue contrast among all imaging modalities, as well as the most sensitive noninvasive way of imaging the brain, spinal cord, or other areas of the body. For the purpose of accurate cerebrovascular segmentation and modelling, it is important to visualize arterial blood flow and blood vessel morphology. As such, utilizing magnetic resonance angiography allows for obtaining the aforementioned characteristics and functionalities.

In this chapter, we review recent methods utilized for cerebrovascular segmentation from MRA images, including their strengths and limitations. Moreover, we introduce a two-level segmentation model for accurate brain blood vessel segmentation from TOF-MRA images, which combines statistical methods with the spatial interaction model between the intensities with the first level statistical model. More precisely, we propose the use of the Gaussian mixture model, followed by applying the MGRF model to refine the initial segmentation. Furthermore, we apply the two-level segmentation on Gaussian scale space data generated from the original data using 3D Gaussian kernels. By combining the scale space data with the use of the majority voting scheme and connectivity analysis, we obtain the final 3D segmentation of the brain vessels from TOF-MRA images.

In conclusion, the presented experimental data indicates that the proposed segmentation algorithm for extracting cerebrovascular trees from TOF-MRA images shows promising results. Moreover, the advantages of the proposed approach include a completely unsupervised segmentation method, without the need for additional pre-processing and post-processing steps to obtain a three-dimensional visualization of the segmented cerebrovascular tree.

References

1. X. Ustrell-Roig and J. Serena-Leal, "Stroke: diagnosis and therapeutic management of cerebrovascular disease," *Revista Espaola de Cardiologa (English Edition)*, vol. 60, no. 7, pp. 753–769, 2007. [Online]. Available: http://www.sciencedirect.com/science/article/pii/S1885585708600110

2. R.-F. Cao, X.-C. Wang, Z.-K. Wu, M.-Q. Zhou, and X.-Y. Liu, "A parallel Markov cerebrovascular segmentation algorithm based on statistical model," *Journal of Computer Science and Technology*, vol. 31, no. 2, p. 400, 2016.
3. V. L. Feigin, "Stroke epidemiology in the developing world," *The Lancet*, vol. 365, no. 9478, pp. 2160–2161, 2005.
4. M. J. Donahue and M. K. Strother, "Novel non-invasive magnetic resonance imaging methods in cerebrovascular disease," 2013.
5. T. Truelsen, S. Begg, and C. Mathers, "The global burden of cerebrovascular disease," *Geneva: World Health Organisation*, 2000.
6. C. Sudlow, C. Warlow *et al*., "Comparable studies of the incidence of stroke and its pathological types," *Stroke*, vol. 28, no. 3, pp. 491–499, 1997.
7. O. Wu, L. H. Schwamm, and A. G. Sorensen, "Imaging stroke patients with unclear onset times," *Neuroimaging Clinics of North America*, vol. 21, no. 2, pp. 327–344, 2011.
8. J. M. Roth, "Recombinant tissue plasminogen activator for the treatment of acute ischemic stroke," in *Baylor University Medical Center. Proceedings*, vol. 24, no. 3, p. 257, 2011.
9. A. Chatzikonstantinou, M. E. Wolf, A. Schaefer, and M. G. Hennerici, "Asymptomatic and symptomatic carotid stenosis: an obsolete classification?" *Stroke Research and Treatment*, vol. 2012, 2012.
10. R. W. Hobson, W. C. Mackey, E. Ascher, M. H. Murad, K. D. Calligaro, A. J. Comerota, V. M. Montori, M. K. Eskandari, D. W. Massop, R. L. Bush *et al*., "Management of atherosclerotic carotid artery disease: clinical practice guidelines of the society for vascular surgery," *Journal of Vascular Surgery*, vol. 48, no. 2, pp. 480–486, 2008.
11. N. Ajiboye, N. Chalouhi, R. M. Starke, M. Zanaty, and R. Bell, "Unruptured cerebral aneurysms: evaluation and management," *The Scientific World Journal*, vol. 2015, 2015.
12. A. El-Baz, A. Farag, and G. Gimelfarb, *Cerebrovascular Segmentation by Accurate Probabilistic Modeling of TOF-MRA Images*. Berlin, Heidelberg: Springer Berlin Heidelberg, 2005, pp. 1128–1137. [Online]. Available: http://dx.doi.org/10.1007/11499145_114.
13. J. Vymazal, A. M. Rulseh, J. Keller, and L. Janouskova, "Comparison of CT and MR imaging in ischemic stroke," *Insights into Imaging*, vol. 3, no. 6, pp. 619–627, 2012.
14. B. Foster, U. Bagci, A. Mansoor, Z. Xu, and D. J. Mollura, "A review on segmentation of positron emission tomography images," *Computers in Biology and Medicine*, vol. 50, pp. 76–96, 2014.
15. S. Sarkar, S. Ghosh, S. K. Ghosh, and A. Collier, "Role of transcranial doppler ultrasonography in stroke," *Postgraduate Medical Journal*, vol. 83, no. 985, pp. 683–689, 2007.
16. V. Hoerr and C. Faber, "Magnetic resonance imaging characterization of microbial infections," *Journal of Pharmaceutical and Biomedical Analysis*, vol. 93, pp. 136–146, 2014, {NMR} Spectroscopy in Pharmaceutical and Biomedical Analysis. [Online]. Available: http://www.sciencedirect.com/science/article/pii/S0731708513004937.
17. A. Saraste, S. G. Nekolla, and M. Schwaiger, "Cardiovascular molecular imaging: an overview," *Cardiovascular Research*, vol. 83, no. 4, p. 643, 2009. [Online]. Available: http://dx.doi.org/10.1093/cvr/cvp209
18. F. E. Boas and D. Fleischmann, "CT artifacts: causes and reduction techniques."
19. Schneider, Prince, Meaney, and Ho, "Magnetic resonance angiography: techniques, indications and practical applications," *Vasa*, vol. 34, no. 3, pp. 213–213, 2005. [Online]. Available: http://dx.doi.org/10.1024/0301-1526.34.3.213b
20. M. P. Hartung, T. M. Grist, and C. J. François, "Magnetic resonance angiography: current status and future directions," *Journal of Cardiovascular Magnetic Resonance*, vol. 13, no. 1, p. 19, 2011. [Online]. Available: http://dx.doi.org/10.1186/1532-429X-13-19
21. A. G. Clifton, "MR angiography," *British Medical Bulletin*, vol. 56, no. 2, pp. 367–377, 2000.
22. B. Battal, M. Kocaoglu, N. Bulakbasi, G. Husmen, H. T. Sanal, and C. Tayfun, "Cerebrospinal fluid flow imaging by using phase-contrast MR technique," *The British Journal of Radiology*, 2014.
23. H. Ha, G. B. Kim, J. Kweon, S. J. Lee, Y.-H. Kim, D. H. Lee, D. H. Yang, and N. Kim, "Hemodynamic measurement using four-dimensional phase-contrast MRI: Quantification of hemodynamic parameters and clinical applications," *Korean Journal of Radiology*, vol. 17, no. 4, pp. 445–462, 2016.
24. A. El-Baz, G. Gimel'farb, V. Kumar, R. Falk, and M. A. El-Ghar, "3D joint Markov-Gibbs model for segmenting the blood vessels from MRS," in *2009 IEEE International Symposium on Biomedical Imaging: From Nano to Macro*, June 2009, pp. 1366–1369.
25. M. P. Hartung, T. M. Grist, and C. J. François, "Magnetic resonance angiography: current status and future directions," *Journal of Cardiovascular Magnetic Resonance*, vol. 13, no. 1, p. 19, 2011.

26. P. D. Schellinger, G. Richter, M. Köhrmann, and A. Dörfler, "Noninvasive angiography (magnetic resonance and computed tomography) in the diagnosis of ischemic cerebrovascular disease," *Cerebrovascular Diseases*, vol. 24, no. Suppl. 1, pp. 16–23, 2007.
27. O. Wink, W. J. Niessen, and M. A. Viergever, "Fast delineation and visualization of vessels in 3-d angiographic images," *IEEE Transactions on Medical Imaging*, vol. 19, no. 4, pp. 337–346, 2000.
28. K. Krissian, G. Malandain, N. Ayache, R. Vaillant, and Y. Trousset, "Model-based detection of tubular structures in 3d images," *Computer Vision and Image Understanding*, vol. 80, no. 2, pp. 130–171, 2000.
29. S. R. Aylward and E. Bullitt, "Initialization, noise, singularities, and scale in height ridge traversal for tubular object centerline extraction," *IEEE Transactions on Medical Imaging*, vol. 21, no. 2, pp. 61–75, 2002.
30. J. S. Suri, K. Liu, L. Reden, and S. Laxminarayan, "A review on MR vascular image processing: skeleton versus nonskeleton approaches: part II." *IEEE Transactions on Information Technology in Biomedicine: A Publication of the IEEE Engineering in Medicine and Biology Society*, vol. 6, no. 4, pp. 338–350, 2002.
31. T. McInerney and D. Terzopoulos, *Medical Image Segmentation Using Topologically Adaptable Surfaces*. Berlin, Heidelberg: Springer Berlin Heidelberg, 1997, pp. 23–32. [Online]. Available: http://dx.doi.org/10.1007/BFb0029221
32. L. M. Lorigo, O. D. Faugeras, W. E. L. Grimson, R. Keriven, R. Kikinis, A. Nabavi, and C.-F. Westin, "Curves: curve evolution for vessel segmentation," *Medical Image Analysis*, vol. 5, pp. 195–206, 2001.
33. M. Descoteaux, L. Collins, and K. Siddiqi, "Geometric flows for segmenting vasculature in MRI: Theory and validation," in *International Conference on Medical Image Computing and Computer-Assisted Intervention*. Springer, 2004, pp. 500–507.
34. D. Nain, A. Yezzi, and G. Turk, "Vessel segmentation using a shape driven flow," *Medical Image Computing and Computer-Assisted Intervention–MICCAI 2004*, pp. 51–59, 2004.
35. A. El-Baz, A. Farag, G. Gimelfarb, and S. Hushek, "Automatic cerebrovascular segmentation by accurate probabilistic modeling of TOF-MRA images," *Medical Image Computing and Computer-Assisted Intervention–MICCAI 2005*, pp. 34–42, 2005.
36. X. Gao, Y. Uchiyama, X. Zhou, T. Hara, T. Asano, and H. Fujita, "A fast and fully automatic method for cerebrovascular segmentation on time-of-flight (tof) MRA image," *Journal of Digital Imaging*, vol. 24, no. 4, pp. 609–625, 2011.
37. D. L. Wilson and J. A. Noble, "An adaptive segmentation algorithm for time-of-flight MRA data," *IEEE Transactions on Medical Imaging*, vol. 18, no. 10, pp. 938–945, Oct 1999.
38. A. El-Baz, A. Farag, G. Gimelfarb, M. El-Ghar, and T. Eldiasty, "A new adaptive probabilistic model of blood vessels for segmenting MRA images," *Medical Image Computing and Computer-Assisted Intervention–MICCAI 2006*, pp. 799–806, 2006.
39. M. S. Hassouna, A. Farag, S. Hushek, and T. Moriarty, "Cerebrovascular segmentation from {TOF} using stochastic models," *Medical Image Analysis*, vol. 10, no. 1, pp. 2–18, 2006. [Online]. Available: http://www.sciencedirect.com/science/article/pii/S1361841505000186.
40. I. Despotović, B. Goossens, and W. Philips, "MRI segmentation of the human brain: challenges, methods, and applications," *Computational and Mathematical Methods in Medicine*, vol. 2015, 2015.
41. A. P. Dempster, N. M. Laird, and D. B. Rubin, "Maximum likelihood from incomplete data via the EM algorithm," *Journal of the Royal Statistical Society. Series B (methodological)*, pp. 1–38, 1977.
42. A. A. Farag, A. S. El-Baz, and G. Gimel'farb, "Precise segmentation of multimodal images," *IEEE Transactions on Image Processing*, vol. 15, no. 4, pp. 952–968, 2006.
43. G. Gimelfarb, *Image Textures and Gibbs Random Fields*.
44. A. El-Baz, G. Gimel'farb, V. Kumar, R. Falk, and M. A. El-Ghar, "3D joint Markov-Gibbs model for segmenting the blood vessels from MRA," in *Proceedings of IEEE International Symposium on Biomedical Imaging: From Nano to Macro (ISBI'09)*, 2009, pp. 1366–1369.
45. A. A. Farag, A. El-Baz, and G. Gimel'farb, "Density estimation using modified expectation-maximization algorithm for a linear combination of Gaussians," in *2004 International Conference on Image Processing (ICIP'04)*, vol. 3, IEEE, 2004, pp. 1871–1874.

6 Left Atrial Scarring Segmentation from Delayed-Enhancement Cardiac MRI Images: A Deep Learning Approach

Guang Yang[1], Xiahai Zhuang[2], Habib Khan[3], Eva Nyktari[3], Shouvik Haldar[3], Lei Li[4], Rick Wage[3], Xujiong Ye[5], Greg Slabaugh[6], Raad Mohiaddin[1], Tom Wong[1], Jennifer Keegan[1], David Firmin[1]

[1]Royal Brompton Hospital and Imperial College London
[2]Fudan University
[3]Royal Brompton Hospital
[4]Shanghai Jiao Tong University
[5]University of Lincoln
[6]City University London

CONTENTS

6.1 INTRODUCTION

6.1.1 Background

Atrial fibrillation (AF) is the most common arrhythmia of clinical significance, and it affects approximately 1–2% of the population, a figure that is rising fast with ageing [1], [2]. AF occurs when chaotic and disorganized electrical activity develops in the atria, causing muscle cells to contract irregularly and rapidly. Moreover, it is associated with structural remodelling, including fibrotic changes in the left atrial substrate [3]. AF can cause increased morbidity, especially stroke and heart failure, and result in poor mental health, dementia, and increased mortality [2], [4], [5].

Pharmacological treatment of AF aims to restore and maintain sinus rhythm [6]. However, AF recurrence, side effects of antiarrhythmic drugs, and risks of proarrhythmia may offset the benefits of pharmacological treatment [7]. Consequently, there have been increasing efforts to develop non-pharmacological methods to treat AF patients such as percutaneous catheter ablation (CA) and surgical ablation (SA). Since the importance of pulmonary vein (PV) triggers in the initiation of AF was found [8], CA, which electrically isolates the PVs, has developed into an important interventional therapy [9]. However, despite efforts to improve targeting and delivery of CA, the success rate for a single procedure is just 30–50% at 5 years follow-up [10], [11]. Thoracoscopic SA has shown higher long-term success rates for a single procedure [12]–[14], but this comes with a procedural major adverse event rate of 23% [15].

The high failure rate of ablation in AF patients can be attributed to: (1) inadequate understanding of the arrhythmia mechanisms and arrhythmogenic substrates; (2) difficulty in identifying the potential non-responders of ablation; (3) inability to establish the ideal ablation strategy for each patient; (4) inadequate information of lesion integrity and longevity; and (5) limitations in the information about the location and extent of the ablation-induced scarring during and/or after the procedure [16], [17]. These have motivated researchers to develop better fibrosis imaging and assessment techniques to provide accurate guidance of the pre- and post-ablation procedures and improve their performance.

The current clinical gold standard for assessment of atrial scarring is electro-anatomical mapping (EAM), performed during an electrophysiological (EP) study [17]. The electrical activity of the left atrium (LA) is recorded using a mapping catheter prior to CA, with regions of scarring being associated with low voltage (<0.5mV). The main limitations of this technique are its invasiveness, the use of ionizing radiation, and the suboptimal accuracy, with reported errors of up to 10 mm in the localization of scar tissue [18], [19].

Late gadolinium enhancement (LGE) magnetic resonance imaging (MRI) is an established noninvasive technique for detecting myocardial scar tissue [20]. With this technique, healthy and scar tissues are differentiated by their altered wash-in and wash-out contrast agent kinetics, which result in scar tissue being seen as a region of enhanced or high signal intensity while healthy tissue is nulled. While 2D breath-hold LGE MRI is well-established for ventricular imaging, there is a growing interest in imaging the thinner walled atria for identification of native and ablation scarring in AF patients [21]–[24]. This requires higher spatial resolution and contiguous coverage, and data are best acquired as a 3D volume during free-breathing with diaphragmatic respiratory-gating. Atrial 3D LGE imaging has been used to: (1) assess patient suitability for AF ablation by identifying potential non-responders [22], [25]–[30], and (2) define the most appropriate ablation approach [26], [27], [31]. In addition, visualization and quantification of native and post-ablation atrial scarring derived from LGE MRI has been used to guide initial and follow-up ablation procedures [27],

[28], [32]–[35]. Histopathological studies have validated LGE MRI for quantification of native AF fibrosis [30], [36] and for characterization of AF ablation-induced wall injury [37].

Visualization and quantification of atrial scarring requires objective, robust, and accurate segmentation of the enhanced scar regions from the LGE MRI images. Essentially, there are two segmentations required: one showing the cardiac anatomy (geometry), particularly the LA wall and PVs, the other delineating the enhanced scar regions. The former segmentation is required to rule out confounding enhanced tissues from other parts of the heart (e.g., the mitral valve and aorta), or the enhancement from non-heart structures, while the latter is a prerequisite for insightful visualization and meaningful quantification. Segmentation of the atrial scarring from LGE MRI images is a very challenging problem. Firstly, the LA wall is very thin, and scarring is hard to distinguish even by experienced expert cardiologists specialized in cardiac MRI. Secondly, residual respiratory motion, heart rate variability, low signal-to-noise ratio (SNR), and contrast agent wash-out during the long acquisition (current scanning time $\approx$ 10mins) frequently result in image quality being poor. In addition, artifactual enhanced signal from surrounding tissues may result in a large number of false positives.

6.1.2 Related Work

Oakes et al. [22] quantified the enhanced atrial scarring by analyzing the intensity histogram of the manually segmented LA wall. Perry et al. [38] applied k-means clustering to quantitatively assess normal and scarred tissue from manual LA wall segmentation. A grand challenge was carried out for evaluation and benchmarking of various atrial scarring segmentation methods, including histogram analysis, simple and advanced thresholding, k-means clustering, and graph-cuts [39]. Although these pioneering studies have shown promising results on the segmentation and quantification of atrial scarring using LGE MRI images, most have relied on manual segmentation of the LA wall and PVs. This has several drawbacks: (1) it is a time-consuming task; (2) there are intra- and inter-observer variations; (3) it is less reproducible for a multi-center and multi-scanner study. Moreover, some previous studies have assumed a fixed thickness of the LA wall, while there is no evidence that this is the case, and re-orientation and interpolation of the MR images can result in partial volume effects and increase the variance of the wall thickness. Inaccurate manual segmentation of the LA wall and PVs can further complicate the delineation of the atrial scarring, and its quantification can be error-prone. This could be one of the major reasons that there are ongoing concerns regarding the correlation between atrial scarring identified by LGE MRI (enhanced regions) and the gold standard EAM (low voltage regions) [30], [40].

The LA and PVs would ideally be segmented from the cardiac and respiratory-gated LGE MRI dataset. However, this is difficult as normal tissue is nulled and only scar tissue is seen with high signal. Other options are to segment them from a separately acquired breath-hold magnetic resonance angiogram (MRA) study [29], [41], [42] or from a respiratory and cardiac gated 3D Roadmap acquisition, that is, using a balanced steady state free precession (b-SSFP) sequence [43]. While MRA shows the LA and PVs with high contrast, these acquisitions are generally un-gated and acquired in an inspiratory breath-hold. The anatomy extracted from MRA therefore can be highly deformed compared to that in the LGE MRI study. Although the 3D Roadmap acquisition takes longer to acquire, it is in the same respiratory phase as the LGE MRI, and the extracted anatomy can be better matched. Ravanelli et al. [29] proposed to manually segment the LA wall and PVs using MRA images in 3D, for which both efficiency and accuracy have been claimed. The segmented LA and PVs were then mapped to LGE MRI and this was followed by a thresholding-based segmentation of the atrial scarring [29]. Recently, Tao et al. [42] combined atlas-based segmentation of LGE MRI and MRA to define the cardiac anatomy. After image fusion of the LGE MRI and MRA, accurate LA chamber and PVs segmentation has been achieved by a level set based local refinement, based on which an objective atrial scarring assessment is envisaged in future development [42]. Instead of using MRA, Karim et al. [43] used b-SSFP whole-heart acquisition to define the cardiac anatomy.

TABLE 6.1
Previous Studies on Atrial Scarring.

Methods	Subjects No.	LA Wall Segmentation	Scarring Segmentation	Evaluation Methods for Scarring Segmentation
Oakes et al., 2009 [22]	81	Manual	2-4 SD	Scar Percentage
Knowles et al., 2010 [41]	7	Semi-Auto	Maximum Intensity Projection	Scar Percentage
Perry et al., 2012 [44]	34	Manual	k-means Clustering	Dice Score
Ravanelli et al., 2014 [29]	10	Manual	4 SD	Dice Score
Karim et al., 2014 [43]	15	Semi-Auto	Graph-Cuts	Dice Score, ROC, Scar Percentage
Tao et al., 2016 [42]	46	Automatic Atlas	Maximum Intensity Projection	Qualitative Visualization
Veni et al., 2017 [45]	72	Automatic ShapeCut	Threshold/k-Means Clustering	Scar Percentage
Ours	20	Automatic Atlas	Super-Pixel and Deep Learning	Multiple Quantitative Metrics

The cardiac anatomy was resolved using a statistical shape model, and the atrial scarring was then segmented using a graph-cut model assuming that the LA wall is ±3mm from the endocardial border obtained from the LA geometry extraction [43]. Table 6.1 provides a summary of previously published methods on atrial scarring segmentation using LGE MRI.

6.1.3 Our Contributions

In this chapter, we present a novel fully automatic segmentation and objective assessment of atrial scarring for longstanding persistent AF patients scanned by LGE MRI. The LA chamber and PVs are defined using a multi-atlas based whole heart segmentation (MA-WHS) method on Roadmap MRI images, which are acquired using a respiratory and cardiac gated 3D b-SSFP sequence. LA and PVs geometry is resolved by mapping the segmented Roadmap anatomy to LGE MRI using the DICOM header data, and is further refined by affine and nonrigid registration steps. The LGE MRI images are over-segmented by a novel Simple Linear Iterative Clustering (SLIC) based super-pixels method [46]. Then a fully automatic supervised deep learning classification method is applied to segment the atrial scarring within the segmented LA and PVs geometry. In this study, two validation steps have been performed: one for the LA chamber and PVs segmentation; and one for the atrial scarring segmentation—both against established ground truths from manual segmentations by experienced expert-cardiologists specialized in cardiac MRI. This chapter is based on our previous work on atrial scarring segmentation [47]–[49].

The rest of this manuscript is organized as follows. Section 2 details the materials and main methods of this study. Section 3 demonstrates our experimental results, which are followed by discussions and a conclusion (Sections 4 and 5).

6.2 METHOD

6.2.1 Study Population

Cardiac MRI was performed in longstanding persistent AF patients between 2011–2013 in agreement with the local regional ethics committee. A Likert-type scale was applied to score the image quality of each LGE MRI scan, e.g., 0 (non-diagnostic), 1 (poor), 2 (fair), 3 (good), and 4 (very good) depending on the level of SNR, appropriate inversion time, and the existence of navigator beam and ghost artefacts.

Ten pre-ablation scans with image quality ≥2 have been retrospectively entered into this study (~60% of all the scanned pre-ablation cases). To make a balanced dataset, we randomly selected 10 post-ablation cases from all the 26 post-ablation scans with image quality ≥2 (~92% of all the scanned post-ablation cases).

6.2.2 MRI Protocol

Cardiac MR data were acquired on a Siemens Magnetom Avanto 1.5T scanner (Siemens Medical Systems, Erlangen, Germany).

Transverse navigator-gated 3D LGE MRI [21], [22], [50] was performed using an inversion prepared segmented gradient echo sequence (TE/TR 2.2ms/5.2ms) 15 minutes after gadolinium (Gd) administration (Gadovist—gadobutrol, 0.1mmol/kg body weight, Bayer-Schering, Berlin, Germany) when a transient steady-state of Gd wash-in and wash-out of normal myocardium had been reached [51]. Detailed scanning parameters are: 30–34 slices at 1.5×1.5×4mm^3, reconstructed to 60–68 slices at 0.75×0.75×2mm^3, field-of-view 380×380mm^2, acceleration factor of 2 using generalized auto-calibrating partially parallel acquisition (GRAPPA), acquisition window 125ms positioned within the subject-specific rest period, single R-wave gating, chemical shift fat suppression, flip angle 20°. Data were acquired during free-breathing using a crossed-pairs navigator positioned over the dome of the right hemi-diaphragm with navigator acceptance window size of 5mm and CLAWS respiratory motion control [52]. The nominal acquisition duration was 204–232 cardiac cycles assuming 100% respiratory efficiency.

Coronal navigator-gated 3D b-SSFP (TE/TR 1ms/2.3ms) Roadmap data were acquired with the following parameters: 80 slices at 1.6×1.6×3.2mm^3, reconstructed to 160 slices at 0.8×0.8×1.6mm^3, field-of-view 380×380mm^2, acceleration factor of 2 using GRAPPA, partial Fourier 6/8, acquisition window 125ms positioned within the subject-specific rest period, single R-wave gating, chemical shift fat suppression, flip angle 70°. Data were acquired during free-breathing using a crossed-pairs navigator positioned over the dome of the right hemi-diaphragm with navigator acceptance window size of 5mm and CLAWS respiratory motion control [52]. The nominal acquisition duration was 241 cardiac cycles assuming 100% respiratory efficiency. More details of the acquisition parameters can be found in Table 6.2.

6.2.3 Multi-Atlas Whole Heart Segmentation (MA-WHS)

A multi-atlas approach [53], [54] was developed to derive the whole heart segmentation of the Roadmap acquisition and then mapped to LGE MRI [55], [56]. This segmentation consists of two major steps: (1) atlas propagation based on image registration algorithms and (2) label fusion from multi-atlas propagated segmentation results.

First we obtained 30 MRI Roadmap studies from the Left Atrium Segmentation Grand Challenge organized by King's College London [57] together with manual segmentations of the left atrium,

TABLE 6.2

MRI Sequence Details for the 3D Roadmap and 3D LGE MRI Acquisitions.

Sequence	ST (mm)	FOV (cm)	NEX	AM	RM	TR/TE/FA
3D Roadmap	1.6	38 × 38	1	256 × 256	512 × 512	2.3ms/1ms/70°
3D LGE MRI	2	38 × 38	1	256 × 256	512 × 512	5.2ms/2.2ms/20°

ST = reconstructed slice thickness; FOV = field of view; NEX = number of excitations; AM = acquisition matrix; RM = reconstruction matrix; TR/TE/FA = repetition time/echo time/flip angle.

pulmonary veins, and appendages. In these, we further labelled the right and left ventricles, the right atrium, the aorta, and the pulmonary artery, to generate 30 whole heart atlases. These 30 MRI Roadmap studies were employed only for building an independent multi-atlas dataset, which will then be used for segmenting our Roadmap studies that linked with the LGE MRI scans for the AF patients.

Let I be the target image to be segmented, $\{(\mathfrak{I}_a, \mathfrak{L}_a) \,|\, a = 1, \ldots N\}$ be the set of atlases, where $N = 30$, $\mathfrak{I}_a$ and $\mathfrak{L}_a$ are respectively the intensity image and corresponding segmentation label image of the a-th atlas. For each atlas, MA-WHS performs an atlas-to-target registration, by maximizing the similarity between the images, to derive the set of warped atlases,

$$T_a = \arg\max_{T_a} \text{ ImageSimilarity}(I, \mathfrak{I}_a), \text{ and } \begin{cases} A_a = T_a(\mathfrak{I}_a) \\ L_a = T_a(\mathfrak{L}_a) \end{cases}, \tag{6.1}$$

in which T_a is the resulting transformation of the registration, and $\{(A_a, L_a) \,|\, a = 1, \ldots N\}$ are respectively the warped atlas intensity image and corresponding segmentation result. Here, we employ the hierarchical registration for segmentation propagation, which was specifically designed for the whole heart MRI images and consists of three steps, namely the global affine registration for localization of the whole heart, the local affine registration for the initialization of the substructures, and the fully deformable registration for local detail refinement [58]. Image similarity metrics evaluate how similar the atlas and target image are. In this work we propose to use the spatially encoded mutual information (SEMI) method, which has been shown to be robust against intensity non-uniformity and different intensity contrast [59], that is

$$\text{ImageSimilarity}(I, \mathfrak{I}_a) = \left\{S_1, \ldots, S_{n_s}\right\} \tag{6.2}$$

where $\left\{S_1, \ldots, S_{n_s}\right\}$ are the SEMI and computed based on the spatially encoded joint histogram,

$$H_s(I, \mathfrak{I}_a) = \sum_{x \in \Omega} w_1(I(x)) w_2(\mathfrak{I}_a(x)) W_s(x). \tag{6.3}$$

Here, $w_1(I(x))$ and $w_2(\mathfrak{I}_a(x))$ are Parzen window estimation and $W_s(x)$ is a weighting function to encode the spatial information [59].

After the multi-atlas propagation, a label fusion algorithm is required to generate one final segmentation of the LA from the 30 propagated results,

$$L_I = \text{LabelFusion}\left(\{(A_1, L_1) \ldots (A_N, L_N)\}\right). \tag{6.4}$$

The label fusion decides how to combine the multiple classification results into one labelling result. Since the atlases can produce segmentations with dramatically different accuracy at different locations, it should evaluate the performance of each atlas locally and assign different weights for the atlases at each pixel of the target image in decision fusion.

The recent literatures have many new methods [60]–[67] on improving multi-atlas segmentation using sophisticatedly designed algorithms, which generally need to evaluate local similarity between patches from the atlases and the target image for local weighted label fusion,

$$L_I(x) = \text{argmax}_{l \in \{l_{bk}, l_{la}\}} \sum_a w_a\left(S(I, A_a, x)\right) \delta(L_a(x), l), \tag{6.5}$$

in which l_{bk} and l_{la} indicate the labels of the background and left atrium, respectively, and the local weight $w_a(\cdot) \propto S(\cdot)$ is determined by the local similarity $S(\cdot)$ between the target image and the atlas. $\delta(a,b)$ is the Kronecker delta function which returns 1 when $a = b$ and returns 0 otherwise.

For the LA segmentation, we propose to use the multi-scale patch based label fusion (MSP-LF). This is because the intensity distribution of the blood pool in the LA is almost identical to that of the blood pool in the other chambers and great vessels. The multi-scale space theory can handle different level information within a small patch and has been applied to feature extraction/detection and image matching [54], [67]–[73]. The patches we compute from different scale spaces can represent the different levels of structural information, with low scale capturing local fine structure and high scale suppressing fine structure but providing global structural information of the image. This is different from the conventional patch-based methods, which only compute the local structural information within the patch. To avoid increasing the computational complexity, we adopt the multi-resolution implementation and couple it with the MSP where the high-scale patch can be efficiently computed using a low-resolution image space. The local similarity between two images using the MSP measure is computed, as follows,

$$S_{\text{msp}}\left(I, A_a, x\right) = \sum_s S\left(I^{(s)}, A_a^{(s)}, x\right) \tag{6.6}$$

where $I^{(s)} = I * \text{Gaussian}(0, \sigma_s)$ is the target image from s scale-space, which is computed from the convolution of the target image with Gaussian kernel function with scale s. Here, we compute the local similarity in multi-scale image using the conditional probability of the images,

$$S\left(I^{(s)}, A_a^{(s)}, x\right) = p\left(i_x \middle| j_x\right) = \frac{p\left(i_x, j_x\right)}{p\left(j_x\right)} \tag{6.7}$$

where $i_x = I^{(s)}(x)$ and $j_x = A_a^{(s)}(x)$ and the conditional image probability is obtained from the joint and marginal image probability, which can be calculated using the Parzen window estimation [74].

For each patient, the Roadmap dataset was then registered to the LGE MRI dataset using the DICOM header data, and then refined by affine and nonrigid registration steps [59]. The resulting transformation was applied to the MA-WHS derived cardiac anatomy to define the endocardial LA boundary and PV on the LGE MRI dataset for each patient.

6.2.4 Image Over-Segmentation Using SLIC Super-Pixels

We used a Simple Linear Iterative Clustering (SLIC) based super-pixel method [46] to over-segment LGE MRI images in order to separate potential enhanced atrial scarring regions from other tissues. The SLIC method has been used successfully in many medical image analysis problems [75]–[77]. The SLIC super-pixel method, which is an unsupervised learning [78] based method, groups pixels into perceptually meaningful patches with similar size, which can be used to replace the regular pixel grid. Consequently, the derived super-pixel patches can capture and mitigate image redundancy, and therefore provide a significant primitive from which image features can be calculated effectively and efficiently.

In summary, super-pixel methods have been proven to have the following benefits: (1) super-pixels can adhere well to perceptually meaningful object boundaries in images; (2) super-pixels can reduce computational complexity of extracting image features; (3) for segmentation applications, super-pixels can improve performance while reducing the computation time [79]. In this study, we proposed to use a SLIC based super-pixel method, which has been successfully applied to solve various medical image analysis problems (e.g., [75], [80]). It has also demonstrated better segmentation accuracy and superior adherence to object boundaries, and it is faster and more memory efficient

compared to other state-of-the-art super-pixels methods [46]. Based on local k-means clustering, the SLIC method iteratively groups pixels into super-pixels. The clustering proximity is estimated in both intensity and spatial domains that is

$$D = \sqrt{d_c^2 + \left(\frac{d_s}{S}\right)^2 m^2}, \tag{6.8}$$

in which $d_c = \sqrt{(I_j - I_i)^2}$ measures the pixel intensity difference of a gray scale image and $d_s = \sqrt{(x_j - x_i)^2 + (y_j - y_i)^2}$ describes the spatial distance between each pixel and the geometric center of the super-pixel. SLIC is initialized by sampling the target slice of the LGE MRI image into a regular grid space with grid interval of S pixels. To speed up the iteration, SLIC limits the size of search region of similar pixels to $2S \times 2S$ around the super-pixel center (namely, local k-means clustering). In addition, parameter m balances the weighting between intensity similarity d_c and spatial proximity d_s. In this study we initialized S to 4 pixels that is 2.8×2.8mm^2 considering the LA wall thickness is approximately 3mm [23], [81], and also take into account that the super-pixel size is still large enough to extract statistics of the grouped pixel intensities. In addition, m was chosen by visual inspection of the over-segmented results, and it was fixed when the super-pixel results adhered well with the LA wall boundary.

6.2.5 Atrial Scarring Segmentation Based on Super-Pixels Classification

The LA regions, including LA wall, blood pool and atrial scarring, have been over-segmented into super-pixel patches. Next the atrial scarring segmentation will be based on classification of these super-pixel patches. This can be categorized as a supervised learning based segmentation method (Figure 6.1). First, we need to construct a training dataset with ground truth labelling, that is, each super-pixel patch will be labelled as scar or non-scar. Second, we can train our classifier based on the paired super-pixel patches and their labels. Finally, the trained model will be used to predict the atrial scarring in new input LGE MRI images.

6.2.5.1 Training Data Construction and Ground Truth Definition

In order to train the following classifier, we built a training dataset containing enhanced and non-enhanced super-pixel patches. This has been done by (1) experienced expert-cardiologists specialized in cardiac MRI performing manual mouse clicks to select the enhanced scar regions; (2) combining the mouse clicks and SLIC segmentation to label the enhanced super-pixels; (3) applying morphological dilation (3mm) to the segmented endocardial LA boundary and PV from MA-WHS to extract the LA wall and PV; (4) finding the overlapped regions of the LA wall and PV and

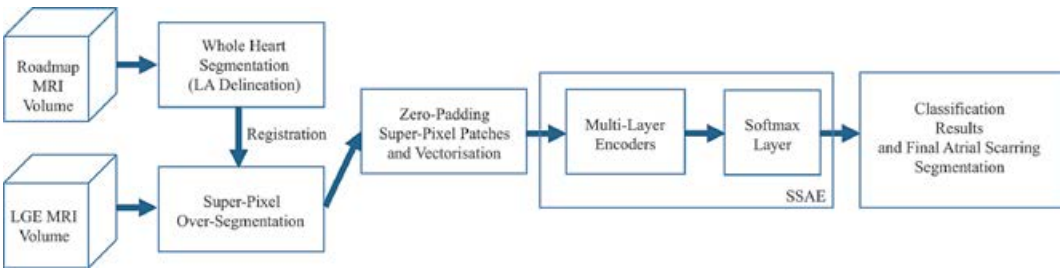

FIGURE 6.1 Whole pipeline of the atrial scarring segmentation workflow.

the labelled enhanced super-pixels; and (5) labelling the other super-pixels overlapped with LA wall and PV as non-enhancement. Details of each step are given as following:

1. Manual mouse clicks: Instead of manually drawing the boundaries of the enhanced atrial scarring regions, we asked experienced cardiologists specialized in cardiac MRI to perform manual mouse clicks on the LGE MRI images to label the regions that they believed to be enhanced (i.e., atrial scarring tissue). This is because manual boundary drawing of enhancement on the thin LA wall is a very challenging task and subject to large inter- and intra-observer variances. Mouse clicks on the enhancement regions are much easier and much more efficient. The manual mouse clicks were done on the original LGE MRI images without the super-pixel grid overlaid. This is because: (a) the mouse clicks will not be biased by super-pixel patches and (b) the super-pixel grid may reduce the visibility of the enhancement on LGE MRI images.
2. The coordinates of the mouse clicks were used to select the enhanced super-pixels. Because our cardiologists performed the mouse clicks on the original LGE MRI images without having prior knowledge about the super-pixels, we asked them to have relatively dense mouse clicks. These mouse clicks will ensure all the enhanced regions can be included, but only one mouse click will be taken into account if multiple clicks dwell in the same super-pixel.
3. The endocardial LA boundary and PV were extracted using our MA-WHS method. We then applied a morphological dilation to extract the LA wall and PV assuming that the thickness of LA wall is 3mm. The blood pool regions were extracted by a morphological erosion (5mm) from the endocardial LA boundary. And the pixel intensities were normalized according to the mean and standard deviation of the blood pool intensities [39].
4. We masked the selected enhanced super-pixels [derived from step (2)] using the LA wall and PV segmentation. Only the super-pixels having a defined overlap with the LA wall and PV segmentation were selected as enhancement for building the training data (overlapping ratio was set to $\geq 20\%$). Other super-pixels (overlapping ratio $< 20\%$) were discarded as they were considered as enhancement from other substructures of the heart (such as the mitral valve and aorta) but not enhancement of the LA wall and PV. Although we assumed that the LA wall thickness is 3mm, our enhanced super-pixels are not restricted to this wall thickness.
5. The other super-pixels overlapped with the LA wall and PV but not selected as enhancement were considered as non-enhancement (overlapping ratio was set to $\geq 20\%$).

By performing these five steps, we constructed a training dataset that contains super-pixel patches labelled either enhancement or non-enhancement within the LA wall and PV.

In order to form the ground truth of the enhanced atrial scarring on the LGE MRI images, we performed the following two further steps:

6. Once we extracted the enhanced super-pixels, they were combined to create a binary image for each slice (i.e., 1 for enhanced super-pixels and 0 for unenhanced).
7. The binary image was overlaid on the original LGE MRI images, and our cardiologists performed manual corrections to create the final boundaries (ground truth) of the enhanced atrial scarring. In so doing, we minimized the bias toward a better performance of the segmentation using classified super-pixels.

6.2.5.2 Deep Learning Using Stacked Sparse Auto-Encoders

The segmentation of the atrial scarring is performed using the classification of the over-segmented super-pixels. Conventional classification tasks are normally solved using particular machine

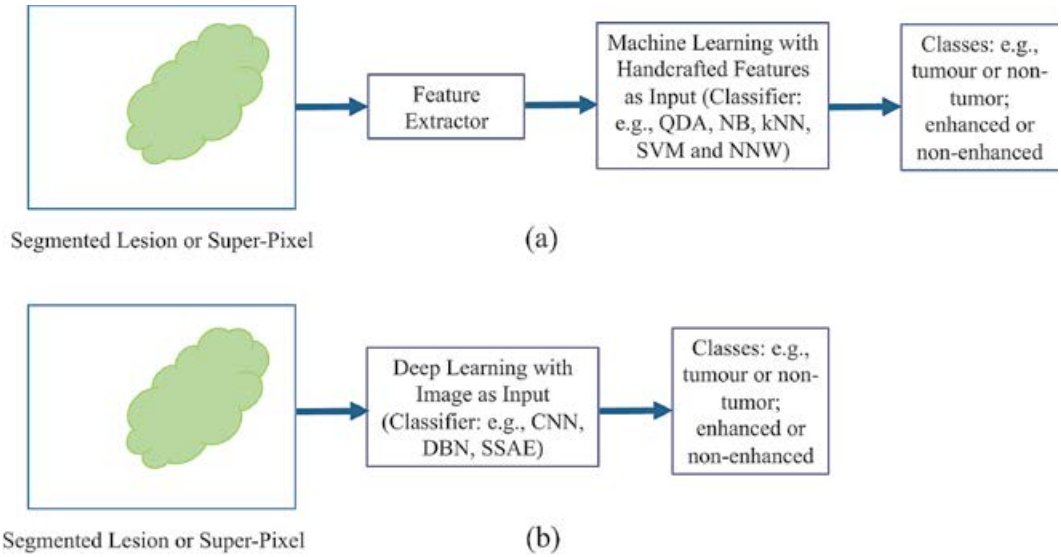

FIGURE 6.2 Machine learning and deep learning for classification. (a) Conventional machine learning for a general classification task (i.e., machine learning with feature input or feature-based machine learning) in the field of medical image analysis. Handcrafted features (e.g., contrast, circularity, and effective diameter) are extracted from a segmented lesion or super-pixels in an image. (b) Deep learning based classification: deep learning with image input. Thus, one of the major and essential differences between machine learning and deep learning is the direct training of pixels in images.

learning algorithms. In this use, a machine learning algorithm is often called a classifier. Widely used classification methods include quadratic discriminant analysis (QDA) [82], Naïve Bayes (NB) [83], k-Nearest Neighbor algorithm (kNN) [84], Support Vector Machines (SVM) [85] [86], and shallow Neural Networks (NNW) [87] [88]. A crucial step in the design of such a classification framework is the extraction of discriminant features from the images (or over-segmented super-pixel patches in our case). This process is normally done by human researchers or a particular automated filtering pre-processing that is denoted as handcrafted features (Figure 6.2a). However, meaningful or task-related handcrafted features are designed mostly by human experts on the basis of their domain knowledge, making it hard for non-experts to exploit machine learning techniques for their own studies. Moreover, filtering based feature engineering methods may be biased to the particular pre-defined basis function that is only sensitive to specific features of the images.

Recently, deep learning based methods (e.g., Convolutional Neural Networks [CNN] and Deep Belief Network [DBN]) are rapidly becoming the state of the art, leading to superior performance in different medical image reconstruction, segmentation, and analysis applications [89]–[91]. Compared to conventional machine learning based classification methods, deep learning has overcome the obstacles of handcrafted features by incorporating the feature engineering step into a learning step. That is, instead of extracting features manually or using pre-defined filtering, deep learning requires only a set of data with minimal preprocessing and discovers the informative representations in a self-taught manner [92] (Figure 6.2b). In so doing, the burden of feature engineering has shifted from humans (subjective) to computers (objective), allowing non-experts in machine learning to effectively use deep learning for their own applications, especially in medical image analysis [92].

In this study, after we obtained the over-segmented super-pixels, the Stacked Sparse Auto-Encoders (SSAE) [93] were used to perform the classification. The SSAE were initially pre-trained

in an unsupervised manner without using the labels of the super-pixels. An auto-encoder neural network tries to learn an approximation to the identity function to replicate its input at its output using a back-propagation algorithm, that is $\hat{\mathrm{X}} = h_{\mathrm{W,b}}(\mathrm{X}) \approx \mathrm{X}$, in which $\mathrm{X} = \{x_1, x_2, \ldots, x_m\}$, $\mathrm{X} \in \Re^{n \times m}$ is a matrix storing all the input training vectors $x_i \in \Re^n$. Each input vector x_i was formed by: (1) zero-padding all the super-pixels into a 20×20 matrix, which is the smallest bounding box for the largest super-pixel dimensions, and (2) vectorizing the 20×20 matrix into a 400×1 vector. The cost function of this pre-training can be written as

$$\arg\min_{\mathrm{W}^l} J_a\left(\mathrm{W}^l\right) = \frac{1}{2m}\sum_{i=1}^{m}\left\|\hat{x}_i - x_i\right\|_2^2 + \frac{\lambda}{2}\left\|\mathrm{W}^l\right\|_2^2 + \beta\sum_{j=1}^{k}\mathrm{KL}\left(\rho\left\|\hat{\rho}_j\right.\right), \tag{6.9}$$

where m is the number of input training vectors, k is the number of hidden nodes, λ is the coefficient for the L_2 regularization term, β is the weight of sparsity penalty, KL is the Kullback-Leibler divergence function $\mathrm{KL}(\rho\left\|\hat{\rho}_j\right.) = \rho\log\frac{\rho}{\hat{\rho}_j} + (1-\rho)\log\frac{1-\rho}{1-\hat{\rho}_j}$, ρ is sparsity parameter that specifies the desired level of sparsity, $\hat{\rho}_j$ is probability of firing activity that is $\hat{\rho}_j = \frac{1}{m}\sum_{i=1}^{m} h_j(x_i)$. The unsupervised pre-training is performed one layer at a time by minimizing the error in reconstructing its input and learning an encoder and a decoder, which yields an optimal set of weights W and biases b stored in W^l. If the number of hidden nodes k is less than the number of visible input nodes n, then the network is forced to learn a compressed and sparse representation of the input [93].

Second, a Softmax layer was added as the activity classification model $h_\theta(x_i)$ to accomplish the super-pixels classification task [93]. In addition, it can be jointly trained with the SSAE during fine-tuning of the parameters with labeled instances in a *supervised fashion*. The weight matrix θ is obtained by solving the convex optimization problem as follows.

$$\arg\min_{\theta} J_s(\theta) = -\frac{1}{m}\sum_{i=1}^{m}\sum_{c=1}^{C}\mathbf{1}\{y_i = c\}\times\log P\left(y_i = c\left|x_i;\theta\right.\right) + \frac{\lambda}{2}\|\theta\|_2^2, \tag{6.10}$$

where $c \in \{1, C = 2\}$ is the class label, $\tilde{\mathrm{X}} = \{(x_1, y_1), (x_2, y_2), \ldots, (x_m, y_m),\}$ represents a set of labeled training instances, and the last term for the L_2 regularization.

Finally, fine-tuning was applied to boost the classification performance, and it treats all layers of the SSAE and the Softmax layer as a single model and improves all the weights of all layers in the network by using the backpropagation technique [93].

6.2.5.3 Hyper-Parameters Settings

Figure 6.3 shows the detailed network architecture of the implemented SSAE. Hyper-parameters were not optimized explicitly but were determined via trial and error. Here are the final defined

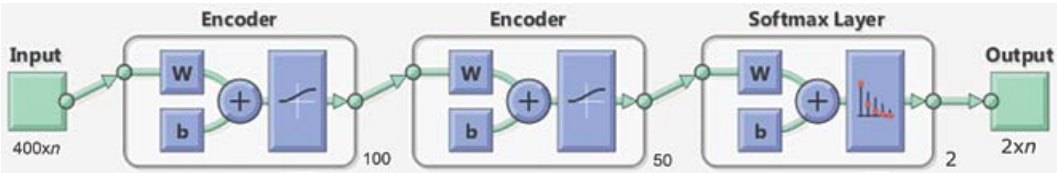

FIGURE 6.3 Detailed network architecture of the implemented SSAE.

hyper-parameters (values) used in this study: maximum epochs of the SSAE (200), maximum epochs of the Softmax and fine-tuning (500), hidden layers size of the SSAE (100 and 50), sparsity parameter ρ (0.1), sparsity penalty β (5), L_2 regularization term λ for the SSAE and the Softmax (0.0001).

6.2.6 Validation Approaches

6.2.6.1 Validation for the Whole Heart Segmentation

One experienced cardiologist (>5 years' experience and specialized in cardiac MRI) manually segmented the endocardial LA boundary and labelled the PV slice-by-slice in the LGE MRI images for all the patients. A second senior cardiologist (>25 years' experience and specialized in cardiac MRI) confirmed the manual segmentation. The evaluation and validation of our MA-WHS has been done against this manual segmentation, which is assumed to be the ground truth. We used three metrics: Dice Score [94], [95], Hausdorff Distance (HD) [96] and Average Surface Distance (ASD). Dice Score, which is defined as $\text{Dice Score} = \frac{2\times|F_{Manual}\cap F_{Auto}|}{|F_{Manual}|+|F_{Auto}|}$ (F_{Manual}: ground truth segmentation; F_{Auto}: automatic segmentation; $|\bullet|$: the number of pixels assigned to the segmentation), measures the overlap between two segmentations. The higher the values of Dice Score, the better the overall performance of the segmentation will be. HD and ASD measure the boundary distance (in mm) between two contours of segmentation, which are defined as

$$\begin{aligned} &HD(P_{Manual},P_{Auto}) = \max\left(d(P_{Manual},P_{Auto}),d(P_{Auto},P_{Manual})\right)\\ &\text{where}\quad d(P_{Manual},P_{Auto}) = \sup_{p_m\in P_{Manual}}\inf_{p_a\in P_{Auto}}\|p_m-p_a\|\\ &d(P_{Auto},P_{Manual}) = \sup_{p_a\in P_{Auto}}\inf_{p_m\in P_{Manual}}\|p_m-p_a\|, \end{aligned} \tag{6.11}$$

$$ASD = \frac{1}{2}\left(\frac{\sum_{p_m\in P_{Manual}}\min_{p_a\in P_{Auto}}\|p_m-p_a\|}{\sum_{p_m\in P_{Manual}}1}+\frac{\sum_{p_a\in P_{Auto}}\min_{p_m\in P_{Manual}}\|p_m-p_a\|}{\sum_{p_a\in P_{Auto}}1}\right), \tag{6.12}$$

in which $P_{Manual}=\{p_{m1},\ldots,p_{mn}\}$ and $P_{Auto}=\{p_{a1},\ldots,p_{an}\}$ are two finite point sets of the two segmented contours (using the ground truth segmentation and automatic segmentation), $\|\bullet\|$ denotes L_2 norm, sup denotes supremum and inf denotes infimum. The lower the values of HD and ASD, the better agreement between manual delineation and fully automatic segmentation.

6.2.6.2 Validation for the Atrial Scarring Validation

We evaluated our SSAE based classification by: (i) leave-one-patient-out cross-validation (LOO CV) [78], [97], which provides an unbiased predictor and is capable of creating sufficient training data for studies with small sample size [98] and (ii) the cross-validated classification accuracy, sensitivity, specificity [76], [77], [99], and average area under the receiver operating characteristic (ROC) curve (AUC) [88], [100]. For evaluation of the atrial scarring segmentation, we used the Dice score.

TABLE 6.3
Quantitative Results of the Whole Heart Segmentation and Atrial Scarring Segmentation.

Tasks	Acc.	Sens.	Spec.	AUC	Dice	HD (mm)	ASD (mm)
MM-WHS	-	-	-	-	0.90±0.12	9.53±6.01	1.47±0.89
Atrial Scarring Segmentation	0.91	0.95	0.75	0.95	0.82±0.05	-	-

6.3 RESULTS

6.3.1 Whole Heart Segmentation

The quantitative evaluations show that the MA-WHS based method achieved 0.90±0.12 Dice score, 9.53±6.01mm HD, and 1.47±0.89mm ASD (Table 6.3).

6.3.2 Atrial Scarring Segmentation

For the SSAE based super-pixels classification, we obtained LOO CV accuracy of 0.91, sensitivity of 0.95, specificity of 0.75, AUC of 0.95, and the Dice score for the final atrial scarring segmentation was found to be 0.82±0.05 (Table 6.3).

In addition, for the atrial scarring segmentation, we compared our fully automatic framework with existing semi-automatic methods with manually delineated anatomical structure of the LA and PVs. The four methods we compared in this study were described in the benchmarking work [39], namely simple thresholding (Thr), conventional standard deviation (4 SDs were tested, i.e., SD4), k-means clustering (KM), and fuzzy c-means clustering with graph-cuts (FCM+GC). Figure 6.4 shows that our fully automatic framework obtained more accurate and more consistent results across 20 AF patient cases (Figure 6.4, red dots represent outliers).

Figure 6.5 demonstrates that qualitatively our fully automatic atrial scarring segmentation is in accordance with the manual segmented results. However, if there are enhancements from the nearby mitral valve or blood pool regions, our method may misclassify them as enhanced atrial fibrosis that is the major contribution for the false positives.

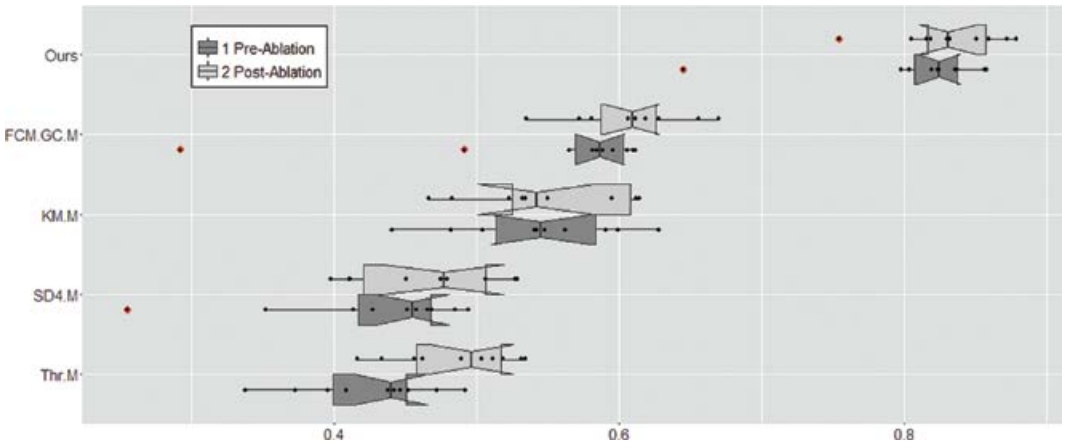

FIGURE 6.4 Boxplot for the comparison results of the Dice scores obtained by our fully automatic framework and other four methods (Thr, SD4, KM, and FCM+GC) with manual delineated LA wall and PVs (+M).

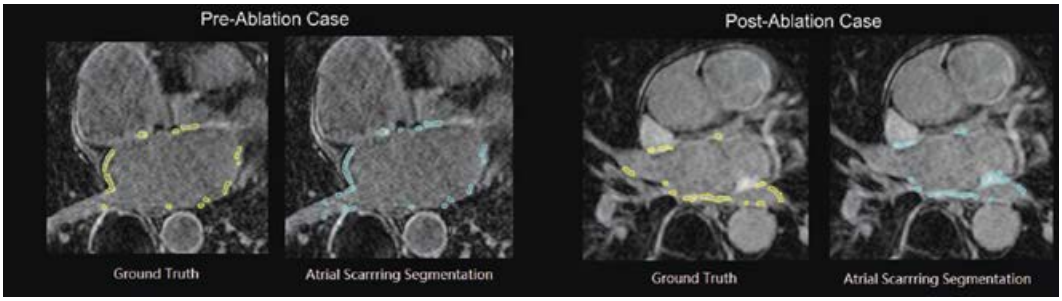

FIGURE 6.5 Final atrial scarring segmentation results (cyan regions) for an example pre-ablation (left) and an example post-ablation (right) case compared to the ground truth (yellow regions).

6.4 DISCUSSION

In this study, we developed a novel fully automatic segmentation pipeline to detect enhanced atrial scarring in LGE MRI images. The achievements of this work are:

a. MA-WHS of Roadmap MRI for cardiac anatomy segmentation: a MA-WHS segmentation method has been proposed with a new MSP-LF scheme to define the LA and PV geometry while minimizing the mis-segmentation from confounding tissues of other substructures of the heart;
b. Super-pixel classification based method for atrial scar segmentation from LGE MRI: the super-pixel classification has two uses. Firstly, it has been used as a by-product tool, which can help cardiologists to easily construct a manual ground truth segmentation by indicating enhanced scarring regions with a number of mouse clicks. This is subject to limited manual corrections and is more efficient and reliable than direct manual drawing around enhanced region borders, especially when the boundaries are highly irregular and ill-defined. Secondly, based on the trained classifier, the super-pixel classification allows a fully automatic atrial scarring segmentation to be achieved by running super-pixel based over-segmentation and classification for the new input LGE MRI data;
c. SSAE based deep learning classifier: the SSAE based classifier has been proposed and implemented that achieved high classification accuracy without any handcrafted features needed;
d. Validation: our developed fully automatic pipeline was tested and validated directly on real clinical datasets.

Compared to manual ground truth construction that took 25mins to 50mins per patient case, the SSAE based prediction only took 5.8±0.9secs to segment one patient case, while for a single loop of the LOO CV, the training on 20 patients took about 20 hours. All the experiments were performed using a Windows 7 workstation with 6-cores 1.9GHz Intel® Xeon® E5-2609v3/64 GB RAM and NVIDIA GeForce® GTX Titan X with an in-house Matlab implementation. With the proven efficiency and efficacy, the application of our method to real clinical problems is straightforward. Overall, results of this study offer compelling evidence that our fully automatic pipeline is capable of detecting enhanced atrial scarring from LGE MRI images acquired from a longstanding persistent AF cohort.

Segmentation of the atrial scarring from LGE MRI images is very challenging. This is not only because the atrial scarring is difficult to distinguish in the thin LA wall but also because the image quality can be poor due to motion artefacts, noise contamination, and contrast agent wash-out during the long acquisition. Moreover, the enhancement from the surrounding tissues (i.e., other substructures of the heart or non-heart tissues) and enhanced blood flow are confounding issues for atrial scarring segmentation and result in increased false positives. For example, the aortic wall is generally enhanced and when close to the LA, can be mistaken for atrial scarring and contribute a

false positive result. Moreover, false positives can be increased from the misclassification of other enhanced regions, for example, other non-heart tissues and other substructures of the heart or fat tissues surrounding the LA. However, most of these confounding enhancement regions can be distinguished subject to accurate heart anatomy delineation using our MA-WHS. Another source of artefact originates from the respiratory navigator and results in enhanced signal from blood flow in the right pulmonary veins. Recent advances in sequence design have reduced navigator artefacts considerably [52], [101]. Due to the subjective understanding of the LGE MRI images, our cardiologists may also miss labelling some enhanced regions.

In this study, we showed good accuracy for segmenting the LA and proximal PVs. The segmentation accuracy in the more distal veins was less good, but this is not an issue for clinical ablation for AF patients as the ablation points or clamps are never placed far away from the LA chamber. In addition, the segmentation of the PVs at the more distal regions might just introduce more artefacts from the enhanced navigator beam regions without improving the accuracy of the actual atrial scarring segmentation. There are some previous studies that endeavoured to segment the detailed sub-branches of PVs and especially at the more distal regions (e.g., [42] using MRA). However, this can only improve the accuracy of LA+PV delineation against manual delineated ground truth, but may not be a benefit for the final atrial scarring segmentation. For the post-ablation cases, the enhancement at or near the PVs can indicate the efficacy of the treatment, for example, identify the gaps in the ablation line. Therefore, based on our experiments and observations, a robust segmentation method to delineate PV anatomy variations is still in demand, and it is a more important task than accurate delineation of the detailed sub-branches of the PVs.

In our study, 2D SLIC was applied instead of using its 3D version. This is because: (1) our 3D LGE MRI data are anisotropic with fine in-plane resolution and relatively coarse resolution in the third dimension (i.e., $0.75\times0.75\times2\text{mm}^3$); therefore, 2D SLIC can provide better adherence to the more detailed anatomical edges shown in the 2D in-plane slice, which has a higher spatial resolution; (2) the clinical image viewing is still a slice-by-slice procedure in 2D, and the 2D SLIC results are more intuitive for manual super-pixel labelling by our expert-cardiologists, which is a necessary step for atrial scarring ground truth construction; (3) the 2D SLIC processing is efficient (8.6±2.6 seconds per 2D slice and ~5mins per patient case) although a slice-by-slice computing was performed. In addition, for our application, we did not perform further optimization for the two parameters of the SLIC algorithm (i.e., the size of the super-pixels S and the compactness m). In our study, the size of the super-pixels was restricted by the LA wall thickness and S was initialized to 4 pixels. The compactness term m controls the regularity of the super-pixel shapes (i.e., the resulting super-pixels can adhere more tightly to object boundaries in the image when m is small), but these super-pixels have less regular shape. We chose $m=4$ based on visual inspections of the over-segmentation results.

As is well known, LGE studies are specifically designed to highlight fibrosis and scarring, and to null all signal from normal tissue. Although it is possible to see the cardiac anatomy in LGE images, the SNR is limited and accurate and automatic segmentation of the LA and PV walls would be very difficult. To the best of our knowledge, all previous studies have relied on manual drawing on LGE images or have used MRA images or b-SSFP based Roadmap scans for the delineation of the LA and PV anatomy. In this current study, we use the 3D Roadmap images to resolve the LA and PV anatomy. For each AF patient in our study, the Roadmap data took ~6.5mins to acquire (241 cardiac cycles at 800ms per cardiac cycle with a typical respiratory efficiency of 50%). In subsequent work, we have reduced the spatial resolution of the 3D Roadmap to $1.8\times1.8\times1.8\text{mm}^3$, which reduces the acquisition duration to ~4mins while preserving good results. In addition, although the requirement for a Roadmap acquisition might be a limitation, in practice, many patients have these as part of their standard clinical cardiac MRI examination.

The comparison work reported in this study is limited. While we validated our techniques against manual segmentation, we also wished to compare our results with other previously published techniques. A number of advanced techniques have been proposed, such as unsupervised learning based clustering and graph-cuts based methods [39]. However, implementation of these is difficult as the

fine-tuned hyper-parameters used are not always clearly described and the methodologies cannot be reproduced exactly. Moreover, our patient cohort is different from that in which these algorithms were optimized and tested. In this study, we have therefore only compared our technique against the simple thresholding and conventional standard deviation based methods, as these have fully standard implementations. When compared to manual segmentation (ground truth) in post-ablation scans, these standard techniques gave median DICE of 38–48%, while our fully automatic technique achieved a median DICE of 82%. The results that we obtained here with the standard techniques are similar to those reported with these same techniques in the benchmarking study described in [39], while the latter score is similar to the best-performing methods reported in that same study.

In general, the segmentation algorithms performed better on post-ablation LGE MRI scans compared to the performance on pre-ablation ones. This is likely due to better image quality post-ablation (when the heart has reverted to sinus rhythm) and to higher levels of fibrosis. For the LA+PV segmentation, many of the algorithms previously published rely on manual segmentation. In our study, we have compared the efficacy of the atrial scarring segmentation algorithms using automatically segmented LA+PV geometry against the same algorithms with manually delineated geometry showing very similar results, thus confirming that our fully automatic MA-WHS method is capable of accurately defining the relevant cardiac anatomy.

In addition, compared to a method of using multi-atlas segmentation for the four chambers [42], our MA-WHS method obtained superior DICE (90% vs. 86% reported by [42]) and ASD (1.5 mm vs. 1.8 mm reported by [42]). Even compared with their results obtained after refinement by MRA [42], our MA-WHS still has comparable results. For the segmentation of the atrial scarring, in our study, the results of the standard segmentation techniques in pre-ablation cases were better than those reported by the benchmarking study [39]. This is likely to be due to our patients all having longstanding persistent AF and therefore having higher levels of pre-ablation scarring. For the post-ablation cases, we have obtained comparable median DICE compared to the best performing algorithm [39]. Of note is that in the benchmarking study the variances of all of the techniques tested are large, while in our manuscript, the results are more consistent with a relatively small variance. This may be due to our patient cohort being more tightly defined, whereas in the previous study, datasets were analyzed from patients at multiple institutions using a variety of imaging protocols. It may also be that our automatic technique is based on supervised learning while previous methods are unsupervised, and the derived model parameters may not be optimized for all the patient cases.

In our study, although techniques like SLIC and super-pixel based classification may be very well known and widely used methods [61], [80], [102]–[105], they are reliable algorithms that, when uniquely combined in the proposed pipeline, enable fully automatic segmentation and assessment of atrial scarring. This is an important advance, as LGE MRI is becoming a preferred method for noninvasive imaging of atrial scarring.

One possible limitation of our study is that the SSAE based classifier has many hyper-parameters, which need to be carefully tuned (e.g., maximum epochs of the SSAE, maximum epochs of the Softmax and fine-tuning, hidden layers size of the SSAE, sparsity parameter ρ, sparsity penalty β, L2 regularization term λ for the SSAE and the Softmax). Currently these hyper-parameters were tuned via trial and error, which may limit the final classification accuracy.

6.5 CONCLUSION

To the best of our knowledge, this is the first study that developed a deep learning based fully automatic segmentation pipeline for atrial scarring segmentation with quantitative validation on LGE MRI scans. The proposed pipeline has demonstrated an effective and efficient way to objectively segment and assess the atrial scarring. The evaluation has been done on 20 LGE MRI scans in longstanding persistent AF patients that contain both pre-ablation and post-ablation cases. The validation results have shown that both our MA-WHS and super-pixel classification based atrial

scarring segmentation have obtained satisfactory accuracy. Based on the results, we can envisage a straightforward deployment of our framework for clinical usage.

Acknowledgments

The studies described in this chapter were funded by the British Heart Foundation Project Grant (Project Number: PG/16/78/32402), the NIHR Cardiovascular Biomedical Research Unit, Royal Brompton Hospital & Harefield NHS Foundation Trust and Imperial College London, and the Chinese NSFC research fund (81301283) and the NSFC-RS fund (81511130090). Data were obtained during the NIHR Efficacy and Mechanism Evaluation Programme (Project Number: 12/127/127).

References

1. Y. Miyasaka, "Secular trends in incidence of atrial fibrillation in Olmsted County, Minnesota, 1980 to 2000, and implications on the projections for future prevalence," *Circulation*, vol. 114, no. 2, pp. 119–125, Jul. 2006.
2. S. S. Chugh, R. Havmoeller, K. Narayanan, D. Singh, M. Rienstra, E. J. Benjamin, R. F. Gillum, Y.-H. Kim, J. H. McAnulty, Z.-J. Zheng, M. H. Forouzanfar, M. Naghavi, G. A. Mensah, M. Ezzati, and C. J. L. Murray, "Worldwide epidemiology of atrial fibrillation: A global burden of disease 2010 study," *Circulation*, vol. 129, no. 8, pp. 837–847, 2014.
3. M. Allessie, "Electrical, contractile and structural remodeling during atrial fibrillation," *Cardiovasc. Res.*, vol. 54, no. 2, pp. 230–246, 2002.
4. S. Stewart, C. L. Hart, D. J. Hole, and J. J. V. McMurray, "A population-based study of the long-term risks associated with atrial fibrillation: 20-year follow-up of the Renfrew/Paisley study," *Am. J. Med.*, vol. 113, no. 5, pp. 359–364, 2002.
5. C. T. January, L. S. Wann, J. S. Alpert, H. Calkins, J. E. Cigarroa, J. C. Cleveland, J. B. Conti, P. T. Ellinor, M. D. Ezekowitz, M. E. Field, K. T. Murray, R. L. Sacco, W. G. Stevenson, P. J. Tchou, C. M. Tracy, and C. W. Yancy, "2014 AHA/ACC/HRS Guideline for the Management of Patients with Atrial Fibrillation: Executive Summary," *J. Am. Coll. Cardiol.*, vol. 64, no. 21, pp. 2246–2280, Dec. 2014.
6. S. H. Hohnloser, K.-H. Kuck, and J. Lilienthal, "Rhythm or rate control in atrial fibrillation—Pharmacological Intervention in Atrial Fibrillation (PIAF): a randomised trial," *Lancet*, vol. 356, no. 9244, pp. 1789–1794, Nov. 2000.
7. I. C. Van Gelder, V. E. Hagens, H. A. Bosker, J. H. Kingma, O. Kamp, T. Kingma, S. A. Said, J. I. Darmanata, A. J. M. Timmermans, J. G. P. Tijssen, and H. J. G. M. Crijns, "A comparison of rate control and rhythm control in patients with recurrent persistent atrial fibrillation," *N. Engl. J. Med.*, vol. 347, no. 23, pp. 1834–1840, Dec. 2002.
8. M. Haïssaguerre, P. Jaïs, D. C. Shah, A. Takahashi, M. Hocini, G. Quiniou, S. Garrigue, A. Le Mouroux, P. Le Métayer, and J. Clémenty, "Spontaneous initiation of atrial fibrillation by ectopic beats originating in the pulmonary veins," *N. Engl. J. Med.*, vol. 339, no. 10, pp. 659–666, Sep. 1998.
9. D. J. Wilber, C. Pappone, P. Neuzil, A. De Paola, F. Marchlinski, A. Natale, L. Macle, E. G. Daoud, H. Calkins, B. Hall, V. Reddy, G. Augello, M. R. Reynolds, C. Vinekar, C. Y. Liu, S. M. Berry, D. A. Berry, and ThermoCool AF Trial Investigators, "Comparison of antiarrhythmic drug therapy and radiofrequency catheter ablation in patients with paroxysmal atrial fibrillation: a randomized controlled trial," *JAMA*, vol. 303, no. 4, pp. 333–340, Jan. 2010.
10. F. Ouyang, R. Tilz, J. Chun, B. Schmidt, E. Wissner, T. Zerm, K. Neven, B. Köktürk, M. Konstantinidou, A. Metzner, A. Fuernkranz, and K. H. Kuck, "Long-term results of catheter ablation in paroxysmal atrial fibrillation: lessons from a 5-year follow-up," *Circulation*, vol. 122, no. 23, pp. 2368–2377, 2010.
11. R. Weerasooriya, P. Khairy, J. Litalien, L. MacLe, M. Hocini, F. Sacher, N. Lellouche, S. Knecht, M. Wright, I. Nault, S. Miyazaki, C. Scavee, J. Clementy, M. Haissaguerre, and P. Jais, "Catheter ablation for atrial fibrillation: are results maintained at 5 years of follow-up?" *J. Am. Coll. Cardiol.*, vol. 57, no. 2, pp. 160–166, 2011.
12. J. R. Edgerton, J. H. McClelland, D. Duke, M. W. Gerdisch, B. M. Steinberg, S. H. Bronleewe, S. L. Prince, M. A. Herbert, S. Hoffman, and M. J. Mack, "Minimally invasive surgical ablation of atrial fibrillation: six-month results," *J. Thorac. Cardiovasc. Surg.*, vol. 138, no. 1, pp. 109–113; discussion 114, Jul. 2009.
13. J. R. Edgerton, W. M. Jackman, C. Mahoney, and M. J. Mack, "Totally thoracoscopic surgical ablation of persistent AF and long-standing persistent atrial fibrillation using the 'Dallas' lesion set," *Heart Rhythm*, vol. 6, no. 12 Suppl, pp. S64–S70, Dec. 2009.

14. S. P. J. Krul, A. H. G. Driessen, W. J. van Boven, A. C. Linnenbank, G. S. C. Geuzebroek, W. M. Jackman, A. A. M. Wilde, J. M. T. de Bakker, and J. R. de Groot, "Thoracoscopic video-assisted pulmonary vein antrum isolation, ganglionated plexus ablation, and periprocedural confirmation of ablation lesions: first results of a hybrid surgical-electrophysiological approach for atrial fibrillation," *Circ. Arrhythm. Electrophysiol.*, vol. 4, no. 3, pp. 262–70, Jun. 2011.
15. L. V. A. Boersma, M. Castella, W. van Boven, A. Berruezo, A. Yilmaz, M. Nadal, E. Sandoval, N. Calvo, J. Brugada, J. Kelder, M. Wijffels, and L. Mont, "Atrial fibrillation catheter ablation versus surgical ablation treatment (FAST): a 2-center randomized clinical trial," *Circulation*, vol. 125, no. 1, pp. 23–30, Jan. 2012.
16. T. J. Badger, R. S. Oakes, M. Daccarett, N. S. Burgon, N. Akoum, E. N. Fish, J. J. E. Blauer, S. N. Rao, Y. Adjei-Poku, E. G. Kholmovski, S. Vijayakumar, E. V. R. Di Bella, R. S. MacLeod, and N. F. Marrouche, "Temporal left atrial lesion formation after ablation of atrial fibrillation," *Hear. Rhythm*, vol. 6, no. 2, pp. 161–168, 2009.
17. H. Calkins, K. H. Kuck, R. Cappato, J. Brugada, A. J. Camm, S.-A. Chen, H. J. G. Crijns, R. J. Damiano, D. W. Davies, J. DiMarco, J. Edgerton, K. Ellenbogen, M. D. Ezekowitz, D. E. Haines, M. Haissaguerre, G. Hindricks, Y. Iesaka, W. Jackman, J. Jalife, P. Jais, J. Kalman, D. Keane, Y.-H. Kim, P. Kirchhof, G. Klein, H. Kottkamp, K. Kumagai, B. D. Lindsay, M. Mansour, F. E. Marchlinski, P. M. McCarthy, J. L. Mont, F. Morady, K. Nademanee, H. Nakagawa, A. Natale, S. Nattel, D. L. Packer, C. Pappone, E. Prystowsky, A. Raviele, V. Reddy, J. N. Ruskin, R. J. Shemin, H.-M. Tsao, D. Wilber, and Heart Rhythm Society Task Force on Catheter and Surgical Ablation of Atrial Fibrillation, "2012 HRS/EHRA/ECAS expert consensus statement on catheter and surgical ablation of atrial fibrillation: recommendations for patient selection, procedural techniques, patient management and follow-up, definitions, endpoints, and research trial design," *Heart Rhythm*, vol. 9, no. 4, pp. 632–696.e21, Apr. 2012.
18. H. Zhong, J. M. Lacomis, and D. Schwartzman, "On the accuracy of CartoMerge for guiding posterior left atrial ablation in man," *Heart Rhythm*, vol. 4, no. 5, pp. 595–602, May 2007.
19. E. J. Schmidt, R. P. Mallozzi, A. Thiagalingam, G. Holmvang, A. D'Avila, R. Guhde, R. Darrow, G. S. Slavin, M. M. Fung, J. Dando, L. Foley, C. L. Dumoulin, and V. Y. Reddy, "Electroanatomic mapping and radiofrequency ablation of porcine left atria and atrioventricular nodes using magnetic resonance catheter tracking," *Circ. Arrhythm. Electrophysiol.*, vol. 2, no. 6, pp. 695–704, Dec. 2009.
20. P. Kellman and A. E. Arai, "Cardiac imaging techniques for physicians: late enhancement," *J. Magn. Reson. Imaging*, vol. 36, no. 3, pp. 529–542, Sep. 2012.
21. D. C. Peters, J. V Wylie, T. H. Hauser, K. V. Kissinger, R. M. Botnar, V. Essebag, M. E. Josephson, and W. J. Manning, "Detection of pulmonary vein and left atrial scar after catheter ablation with three-dimensional navigator-gated delayed enhancement MR imaging: initial experience," *Radiology*, vol. 243, no. 3, pp. 690–695, 2007.
22. R. S. Oakes, T. J. Badger, E. G. Kholmovski, N. Akoum, N. S. Burgon, E. N. Fish, J. J. E. Blauer, S. N. Rao, E. V. R. Dibella, N. M. Segerson, M. Daccarett, J. Windfelder, C. J. McGann, D. Parker, R. S. MacLeod, and N. F. Marrouche, "Detection and quantification of left atrial structural remodeling with delayed-enhancement magnetic resonance imaging in patients with atrial fibrillation," *Circulation*, vol. 119, no. 13, pp. 1758–1767, 2009.
23. M. Akçakaya, H. Rayatzadeh, T. Basha, S. N. Hong, R. H. Chan, K. V Kissinger, T. H. Hauser, M. E. Josephson, and W. J. Manning, "Accelerated late gadolinium enhancement cardiac MR imaging with isotropic spatial resolution using compressed sensing: initial experience," *Radiology*, vol. 264, no. 3, pp. 691–699, 2012.
24. G. R. Vergara, S. Vijayakumar, E. G. Kholmovski, J. J. E. Blauer, M. a. Guttman, C. Gloschat, G. Payne, K. Vij, N. W. Akoum, M. Daccarett, C. J. McGann, R. S. MacLeod, and N. F. Marrouche, "Real-time magnetic resonance imaging-guided radiofrequency atrial ablation and visualization of lesion formation at 3 Tesla," *Hear. Rhythm*, vol. 8, no. 2, pp. 295–303, 2011.
25. N. F. Marrouche, D. Wilber, G. Hindricks, P. Jais, N. Akoum, F. Marchlinski, E. Kholmovski, N. Burgon, N. Hu, L. Mont, T. Deneke, M. Duytschaever, T. Neumann, M. Mansour, C. Mahnkopf, B. Herweg, E. Daoud, E. Wissner, P. Bansmann, and J. Brachmann, "Association of atrial tissue fibrosis identified by delayed enhancement MRI and atrial fibrillation catheter ablation: the DECAAF study," *JAMA*, vol. 311, no. 5, pp. 498–506, 2014.
26. N. Akoum, M. Daccarett, C. McGann, N. Segerson, G. Vergara, S. Kuppahally, T. Badger, N. Burgon, T. Haslam, E. Kholmovski, R. MacLeod, and N. Marrouche, "Atrial fibrosis helps select the appropriate patient and strategy in catheter ablation of atrial fibrillation: a DE-MRI guided approach," *J. Cardiovasc. Electrophysiol.*, vol. 22, no. 1, pp. 16–22, 2011.

27. G. R. Vergara and N. F. Marrouche, "Tailored management of atrial fibrillation using a LGE-MRI based model: from the clinic to the electrophysiology laboratory," *J. Cardiovasc. Electrophysiol.*, vol. 22, no. 4, pp. 481–487, 2011.
28. L. C. Malcolme-Lawes, C. Juli, R. Karim, W. Bai, R. Quest, P. B. Lim, S. Jamil-Copley, P. Kojodjojo, B. Ariff, D. W. Davies, D. Rueckert, D. P. Francis, R. Hunter, D. Jones, R. Boubertakh, S. E. Petersen, R. Schilling, P. Kanagaratnam, and N. S. Peters, "Automated analysis of atrial late gadolinium enhancement imaging that correlates with endocardial voltage and clinical outcomes: a 2-center study," *Hear. Rhythm*, vol. 10, no. 8, pp. 1184–1189, 2013.
29. D. Ravanelli, E. C. Dal Piaz, M. Centonze, G. Casagranda, M. Marini, M. Del Greco, R. Karim, K. Rhode, and A. Valentini, "A novel skeleton based quantification and 3-D volumetric visualization of left atrium fibrosis using late gadolinium enhancement magnetic resonance imaging," *IEEE Trans. Med. Imaging*, vol. 33, no. 2, pp. 566–576, 2014.
30. C. McGann, N. Akoum, A. Patel, E. Kholmovski, P. Revelo, K. Damal, B. Wilson, J. Cates, A. Harrison, R. Ranjan, N. S. Burgon, T. Greene, D. Kim, E. V. R. DiBella, D. Parker, R. S. MacLeod, and N. F. Marrouche, "Atrial fibrillation ablation outcome is predicted by left atrial remodeling on MRI," *Circ. Arrhythmia Electrophysiol.*, vol. 7, no. 1, pp. 23–30, 2014.
31. A. S. Jadidi, H. Cochet, A. J. Shah, S. J. Kim, E. Duncan, S. Miyazaki, M. Sermesant, H. Lehrmann, M. Lederlin, N. Linton, A. Forclaz, I. Nault, L. Rivard, M. Wright, X. Liu, D. Scherr, S. B. Wilton, L. Roten, P. Pascale, N. Derval, F. Sacher, S. Knecht, C. Keyl, M. Hocini, M. Montaudon, F. Laurent, M. Haïssaguerre, and P. Jaïs, "Inverse relationship between fractionated electrograms and atrial fibrosis in persistent atrial fibrillation: combined magnetic resonance imaging and high-density mapping," *J. Am. Coll. Cardiol.*, vol. 62, no. 9, pp. 802–812, 2013.
32. V. Y. Reddy, E. J. Schmidt, G. Holmvang, and M. Fung, "Arrhythmia recurrence after atrial fibrillation ablation: can magnetic resonance imaging identify gaps in atrial ablation lines?" *J. Cardiovasc. Electrophysiol.*, vol. 19, no. 4, pp. 434–437, 2008.
33. T. J. Badger, M. Daccarett, N. W. Akoum, Y. a. Adjei-Poku, N. S. Burgon, T. S. Haslam, S. Kalvaitis, S. Kuppahally, G. Vergara, L. McMullen, P. A. Anderson, E. Kholmovski, R. S. MacLeod, and N. F. Marrouche, "Evaluation of left atrial lesions after initial and repeat atrial fibrillation ablation; Lessons learned from delayed-enhancement MRI in repeat ablation procedures," *Circ. Arrhythmia Electrophysiol.*, vol. 3, no. 3, pp. 249–259, 2010.
34. S. Kapa, B. Desjardins, D. J. Callans, F. E. Marchlinski, and S. Dixit, "Contact electroanatomic mapping derived voltage criteria for characterizing left atrial scar in patients undergoing ablation for atrial fibrillation," *J. Cardiovasc. Electrophysiol.*, vol. 25, no. 10, pp. 1044–1052, Oct. 2014.
35. F. Bisbal, E. Guiu, P. Cabanas-Grandío, A. Berruezo, S. Prat-Gonzalez, B. Vidal, C. Garrido, D. Andreu, J. Fernandez-Armenta, J. M. Tolosana, E. Arbelo, T. M. De Caralt, R. J. Perea, J. Brugada, and L. Mont, "CMR-guided approach to localize and ablate gaps in repeat AF ablation procedure," *JACC Cardiovasc. Imaging*, vol. 7, no. 7, pp. 653–663, 2014.
36. K. Higuchi, M. Akkaya, N. Akoum, and N. F. Marrouche, "Cardiac MRI assessment of atrial fibrosis in atrial fibrillation: implications for diagnosis and therapy," *Heart*, vol. 100, no. 7, pp. 590–596, 2014.
37. J. L. Harrison, H. K. Jensen, S. A. Peel, A. Chiribiri, A. K. Grondal, L. O. Bloch, S. F. Pedersen, J. F. Bentzon, C. Kolbitsch, R. Karim, S. E. Williams, N. W. Linton, K. S. Rhode, J. Gill, M. Cooklin, C. A. Rinaldi, M. Wright, W. Y. Kim, T. Schaeffter, R. S. Razavi, and M. D. O'Neill, "Cardiac magnetic resonance and electroanatomical mapping of acute and chronic atrial ablation injury: a histological validation study," *Eur. Heart J.*, vol. 35, no. 22, pp. 1486–1495, 2014.
38. D. Perry, A. Morris, N. Burgon, C. McGann, R. MacLeod, and J. Cates, "Automatic classification of scar tissue in late gadolinium enhancement cardiac MRI for the assessment of left-atrial wall injury after radiofrequency ablation," in *In SPIE Medical Imaging*, 2012, p. 83151D.
39. R. Karim, R. J. Housden, M. Balasubramaniam, Z. Chen, D. Perry, A. Uddin, Y. Al-Beyatti, E. Palkhi, P. Acheampong, S. Obom, A. Hennemuth, Y. Lu, W. Bai, W. Shi, Y. Gao, H.-O. Peitgen, P. Radau, R. Razavi, A. Tannenbaum, D. Rueckert, J. Cates, T. Schaeffter, D. Peters, R. MacLeod, and K. Rhode, "Evaluation of current algorithms for segmentation of scar tissue from late gadolinium enhancement cardiovascular magnetic resonance of the left atrium: an open-access grand challenge," *J. Cardiovasc. Magn. Reson.*, vol. 15, pp. 105–122, 2013.
40. J. L. Harrison, C. Sohns, N. W. Linton, R. Karim, S. E. Williams, K. S. Rhode, J. Gill, M. Cooklin, C. A. Rinaldi, M. Wright, T. Schaeffter, R. S. Razavi, and M. D. O'Neill, "Repeat left atrial catheter ablation: cardiac magnetic resonance prediction of endocardial voltage and gaps in ablation lesion sets," *Circ. Arrhythmia Electrophysiol.*, vol. 8, no. 2, pp. 270–278, Apr. 2015.

41. B. R. Knowles, D. Caulfield, M. Cooklin, C. A. Rinaldi, J. Gill, J. Bostock, R. Razavi, T. Schaeffter, and K. S. Rhode, "3-D visualization of acute RF ablation lesions using MRI for the simultaneous determination of the patterns of necrosis and edema," *IEEE Trans. Biomed. Eng.*, vol. 57, no. 6, pp. 1467–1475, 2010.
42. Q. Tao, E. G. Ipek, R. Shahzad, F. F. Berendsen, S. Nazarian, and R. J. van der Geest, "Fully automatic segmentation of left atrium and pulmonary veins in late gadolinium-enhanced MRI: towards objective atrial scar assessment," *J. Magn. Reson. Imaging*, vol. 44, no. 2, pp. 346–354, Jan. 2016.
43. R. Karim, A. Arujuna, R. J. Housden, J. Gill, H. Cliffe, K. Matharu, C. A. Rinaldi, M. O'Neill, D. Rueckert, R. Razavi, T. Schaeffter, and K. Rhode, "A method to standardize quantification of left atrial scar from delayed-enhancement MR Images," *Transl. Eng. Heal. Med. IEEE J.*, vol. 2, pp. 1–15, 2014.
44. D. Perry, A. Morris, N. Burgon, C. McGann, R. MacLeod, and J. Cates, "Automatic classification of scar tissue in late gadolinium enhancement cardiac MRI for the assessment of left-atrial wall injury after radiofrequency ablation," 2012, p. 83151D.
45. G. Veni, S. Y. Elhabian, and R. T. Whitaker, "ShapeCut: Bayesian surface estimation using shape-driven graph.," *Med. Image Anal.*, vol. 40, pp. 11–29, Aug. 2017.
46. R. Achanta, A. Shaji, K. Smith, and A. Lucchi, "SLIC superpixels compared to state-of-the-art superpixel methods," *IEEE Trans. Pattern Anal. Mach. Intell.*, vol. 34, no. 11, pp. 2274–2281, 2012.
47. G. Yang, X. Zhuang, H. Khan, S. Haldar, E. Nyktari, X. Ye, G. Slabaugh, T. Wong, R. Mohiaddin, J. Keegan, and D. Firmin, "Segmenting atrial fibrosis from late gadolinium-enhanced cardiac MRI by deep-learned features with stacked sparse auto-encoders," in *Annual Conference on Medical Image Understanding and Analysis, Communications in Computer and Information Science*, 2017, pp. 195–206.
48. G. Yang, X. Zhuang, H. Khan, S. Haldar, E. Nyktari, L. Li, R. Wage, X. Ye, G. Slabaugh, R. Mohiaddin, T. Wong, J. Keegan, and D. Firmin, "Fully automatic segmentation and objective assessment of atrial scars for longstanding persistent atrial fibrillation patients using late gadolinium-enhanced MRI," *Med. Phys.*, vol. 45, no. 4, pp. 1562–1576, 2018.
49. G. Yang, X. Zhuang, H. Khan, S. Haldar, E. Nyktari, X. Ye, G. Slabaugh, T. Wong, R. Mohiaddin, J. Keegan, and D. Firmin, "A fully automatic deep learning method for atrial scarring segmentation from late gadolinium-enhanced MRI images," in *2017 IEEE 14th International Symposium on Biomedical Imaging (ISBI 2017)*, 2017, pp. 844–848.
50. D. C. Peters, J. V. Wylie, T. H. Hauser, R. Nezafat, Y. Han, J. J. Woo, J. Taclas, K. V. Kissinger, B. Goddu, M. E. Josephson, and W. J. Manning, "Recurrence of atrial fibrillation correlates with the extent of post-procedural late gadolinium enhancement. A pilot study," *JACC Cardiovasc. Imaging*, vol. 2, no. 3, pp. 308–316, 2009.
51. J. Keegan, P. Jhooti, S. V. Babu-Narayan, P. Drivas, S. Ernst, and D. N. Firmin, "Improved respiratory efficiency of 3D late gadolinium enhancement imaging using the continuously adaptive windowing strategy (CLAWS)," *Magn. Reson. Med.*, vol. 71, no. 3, pp. 1064–1074, 2014.
52. J. Keegan, P. Drivas, and D. N. Firmin, "Navigator artifact reduction in three-dimensional late gadolinium enhancement imaging of the atria," *Magn. Reson. Med.*, vol. 785, pp. 779–785, 2013.
53. X. Zhuang, W. Bai, J. Song, S. Zhan, X. Qian, W. Shi, Y. Lian, and D. Rueckert, "Multiatlas whole heart segmentation of CT data using conditional entropy for atlas ranking and selection," *Med. Phys.*, vol. 42, no. 7, pp. 3822–3833, 2015.
54. X. Zhuang and J. Shen, "Multi-scale patch and multi-modality atlases for whole heart segmentation of MRI," *Med. Image Anal.*, vol. 31, pp. 77–87, Jul. 2016.
55. G. Yang, X. Zhuang, H. Khan, S. Haldar, E. Nyktari, L. Li, X. Ye, G. Slabaugh, T. Wong, R. Mohiaddin, J. Keegan, and D. Firmin, "Multi-atlas propagation based left atrium segmentation coupled with super-voxel based pulmonary veins delineation in late gadolinium-enhanced cardiac MRI," in *SPIE Medical Imaging*, 2017, pp. 1013313–1.
56. G. Yang, X. Ye, G. Slabaugh, J. Keegan, R. Mohiaddin, and D. Firmin, "Differentiation of pre-ablation and post-ablation late gadolinium-enhanced cardiac MRI scans of longstanding persistent atrial fibrillation patients," in *SPIE Medical Imaging*, 2017, p. 1013400–1.
57. C. Tobon-Gomez, A. Geers, J. Peters, J. Weese, K. Pinto, R. Karim, T. Schaeffter, R. Razavi, and K. Rhode, "Benchmark for algorithms segmenting the left atrium from 3D CT and MRI datasets," *IEEE Trans. Med. Imaging*, vol. 34, no. 7, pp. 1460–1473, Feb. 2015.
58. X. Zhuang, K. S. Rhode, R. S. Razavi, D. J. Hawkes, and S. Ourselin, "A registration-based propagation framework for automatic whole heart segmentation of cardiac MRI," *IEEE Trans. Med. Imaging*, vol. 29, no. 9, pp. 1612–1625, 2010.
59. X. Zhuang, S. Arridge, D. J. Hawkes, and S. Ourselin, "A nonrigid registration framework using spatially encoded mutual information and free-form deformations," *IEEE Trans. Med. Imaging*, vol. 30, no. 10, pp. 1819–28, Oct. 2011.

60. X. Artaechevarria, A. Munoz-Barrutia, and C. Ortiz-de-Solorzano, "Combination strategies in multi-atlas image segmentation: application to brain MR data," *IEEE Trans. Med. Imaging*, vol. 28, no. 8, pp. 1266–1277, Aug. 2009.
61. W. Bai, W. Shi, C. Ledig, and D. Rueckert, "Multi-atlas segmentation with augmented features for cardiac MR images," *Med. Image Anal.*, vol. 19, no. 1, pp. 98–109, 2015.
62. P. Coupé, J. V. Manjón, V. Fonov, J. Pruessner, M. Robles, and D. L. Collins, "Nonlocal patch-based label fusion for hippocampus segmentation," in *Medical Image Computing and Computer-Assisted Intervention*, 2010, pp. 129–136.
63. S. F. Eskildsen, P. Coupé, V. Fonov, J. V. Manjón, K. K. Leung, N. Guizard, S. N. Wassef, L. R. Østergaard, and D. L. Collins, "BEaST: Brain extraction based on nonlocal segmentation technique," *Neuroimage*, vol. 59, no. 3, pp. 2362–2373, Feb. 2012.
64. S. Hu, P. Coupé, J. C. Pruessner, and D. L. Collins, "Nonlocal regularization for active appearance model: application to medial temporal lobe segmentation," *Hum. Brain Mapp.*, vol. 35, no. 2, pp. 377–395, Feb. 2014.
65. M. R. Sabuncu, B. T. T. Yeo, K. Van Leemput, B. Fischl, and P. Golland, "A generative model for image segmentation based on label fusion," *IEEE Trans. Med. Imaging*, vol. 29, no. 10, pp. 1714–29, Oct. 2010.
66. H. Wang, J. W. Suh, S. R. Das, J. B. Pluta, C. Craige, and P. A. Yushkevich, "Multi-atlas segmentation with joint label fusion," *IEEE Trans. Pattern Anal. Mach. Intell.*, vol. 35, no. 3, pp. 611–623, Mar. 2013.
67. G. Wu, M. Kim, G. Sanroma, Q. Wang, B. C. Munsell, D. Shen, and Alzheimer's Disease Neuroimaging Initiative, "Hierarchical multi-atlas label fusion with multi-scale feature representation and label-specific patch partition," *Neuroimage*, vol. 106, pp. 34–46, Feb. 2015.
68. T. Lindeberg, "Feature detection with automatic scale selection," *Int. J. Comput. Vis.*, vol. 30, no. 2, pp. 79–116, 1998.
69. T. Lindeberg, "Generalized Gaussian Scale-Space Axiomatics Comprising Linear Scale-Space, Affine Scale-Space and Spatio-Temporal Scale-Space," *J. Math. Imaging Vis.*, vol. 40, no. 1, pp. 36–81, May 2011.
70. M. Holden, L. D. Griffin, N. Saeed, and D. L. G. Hill, "Multi-channel mutual information using scale space," in *Medical Image Computing and Computer-Assisted Intervention*, 2004, pp. 797–804.
71. D. G. Lowe, "Distinctive image features from scale-invariant keypoints," *Int. J. Comput. Vis.*, vol. 60, no. 2, pp. 91–110, Nov. 2004.
72. S. Leutenegger, M. Chli, and R. Y. Siegwart, "BRISK: Binary robust invariant scalable keypoints," in *2011 International Conference on Computer Vision*, 2011, pp. 2548–2555.
73. Y. Wu, G. Liu, M. Huang, J. Guo, J. Jiang, W. Yang, W. Chen, and Q. Feng, "Prostate segmentation based on variant scale patch and local independent projection," *IEEE Trans. Med. Imaging*, vol. 33, no. 6, pp. 1290–1303, Jun. 2014.
74. P. Thévenaz and M. Unser, "Optimization of mutual information for multiresolution image registration," *IEEE Trans. Image Process.*, vol. 9, no. 12, pp. 2083–99, 2000.
75. M. Soltaninejad, G. Yang, T. Lambrou, N. Allinson, T. L. Jones, T. R. Barrick, F. A. Howe, and X. Ye, "Automated brain tumour detection and segmentation using superpixel-based extremely randomized trees in FLAIR MRI," *Int. J. Comput. Assist. Radiol. Surg.*, Sep. 2016.
76. M. Soltaninejad, X. Ye, G. Yang, N. Allinson, and T. Lambrou, "An image analysis approach to MRI brain tumour grading," *Oncol. News*, vol. 9, no. 6, pp. 204–207, Jan. 2015.
77. M. Soltaninejad, X. Ye, G. Yang, N. Allinson, and T. Lambrou, "Brain tumour grading in different MRI protocols using SVM on statistical features," in *Medical Image Understanding and Analysis*, 2014.
78. G. Yang, F. Raschke, T. R. Barrick, and F. A. Howe, "Manifold learning in MR spectroscopy using nonlinear dimensionality reduction and unsupervised clustering," *Magn. Reson. Med.*, vol. 74, no. 3, pp. 868–878, 2015.
79. X. Ye, G. Beddoe, and G. Slabaugh, "Automatic graph cut segmentation of lesions in CT using mean shift superpixels.," *Int. J. Biomed. Imaging*, vol. 2010, p. 983963, Jan. 2010.
80. Y. Zhao, Y. Zheng, Y. Liu, J. Yang, Y. Zhao, D. Chen, and Y. Wang, "Intensity and compactness enabled saliency estimation for leakage detection in diabetic and malarial retinopathy," *IEEE Trans. Med. Imaging*, vol. 36, no. 1, pp. 51–63, Jan. 2017.
81. K. Lemola, M. Sneider, B. Desjardins, I. Case, J. Han, E. Good, K. Tamirisa, A. Tsemo, A. Chugh, F. Bogun, F. Pelosi, E. Kazerooni, F. Morady, and H. Oral, "Computed tomographic analysis of the anatomy of the left atrium and the esophagus: implications for left atrial catheter ablation," *Circulation*, vol. 110, no. 24, pp. 3655–60, Dec. 2004.

82. P. A. Lachenbruch and M. Goldstein, "Discriminant analysis," *Biometrics*, vol. 35, no. 1, pp. 69–85, 1979.
83. G. John and P. Langley, "Estimating continuous distributions in Bayesian classifiers," *Proc. Elev. Conf. Uncertain. Artif. Intell.*, pp. 338–345, 1995.
84. J. Friedman, J. Bentley, and R. Finkel, "An algorithm for finding best matches in logarithmic expected time," *ACM Trans. Math. Softw.*, vol. 1549, pp. 209–226, 1977.
85. N. Cristianini and J. Shawe-Taylor, *An Introduction to Support Vector Machines and Other Kernel-based Learning Methods*, First. Cambridge University Press, 2000.
86. G. Yang, T. L. Jones, F. A. Howe, and T. R. Barrick, "Morphometric model for discrimination between glioblastoma multiforme and solitary metastasis using three-dimensional shape analysis," *Magn. Reson. Med.*, Jul. 2015.
87. M. T. Hagan, H. B. Demuth, and M. H. Beale, *Neural Network Design*. PWS Pub. Co., 1996.
88. G. Yang, T. L. Jones, T. R. Barrick, and F. A. Howe, "Discrimination between glioblastoma multiforme and solitary metastasis using morphological features derived from the p:q tensor decomposition of diffusion tensor imaging," *NMR Biomed.*, vol. 27, no. 9, pp. 1103–1111, Sep. 2014.
89. Y. Mo, F. Liu, J. Zhang, G. Yang, T. He, and Y. Guo, "Deep poincare map for robust medical image segmentation," Mar. 2017.
90. H. Dong, G. Yang, F. Liu, Y. Mo, and Y. Guo, "Automatic brain tumor detection and segmentation using U-Net based fully convolutional networks," in *Annual Conference on Medical Image Understanding and Analysis, Communications in Computer and Information Science*, 2017, pp. 506–517.
91. S. Yu, H. Dong, G. Yang, G. Slabaugh, P. L. Dragotti, X. Ye, F. Liu, S. Arridge, J. Keegan, D. Firmin, and Y. Guo, "Deep de-aliasing for fast compressive sensing MRI," May 2017. arXiv:1705.07137
92. D. Shen, G. Wu, and H.-I. Suk, "Deep learning in medical image analysis," *Annu. Rev. Biomed. Eng.*, vol. 19, pp. 221–248, Jun. 2017.
93. M. Hasan and A. K. Roy-Chowdhury, "A continuous learning framework for activity recognition using deep hybrid feature models," *IEEE Trans. Multimed.*, vol. 17, no. 11, pp. 1909–1922, Nov. 2015.
94. X. Zhuang, "Challenges and methodologies of fully automatic whole heart segmentation: a review," *J. Healthc. Eng.*, vol. 4, no. 3, pp. 371–408, 2013.
95. G. Yang, J. H. Hipwell, M. J. Clarkson, C. Tanner, T. Mertzanidou, S. Gunn, S. Ourselin, D. J. Hawkes, and S. R. Arridge, "Combined reconstruction and registration of digital breast tomosynthesis," in *Lecture Notes in Computer Science (including subseries Lecture Notes in Artificial Intelligence and Lecture Notes in Bioinformatics)*, vol. 6136 LNCS, pp. 760–768, 2010.
96. D. P. Huttenlocher, G. A. Klanderman, and W. J. Rucklidge, "Comparing images using the Hausdorff distance," *IEEE Trans. Pattern Anal. Mach. Intell.*, vol. 15, no. 9, pp. 850–863, 1993.
97. G. Yang, F. Raschke, T. R. Barrick, and F. A. Howe, "Classification of brain tumour 1H MR spectra: extracting features by metabolite quantification or nonlinear manifold learning?" in *2014 IEEE 11th International Symposium on Biomedical Imaging (ISBI)*, IEEE, 2014, pp. 1039–1042.
98. B. Efron, "Estimating the error rate of a prediction rule: improvement on cross-validation," *J. Am. Stat. Assoc.*, vol. 78, no. 382, p. 316, 1983.
99. T. L. Jones, T. J. Byrnes, G. Yang, F. A. Howe, B. A. Bell, and T. R. Barrick, "Brain tumor classification using the diffusion tensor image segmentation (D-SEG) technique," *Neuro. Oncol.*, vol. 17, no. 3, pp. 466–476, Aug. 2014.
100. K. Murphy, *Machine Learning: A Probabilistic Perspective*. MIT Press, 2012.
101. M. H. Moghari, D. C. Peters, J. Smink, L. Goepfert, K. V Kissinger, B. Goddu, T. H. Hauser, M. E. Josephson, W. J. Manning, and R. Nezafat, "Pulmonary vein inflow artifact reduction for free-breathing left atrium late gadolinium enhancement," *Magn. Reson. Med.*, vol. 66, no. 1, pp. 180–6, Jul. 2011.
102. B. Irving, J. M. Franklin, B. W. Papież, E. M. Anderson, R. A. Sharma, F. V. Gleeson, S. M. Brady, and J. A. Schnabel, "Pieces-of-parts for supervoxel segmentation with global context: application to DCE-MRI tumour delineation," *Med. Image Anal.*, vol. 32, pp. 69–83, Aug. 2016.
103. F. Kanavati, T. Tong, K. Misawa, M. Fujiwara, K. Mori, D. Rueckert, and B. Glocker, "Supervoxel classification forests for estimating pairwise image correspondences," *Pattern Recognit.*, vol. 63, pp. 561–569, Mar. 2017.
104. M. P. Heinrich, I. J. A. Simpson, B. W. Papież, S. M. Brady, and J. A. Schnabel, "Deformable image registration by combining uncertainty estimates from supervoxel belief propagation," *Med. Image Anal.*, vol. 27, pp. 57–71, Jan. 2016.
105. Z. Tian, L. Liu, Z. Zhang, and B. Fei, "Superpixel-based segmentation for 3D prostate MR images," *IEEE Trans. Med. Imaging*, vol. 35, no. 3, pp. 791–801, 2016.

7 Cardiovascular Health Informatics Computing Powered by Unobtrusive Sensing Computing, Medical Image Computing, and Information Fusion Analysis

Chengjin Yu[1], Xiuquan Du[1], Yanping Zhang[1], Heye Zhang[2]
[1]Anhui University
[2]Shenzhen Institutes of Advanced Technology

CONTENTS

7.1 INTRODUCTION

Cardiovascular disease (CVD) is the leading cause of death in the world. As of 2015, 17.7 million people die each year from cardiovascular disease, estimated at 31% of total deaths [1]. Two-thirds of all the deaths caused by CVD happened outside the hospital [2], and over 82% of CVD deaths took place in low-income and middle-income countries [1]. Many researchers have been working to improve the quality of care for patients and to reduce costs through early detection/intervention and more effective disease/patient management. This requires more advanced sensing, computing, and analysis.

Accompanied by the emergence of a large variety of new technologies, no aspect of human life can escape the impact of the information age. Perhaps in no area of life is information more

critical than in health and medicine [3]. There is now a consensus that the systematic health informatics approach—the acquisition, management, and use of health information—can greatly improve the quality and efficiency of health care. Furthermore, advancing health informatics is considered to be one of the 14 grand challenges for engineering in the 21st century by the U.S. National Academy of Engineering [3]. It is also a reliable method to realizing p-Health technologies including Predictive, Personalized, Precise, Pervasive, Participatory, and Preemptive healthcare [4].

This section focuses on computing in cardiovascular health informatics, which includes sensing computing, medical image computing, and information fusion analysis. In the past, doctors and researchers collected medical data by sensing and imaging. Limited time and effort can be put into the analysis of the data. With the enhancement of computing power and the miniaturization of electronic devices, the ideal of continuous unobtrusive sensing becomes reality. It is very desirable for us to develop computer-aided diagnosis systems and even fully operative computer diagnosis systems when we face big data. An example is given in Figure 7.1, which describes the evolution of the electrocardiogram (ECG) device. Electronic devices evolved from water buckets and bulky vacuum tubes to discrete transistors-based machines. Their size also evolved from desktop sized to small, wearable equipment [5]. A clear trend is that they will become smaller, lighter, and more comfortable to wear.

With the exponential increase of data, whether it is sensing data or imaging data, researchers are increasingly inclined to use big data technology and artificial intelligence technology for data processing, and to dig out the information to help diagnose, or help to understand the pathophysiology of disease. These techniques have changed traditional medicine. In the past, enough experience was needed for a doctor to extract disease information from medical data. But now, many diseases can be automatically identified based on a computer. For example, Figure 7.2 illustrates a myocardial infarction area that was predicted by a deep learning method [7]. This example of excellent results show the great potential of computing based imaging methods.

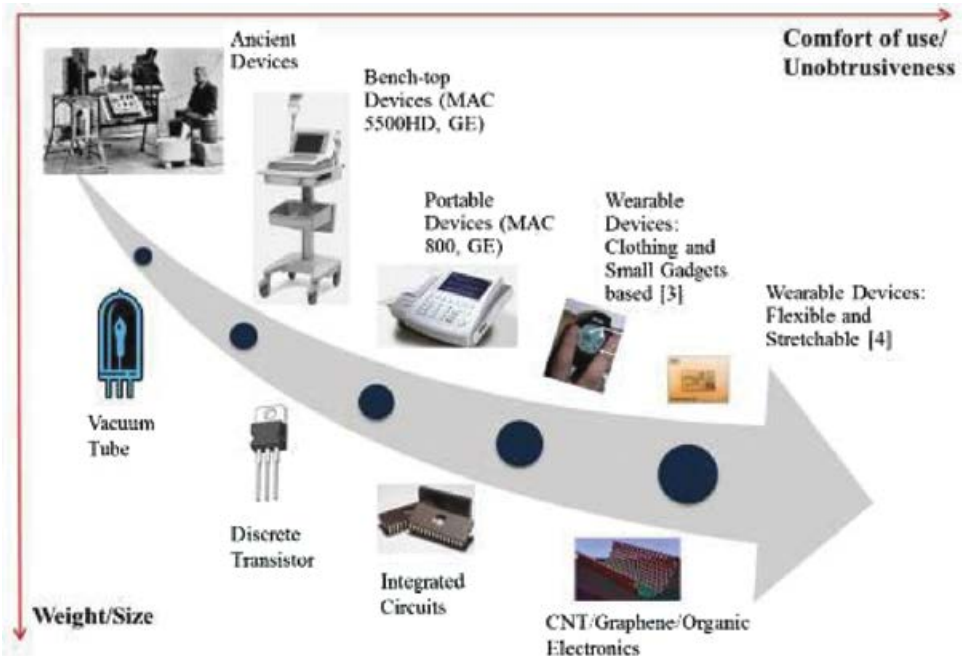

FIGURE 7.1 The timelines of medical devices for ECG measurement with the evolution of electronic technology.

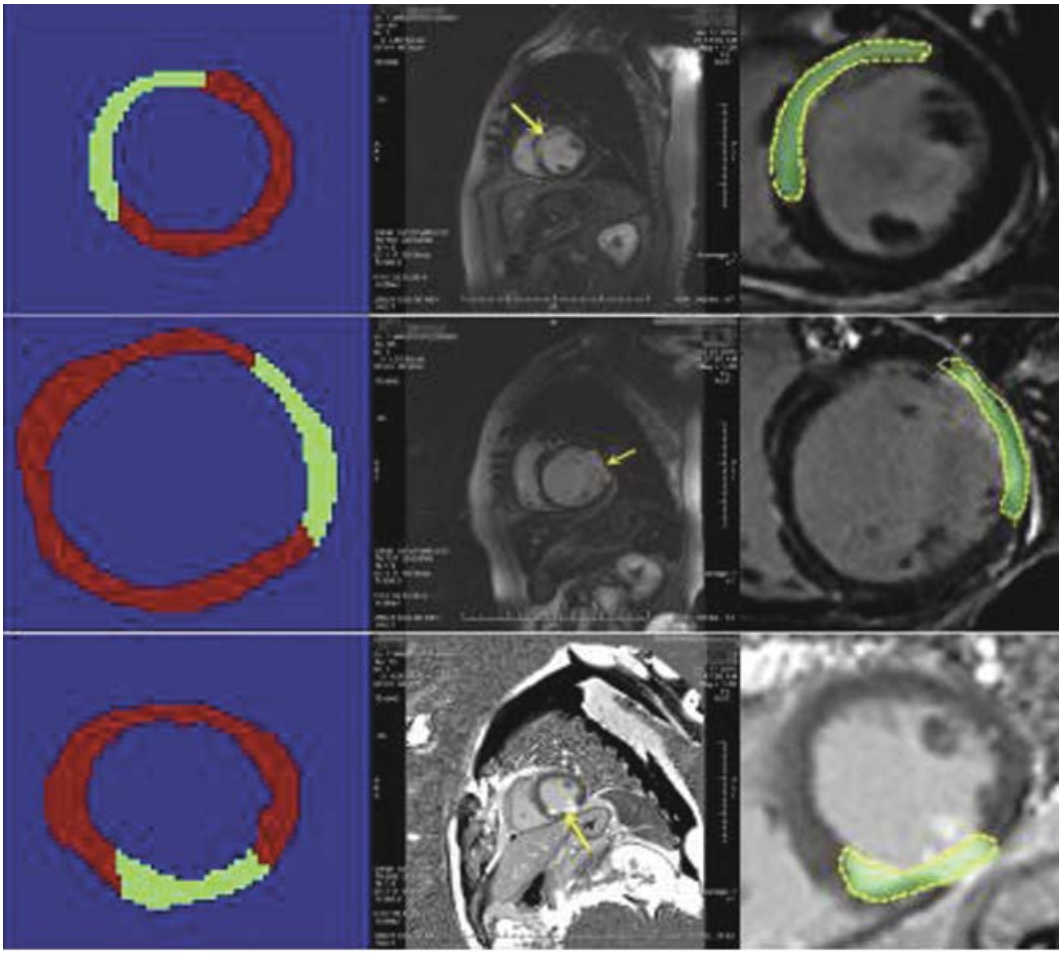

FIGURE 7.2 (a-b) MI area (the green zone) predicted by [7] can be a good fit for the ground truth (the yellow arrow) (c) MI area (the green zone) predicted by [7] can be a good fit for the ground truth (the yellow dotted line).

The objectives of this chapter are to provide an overview of the state-of-the-art of cardiovascular health informatics computing. The development of the field is reviewed from the perspective of sensing computing, image computing, and information fusion analysis, respectively.

The rest of this chapter is organized as follows: Section 2 will discuss unobtrusive sensing computing. Section 3 will present the recent advances and core technologies of image computing, and will also highlight the recent deep learning model. Section 4 will discuss data fusion analysis, as well as the impact of big data in healthcare. Section 5 will give the conclusion.

7.2 UNOBTRUSIVE SENSING COMPUTING

7.2.1 Unobtrusive Sensors for the Real-Time and Continuous Acquisition of Cardiovascular Health Information

Unobtrusive sensors can achieve continuous monitoring of physical activities and behaviors, and record the physiological signals of the human body and other information, such as electrocardiograph (ECG), photoplethysmography (PPG), respiratory rate, heart rate, body temperature,

blood oxygen saturation, blood pressure (BP), posture, and physical activities. It does not intrude on one's normal life. In fact, often the user is unaware of the signal while the information is being collected via unobtrusive sensors. A sample model of a home setting for ongoing physiological monitoring is shown in Figure 7.3.

Generally, unobtrusive sensors can be implemented in two ways: (1) wearable sensors are worn by the subject, such as in the form of shoes, eyeglasses, earrings, clothing, gloves, and watches, or (2) sensors are embedded into the ambient environment or as smart objects interacting with the subjects, such as a chair [4], car seat [11], mattress [12], mirror [8], steering wheel [14], mouse [15], toilet seat [16], and bathroom scale [17]. Figure 7.3 shows several unobtrusive sensors that were developed by different groups. We can further divide unobtrusive sensors into two categories, depending on whether the source of the signal is passive or active. For example, capacitive-coupling-based ECG can be realized by detecting signals from the human body. The active sensing methods send energy to the human body and detect the reflected or backscattered energy, such as using radio or radar to detect heart rate remotely, or remote infrared temperature measurements.

Acquired physiological health information from unobtrusive sensors can be transmitted to a remote control center for storage and analysis based on wireless communication technologies. In this way, the patient's cardiovascular health information can be obtained out-of-hospital in real time. Not only can the medical costs caused by frequent visits to the hospital be reduced, but also these devices allow for taking preemptive actions in response to acute cardiac cardiovascular disease events. Sometimes, out-of-hospital measurement results are often more significant than the clinical diagnosis. It has been widely recognized that clinical blood pressure measurements may fail to reflect true information and may even provide some false clinical diagnostic information, such as white-coat hypertension. The experts suggest that patients with known or suspected hypertension are more likely to use a home-based blood pressure monitoring method [18]. In addition, it has been confirmed that independent risk factors for the prediction of cardiac cardiovascular disease mortality can be extracted from 24-hour blood pressure measurements, according to some clinical studies. The Ohasama clinical study shows that there is a significant linear relationship between relative hazard ratios and cardiac cardiovascular disease death [19]. Therefore, the acquisition of cardiovascular health information should not be confined to the hospital or physical examination center, but should cover daily life in every moment.

Many unobtrusive monitoring devices in cardiac cardiovascular disease healthcare have been developed. Recently, capacitance-coupled technique based dry/noncontact electrodes are

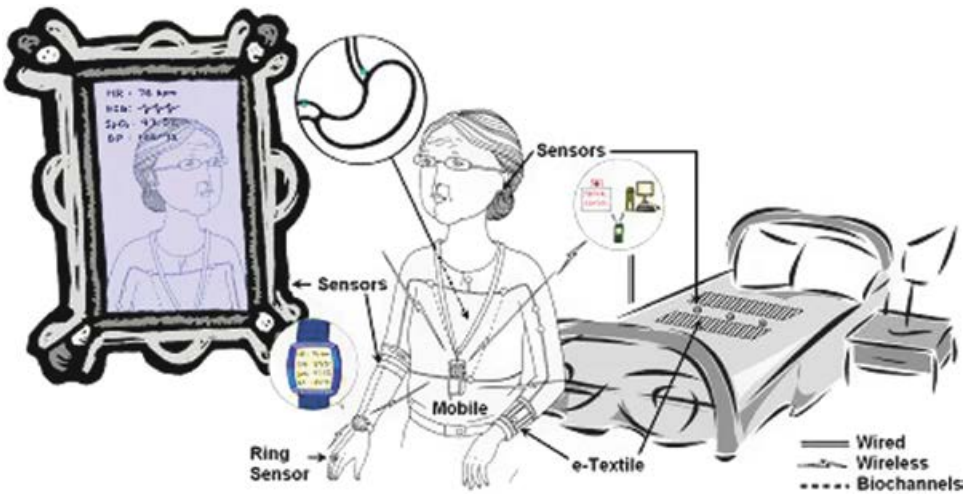

FIGURE 7.3 Illustration of unobtrusive physiological measurements in a home environment [5].

TABLE 7.1
Different Implementations of Capacitive ECG Sensors

Systems	Location of ECG electrodes	Measured signals and parameters
Bed [23]	Bed cushion	ECG, PPG, heart rate, BP
Wearable ECG system [26]	Cloth and belt	ECG
BP monitoring chair [21]	Chair pad and arms	ECG, PPG, heart rate, BP
Non-contact chair based system [25]	Chair back	ECG, BCG, heart rate, BP
Aachen Smart Chair [25]	Chair backrest and pad	ECG
Ambulatory ECG monitoring over cloth [29]	Integrated on underwear	ECG
Textile integrated long-term ECG monitor [30]	Integrated into garment	ECG
Non-contact ECG/EEG electrodes [31]	Embedded within fabric and clothing	ECG
Wireless wearable ECG sensor [32]	Integrated into a cotton T-shirt	ECG

embedded in furniture, which can provide unobtrusive sensing for an electrocardiogram. For this method, the skin and electrodes form two layers of capacitors. It also avoids direct contact with the human body, and prevents skin infection and the signal deterioration caused by the adhesive electrode in the long-term monitoring. Table 7.1 summarizes some typical implementations of capacitive ECG sensing. But there are still some challenges in capacitance-coupled technique based sensing. The major problems are modulation of the bioelectric potential signals from motion-related source impedance changes and electronic noise when designing these non-contact electrodes [28]. Some recent works propose to overcome those problems. For instance, gradiometer electrodes are adopted to reduce the influence of motion artifacts [34]. The preamplifier immediately following the ECG electrode is the major contributor to the overall electronic noise level [30] and may be addressed by employing careful preamplifier design. And electronic noise may be addressed by employing careful preamplifier design due to the fact that the preamplifier immediately following the ECG electrode is the major contributor to overall electronic noise levels [22].

Photoplethysmographic (PPG) is a simple, low-cost technique that can monitor changes in blood volume in capillaries. It contains a light source that can emit light into tissue and then a photodetector to collect the light reflected from or transmitted through the tissue. Photoplethysmographic (PPG) technique based devices are often portable and noninvasive, so they are widely used for measurement of many vital signs, such as SpO2, heart rate, respiration rate, and BP. Recent research shows that sensors can be integrated into daily living accessories or gadgets such as earrings, gloves, and hats, to achieve unobtrusive measurements. Table 7.2 summarizes different applications for PPG techniques. Recently, Jae et al. [26] proposed an indirect-contact sensor for PPG measurement over clothes. A control circuit was adopted to adaptively adjust the light intensity for various clothing types. In other research, Poh et al. [27] showed that heart rate and respiration rate can be derived from PPG that is remotely captured from a subject's face using a simple digital camera. However, the temporal resolution of the blood volume detected by this method was restricted by the sample rate of the camera, thus affecting its accuracy.

The pulse wave propagation based method is a promising technique for continuous and cuffless BP measurement. It has been shown that there is a strong correlation between pulse wave velocity (PWV) and arterial pressure. Pulse transit time (PTT) is the time that pulse travels from the heart to the periphery. Clinically, PTT can be estimated rapidly via ECG and PPG signals. Much recent work has proved the feasibility of PTT based BP measuring. According to the experimental results from [47][48][49][50][51][52], the error of systolic and diastolic blood pressure between PTT based BP and reference are 0.6 ± 9.8 mmHg and 0.9 ± 5.6 mmHg, respectively. Such results basically

TABLE 7.2
PPG Measuring Devices at Different Sites of the Body

Devices	Location of Sensor/Operation mode	Measured Parameters
PPG ring [33]	Finger/Reflective	Heart rate and its variability, SpO_2
Pulsear [35]	External ear cartilage/Reflective	Heart rate
Forehead mounted sensor [36]	Forehead /Reflective	SpO_2
e-AR [37]	Posterior, inferior and anterior auricular /Reflective	Heart rate
IN-MONIT system [18]	Auditory canal /Reflective	Heart activity and heart rate
Glove and hat based PPG sensor [39]	Finger and forehead/Reflective	Heart rate and pulse wave transit time
Ear-worn monitor [19]	Superior Auricular, superior Tragus and Posterior Auricular /Reflective	Heart rate
Headset [40]	Ear lobe/Transmissive	Heart rate
Heartphone [41]	Auditory canal /Reflective	Heart rate
Magnetic earring sensor [42]	Earlobe /Reflective	Heart rate
Eyeglasses [43]	Nose bridge/Reflective	Heart rate and pulse transit time
Ear-worn PPG sensor [44]	Ear lobe /Reflective	Heart rate
Smartphone [45]	Finger /Reflective	Heart rate

meet the accuracy requirements (5 ± 8 mmHg for systolic and diastolic BP estimation) of the American Medical Devices Promotion Council (AAMI) [51], as shown in Figure 7.4(a). The hydrostatic pressure approach is adopted to achieve individual calibration by Poon [53]. In this method, subjects need to lift their hands to a specific height below the heart. Then, the relationship between PTT, BP, and height can be written as follows:

$$PTT = \begin{cases} \dfrac{L\sqrt{\rho b}}{1+\exp(bP_i)} & ; \quad h = 0 \\ \dfrac{2L}{\sqrt{\rho b g h}} \ln \left| \dfrac{\sqrt{\exp[b(P_i - P_h)]} + \exp(-bP_h) - \sqrt{\exp(-bP_h)}}{\sqrt{\exp[b(P_i - P_h)]} + 1 - 1} \right| & ; \quad h \neq 0 \end{cases} \tag{7.1}$$

where b is the subject-dependent parameter characterizing the artery properties, L is the distance traveled by the pulse, P_h is the hydrostatic pressure ρgh, and P_i is the internal pressure. The parameters in the PTT based model are easy to obtain from simple movements. Therefore, the PTT based model can be easily implemented into furniture such as a normal chair [25], and a pillow [23] among others, as shown in Figure 7.4(b).

In addition to sensing technology, user-friendly design is another important issue in the development of unobtrusive devices. In recent years, the technique of intelligent textiles has been greatly improved, which provides effective solutions for unobtrusive sensors. Due to the critical features of intelligent textiles, such as flexible structure, light weight, and biocompatibility, it is easy to integrate wearable wireless sensors into our clothes [54][55]. Thus, continuous monitoring in daily life can be naturally achieved.

Though significant progress has been made in the field of unobtrusive sensing, there are still several challenges to overcome. Poon [57] summarizes some key techniques as "MINDS" (Miniaturization, Intelligence, Networking, Digitalization, Standardization). In addition, information security, energy-efficiency, robustness, and personalization are also proposed by [58], which are important for the future development of wearable technologies.

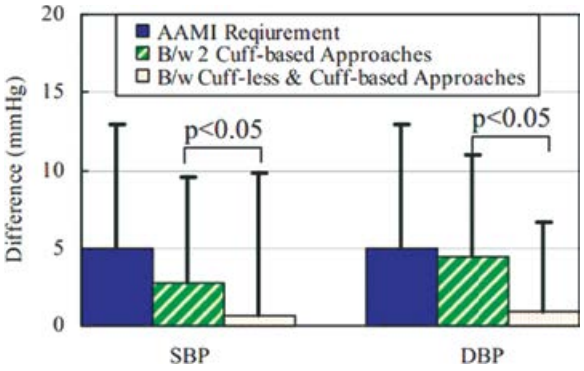

(a)

(b)

FIGURE 7.4 Unobtrusive sensing devices with sensors embedded in daily objects, such as: mirror [8], bed [28], chair [21], steering wheel [9], and toilet seat [10].

7.2.2 High Resolution Imaging for Cardiovascular Disease Diagnosis

Developing high resolution biomedical imaging is crucial for early prevention of CVD. Atherosclerosis is the main cause of acute cardiovascular disease [60]. The development of atherosclerosis will lead to unstable atherosclerotic plaques or vulnerable plaque, which is characterized as active inflammation, a thin fibrous cap with a large lipid core, erosion or fissure of the plaque surface, intra-plaque hemorrhage, and superficial calcified nodules [60][61]. Vulnerable plaque will narrow blood vessels or even occlude the vessel, resulting in the block of blood flow to vital organs, such as the heart and the brain. If the treatment of atherosclerosis is delayed, subsequently the rupture of vulnerable plaque will cause acute coronary death or stroke [60]. In addition, other kinds of cardiac diseases, such as myocarditis, electrophysiological disorders, valvular heart disease, and other cardiomyopathies (hypertrophic, dilated, or restrictive) are often related to vulnerable myocardium, and vulnerable plaques, which have a high likelihood of thrombotic complications and rapid progression, and so should be diagnosed and treated as early as possible [25][10].

Both invasive and noninvasive imaging modalities have provided insight into the structure and progression of asymptomatic atherosclerosis, vulnerable myocardium and plaque [59,10]. Some invasive imaging modalities such as catheterization or mini-invasive tests such as optical coherence tomography (OCT) and intravascular ultrasound (IVUS) have been used clinically for evaluating the vulnerability of plaque. Photoacoustic imaging technique opens a new area for intravascular imaging [62][63]. In comparison with IVUS, photoacoustic imaging techniques with high spatial resolution can provide more detailed information about plaques.

Because of the convenience and cost-effectiveness, noninvasive imaging modalities are more frequently used for screening subclinical atherosclerosis, high-risk plaque, and myocardium vulnerability. Now many well-established risk factors are measured by standard clinical imaging modalities, such as carotid intima-media thickness (CIMT) and ankle brachial index (ABI) captured by ultrasound (US) imaging, and the coronary artery calcium score (CACS) calculated by computerized tomography (CT) imaging. These risk factors have been proved to be highly associated with the occurrence of fatal events, and are widely used in the clinical guidelines for the assessment of cardiovascular risk in asymptomatic adults [64].

Figure 7.5 provides some examples of using noninvasive imaging techniques for identification of CVD [10]. Prominently, CT technology can assess plaque composition, level of calcification, and coronary stenosis [10]. Magnetic resonance imaging (MRI) can reliably detect and quantify carotid/aortic plaque components such as lipids, fibro-cellular tissue, calcium, intra-plaque hemorrhage [65], atherosclerotic burden, and potentially, plaque perfusion in non-coronary arteries [10]. Several promising approaches to improve the MRI resolution have been reported, such as multi-channel coil design [66].

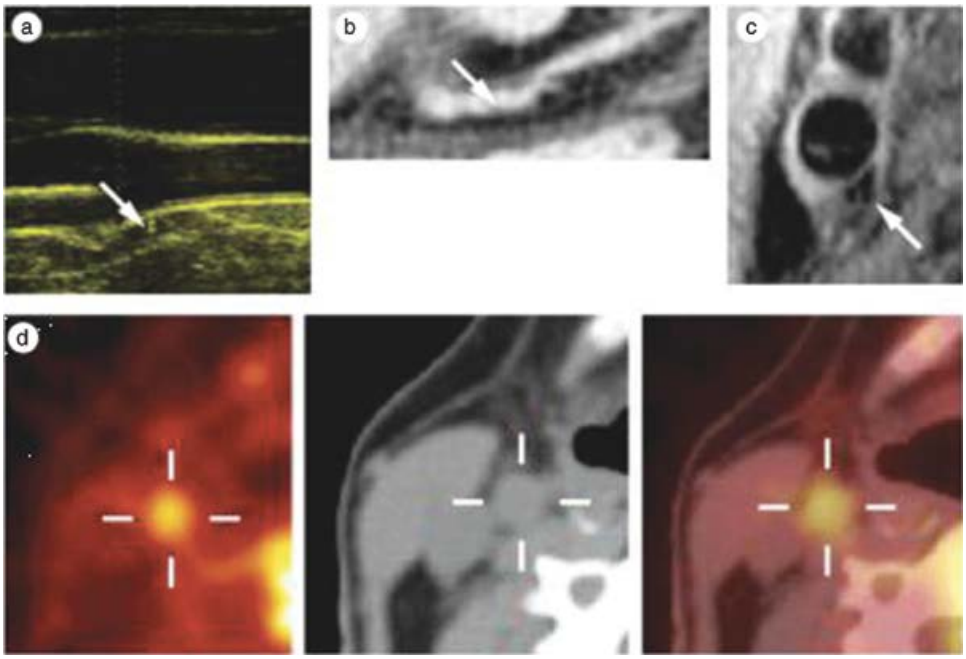

FIGURE 7.5 Noninvasive imaging techniques for early identification of cardiovascular disease. Reproduced from [10]. a. Example of an image captured by ultrasonography. The arrow indicates plaque burden. b. Example of an image captured by CT technology. The arrow shows calcification. c. Example of an image captured by MRI. The arrow indicates lipid deposit. d. Examples of images captured by PET, CT, and combined PET/CT. The visual target outlines the carotid artery.

TABLE 7.3
Noninvasive Imaging for Screening Atherosclerotic Plaque

Technology	Resolution (μm)		Penetration	Calcium	Fibrous cap	Lipid core	Thrombus	Inflammation	Status
	Spatial	Axial							
Ultrasound	600	400	9cm	+	+	+	+	+	Clinically applied
CT	400	400	–	++++	+	++	+	+	Clinical studies
MRI	250	3000	–	++	++	+++	++	+++	Clinical studies
SPECT	10000	–	–	+	+	++	++	+++	Preclinical studies
PET	4000	–	–	+	+	++	++	+++	Preclinical studies

–, represents nonapplicable; ++++, sensitivity > 90%; +++, sensitivity 80–90%; ++, sensitivity 50–80%; +, sensitivity <50%

Table 7.3 presents the sensitivity and application status of using noninvasive imaging techniques for screening atherosclerotic plaque, which was collected by Jan G. Kips, et al. [59]. As can be seen from the table, each of the current technologies has one or more limitations upon spatial/axial resolutions, penetration depth, and tissue characterizing capability, which will affect detection of vulnerable plaques in time [59]. Other limitations, such as the high investment of imaging machines (e.g., MRI, Multidetector CT), high expenditure on the tests using these devices, and potential risk derived from radiation exposure of CT, SPECT, PET, prevent current imaging modalities from being used for conventional examinations in daily clinical practices. In the end, because the movement of the cardiac system, respiratory, swallow, blood flow, and casual body movement will cause blurred images, poor contrast ratio, and even failure of the examination, the duration of the 3D volume imaging of the heart, especially MRI, should be greatly reduced [67].

Therefore, improving both temporal and spatial resolution of biomedical imaging is crucially important for CVD applications. Higher resolution imaging will allow the early screening of vulnerable plaque and vulnerable myocardium, and early identification of atherosclerosis during clinical practices. Grand technical challenges in this area are to develop high-resolution imaging modalities with high sensitivity that can be used for the objective evaluation of vulnerable plaque including its morphostructure and components, and for the detection of pathological markers.

7.3 MEDICAL IMAGE COMPUTING

Many issues in cardiac image processing and analysis can be summarized as optimization problems. Thus optimization techniques become an effective way to provide solutions in that field. Previous optimization techniques to address the problems were mainly based on approximation optimization techniques and state-space approaches. More recently, deep learning techniques [69, 70] have been successfully used to handle the challenges of cardiac image processing and analysis. To date, the areas where those optimization techniques are being applied include image segmentation, motion and deformation reconstruction, material property estimation, and other tasks. Next, we will detail the application of different optimization techniques in the field of cardiac image analysis. And the future direction will be pointed out in the end.

7.3.1 Approximation Optimization Techniques

The gradient descent method [72] is the earliest, simplest, and most commonly used optimization method. Its basic idea is to use the negative gradient direction of the current position as the search direction. The closer the gradient descent method is to the target, the smaller the step length and the slower the progression. Duncan et al. [73] proposed a contour shape descriptors based method

that successfully measures the non-rigid motion of deformable objects from image sequences via a gradient descent algorithm. In such an approach, gradient descent algorithm is used to minimize the deformation between the segments using a measure of bending energy. Compared with gradient descent algorithm, the conjugate gradient descent method [72] can also be used to solve unconstrained optimization problems. In [73,74], B-spline cubic deformable models were introduced for analysis of cardiac motion. And model fitting was posed as an energy minimization problem. Fitting was performed by optimizing an objective function, which encoded the distance (external energy) between isoparametric planes of the model and MRI tag planes. In the end, such an optimization problem was numerically solved by an adaptive conjugate gradient descent algorithm.

In a dynamic programming method [75], the multi-stage process is transformed into a series of single stage problems, and the relationships among phases are solved one by one. Amini et al. presented two optimization approaches for active contours based on dynamic programming [76][77]. The optimization problem is set up as a discrete multi-stage decision process. And this formulation leads to a stable behavior for the active contours over iterations.

The least-squares [78] are important techniques in data fitting. The best fit in the least-squares sense minimizes the sum of squared residuals. Declerck et al. [79] have introduced a spatio-temporal model to segment the LV and to analyze motion from gated-SPECT sequences. Corresponding point pairs in different frames are selected by least squares optimization [80][81][82].

Even if excellent results can be obtained via those approximation optimization techniques, they treat the problems as a static process and calculate only after the external force is applied. When the noises increase, it can hardly obtain meaningful results.

7.3.2 State-Space Based Approaches

In control engineering, a state-space representation is a mathematical model of a physical system as a set of input, output, and state variables related by first-order differential equations. Generally, state-space approaches include Kalman filter, unscented Kalman filter, extended Kalman filter, and H filter [84]. And they are widely applied concepts in time series analysis used in the field and can deliver reliable results efficiently.

Meyer et al. [85] proposed a method to adopt the Kalman filter to estimate myocardial deformation and achieve a lower average error. However, the movements of the block between two neighboring imaging frames are modeled as a constant process, and this may provide a biased motion of the myocardial surface because of its nonlinear dynamics. In order to properly handle the nonlinear dynamics, researchers often built a nonlinear state-space approach based on the nonlinear periodic function [86][87], and solve problems by extended Kalman filter [88][89][90] or unscented Kalman filter [91].

The main problem of Kalman filter is under the Gaussian statistics assumptions [84]. However, uncertainties, such as image noise, sparse image data, and model uncertainty, often encountered in practical cases, might not be Gaussian statistics. Meanwhile, the mini-max strategy does not impose such restrictions and only makes assumptions on the finite disturbance energy. It is thus more robust and less sensitive to noise variations and modeling assumptions [68]. As a result, Liu et al. [93] presented an integrated robust estimation framework for the joint recovery of dense field cardiac motion and material parameters, and Gao et al. [95][96] also achieved a robust estimation of carotid artery wall motion based on H+ filter.

7.3.3 Deep Learning

Deep learning can imitate the function of human learning by training a multi-layer network. As a result, it can perform corresponding tasks as well as the human. The general concept behind deep learning is to learn hierarchical feature representations by first inferring simple representations and then progressively building up more complex representations from the previous level. The most successful type of models for image analysis to date are convolutional neural networks (CNNs).

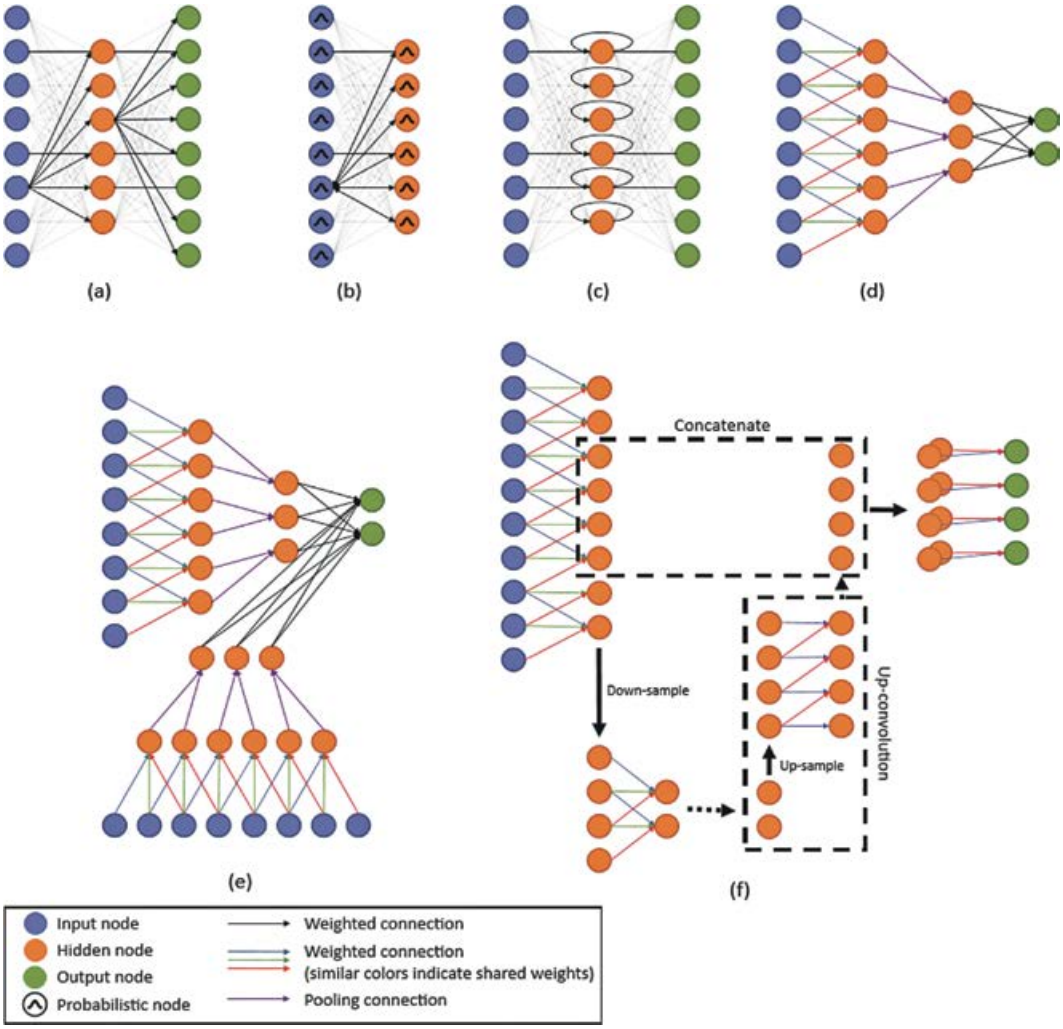

FIGURE 7.6 A graphic representation of different deep learning models.

CNNs contain many layers that transform their input with convolution filters of a small extent [70]. Besides, recurrent neural networks (RNNs), deep belief networks (DBNs) and their improved models are also widely used. Figure 7.6 shows the different deep learning models.

Deep learning has been applied to many aspects of cardiac image analysis. Left ventricle segmentation is the most common, but the number of applications is highly diverse: segmentation, tracking, slice classification, image quality assessment, automated calcium scoring and coronary centerline tracking, and super-resolution.

The work in [97–106] concentrate on left ventricle segmentation. Most of them [97–101] use simple CNNs and analyze data slice by slice. DBNs are adopted in [99–105], but they are only used to extract features and are integrated in compound segmentation frameworks. As an extension of [104], [103] achieves left ventricle tracking. Furthermore, Lessmann et al. [107] and Wolterink et al. [108] also use CNNs to detect coronary calcium from gated CT and ungated CT, respectively. And Oktay et al. [109] propose a super-resolution method based on CNNs.

Meanwhile, some other papers are exceptional because they combine CNNs with RNNs so that they can address more complex tasks. Xu et al. [7] propose an end-to-end deep-learning algorithm

framework to detect the myocardial infarction area. In such a method, Fast R-CNN is used to crop the region-of-interest (ROI) sequences; then the local motion features are generated by LSTM-RNN. In the end, they use SAEs to further learn these features, and identify the infarction by a softmax classifier. Kong et al. [111] also proposed a TempReg-Net framework, combining CNNs and RNNs, to identify specific frames and a cardiac sequence. Poudel et al. introduced a recurrent connection within the U-net architecture to segment the left ventricle slice by slice and learn what information to remember from the previous slices when segmenting the next one.

7.4 INFORMATION FUSION ANALYSIS

The development of sensing and imaging technologies increase the sensor's capability of acquiring data, such as physiological monitoring, high resolution imaging, biomarker detection, gene sequencing and so on. This increase has provided a huge amount of information of the heart, spinning multi-scales from gene, protein, cell, tissue, organ, to the system [11]. However, it is still a great challenge to deal with multi-sensing information fusion and generate a unified paradigm to support clinical diagnosis and treatment [113]. To date, several definitions of information fusion have emerged. F. E. White [120] proposed a definition of data fusion as a "multi-level, multifaceted process handling the automatic detection, association, correlation, estimation, and combination of data and information from several sources." Recently, in [6], information fusion is defined as a means "to develop efficient methods for automatically or semi-automatically translating the information from multiple sources into a structured representation so that human or automated decisions can be made accurately." As a multi-disciplinary research area, information fusion often can be met by developing model based fusion frameworks or technologies to personalize multiphysics models using personal multiscale health information obtained by multi-parameter sensing and multimodal imaging techniques. In this section, we will discuss multi-sensor fusion methods and the impact of big health data for clinical decision support.

7.4.1 Multi-Sensor Fusion Methods

In order to achieve early prediction of cardiac cardiovascular disease, many fusion works have been proposed in the literature. For instance, in a European Commission funded project, euHeart, a probabilistic fusion framework was developed to assimilate different health data into a multi-physics cardiac model by acting on the discrepancy between the measurements and the values derived from the computational model across scales (e.g., protein level ion channels flux and whole organ deformation) and functions (e.g., mechanical contraction and electrical activation), and then discover the new knowledge using the personalized model after the assimilated process [13]. By integrating continuous and real-time sensing data from unobtrusive/wearable devices with other health data, the real-time prediction of acute events of CVDs may become possible. Zhang's team has proposed a personalized framework for quantitative assessment of the risk of acute cardiovascular events based on vulnerable plaque rupturing mechanisms as shown in Figure 7.7. This framework does not only take traditional risk factors, sensitive biomarkers, blood biochemistry, vascular morphology, plaque information, and functional image information as inputs of the prediction model, but it also gathers physiological information continuously from unobtrusive devices and body sensor networks as the trigger factors aiming for real-time risk assessment of acute cardiovascular events.

Some other works try to find the cause of cardiac cardiovascular disease. They concentrated on simulating the physiology and pathology of the cardiovascular system, and efforts have been spent on developing computational models in the field. The capabilities of these models vary significantly from simulating the heart function, hemodynamics of the arterial system, to the whole cardiovascular system, including blood circulation [68][115]. So is the complexity of these models, from the simple zero-dimensional Windkessel model to complex multi-scale, multi-physics models which incorporate cells to systemic circulation [115].

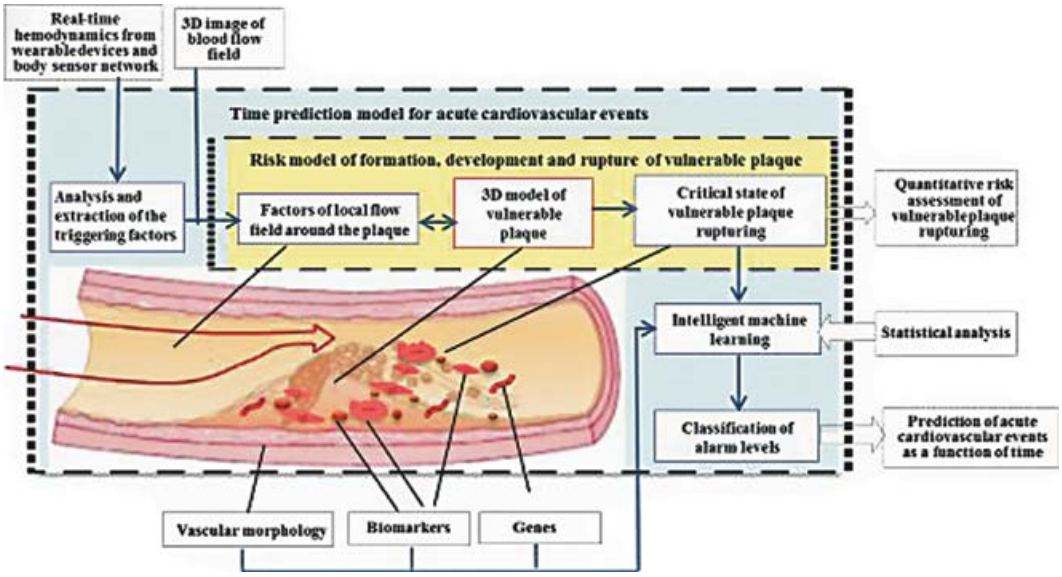

FIGURE 7.7 The proposed framework for the quantitative assessment of the risk of acute cardiovascular events. Reproduced from H. Gao, C. C. Y. Poon (2010).

One particularly great collaboration should be emphasized here, the Cardiac Physiome Project. With an international contribution, this project has made a great progress in developing a multi-physics model, which has the coupling of metabolic, electrophysiological, and biomechanical processes, for integrating the cardiac structure-function relations at multi-scale across from cell, tissue, to organ levels as shown in Figure 7.8. In this project, the biomodel-based coupling approaches

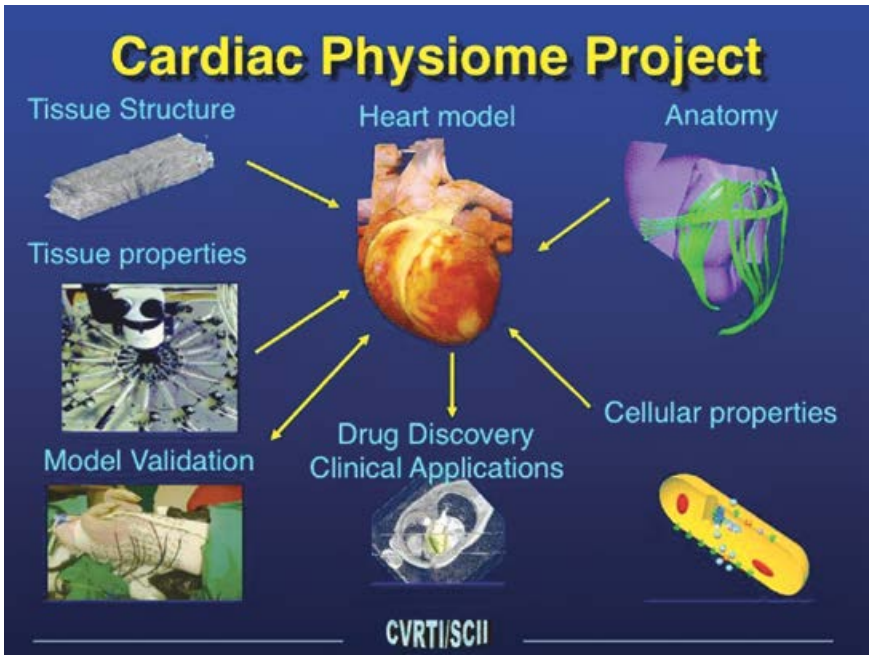

FIGURE 7.8 Diagram of Cardiac Physiome Project. Reproduced from [68].

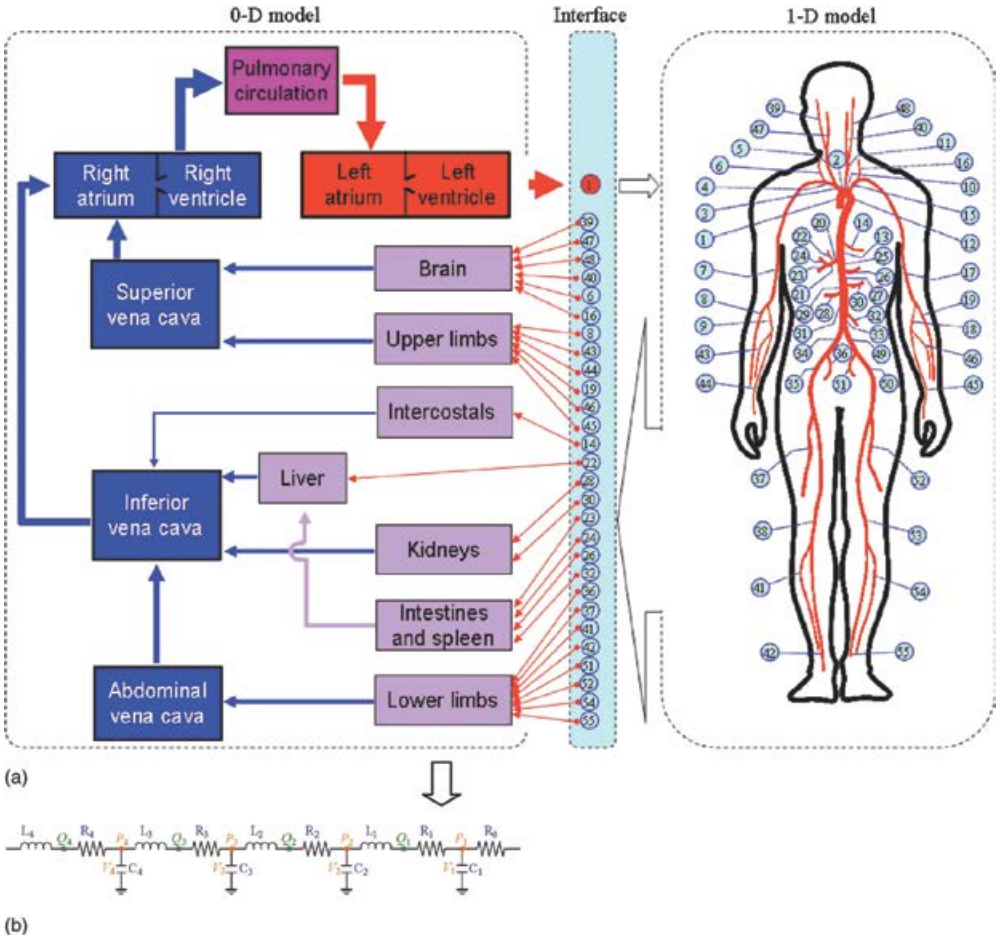

FIGURE 7.9 The illustration of multi-scale modelling of the cardiovascular system. Reproduced from [119].

have been intensely used for combining cardiac continuum tissue mechanics with electrophysiology, ventricular blood flow, and coronary hemodynamics in a meaningful physiological sense [117]. Another similar multi-scale framework is the Virtual Physiological Rat Project, which develops a multi-model platform with a coupling of metabolic and electrophysiological processes [118].

7.4.2 Impact of Big Health Data

The development of sensing technology has largely increased the sensor's capability of acquiring data, and multiple sensors are expected to provide different viewpoints of the health status of the patient. However, multi-sensor data fusion is a great challenge because the heterogeneous data need to be processed in order to generate unified and meaningful conclusions for clinical diagnosis and treatment [120]. The fusion of sensing data with other health data such as imaging, biomarkers, gene sequencing, etc. is even more challenging.

The definitions of data fusion are different in the literature. In [121], data fusion is defined as a "multi-level, multifaceted process handling the automatic detection, association, correlation, estimation, and combination of data and information from several sources." A comprehensive

FIGURE 7.10 Various wearable garments for physiological and activity monitoring. (a) The Georgia Tech Wearable Motherboard™ (Smart Shirt) for the measurement of ECG, heart rate, body temperature, and respiration rate [127]; (b) the EKG Shirt system which used interconnection technology based on embroidery of conductive yarn for heart rate [128]; (c) the LifeShirt system for the measurement of ECG, heart rate, posture and activity, respiration parameters, BP (peripheral is needed), temperature, SpO_2 [129]; (d) the ProTEX garment for the measurement of heart rate, breathing rate, body temperature, SpO_2, position, activity and posture [130]; (e) the WEALTHY system with knitted integrated sensors for the measurement of ECG, heart rate, respiration, activity monitoring [131]; (f) the VTAMN system for the measurement of heart rate, breathing rate, body temperature and activity [132]; (g) the h-Shirt system for the measurement of ECG, PPG, heart rate, and BP [133].

review and discussion of data fusion definitions are presented in [122]. We propose the definition of data fusion as: "to develop efficient methods for automatically or semi-automatically translating the information from multiple sources into a structured representation so that human or automated decisions can be made accurately." Data fusion is definitely a multi-disciplinary research area, which has integrated many techniques, such as signal processing, information theory, statistical estimation and inference, and artificial intelligence. In this section, we will discuss multi-sensor fusion methods and the fusion of sensing data with other types of health data for clinical decision support.

Since most health data are accompanied with a large number of noisy, irrelevant and redundant information, which may give spurious signals in clinical decision support, it is therefore necessary to filter the data before the fusion. To address this issue, ranked lists of events or attributes clearly relevant to clinical decision-making should be created [123]. Temporal reasoning method has been suggested for detecting associations between clinical entities [124]. More sophisticated methods such as contextual filters [125], and statistical shrinkage toward the null hypothesis of no association [126] were also proposed. How to filter information that is clinically meaningful would become more and more important but challenging due to the ever-increasing data types and volumes.

7.5 CONCLUSION

As Eric Topol described in [134]: "By bringing the era of big data and personal technology to the clinic, laboratory, and hospital, doctors can see a full, continuously updated picture of each patient and treat each individually." The emerging technologies in cardiovascular health informatics has dramatically changed the way we acquire, process, fuse and explain multi-scale and multi-modal cardiovascular health information. It provides us with new opportunities to understand the pathologies of CVDs. Furthermore, we can develop personalized, accurate risk assessment tools to screen high-risk patients at an early stage, and eventually achieve the goal of early detection, early prediction, early diagnosis, and early treatment of CVDs.

In this chapter, we summarize the development of cardiovascular health informatics from three aspects: unobtrusive sensing computing, medical image computing, and information fusion analysis. We introduce development process and the latest research results of each aspect. We can see the trend is: Cardiovascular health informatics is not only limited to the hospital, it will be integrated into our daily life. Although significant progress for healthcare applications had been made in the past decades, issues such as user acceptance, medical costs, real-time imaging, and efficiency of computing remain. No matter what technology we focus on, our ultimate goal is to apply possibility to reality, especially to serve more middle and lower income patients and populations. Another important requirement is the generalization of technologies; feasibility and user friendliness play an important role in promotion. In the following, we put forward some promising directions on the development of cardiovascular health informatics computing for future research:

1. To develop flexible, stretchable, and printable devices for unobtrusive physiological and biochemical monitoring. Research on a variety of semiconductor materials, including small-molecule organics and polymers, inorganic semiconducting materials. To develop flexible and stretchable sensors, which are very comfortable to wear.
2. To develop systematic data fusion framework. Integrate the multi-modal and multi-scale big health data from sensing, blood testing, biomarker detection, structural and functional imaging for the quantitative risk assessment and the early prediction of chronic diseases.
3. To extract new risk factors based on fusion analysis with both high sensitivity and specificity, and to integrate real-time and continuous physiological information, biomarker information and blood biochemistry with high-resolution cardiovascular imaging information for screening vulnerable plaque and vulnerable patients.

At the end, we should point out that the prevention of CVD is easier than the cure of CVD. Most CVD is preventable by adopting a healthy lifestyle, such as exercise, diet modification, and non-pharmacological means of blood pressure regulation (reduced salt, etc.).

References

1. World Health Organization. Cardiovascular diseases (CVDs). 2015. http://www.who.int/mediacentre/factsheets/fs317/en/ (accessed 4 Aug 2015).
2. J. Mackay, G. A. Mensah, S. Mendis, and K. Greenlund. *The Atlas of Heart Disease and Stroke*. Geneva, Switzerland: World Health Organization. 2004.
3. National Academy of Engineering. Advance health informatics [Online]. Available: http://www.engineeringchallenges.org/cms/8996/8938.aspx
4. Y. T. Zhang, C. C. Y. Poon, and E. MacPherson. Editorial note on health informatics. *IEEE Trans. Inf. Technol. Biomed.,* vol. 13, no. 3, pp. 281–283, May 2009.
5. C. C. Y. Poon, Y. M. Wong, and Y.-T. Zhang. M-Health: the development of cuff-less and wearable blood pressure meters for use in body sensor networks. *IEEE/NLM Life Science Systems and Applications Workshop*, Bethesda, MD, 2006, pp. 1–2.
6. Y. L. Zheng, X. R. Ding, C. C. Poon, B. P. Lo, H. Zhang, X. L. Zhou, et al. Unobtrusive sensing and wearable devices for health informatics. *IEEE Transactions on Biomedical Engineering*, vol. 61, no. 5, pp. 1538–1554, 2014.

7. C. Xu, L. Xu, Z. Gao, S. Zhao, H. Zhang, Y. Zhang, et al. Direct detection of pixel-level myocardial infarction areas via a deep-learning algorithm. *Medical Image Computing and Computer-Assisted Intervention – MICCAI 2017.*
8. M. Z. Poh, D. McDuff, and R. Picard. A medical mirror for non-contact health monitoring. *ACM SIGGRAPH 2011 Emerging Technologies*. Vancouver, British Columbia, Canada, 2011, p. 1.
9. Gomez-Clapers and R. Casanella. A fast and easy-to-use ECG acquisition and heart rate monitoring system using a wireless steering wheel. *IEEE Sens. J.*, vol. 12, no. 3, pp. 610–616, Mar. 2012.
10. K. Ko Keun, L. Yong Kyu, and P. Kwang-Suk. The electrically noncontacting ECG measurement on the toilet seat using the capacitively-coupled insulated electrodes. *26th Annual International Conference of the IEEE Engineering in Medicine and Biology Society.* San Francisco, CA, USA, 2004, pp. 2375–2378.
11. P. J. Hunter and T. K. Borg. Integration from proteins to organs: the Physiome Project. *Nat. Rev. Mol. Cell Biol.*, vol. 4, no. 3, pp. 237–243, Mar. 2003.
12. Wellcome trust heart physiome project [Online]. http://heart.physiomeproject.org/index.html
13. euHeart [Online]. http://www.euheart.eu/index.php?id=32
14. Europen Union. HeartCycle project [Online]. http://www.heartcycle.eu/.
15. J. G. Kips, P. Segers, and L. M. Bortel. Identifying the vulnerable plaque: a review of invasive and non-invasive imaging modalities. *Artery Research*, vol. 2, pp. 21–34, 2008.
16. V. Fuster, F. Lois, and M. Franco. Early identification of atherosclerotic disease by noninvasive imaging. *Nat. Rev. Cardiol.*, vol. 7, no. 6, pp. 327–333, Jun. 2010.
17. M. Kikuya, A. Hozawa, T. Ohokubo, I. Tsuji, M. Michimata, M. Matsubara, M. Ota, K. Nagai, T. Araki, H. Satoh, S. Ito, S. Hisamichi, and Y. Imai. Prognostic significance of blood pressure and heart rate variabilities: The Ohasama study. *Hypertension*, vol. 36, no. 5, pp. 901–906, Nov. 2000.
18. S. Vogel, M. Hulsbusch, T. Hennig, V. Blazek, and S. Leonhardt. In-ear vital signs monitoring using a novel microoptic reflective sensor. *IEEE Trans. Inf. Technol. Biomed.*, vol. 13, no. 6, pp. 882–889, 2009.
19. J. A. C. Patterson, D. G. McIlwraith, and G.-Z. Yang. A flexible, low noise reflective PPG sensor platform for ear-worn heart rate monitoring. *Sixth International Workshop on Wearable and Implantable Body Sensor Networks*. Berkeley, CA, 2009, pp. 286–291.
20. J. A. C. Patterson, D. G. McIlwraith, and G.-Z. Yang. A flexible, low noise reflective PPG sensor platform for ear-worn heart rate monitoring. *Sixth International Workshop on Wearable and Implantable Body Sensor Networks*. Berkeley, CA, 2009, pp. 286–291.
21. K. F. Wu, C. H. Chan, and Y. T. Zhang. Contactless and cuffless monitoring of blood pressure on a chair using e-textile materials. *3rd IEEE/EMBS International Summer School on Medical Devices and Biosensors*. Cambridge, MA, 2006, pp. 98–100.
22. Y. M. Chi, T. P. Jung, and G. Cauwenberghs. Dry-contact and noncontact biopotential electrodes: methodological review. *IEEE Rev. Biomed. Eng.*, vol. 3, pp. 106–119, 2010.
23. W. B. Gu, C. C. Y. Poon, H. K. Leung, M. Y. Sy, M. Y. M. Wong, and Y. T. Zhang. A novel method for the contactless and continuous measurement of arterial blood pressure on a sleeping bed. *Annual International Conference of the IEEE Engineering in Medicine and Biology Society*, 2009, pp. 6084–6086.
24. P. Chulsung, P. H. Chou, B. Ying, R. Matthews, and A. Hibbs. An ultra-wearable, wireless, low power ECG monitoring system. *IEEE Biomedical Circuits and Systems Conference*. London, 2006, pp. 241–244.
25. H. Baek, G. Chung, K. Kim, and K. Park. A smart health monitoring chair for nonintrusive measurement of biological signals. *IEEE Trans. Inf. Technol. Biomed.*, vol. 16, no. 1, pp. 150–158, 2012.
26. B. Hyun Jae, C. Gih Sung, K. Ko Keun, K. Jung Soo, and P. Kwang Suk. Photoplethysmogram measurement without direct skin-to-sensor contact using an adaptive light source intensity control. *IEEE Trans. Inf. Technol. Biomed.*, vol. 13, no. 6, pp. 1085–1088, Nov. 2009.
27. M. Ishijima. Monitoring of electrocardiograms in bed without utilizing body surface electrodes. *IEEE Trans. Biomed. Eng.*, vol. 40, no. 6, pp. 593–594, Jun 1993.
28. A. Aleksandrowicz and S. Leonhardt. Wireless and non-contact ECG measurement system–the Aachen SmartChair. *Acta Polytechnica*, vol. 2, pp. 68–71, 2007.
29. Y. Yama, A. Ueno, and Y. Uchikawa. Development of a wireless capacitive sensor for ambulatory ECG monitoring over clothes. *29th Annual International Conference of the IEEE Engineering in Medicine and Biology Society.* Lyon, 2007, pp. 5727–5730.
30. S. Fuhrhop, S. Lamparth, and S. Heuer. A textile integrated long-term ECG monitor with capacitively coupled electrodes. *IEEE Biomedical Circuits and Systems Conference*. Beijing, 2009, pp. 21–24.
31. Y. M. Chi and G. Cauwenberghs. Wireless non-contact EEG/ECG electrodes for body sensor networks. *International Conference on Body Sensor Networks.* Singapore, 2010, pp. 297–301.

32. E. Nemati, M. J. Deen, and T. Mondal. A wireless wearable ECG sensor for long-term applications. *IEEE Commun. Mag.*, vol. 50, no. 1, pp. 36–43, 2012.
33. H. H. Asada, P. Shaltis, A. Reisner, R. Sokwoo, and R. C. Hutchinson. Mobile monitoring with wearable photoplethysmographic biosensors. *IEEE Eng Med Biol*, vol. 22, no. 3, pp. 28–40, 2003.
34. P. GuoChen and M. F. Bocko. Non-contact ECG sensing employing gradiometer electrodes. *IEEE Trans. Biomed. Eng.*, vol. 60, no. 1, pp. 179–183, Jan. 2013.
35. P. Celka, C. Verjus, R. Vetter, P. Renevey, and V. Neuman. Motion resistant earphone located infrared based heart rate measurement device. *Biomed. Eng.*, 2004.
36. Y. Mendelson, R. J. Duckworth, and G. Comtois. A wearable reflectance pulse oximeter for remote physiological monitoring. *28th Annual International Conference of the IEEE Engineering in Medicine and Biology Society.* New York, NY, 2006, pp. 912–915.
37. W. Lei, B. Lo, and G.-Z. Yang. Multichannel reflective PPG earpiece sensor with passive motion cancellation. *IEEE Trans. Biomed. Circuits Syst.*, vol. 1, no. 4, pp. 235–241, 2007.
38. J. Spigulis, R. Erts, V. Nikiforovs, and E. Kviesis-Kipge. Wearable wireless photoplethysmography sensors. *Photonics Europe*, 2008, pp. 69912O1-7.
39. S. Vogel, M. Hulsbusch, T. Hennig, V. Blazek, and S. Leonhardt, "In-ear vital signs monitoring using a novel microoptic reflective sensor," *IEEE Trans. Inf. Technol. Biomed.*, vol. 13, no. 6, pp. 882–889, 2009.
40. K. Shin, Y. Kim, S. Bae, K. Park, and S. Kim. A novel headset with a transmissive PPG sensor for heart rate measurement. *13th International Conference on Biomedical Engineering,* vol. 23. C. Lim and J. H. Goh, eds. Springer Berlin Heidelberg, 2009, pp. 519–522.
41. M.-Z. Poh, K. Kim, et al. Cardiovascular monitoring using earphones and a mobile device. *IEEE Pervasive Comput.*, vol. 11, no. 4, pp. 18–26, 2012.
42. M. Z. Poh, N. C. Swenson, and R. W. Picard. Motion-tolerant magnetic earring sensor and wireless earpiece for wearable photoplethysmography. *IEEE Trans. Inf. Technol. Biomed.*, vol. 14, no. 3, pp. 786–794, 2010.
43. Y. L. Zheng, B. Leung, S. Sy, Y. T. Zhang, and C. C. Y. Poon. A clip-free eyeglasses-based wearable monitoring device for measuring photoplethysmograhic signals. *34th Annual International Conference of the IEEE Engineering in Medicine and Biology Society* (EMBC). San Diego, 2012, pp. 5022–5025.
44. Y. H. Lin, C. F. Lin, and H. Z. You. A driver's physiological monitoring system based on a wearable PPG sensor and a smartphone. *Security-Enriched Urban Computing and Smart Grid*, vol. 223. R.-S. Chang, et al., eds. Springer Berlin Heidelberg, 2011, pp. 326–335.
45. F. Lamonaca, Y. Kurylyak, D. Grimaldi, and V. Spagnuolo. Reliable pulse rate evaluation by smartphone. *IEEE International Symposium on Medical Measurements and Applications Proceedings*. Budapest, 2012, pp. 1–4.
46. W. Chen, T. Kobayashi, S. Ichikawa, Y. Takeuchi, and T. Togawa. Continuous estimation of systolic blood pressure using the pulse arrival time and intermittent calibration. *Medical & Biological Engineering & Computing,* vol. 38, no. 5, pp. 569–574, Sep. 2000.
47. C. C. Poon and Y. T. Zhang. Cuff-less and noninvasive measurements of arterial blood pressure by pulse transit time. *Proc. 27th Annu. Int. Conf. IEEE Engineering in Medicine and Biology Society*. Shanghai, China, 2005, pp. 5877–5880.
48. D. B. McCombie, A. T. Reisner, and H. H. Asada. Adaptive blood pressure estimation from wearable PPG sensors using peripheral artery pulse wave velocity measurements and multi-channel blind identification of local arterial dynamics. *Proc. 28th Annu. Int. Conf. IEEE Engineering in Medicine and Biology Society.* New York, USA, 2006, pp. 3521–3524.
49. H. Gesche, D. Grosskurth, G. Kuchler, and A. Patzak. Continuous blood pressure measurement by using the pulse transit time: comparison to a cuff-based method. *European Journal of Applied Physiology*, vol. 112, no. 1, pp. 309–315, Jan. 2012.
50. J. Y. A. Foo, C. S. Lim, and P. Wang. Evaluation of blood pressure changes using vascular transit time. *Blood Press Monitoring*, vol. 27, no. 8, pp. 685–694, Aug. 2006.
51. Y. Chen, C. Wen, G. Tao, M. Bi, and G. Li. Continuous and noninvasive blood pressure measurement: a novel modeling methodology of the relationship between blood pressure and pulse wave velocity. *Ann. Biomed. Eng.*, vol. 37, no. 11, pp. 2222–2233, Nov. 2009.
52. C. C. Poon, Y.-T. Zhang, and Y. Liu. Modeling of pulse transit time under the effects of hydrostatic pressure for cuffless blood pressure measurements. *3rd IEEE/EMBS International Summer School on Medical Devices and Biosensors*, 2006, pp. 65–68.
53. F. Axisa, P. M. Schmitt, C. Gehin, G. Delhomme, E. McAdams, and A. Dittmar. Flexible technologies and smart clothing for citizen medicine, home healthcare, and disease prevention. *IEEE Trans. Inf. Technol. Biomed.,* vol. 9, no. 3, pp. 325–336, Sep. 2005.

54. D. H. Kim, N. Lu, R. Ma, Y. S. Kim, R. H. Kim, S. Wang, J. Wu, S. M. Won, H. Tao, A. Islam, K. J. Yu, T. I. Kim, R. Chowdhury, M. Ying, L. Xu, M. Li, H. J. Chung, H. Keum, M. McCormick, P. Liu, Y. W. Zhang, F. G. Omenetto, Y. Huang, T. Coleman, and J. A. Rogers. Epidermal electronics. *Science*, vol. 333, no. 6044, pp. 838–843, Aug 12, 2011.
55. W. B. Gu, C. C. Poon, H. K. Leung, M. Y. Sy, M. Y. Wong, and Y. T. Zhang. A novel method for the contactless and continuous measurement of arterial blood pressure on a sleeping bed. *Proc. Annu. Int. Conf. IEEE Engineering in Medicine and Biology Society.* Minneapolis, USA, 2009, pp. 6084–6086.
56. R. A. Payne, C. N. Symeonides, D. J. Webb, and S. R. Maxwell. Pulse transit time measured from the ECG: an unreliable marker of beat-to-beat blood pressure. *J. Appl. Physiol.*, vol. 100, no. 1, pp. 136–141, Jan. 2006.
57. Y. T. Zhang, C. C. Y. Poon, and E. MacPherson. Editorial note on health informatics. *IEEE Trans. Inf. Technol. Biomed.*, vol. 13, no. 3, pp. 281–283, May 2009.
58. Y. Lin. A natural contact sensor paradigm for nonintrusive and real-time sensing of biosignals in human-machine interactions. *IEEE Sens. J.*, vol. 11, no. 3, pp. 522–529, Mar. 2011.
59. W. B. Gu, C. C. Y. Poon, M. Y. Sy, H. K. Leung, Y. P. Liang, and Y. T. Zhang. A h-shirt-based body sensor network for cuffless calibration and estimation of arterial blood pressure. *Sixth International Workshop on Wearable and Implantable Body Sensor Networks* (BSN). Berkeley, CA, 2009, pp. 151–155.
60. B. Lo, G.-Z. Yang, and J. Pansiot. Bayesian analysis of sub-plantar ground reaction force with BSN. *Sixth International Workshop on Wearable and Implantable Body Sensor Networks.* Berkeley, CA, 2009, pp. 133–137.
61. T. Yamada, Y. Hayamizu, Y. Yamamoto, Y. Yomogida, A. Izadi-Najafabadi, D. N. Futaba, and K. Hata. A stretchable carbon nanotube strain sensor for human-motion detection. *Nat. Nanotechnol.*, vol. 6, no. 5, pp. 296–301, May 2011.
62. Y. C. Wu, C. S. Chang, Y. Sawaguchi, W. C. Yu, M. J. Chen, J. Y. Lin, S. M. Liu, C. C. Han, and W. Liang. A mobile-phone-based health management system. *Health Management - Different Approaches and Solutions*, K. Śmigórski, ed. InTech, 2011.
63. C. C. Y. Poon and Y. T. Zhang. Perspectives on high technologies for low-cost healthcare. *IEEE Eng Med Biol*, vol. 27, no. 5, pp. 42–47, 2008.
64. L. Atallah, et al. Sensor positioning for activity recognition using wearable accelerometers. *IEEE Trans. Biomed. Circuits Syst.*, vol. 5, no. 4, pp. 320–329, Aug. 2011.
65. N. Golmie, D. Cypher, and O. Rébala. Performance analysis of low rate wireless technologies for medical applications. *Comput. Commun.*, vol. 28, no. 10, pp. 1266–1275, 2005.
66. K. Kang, J. Ryu, J. Hur, and L. Sha. Design and QoS of a wireless system for real-time remote electrocardiography. *IEEE Journal of Biomedical and Health Informatics*, vol. 17, no. 3, pp. 745–755, 2013.
67. P. J. Hunter and T. K. Borg. Integration from proteins to organs: the Physiome Project. *Nat. Rev. Mol. Cell Biol.*, vol. 4, no. 3, pp. 237–243, Mar 2003.
68. A. F. Frangi, W. J. Niessen, and M. A. Viergever. Three-dimensional modeling for functional analysis of cardiac images: a review. *IEEE Transactions on Medical Imaging*, vol. 20, no. 1, pp. 2–25, 2001.
69. H. Wang and A. A. Amini. Cardiac motion and deformation recovery from MRI: a review. *IEEE Transactions on Medical Imaging*, vol. 31, no. 2, pp. 487–503, 2012.
70. Y. Lecun, Y. Bengio, and G. Hinton. Deep learning. *Nature*, vol. 521, no. 5773, pp. 436–444, 2015.
71. G. Litjens et al. A Survey on Deep Learning in Medical Image Analysis (2017).
72. J. S. Duncan et al. Measurement of non-rigid motion using contour shape descriptors. *Proceedings Computer Vision and Pattern Recognition, CVPR '91.* IEEE, 1991, pp. 318–324.
73. W. Press et al. Numerical recipes. *The Art of Scientific Computing.* New York: Cambridge Univ. Press. 1988.
74. A. Radeva, A. Amini, and J. Huang. Deformable B-solids and implicit snakes for 3D localization and tracking of SPAMM MRI data. *Comput. Vis. Image Understand.*, vol. 66, no. 2, pp. 163–178, May 1997.
75. J. Huang, D. Abendschein, V. G. Dávila-Román, and A. A. Amini. Spatio-temporal tracking of myocardial deformations with a 4-D B-spline model from tagged MRI. *IEEE Trans. Med. Imag.*, vol. 18, no. 10, pp. 957–972, Oct. 1999.
76. R. E. Bellman and S. E. Dreyfus. *Applied Dynamic Programming.* Princeton University. 1962.
77. A. Amini, S. Tehrani, and T. Weymouth. Using dynamic programming for minimizing the energy of active contours in the presence of hard constraints. *Proc. Second Int. Conf. Computer Vision*, Tarpon Springs, FL, Dec. 1988.
78. A. A. Amini, T. E. Weymouth, and R. C. Jain. Using dynamic programming for solving variational problems in vision. *IEEE Transactions on Pattern Analysis & Machine Intelligence*, vol. 12, no. 9, pp. 855–867, 1990.

79. S. M. Stigler. Gauss and the invention of least squares. *Annals of Statistics*, vol. 9, no. 3, pp. 465–474, 1981.
80. J. Declerck, J. Feldmar, and N. Ayache. Definition of a four-dimensional continuous planisferic transformation for the tracking and the analysis of the left-ventricle motion. *Med. Image Anal.*, vol. 2, no. 2, pp. 197–213, June 1998.
81. J. Declerck, J. Feldmar, M. L. Goris, and F. Betting. Automatic registration and alignment on a template of cardiac stress and rest SPECT images. *IEEE Trans. Med. Imag.*, vol. 16, pp. 727–737, Dec. 1997.
82. P. J. Besl and N. D. McKay. A method for registration of 3D shapes. *IEEE Trans. Pattern Anal. Machine Intell.*, vol. 14, pp. 239–255, Feb. 1992.
83. T. W. Sederberg and S. R. Parry. Free-form deformation of solid geometric models. *Proc. SIGGRAPH'86,* vol. 20, pp. 151–160.
84. T. Basar. A new approach to linear filtering and prediction problems. *Control Theory: Twenty-Five Seminal Papers (1932–1981).* Wiley-IEEE Press, 2009, pp. 167–179.
85. S. Dan. *Optimal State Estimation: Kalman, H∞, and Nonlinear Approaches*. Wiley-Interscience, 2006.
86. F. G. Meyer et al. Tracking myocardial deformation using phase contrast MR velocity fields: a stochastic approach. *IEEE Transactions on Medical Imaging*, vol. 15, no. 4, pp. 453–465, 1996.
87. J. Stoitsis et al. A mathematical model of the mechanical deformation of the carotid artery wall and its application to clinical data. *International Conference of the Engineering in Medicine and Biology Society*, 2007, pp. 2163–2166.
88. S. Golemati et al. Comparison of block matching and differential methods for motion analysis of the carotid artery wall from ultrasound images. *IEEE Transactions on Information Technology in Biomedicine A Publication of the IEEE Engineering in Medicine & Biology Society*, vol. 16, no. 5, pp. 852–858, 2012.
89. P. Shi and H. Liu. Stochastic finite element framework for cardiac kinematics function and material property analysis. *Medical Image Computing and Computer-Assisted Intervention MICCAI 2002*. Springer Berlin Heidelberg, 2002, pp. 634–641.
90. Z. Gao, et al. Carotid artery wall motion estimated from ultrasound imaging sequences using a nonlinear state space approach. *Medical Image Computing and Computer-Assisted Intervention MICCAI 2016*. Springer International Publishing, 2016.
91. M. Lu, et al. Reconstruction of elasticity: a stochastic model-based approach in ultrasound elastography. *Biomedical Engineering Online*, vol. 12, no. 1, p. 79, 2013.
92. K. C. L. Wong, et al. Physiological fusion of functional and structural data for cardiac deformation recovery. *IEEE Transactions on Medical Imaging*, vol. 30, no. 4, pp. 990–1000, 2011.
93. B. Hassibi, A. H. Sayed, and T. Kailath. Indefinite-quadratic estimation and control: a unified approach to H 2, and, H∞, theories. *Society for Industrial and Applied Mathematics*, 1999.
94. H. Liu and P. Shi. Cardiac motion and elasticity characterization with iterative sequential, H_∞ criteria. *Medical Image Computing and Computer-Assisted Intervention – MICCAI 2004*. Springer Berlin Heidelberg, 2004, pp. 34–42.
95. E. W. B. Lo, H. Liu, and P. Shi. H∞, filtering and physical modeling for robust kinematics estimation. *Proceedings IEEE Xplore, International Conference on Image Processing, ICIP*, vol. 3, 2003, pp. II-169–172.
96. Z. Gao, et al. Motion estimation of common carotid artery wall using a H∞ filter based block matching method. *International Conference on Medical Image Computing and Computer Assisted Intervention*, 2015, pp. 443–450.
97. Z. Gao, H. Xiong, X. Liu, et al. Robust estimation of carotid artery wall motion using the elasticity-based state-space approach. *Medical Image Analysis*, vol. 37, 2017, p. 1.
98. M. R. Avendi, A. Kheradvar, and H. Jafarkhani. A combined deep-learning and deformable-model approach to fully automatic segmentation of the left ventricle in cardiac MRI. *Medical Image Analysis*, vol. 30, pp. 108–119, 2016.
99. R. P. K. Poudel, P. Lamata, and G. Montana. Recurrent fully convolutional neural networks for multi-slice MRI cardiac segmentation. *Reconstruction, Segmentation, and Analysis of Medical Images.* Springer International Publishing, 2016.
100. C. Rupprecht, et al. *Deep Active Contours*. 2016.
101. P. V. Tran. A fully convolutional neural network for cardiac segmentation in short-axis MRI. arXiv:1604.00494, 2016.
102. H. Yang, et al. *Deep Fusion Net for Multi-Atlas Segmentation: Application to Cardiac MR Images*, 2016.

103. T. A. Ngo, Z. Lu, and G. Carneiro. Combining deep learning and level set for the automated segmentation of the left ventricle of the heart from cardiac cine magnetic resonance. *Medical Image Analysis*, vol. 35, p. 159, 2017.
104. G. Carneiro and J. C. Nascimento. Combining multiple dynamic models and deep learning architectures for tracking the left ventricle endocardium in ultrasound data. *IEEE Transactions on Pattern Analysis & Machine Intelligence*, vol. 35, no. 11, pp. 2592–2607, 2013.
105. G. Carneiro, J. C. Nascimento, and A. Freitas. The segmentation of the left ventricle of the heart from ultrasound data using deep learning architectures and derivative-based search methods. *IEEE Transactions on Image Processing A Publication of the IEEE Signal Processing Society*, vol. 21, no. 3, pp. 968–982, 2012.
106. J. C. Nascimento and G. Carneiro. Multi-atlas segmentation using manifold learning with deep belief networks. *International Symposium on Biomedical Imaging*, IEEE, 2016, pp. 867–871.
107. M. Zreik et al. Automatic segmentation of the left ventricle in cardiac CT angiography using convolutional neural networks. *International Symposium on Biomedical Imaging*, IEEE, 2016, pp. 40–43.
108. N. Lessmann et al. Deep convolutional neural networks for automatic coronary calcium scoring in a screening study with low-dose chest CT. 2016, p. 978511.
109. J. M. Wolterink, et al. Automatic coronary calcium scoring in cardiac CT angiography using convolutional neural networks. *Medical Image Computing and Computer-Assisted Intervention – MICCAI 2015*. Springer International Publishing, 2015, pp. 589–596.
110. O. Oktay, et al. Multi-input cardiac image super-resolution using convolutional neural networks. *International Conference on Medical Image Computing and Computer-Assisted Intervention*, Springer International Publishing, 2016, pp. 246–254.
111. B. Kong, Y. Zhan, M. Shin, M., et al. Recognizing end-diastole and end-systole frames via deep temporal regression network. *Med Image Comput Comput Assist Interv.*, vol. 9901 of *Lect Notes Comput Sci.*, pp. 264–272, 2016.
112. R. P. K. Poudel, P. Lamata, and G. Montana. Recurrent fully convolutional neural networks for multi-slice MRI cardiac segmentation. *Reconstruction, Segmentation, and Analysis of Medical Images*. Springer International Publishing, 2016.
113. B. Khaleghi. *Multisensor Data Fusion: A Review of the State-of-the-Art*. 2013.
114. S. Paeme, K. T. Moorhead, J. G. Chase, B. Lambermont, P. Kolh, V. D'Orio, L. Pierard, M. Moonen, P. Lancellotti, P. C. Dauby, and T. Desaive. Mathematical multi-scale model of the cardiovascular system including mitral valve dynamics. Application to ischemic mitral insufficiency. *Biomed. Eng. Online*, vol. 10, pp. 86, 2011.
115. H. K. Yun. Book Review: the creative destruction of medicine: how the digital revolution will create better healthcare. *Journal of Gynecologic Oncology*, vol. 24, no. 1, pp. 98–99, 2013.
116. D. A. Nordsletten, S. A. Niederer, M. P. Nash, P. J. Hunter, and N. P. Smith. Coupling multi-physics models to cardiac mechanics. *Prog. Biophys. Mol. Biol.*, vol. 104, no. 1–3, pp. 77–88, Jan. 2011.
117. D. A. Beard, M. L. Neal, N. Tabesh-Saleki, C. T. Thompson, J. B. Bassingthwaighte, M. Shimoyama, and B. E. Carlson. Multiscale modeling and data integration in the virtual physiological rat project. *Ann. Biomed. Eng.*, vol. 40, no. 11, pp. 2365–2378, Nov. 2012.
118. F. Y. Liang, S. Takagi, R. Himeno, and H. Liu. Biomechanical characterization of ventricular-arterial coupling during aging: a multi-scale model study. *J. Biomech.*, vol. 42, no. 6, pp. 692–704, Apr. 16, 2009.
119. B. Khaleghi, A. Khamis, F. O. Karray, and S. N. Razavi. Multisensor data fusion: a review of the state-of-the-art. *Inf. Fusion*, vol. 14, no. 1, pp. 28–44, 2013.
120. F. E. White. *Data Fusion Lexicon*. San Diego: Joint Directors of Laboratories, Technical Panel for C3, Data Fusion Sub-Panel, Naval Ocean Systems Center. 1991.
121. H. Boström, S. F. Andler, M. Brohede, R. Johansson, A. Karlsson, J. van Laere, L. Niklasson, M. Nilsson, A. Persson, and T. Ziemke. *On the Definition of Information Fusion as a Field of Research*. University of Skövde, School of Humanities and Informatics. 2007.
122. Y. Huang, P. McCullagh, N. Black, and R. Harper. Feature selection and classification model construction on type 2 diabetic patients' data. *Artif. Intell. Med.*, vol. 41, no. 3, pp. 251–262, Nov. 2007.
123. M. J. O'Connor, R. D. Shankar, D. B. Parrish, and A. K. Das. Knowledge-data integration for temporal reasoning in a clinical trial system. *Int. J. Med. Inform.*, vol. 78, Supplement 1, pp. S77–S85, 2009.
124. X. Wang, H. Chase, M. Markatou, G. Hripcsak, and C. Friedman. Selecting information in electronic health records for knowledge acquisition. *J. Biomed. Inform.*, vol. 43, no. 4, pp. 595–601, 2010.
125. G. N. Noren, J. Hopstadius, A. Bate, K. Star, and I. R. Edwards. Temporal pattern discovery in longitudinal electronic patient records. *Data Min. Knowl. Discov.*, vol. 20, no. 3, pp. 361–387, May 2010.

126. B. Firoozbakhsh, N. Jayant, S. Park, and S. Jayaraman. Wireless communication of vital signs using the Georgia Tech Wearable Motherboard. *IEEE International Conference on Multimedia and Expo* (ICME), New York, 2000, pp. 1253–1256.
127. T. Linz, C. Kallmayer, R. Aschenbrenner, and H. Reichl. Fully integrated EKG shirt based on embroidered electrical interconnections with conductive yarn and miniaturized flexible electronics. *International Workshop on Wearable and Implantable Body Sensor Networks*, Cambridge, MA, 2006.
128. P. Grossman. The LifeShirt: a multi-function ambulatory system monitoring health, disease, and medical intervention in the real world. *Wearable ehealth Systems for Personalised Health Management: State of the Art and Future Challenges.* A. Lymberis and D. E. D. Rossi, eds. Headington: IOS Press. 2004. pp. 133–141.
129. D. Curone, E. L. Secco, A. Tognetti, G. Loriga, G. Dudnik, M. Risatti, R. Whyte, A. Bonfiglio, and G. Magenes. Smart garments for emergency operators: The ProeTEX project. *IEEE Trans. Inf. Technol. Biomed.*, vol. 14, no. 3, pp. 694–701, May 2010.
130. R. Paradiso, G. Loriga, and N. Taccini. A wearable health care system based on knitted integrated sensors. *IEEE Trans. Inf. Technol. Biomed.*, vol. 9, no. 3, pp. 337–344, Sep. 2005.
131. N. Noury, A. Dittmar, C. Corroy, R. Baghai, J. L. Weber, D. Blanc, F. Klefstat, A. Blinovska, S. Vaysse, and B. Comet. VTAMN - A smart cloth for ambulatory remote monitoring of physiological parameters and activity. *26th Annual International Conference of the IEEE Engineering in Medicine and Biology Society*, San Francisco, CA, 2004, pp. 3266–3269.
132. W. B. Gu, C. C. Y. Poon, M. Y. Sy, H. K. Leung, Y. P. Liang, and Y. T. Zhang. A h-shirt-based body sensor network for cuffless calibration and estimation of arterial blood pressure. *Sixth International Workshop on Wearable and Implantable Body Sensor Networks (BSN).* Berkeley, CA, 2009, pp. 151–155.
133. H. K. Yun. Book Review: the creative destruction of medicine: how the digital revolution will create better healthcare. *Journal of Gynecologic Oncology*, vol. 24, no. 1, pp. 98–99, 2013.

8 Automatic Segmentation of Cardiac Substructures for Radiation Oncology Applications

Jinzhong Yang[1], *Rongrong Zhou*[2], *Yangkun Luo*[3], *Zhongxing Liao*[1]
[1]University of Texas MD Anderson Cancer Center
[2]Central South University
[3]Sichuan Cancer Hospital

CONTENTS

8.1 INTRODUCTION

Modern radiotherapy techniques such as intensity-modulated radiation therapy (IMRT) and combinations of those techniques with chemotherapy have greatly improved the overall survival of cancer patients. However, radiation-induced cardiac side effects, which often manifest years after treatment, have been shown to offset this improvement [1–4]. Cardiac toxicity has been seen in patients treated for lymphoma, breast cancer, and lung cancer [5–9]. Cardiac exposure was shown as a negative prognostic factor for patients with lung cancer after concurrent chemotherapy and radiotherapy. In the most recent report of a phase III trial, the volume of the heart received as low as 5 Gy negatively impacted on the overall survival [10]. Cardiac injury is not limited to the myocardium. Radiation may also damage the vascular endothelium and capillary vessels, resulting in peripheral, coronary, and carotid artery disease [11]. Most previous reports used the whole heart as a single region of interest; however, the relationship between dose to cardiac substructures and subsequent toxicity is of great interest and has not been well defined, mainly due to the inconsistency and demand of time in cardiac substructure delineation from computed tomography (CT) images [2].

Manual contouring of cardiac substructures from CT images requires clinical knowledge, time, and effort. Cardiac substructures are not clearly distinguishable in the noncontrast CT normally used for treatment planning. Although cardiac substructures are more visible on magnetic resonance images and contrast CT images, these image modalities are usually unavailable for treatment planning. In addition, cardiac and respiratory motions and anatomical variations also present a great challenge to defining cardiac substructures. Furthermore, manual contouring of structures with inadequate image contrast, like cardiac substructures, can be unreliable because of substantial inter-observer variability [12,13].

Although heart dose is an important factor in overall survival, to date substantial variability in heart contouring has prevented accurate correlative study of heart dose and cardiac toxicity [10]. Heart exposure is associated with a broad spectrum of cardiac toxicity depending on the extent of damage to various heart substructures [6]. Determining the relationship between heart dose and cardiac toxicity requires ways of consistently and accurately generating contours for cardiac substructures. A few studies have been reported on the use of automatic segmentation of cardiac substructures [14,15]. Our previous study of using a set of cardiac atlases with multi-atlas segmentation to automatically contour 15 cardiac substructures revealed that automatic-segmentation contouring was within one standard deviation of the variability of manual contouring by experts [16]. Auto-segmented contours could still need modification by clinical specialists to conform to the corresponding anatomy; however, whether modification is needed when auto-segmented contours are used for dosimetric analysis is unknown.

In this chapter, we reported our development of a set of cardiac atlases with well-defined cardiac substructure contours for multi-atlas segmentation. We validated the auto-contouring using these cardiac atlases by comparing auto-segmentation with manual delineation and inter-observer variability. We demonstrated that accurate and consistent cardiac contours could be generated with this development. In addition, we evaluated the extent of the modification needed for auto-segmented cardiac substructures and whether those modifications would influence dosimetric variables in clinical practice.

8.2 METHODS AND MATERIALS

8.2.1 Patient Data

This study was approved by the institutional review board of the MD Anderson Cancer Center. First, six patients with malignancies located in the thorax were retrospectively identified as the first group of patients for this study. The selection criteria were that they all had both contrast and noncontrast diagnostic chest CT scans acquired in the same imaging session and the noncontrast

CT images could be reconstructed to the same display field of view similar to those used for thoracic radiation treatment planning. These six patients were used as the development dataset to generate gold standard cardiac atlas. As a regular procedure, the images were acquired while the patients held their breath and had their arms above their heads. A pre-contrast CT image was acquired first. With the patient still on the table, a post-contrast CT image was acquired about 3 minutes later. For post-contrast CT image acquisition, systolic- and diastolic-phase images were scanned and averaged.

Next, 55 patients with non-small cell lung cancer (NSCLC) treated with definitive chemoradiation with IMRT or passive scattering proton beam therapy to a dose of 74 Gy in 37 fractions in a randomized clinical trial were retrospectively identified for this study, and their treatment plans, including simulation CT scans and dose distribution, were extracted from an institutional database. They were selected randomly without special restrictions on gender, heart anatomy, or body anatomy. As a selection criterion, only those patients receiving substantial heart dose were included. Patients with significant lung necrosis or lung collapse were excluded. Treatment simulation was performed with the patients' arms above their heads in the supine position and immobilization with custom Vac-Lok cradles (Civco Medical Solutions, Kalona, IA). All 55 patients underwent four-dimensional CT (4DCT) for treatment planning, and the averaged 4DCT image was used for planning CT, on which the cardiac contours were delineated. All CT images in two groups had an in-slice resolution of 1.0 mm and slice spacing of 2.5 mm. The CT image quality is normal in our current clinical practice.

8.2.2 Cardiac Atlas Development

In combined previous studies [17–19] and our own experience, we found that a total of 12 atlases can be sufficient for obtaining robust multi-atlas segmentation for thoracic CT images. Because of the limitation of available contrast CT images, here we developed 12 cardiac atlases in two phases. First, contours were drawn manually on the first group of six patients with both contrast and non-contrast CT images. Because cardiac substructures are almost indistinguishable in noncontrast CT images, contrast CT is considered the gold standard for delineation of the heart substructures and can help reduce ambiguity in manual contouring. Second, the set of atlases was expanded to include a second group of six additional patients. The overall atlas development process was described in Figure 8.1.

8.2.2.1 Phase I: Manual Contouring

The diagnostic images of the first group of six patients were imported into the Pinnacle treatment planning system (Philips Medical Systems, Fitchburg, WI) for manual contouring. The contrast CT image was fused with the noncontrast CT image using rigid-registration in Pinnacle. Manual contouring was performed by eight radiation oncologists: two specialists in thoracic cancer radiotherapy, two specialists in lymphoma radiotherapy, and four radiation oncologists trained outside the United States with various levels of experience. Before manual delineation, the eight radiation oncologists reviewed the RTOG (Radiation Therapy Oncology Group) 1106 organ-at-risk contouring guideline [20] and a published cardiac atlas consensus contouring guideline [21] as a group. Each of the eight oncologists manually and independently delineated 15 cardiac structures on noncontrast CT images by referring to the fused contrast CT image and *Netter's Atlas of Human Anatomy* [22] and by following the aforementioned contouring guidelines. The 15 delineated structures were the whole heart, the four heart chambers (left atrium, right atrium, left ventricle, and right ventricle), four coronary arteries (left main coronary artery, left anterior descending artery, left circumflex artery, and right coronary artery), and six great vessels (superior vena cava, inferior vena cava, pulmonary artery, pulmonary vein, ascending aorta with the aortic arch, and descending aorta). The contours of each structure delineated by the eight radiation oncologists were fused to

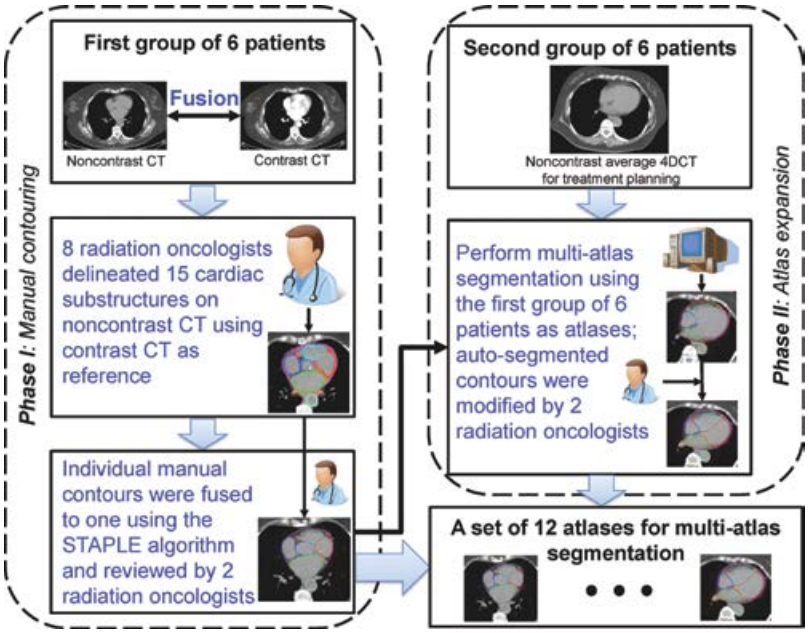

FIGURE 8.1 The overall framework of the atlas development. Please refer to the text for details.

one using the simultaneous truth and performance level estimation (STAPLE) algorithm for each patient [23]. The fused contours were further reviewed and edited by two radiation oncologists to ensure consistency across patients.

8.2.2.2 Phase II: Atlas Expansion

The noncontrast CT images of the first group of six patients and the modified contours were used in conjunction with the in-house Multi-Atlas Contouring Service (MACS) software (detailed in the next section) to automatically delineate the cardiac structures of six patients that were randomly selected from the 55 NSCLC patients. The auto-segmented contours for the second group of six patients were used as templates for manual contouring, and two radiation oncologists jointly contoured these six patients on the basis of the templates. Thus, a total of 12 patients, including the noncontrast CT images with well-defined contours, served as the final atlases for multi-atlas segmentation.

8.2.3 Multi-Atlas Segmentation

The in-house MACS software was used to perform multi-atlas segmentation. MACS has a user interface in the Pinnacle treatment planning system. For a new image to be segmented, users can submit the request in Pinnacle. MACS processes segmentation on a central server. The aforementioned 12 cardiac atlases were stored on the server. First, each atlas was separately registered to the new image using a dual-force Demons deformable registration algorithm [24]. The resultant deformation vector fields that characterized the individual deformable registration were used to deform the contours in each atlas to obtain individual segmentations [25]. Finally, we used the STAPLE algorithm with a built-in tissue appearance model [26] to combine the individual segmentations, generating a fusion contour that approximated the true segmentation. The contour fusion process allowed us to minimize variations among segmentations obtained from different atlases and random errors in deformable image registration. The MACS server sends the final fusion contour back

to Pinnacle to complete the auto-segmentation. The auto-segmentation in MACS is independent to treatment planning systems.

8.2.4 Evaluation Metrics

Let R and T represent two binary volumes and ∂R and ∂T represent the surface of these two volumes, respectively. The surface was generated from the binary volume using the marching cube algorithm from Insight Toolkit software [27] and represented by a triangular mesh with vertices resampled to be approximately 3 within 1 mm^3 space. We calculated the Dice similarity coefficient (DSC) for volumes R and T as:

$$DSC(R,T) = \frac{2|R \cap T|}{|R| + |T|}. \tag{8.1}$$

The DSC has a value between 0 and 1, with 1 indicating perfect agreement and 0 indicating no overlap. We also calculated the symmetric mean surface distance (MSD) between the two surfaces ∂R and ∂T [28]:

$$MSD(\partial R, \partial T) = \frac{1}{2}\left[\frac{\sum_{r\in\partial R} \min_{t\in\partial T} d(r,\, t)}{|\partial R|} + \frac{\sum_{t\in\partial T} \min_{r\in\partial R} d(t,\, r)}{|\partial T|}\right]. \tag{8.2}$$

where $d(\cdot,\cdot)$ stands for the Euclidian distance of two points and $|\cdot|$ denotes the number of points on a surface.

8.2.5 Atlas Validation

To validate the cardiac atlases we developed in section 2.2, we compared the auto-segmented contours using these atlases with the expert manual contours in terms of the inter-observer variability. In addition, we performed leave-one-out tests in using these atlases for auto-segmentation, by comparing the auto-segmented contours with the consensus contours generated from experts.

8.2.5.1 Inter-Observer Variability

Inter-observer variability was evaluated by comparing individual expert contours with the STAPLE fused contours for the first group of six patients. For each structure in each patient, the eight expert contours were compared with the fused contours individually using DSC and MSD metrics. For each structure, the mean ($\overline{DSC}_0$ and $\overline{MSD}_0$) and standard deviation (σ_{DSC_0} and σ_{MSD_0}) of 48 DSC and 48 MSD values were calculated to measure inter-observer variability. At the same time, we performed leave-one-out auto-segmentation using the fused contours without any modification for the six patients and evaluated the auto-segmented contours against the fused contours using DSC and MSD metrics. The mean ($\overline{DSC}_1$ and $\overline{MSD}_1$) and standard deviation of DSC and MSD were calculated for the six tests. Auto-segmentation was compared with inter-observer variability to evaluate the performance of auto-contouring for each structure using the following metric:

$$PV = \frac{1}{2}\left[\frac{\overline{DSC}_1 - \overline{DSC}_0}{\sigma_{DSC_0}} + \frac{\overline{MSD}_1 - \overline{MSD}_0}{\sigma_{MSD_0}}\right], \tag{8.3}$$

where $PV < 1$ means that auto-segmentation is within one standard deviation of expert contouring variability, indicating that auto-segmentation is comparable with manual contouring.

8.2.5.2 Leave-One-Out Validation

To validate the use of the atlases for auto-contouring, we performed 12 leave-one-out tests for the 12 cardiac atlas patients. In each test, one patient served as the test patient and the remaining 11 patients were used as atlases to auto-contouring the cardiac structures for the test patient using multi-atlas segmentation. We compared the auto-segmented contours with the atlas contours in the 12 tests in terms of DSCs and MSDs. The mean and standard deviation for the 12 tests were calculated to evaluate agreement for each structure.

8.2.6 Auto-Contouring Validation

The 12 cardiac atlases were used in MACS to delineate 11 cardiac substructures automatically for the remaining 49 NSCLC patients in the second patient group. The 11 cardiac substructures included the whole heart, the four heart chambers (left atrium, left ventricle, right atrium, and right ventricle), and the six great vessels (the ascending aorta, descending aorta, superior vena cava, inferior vena cava, pulmonary artery, and pulmonary vein). The coronary arteries were not included because we found that it is not possible to auto-segment them from noncontrast CT images in the atlas validation. The auto-segmented contours were then modified jointly by two experienced radiation oncologists who followed the contouring guidelines from RTOG 1106 [20] and a published consensus guideline on cardiac atlas contouring [21].

8.2.6.1 Geometric Evaluation

We quantitatively evaluate the geometric agreement between the modified and auto-segmented contours using DSC and MSD described in section 2.4. Previous studies have shown that a DSC > 0.7 was considered as a good agreement and possibly clinically acceptable [29, 30]. The MSD evaluated the distance between two contours and was used with DSC to determine a good geometric agreement or not. A smaller MSD indicates better agreement between two contours.

8.2.6.2 Dosimetric Evaluation

Dose-volume histograms (DVHs) were generated for both the auto-segmented and modified contours for each cardiac substructure. Representative metrics evaluated included the mean dose (Dmean) to the heart and its four chambers; the heart V30 (heart volume receiving dose ≥30 Gy); and the maximum dose (Dmax) to all six great vessels. We performed hypothesis testing to identify statistically significant differences between auto-segmented contours and modified contours in terms of dosimetric variables. We used paired Student's *t* tests for normally distributed data and Wilcoxon signed rank tests for non-normally distributed data. All analyses were done with SPSS version 17.0 (SPSS, Chicago, IL, USA). *P* values of <0.05 was considered to indicate statistically significant differences.

8.3 RESULTS

8.3.1 Cardiac Atlases

The final cardiac atlases were composed of 12 patients: the first group of six patients with diagnostic CT scans and the second group of six NSCLC patients. The first group included the noncontrast CT image and the edited fused contours, while the second group included the averaged 4DCT image and the edited auto-segmented contours. The atlases were used together with MACS to

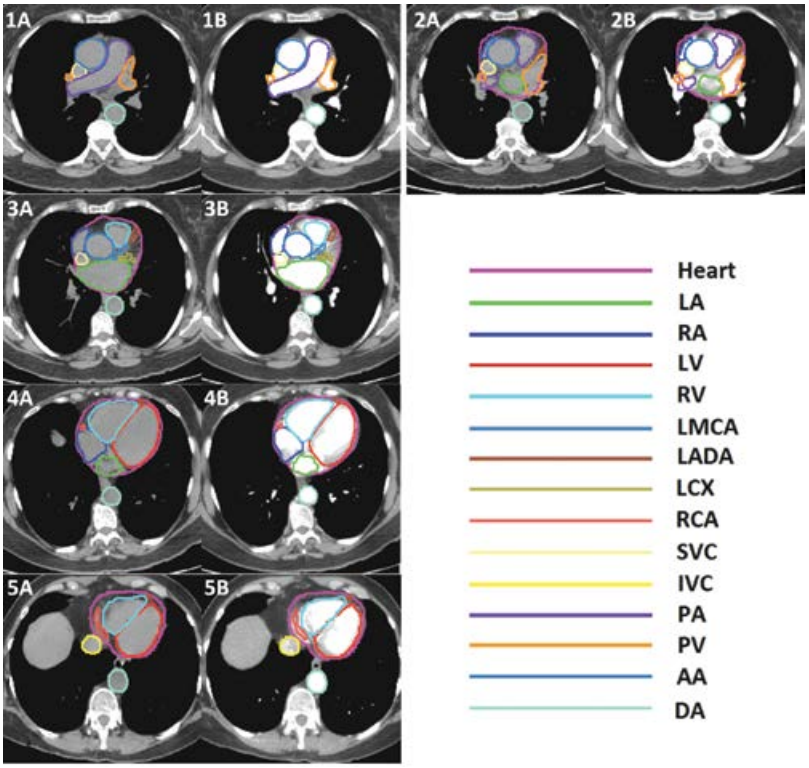

FIGURE 8.2 Atlas contours overlaid on noncontrast (panels A) and contrast (panels B) CT images from one patient. LA = left atrium; RA = right atrium; LV = left ventricle; RV = right ventricle; LMCA = left main coronary artery; LADA = left anterior descending artery; LCX = left circumflex artery; RCA = right coronary artery; SVC = superior vena cava; IVC = inferior vena cava; PA = pulmonary artery; PV = pulmonary vein; AA = ascending aorta and aortic arch; DA = descending aorta.

automatically delineate cardiac substructures in the Pinnacle treatment planning system. Figure 8.2 shows one atlas with contours overlaid on the contrast and noncontrast CT images. The average time for manually contouring the 15 cardiac substructures was about 40 minutes (range: 35 to 50 minutes), with the contrast CT available for reference. The average time for the MACS to automatically delineate the 15 cardiac substructures was about 10 minutes per patient, with the MACS running on a Microsoft Windows PC with an eight-core CPU (2 Intel Xeon X5472 quad-core processors at 3GHz) and 8GB of memory.

8.3.2 Atlas Validation

8.3.2.1 Inter-Observer Variability

Figure 8.3 shows a comparison of inter-observer variability in manual contouring with auto-segmentation for the first group of six patients. Inter-observer variability was smaller for the heart, the four chambers, and the aorta than for other structures that were not clearly distinguishable on the CT image, such as the pulmonary vein and coronary arteries. The mean DSCs for individual expert contours relative to the fused contours were less than 0.5 for coronary arteries and the pulmonary vein, and the mean MSDs were greater than 4.0 mm, indicating a very large inter-observer variability. The largest MSD for deviation of expert contours from

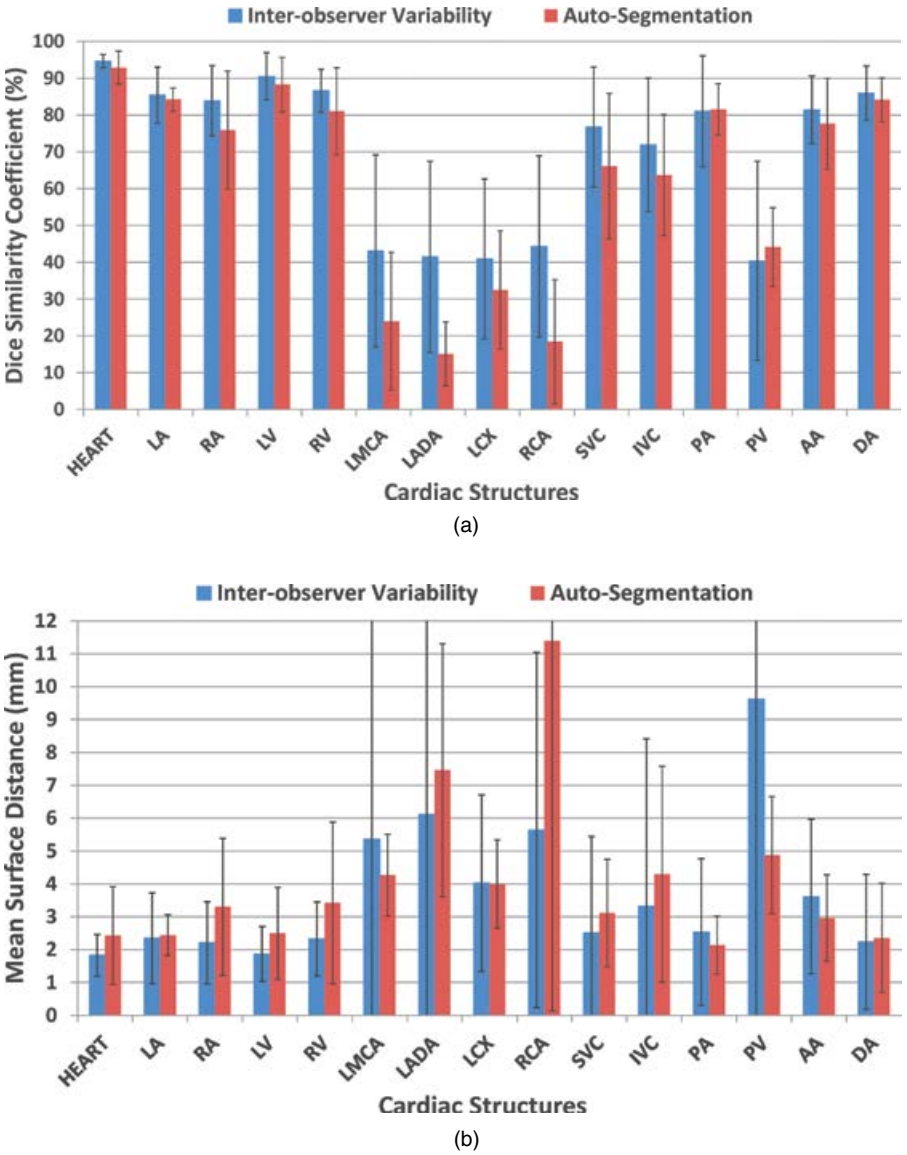

FIGURE 8.3 Comparison of inter-observer variability with auto-segmentation using (a) Dice similarity coefficient (DSC) and (b) mean surface distance (MSD) metrics. The error bars indicate one standard deviation. For abbreviations, see the legend to Figure 8.2.

the fused contours was 5.4 cm for the pulmonary vein. This disagreement is mostly due to the complex shape of these structures and their low contrast on the CT images. The interface of pulmonary vein to heart chambers has the most disagreement among experts. The mean DSCs and mean MSDs of auto-segmented contours were within one standard deviation of the mean DSCs and mean MSDs of expert contouring variability for all structures when measured by the *PV* metric defined in Eq. (8.3) (Table 8.1). These findings demonstrated that auto-segmentation of most cardiac structures was at least comparable to manual delineation. Figure 8.4 shows examples of inter-observer variability for the heart and the four chambers. Contouring variability can be clearly seen for different structures. For example, the most variable heart contours were in the superior region.

TABLE 8.1

Multi-atlas segmentation results of leave-one-out tests using the fused contours of the first group of 6 patients. The auto-segmented contours in each were compared with the fused contours for 15 cardiac structures using Dice similarity coefficient and mean surface distance metrics. Auto-segmentation was compared with expert contouring variability using the *PV* value defined in Eq. (8.3). *PV* < 1 indicates that auto-segmentation is comparable with manual contouring.

	Dice similarity coefficient														
Patient	**Heart**	**LA**	**RA**	**LV**	**RV**	**LMCA**	**LADA**	**LCX**	**RCA**	**SVC**	**IVC**	**PA**	**PV**	**AA**	**DA**
1	0.96	0.84	0.82	0.92	0.86	0.03	0.04	0.39	0.34	0.82	0.59	0.86	0.54	0.82	0.84
2	0.96	0.89	0.86	0.94	0.89	0.20	0.07	0.25	0.14	0.81	0.75	0.68	0.30	0.74	0.82
3	0.94	0.84	0.72	0.89	0.78	0.45	0.29	0.61	0.00	0.47	0.64	0.88	0.37	0.85	0.90
4	0.94	0.86	0.87	0.94	0.89	0.49	0.17	0.14	0.40	0.80	0.81	0.81	0.38	0.86	0.89
5	0.93	0.83	0.84	0.87	0.87	0.15	0.18	0.29	0.23	0.71	0.70	0.85	0.54	0.86	0.86
6	0.84	0.80	0.45	0.74	0.58	0.12	0.19	0.27	0.00	0.36	0.34	0.83	0.53	0.54	0.73
Mean	**0.93**	**0.84**	**0.76**	**0.88**	**0.81**	**0.24**	**0.16**	**0.33**	**0.19**	**0.66**	**0.64**	**0.82**	**0.44**	**0.78**	**0.84**
SD	**0.05**	**0.03**	**0.16**	**0.07**	**0.12**	**0.19**	**0.09**	**0.16**	**0.17**	**0.20**	**0.17**	**0.07**	**0.11**	**0.12**	**0.06**
	Mean surface distance (mm)														
Patient	**Heart**	**LA**	**RA**	**LV**	**RV**	**LMCA**	**LADA**	**LCX**	**RCA**	**SVC**	**IVC**	**PA**	**PV**	**AA**	**DA**
1	1.2	2.2	2.5	1.8	2.4	6.0	5.1	3.7	2.9	1.8	4.0	1.5	2.9	2.5	1.7
2	1.5	1.7	2.1	1.4	2.2	4.1	4.2	4.7	6.3	1.7	2.3	3.6	6.5	3.5	2.0
3	2.2	2.8	3.6	2.3	3.3	2.4	2.6	1.7	14.9	4.4	3.1	1.5	4.6	2.1	1.3
4	2.0	2.0	1.7	1.5	2.1	3.0	5.1	4.0	2.8	1.9	2.0	2.0	6.8	1.8	1.3
5	2.2	3.4	2.6	3.0	2.2	4.8	8.5	4.7	4.1	2.9	2.7	2.0	4.0	2.3	1.9
6	5.5	2.6	7.3	5.0	8.4	3.1	11.3	2.3	29.5	5.5	10.2	1.8	3.5	5.3	5.5
Mean	**2.4**	**2.4**	**3.3**	**2.5**	**3.4**	**3.9**	**6.1**	**3.5**	**10.1**	**3.1**	**4.1**	**2.1**	**4.7**	**2.9**	**2.3**
SD	**1.5**	**0.6**	**2.1**	**1.4**	**2.5**	**1.3**	**3.2**	**1.3**	**10.5**	**1.6**	**3.1**	**0.8**	**1.6**	**1.3**	**1.6**
	Comparison of auto-segmentation with expert contouring variability														
	Heart	**LA**	**RA**	**LV**	**RV**	**LMCA**	**LADA**	**LCX**	**RCA**	**SVC**	**IVC**	**PA**	**PV**	**AA**	**DA**
PV	0.99	0.11	0.85	0.54	0.97	0.45	0.50	0.29	0.94	0.42	0.30	0.12	0.31	0.35	0.15

LA = left atrium; RA = right atrium; LV = left ventricle; RV = right ventricle; LMCA = left main coronary artery; LADA = left anterior descending artery; LCX = left circumflex artery; RCA = right coronary artery; SVC = superior vena cava; IVC = inferior vena cava; PA = pulmonary artery; PV = pulmonary vein; AA = ascending aorta and aortic arch; DA = descending aorta; SD = standard deviation.

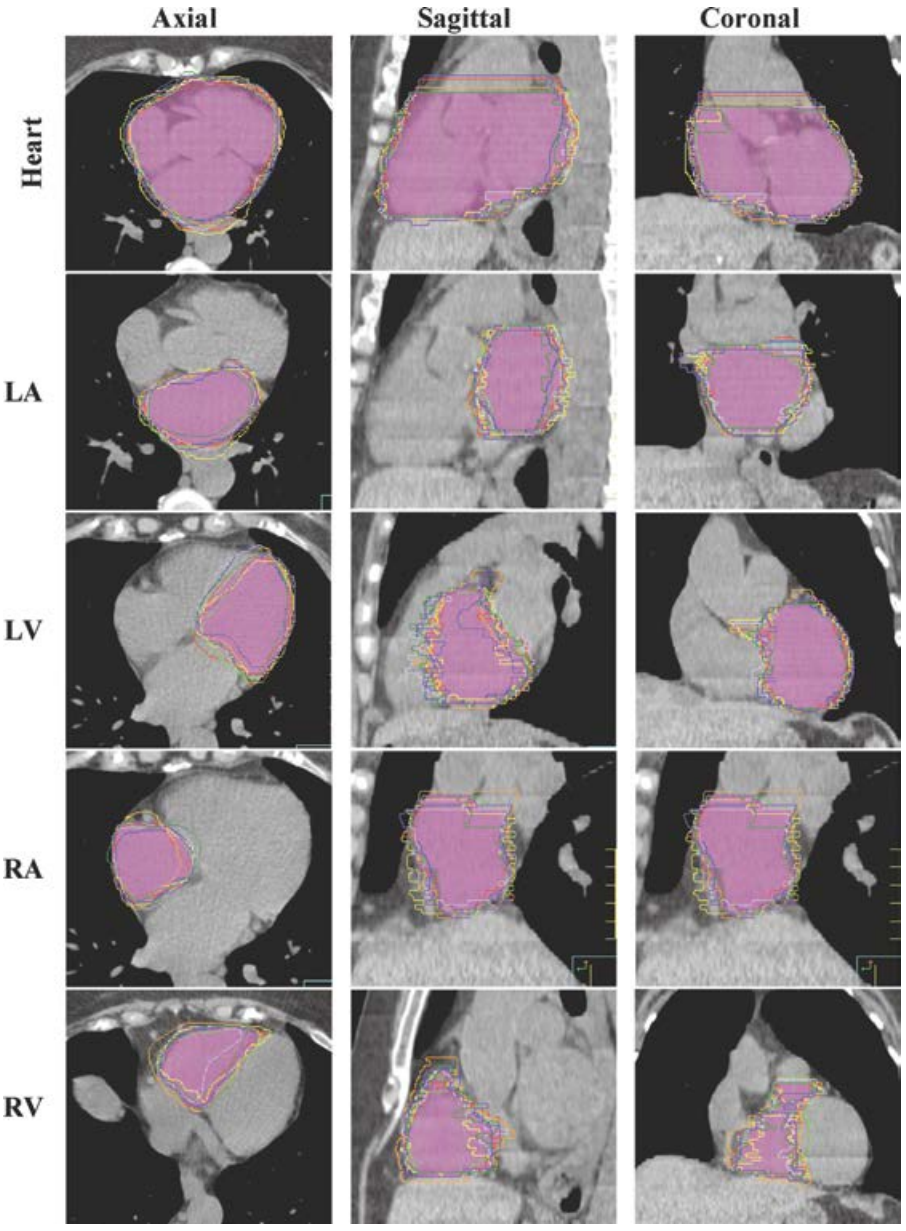

FIGURE 8.4 Inter-observer variability in manual contouring of the whole heart, left atrium (LA), right atrium (RA), left ventricle (LV), and right ventricle (RV). The manual contours delineated by eight radiation oncologists are shown in different colors, and the color-wash represents the fused consensus contours.

8.3.2.2 Leave-One-Out Validation

The leave-one-out validation results are shown in Figure 8.5. Good agreement between the auto-segmented contours and atlas contours was observed for the heart, the chambers, and the great vessels, with the mean DSC greater than 0.7 and mean MSD less than 3 mm, except for the pulmonary vein, with DSC = 0.64 ± 0.09 and MSD = 2.6 ± 0.7 mm. Heart segmentation had the best agreement, with DSC = 0.95 ± 0.03 and MSD = 1.9 ± 1.1 mm. Coronary arteries were difficult to delineate automatically, with the mean DSC below 0.4 for all coronary structures. Figure 8.6 shows some

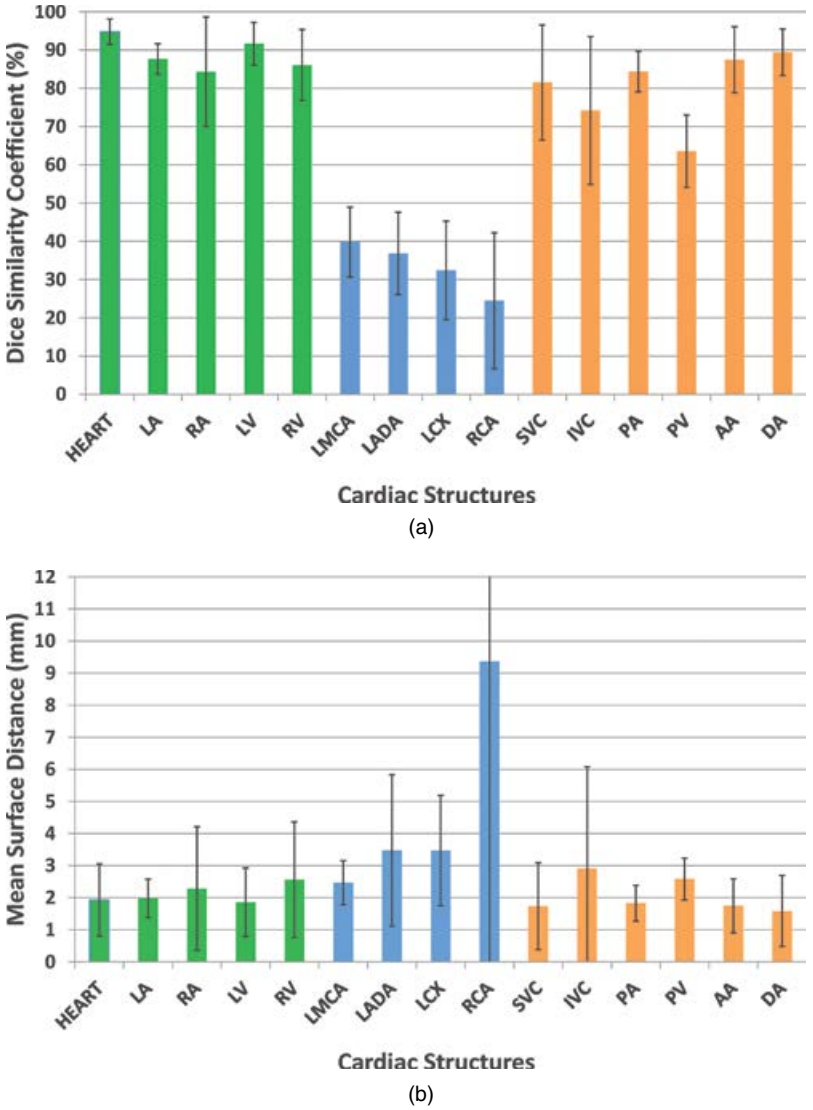

FIGURE 8.5 Comparison of auto-segmented contours with atlas contours for the leave-one-out validation for 12 atlases using (a) Dice similarity coefficient (DSC) and (b) mean surface distance (MSD) metrics. The error bars indicate one standard deviation. For abbreviations, see the legend to Figure 8.2.

comparisons between auto-segmented contours and atlas contours. Good agreement was observed for most structures. Detailed leave-one-out results are listed in Table 8.2.

8.3.3 Auto-Contouring Validation

The mean time for the MACS to automatically delineate the 11 cardiac substructures (excluding coronary artery structures) was 10 minutes per patient. The time (mean ± SD) to modify the contours of all 11 cardiac substructures was 40.2 ± 4.24 minutes for the first 10 patients and 27.2 ± 3.50 minutes for the second 10 patients (Figure 8.7); by comparison, contouring from scratch would take several hours. The time needed to modify the contours of the various structures declined as the radiation oncologists who were doing the modifying became more familiar with the rules for doing so.

TABLE 8.2

Multi-atlas segmentation results of leave-one-out tests for the 12 atlases. The auto-segmented contours in each test were compared with the atlas contours for 15 cardiac structures using Dice similarity coefficient and mean surface distance.

	Dice similarity coefficient (%)														
Atlas	**Heart**	**LA**	**RA**	**LV**	**RV**	**LMCA**	**LADA**	**LCX**	**RCA**	**SVC**	**IVC**	**PA**	**PV**	**AA**	**DA**
1	0.96	0.87	0.85	0.93	0.89	0.41	0.39	0.26	0.09	0.81	0.78	0.85	0.56	0.89	0.87
2	0.95	0.89	0.90	0.93	0.89	0.48	0.29	0.15	0.05	0.84	0.81	0.77	0.53	0.83	0.84
3	0.94	0.89	0.80	0.91	0.80	0.37	0.41	0.38	0.17	0.59	0.62	0.89	0.63	0.88	0.92
4	0.95	0.88	0.89	0.95	0.90	0.28	0.43	0.43	0.43	0.85	0.84	0.81	0.53	0.90	0.92
5	0.93	0.83	0.86	0.88	0.86	0.37	0.45	0.25	0.49	0.87	0.79	0.86	0.64	0.90	0.86
6	0.85	0.81	0.41	0.75	0.59	0.27	0.12	0.32	0.00	0.43	0.19	0.85	0.57	0.62	0.74
7	0.96	0.94	0.92	0.96	0.92	0.56	0.34	0.39	0.19	0.90	0.64	0.88	0.75	0.94	0.95
8	0.97	0.92	0.91	0.95	0.91	0.41	0.45	0.47	0.22	0.89	0.75	0.92	0.76	0.93	0.91
9	0.96	0.84	0.90	0.95	0.93	0.39	0.21	0.43	0.45	0.86	0.84	0.87	0.71	0.91	0.95
10	0.97	0.88	0.87	0.93	0.87	0.52	0.46	0.38	0.12	0.93	0.87	0.84	0.73	0.93	0.90
11	0.98	0.92	0.93	0.94	0.94	0.29	0.43	0.04	0.24	0.91	0.89	0.87	0.72	0.92	0.95
12	0.96	0.84	0.88	0.92	0.84	0.44	0.45	0.38	0.50	0.91	0.88	0.73	0.51	0.84	0.93
Mean	**0.95**	**0.88**	**0.84**	**0.92**	**0.86**	**0.40**	**0.37**	**0.32**	**0.25**	**0.82**	**0.74**	**0.84**	**0.64**	**0.88**	**0.89**
SD	**0.03**	**0.04**	**0.14**	**0.06**	**0.09**	**0.09**	**0.11**	**0.13**	**0.18**	**0.15**	**0.19**	**0.05**	**0.09**	**0.09**	**0.06**
	Mean surface distance (mm)														
Atlas	**Heart**	**LA**	**RA**	**LV**	**RV**	**LMCA**	**LADA**	**LCX**	**RCA**	**SVC**	**IVC**	**PA**	**PV**	**AA**	**DA**
1	1.4	1.9	2.1	1.5	1.9	2.4	2.5	3.3	11.4	1.7	2.1	1.8	3.0	1.5	1.4
2	1.7	2.1	1.5	1.5	2.1	1.9	2.8	4.2	15.9	1.4	1.8	2.6	2.6	2.1	2.4
3	1.9	1.9	2.6	2.0	2.9	2.3	2.6	3.5	5.0	4.3	3.5	1.3	2.7	1.8	1.1
4	1.8	1.7	1.4	1.3	2.1	4.2	2.4	2.0	2.8	1.4	1.5	2.0	2.7	1.3	0.9
5	2.4	3.3	2.2	2.7	2.4	2.6	3.0	3.3	3.1	1.3	1.8	1.9	2.8	1.8	2.0
6	5.3	2.5	8.2	5.0	8.1	3.3	10.7	4.6	40.3	4.8	12.6	1.6	3.1	4.1	4.7
7	1.5	1.1	1.2	1.2	1.7	1.6	4.3	2.7	6.1	1.0	3.8	1.7	1.7	1.0	0.7
8	1.2	1.3	1.2	1.0	1.5	2.7	2.6	1.9	4.4	0.8	2.3	0.9	1.5	1.1	1.5
9	1.7	2.4	1.7	1.3	1.6	1.9	3.5	2.4	2.7	1.6	1.7	1.8	2.2	1.4	1.0
10	1.5	2.2	2.2	1.6	2.4	2.2	2.1	2.8	7.3	0.8	1.3	1.8	2.5	1.3	1.2
11	1.0	1.3	1.1	1.5	1.3	2.6	2.8	8.3	10.7	0.9	1.3	1.4	2.1	1.3	0.8
12	1.9	2.1	1.8	1.8	2.7	2.1	2.6	2.6	2.6	0.9	1.3	3.0	4.0	2.2	1.3
Mean	**1.9**	**2.0**	**2.3**	**1.9**	**2.6**	**2.5**	**3.5**	**3.5**	**9.4**	**1.7**	**2.9**	**1.8**	**2.6**	**1.8**	**1.6**
SD	**1.1**	**0.6**	**1.9**	**1.1**	**1.8**	**0.7**	**2.4**	**1.7**	**10.6**	**1.4**	**3.2**	**0.6**	**0.7**	**0.8**	**1.1**

LA = left atrium; RA = right atrium; LV = left ventricle; RV = right ventricle; LMCA = left main coronary artery; LADA = left anterior descending artery; LCX = left circumflex artery; RCA = right coronary artery; SVC = superior vena cava; IVC = inferior vena cava; PA = pulmonary artery; PV = pulmonary vein; AA = ascending aorta and aortic arch; DA = descending aorta; SD = standard deviation.

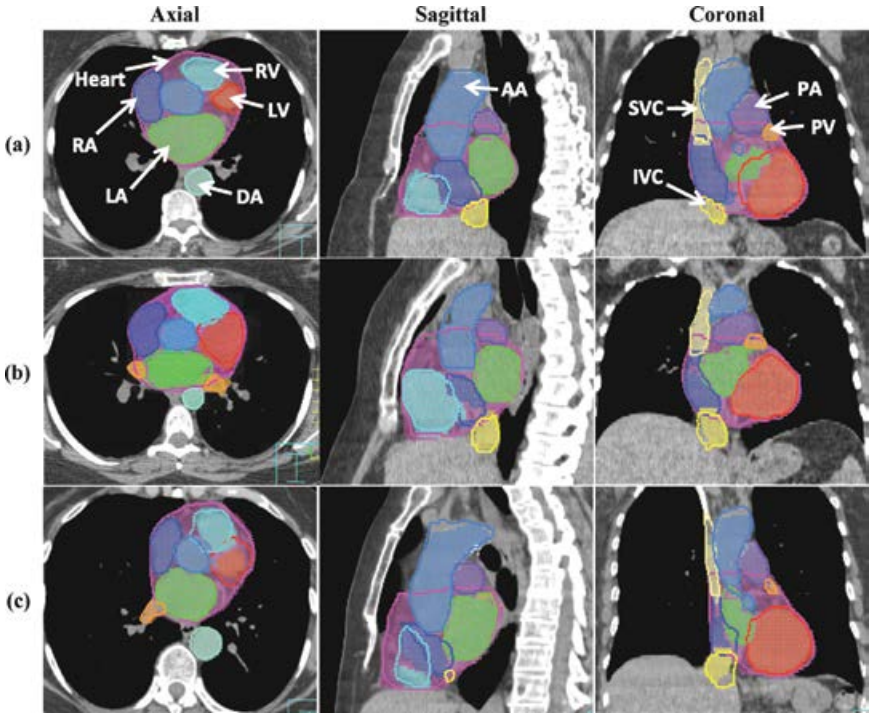

FIGURE 8.6 Comparison of auto-segmented contours with atlas contours for three representative patients (a, b, and c). The auto-segmented contours (lines) were compared with the atlas contours (color-wash) in the axial, sagittal, and coronal planes for the heart, the chambers, and the great vessels. For abbreviations, see the legend to Figure 8.2.

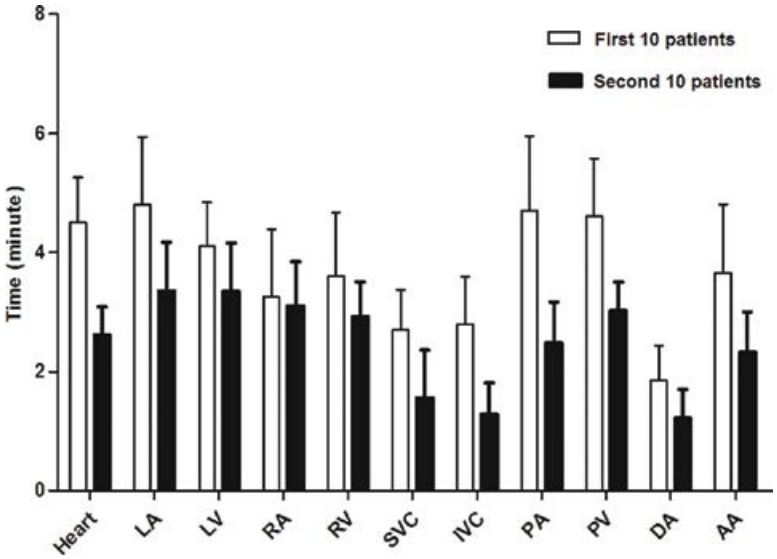

FIGURE 8.7 Average time needed to modify contours of 11 cardiac substructures per patient for the first 10 patients (clear bars) and for the second 10 patients (solid bars). Error bars represent one standard deviation. For abbreviations, see the legend to Figure 8.2.

TABLE 8.3
Comparability of modified contours versus auto-segmented contours of 11 cardiac substructures

	Dice Similarity Coefficient, Mean ± SD	Mean Surface Distance, mm, Mean ± SD
Heart	0.95 ± 0.04	2.1 ± 1.8
Left atrium	0.89 ± 0.05	1.8 ± 0.7
Left ventricle	0.91 ± 0.06	2.2 ± 1.8
Right atrium	0.86 ± 0.12	2.3 ± 2.2
Right ventricle	0.87 ± 0.10	2.7 ± 2.2
Superior vena cava	0.84 ± 0.14	1.7 ± 1.3
Inferior vena cava	0.78 ± 0.15	2.9 ± 5.1
Pulmonary artery	0.86 ± 0.05	2.2 ± 0.7
Pulmonary vein	0.73 ± 0.08	2.0 ± 0.7
Descending aorta	0.92 ± 0.04	1.3 ± 0.6
Ascending aorta	0.92 ± 0.06	1.4 ± 0.8

Abbreviation: SD, standard deviation

8.3.3.1 Geometric Evaluation

Geometric overlap between the modified and the auto-segmented contours for the 49 patients, quantified in terms of DSC and MSD, are shown in Table 8.3. Of the 11 structures, the average DSC values ranged from 0.73 ± 0.08 to 0.95 ± 0.04, and the average MSD values ranged from 1.3 ± 0.6 mm to 2.9 ± 5.1 mm for all 49 patients. Overall, the mean DSC for all of these structures was >0.7, indicating that no substantial modification was needed for the auto-segmented contours. Among the 11 structures, the pulmonary vein and inferior vena cava had lower DSC values (0.73 ± 0.08 and 0.78 ± 0.15), and higher MSD values (2.0 ± 0.7 mm and 2.9 ± 5.1 mm) than other structures, suggesting that contours for these two structures needed more modification than did the contours for the other structures.

8.3.3.2 Dosimetric Evaluation

To investigate whether the auto-segmented contours could be used to study the cardiac dose-response directly in clinical practice, we evaluated dosimetric differences between the modified and auto-segmented contours for the 49 patients. The DVH of the 11 cardiac substructures were calculated from the original dose distribution on the clinical treatment plan. Dosimetric variables are compared in Table 8.4. For all patients, the heart V30 and mean dose to the entire heart and the four heart chambers did not show statistically significant difference for modified versus auto-segmented contours. The maximum dose to the great vessels also did not show statistically significant difference for the modified versus auto-segmented contours, except for the pulmonary vein (modified 78.11 ± 13.24 Gy, auto-segmented 76.44 ± 14.23 Gy, $P = 0.01$).

8.4 DISCUSSION

The risk of radiation-related cardiac toxicity is an important issue in radiotherapy for breast cancer, Hodgkin lymphoma, and lung cancer, among others. However, little has been reported on the relationship between cardiac toxicity and radiation dose-volumes for the heart, and even less for the specific cardiac substructures. This probably reflects the inability to delineate those structures

TABLE 8.4

Dosimetric comparability of modified contours versus auto-segmented contours

Structures and Dosimetric Variables	Modified Contours, Mean ± SD	Auto-Segmented Contours, Mean ± SD	*P*-Values*
Heart			
Dmean, Gy	10.81 ± 7.78	10.85 ± 7.84	0.86
V30, %	13 ± 11	14 ± 11	0.89
Left atrium			
Dmean, Gy	20.71 ± 16.21	20.81 ± 16.07	0.66
Left ventricle			
Dmean, Gy	4.02 ± 7.11	4.02 ± 7.12	0.33
Right atrium			
Dmean, Gy	997 ± 1014	10.83 ± 10.58	0.11
Right ventricle			
Dmean, Gy	5.03 ± 6.15	5.02 ± 6.08	0.24
Superior vena cava			
Dmax, Gy	74.04 ± 17.06	74.19 ± 17.04	0.14
Inferior vena cava			
Dmax, Gy	6.97 ± 15.84	7.91 ± 16.74	0.20
Pulmonary artery			
Dmax, Gy	80.75 ± 7.60	80.39 ± 7.47	0.08
Pulmonary vein			
Dmax, Gy	78.11 ± 13.24	76.44 ± 14.23	0.01
Descending aorta			
Dmax, Gy	63.41 ± 21.38	62.41 ± 21.68	0.18
Ascending aorta			
Dmax, Gy	10.81 ± 7.78	10.85 ± 7.84	0.86

Abbreviations: V30, percentage volume receiving dose ≥ 30 Gy; SD, standard deviation

* From paired Student's *t*-tests (normally distributed data) or Wilcoxon signed-rank test (non-normally distributed data).

efficiently on treatment planning images. In addition, substantial variability in heart contouring has been reported in NSCLC [10] and could affect the validity of dosimetric analyses of cardiac toxicity. In this study we developed a set of cardiac atlases to be used with multi-atlas segmentation for auto-contouring cardiac substructures. We showed that manual contouring has high inter-observer variability, and variability in automatic segmentation was at least comparable to inter-observer variability in manual delineation of cardiac substructures. We have demonstrated that accurate and consistent contours can be automatically delineated for cardiac substructures except for coronary arteries. In addition, we further evaluated the dosimetric implications of automatic segmentation and found that modification of the auto-segmented contours had little effect on the dose-volume response, which suggests that using automatic segmentation may be feasible for dose-volume response studies.

Our results have clinically significant implications. First, the cardiac atlases can aid treatment planning in radiotherapy and potentially save time for clinicians in cardiac delineation. Our results

have shown that auto-segmentation of most cardiac substructures was at least comparable to manual delineation. Accurate and consistent contours can also improve heart dose sparing in treatment planning and thereby improve treatment outcomes. Second, accurate and consistent cardiac substructure contouring can facilitate volume dose analysis, allowing assessment of radiation doses to specific cardiac structures for toxicity analysis to achieve cardiac risk control [2]. Recent efforts have shown that with the advances of radiation therapy planning, avoiding heart structures is possible and desirable, especially for young patients with a high cure rate and long-term survival like lymphoma patients [8]. A standard and consistent heart contour is also important to reporting and comparison of the heart dose volume histogram and heart toxicities [10].

Validation of auto-segmentation is frequently subject to the impact of inter-observer variability when manual contours are used as the ground truth [31–33]. In this study, we performed an inter-observer variability analysis, used consensus contours as the ground truth to evaluate auto-segmented contours, and compared auto-segmentation with inter-observer variability to evaluate auto-segmentation. We thereby essentially minimized the impact of human factors in manual contouring and evaluated auto-segmentation for practical clinical use as an alternative to traditional manual contouring. However, the large inter-observer variability indicates that the manual contours were far from perfect. The major cause of the uncertainty in manual contouring may be cardiac motion. The contrast CT used in this study had both systolic- and diastolic-phase images, but the noncontrast CT did not. In general, cardiac-phase images are not available for treatment planning. Due to cardiac motion, fusion of contrast and noncontrast CT images may not be perfect. This imperfect fusion may have a considerable effect on contouring of small structures such as coronary arteries because a small deviation in fusion may cause a large discrepancy in contouring. On the other hand, even with contrast CT, the boundaries of some structures, such as coronary arteries, were still not clearly discernible. Contouring those structures still relied a lot on individual judgment, thereby resulting in large inter-observer variability in manual contouring. Accurate anatomical identification of coronary arteries therefore remains challenging and will be a major barrier for auto-contouring.

Image resolution may limit the capability of auto-contouring the small structures as well. Coronary arteries may not be discernible in older planning CT scans with a large voxel size. Auto-contouring is also subject to the effects of inter-patient variation. A tumor close to the heart can significantly change the shape and appearance of a cardiac structure in CT images. Our auto-segmentation relies on accurate matching of the anatomy between atlas images and the new image for segmentation. If a large difference exists, the matching is not accurate. We indeed found that when a large tumor was near the heart, the accuracy of auto-contouring was low.

The choice of metrics can also affect evaluation results. DSC-based evaluations are known to be favorable for large volumes. It is not surprising to see larger DSCs for the heart, chambers, or great vessels than for coronary arteries. Therefore, distance-based metrics should also be used. However, distance-based metrics are subject to the effect of voxel size. Images with higher resolution (or smaller voxel size) tend to produce better distance-based evaluation for auto-segmentation. In our study, all images had slice spacing of 2.5 mm, which may limit distance-based assessment. By considering the limitation of image resolution, our auto-segmentation approach is comparable to state-of-the-art cardiac segmentation methods [34–36], which were applied to contrast CT images with sub-millimeter resolution for diagnosis of cardiovascular diseases. On the other hand, this showed that the atlases we developed are useful for auto-contouring the cardiac substructures.

We found good agreement between the modified and auto-segmented contours, implying that no substantial modifications were needed for the auto-segmented contours. Among the contoured structures we evaluated, the pulmonary vein and inferior vena cava showed less agreement than others, mainly because of their relatively small volumes and indistinguishable anatomical boundaries on the CT images, and thus modifications are likely to be needed for these types of structures. Other studies have shown similar findings [37,38]. In addition, auto-segmenting these structures has several specific challenges. First, the junction between the inferior vena cava and

the right atrium is difficult to contour because of the lack of distinct contrast between them. In our study, modifications had to be made to correct part of the inferior vena cava to be the right atrium. Second, the complex anatomic shape of the pulmonary vein makes automatic segmentation difficult. Third, we noticed that pulmonary veins were susceptible to tumor invasion for some patients, which can cause segmentation errors. Therefore, one would expect more modifications for these two structures.

Geometric evaluation measured by the DSC or MSD serves directly for the purpose to validate the accuracy of auto-segmentation. However, geometric evaluation is generally not directly interpretable in clinical settings. Rather, the dose-volume response is often compared with clinical outcomes in analyses of radiation-induced toxicity [39]. Traditionally, the parameters of mean dose and the volume receiving a certain amount of dose are used to evaluate the heart and chamber doses, and the parameter of maximum dose is used to evaluate the dose to the great vessels. We found no statistically significant differences between the modified and the auto-segmented contours, except for the pulmonary vein ($P = 0.01$). This finding implies that small geometric differences between auto-segmented and modified contours have negligible effects on dosimetry. On the other hand, previous studies have found the whole heart; heart chambers including endocardium, myocardium, and epicardium; and coronary arteries to be the most important substructures related to radiation-induced cardiac toxicity, but the pulmonary vein did not show direct correlation with cardiac toxicity [6, 40]. Thus, our results presumably suggest that auto-segmented contours can be used directly for studying cardiac dose-response, although the pulmonary artery or pulmonary vein may need some minor modifications for some individuals. Indeed, this auto-segmentation tool can be used to quickly evaluate dose-volume response for patients undergoing radiotherapy and would be desirable for quality assurance in multi-institutional trials or large population-based dosimetric studies.

8.5 CONCLUSION

To conclude, it is possible to automatically delineate the heart, the heart chambers, and the great vessels from noncontrast CT images for radiation oncology applications, especially on clinical trials to evaluate the radiation-induced cardiac toxicities. We found that automatic segmentation of cardiac substructures did not require substantial modifications, and dosimetric evaluation showed no statistically significant differences between the auto-segmented and modified contours except for the pulmonary vein. These findings suggest that using auto-segmented contours to study cardiac dose-response is feasible in current clinical practice. However, accurate identification of coronary arteries in CT images is difficult and their auto-contouring needs further investigation.

Acknowledgments

This research was supported in part by The University of Texas MD Anderson Cancer Center Institutional Research Grant (IRG) Program and MD Anderson Cancer Center support grant CA016672. The authors would like to thank Drs. Daniel Gomez, Bouthaina Dabaja, Quynh-Nhu Nguyen, Sarah Migrom, Chelsea Pinnix, Anhui Shi, Ju Yang, Ying Liu, and Tinsu Pan for their contribution to this work. The authors would also like to thank Drs. Laurence Court and Peter Balter for their valuable discussions.

References

1. Albini A, Pennesi G, Donatelli F, Cammarota R, De Flora S, Noonan DM. Cardiotoxicity of anticancer drugs: the need for cardio-oncology and cardio-oncological prevention. *Journal of the National Cancer Institute* 2010;102:14–25.
2. Gagliardi G, Constine LS, Moiseenko V, et al. Radiation dose-volume effects in the heart. *Int J Radiat Oncol Biol Phys* 2010;76:S77–S85.

3. Lancellotti P, Nkomo VT, Badano LP, et al. Expert consensus for multi-modality imaging evaluation of cardiovascular complications of radiotherapy in adults: a report from the European Association of Cardiovascular Imaging and the American Society of Echocardiography. *J Am Soc Echocardiogr* 2013;26:1013–1032.
4. Mulrooney DA, Yeazel MW, Kawashima T, et al. Cardiac outcomes in a cohort of adult survivors of childhood and adolescent cancer: retrospective analysis of the Childhood Cancer Survivor Study cohort. *BMJ* 2009;339:b4606.
5. Demirci S, Nam J, Hubbs JL, Nguyen T, Marks LB. Radiation-induced cardiac toxicity after therapy for breast cancer: interaction between treatment era and follow-up duration. *Int J Radiat Oncol Biol Phys* 2009;73:980–987.
6. Darby SC, Cutter DJ, Boerma M, et al. Radiation-related heart disease: current knowledge and future prospects. *Int J Radiat Oncol Biol Phys* 2010;76:656–665.
7. Sardaro A, Petruzzelli MF, D'Errico MP, Grimaldi L, Pili G, Portaluri M. Radiation-induced cardiac damage in early left breast cancer patients: risk factors, biological mechanisms, radiobiology, and dosimetric constraints. *Radiother Oncol* 2012;103:133–142.
8. Maraldo MV, Brodin NP, Vogelius IR, et al. Risk of developing cardiovascular disease after involved node radiotherapy versus mantle field for Hodgkin lymphoma. *Int J Radiat Oncol Biol Phys* 2012;83:1232–1237.
9. van Eggermond AM, Schaapveld M, Lugtenburg PJ, et al. Risk of multiple primary malignancies following treatment of Hodgkin lymphoma. *Blood* 2014;124:319–327; quiz 466.
10. Bradley JD, Paulus R, Komaki R, et al. Standard-dose versus high-dose conformal radiotherapy with concurrent and consolidation carboplatin plus paclitaxel with or without cetuximab for patients with stage IIIA or IIIB non-small-cell lung cancer (RTOG 0617): a randomised, two-by-two factorial phase 3 study. *Lancet Oncol* 2015;16:187–199.
11. Yusuf SW, Sami S, Daher IN. Radiation-induced heart disease: a clinical update. *Cardiology Research and Practice* 2011;2011:317659.
12. Collier DC, Burnett SS, Amin M, et al. Assessment of consistency in contouring of normal-tissue anatomic structures. *Journal of Applied Clinical Medical Physics* 2003;4:17–24.
13. Yang J, Woodward WA, Reed VK, et al. Statistical modeling approach to quantitative analysis of interobserver variability in breast contouring. *Int J Radiat Oncol Biol Phys* 2014;89:214–221.
14. Weiss E, Wijesooriya K, Ramakrishnan V, Keall PJ. Comparison of intensity-modulated radiotherapy planning based on manual and automatically generated contours using deformable image registration in four-dimensional computed tomography of lung cancer patients. *Int J Radiat Oncol Biol Phys* 2008;70:572–581.
15. Lorenzen EL, Ewertz M, Brink C. Automatic segmentation of the heart in radiotherapy for breast cancer. *Acta Oncol* 2014;53:1366–1372.
16. Zhou R, Liao Z, Pan T, et al. Cardiac atlas development and validation for automatic segmentation of cardiac substructures. *Radiother Oncol* 2017;122:66–71.
17. Aljabar P, Heckemann RA, Hammers A, Hajnal JV, Rueckert D. Multi-atlas based segmentation of brain images: atlas selection and its effect on accuracy. *NeuroImage* 2009;46:726–738.
18. Yang J, Amini A, Williamson R, et al. Automatic contouring of brachial plexus using a multi-atlas approach for lung cancer radiation therapy. *Practical Radiation Oncology* 2013;3:e139–e147.
19. Yang J, Haas B, Fang R, et al. Atlas ranking and selection for automatic segmentation of the esophagus from CT scans. *Physics in Medicine and Biology* 2017;62:9140–9158.
20. Kong F, Quint L, Machtay M, Bradley J. Atlases for organs at risk (OARs) in thoracic radiation therapy, 2013.
21. Feng M, Moran JM, Koelling T, et al. Development and validation of a heart atlas to study cardiac exposure to radiation following treatment for breast cancer. *Int J Radiat Oncol Biol Phys* 2011;79:10–18.
22. Netter FH. *Atlas of Human Anatomy*. Elsevier Health Sciences, 2010.
23. Warfield SK, Zou KH, Wells WM. Simultaneous truth and performance level estimation (STAPLE): an algorithm for the validation of image segmentation. *IEEE Trans Med Imaging* 2004;23:903–921.
24. Wang H, Dong L, Lii MF, et al. Implementation and validation of a three-dimensional deformable registration algorithm for targeted prostate cancer radiotherapy. *International Journal of Radiation Oncology, Biology, Physics* 2005;61:725–735.
25. Yang J, Zhang Y, Zhang L, Dong L. Automatic segmentation of parotids from CT scans using multiple atlases. In: van Ginneken B, Murphy K, Heimann T, Pekar V, and Deng X, eds. *Medical Image Analysis for the Clinic: A Grand Challenge*, 2010;323–330.
26. Yang J, Garden A, Zhang Y, Zhang L, Court L, Dong L. WE-E-213CD-09: Multi-atlas fusion using a tissue appearance model. *Med Phys* 2012;39:3961.

27. Ibanez L, Schroeder W, Ng L, Cates J. *The ITK Software Guide*. Clifton Park, NY: Kitware Inc., 2005.
28. Korsager AS, Fortunati V, van der Lijn F, et al. The use of atlas registration and graph cuts for prostate segmentation in magnetic resonance images. *Medical Physics* 2015;42:1614–1624.
29. Zijdenbos AP, Dawant BM, Margolin RA, Palmer AC. Morphometric analysis of white-matter lesions in MR-images - method and validation. *IEEE Transactions on Medical Imaging* 1994;13:716–724.
30. Zou KH, Warfield SK, Bharatha A, et al. Statistical validation of image segmentation quality based on a spatial overlap index: scientific reports. *Academic Radiology* 2004;11:178–189.
31. Stapleford LJ, Lawson JD, Perkins C, et al. Evaluation of automatic atlas-based lymph node segmentation for head-and-neck cancer. *Int J Radiat Oncol Biol Phys* 2010;77:959–966.
32. Teguh DN, Levendag PC, Voet PW, et al. Clinical validation of atlas-based auto-segmentation of multiple target volumes and normal tissue (swallowing/mastication) structures in the head and neck. *Int J Radiat Oncol Biol Phys* 2011;81:950–957.
33. Yang J, Wei C, Zhang L, Zhang Y, Blum RS, Dong L. A statistical modeling approach for evaluating auto-segmentation methods for image-guided radiotherapy. *Comput Med Imaging Graph* 2012;36:492–500.
34. Ecabert O, Peters J, Walker MJ, et al. Segmentation of the heart and great vessels in CT images using a model-based adaptation framework. *Med Image Anal* 2011;15:863–876.
35. Kirisli HA, Schaap M, Klein S, et al. Evaluation of a multi-atlas based method for segmentation of cardiac CTA data: a large-scale, multicenter, and multivendor study. *Med Phys* 2010;37:6279–6291.
36. Zhuang X, Bai W, Song J, et al. Multiatlas whole heart segmentation of CT data using conditional entropy for atlas ranking and selection. *Med Phys* 2015;42:3822–3833.
37. Isambert A, Dhermain F, Bidault F, et al. Evaluation of an atlas-based automatic segmentation software for the delineation of brain organs at risk in a radiation therapy clinical context. *Radiother Oncol* 2008;87:93–99.
38. Anders LC, Stieler F, Siebenlist K, Schafer J, Lohr F, Wenz F. Performance of an atlas-based autosegmentation software for delineation of target volumes for radiotherapy of breast and anorectal cancer. *Radiother Oncol* 2012;102:68–73.
39. Voet PW, Dirkx ML, Teguh DN, Hoogeman MS, Levendag PC, Heijmen BJ. Does atlas-based autosegmentation of neck levels require subsequent manual contour editing to avoid risk of severe target underdosage? A dosimetric analysis. *Radiotherapy and Oncology* 2011;98:373–377.
40. Taunk NK, Haffty BG, Kostis JB, Goyal S. Radiation-induced heart disease: pathologic abnormalities and putative mechanisms. *Front Oncol* 2015;5:39.

Taylor & Francis
Taylor & Francis Group
http://taylorandfrancis.com

9 Detection of Calcification from Abdominal Aortic Aneurysm

Safa Salahat[1], Ahmed Soliman[2], Harish Bhaskar[1], Tim McGloughlin[1], Ayman El-Baz[2], Naoufel Werghi[1]
[1]University of Khalifa
[2]University of Louisville

CONTENTS

9.1 INTRODUCTION

The aorta is the largest blood vessel in the human body starting from the left ventricle of the heart going down into the abdomen. An aneurysm is an irreversible localized dilatation of a vessel [1–2]. Abdominal aortic aneurysm (AAA) is a cardiovascular disease which is identified when the abdominal aorta expands, reaching a maximum diameter of 3 cm or larger. AAAs with smaller maximum diameter are considered healthy (see Figure 9.1) [3–4]. AAA is asymptomatic in most cases until rupture, or being occasionally discovered when the patient has radiologic testing for other purposes [4–6].

Clinical risk factors for the development of AAA include smoking, hypertension, gender, obesity, age, genetics, and family history, while smoking remains the most dominant factor. Smoking boosts the rupture risk up to seven times the original risk [7–8]. Aging and hypertension lead to a stiffer aorta.

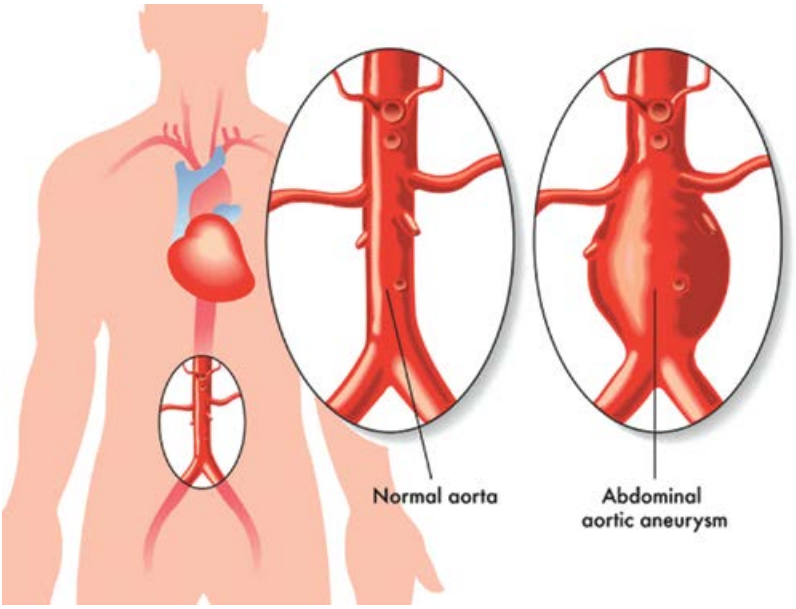

FIGURE 9.1 Examples of healthy and diseased aortas (see [81]).

AAA is more common in males than females. This can be referred to the fact that the number of male smokers is much higher than female smokers. Since the number of female smokers is on the increase, this factor may not be a valid one in the future.

Surgical intervention occurs when the aneurysm reaches a maximum diameter of 5.5 cm, or when a high growth rate is observed. There are two surgical techniques for AAA treatment, which are open aneurysm repair (OR) and endovascular aneurysm repair (EVAR) [8–9]. The expanded part of the aorta is replaced by graft in OR, while the graft is inserted within the aorta at the aneurysm site in EVAR. OR is riskier in the short term [10], but safer in the long term, while it is the opposite for EVAR because the graft may migrate, causing some complications that might require careful follow-up later (endoleak or kinking the graft) [11–12].

While the maximum diameter of the AAA is still considered as the primary indicator of whether a medical intervention is required or not, some studies [79–80] indicated that biomechanical wall stress of the aortic wall can serve as a more accurate predictor of rupture risk than the maximum diameter. In most AAA patients, varying amounts of calcification deposits were observed. It was reported in [13] that calcification is directly related to increasing AAA rupture risk, which clearly calls for the development of an invasive medical tool capable of detecting calcification in vivo. This research is expected to lead to better diagnosis, reducing the number of fatalities related to this disease, and leading to more consistent diagnosis among radiologists and clinicians [14].

In this chapter, section 9.2 provides a detailed literature review of existing contributions to segment the aneurysm and its components. In this review, literature contributions were divided into four main categories based on the major algorithm used for the segmentation: deformable models, graph, fuzzy c-means, and other contributions in which a sequence or combination of algorithms, not covered by the previous three categories, are used to perform the segmentation. Section 9.3 demonstrates the details of a newly proposed aneurysm segmentation method, and section 9.4 suggests the usage of a classifier-based approach utilizing the Bayesian classifier to solve the calcification detection problem from AAA.

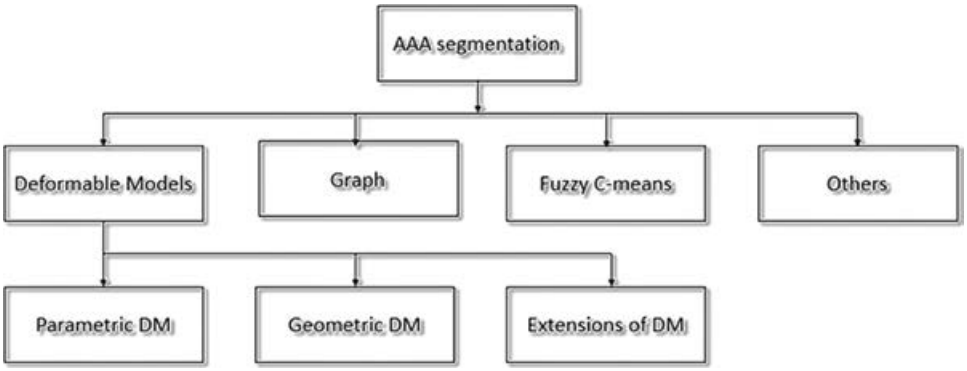

FIGURE 9.2 AAA segmentation methods.

9.2 LITERATURE REVIEW

This section reviews the algorithms and techniques used for abdominal aortic aneurysm segmentation, which are summarized in Figure 9.2. These methods were divided into four main categories, deformable model based methods, graph based methods, fuzzy c-means based methods, and others. The contributions in the last category use a combination or sequence of image processing algorithms that don't belong to any of the first three categories to perform the segmentation task.

9.2.1 Deformable Models

Deformable models (DMs) are curves or surfaces controlled by internal and external forces, which maintain the smoothness of the evolving curve or surface, and draw the model to certain features, respectively.

9.2.1.1 Parametric Deformable Models

The lumen and thrombus were 3D segmented from CTA images in [15–16] based on deformable models. Once the operator specifies two points in the lumen, the thrombus is segmented using deformable models utilizing the surface resulting from lumen segmentation, which is as well segmented using deformable models. The vertices of the mesh evolve through a 3D active object method. In order to build the initial tube that segments the lumen, four positions are required, where two of them specify the proximal and distal slices, and the other two specify the lumen axis. Bi-level image thresholds are required for the deformation process. The area of each face in the mesh must satisfy the provided mesh resolution parameter (within a certain tolerance) which adjusts the mesh through consecutive split and merge operations. The internal force ensures uniform distribution of the mesh vertices, and controls mesh smoothness. The external force may shrink, expand, or stabilize depending on the location of the vertex x (i.e., outside, inside, or at the boundary). To determine the location, k-nearest neighbor identifies the appropriate class for the pattern taken at the vertex. Difference in volume and total mesh displacement were tested as stopping criteria, by comparing them to a predefined threshold value.

Motivated by the work of Huang et al. [17], Demirci et al. [18] developed a hybrid deformable model that utilizes both local and global image statistics to semi-automatically segment the thrombus from CTA scans. Aortic lumen volume is needed to serve as initialization for the deformable model aiming to segment the thrombus. The lumen area was covered by the thrombus mean intensity value, so that the model wouldn't get drawn to it. The deformation process is led by both local and global information, in addition to shape constraints. B-spline surfaces and distance functions utilized in this work would prevent the breaching of neighboring regions where the edge is weak.

Das et al. [19] presented a 2D thrombus segmentation method from CT using an active contour model [20]. In order to remove obstacles that may hinder the snake, streak artifacts are suppressed using morphological closing, bone structures are removed using AutoBone [21], and the lumen is filled with the thrombus mean intensity value. Once the snake is manually initialized, the introduced objectness property would control the deformation of the snake, while still being constrained by a narrow band that limits its movement through iterations. To control snake deformation, pixel objectness is calculated as a subtraction of its probability of being a background pixel from the probability of being an object, causing it to expand, shrink, or stand still. A narrow band of uniform width prevents the snake from breaching thrombus neighboring structures of fuzzy edges. The segmentation result of a slice is passed to the next one to initialize the next deformation.

In [22] Disseldorp et al. performed 3D segmentation of the aorta from ultrasound and compared it to CT. In order to ensure that the whole AAA volume is acquired, additional proximal and distal volumes had to be registered with the whole 3D volume, so that the active contour model suggested by Kass et al. [20] would be used next to segment the volume in 3D. The active contour model relies on internal and image derived external forces and user constraints to control the deformation process. CT volume was segmented using Hemodyn.

9.2.1.2 Geometric Deformable Models

The work developed by Zohiosa et al. [23] is among the first to exploit the level set method (LSM) to segment both the thrombus and outer aortic wall boundaries from CTA. The authors state that the level set method has been limited for lumen segmentation only because the surrounding structures for the thrombus have strong edges and similar intensity values, which may lead the advancing front to fall into wrong regions, in addition to the fact that it is computationally expensive. New geometrical methods are introduced in this chapter to solve this leakage problem. The proposed segmentation method utilizes the presence of calcification for the LSM, and the wall is interpolated from neighboring regions in case a source of contrast is not present. The main limitations of this work are (1) the presence of calcification is critical for the initialization for this method, (2) the calcifications are assumed to be contained within the aortic wall, while it may be present within the thrombus, and (3) some calcification is lost due to the high threshold used, to prevent the LSM from leaking to the spine.

Subaši´c et al. [24] proposed an AAA segmentation method for the inner and outer aortic wall boundaries using CTA that requires minimal user interaction. In order to obtain the inner aortic wall boundary, the geometric deformable model is used, followed up by post processing. The outer aortic boundary requires a preprocessing step that assumes an oval shape for the aorta before the geometric deformable model (GDM) and the morphological operations are applied.

The objective of the study in [26] is the 3D reconstruction of the aorta for aortic stent graft implantation. A geometric active contour model that utilizes a Gaussian filter was modified to reduce edge blurring while reducing noise in AAA images for better edge detection. In order to achieve that, a morphological gradient and a morphological gradient function were used. The 3D volume is reconstructed using the Rhinoceros (Robert McNeel and Associates) surface-rendering tool.

Kim et al. [27] improved the geometric active contour model by adopting a hybrid median filter preprocessed morphological gradient edge function instead of Gaussian blurred images to improve segmentation accuracy. Minimum distance error and mismatched area of salt-and-pepper noised synthetic images suggest improved accuracy, while no quantitative evaluation of the AAA images was provided.

Loncaric et al. [28] developed a level set based 3D segmentation method for AAA from CTA that could be utilized for accurate stent graft measurements. Level set described in [29] and [30]

was the method of choice to extract the 3D model because it is capable of handling bifurcations in arteries easily. The 3D surface deforms through a number of iterations, where the motion at a certain point is determined by the summation of constant, curvature, and image derived velocities, which represent inflation, internal, and external (image gradient) forces, respectively. A sphere is used as the initial surface, where the radius and the center are manually specified by the user such that it is inside the aorta.

As the authors further discuss their work in [31–33], it was pointed out that the previously mentioned method was used for segmenting the inner aortic wall due to the high contrast of the lumen to the thrombus and aortic wall because of the contrast agent injected into the patient. To segment the outer aortic wall that has a large contact area with other structures of similar intensity values, the authors applied 2D level set for each slice, and added an extra stopping criterion that assumes the aorta to be smooth and round. A circle is initialized utilizing the surface resulting from the inner aortic wall segmentation.

Nakhjavanlo et al. [34] performed 3D segmentation of abdominal and thoracic thrombus from CTA. This segmentation method utilized level set along with anisotropic diffusion [35], which would suppress noise and maintain sharp edges at the same time. The test set included 2D and 3D CTA data. Experiments proved that this approach leads to better accuracy and speed than the standard implementation of level set.

In [36] Hong et al. relied on deep learning to develop a fully autonomous method for AAA segmentation from CT. There are two major steps prior to AAA measurement, which are localization of the aneurysm followed by segmentation. Training and testing data were obtained from a single patient CT slices. Four classes were used to train the deep belief network, where the fourth class represents the aneurysm, and the other three classes represent other structures. Patches with more than one circular object or that didn't satisfy certain conditions were excluded. The procedure suggested by Majd et al. [37] was utilized subsequently to segment the aorta. The center of the lumen obtained by thresholding would initialize the level set method to extract the outer boundary of the aorta.

9.2.1.3 Extensions of Deformable Models

Bruijne et al. [38] suggested a semi-automatic segmentation method for AAA based on Active Shape Model (ASM). The contours from previous slices are used to find the contour at a particular slice. The contour of the first slice is obtained manually. If the contour for a particular slice is not correct, the user can correct it manually. Since AAA doesn't have a particular shape or intensity, the linear model was modified to use maximum intensity correlation from adjacent slices instead of the training data.

Bruijne in [39] compared the aorta segmentation results from 3D volume using level set and deformable model. The deformable model was implemented in a previous work for the authors in [40]. The average in slice plane error (in mm) using deformable models was slightly higher than that using level set. At the end of the paper, the authors suggested a better solution, which takes the advantages of both methods. This new system initially segments the aorta using deformable models, then uses level set to improve the segmentation result. This last system is implemented in [41]. This hybrid system has the capability to segment small structures, like renal arteries, is more computationally efficient than level set, and most importantly is more accurate than [40] and [39].

9.2.2 Graph-Based Segmentation

In a graph, vertices are connected through edges. The main technique used for segmenting the AAA in this section is the graph cut method.

A 3D thrombus segmentation method utilizing 3D multi-detector computed tomography angiography (CTA) images is developed in [42]. While the segmentation of aortic lumen is relatively easy due to the contrast agents injected into the patient which provides better visibility for the lumen, the segmentation of the thrombus is more difficult because the shape of the thrombus is irregular, and it can be obscured in some scenarios with the surrounding structures that may have similar intensity values to the thrombus. This method starts with a preprocessing step that requires an initial approximation of the lumen that is later used for an accurate segmentation of the lumen and thrombus using a graph search based on a triangular mesh. Then, the user gets to manually improve the segmentation result.

In [43], a semi-automatic graph cut based 3D segmentation method that works both for CT and MR was developed. This method segments the lumen and aortic wall, and was tested on patients with and without AAA, and synthetic images. This method doesn't over segment, nor does it require prior information on the shape. This segmentation method is based on graph cut, in which the graph consists of nodes and undirected edges of weighted capacity, and a source and a sink nodes, in order to find the minimum cut. The graph cut method classifies the nodes into two subsets that either exist inside or outside the segmented area. The other nodes used to separate the two sets represent the edges. The volume consists of L images of $N \times M$ pixels each, and the user needs to manually initialize the region of interest, which would result in inside, outside, and neutral volumes.

Hraiech et al. [44] developed a 3D lumen segmentation method based on graph cut from CTA. In graph cut, the image pixels are represented by nodes connected to their neighboring pixels through weighted links. Also, each node in the graph is connected to source s and sink t nodes. These two types are known as n-link and t-link, respectively. To find the minimal cut, a cut of a certain cost that separates the vertices connected to the source and the sink is made. The objective is to keep this cost to a minimum. The moving average filter was used for noise reduction, and the user manually specifies the seeds of the background and the object to generate a binary image through graph cut, followed by a connected component analysis to exclude other irrelevant structures, and Laplacian smoothing in each slice before building the surface model.

Freiman et al. [45] aimed to segment the thrombus from CTA using graph-cut constrained by a geometric parametric model, so that neighboring tissue won't be considered as part of the thrombus. The lumen volume is segmented as discussed in [46] so that it can be used for thrombus segmentation. To reduce user intervention, improve the accuracy, and include shape related information of the object to be segmented, a new energy function is iteratively minimized instead of the standard graph cut in [47], such that it incorporates both intensity and shape constraint. The labeling map is obtained using graph min-cut, and the method in [48] is used to fit an ellipse into the thrombus. This process is repeated until the geometric parametric model converges.

Rieke et al. in [49] segmented the aorta relying on graph based and random walks from structure tensor ultrasound images and intensity ultrasound images. Graph-based methods don't usually produce satisfactory results when applied to ultrasound intensity images, therefore the authors suggested that the pixel context can be more useful to the segmentation process than the intensity value alone. Graph cut and random walk were applied to structure tensor ultrasound images, which led to a better accuracy than intensity ultrasound images.

9.2.3 Fuzzy C-Means Clustering-Based Segmentation

Fuzzy c-means is a clustering method often used in image segmentation. In this section, we discuss various contributions to the AAA segmentation problem, including different variations and improvements of the originally suggested fuzzy c-means method.

In [50], a method is proposed to segment the lumen and aortic wall from MRI. The method requires two steps through which the lumen, thrombus and aortic wall are segmented. The

segmentation of the lumen is performed utilizing fuzzy c-means and morphological operations in the first step. The result from the first step is used to avoid manual initialization in the second step which uses the graph cut method to obtain the aortic wall and thrombus. The main advantage of this work is that it is fully automatic, in addition to its computational simplicity.

Pham in [51] proposed an autonomous geostatistically constrained fuzzy c-means method that contributes to the AAA segmentation process. The result of this method is compared to Otsu's method, geo-thresholding, and fuzzy c-means. It is observed that these three techniques obtain the entire aorta, which contains the lumen, thrombus, and calcification as one region, while the proposed geostatistically constrained FCM method labels the lumen and calcification as different regions.

Majd et al. [52] suggested an algorithm based on spatial fuzzy c-means that contributes to the AAA thrombus and lumen segmentation problem. Spatial fuzzy c-means [53] algorithm is an improved version of the c-means clustering method. While c-means only considers the distance between cluster centers and the pixels, spatial fuzzy c-means takes into account pixels' correlation at a local neighborhood to improve the clustering result. Once spatial fuzzy c-means is applied to the CT image, fuzzy thresholding, morphological erosion and thinning, and global thresholding are applied to obtain the final binary CT image. This algorithm led to better results than FCM and GCFCM, previously discussed in [51].

9.2.4 Other Methods

In this section, we include contributions that have used a wide range of algorithms and techniques to solve the AAA segmentation problem. It consists of machine learning, region growing, and other basic image processing operations such as image thresholding and morphological operations. It further contains other noteworthy contributions to estimate AAA geometry.

The method proposed in [54] is based on active learning, through which interaction between the user and the classifier occurs, for 3D segmentation of the AAA thrombus from CTA images that requires minimal user interaction. Random forest classifier is used for feature classification, and the classifier is retrained by including uncertain voxels which are manually labeled by the user.

An automatic method that provides fast and reliable patient specific 3D shape reconstruction of the AAA from CT, which can be used for biomechanical analysis to predict AAA rupture, is suggested in [55]. Free form deformation (FFD) has limited deformations for low order polynomials, and generates many variables for higher order ones. In addition, extended FFD is needed because FFD doesn't produce good results for complex structures as in the case of AAA. Unlike FFD, extended free form deformation (EFFD) doesn't require a 3D parallelepiped lattice. The objective of the optimization process is to find lattice parameters that provide minimum distance between the manually labeled aorta contours in a CT scan and the 2D contours of the deforming template model of the provided healthy aorta, with the aim of producing a patient specific structure. Sequential quadratic programming is used to handle this task. In order to smooth the deformed model geometry, a higher order polynomial function is used for EFFD.

Biasi et al. in [56] performed 2D segmentation for AAA using a series of algorithms. The CT image is thresholded, and morphological closing is used to improve the result. The initial segmentation utilizes canny edge detector and watershed algorithm resulting in several segments of interest (SOI). Neural networks with the same number of training data for both classes would classify whether an SOI is a lumen or another structure. SOI are then passed to a Region Growing Method for a second segmentation stage. After that, extCLP was used to merge different segments that belong to the aneurysm. 3D reconstruction is then performed based on the polygon calculated from the detected edges using VDRF filter.

Bruijne et al. [57] took the initiative to develop a system that segments aortic endografts from CTA. Radiopaque markers of predetermined configuration were utilized to easily identify the location of the graft, and provide a priori knowledge in the marker detection process. Platinum

cylinders served as markers and were sewn along the Ancure endograft. In the marker detection step, the product of eigenvalues of the Hessian matrix is calculated at each voxel to determine local minimums, which represent candidate centers of the markers. A voxel (or center of gravity) is considered to be a local minimum if voxels in its neighborhood have higher intensity values. In order to distinguish between the true markers and other similar structures, a tracking method was suggested that starts with a small search space which is enlarged if the smaller one fails to find a marker. If the larger search space doesn't find a successive marker or the tracked markers from the proximal and distal ends manually initialized by the operator meet, the process is terminated. These markers estimate the central axis and boundary location needed for graft segmentation.

Feinen et al. [58] developed a 3D registration technique that can be used to compare AAA pre and post the operation from CT images. This registration technique requires two main steps, lumen segmentation and graph matching. Lumen segmentation is based on the hybrid level set segmentation method described in [59], and the skeleton matching adopts the path similarity approach in [60], where the skeleton is generated as depicted in [61]. The clustering method in [62] is used to segment the kidneys and L4 of the lumbar spine to orient the skeleton correctly.

Dehmeshki et al. [63] built a fully automatic system that segments the aorta from CTA images and determines whether an aneurysm exists. The lumen is first segmented through thresholding, followed by morphological erosion to isolate it from other structures. Then the thin and lengthy object at the center of the body is taken to be the lumen. The abdominal section is the part bounded by the Celiac Trunk and the Iliac Junction. Once non-aneurysmal structures are identified, an ellipsoid fitting algorithm is utilized to obtain the aorta. Aorta maximum diameter, lumen shape irregularity and displacement are the parameters needed to check for the existence of the aneurysm.

Hosseini et al. [64] segmented the lumen and the thrombus based on the information derived from the histogram of the CT slice, and assumptions on the shape of the AAA. Contrast enhanced and non-contrast enhanced scans are included in this study. First the lumen is segmented. In contrast enhanced images, a threshold of 200 is used to remove objects of lower intensity values, then a median filter is applied followed by a morphological operation. Then a search method is employed to segment the lumen. In case of poor contrast, lumen is identified as the object with circular appearance. In order to extract the thrombus in non-contrast enhanced CTA, the search is HU 950 to 1200. Some constraints based on experimental observations are defined to increase the lower limit if needed. In contrast enhanced images, the segmentation of the thrombus is guided by the boundary of the extracted lumen and the histogram of the scan, the thrombus occupies the range between the first two peaks in the histogram.

Rouet et al. [65] suggested a new method for monitoring AAA from 3D ultrasound images. This work mainly attempts to solve some limitations usually faced when using 2D ultrasound to monitor AAA growth. This method aims to obtain a better reproducibility than that of 2D ultrasound measurements for estimating AAA maximum diameter and geometry, and enables 3D cross-sectional reconstruction for medical experts' offline reviews in a similar way to CT and MRI. The aneurysm is semi-automatically segmented using the method proposed by Mory et al. in [66], and the proximal and distal ends are manually specified by the user to generate a referential centerline which is needed to obtain 2D contours of cross-sections and measure the volume. Cross-sections are described through an elliptic model, instead of circular, to get more accurate measurement for the maximum diameter as the aneurysm can have an irregular shape.

Maiora and Graña in [67] semi-automatically segmented the thrombus and lumen of eight datasets from CT utilizing random forest classifier [68] and active learning [69]. Active learning is needed to select best features for training and keep their number to a minimum, so that the classifier would be able to more efficiently classify a new test data. Through active learning,

the operator would label pixels that are most ambiguous, so that they would be added to the training set. In this paper, the classification result of four classifiers were compared (SVM, RBF, MLP, RF), where the random forest (RF) scored highest in terms of sensitivity, specificity, and accuracy. Finally, morphological closing was used to acquire the final segmentation of the thrombus.

Almuntashri et al. [70] designed a system to segment aortic lumen from non-contrast enhanced 2D CT and PC-MR via combining a number of algorithms. A region of interest that contains the lumen is specified at first, and the image is cropped. Then the noise would be suppressed via a method previously suggested by the authors in [71], where the Laplacian of Gaussian is computed, and only pixels whose values are greater or equal to LoG values are kept. After that, the second derivative-like measure of enhancements specifies intensity mapping and parameters for anisotropic diffusion and region growing in the next step. The edge detector used was also developed by the authors in a previous work [72], through which the logarithmic ratio of two morphological filters are used for edge detection. The user should provide an initial point inside the lumen to initialize the region growing algorithm for the first image, and the mask centroid is computed, so that it can be used for initialization for the next image. The authors also claim that their method is more accurate and computationally more efficient than deformable models, although quantitative evaluation wasn't provided.

Shum et al. in [74] segmented the abdominal aortic wall providing a thorough quantitative evaluation. In order to segment the lumen, the user would provide a single click to specify a pixel within the lumen, and the lumen boundary is determined by the high gradient from the gradient computed image. Each slice is thresholded and the connected region of maximum area that contains the selected point is taken as the lumen. The threshold value can be modified by the user for a different slice. The user then specifies a threshold value to generate a boundary such that it encapsulates the lumen and satisfies some conditions. Manual intervention might be needed to correct the result or in case the detection fails. For wall thickness detection, the contrast of the image is improved then segmented in parallel, based on histogram and neural network, which results into two images with lumen, thrombus, and background. The wall image is obtained by subtracting the two images followed by smoothing and interpolation. The wall thickness is computed as the shortest distance between corresponding pixels in the inner and outer walls of the vessel. Twenty image datasets, half of which are ruptured, were used for testing. The lumen error between the averaged manual segmentation of the two surgeons and Simpleware is double the error of that when compared to the proposed method. Through wall thickness evaluation, it was observed that wall thickness for ruptured cases is greater than un-ruptured.

Macía et al. in [75] segmented the lumen and thrombus in 3D from CT. The user needs to specify the initial points for the region growing algorithm, followed by morphological closing to segment the lumen, so that the lumen centerline would be computed. Centroids of connected components in a certain slice is compared to the centroid in the previous slice, and the centroid of minimum Euclidean distance is picked as lumen centroid for this slice. The thrombus is represented by radial functions in cylindrical coordinates which encapsulate the thrombus, with the centerline as their origin. The outer function requires prior knowledge of the thrombus.

Bodur et al. in [76] proposed a segmentation for the outer boundary of the aorta from CTA. The user first provides two points that belong to the lumen, and the histogram of neighboring regions is calculated, and the intensity of each voxel is checked to determine the probability of it belonging to the lumen. Distance tree in [77] is then utilized to extract the centerline defined as the path connecting the two input points, so that the slices orthogonal to it would be computed. The nodes where the centerline crosses the new slices are required to detect the aortic border. Afterwards, the isoperimetric segmentation method described in [78] was modified such that it enforces circular constraints to obtain the outer boundary.

TABLE 9.1
Quantitative comparison of AAA segmentation methods.

Paper	Evaluation Metrics	Value
[16]	Thrombus volume error	4.5±5.6%
	Max distance	5.5±3.7 mm
[18]	Mean overlap ratio,	0.9316
	sensitivity,	0.9354
	specificity	0.9837
[19]	Disc similarity coefficient	85.08%~93.16%
[20]	SI of merged volume	0.88
	HD of merged volume	8.4 mm
[22]	Outer wall Hausdorff Distance	4.160±1.096 mm
	Outer wall area overlap	94.6±1.8%
[31]	AAA correlation between proposed and manually corrected	0.93
	AAA relative error between proposed and manually corrected	12.35±13.92
[37]	AAA average volume overlap	95.8%
	AAA Average relative volume difference	1.5%
[38]	Average of two mean AAA segmentation errors	0.732 mm
[40]	AAA Minimum distance error	0.57 mm
[41]	Luminal surface error	0.99±0.18mm
	Thrombotic surface error	1.9±0.72mm
[42]	Lumen/wall volume overlap in CT	87.69±6.83 90.93±4.90
	Lumen/wall Hausdorff distance in CT	2.68±1.25 mm 3.09±1.81 mm
	Max diameter distance in CT	2.86±1.77 mm
[44]	Thrombus mean absolute volume difference	8.0%
	Thrombus mean volumetric overlap error	12.9%
[49]	Aortic wall average contour overlapping	79%
[54]	Average area error using 15 CT images.	less than 5%
[56]	Markers detected	262 out of 266
	Average relative graft volume overlap	92%
[57]	Mean accuracy: correctly matched points	97%
[62]	Detection	98%
	Mean volume overlap	0.95
[66]	AAA dice Similarity measure	Above 0.9
[72]	Average classification accuracy per scan: accuracy, sensitivity, specificity	97.7%, 91.9%, 98.6%.
[73]	Mean relative lumen area error	5.14% for un-ruptured, 2.98% for ruptured
	The mean wall thickness	1.78±0.39 mm for ruptured 1.48±0.22 mm for un-ruptured
[75]	Auto X/Man Diam and Auto X/Auto Diam	0.342±0.245 cm.

9.2.5 Summary

A summary of section 9.2 quantitative evaluation results is provided in Table 9.1.

9.3 PROPOSED TOPOLOGY PRIOR MODEL BASED AAA SEGMENTATION

In this section, a statistical based method using a topology prior model, integrating both intensity and shape information, to segment abdominal aortic aneurysm (AAA) from computed tomography angiography (CTA) scans is proposed.

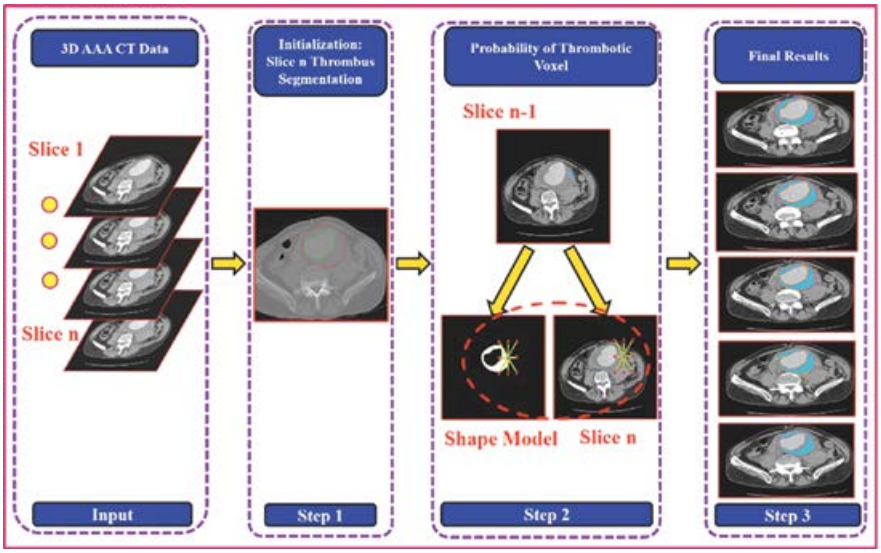

FIGURE 9.3 Block diagram of the AAA segmentation.

9.3.1 Methodology

The proposed framework for segmenting the AAA thrombus and the lumen from 3D-CTA data (depicted in Figure 9.3) utilizes a label propagation, with topology preservation, scheme using both a patient specific shape model and first-order adaptive intensity model to overcome the problem of intensity homogeneity between thrombus and its adjacent structures. Details of each model component are discussed.

9.3.1.1 Patient-Specific Shape Model

Accurate segmentation of the abdominal aortic aneurysm (AAA) wall is very difficult since the intensities/grey levels of the AAA wall are very close to the intensities of other abdominal tissues. Thus, inclusion of information on the shape or topology of AAA wall will provide a guiding feature during the segmentation process and potentially enhance the segmentation accuracy. The primary challenge in creating a prior shape model of the AAA wall is the high intra-patient variability, especially due to pathology. To overcome this challenge, we introduced adaptive shape-specific model that is based on manual delineation of the inner and outer borders of AAA. Subsequently, the appearance and the topology of the manually segmented AAA wall will be used to guide the segmentation of the adjacent slice. Each slice segmentation will drive its adjacent one, which can be viewed as an adaptive label propagation process (see Figure 9.4).

9.3.1.2 First-Order Adaptive Intensity Model

Unlike traditional shape models that depend only on the mapped voxel location to calculate the probabilistic map, our first-order adaptive intensity model ensures that only the visually similar voxels will contribute in the probability map calculations for the slice to be segmented to provide an accurate segmentation result.

The complete framework proceeds as follows: Starting from the last slice, (1) the lumen and the thrombus are manually segmented by the operator, which results in two binary masks, which are subtracted to produce the binary mask representing the thrombotic region in the first slice (see Figure 9.5). (2) Then moving backward each slice i is segmented referring to the previously segmented slice $(i+1)$ This procedure is performed as follows: at each voxel in the slice i an $N1\times N2$ window $\boldsymbol{w}$ is generated around its counterpart in slice $(i+1)$, then voxels in that window whose Hounsfield values fall within a predefined tolerance $\pm\tau$ are selected. (3) If no voxels are found, window size

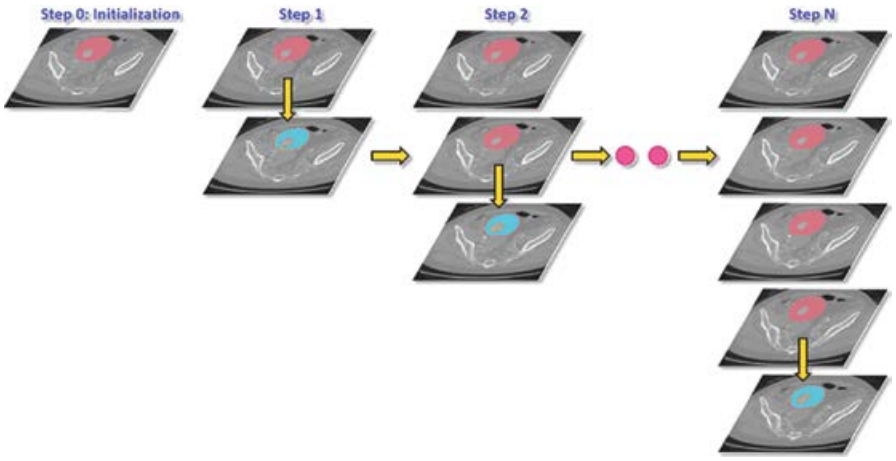

FIGURE 9.4 Step-by-step illustration of the guiding shape model.

is increased until such voxel(s) are found, or maximum window size is reached. (4) Then the probability of each voxel to be part of the thrombus is calculated as the occurrence of positively labeled voxels from the total voxels in slice $i+1$ which are within the window whose Hounsfield values are close to the voxel in slice i. Therefore, if we have k similar voxels within the window, of which m are labeled as *1*, then the probability of this voxel in slice i to belong to the thrombus is simply $p_{TH}(x) = m/k$. If $(p_{TH}(x) > 0.5)$ then this voxel x belongs to the thrombus, and background otherwise. (5) 2D median is then applied for each slice independently to improve the 2D segmentation result. (6) 3D-median filter is applied to the whole volume to improve segmentation consistency and surface smoothness. The final result is a binary volume that labels the thrombus across the slices.

To further illustrate this, we provide the following simple example. After the lumen and thrombus boundaries of slice n (last slice) are labeled to generate the binary mask in Figure 9.5, for each voxel in slice *n-1*, a 3×3 window in slice n is established as shown in Figure 9.5. If k voxels in slice n are

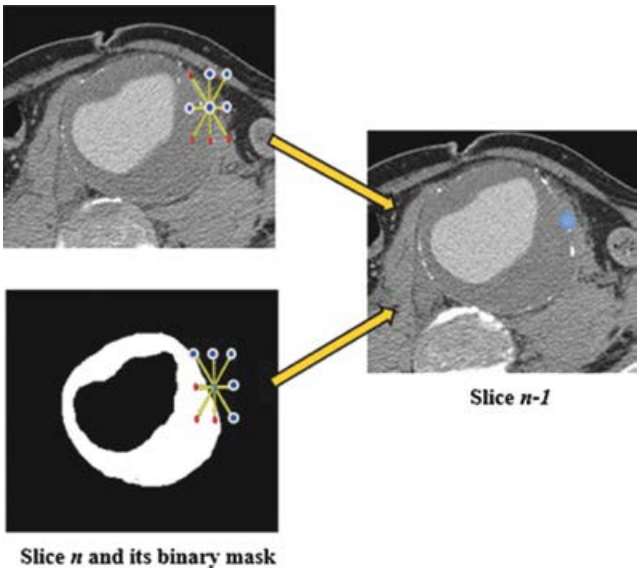

FIGURE 9.5 The window centered at voxel x location in slice n. The window contains four visually similar voxels (highlighted in red), of which three are labeled as 1 resulting in $Pth = 3/4$.

similar to voxel x (current voxel in slice $n\text{-}1$) Hounsfield value (within the given tolerance), and m out of these k voxels are labeled as 1, then $p_{TH}(x) = m/k$. If $p_{TH}(x) > 0.5$ then this voxel is thrombotic.

The related algorithm of the procedure can be described in more detail as follows:

ALGORITHM 1 TOPOLOGY BASED SEGMENTATION

1. Manually label the outer boundaries of the lumen and the thrombus in slice n.
2. Derive a mask related to the thrombotic region labeled as 1 for thrombotic voxel and 0 for background.
3. For each slice i, i=n-1to1
   For each voxel x in slice i
   a. Construct a window w around the counterpart of voxel x in slice $i+1$
   b. Find voxels with Hounsfield values that fall within a predefined tolerance $\pm\tau$ in w
   c. If no voxels are found to satisfy (b), increase size of w until correspondences are found or the maximum size allowed for w is reached
   d. Calculate the probability $p(x)$ of each voxel belonging to the thrombus based on the occurrences of white voxels from the total corresponding voxels which satisfy (b) in slice $i+1$
   e. If $(p_{TH}(x) > 0.5)$, x is part of the thrombus, background otherwise
   End For
   Apply 2D median filter on the 2D segmented binary image.
   End For
4. Apply 3D median filter on the reconstructed 3D volume

9.3.2 Evaluation

This method has been tested on CT datasets collected from six patients, the region of interest to be segmented appears in eight slices each, who were diagnosed with AAA, which was provided by Limerick University. The in-plane voxel spacing ranges from 0.7031×0.7031 to 0.8984×0.8984, while the slice thickness ranges from 1.25mm to 5mm. Final results obtained are visualized in Figure 9.6. To evaluate the accuracy of our method, we have used the Dice similarity coefficient (DC) and Hausdorff distance, that characterize the spatial overlap and surface-to-surface distances, in addition to other commonly used metrics, for comparison purpose, as illustrated in Table 9.2. An expert-radiologist manually labeled the thrombus and the lumen of the aneurysm to acquire the ground truth data to be utilized to evaluate the accuracy of our proposed method.

TABLE 9.2
Evaluation of the proposed thrombus segmentation method tested on the six patients.

Metric	$\text{Mean}_{\pm\text{Std}}$
Dice Coefficient	$0.9303_{\pm 0.0499}$
Sensitivity	$0.9138_{\pm 0.0621}$
Specificity	$0.9989_{\pm 0.0005}$
Volume overlap %	$87.350_{\pm 8.1800}$
Hausdorff distance (mm)	$3.5703_{\pm 3.1941}$
Mean absolute surface distance (mm)	$0.2578_{\pm 0.2274}$
Mean absolute volume difference %	$5.3665_{\pm 2.3786}$
Mean symmetric absolute surface distance	$0.4753_{\pm 0.4119}$

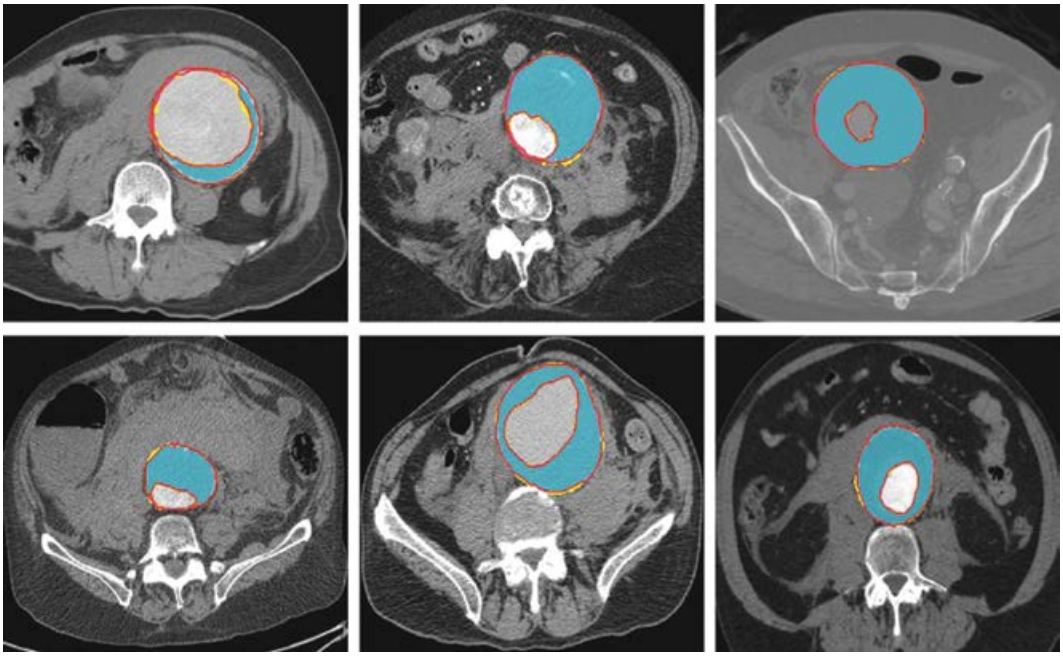

FIGURE 9.6 Example thrombus segmentation result taken from different patients with color-coded ground truth edges, false positive errors, and false negative errors (red, yellow, and pink, respectively).

Figure 9.6 shows a 2D axial projection for sample results obtained by our proposed method, from different subjects, where the ground truth edges are plotted in red along our segmentation in addition to false positive and false negative (in green, yellow, and pink, respectively). It is clear from the sample results that our proposed method accurately segments the thrombus from its neighbors with little false positive segmentation as a result of high homogeneity of neighboring tissues. This proposed method managed to achieve results that are comparable to the best results reported in the literature. The mean Dice coefficient obtained was $0.9303_{\pm 0.0499}$, and the mean Hausdorff distance for the thrombus was $3.5703_{\pm 3.1941}$ mm. Our results are summarized in Table 9.2, which also provides a comparison with the best results from the literature provided in Table 9.3.

TABLE 9.3
Best literature reported thrombus segmentation results.

Ref.	Metric	Value	S/P
19	Dice Coefficient	0.8508 to 0.9316	7/-
18	Sensitivity	0.9354	5/-
18	Specificity	0.9837	5/-
16	Volume overlap%	$95_{\pm 3.30}$	125/17
43	Outer wall Hausdorff distance (mm)	$3.09_{\pm 1.81}$	24/-
42	Mean unsigned error for thrombotic surface (mm)	$1.9_{\pm 0.72}$	1300/9
45	Mean absolute volume difference%	$8.0_{\pm 7.00}$	-/8
45	Average symmetric surface distance	$1.46_{\pm 0.40}$ mm	-/8

*S/P = Slices/Patients

TABLE 9.4
Parameter producing best results for each patient.

Patient No.	Max Window Size	Tolerance
1	15	3
2	19	0
3	17	1
4	17	0
5	5	3
6	15	2

The test set used in [18, 19] is very limited. Although the testing was performed on a large dataset in [42], it requires several manual initializations and user guidance throughout the segmentation process, which explains the high performance obtained. It can be observed that our results surpass the best results reported in the literature for some metrics, and produce comparable results for others, except for the volume overlap metric where our method is approximately 7.65% less than the highest reported value.

The most important parameters that affect the segmentation result are the tolerance τ, which controls the voxels that will contribute in the current voxel probability calculation, and the maximum window size, which determines the search space for these voxels. Both of $N1$ and $N2$ are equal, starting with 3×3 until the maximum window size is reached. Maximum allowable tolerance τ has to be specified as well. The Dice similarity coefficient and Hausdorff distance are the most important metrics. Varying these two parameters ($N1 = N2$, and τ) doesn't or slightly affects these metrics. This means that the performance of the system is stable. Because we are quantitatively comparing our work with the best values from the literature, we picked the parameters that would produce best results as well. Table 9.4 specifies the parameters used for each patient, which would produce the best performance.

9.3.3 Summary

In conclusion, this chapter has suggested a new statistical-based method for abdominal aortic aneurysm (AAA) segmentation from 3D-CT, which utilizes topology (both intensity and shape) information to perform the segmentation. The results obtained are competitive to the best results reported in literature. This makes it a promising robust medical tool to perform aneurysm segmentation to reduce the burden on radiologists.

9.4 DETECTION OF CALCIFICATION FROM AAA

Once the thrombus containing calcification deposits has been successfully segmented, the next step would be the detection of calcification. We use Bayesian classifier for this task. This can serve as a medical tool for detection and quantification of calcification, so that calcification can be included in rupture risk models to reduce fatalities and provide more accurate diagnosis.

Upon reviewing the literature, we didn't find any contributions that attempt to detect calcification specifically from AAA. This makes us the first to attempt to detect calcification from AAA.

9.4.1 Methodology

A total of 25 slices and 22 slices were used for testing and training. 4357 and 120473 data samples were used to train the calcification and thrombus (without the calcification) respectively, and

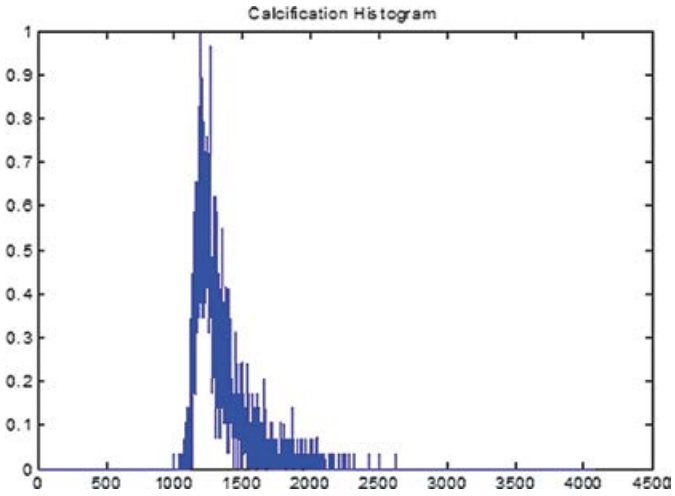

FIGURE 9.7 Normalized histogram of data used to train the calcification class.

145945 data were used for testing. Hounsfield value was the feature selected to train the two classes, because they are visually distinguishable.

Bayesian classification is a probabilistic classification well established in pattern classifications. A voxel x is considered part of calcification region if

$$p(calcification \backslash x) > p(thrombus \backslash x) \tag{9.1}$$

Using the Bayes theorem we can write the above inequality as

$$p(calcification)\,p(x/calcification)/p(x) > p(thrombus)\,p(x/thrombus)/p(x) \tag{9.2}$$

Assuming that the prior *p(calcification)* and *p(thrombus)* are equal (this is a reasonable assumption as nearly all the slices derived from the patients' scans contain these two regions), we can bring the inequality to the following expression

$$p(x/calcification) > p(x/thrombus) \tag{9.3}$$

The class-conditional probabilities densities functions *p(x/calcification)* and *p(x/thrombus)* are computed using histograms derived from the training data and normalized afterwards. These two histograms are illustrated in Figure 9.7 and Figure 9.8, respectively. Now, for a new test data of certain Hounsfield value, this value will be compared with the probabilities of the two classes. The higher probability value will determine to which class this new test data belongs. Sample segmentation results are depicted in Figure 9.9.

9.4.2 Evaluation

It important to note that due to the fact that calcification deposits have a small area, and in order to have a meaningful evaluation, sensitivity and specificity were used to evaluate calcification detection accuracy. In order to improve calcification detection accuracy, the effect of using the actual priori probabilities and morphological closing are studied as well. Bayesian classifier results for different scenarios are summarized in Table 9.5.

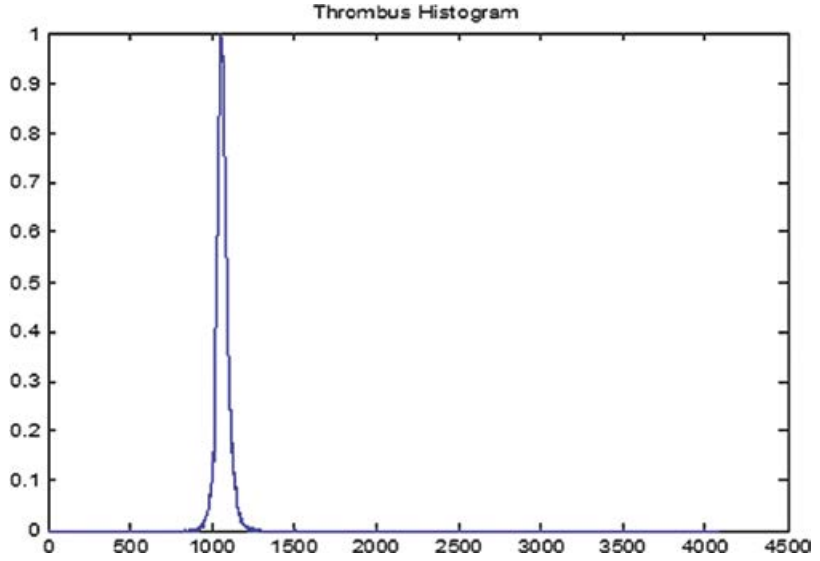

FIGURE 9.8 Normalized histogram of data used to train the thrombus class.

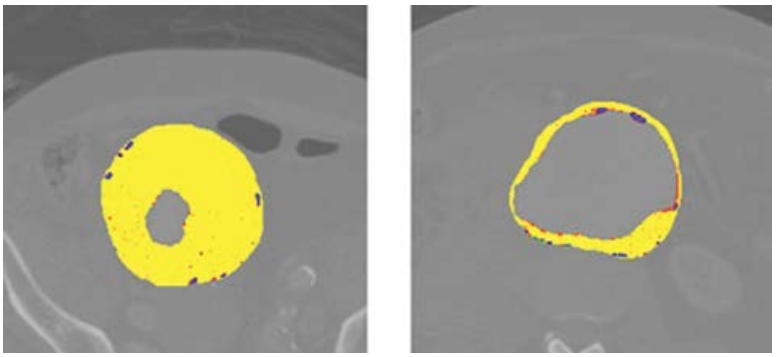

FIGURE 9.9 Sample results of detected calcification using Bayesian classifier. Blue pixels are TPs, yellow are TNs, green are FNs, reds are FPs.

TABLE 9.5
Calcification evaluation results.

Metric/ Classifier	Bayesian (equi-probable)	$p(c) = 0.1$, $p(t) = 0.5$	$p(c) = 0.0349$, $p(t) = 0.96509$ (*using actual priori probabilities*)	After morphological closing (equi-probable)	After morphological closing $p(c) = 0.0349$, $p(t) = 0.96509$	Removing regions with area < 2 $p(c) = 0.0349$, $p(t) = 0.96509$
Sensitivity	0.9580	0.9235	0.8188	0.9626	0.8250	0.8142
Specificity	0.9428	0.9767	0.9937	0.9328	0.9932	0.9960
Accuracy	0.9433	0.9750	0.9880	0.9338	0.9877	0.9900

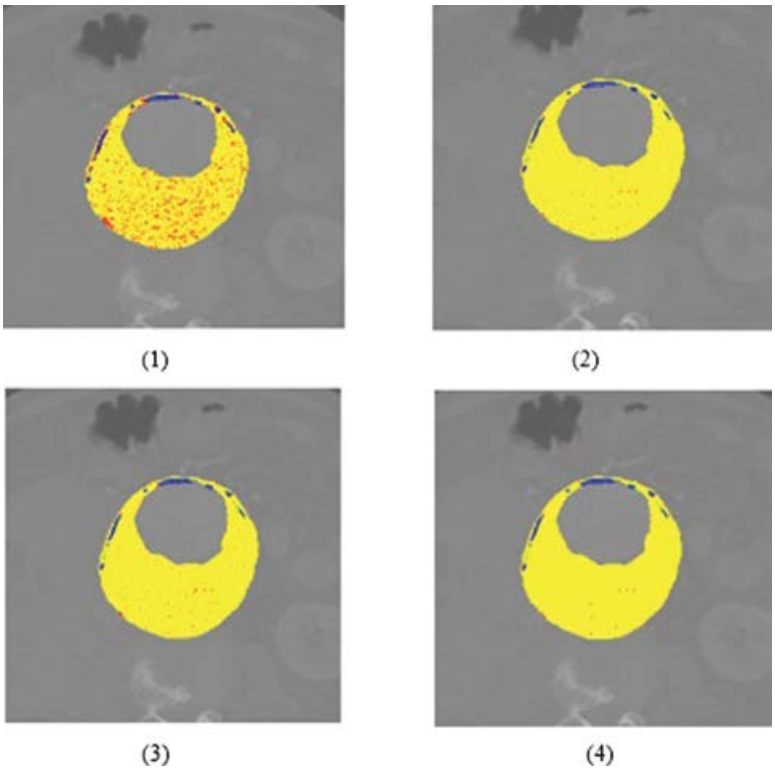

FIGURE 9.10 Sample results of detected calcification using Bayesian classifier in case (1) equiprobable classes, (2) using the actual priori probabilities, and (3) result of applying morphological closing on (2). (4) Result of removing regions less than 2 voxels (2). Blue pixels are TPs, yellow are TNs, green are FNs, reds are FPs.

The radius used for morphological closing (disk) for the equi-probable case is *1*. Increasing this radius any further slightly improved sensitivity, but significantly dropped specificity and accuracy. 0.9630, 0.8965, and 0.8987 were obtained for radius of *2* the three above metrics, respectively. Sensitivity of 0.8301, specificity of 0.9922, and accuracy of 0.9869 were obtained using a disc of radius *2 with* $p(c) = 0.0349$ and $p(t) = 0.96509$. It should be noted that the result was still visually similar to (2) even after applying morphological closing, so connected components with voxels less than 2 were removed instead (using the actual priori probabilities). These results are illustrated in Figure 9.10.

9.4.3 Summary

Good calcification detection results were obtained from segmented abdominal aortic aneurysms using Bayesian classifier. Larger training and test sets are to be used next, and other types of classifiers are to be tested to determine which leads to the highest sensitivity and specificity.

9.5 CONCLUSION AND FUTURE RESEARCH

From the literature review, a few conclusions can be drawn. The segmentation of the lumen is a straightforward task, and has been successfully performed in multiple ways as illustrated earlier. For the more difficult task of thrombus segmentation, further research still can be conducted to develop an efficient solution to the leakage problem faced by most of the existing methods. More importantly, to build a more precise biomechanical model for rupture risk

prediction, the problems of vessel wall segmentation and calcification detection have to be addressed properly by the image processing community. There are four main criteria that have to be present in future designed solutions. They need to be highly accurate such that they at least produce comparable results to the manual segmentation performed by the medical expert. The total volume processing and user interaction time, which guides throughout the segmentation process, should be a few seconds at maximum, and the manual correction step afterwards should be canceled. It is also needless to mention that the developed tool needs to be reliable and robust enough to handle different AAA scenarios and variations, and achieve an acceptable reproducibility.

In future work, we plan to:

a. Further improve the proposed thrombus segmentation method so that it would score best for all evaluation metrics when compared to the literature.
b. Improve methods of automation. This can be done by automatically segmenting the lumen in the last slice once the outer boundary of the aneurysm has been labelled by the user/operator. Lumen detection can be performed in multiple ways as previously discussed in the literature.
c. Explore other directions to increase calcification detection accuracy.
d. Perform further testing on a larger test set. We plan to introduce this as a formal dataset to provide ground truth data, and our segmented results for comparison purposes.
e. Use this tool to include calcification in RR prediction models to prove that the inclusion of calcification data in the models coupled with the maximum diameter parameters would enhance RR prediction methods. Such an approach could lead clinicians to formally adopt and accept this new method for rupture prediction.
f. Introduce a standard online dataset that can be used by other researchers, to have meaningful and fair comparisons between different contributions.

References

1. M. Belkin, M. C. Donaldson, and A. D. Whittemore, "Abdominal Aortic Aneurysms," *Current Opinion in Cardiology,* vol. 9, no. 5, pp. 581–590, 1994.
2. U. G. Jr. and S. TA, "Abdominal Aortic Aneurysm," *Am Fam Physician*, vol. 73, no. 7, pp. 1198–1204, 2006.
3. F. Moll, J. Powell, G. Fraedrich, F. Verzini, S. Haulon, M. Waltham, J. v. Herwaarden, P. Holt, J. v. Keulen, B. Rantner, F. Schlösser, F. Setacci, and J.-B. Ricco, "Management of Abdominal Aortic Aneurysms Clinical Practice Guidelines of the European Society for Vascular Surgery," *European Journal of Vascular and Endovascular Surgery*, vol. 41, no. 1, pp. 1–58, 2011.
4. E. C. B., "Abdominal Aortic Aneurysms," *New England Journal of Medicine*, vol. 328, no. 16, pp. 1167–1172, 1993.
5. K. A. Vardulaki, T. C. Prevost, N. M. Walker, N. E. Day, A. B. Wilmink, C. R. Quick, H. A. Ashton, and R. A. Scott, "Growth Rates and Risk of Rupture of Abdominal Aortic Aneurysms," *British Journal of Surgery*, vol. 85, no. 12, pp. 1674–1680, 1998.
6. C. M. Scotti, A. Shkolnik, S. C. Muluk, and E. A. Finol, "Fluid-Structure Interaction in Abdominal Aortic Aneurysms: Effects of Asymmetry and Wall Thickness," *BioMedical Engineering OnLine*, vol. 4, no. 64, pp. 64–86, 2005.
7. E. Choke, G. Cockerill, W. Wilson, S. Sayed, J. Dawson, I. Loftus, and M. Thompson, "A Review of Biological Factors Implicated in Abdominal Aortic Aneurysm Rupture," *European Journal of Vascular and Endovascular Surgery*, vol. 30, no. 3, pp. 227–244, 30.
8. C. K. Zarins, R. A. White, D. Schwarten, E. Kinney, E. B. Diethrich, K. J. Hodgson, and T. J. Fogarty, "AneuRx Stent Graft Versus Open Surgical Repair of Abdominal Aortic Aneurysms: Multicenter Prospective Clinical Trial," *Journal of Vascular Surgery*, vol. 29, no. 2, pp. 292–305, 1999.
9. R. C. Darling, C. R. Messina, D. C. Brewster, and L. W. Ottinger, "Autopsy Study of Unoperated Abdominal Aortic Aneurysms. The Case for Early Resection," *Circulation*, vol. 56, no. 3, pp. 161–164, 1977.

10. K. P. Conway, J. Byrne, M. Townsend, and I. F. Lane, "Prognosis of Patients Turned Down for Conventional Abdominal Aortic Aneurysm Repair in the Endovascular and Sonographic Era: Szilagyi Revisited?" *Journal of Vascular Surgery*, vol. 33, no. 4, pp. 752–757, 2001.
11. E. Georgakarakos, C. V. Ioannou, Y. P. T. K. Y. Kamarianakis, E. Manousaki, and A. N. Katsamouris, "The Role of Geometric Parameters in the Prediction of Abdominal Aortic Aneurysm Wall Stress," *European Journal of Vascular and Endovascular Surgery*, vol. 39, no. 1, pp. 42–48, 2010.
12. A. K. Venkatasubramaniam, M. J. Fagan, T. Mehta, K. J. Mylankal, B. Ray, G. Kuhan, I. C. Chetter, and P. T. McCollum, "A Comparative Study of Aortic Wall Stress using Finite Element Analysis for Ruptured and Non-ruptured Abdominal Aortic Aneurysms," *European Journal of Vascular and Endovascular Surgery*, vol. 28, no. 2, pp. 168–176, 2004.
13. S. A. O'Leary, J. J. Mulvihill, H. E. Barrett, E. G. Kavanagh, M. T. Walsh, T. M. McGloughlin, and B. J. Doyle, "Determining the Influence of Calcification on the Failure Properties of Abdominal Aortic Aneurysm (AAA) Tissue," *Journal of the Mechanical Behavior of Biomedical Materials*, vol. 42, pp. 154–167, 2015.
14. D. A. Vorp, M. L. Raghavan, and M. W. Webster, "Mechanical Wall Stress in Abdominal Aortic Aneurysm: Influence of Diameter and Asymmetry," *Journal of Vascular Surgery*, vol. 27, no. 4, pp. 632–639, 1998.
15. J. J. Wever, J. D. Blankensteijn, J. C. v. Rijn, I. A. M. J. Broeders, B. C. Eikelboom, and W. P. T. M. Mali, "Inter- and Intraobserver Variability of CT Measurements Obtained after Endovascular Repair of Abdominal Aortic Aneurysms," *American Journal of Roentgenology*, vol. 175, no. 5, pp. 1279–1282, 2000.
16. S. D. Olabarriaga, J. M. Rouet, M. Fradkin, M. Breeuwer, and W. J. Niessen, "Segmentation of Thrombus in Abdominal Aortic Aneurysms from CTA with Non-Parametric Statistical Grey Level Appearance Modelling," *IEEE Trans. on Medical Imaging*, vol. 24, no. 4, pp. 477–485, Apr. 2005.
17. X. Huang, D. Metaxas, and T. Chen, "MetaMorphs: Deformable Shape and Texture Models," in *IEEE Computer Society Conference on Computer Vision and Pattern Recognition*, Washington, 27 Jun.-2 Jul. 2004.
18. S. Demirci, G. Lejeune, and N. Navab, "Hybrid Deformable Model for Aneurysm Segmentation," in *IEEE International Symposium on Biomedical Imaging: From Nano to Macro*, Boston, 28 Jun.-1 Jul. 2009.
19. B. Das, Y. Mallya, S. Srikanth, and R. Malladi, "Aortic Thrombus Segmentation Using Narrow Band Active Contour Model," in *International Conference of the IEEE Engineering in Medicine and Biology Society*, New York, Aug.-3 Sept. 2006.
20. M. Kass, A. Witkin, and D. Terzopoulos, "Snakes: Active Contour Models," *International Journal of Computer Vision*, vol. 1, no. 4, pp. 321–331, 1988.
21. R. Mullick, R. Avila, J. F. Platt, Y. Mallya, R. F. Senzig, and J. Knoplioch, "Automatic Bone Removal for Abdomen CTA: A Clinical Review," *RSNA*, vol. 225, p. 646, 2002.
22. E. v. Disseldorp, J. v. Dronkelaar, J. Pluim, F. v. d. Vosse, M. v. Sambeek, and R. Lopata, "Automatic Segmentation and Registration of Abdominal Aortic Aneurysms Using 3D Ultrasound," in *IEEE International Ultrasonics Symposium, Tours*, 18–21 Sept. 2016.
23. C. Zohiosa, G. Kossiorisa, and Y. Papaharilaou, "Geometrical Methods for Level Set Based Abdominal Aortic Aneurysm Thrombus and Outer Wall 2D Image Segmentation," *Computer Methods and Programs in Biomedicine*, vol. 107, no. 2, pp. 202–217, 2012.
24. M. Subašić, S. Lončarića, and E. Sorantin, "Model-Based Quantitative AAA Image Analysis Using a Priori Knowledge," *Computer Methods and Programs in Biomedicine*, vol. 80, no. 2, pp. 103–114, 2005.
25. S. Loncaric, D. Kovacevic, and E. Sorantin, "Semi-Automatic Active Contour Approach to Segmentation of Computed Tomography Volumes," in *SPIE Medical Imaging*, San Diego, 2000.
26. H. C. Kim, S. W. Park, K. W. Nam, H. Choi, E. J. Choi, S. Jin, M. G. Kim, and K. Sun, "Determination of Accurate Stent Graft Configuration in Abdominal Aortic Aneurysm Using Computed Tomography: A Preliminary Study," *Clinical Imaging*, vol. 34, no. 4, pp. 255–262, 2010.
27. H. C. Kim, Y. H. Seol, S. Y. Choi, J. S. Oh, M. G. Kim, and K. Sun, "A Study of AAA Image Segmentation Technique using Geometric Active Contour Model with Morphological Gradient Edge Function," in *International Conference of the IEEE Engineering in Medicine and Biology Society*, Lyon, 22–26 Aug. 2007.
28. S. Loncaric, M. Subasic, and E. Sorantin, "3-D Deformable Model for Aortic Aneurysm Segmentation from CT Images," in *International Conference of the IEEE Engineering in Medicine and Biology Society*, Chicago, IL, 23–28 Jul. 2000.

29. S. Osher and J. A. Sethian, "Fronts Propagating with Curvature Dependent Speed: Algorithms Based on Hamilton-Jacobi Formulation," *Computational Physics*, vol. 79, no. 1, pp. 12–49, 1988.
30. R. Malladi, J. A. Sethian, and B. C. Vemuri, "Shape Modeling with Front Propagation: A Level Set Approach," *IEEE Trans. on Pattern Analysis and Machine Intelligence*, vol. 17, no. 2, pp. 158–175, Feb. 1995.
31. S. Loncaric, M. Subasic, and E. Sorantin, "3-D Deformable Model for Abdominal Aortic Aneurysm Segmentation from CT Images," in *International Workshop on Image and Signal Processing and Analysis*, Pula, 23–28 Jul. 2000.
32. M. Subasic, S. Loncaric, and E. Sorantin, "3-D Image Analysis of Abdominal Aortic Aneurysm," in *SPIE Medical Imaging*, San Diego, CA, 2001.
33. M. Subasic, S. Loncaric, and E. Sorantin, "Region-based Deformable Model for Aortic Wall Segmentation," in *Symposium on Image and Signal Processing and Analysis*, Rome, 18–20 Sept. 2003.
34. B. B. Nakhjavanlo, T. J. Ellis, P. H. Soan, and J. Dehmeshki, "3D Medical Image Segmentation Using Level Set Models and Anisotropic Diffusion," in *International Conference on Signal Image Technology & Internet-Based Systems*, Dijon, 28 Nov.-1 Dec. 2011.
35. P. Perona and J. Malik, "Scale-Space and Edge Detection Using Anisotropic Diffusion," in *IEEE Trans. on Pattern Analysis and Machine Intelligence*, vol. 12, no. 7, pp. 629–639, Jul. 1990.
36. H. A. Hong and U. U. Sheikh, "Automatic Detection, Segmentation and Classification of Abdominal Aortic Aneurysm Using Deep Learning," in *IEEE International Colloquium on Signal Processing & Its Applications*, Malacca, 4–6 Mar. 2016.
37. E. M. Majd, "Segmentation of Abdominal Aortic Aneurysm Using a Bayesian Level Set Approach in Computed Tomography Angiography Images," MSc. thesis, Faculty of Elect. Eng., Universiti Teknologi Malaysia, Skudai, 2011.
38. M. d. Bruijne, B. v. Ginneken, M. A. Viergever, and W. J. Niessen, "Interactive Segmentation of Abdominal Aortic Aneurysms in CTA Images," *Medical Image Analysis*, vol. 8, no. 2, pp. 127–138, 2004.
39. D. Magee, A. Bulpitt, and E. Berry, "Level Set Methods for the 3D Segmentation of CT Images of Abdominal Aortic Aneurysms," in *Medical Image Understanding and Analysis*, 2001.
40. A. J. Bulpitt and E. Berry, "Spiral CT of Abdominal Aortic Aneurysms: Comparison of Segmentation with An Automatic 3D Deformable Model and Interactive Segmentation," in *The International Society for Optical Engineering*, San Diego, 1998.
41. D. Magee, A. Bulpitt, and E. Berry, "Combining 3D Deformable Models and Level Set Methods for the Segmentation of Abdominal Aortic Aneurysms," in *British Machine Vision Conference*, Manchester, 2001.
42. K. Lee, R. K. Johnson, Y. Yin, A. Wahle, M. E. Olszewski, T. D. Scholz, and M. Sonka, "Three-Dimensional Thrombus Segmentation in Abdominal Aortic Aneurysms Using Graph Search Based on a Triangular Mesh," *Computers in Biology and Medicine*, vol. 40, no. 3, p. 271–278, 2010.
43. A. A. Duquette, P.-M. Jodoin, O. Bouchot, and A. Lalande, "3D Segmentation of Abdominal Aorta from CT-Scan and MR Images," *Computerized Medical Imaging and Graphics*, vol. 36, no. 4, pp. 294–303, 2012.
44. N. Hraiech, M. Carroll, M. Rochette, and J. L. Coatrieux, "3D Vascular Shape Segmentation for Fluid-Structure Modeling," in *IEEE International Conference on Shape Modeling and Applications*, Lyon, 13–15 Jun. 2007.
45. M. Freiman, S. J. Esse, L. J., and J. Sosna, "An Iterative Model-Constrained Graph-Cut Algorithm for Abdominal Aortic Aneurysm Thrombus Segmentation," in *IEEE International Symposium on Biomedical Imaging: From Nano to Macro*, Rotterdam, 14–17 April 2010.
46. M. Freiman, N. Broide, M. Natanzon, E. Nammer, O. Shilon, L. Weizman, L. Joskowicz, and J. Sosna, "Vessels-Cut: A Graph Based Approach to Patient-Specific Carotid Arteries Modeling," in *Modelling the Physiological Human*, Springer Berlin Heidelberg, 2009, pp. 1–12.
47. Y. Boykov and G. Funka-Lea, "Graph Cuts and Efficient N-D Image Segmentation," *International Journal of Computer Vision*, vol. 70, no. 2, pp. 109–131, 2006.
48. P. J. Besl and H. D. McKay, "A Method for Registration of 3-D Shapes," *IEEE Trans. on Pattern Analysis and Machine Intelligence*, vol. 14, no. 2, pp. 239–256, Feb. 1992.
49. N. Rieke, C. Hennersperger, D. Mateus, and N. Navab, "Ultrasound Interactive Segmentation with Tensor-Graph Methods," in *IEEE International Symposium on Biomedical Imaging*, Beijing, 29 Apr.-2 May 2014.
50. S. Martinez-Muñoz, D. Ruiz-Fernandez, Galiana-Merino, and J. Jose, "Automatic Abdominal Aortic Aneurysm Segmentation in MR Images," *Expert Systems with Applications*, vol. 54, pp. 78–87, 2016.

51. T. D. Pham and J. Golledge, "Geostatistically Constrained Fuzzy Segmentation of Abdominal Aortic Aneurysm CT Images," in *IEEE International Conference on Fuzzy Systems*, Hong Kong, 1–6 Jun. 2008.
52. E. M. Majd, U. U. Sheikh, and S. A. R. Abu-Bakar, "Automatic Segmentation of Abdominal Aortic Aneurysm in Computed Tomography Images," in *Signal-Image Technology and Internet Based Systems*, Kuala Lumpur, 15–18 Dec. 2010.
53. K.-S. Chuang, H.-L. Tzeng, S. Chen, J. Wu, and T. Chen, "Fuzzy C-Means Clustering with Spatial Information for Image Segmentation," *Computerized Medical Imaging and Graphics*, vol. 30, no. 1, pp. 9–15, 2006.
54. J. Maiora, B. Ayerdi, and M. Graña, "Random Forest Active Learning for AAA Thrombus Segmentation in Computed Tomography Angiography Images," *Neurocomputing*, vol. 126, pp. 71–77, 2014.
55. M.-B. Shim, M. Gunay, and K. Shimada, "Three-Dimensional Shape Reconstruction of Abdominal Aortic Aneurysm," *Computer-Aided Design*, vol. 41, no. 8, pp. 555–565, 2009.
56. H. D. Biasi, A. v. Wangenheim, P. G. Silveira, and E. Comunello, "3D Reconstruction of Abdominal Aortic Aneurysms," in *IEEE Symposium on Computer-Based Medical Systems*, Maribor, 2002.
57. M. d. Bruijne, W. J. Niessen, J. B. A. Maintz, and M. A. Viergever, "Localization and Segmentation of Aortic Endografts Using Marker Detection," *IEEE Trans. on Medical Imaging*, vol. 22, no. 4, pp. 473– 482, Apr. 2003.
58. C. Feinen, J. Czajkowska, M. Grzegorzek, M. Raspe, and R. Wickenhöfer, "Skeleton-Based Abdominal Aorta Registration Technique," in *International Conference of the IEEE Engineering in Medicine and Biology Society*, Chicago, IL, 26–30 Aug. 2014.
59. Y. Zhang, B. J. Matuszewski, L. K. Shark, and C. J. Moore, "Medical Image Segmentation Using New Hybrid Level-Set Method," in *International Conference BioMedical Visualization: Information Visualization in Medical and Biomedical Informatics*, London, 9–11 Jul. 2008.
60. X. Bai and L. J. Latecki, "Path Similarity Skeleton Graph Matching," *IEEE Trans. on Pattern Analysis and Machine Intelligence*, vol. 30, no. 7, pp. 1282–1292, Jul. 2008.
61. V. U. Robert and B. Ingmar, "Subvoxel Precise Skeletons of Volumetric Data Based on Fast Marching Methods," *Medical Physics*, vol. 34, no. 3, pp. 627–638, 2007.
62. J. Kawa and E. Pietka, "Kernelized Fuzzy C-Means Method in Fast Segmentation of Demyelination Plaques in Multiple Sclerosis," in *International Conference of the IEEE Engineering in Medicine and Biology Society*, Lyon, 22–26 Aug. 2007.
63. J. Dehmeshki, H. Amin, M. Ebadian-Dehkordi, A. Jouannic, and S. Qanadli, "Computer Aided Detection and Measurement of Abdominal Aortic Aneurysm Using Computed Tomography Digital Images," in *International Conference on Digital Society*, Cancun, Feb. 2009.
64. B. Hosseini, S. V. Mashak, E. M. Majd, U. U. Sheikh, and S. A. R. Abu-Bakar, "Automatic Segmentation of Abdominal Aortic Aneurysm Using Logical Algorithm," in *UKSim European Symposium on Computer Modeling and Simulation*, Pisa, 17–19 Nov. 2010.
65. L. Rouet, R. Ardon, J. M. Rouet, B. Mory, C. Dufour, and A. Long, "Semi-Automatic Abdominal Aortic Aneurysms Geometry Assessment Based on 3D Ultrasound," in *IEEE International Ultrasonics Symposium*, San Diego, 11–14 Oct. 2010.
66. B. Mory, R. Ardon, A. J. Yezzi, and J.-P. Thiran, "Non-Euclidean Image-Adaptive Radial Basis Functions for 3D Interactive Segmentation," in *IEEE International Conference on Computer Vision*, Kyoto, 29 Sept. –2 Oct. 2009.
67. J. Maiora and M. Graña, "Abdominal CTA Image Analysis through Active Learning and Decision Random Forests: Application to AAA Segmentation," in *International Joint Conference on Neural Networks*, Brisbane, 10–15 Jun. 2012.
68. L. Breiman, "Random Forests," *Machine Learning*, vol. 45, no. 1, pp. 5–32, 2001.
69. M. Yaqub, M. Javaid, C. Cooper, and J. Noble, "Improving the Classification Accuracy of the Classic RF Method by Intelligent Feature Selection and Weighted Voting of Trees with Application to Medical Image Segmentation," *Machine Learning in Medical Imaging*, vol. 7009, pp. 184–192, 2011.
70. A. Almuntashri, E. Finol, and S. Agaian, "Automatic Lumen Segmentation in CT and PC-MR Images of Abdominal Aortic Aneurysm," in *IEEE International Conference on Systems, Man, and Cybernetics*, Seoul, 2012.
71. S. Agaian and A. Almuntashri, "Noise-Resilient Edge Detection Algorithm for Brain MRI Images," in *IEEE Engineering in Medicine and Biology Society*, Minneapolis, 2009.
72. S. Agaian and A. Almuntashri, "A New Edge Detection Algorithm in Image Processing Based on LIP-Ratio Approach," in *SPIE*, San Francisco, 2010.

73. I. Išgum, B. v. Ginneken, and M. A. Viergever, "Automatic Detection of Calcifications in the Aorta from Abdominal CT Scans," *Computer Assisted Radiology and Surgery*, vol. 1256, pp. 1037–1042, 2003.
74. J. Shum, E. S. DiMartino, A. Goldhammer, D. H. Goldman, L. C. Acker, G. Patel, J. H. Ng, G. Martufi, and E. A. Finol, "Semiautomatic Vessel Wall Detection and Quantification of Wall Thickness in Computed Tomography Images of Human Abdominal Aortic Aneurysms," *Medical Physics*, vol. 37, no. 2, pp. 638–648, 2010.
75. I. Macía, J. H. Legarreta, C. Paloc, M. Graña, J. Maiora, G. García, and M. d. Blas, "Segmentation of Abdominal Aortic Aneurysms in CT Images Using a Radial Model Approach," in *Intelligent Data Engineering and Automated Learning - IDEAL* 2009, vol. 5788, Berlin, Springer Berlin Heidelberg, 2009, pp. 664–671.
76. O. Bodur, L. Grady, A. Stillman, G. Setser, R. Funka-Lea, and T. O'Donnell, "Semi-Automatic Aortic Aneurysm Analysis," in *The International Society for Optical Engineering*, San Jose, 2007.
77. L. Grady, "Fast, Quality, Segmentation of Large Volumes – Isoperimetric Distance Trees," in *European Conference on Computer Vision*, Graz, 7–13 May 2006.
78. L. Grady and E. L. Schwartz, "Isoperimetric Graph Partitioning for Image Segmentation," *IEEE Trans. on Pattern Analysis and Machine Intelligence*, vol. 28, no. 3, pp. 469–475, Mar. 2006.
79. T. C. Gasser, "Biomechanical Rupture Risk Assessment - A Consistent and Objective Decision-Making Tool for Abdominal Aortic Aneurysm Patients," *AORTA Journal*, vol. 4, no. 2, pp. 42–60, April 2016.
80. N. Kontopodis, D. Pantidis, A. Dedes, N. Daskalakis, and C. V. Ioannou, "The – Not So – Solid 5.5 cm Threshold for Abdominal Aortic Aneurysm Repair: Facts, Misinterpretations, and Future Directions," *Frontiers in Surgery*, vol. 3, p. 1, 2016.
81. P. Myers, "What Is an AAA." [Online]. http://www.huntervascular.com/aaa/. [Accessed 10 December 2016].

Taylor & Francis
Taylor & Francis Group
http://taylorandfrancis.com

10 Hermite-Based Deformable Models for Cardiac Image Segmentation

Jimena Olveres[1], Erik Carbajal-Degante[1], Boris Escalante-Ramírez[1], Leiner Barba-J[2], Lorena Vargas-Quintero[2], Enrique Vallejo Venegas[3], Lisbeth Camargo Marín[4], Mario Guzmán Huerta[4]

[1]Universidad Nacional Autónoma de México
[2]Universidad Popular del Cesar
[3]Centro Médico ABC
[4]Instituto Nacional de Perinatología

CONTENTS

10.1 INTRODUCTION

Cardiac image analysis has become an important tool for improving medical diagnosis and planning treatments. It involves volume or still image segmentation and classification of different anatomical structures, such as the heart and its cavities as mentioned in the method's reviews by [1, 2, 3], or isolated structures like ventricles as in [4, 5, 6, 7], or different analysis such as heart movement measurement [8]. All of these tasks play a critical role in understanding image content and facilitating extraction of the anatomical organ or region-of-interest. They may also help towards the construction of reliable computer-aided diagnosis systems.

Cardiac segmentation is still a challenging task due to biological aspects that depend on the diverse organ anatomy and physical issues that image modalities must face. These include, for example, noise due to unwanted movements as well as from the respiratory system, cardiac synchronization, and differences in anatomy when a pathology occurs. Defining heart's edges and structures is of considerable importance in medical imaging, and results are not always as expected. If, in addition, we add organ movement, it increases the difficulty of the task. Such is the case of the heart and its corresponding expansion and contraction. The visualization of human organs also depends on the type of image technology used.

Cardiac computed tomography (CT), nuclear cardiology, echocardiography, cardiovascular magnetic resonance (CMR), positron emission computed tomography (PET), and coronary angiography are imaging modalities that have been used to measure myocardial perfusion, left ventricular function, and coronary anatomy for clinical management and research.

The practical clinical application of these modalities depends heavily on their specific inherent strengths and weaknesses. This large variety of imaging techniques has resulted in a lack of standardization and has made accurate intra- and cross-modality comparisons for clinical patient management and research very difficult.

In the case of left ventricular systolic dysfunction, the most pressing consideration is to determine if coronary artery disease, valvular disease, or any other etiology is responsible for [9]. If heart failure occurs, the heart shows reduced function. This may cause the left ventricle (LV) to lose its ability to contract or relax normally. In response, LV compensates for this stress by modifying its behavior, which creates hypertrophy that causes enlargement and hardening of the LV muscles and progresses to congestive heart failure [10].

Non-invasive imaging evaluations and clinical controls increase the probability of the survival of patients. They are also very important in the initial assessment of patients with new-onset heart failure [11]. Information about the current condition of the anatomical structures of the heart is needed for an early and accurate diagnosis. In the case of suspected heart failure, the most common image modality is the ultrasound-echocardiography due to its low cost and good spatial resolution. However, the reproducibility of quantitative measurements is user dependent and can be variable [9]. Magnetic resonance imaging (MRI) has also been used as a reference method [1]. It is useful for scanning and detecting abnormalities in soft organs, and there is no involvement of any kind of radiation, yet it is expensive and presents limited availability compared with computed tomography (CT) [12]. MR technology offers high resolution and SNR among other characteristics, however, it is an expensive alternative that few hospitals can afford.

CT has the advantage of being more accessible. In the X-ray technology, the calibration curves needed are well known, while in MR there are large characteristic variations to consider for its procedures. Most medical segmentation algorithms are created for magnetic resonance images because of the good contrast offered by this technology. Although CT imaging does not provide suitable contrast resolution in comparison with MRI, it is far more accessible and has enough spatial resolution to distinguish adjacent organs [13]. In addition, it is a growing tendency for the cardiac CT studies because of its cost [14] and other advantages. However, it is well-known that CT-based heart segmentation is sensitive to initialization, noise, and image characteristics. In the case of heart failure along with coronary artery disease, CT imaging provides insights and detailed information of the heart that support and tailor treatments. Furthermore, heart examination using CT generates 2D and

3D high-resolution images throughout the entire cardiac cycle, which are useful for segmentation tasks. In addition, the use of contrast agents can improve endocardial border definition.

Several techniques have been developed for epicardium and endocardium segmentation using the short axis view. Petitjean and Dacher [2] presented a review of a large group of automated and semi-automated segmentation methods. Kang et al. [1] also wrote a review about the most used methods in cardiac segmentation. The review includes methods based on atlases, deformable models such as level sets (LS), and statistical models with prior knowledge such as active shape models (ASM). However, these methods are focused on MRI. Also, some methods mentioned, such as classic active contours and level sets, are associated with a minimum functional, which often leads to over-segmentation [15].

Therefore, other studies have suggested that the combination of different techniques may improve organ segmentation [16, 17, 18, 19]. For instance, in [6], the authors improved the weighted C-means clustering [20] with a fitting model. In [18], Kronman et al. proposed an adjustment to the segmentation by using active contours based on level sets and a correction of the segmentation leaks using a ray casting method. Ma et al. [5] used a Haar classifier to detect the heart area. Then, the segmentation is performed with an ASM. Dolz et al. [21] showed a hybrid approach combining a watershed transformation with graph-cut segmentation in order to delineate organs such as the spinal canal, lungs, heart, and pericardium. Antunes et al. [7] used level sets to extract the cardiac surface from multi-detector computed tomographic data. The authors coupled a 3D level set with a stopping function based on a multi-scale second derivative Gaussian filter. The results show that the combination of methods outperforms single approaches.

Ultrasound analysis is the standard modality in the evaluation of fetal heart during pregnancy due to the low risk that this medical imaging technique represents for the fetus and mother. Ultrasound systems are used for the assessment of the cardiac function. For evaluation and diagnoses in fetal echocardiography, it is commonly needed to perform quantitative analysis. Some measures that can be obtained for this task are stroke volume, ejection fraction, and dimensions of the ventricular wall. Motion estimation of the heart cavities can be also performed for heart evaluation. Current advances in ultrasound systems allow the acquisition of data in two, three, and four dimensions.

In recent years, different approaches have been proposed to evaluate the cardiac cavities in order to detect heart diseases and cardiac defects of the fetuses. Some of them are focused in determining the size and dimension of the cavity structures. Normally, these annotations on the fetal heart are manually realized by the expert, which is time consuming, tedious, and operator-dependent. For this reason, automatic segmentation methods are necessary for fetal assessment. However, this task is challenging because of the characteristics of ultrasound images and the changes that might suffer the cardiac cavities during gestational ages [22, 23, 24, 25].

Ultrasound data has many limitations for analysis, which result in quality loss, such as low contrast, lack of contours, and artefacts. These limitations hinder the examination and diagnostic accuracy of the studies. These problems also influence the development and effectiveness of segmentation techniques. Different methods have been proposed to address this. One of the methods frequently used in the analysis is a prior knowledge-based technique that uses a training set to code the variability of known shapes [26, 27, 28, 29, 30].

On the other hand, methods that resemble the human visual system have increased in popularity because they allow images to expand into a local decomposition that describes intrinsic attributes related to important cues and highlights structures that are useful for segmentation [31]. The Hermite transform (HT) [32, 33] has been used successfully as a texture descriptor in [34] and [35]. The HT is a special case of the polynomial transform and is based on Gaussian derivatives, thus it is possible to compute local orientation analysis.

In this chapter, four approaches are proposed to improve actual segmentation on cardiac studies with local analysis.

The segmentation schemes were applied on endocardium and/or epicardium, and are based on various active contour and statistical algorithms using steered Hermite coefficients as local descriptors.

10.2 SEGMENTATION METHODS

This section briefly presents the foundations of segmentation models used in this research. As mentioned previously, adequate border delineation is highly desirable in many organ structures. Some early models used for this objective were the active contours and deformable models, which provide powerful advantages to the image analysis field. Segmentation tasks are still challenging because of the nature of the organ anatomy, their function and their image characteristics, such as noise, artifacts, and acquisition protocols. The most common segmentation techniques can be classified in two sets [1]:

Segmentation techniques without previous knowledge of the segmented object or with very little information. They include most of the basic methods based on image information or pixel classification. These techniques include algorithms such as thresholding, border detection, region growing and graph-cuts, as well as basic level sets.

Segmentation techniques with more elaborated previous knowledge, like deformable models, active shape models, active appearance models, and atlas based methods. The prior knowledge can be a speed restriction, a maximal statistical distance between two or more organs, or a shape restriction that modifies the curve evolution.

This chapter's objective is to show how to improve different schemes of segmentation techniques, such as active contours and deformable models, which belong to the more robust segmentation category, making use of local analysis methods. These models rely on the idea that a curve from a given image, subjected to some constraints, can evolve in order to detect objects and sometimes even specific shapes. This chapter is focused on two different models: statistical models and deformable models implemented by level sets.

Active shape models (ASM) and active appearance models (AAM) [36], [37] are part of the statistical deformable models; they can detect objects with specific shape boundaries. Cootes et al. [36], [37] argue that a shape model can deform to some extent within a certain variability. Therefore, ASMs and AAMs are able to deform their shape so that they resemble the real organ. Other studies such as [38] and [4], have applied ASMs to different anatomical organs, such as heart and pediatric cerebellum.

Deformable models and their implementation by level sets proposed in [39] have been widely used in medical image segmentation [40]. They deform according to the image features used to handle the curve evolution, and they can be categorized as edge based [41], region based [42], [43], and model shape based [44], [45]. An extension of the method for vector-value images was proposed by Chan and Vese [46] and was applied to color images. Additionally, Paraggios et al. [47] applied it to supervised texture segmentation problems. The vector value extension allows for the introduction of different kinds of features at the same time without requiring any prior knowledge. For example, Brox et al. [48] simultaneously introduced texture features, gray level, and optic flow for the segmentation process.

10.2.1 Hermite Transform

The Hermite transform is a special case of a polynomial transform that incorporates biological properties due to the similarity between Gaussian derivatives and receptive fields in the human visual system [49, 32, 33]. The main advantage of this tool is the easy extraction of important details as lines, edges, and texture information by applying a decomposition scheme.

The Hermite analysis functions D_n are a set of polynomials obtained from the product of a Gaussian window and the Hermite polynomials H_n, the latter functions are obtained using the Rodrigues' formula [50]. The value of n indicates the order of analysis and σ the spread of Gaussian window,

$$D_n(x) = \frac{(-1)^n}{\sqrt{2^n n!}} \frac{1}{\sigma\sqrt{\pi}} H_n\left(\frac{x}{\sigma}\right) \exp\left(\frac{-x^2}{\sigma^2}\right) \tag{10.1}$$

FIGURE 10.1 Spatial Hermite filters (left) and their corresponding frequency response (left center). Hermite coefficients of a cardiac CT image in the cartesian form (right center) and the steered version (right) from order 0 up to 3.

These functions in Eq. (10.1) are used to expand a signal at every window position providing a localized representation. For the two-dimensional case (see Figure 10.1), an image $I(x,y)$ can be projected into the analysis functions since they are spatially separable and rotationally symmetric, that is $D_{n-m,m}(x,y) = D_{n-m}(x)D_m(y)$.

$$L_{n-m,m}\left(x_0,y_0\right) = \int_{-\infty}^{\infty}\int I(x,y)\, D_{n-m,m}\left(x_0-x, y_0-y\right)dx\,dy, \tag{10.2}$$

for $n = 0,1,\ldots,\infty$ and $m = 0,\ldots,n$.

A steered version of the Hermite transform (SHT) is based on the principle of steerable filters [51] and implemented by linearly combining the cartesian Hermite coefficients, Eq. (10.3) and Eq. (10.4). The steering property is useful to adapt local orientation content according to a criterion of maximum oriented energy, then achieving compaction [52].

$$L^{\theta}_{n-m,m}\left(x_0,y_0\right) = \sum_{k=0}^{n} L_{n-k,k}\left(x_0,y_0\right) R_{n-k,k}(\theta), \tag{10.3}$$

$$R_{n-m,m}(\theta) = \sqrt{\binom{m}{n}}\cos^{n-m}\theta \sin^{m}\theta, \tag{10.4}$$

where $R_{n-m,m}(\theta)$ are known as the cartesian angular functions, which indicate the direction of maximum oriented energy at all window positions. This energy is preserved in terms of its coefficients and can be expressed by the Parseval's formula:

$$E_{\infty} = \sum_{n=0}^{\infty}\sum_{m=0}^{n}\left[L_{n-m,m}\right]^2 = \sum_{n=0}^{\infty}\sum_{m=0}^{n}\left[L^{\theta}_{n-m,m}\right]^2 \tag{10.5}$$

An extension to three-dimensional signals is straightforward since the Gaussian function is separable. Following the decomposition scheme for the 3D case, the expansion can be performed by convolving a volume $I(x,y,z)$ with the set of Hermite filters in x, y and z coordinates.

10.2.2 Active Appearance Model for Fetal Ultrasound Left Ventricle

Active appearance models (AAM) are very popular and well-known methods for medical image analysis. In cardiac segmentation of ultrasound images, AAM has demonstrated being highly robust to typical limitations such as missing edges and low contrast.

The AAM technique consists of computing a statistical model from a training set, which codes the shape and texture changes of the specific structure under analysis. In the AAM scheme, the shape and appearance parameters are combined. The statistical model is built from a set of annotated shapes that correspond to the structures of interest. In this way, the point's information given by the landmarks represent the shape and the gray levels corresponding to the texture of the marked structures. Initially, a specific number of training samples is selected from the dataset. Therefore, the prior knowledge used in this technique is a remarkable advantage when comparing with other methods. The standard AAM basically involves three stages. In the first stage, a statistical model is built considering the shape of the object. Afterwards, a statistical texture model is obtained using the appearance features inside of the marked region. Finally, shape and appearance models are combined.

10.2.2.1 Point Distribution Model

The statistical shape model is obtained from a set of N training images in which manual annotations are realized on the structure of interest. An important aspect of this method is that each shape S_i (with $i = 1,2,\ldots,N$) of the dataset must contain the same quantity of landmarks. Then, $S_i = \{F_{i1}, F_{i2}, \ldots, F_{im}\}$ where $F_{ik} = (x_i, y_i)$, $k = 1,2,\ldots,m$. Here, m is the number of landmarks used for the shapes, and N is the number of samples. An alignment process is applied to all shapes with the aim of reducing the differences regarding the scale, translation, and rotation [53, 54]. Figure 10.2a shows an example of an annotated shape corresponding to the LV.

Principal component analysis is calculated for reducing data dimensionality and determining the main variation modes visible in the training set. The shape model associates the mean shape with the matrix $\mathbb{Z}$ which contains the eigenvectors given by PCA. The shape model is obtained by the following expression

$$S = \overline{S} + \mathbb{Z}\, b \tag{10.6}$$

where $\overline{S}$ represents the mean shape computed from the set of aligned points. $\mathbb{Z}$ is the eigenvector matrix corresponding to the highest eigenvalues λ_s computed through PCA. The shape parameter b varies in the range defined by $-3\sqrt{\lambda_s} \le b_s \le 3\sqrt{\lambda_s}$ [12, 13].

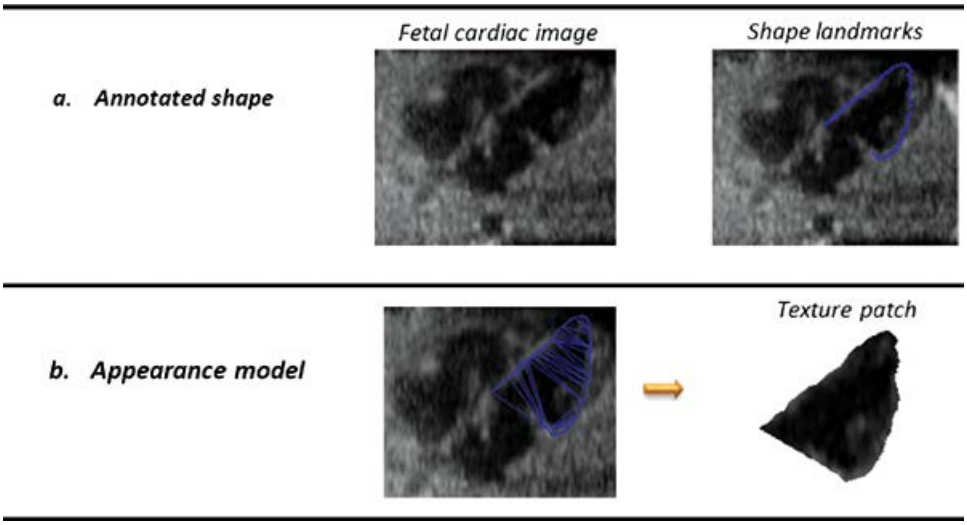

FIGURE 10.2 Example of the shape and texture patch selected from a training sample.

10.2.2.2 Statistical Texture Model

The appearance model is a robust technique that uses texture attributes for analysis and image modeling. The texture information is obtained from the intensity levels of the object of interest. The patch enclosed by the shape points must be selected. A vector G_i of gray levels is built for each structure of the training set. Then, $G_i = [g_{i1}, g_{i2}, \ldots, g_{ik}]$, where $i = 1,2,\ldots,N$. Here, k is the number of elements of the vector and g_{ik} represents the gray level intensity. An example of a texture patch obtained from an annotated echocardiography image is shown in Figure 10.2.

An alignment process is performed with a selected reference texture. A normalization process is also required [53]. In order to obtain the same number of pixels, an affine transformation [55, 56] and triangulation methods are used [57]. Similar to the shape model, the mean texture and PCA are found to build a statistical texture model. Therefore, the eigenvector matrix T corresponding to the highest eigenvalues σ_n is used to build the texture model, which is written as

$$G = \bar{G} + Br, \tag{10.7}$$

where r is the parameter that allows deforming the model. This variable is known as the texture parameter, and it has a variation range defined by $-3\sqrt{\sigma_n} \leq r_n \leq 3\sqrt{\sigma_n}$.

10.2.2.3 Statistical Model Combination

As mentioned, AAM is a combination of the texture and shape models. These features allow better appearance modeling, which generates a robust method. A concatenation of the shape and texture parameters must be performed. Then, the combined model can be defined as

$$h = \begin{bmatrix} \rho b \\ r \end{bmatrix} = \begin{bmatrix} \rho \ \mathbb{Z}^T \left(S_i - \bar{S}\right) \\ B^T \ (\mathbb{G}_i - \bar{G}) \end{bmatrix}, \tag{10.8}$$

where the term ρ is a weight matrix that balances the differences found in the variation range between b and r. This variable is needed because these parameters measure different magnitudes. PCA is applied to the combined model h. Finally, the statistical model that incorporates shape and texture features is calculated as:

$$h = Qc, \tag{10.9}$$

where Q contains the eigenvectors given by the significant eigenvalues ϑ_f, and c is the final parameter, which deforms the shape and texture model at the same time. The variation range of c is specified by $-3\sqrt{\vartheta_f} \leq c_f \leq 3\sqrt{\vartheta_f}$. Equations (10.6) and (10.7) are then rewritten as:

$$S = \bar{S} + \mathbb{Z}\, \rho^{-1} Q_S c \tag{10.10}$$

$$G = \bar{G} + BQ_G c, \tag{10.11}$$

where Q_S is the eigenvector matrix of the shape model, and Q_G is the eigenvector matrix found for the texture model.

10.2.2.4 Segmentation Using AAM

The method used to segment new samples computes the smallest difference between the target image from the model and a new input image. The difference vector is determined by

$$\delta I = I_{input\ \ image} - I_{trained\ \ model} \tag{10.12}$$

During the process, the parameter c must be calculated iteratively (see Eq. 10.13). For this purpose, a regression matrix must be used. This regression matrix is found in the training process and is used to code the variation of shape and texture of the structure of interest [36, 53]. The process finishes until the parameter does not change its value.

10.2.2.5 AAM Multi-Texture Scheme Based on the Steered Hermite Transform Applied to Fetal Echocardiography

Common problems found in ultrasound images can substantially reduce the efficiency of the segmentation methods such as AAM [58, 59]. The problem is more severe when working on fetal echocardiography. The image is significantly degraded by the speckle pattern and other artifacts that hinder the ability to detect some characteristics such as boundaries and homogeneous regions. Many researches have proposed denoising techniques to improve the segmentation performance on echocardiography, while other authors consider the speckle pattern to be essential for the analysis [60, 61]. Following this assumption, we can use the steered Hermite transform to code the texture information. As described, the AAM uses texture patches to build a statistical model. Since the Hermite transform is an operator with remarkable abilities for coding texture features, it can be combined with AAM.

The method described here uses the steered coefficients of the Hermite transform to build a multitexture AAM scheme. This method was proposed by Vargas et al. [62]. Here, coefficients $L^{\theta}_{0,0}$, $L^{\theta}_{1,0}$ and $L^{\theta}_{2,0}$ are used to code the texture features in AAM. These coefficients concentrate the maximum energy of the transformation. Figure 10.3 presents an example of the Hermite transform and the rotated version applied to a cardiac fetal ultrasound image. Each coefficient is independently used to build an AAM. Finally, the three models are combined using a weighted scheme. With these

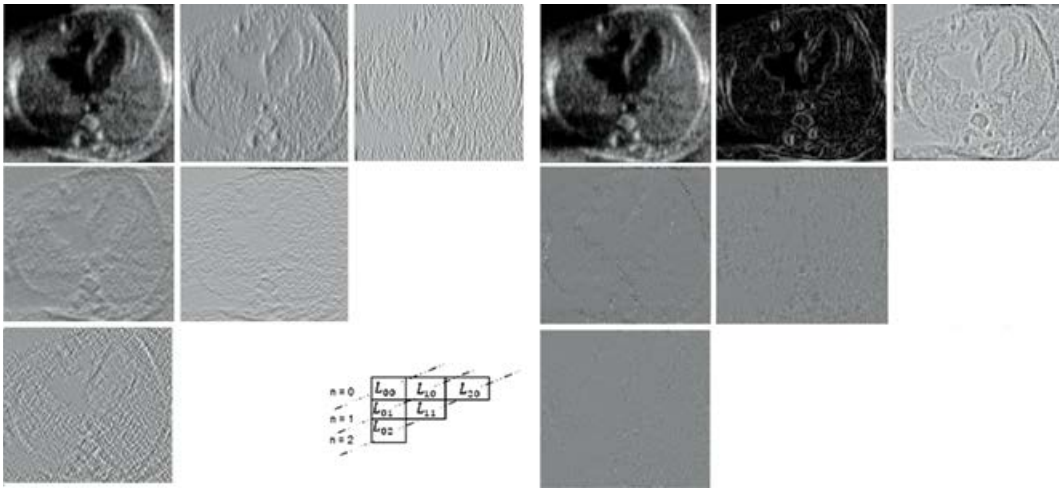

a. *Cartesian coefficients* b. *Steered coefficients*

FIGURE 10.3 The Hermite transform applied to a cardiac ultrasound image.

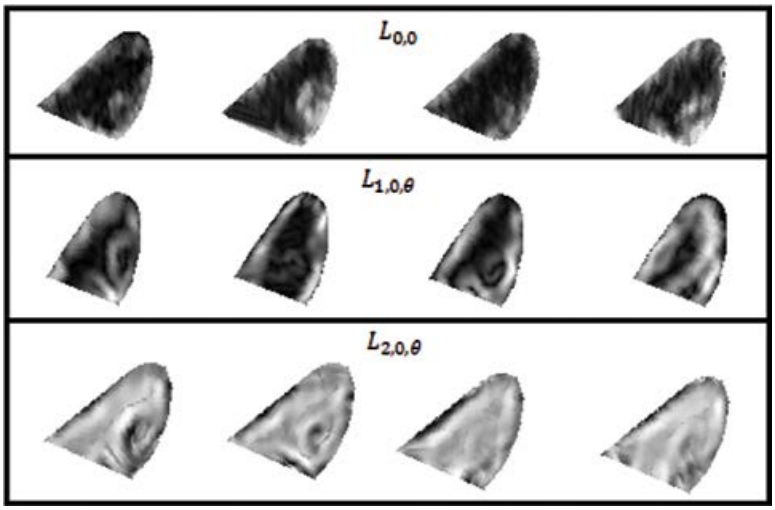

FIGURE 10.4 Modes of variation generated using three SHT coefficients.

coefficients, we can code intensity, edges and zero-crossing features. The steered coefficients are used because they provide directional analysis, which is an important property when working with textures.

During the segmentation, an AAM-based search must be performed using the texture Hermite coefficients of the input image. Similarly, the differences (Eq. 10.12) and the statistical models for each steered coefficient must be found. Then, the optimum parameters $\mathbb{C}_{j0}$ are calculated as

$$\mathbb{C}_{j0}^{It} = \mathbb{C}_{j0}^{It-1} - \mathcal{R}_{j0}\ \delta B_{j0} \tag{10.13}$$

where $j0$ with $j = 0, 1, 2$ correspond to the SHT coefficients. Here, $\mathcal{R}_{j0}$ is the regression matrix obtained from the training stage and It is the current iteration. The process requires an initial parameter $\mathbb{C}_{j0}$ which is commonly set to zero. Therefore, the texture model is updated using Eq. (10.11) for each steered Hermite coefficient. The main objective is to obtain the contour of the cardiac structure. A general statistical shape model is obtained by using a weighted combination of the three shape models. Then,

$$S_t = \sum_{j=0}^{2} a_j \left(\overline{S}_{j0} + \mathbb{Z}_{j0}\rho_{j0}^{-1} Q_{j0} co_{j0}^{t}\right) \tag{10.14}$$

where a_j is the weight parameter normalized to $\sum_{j=0}^{2} a_j = 1$. Figure 10.4 shows examples of the modes of variation captured for a multitexture AAM associated to the steered Hermite coefficients.

10.2.2.6 Segmentation Examples

Figure 10.5 illustrates some examples of the segmentation achieved using the AAM method based on the steered Hermite transform. Images correspond to two examples of fetal echocardiography. Each row represents a different image. Examples are shown for several iterations. It can be noted how the initial contour, shown in Figure 10.5a, is updated until reaching the final segmentation (Figure 10.5d). In the last column, both contours, the initial shape (green contour) and the final one (red contour), are drawn together with the aim of illustrating the deformation suffered by the initial shape.

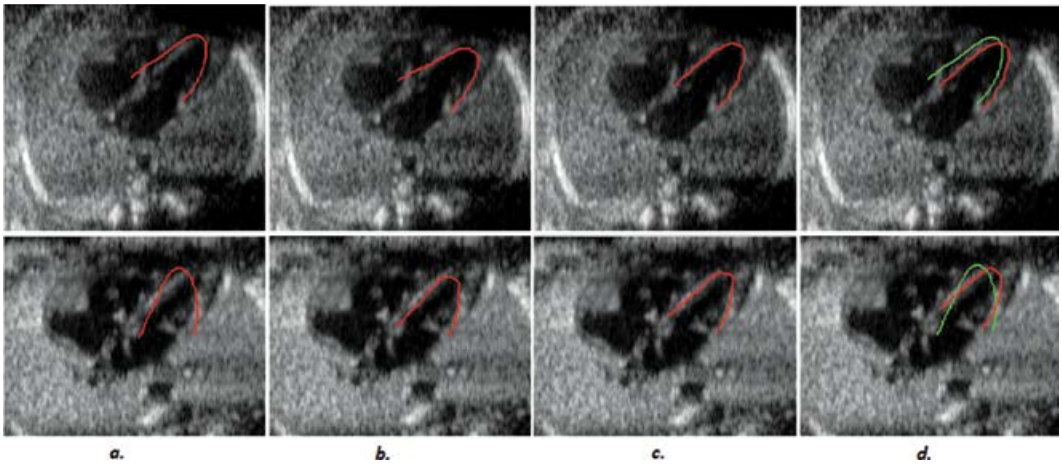

FIGURE 10.5 Segmentation example using the AAM based on the SHT. Each row represents different examples. a-d. Iterations of the method until reaching the desired segmentation (red contour).

In the examples described previously, it was assumed that an initial shape was available, which is a requirement for AAM-based methods because they consist of local techniques. Finding an acceptable initial shape is another challenging problem that must be resolved. Vargas et al. [62] proposed an interesting initialization scheme for these types of applications.

The segmentation obtained with this method can be used for computing some clinical measurements that are useful for assessment of the fetal heart. Moreover, the segmentation might contribute to evaluating the motion of the LV if performed in all images of an echocardiographic sequence.

10.2.3 Active Shape Model for CT Left Ventricle

In [36], Cootes et al. proposed active shape models (ASM) as a refinement of statistical deformable models. As part of the method it trains a known shape, with the final purpose of recognizing it in a new image. An ASM creates a point distribution model (PDM) from a certain number of similar shapes and from there obtains an average shape $\bar{X}$. The goal of the approach is based on the idea that it is possible to deform $\bar{X}$ to some extent to produce certain variability until the ASM meets the boundaries of the object of interest.

The algorithm consists basically of two steps: build a statistical shape and gray model from a set of aligned shapes and at the same time compute a gray level appearance model to obtain specific characteristics of boundary points; and execute an ASM search, to recognize a similar model shape.

Statistical shape model is obtained by executing a statistical shape and a gray-level profile model.

1. A set of M aligned shapes is built. We use manual annotations for each volume to be involved in the training phase, delineating contour lines of the shape for each image. An alignment is applied to each shape involving translation, rotation, and size transformations. For each training shape, a vector of landmarks is obtained $S_{\{i\}} = ((x_{\{0\}},,y_{\{0\}}),\ldots,(x_{\{n-1\}},,y_{\{n-1\}}))^T$. So that the average shape is the mean shape, $\bar{X}$, is the average of all landmarks $\bar{X} = \frac{1}{M}\sum_{k=0}^{M-1} S_k$.
2. The variations of the mean shape are obtained by computing principal component analysis [36], [37], and single value decomposition is used to find the point distribution model (PDM) parameters [63]. The least significant eigenvalues and eigenvectors are removed to avoid singular correlation matrix and data over-fitting [64].

The number of training datasets is often (very) small in comparison to the number of landmarks, and they can lead to a singular correlation matrix and over-fitting of the training data. To reduce such effects, it is necessary to crop the number of eigenvalues, keeping between 90% and 99.5% of the variance in the training data. The mean shape is deformed within certain limits to recognize a new shape according to $\hat{X} = \overline{X} + Pb$, where P is the matrix of the t first principal components, b is the weight vector, and $\hat{X}$ is the estimated shape.

The **gray-level profile model** is also part of the training statistical model construction. Since shapes are described by points enclosing a contour, gray-level profiles normal to each landmark point are calculated. First and second moments are obtained by calculating the mean and covariance matrix from the training set. Either the gray profile or its normalized derivative can be employed.

10.2.3.1 ASM Search

1. In the search phase $\overline{X}$ is placed close to the object of interest manually. The mean shape is deformed within certain limits to recognize a new shape as follows: $\hat{X} = \overline{X} + Pb$. Each landmark in $\overline{X}$ is compared against its corresponding profile, which is a line of pixels that is perpendicular to the landmark. Then the landmarks are moved iteratively toward those that obtain the lowest distance, using for example the Mahalanobis distance. The new contour coordinates, $\hat{X}$, are an estimate of the original contour.

   It is possible to generate new shapes by modifying a parameter b within certain limits to obtain similar shapes of the object to be recognized [65]. Here, b is constrained to the range $\pm m\sqrt{\lambda_i}$ with m between 2 and 3. This restriction limits shapes within 2 or 3 standard deviations of the distribution of shapes in the training data.
2. When new positions for the landmarks are found, an aligning process must be computed to adjust the shape. Pose parameters are used to calculate final deformations to move the current estimate to a new position. The process is iterative and stops when a specific number of iterations or a threshold is reached (see Figure 10.6).

It is well-known that ASMs are often limited when dealing with texture segmentation because they model contours using only shape. Typically, gray level information is included in the functional that drives the fitting of the contour.

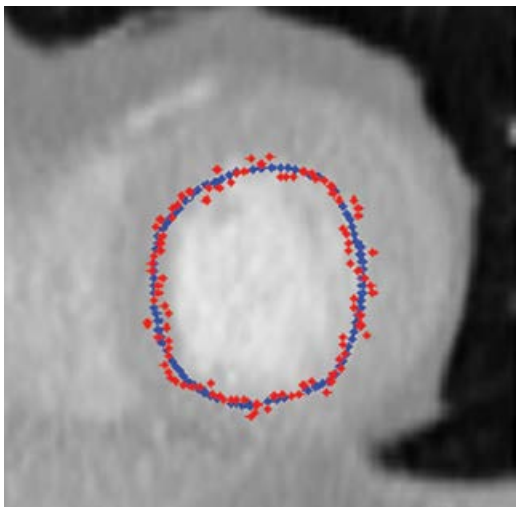

FIGURE 10.6 ASM Adjustment of ventricle shape on a CT image.

The goal of this study is to identify endocardial and epicardial walls that contain myocardium with better precision. In the dataset, the endocardium possesses good contrast, while the epicardium is not always well-defined. Several attempts to segment such structures have been made, such as the ones mentioned in the Introduction, but still better techniques are needed to improve results.

Taking advantage of the SHT, it is feasible to characterize important tissue structures and incorporate the information from the Hermite coefficients (HCs) into the ASMs schemes to improve the segmentation.

A dataset of 28 annotated tomographic cardiac studies was acquired from healthy subjects with a CT Siemens dual source scanner (128 channels) at Centro Médico ABC México. The heart volumes were captured in signed 12-bits DICOM format. The age of subjects ranges from 17 to 81 with an average age of 55; 16 studies belong to males and 12 studies belong to females. All patients present low risk for coronary artery disease and atypical chest pain.

Each study belongs to a single subject and consists of 10 volumes taken at different times during the electrocardiography (ECG)-synchronized cardiac cycle. This method is called ECG-gating, where a volume is acquired only during certain consecutive periods of the cardiac cycle being retrospectively reconstructed. It covers systolic and diastolic cardiac phases.

The studies start on a final diastolic (relaxing) phase, go throughout the systolic (contraction) phase, and return to the diastolic phase, providing images at 0%, 10%, 20%, 30%, 40%, 50%, 60%, 70%, 80%, and 90% of the cardiac cycle. The spatial resolution values range from 0.302734×0.302735×1.5 [mm] to 0.433593×0.433593×1 [mm]. As a prerequisite for left ventricle (LV) visualization, the heart must be oriented in order to obtain a canonical view: horizontal, long, and short axis views. The short axis view shows a plane that is perpendicular to the long axis and gives a suitable cross-sectional view of both ventricles [66], [67]. On the short axis view, the LV is aligned vertically from the base of the heart to the apex (see Figure 10.7).

The first step is to seed a suitable initialization for the ASM algorithms. This is accomplished by estimating the position of the centroid of the LV blood pool during the diastole phase using a compactness metric similar to Lu et al. [16] . This is a simple yet effective way to compute the initial pose. This step is performed on a slice from the mid-third or mid-cavity of the heart volume [3], [68]. A limitation of this step is that in the case of failure the LV cavity center must be manually specified.

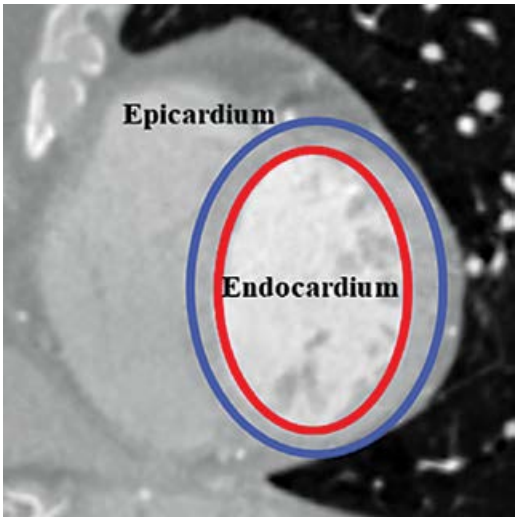

FIGURE 10.7 CT image of the heart displayed using the short axis view where it is possible to see the right and left ventricles. The red ellipse defines the endocardium, whereas the blue ellipse defines epicardium.

10.2.3.2 Combining Active Shape Models with the SHT Coefficients

In [64], the authors proposed to combine ASMs and local binary patterns by considering only landmark profiles. Here, we extend the area of analysis and propose to combine ASMs with HCs to improve the segmentation of the LV. In addition, changes are made to the original ASM algorithm and three methods are explored: ASM, ASM-Profile with HCs, and ASM-Quadratic with HCs.

For all the cases, the initial parameters are set to: number of landmarks = 70, normal profile length = 11, and iterations = 60. These values were chosen based on the results of the experiments. Different combinations were evaluated such as the number of landmarks, profile length, and number of iterations.

In the **ASM/Profile-HC (ASM/PHC)** during the training phase, the Hermite coefficients are calculated over square regions of 9×9 pixels around every landmark based on the approach presented in [64]. Then, a histogram that describes the corresponding landmark is constructed for each Hermite coefficient, and then the final histogram is obtained by concatenating the four local histograms, as shown in Figure 10.8.

The histograms obtained during the recognition phase are compared against the trained model histograms of the corresponding landmarks, so that the closest point to the boundary is the one with the smallest histogram distance. We used the Chi-square distance. This distance can be used as a measure of dissimilarity between distributions, specifically between two histograms. It has also been used in applications such as texture and object classification and image retrieval [69].

The final histogram is created by concatenating the histograms of the HCs as follows:

$$p\left(r_{\{kL_n\}}\right) = \left[n_{\{kL_0\}}, n_{\{kL_1\}}, n_{\{kL_2\}}, n_{\{kL_3\}}\right] \tag{10.15}$$

where $n_{\{k\}}$ represents a k-bin histogram of the Hermite coefficients kL_0, kL_1, kL_2, kL_3 that correspond to the profile $p(r_{\{kL_n\}})$ is the final histogram of the kL_n coefficients that is normalized by the size of the image M (rows) and N (cols). Finally, the landmark position is adjusted by computing the smallest distance between the training landmark histogram and the profile's histograms of the new image according to the Chi-squared function.

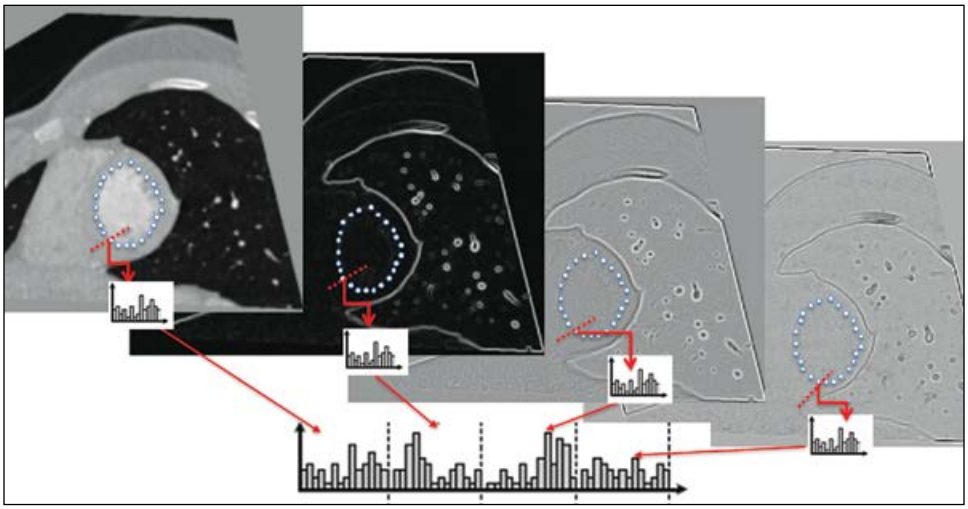

FIGURE 10.8 Histogram concatenation on the Hermite coefficients.

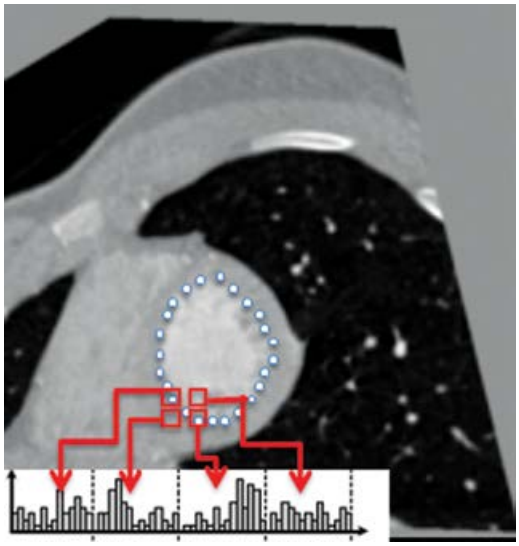

FIGURE 10.9 Histogram concatenation on a squared region.

10.2.3.3 ASM/Quadratic-HC (ASM/QHC)

This proposal computes HCs over four square regions defined by a 7×7 pixel window around the landmarks. The quadratic region used in ASM includes the information from the HCs L_0, L_1, L_2, and L_3 (see Figure 10.9).

A diagram with the description of the general method is shown in Figure 10.10 and 10.11 where we have the training and the recognizing phase.

10.2.3.4 Results

The algorithms were validated against manual annotations made by an expert physician and one assistant in 28 studies throughout the entire cardiac cycle from healthy subjects. Middle slices of

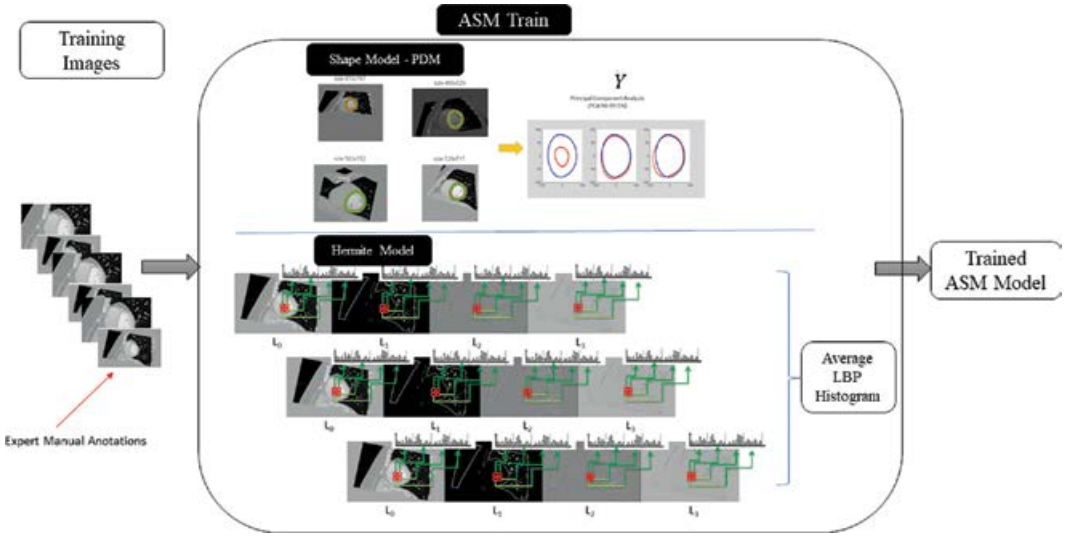

FIGURE 10.10 ASM/Hermite method for the training phase.

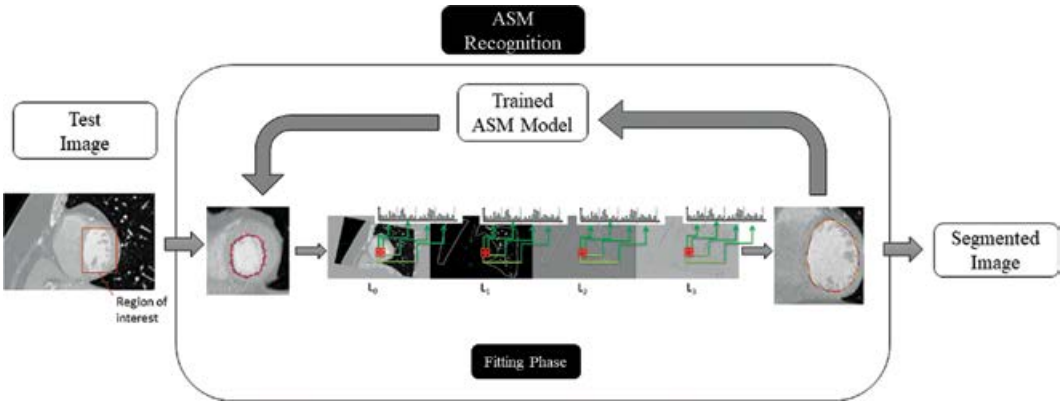

FIGURE 10.11 ASM/Hermite method for the recognition phase.

the volumes are used, so that every study is composed of 10 images that cover diastole and systole phases. The evaluation started with images at 0% cardiac cycle per subject. The same initialization was used throughout the cycle. In order to reduce bias, four-fold cross-validation is used to train the ASM. Every fold was chosen randomly. Our experiments were divided into two groups: endocardium and epicardium segmentation.

With respect to the steered Hermite coefficient computation, different window sizes were evaluated. For the Gaussian sigma values, we used different values on endocardium $\sigma = 5$ and epicardium $\sigma = 7$. A quantitative analysis is performed using two metrics: Hausdorff distance (HD), and Dice index (DI).

In general, throughout the cardiac cycle the ASM-based methods show good results, especially those methods that include texture information like ASM/QHCs, whereas ASM/HCs achieved the poorest results. The average results are summarized in Table 10.1 and Table 10.2.

Consider for instance that Hausdorff distance changes the rank order of the best performing algorithms ASM/QHCs and ASM, throughout the cardiac cycle in comparison with Dice coefficient.

When ASM/QHCs was used for segmenting the epicardium, the results obtained were consistent with good scores. Note how ASM decreases its performance in systole, reaching third and fourth places in the subsequent phases compared to the initial percentages 0% and 10% of the cardiac cycle. The best results were achieved with ASM/QHCs.

Examples of epicardium segmentation is shown in Figure 10.12.

TABLE 10.1

ASM and ASM/HCs methods comparison for left ventricle segmentation with Dice and Hausdorff metrics on 10 percentages of the cardiac cycle for endocardium.

Cardiac cycle	0%	10%	20%	30%	40%	50%	60%	70%	80%	90%
Dice index ASM	0.935	0.908	**0.898**	0.802	0.850	0.878	0.901	0.919	0.890	0.922
Dice index ASM/PHC	0.940	0.918	0.874	0.826	**0.851**	0.875	**0.918**	0.929	**0.928**	0.879
Dice index ASM/QHC	**0.940**	**0.921**	0.865	**0.843**	0.831	**0.885**	0.909	**0.937**	0.916	**0.940**
Hausdorff distance ASM [mm^2]	2.567	3.162	2.922	4.299	3.794	3.547	3.567	2.928	3.915	2.948
Hausdorff distance ASM/PHC [mm^2]	**2.426**	**2.721**	3.346	3.856	**3.382**	3.525	2.914	2.454	**2.910**	3.870
Hausdorff distance ASM/QHC [mm^2]	2.480	2.955	**2.892**	**3.716**	4.272	**4.178**	**2.906**	**2.060**	3.133	**2.398**

TABLE 10.2

ASM and ASM/HCs methods comparison for left ventricle segmentation with Dice and Hausdorff metrics on 10 percentages of the cardiac cycle for epicardium.

Cardiac cycle	0%	10%	20%	30%	40%	50%	60%	70%	80%	90%
Dice index ASM	**0.940**	**0.931**	0.892	0.904	0.906	0.913	0.930	**0.933**	0.926	0.929
Dice index ASM/PHC	0.919	0.916	0.897	0.906	0.906	0.906	0.912	0.912	0.903	0.902
Dice index ASM/QHC	0.928	0.924	**0.918**	**0.932**	**0.930**	**0.935**	**0.936**	0.930	**0.938**	**0.936**
Hausdorff distance ASM [mm^2]	**3.083**	**3.373**	5.080	4.369	4.234	4.041	3.312	**3.124**	**3.444**	3.645
Hausdorff distance ASM/PHC [mm^2]	4.678	4.405	4.705	4.662	4.634	4.725	4.864	5.231	5.382	5.206
Hausdorff distance ASM/QHC [mm^2]	4.545	4.195	**3.966**	**3.494**	**3.409**	**3.322**	**3.283**	3.732	3.451	**3.384**

10.2.4 2D Level Set for CT Left Ventricle

The role of active contour methods is becoming highly important for applications in image processing because they have been extensively used for many different tasks, especially for segmentation. Active contour models are also known as snakes, because they are usually derived by minimizing an energy functional, which is related to the deformation of a curve.

The active contour model without edges proposed by Chan and Vese [42] is a successful method to segment images based on curve evolution. The goal of this method is to identify different objects by dividing the image into distinct regions that share similar information. The main idea of this procedure can be explained as follows: An initial contour with characteristics of shape and position is defined in the image. The algorithm follows an iterative evolution process that leads the contour to capture the shape of the object of interest. The correct initialization of the parameters can help reduce the number of iterations needed to achieve the desired final contour.

In general, internal and external forces are used to guide such curve evolution. A comparison of variations between the foreground and background for a given closed region allows the contour to move into the direction of minimum energy change. The solution of this minimization problem determines the convergence by checking whether the contour is not moving too much between two consecutive iterations. Finally, this process leads to a stationary solution and a complete image segmentation.

Such a method is modeled as a functional that can be solved by the level set (LS) implementation introduced in [70] due to its ability to capture topological changes in the evolving curve (i.e., splitting and merging regions). Furthermore, LS has been proven as an efficient method for moving surfaces on a fixed rectangular grid, which contributes to easily performing computations.

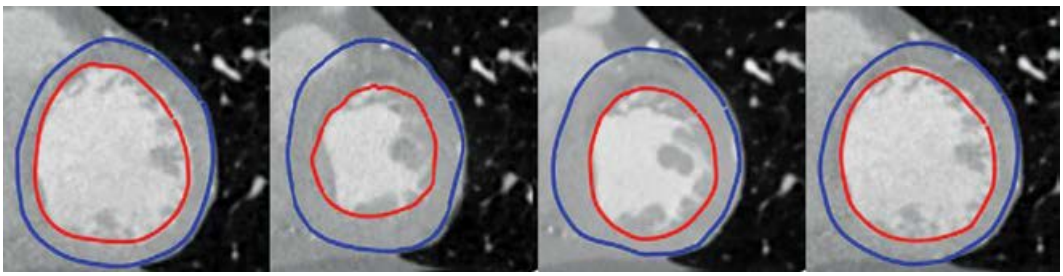

FIGURE 10.12 Segmentation result of the ASM/QHC method for 0%, 30%, 50%, and 90% of cardiac cycle.

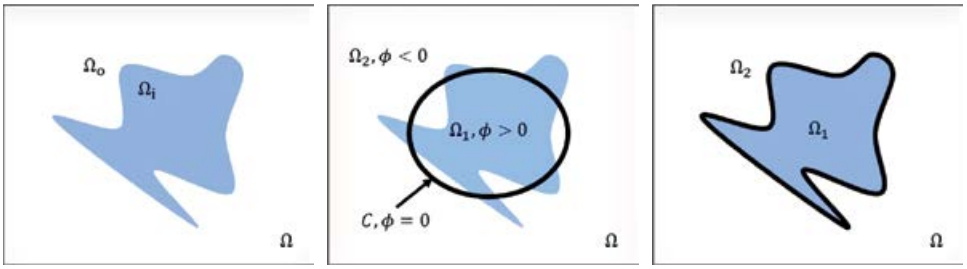

FIGURE 10.13 Contour evolution process for segmentation task. Left: Original image with an irregular shape object. Center: Initial contour. Right: Final segmentation result.

The two-dimensional active contour model based on the Chan-Vese (CV) proposal considers an image I separated by two regions Ω_1 y Ω_2 with a common boundary $\partial\Omega$, where Ω is a bounded open set of $\mathbb{R}^2$. Let C be an evolving curve in Ω such that $\Omega = \Omega_1 \bigcup C \bigcup \Omega_2$, (see Figure 10.13). The aim of the formulation of the energy functional is to identify the best partition as follows:

$$\inf_{c_1, c_2, C} F(c_1, c_2, C), \tag{10.16}$$

$$F(c_1, c_2, C) = \mu \int_C ds + \lambda_1 \int_\Omega (I - c_1)^2 \, dxdy + \lambda_2 \int_\Omega (I - c_2)^2 \, dxdy, \tag{10.17}$$

where c_1 and c_2 represent the two average regions of intensity inside and outside the contour respectively. The parameters λ_1 and λ_2 in Eq. (10.17) are selected by the user for data fitting, and μ is introduced to regularize the surface C. Note that this is a special case of the Mumford-Shah model proposed in [71].

The curve C can be represented via the non-zero level set function ϕ that assigns values of $C = \{(x, y) : \phi(x, y) = 0\}$, $\phi(x, y) > 0$ inside C and $\phi(x, y) < 0$ outside C. Therefore, the functional can be reformulated in terms of the level set as follows:

$$F(c_1, c_2, \phi) = \mu \int_\Omega \delta(\phi) |\nabla \phi| \, dxdy + \int_\Omega \lambda_1 (I - c_1)^2 H(\phi) dxdy + \int_\Omega \lambda_2 (I - c_2)^2 \left(1 - H(\phi)\right) dxdy, \tag{10.18}$$

where the Dirac function δ and the Heaviside function H are used to represent the level set. In numerical implementations, these functions are often regularized in δ_ϵ and H_ϵ respectively. The minimization is solved via the Euler-Lagrange equation for an artificial time $t \leq 0$:

$$\frac{\partial \phi}{\partial t} = \delta_\epsilon(\phi) \left[\mu \cdot \mathrm{div}\left(\frac{\nabla \phi}{|\nabla \phi|} \right) - \lambda_1 (I - c_1)^2 + \lambda_2 (I - c_2)^2 \right] \tag{10.19}$$

An extended version was presented in [46] as a multi-valued active contour. This model was introduced to solve an occlusion problem by analyzing different channels of a color image. The assumption is based on detecting relevant information that can be present in at least one of the channels.

Hence, a single active contour acts over each channel u_i simultaneously. The level set extension to the vector case is:

$$F\left(c_i^+, c_i^-, \phi\right) = \mu \int_\Omega \delta(\phi)|\nabla\phi| dxdy + \int_\Omega \frac{1}{N}\sum_{i=1}^{N} \lambda_i^+ \left(u_i - c_i^+\right)^2 H(\phi) dxdy$$

$$+ \int_\Omega \frac{1}{N}\sum_{i=1}^{N} \lambda_i^- \left(u_i - c_i^-\right)^2 \left(1 - H(\phi)\right) dxdy, \tag{10.20}$$

for $i = 1, \ldots, N$ channels, where c_i^+ and c_i^- are two constant vectors. The non-zero parameters λ_i^+ and λ_i^- are weights defined by the user. Following the solution of the single active contour with level set, we define the multi-valued iterative procedure (VVCV):

$$\frac{\partial\phi}{\partial t} = \delta_\epsilon(\phi)\left[\mu \cdot \mathrm{div}\left(\frac{\nabla\phi}{|\nabla\phi|}\right) - \frac{1}{N}\sum_{i=1}^{N} \lambda_i^+ \left(u_i - c_i^+\right)^2 + \frac{1}{N}\sum_{i=1}^{N} \lambda_i^- \left(u_i - c_i^-\right)^2\right] \tag{10.21}$$

The aim of the proposed methodology (VVCV/SHT) is to include the Hermite coefficients with higher concentration of energy as texture descriptor in the multi-valued active contour:

$$\frac{\partial\phi}{\partial t} = \delta_\epsilon(\phi)\left[\mu \cdot \mathrm{div}\left(\frac{\nabla\phi}{|\nabla\phi|}\right) - \frac{1}{4}\sum_{i=0}^{3} \lambda_i^+ \left(L_{i,0}^\theta - c_i^+\right)^2 + \frac{1}{4}\sum_{i=0}^{3} \lambda_i^- \left(L_{i,0}^\theta - c_i^-\right)^2\right], \tag{10.22}$$

where $L_{i,0}^\theta$ are the image coefficients of the SHT for order $i = 0,1,2,3$. This approach helps identify regions with similar measure of homogeneity and deal with images in the presence of noise.

Approaches based on level set methods employ an initial stage where certain conditions are defined by the user for the semiautomatic process of curve evolution. Firstly, a time step Δt and stopping criterion are used to modify the speed and convergence respectively. The number of iterations depends on these quantities. The initialization of the contour is often placed close to the object of interest, while the parameters of $\lambda^{+,-}$ assign priority to the measure of uniformity. A relation of $\lambda^+ > \lambda^-$ in Eqs. (4,6) and (4,7) improves the delimitation of internal regions because it allows a high variance outside the evolving contour. The latter parameter is helpful to distinguish a single organ structure among many others in the same image.

In the results presented in this section, the parameters were selected experimentally as follows: $\Delta t = 0.1$, $\mu = 0.5$, $\lambda_i^+ = 2$ and $\lambda_i^- = 1.5$, while the stopping criterion was chosen intuitively as a threshold used to detect small energy differences between two consecutive iterations.

In order to validate the proposal, a left ventricle segmentation in heart was carried out [72, 73]. We applied the algorithm over a dataset that consists of 11 annotated tomographic cardiac studies from healthy subjects. These studies were taken and labeled by a highly trained cardiologist using a CT Siemens dual source scanner. Such studies go from the diastolic phase throughout the systolic phase and provide a set of 10 images corresponding to the cardiac cycle from 0% up to 90%. The experiments were evaluated on mid-third slice. To quantify the accuracy of segmentation, we computed two well-known distances according to the expert annotations.

Dice index ranges between 0 to 1 and computes the intersected area between the expert annotations and the recognized contours divided by the sum of both areas. The closer to one, the higher the segmentation accuracy. The Hausdorff distance measures how close the boundaries between

TABLE 10.3

Single active contour and texture-based active contour comparison for left ventricle segmentation with Dice and Hausdorff metrics.

Cardiac cycle	0%	10%	20%	30%	40%	50%	60%	70%	80%	90%
Dice index (VVCV/SHT)	**0.950**	**0.941**	**0.923**	**0.887**	0.832	**0.863**	**0.945**	**0.952**	**0.945**	**0.945**
Dice index (CV)	0.885	0.899	0.862	0.872	**0.882**	0.856	0.940	0.949	0.879	0.881
Hausdorff distance (VVCV/SHT)	**7.10**	**7.19**	**8.90**	11.61	24.07	32.29	**6.70**	**6.07**	**7.18**	**7.38**
Hausdorff distance (CV)	25.13	16.62	17.55	**10.30**	**11.07**	**24.58**	7.65	6.71	27.04	26.05

the segmentation results and manual annotations are. Results in Table 10.3 show that the performance of the algorithms varies with the phase of the cardiac cycle. This can be explained by the organ motion and the irregular shape of the contracted ventricle in the change of phase. Texture-based implementation exhibits better quantitative results than the single active contour algorithm. Figure 10.14 shows the segmentation results compared to manual delineations during the cardiac cycle. We applied a convex hull operation that helps remove papillary muscles.

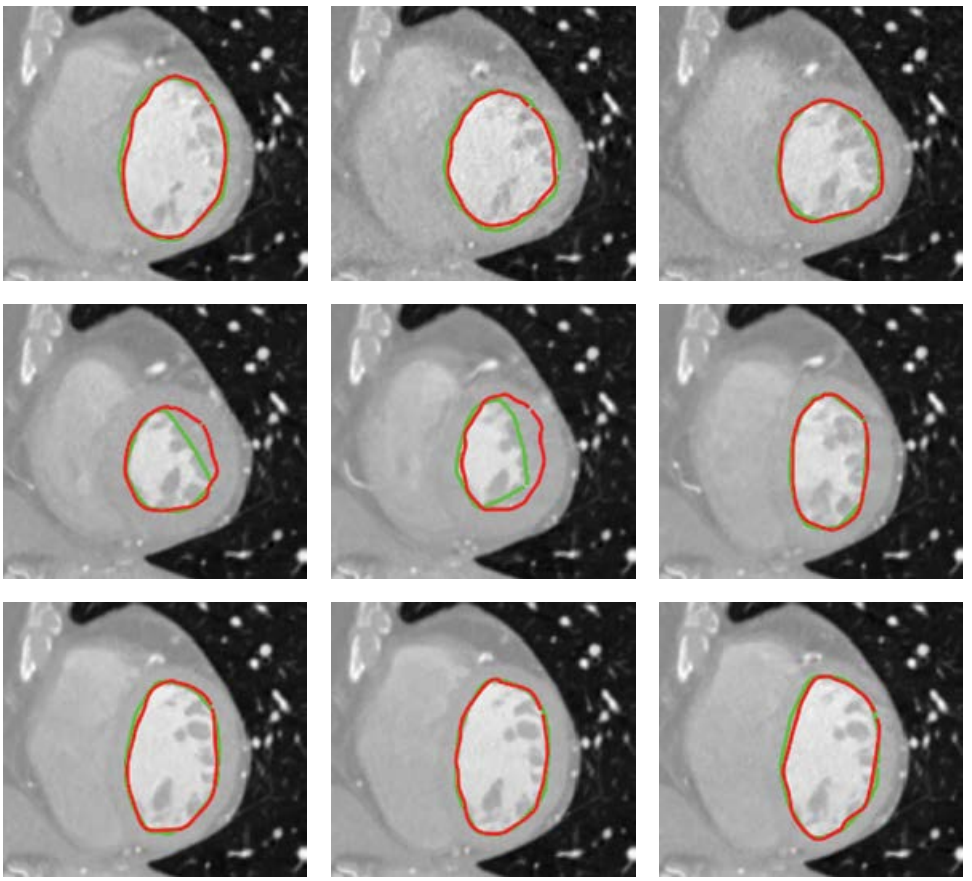

FIGURE 10.14 Endocardium segmentation during cardiac cycle from 0% up to 80%. Red line indicates manual annotation, and the green line displays the final segmentation result with a convex hull operation.

10.2.5 3D Level Set for MR Left Ventricle

Segmentation of cardiac structures must be performed slice by slice when using 2D algorithms for analyzing the entire heart volume. Considering that cardiac cavities are 3D objects, it is of main interest for researchers to design 3D algorithms for segmenting the complete volume. Short axis view is mainly used for detecting cardiac failures and evaluating the LV cavity in all phases of the cardiac cycle. Some clinical indices can be computed from the 3D segmentation of the LV cavity and myocardial wall using this specific view, which is commonly obtained for cardiac MR studies. In this section, we explore how to use a level set algorithm for 3D LV segmentation. One of the main properties of level set techniques is that the extension to higher dimensions is straightforward. We also discuss how a tool like the 3D Hermite transform can be embedded into the energy functional in order to improve the segmentation performance.

The definition of 3D level set is similar to the bidimensional case, but the working space is now defined in $\mathbb{R}^3$. The use of algorithms based on surface evolution techniques instead of propagating 2D contours (applied slice by slice) for segmentation of 3D medical data has been of main concern for many researchers [74, 75, 76]. Since level set techniques do not use parametric schemes, the implementation can be easily performed in any dimension. The implicit definition of the level set function allows its generalization to higher dimensions. The most challenging task in these approaches is to define the velocity field that better describes the segmentation problem. As mentioned, this velocity field can be composed of several functions, which may depend on image features, or geometrical properties [76]. Texture, intensities, edges, and many other image features can be integrated in different ways in these methods. Although many general algorithms have been created [42, 47, 77], new frameworks are always needed when working with specific applications and objects with well-defined shapes. Nonetheless, initialization schemes also become fundamental because solutions found with level set methods are not global.

Figure 10.15 illustrates a general scheme that slightly depicts the deformation of a surface used for segmentation. The surface corresponds to a level set function. As known, it requires an initial surface whose deformation is guided by the velocity field until reaching the desired segmentation.

Analysis of cardiac volumes with short-axis view are interesting applications where level sets methods have gained much relevance. Problems found in these types of images constitute great challenges for segmentation algorithms. Inhomogeneities, diffuse edges, lack of information, low contrast, and irregularity of shapes are the most typical difficulties to be handled from an image processing point of view. Figure 10.16 shows some image examples taken from an MR cardiac volume. The MR study was extracted from the database provided by [78], which was shared for research purposes. As seen, images present many differences regarding the contrast, quality, and variability of shapes, which might affect the performance of the designed methods.

One of the more notorious advantages of level sets approaches is that they allow the combination of several energy functions, each one designed to analyze a specific feature. We will describe how to

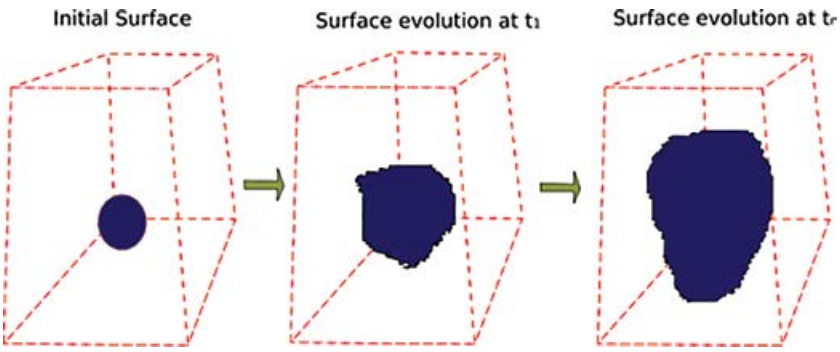

FIGURE 10.15 Surface evolution seen at several instants of time.

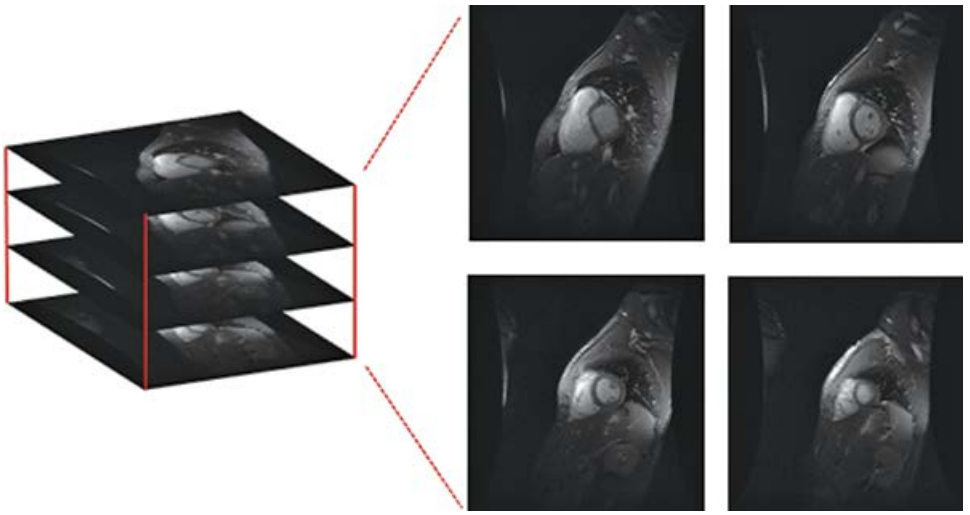

FIGURE 10.16 Example of cardiac MR volume.

build a robust method integrating functions that are able to handle the most typical problems found in cardiac MR volumes.

Let $S = S(X), X \in \mathbb{R}^3$, be an evolving interface used to separate the working space into two regions. We will assume that the part inside the interface is the region of interest needed. This interface can be represented using a level set function φ, it means $S = \{X \mid \phi(X) = 0\}$. Here, S corresponds to the zero level set. The method consists of finding a solution for the motion equation defined as:

$$\frac{\partial \phi}{\partial t} = F|\nabla \varphi|, \tag{10.23}$$

where F is the associated velocity field. Defining the F that better describes the segmentation process is the problem to be solved here. The most used strategy consists of proposing energy functionals, which are then minimized using the calculus of variation. All individual energy functionals are combined, and the minimization process leads to Eq. (10.23).

10.2.5.1 Energy Functionals

In most methods based on level sets, it is common to include an energy functional to evaluate the intensity values of the input images. The region-based functional proposed by Chan-Vese [42] is the most common energy function used for this purpose. It has the advantage of not depending on the edges of the object to perform the segmentation. From Figure 10.16, we can see that the LV cavity and the myocardial wall present different intensity values in all slices of the cardiac volume, which justifies the use of this type of force. The mentioned energy functional can be defined as

$$E_{GR} = \int \left(V(X) - m_1\right)^2 H\left(\phi(X)\right) dX + \int \left(V(X) - m_2\right)^2 \left(1 - H\left(\phi(X)\right)\right) dX, \tag{10.24}$$

where m_1 and m_2 are the average intensity values computed for the regions inside and outside the current surface. The objective of this functional is to guide the evolution of the surface using the intensity information, which characterizes the object and background. The input cardiac volume is V and H is the Heaviside function commonly used to regularize the level set variable. Although this energy functional has demonstrated to be very efficient, even for noisy data, it has the problem that images with inhomogeneity problems are not processed satisfactorily because it only considers global information.

Boundary-based energy functions might also contribute to the segmentation problem in cardiac data. These types of energies are very useful when segmenting images with good contrast and well-defined edges. Several level sets methods based on edge-based functions have been proposed for segmentation of cardiac images [79, 80]. A simple but effective functional to process edge information can be written as

$$E_B = \int gH\big(\phi(X)\big)dX, \tag{10.25}$$

where $g = \frac{1}{1+IG}$ is an asymptotic function that decreases with the image gradient IG. Since the functional only processes edge information, it can be very sensitive to image noise. In this sense, finding an operator that efficiently computes the edge map is the great challenge in this energy function. The problem is even more complicated if we need to compute the edge map of 3D data.

Considering that cardiac MR volumes might contain many inhomogeneous regions due to different factors, it is recommended to include an energy function dedicated to control this problem. Several methods focused on working with inhomogeneous images have been proposed [77, 81]. These methods process the intensity levels using local information because near points are more prone to having similar level intensities. The inhomogeneity problems of the global energy functional can be easily solved by using a similar region term, but locally applied. Then,

$$E_{LR} = \int \big(V(X) - \mu_1(X)\big)^2 H\big(\phi(X)\big)dX + \int \big(V(X) - \mu_2(X)\big)^2 \big(1 - H\big(\phi(X)\big)\big)dX. \tag{10.26}$$

Variables μ_1 and μ_2 are computed in a local region K_w and they consist of the average intensities inside and outside the surface, respectively. K_w corresponds to a window function, which defines a local region around the point X. For 3D data, this window might have spherical, cubic, or Gaussian shape. The intensity values are evaluated directly on the input volume V. The size of the window must be defined as well. The main problem of this energy function is that it requires the initial shape to be near the object of interest.

The described functional are energy terms that depend on the image features of the input volume. It is a common practice to include geometrical constraints because they allow to maintain a regular deformation of the surface during evolution. The following functional is normally used to preserve a smooth surface during the segmentation process

$$E_R = \int \left|\nabla H\big(\phi(X)\big)\right| dX, \tag{10.27}$$

with ∇ being the gradient operator.

Objects in medical images can be also modeled using known geometrical shapes. By looking at the image examples in Figure 10.16, we can see that the LV cavity and the myocardial wall in cardiac volumes with short-axis view are considered to have circular or elliptical shape, seen from each slice. This asseveration was also considered in [76, 82]. The following energy functional can be used for penalizing the deformation of the level set interface when it is evolving far from a previously defined shape. It is described as

$$E_S = \int \big(\phi(X) - \phi_s(X)\big)^2 H\big(\phi(X)\big)dX \tag{10.28}$$

where φ_s is the level set function built from the prior shape considered. If we use moving surfaces for 3D segmentation, φ_s must be built as a 3D shape. Barba-J et at. [76] recently designed a method to construct a distance map from estimated ellipses with the aim of representing the LV in cardiac

MR volumes. It is based on the idea that the LV can be modeled using elliptical shapes in slices obtained from cardiac volumes in short-axis view. The stack of ellipses computed for all slices of the volume are used to finally build the level set function. Similar to the last term, this energy functional only depends on the geometrical properties of the level set function. Here, an elliptical constraint was considered, but it can be generalized to other types of shapes.

10.2.5.2 Combining the Energy Functionals

The complete energy functional is the result of the weighted combination of all the described terms. The segmentation is then achieved by solving the equation

$$E = \alpha_1 E_{GR} + \alpha_2 E_B + \alpha_3 E_{LR} + \alpha_4 E_R + \alpha_5 E_S \tag{10.29}$$

The weight parameters, α_k, k = 1,2,…,5, control the contribution of the individual energy terms. Note that, not all terms might be needed when segmenting a specific volume. The solution of the equation can be found by using the calculus of variation and the gradient descent method, which leads to the following differential equation

$$\frac{\partial \phi}{\partial t} = \left[\alpha_1 \left(-(V - m_1)^2 + (V - m_2)^2 \right) + \alpha_2 g + \alpha_3 \left(-(V - \mu_1)^2 + (V - \mu_2)^2 \right) \right.$$

$$\left. + \alpha_4 Div\left(\frac{\nabla \phi}{|\nabla \phi|} \right) \right] \delta\phi - 2\alpha_5 H(\phi)(\phi - \phi_s). \tag{10.30}$$

The implementation is done by discretizing the above equation. A rule for stopping the level set evolution must be considered as well. An initial shape is also needed, which implies designing an initialization scheme.

Equation (10.30) can be applied to segment both regions, the LV cavity and the myocardial wall. Volumes representing different stages of the cardiac phase can be segmented as well. Naturally, not all terms contribute significantly in all examples. If we want to inhibit the contribution of a specific energy term, its weight value must be set to zero.

10.2.5.3 Using the 3D SHT for Level Set Evolution

The first three energy functionals are computed using different features extracted from the input volume. That means some image processing techniques must be previously performed. The SHT can be competently employed for this purpose because it provides analysis of the input data by extracting different types of features. This transform also has the advantage that the basis functions are separable, which allows its extension to 3D dimensions without major changes. Moreover, directional analysis can be addressed, which becomes a fundamental characteristic when working with features like edges and texture [83].

The global and local energy terms use an input volume for evaluation of the intensity values. The zero-order coefficient of the 3D SHT can be employed as input data in these functionals. Since it consists of a smoothed version of the input volume, image noise is significantly reduced.

As mentioned, the boundary-based energy term requires an edge map, which must be obtained from the input volume. For this case, the first-order coefficients of the 3D SHT provide the edge information of the analyzed volume. One of the most useful advantages of this transformation is that coefficients with order larger than one can be steered to perform directional analysis. The steering process might be done adaptively for each point by selecting the direction of maximum energy [84]. It means that edges are being obtained for any direction. This effective procedure is advantageous because the image noise is significantly reduced by the fact that it is not a directional characteristic. In addition, the 3D edge map can be competently obtained since several orientations are evaluated.

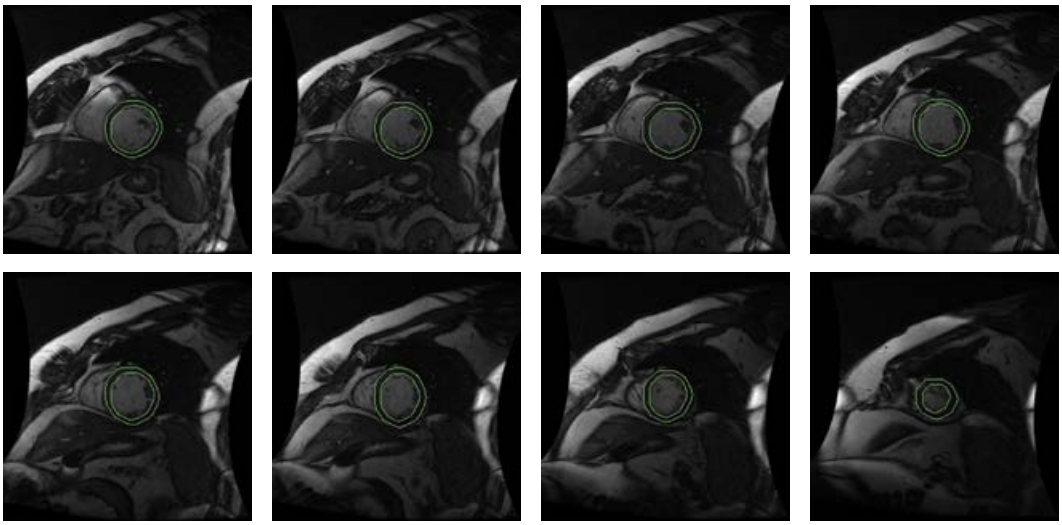

FIGURE 10.17 Segmentation obtained for a MR volume. From left to right and top to bottom, slices show the LV at base, middle and apex of the heart.

In this sense, coefficients of the 3D SHT can be used to guide the evolution of the level set function because it provides the image features needed during the deformation process. The geometrical energy functions are needed to control and maintain a regular deformation of the surface.

10.2.5.4 Segmentation Examples

Figure 10.17 illustrates some volume slices segmented using the described approach. They correspond to data of a cardiac MR volume where the LV cavity and the myocardial wall were segmented. The volume example was selected form the MICCAI MR database [85]. Images show the cardiac structures using a short-axis view.

Figure 10.18 shows the surfaces obtained for the LV cavity and the myocardial wall resulted from the segmentation of a MR study that was selected from the cardiac MR database shared by [78]. Surfaces are illustrated for the end-diastolic and end-systolic phases.

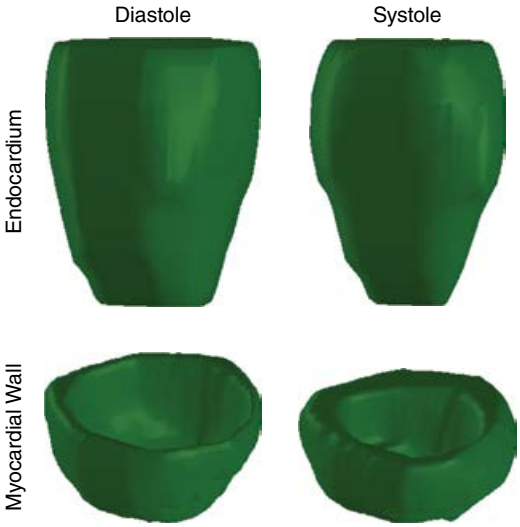

FIGURE 10.18 Surfaces of the LV cavity and myocardial wall obtained for a MR volume. The end-diastolic and end-systolic phases are evaluated.

Once the complete volume has been segmented, at least in the diastole and systole phase, several clinical indices can be computed. These indices are commonly used by physicians to evaluate the behavior of the LV. Two of the most important clinical indices are the ejection fraction (EF) and the dimensions of the myocardial wall. The automatic segmentation can significantly contribute to provide more objective measurements.

Although the method was described for segmentation of cardiac MR volumes, it can be generalized to other modalities such as CT. The combined energy functions in which different image features and geometrical characteristics are processed, allow this method to be configured for other applications as well. The most difficult task in the described method is to find the values of the weight parameters because the importance of each individual functional depends on the characteristics of the input data.

10.3 DISCUSSION

Several techniques that have been developed for human organ segmentation include those based on atlases, deformable models, pixel classification, region and edge detectors, active shape models, active contours and deformable models being some of the most commonly used. However, most of these methods are mainly focused on MRI technology. On the other hand, CT has been shown to be an affordable technique with good image quality results, despite its lower spatial resolution in comparison with MRI. In fetal images, ultrasound analysis is the standard modality because of the low risk that it represents for the fetus. Ultrasound and CT technology is being constantly improved in order to get better image resolution in time and space.

This chapter presents new advances in image segmentation based on deformable models such as active shape models, active appearance models and level sets.

In all cases, the new methods include local textural information given by HCs that is incorporated in the segmentation algorithms to improve shape fitness to the target objects.

The performance of some methods was tested with commonly used metrics, namely Hausdorff distance and Dice index.

The segmentation schemes of the left ventricle presented in this work contribute to the understanding of complex heart dynamics. The results obtained, in some sections, resemble manual clinical delineations in CT imaging and prove that the methods proposed here may help reduce bias in diagnosis and treatment procedures. The joint approach, that is, combining deformable models with HCs, is a reliable option for segmenting the left ventricle, because it is able to differentiate object structures. An advantage of the level sets schemes is the fact that they do not need previous training.

Future work must be done for tasks not covered in this study, such as segmentation of cardiac cavities with different pathologies.

Acknowledgments

The authors thank grants UNAM-PAPIIT IN116917 and SECITI 110/2015.

References

1. D. Kang, J. Woo, P. J. Slomka, D. Dey, G. Germano, C.-C. Jay Kuo, Heart chambers and whole heart segmentation techniques: review, *Journal of Electronic Imaging,* vol. 21, pp. 010901-1–010901-16, 2012.
2. C. Petitjean and J.-N. Dacher, A review of segmentation methods in short axis cardiac MR images, *Medical Image Analysis*, vol. 15, pp. 169–184, 2011.
3. M. D. Cerqueira, N. J. Weissman, V. Dilsizian, A. K. Jacobs, S. Kaul, W. K. Laskey, D. J. Pennell, J. A. Rumberger, T. Ryan, M. S. Verani, Standardized myocardial segmentation and nomenclature for tomographic imaging of the heart, *Circulation*, vol. 105, pp. 539–542, 2002.
4. S. Faghih Roohi and R. Aghaeizadeh Zoroofi, 4D statistical shape modeling of the left ventricle in cardiac MR images, *International Journal of Computer Assisted Radiology and Surgery*, vol. 8, pp. 335–351, 2013.

5. F. Ma, J. Liu, B. Wang, H. Duan, Automatic segmentation of the full heart in cardiac computed tomography images using a Haar classifier and a statistical mode, *Journal of Medical Imaging and Health Informatics*, vol. 6, pp. 1298–1302, 2016.
6. M. N. Bugdol and E. Pietka, Mathematical model in left ventricle segmentation, *Computers in Biology and Medicine*, vol. 57, pp. 187–200, 2015.
7. S. Antunes, A. Esposito, A. Palmisano, C. Colantoni, S. Cerutti, G. Rizzo, Cardiac Multi-detector CT segmentation based on multiscale directional edge detector and 3D level set, *Annals of Biomedical Engineering*, vol. 44, pp. 1487–1501, 2016.
8. E. Moya-Albor, B. Escalante-Ramírez, E. Vallejo, Optical flow estimation in cardiac CT images using the steered Hermite transform, *Signal Processing: Image Communication*, vol. 28, pp. 267–291, 2013.
9. T. C. Wong and P. Soman, Imaging in the evaluation of the patient with new-onset heart failure, *Current Cardiovascular Imaging Reports*, vol. 5, pp. 167–172, 2012.
10. R. Ventura-Clapier, *Encyclopedia of Exercise Medicine in Health and Disease*, Springer Berlin Heidelberg, 2012, p. 175.
11. S. Leschka, S. Waelti, S. Wildermuth, Principles of CT Imaging, in *Cardiac CT and MR for Adult Congenital Heart Disease*, F. Saremi, A cura di, New, York: Springer, 2014.
12. K. Moschetti, S. Muzzarelli, C. Pinget, A. Wagner, G. Pilz, J. Wasserfallen, J. Schulz-Menger, D. Nothnagel, T. Dill, H. Frank, M. Lombardi, O. Bruder, H. Mahrholdt, J. Schwitter, Cost evaluation of cardiovascular magnetic resonance versus coronary angiography for the diagnostic work-up of coronary artery disease: application of the European Cardiovascular Magnetic Resonance registry data to the German, United Kingdom, Swiss, and United States health care systems, *Journal of Cardiovascular Magnetic Resonance*, vol. 14, p. 35, 2012.
13. S. Halliburton, A. Arbab-Zadeh, D. Dey, A. J. Einstein, R. Gentry, R. T. George, T. Gerber, M. Mahesh, W. G. Weigold, State-of-the-art in CT hardware and scan modes for cardiovascular CT, *Journal of Cardiovascular Computed Tomography*, vol. 6, pp. 154–163, 2012.
14. R. J. Gibbons, Noninvasive diagnosis and prognosis assessment in chronic coronary artery disease, *Circulation: Cardiovascular Imaging*, vol. 1, pp. 257–269, 2008.
15. X. Bresson, S. Esedoglu, P. Vandergheynst, J.-P. Thiran, S. Osher, Fast global minimization of the active contour/snake model, *Journal of Mathematical Imaging and Vision*, vol. 28, pp. 151–167, 2007.
16. Y.-L. Lu, K. A. Connelly, A. J. Dick, G. A. Wright, P. E. Radau, Automatic functional analysis of left ventricle in cardiac cine MRI, *Quantitative Imaging in Medicine and Surgery*, vol. 3, 2013.
17. D. Turco and C. Corsi, Advanced PDE-based methods for automatic quantification of cardiac function and scar from magnetic resonance imaging. *Series in Computer Vision in Medical Imaging. Computer Vision: Volume 2*., University of Massachusetts, USA: World Scientific Publishing Company, 2013.
18. A. Kronman and L. Joskowicz, A geometric method for the detection and correction of segmentation leaks of anatomical structures in volumetric medical images, *International Journal of Computer Assisted Radiology and Surgery*, vol. 11, pp. 369–380, 2016.
19. J. J. Cerrolaza, A. Villanueva, R. Cabeza, On hierarchical statistical shape models with application to brain MRI. *Series in Computer Vision in Medical Imaging. Computer Vision: Vol. 2*, University of Massachusetts, USA: World Scientific Publishing Company, 2013.
20. J. Kawa and E. Pietka, Kernelized fuzzy c-means method in fast segmentation of demyelination plaques in multiple sclerosis, in *29th International Conference of the IEEE Engineering in Medicine and Biology Society*, 2007.
21. J. Dolz, H. A. Kirisli, T. Fechter, S. Karnitzki, O. Oehlke, U. Nestle, M. Vermandel, L. Massoptier, Interactive contour delineation of organs at risk in radiotherapy: clinical evaluation on NSCLC patients, *Medical Physics*, vol. 43, pp. 2569–2580, 2016.
22. J. Rychik, N. Ayres, B. Cuneo, N. Gotteiner, L. Hornberger, P. J. Spevak, M. V. D. Veld, American Society of Echocardiography guidelines and standards for performance of the fetal echocardiogram, *Journal of the American Society of Echocardiography*, vol. 17, pp. 803–810, 2004.
23. J. I. E. Hoffman and S. Kaplan, The incidence of congenital heart disease, *Journal of the American College of Cardiology*, vol. 39, pp. 1890–1900, 2002.
24. F. S. Molina, C. Faro, A. Sotiriadis, T. Dagklis, K. H. Nicolaides, Heart stroke volume and cardiac output by four-dimensional ultrasound in normal fetuses, *Ultrasound in Obstetrics & Gynecology*, vol. 32, pp. 181–187, 2008.
25. A. K. Younoszai, D. E. Saudek, S. P. Emery, J. D. Thomas, Evaluation of myocardial mechanics in the fetus by velocity vector imaging, *Journal of the American Society of Echocardiography*, vol. 21, pp. 470–474, 2008.

26. J. A. Noble and D. Boukerroui, Ultrasound image segmentation: a survey, *Medical Imaging, IEEE Transactions on*, vol. 25, pp. 987–1010, 2006.
27. M. Marsousi, A. Eftekhari, A. Kocharian, J. Alirezaie, Endocardial boundary extraction in left ventricular echocardiographic images using fast and adaptive B-spline snake algorithm, *International Journal of Computer Assisted Radiology and Surgery*, vol. 5, pp. 501–513, 2010.
28. N. Paragios, M.-P. Jolly, M. Taron, R. Ramaraj, Active shape models and segmentation of the left ventricle in echocardiography, in *Scale Space and PDE Methods in Computer Vision*, Springer, 2005, pp. 131–142.
29. G. Hamarneh and T. Gustavsson, Combining snakes and active shape models for segmenting the human left ventricle in echocardiographic images, in *Computers in Cardiology 2000*, 2000.
30. T. F. Cootes, A. Hill, C. J. Taylor, J. Haslam, Information processing in medical imaging: use of active shape models for locating structures in medical images, *Image and Vision Computing*, vol. 12, pp. 355–365, 1994.
31. A. Estudillo-Romero and B. Escalante-Ramírez, Rotation-invariant texture features from the steered hermite transform, *Pattern Recognition Letters*, vol. 32, pp. 2150–2162, 2011.
32. J.-B. Martens, The Hermite Transform-Theory, *IEEE Transactions on Acoustics, Speech and Signal Processing*, vol. 38, pp. 1595–1606, 1990.
33. J.-B. Martens, The Hermite transform-applications, *IEEE Transactions on Acoustics, Speech and Signal Processing*, vol. 38, pp. 1607–1618, 1990.
34. Y. Wu and J. Shen, Properties of orthogonal Gaussian-Hermite moments and their applications, *EURASIP Journal on Advances in Signal Processing*, vol. 2005, pp. 1–12, 2005.
35. C. J. Rivero-Moreno and S. Bres, Texture feature extraction and indexing by Hermite filters, in *Proceedings of the 17th International Conference on Pattern Recognition*, 2004.
36. T. F. Cootes, G. J. Edwards, C. J. Taylor, Active appearance models, in *5th European Conference on Computer Vision, Proceedings*, Volume II, Berlin, 1998.
37. T. F. Cootes, C. J. Taylor, D. H. Cooper, J. Graham, Active shape models: their training and application, *Comput. Vis. Image Underst.*, vol. 61, pp. 38–59, 1995.
38. B. G. Becker, F. A. Cosío, M. E. G. Huerta, J. A. Benavides-Serralde, Automatic segmentation of the cerebellum of fetuses on 3D ultrasound images, using a 3D Point Distribution Model, in *Annual International Conference of the IEEE Engineering in Medicine and Biology Society*, 2010.
39. S. Osher and N. Paragios, *Geometric Level Set Methods in Imaging, Vision, and Graphics*, Secaucus, NJ: Springer-Verlag New York, Inc., 2003.
40. J. S. Suri, K. Liu, S. Singh, S. N. Laxminarayan, X. Zeng, L. Reden, Shape recovery algorithms using level sets in 2-D/3-D medical imagery: a state-of-the-art review, *Information Technology in Biomedicine, IEEE Transactions on*, vol. 6, pp. 8–28, 2002.
41. V. Caselles, R. Kimmel, G. Sapiro, Geodesic active contours, *Int. J. Comput. Vision*, vol. 22, pp. 61–79, 1997.
42. T. F. Chan and L. A. Vese, Active contours without edges, *IEEE Transactions on Image Processing*, vol. 10, pp. 266–277, 2001.
43. S. Gao and T. D. Bui, Image segmentation and selective smoothing by using Mumford-Shah model, *IEEE Transactions on Image Processing*, vol. 14, pp. 1537–1549, 2005.
44. C.-L. Huang, Shape-based level set method for image segmentation, in *Ninth International Conference on Hybrid Intelligent Systems*, 2009.
45. T. Kohlberger, M. G. Uzunbaş, C. Alvino, T. Kadir, D. Slosman, G. Funka-Lea, Organ segmentation with level sets using local shape and appearance priors, in *Medical Image Computing and Computer-Assisted Intervention (MICCAI)*, vol. 5762, G. Yang, D. Hawkes, D. Rueckert, A. Noble, C. Taylor, *A cura di*, Springer Berlin Heidelberg, 2009, pp. 34–42.
46. T. F. Chan, B. Y. Sandberg, L. A. Vese, Active contours without edges for vector-valued images, *Journal of Visual Communication and Image Representation*, vol. 11, pp. 130–141, 2000.
47. N. Paragios and R. Deriche, Geodesic active regions: a new framework to deal with frame partition problems in computer vision, *Journal of Visual Communication and Image Representation*, vol. 13, pp. 249–268, 2002.
48. T. Brox, M. Rousson, R. Deriche, J. Weickert, Colour, texture, and motion in level set based segmentation and tracking, *Image and Vision Computing*, vol. 28, pp. 376–390, 2010.
49. R. Young, R. Lesperance, W. W. Meyer, The Gaussian derivative model for spatial-temporal vision: I. Cortical model, *Spatial Vision*, vol. 14, pp. 261–319, 2001.
50. M. Abramowitz, *Handbook of Mathematical Functions, with Formulas, Graphs and Mathematical Tables*, Dover Publications, Incorporated, 1974.

51. W. T. Freeman and E. H. Adelson, The design and use of steerable filters, *IEEE Transactions on Pattern Analysis and Machine Intelligence*, vol. 13, pp. 891–906, 1991.
52. A. M. Dijk and J.-B. Martens, Image representation and compression with steered Hermite transforms, *Signal Processing*, vol. 56, pp. 1–16, 1997.
53. T. F. Cootes and C. J. Taylor, Constrained active appearance models, in *Computer Vision, 2001. ICCV 2001. Proceedings. Eighth IEEE International Conference*, 2001.
54. C. Goodall, Procrustes methods in the statistical analysis of shape, *Journal of the Royal Statistical Society. Series B (Methodological)*, pp. 285–339, 1991.
55. M. Stegmann, *Generative Interpretation of Medical Images*, Technical University of Denmark, 2004, pp. 1–248.
56. Y. Q. Shi and H. Sun, *Image and Video Compression for Multimedia Engineering: Fundamentals, Algorithms, and Standards*, 2nd. Boca Raton, FL, USA: CRC Press, Inc., 2008.
57. Y. Correc and E. Chapuis, Fast computation of Delaunay triangulations, *Advances in Engineering Software (1978)*, vol. 9, pp. 77–83, 1987.
58. T. F. Cootes and C. J. Taylor, On representing edge structure for model matching, in *Computer Vision and Pattern Recognition, 2001. CVPR 2001. Proceedings of the 2001 IEEE Computer Society Conference on*, 2001.
59. Y. Ge, D. Yang, J. Lu, B. Li, X. Zhang, Active appearance models using statistical characteristics of Gabor based texture representation, *Journal of Visual Communication and Image Representation*, vol. 24, pp. 627–634, 2013.
60. V. Damerjian, O. Tankyevych, N. Souag, E. Petit, Speckle characterization methods in ultrasound images: a review, *IRBM,* vol. 35, pp. 202–213, 2014.
61. B. Wang and D. C. Liu, A novel edge enhancement method for ultrasound imaging, in *2008 2nd International Conference on Bioinformatics and Biomedical Engineering*, 2008.
62. L. Vargas-Quintero, B. Escalante-Ramírez, L. Camargo Marín, M. Guzmán Huerta, F. Arámbula Cosio, H. Borboa Olivares, Left ventricle segmentation in fetal echocardiography using a multi-texture active appearance model based on the steered Hermite transform, *Computer Methods and Programs in Biomedicine*, vol. 137, pp. 231–245, 2016.
63. D. J. Kroon, Segmentation of the Mandibular Canal in Cone-Beam CT Data, University of Twente, 2011.
64. J. Olveres, R. Nava, B. Escalante-Ramírez, G. Cristóbal, C. M. García-Moreno, Midbrain volume segmentation using active shape models and LBPs, in *Proc. SPIE Europe*, 2013.
65. R. Abu-gharbieh, G. Hamarneh, T. Gustavsson, Review - active shape models - part II: Image search and classification, in *In Proc. Swedish Symposium on Image Analysis*, 1998.
66. U. J. Schoepf, C. R. Becker, L. K. Hofmann, Y. E. Kent, Multidetector-row CT of the heart, *Radiologic Clinics*, vol. 42, pp. 635–649, 2004.
67. R. Fischbach, Cardiac and cardiothoracic anatomy in CT, in *Multi-slice and Dual-source CT in Cardiac Imaging*, B. M. Ohnesorge, T. G. Flohr, C. R. Becker, A. Knez, M. F. Reiser, eds. Springer Berlin Heidelberg, 2007, pp. 23–39.
68. P. M. B. Natalia A. Trayanova, Cardiac arrhythmias: mechanistic knowledge and innovation from computer models, in *Modeling the Heart and the Circulatory System*, M. D. Gellman and J. R. Turner, eds. New, York: Springer International Publishing, 2015, pp. 27–29.
69. O. Pele and M. Werman, The quadratic-chi histogram distance family, in *Computer Vision – ECCV 2010: 11th European Conference on Computer Vision, Proceedings, Part II*, 2010.
70. S. Osher and J. A. Sethian, Fronts propagating with curvature-dependent speed: algorithms based on Hamilton-Jacobi formulations, *J. Comput. Phys.*, vol. 79, pp. 12–49, 1988.
71. D. Mumford and J. Shah, Optimal approximations by piecewise smooth functions and associated variational problems, *Communications on Pure and Applied Mathematics*, vol. 42, pp. 577–685, 1989.
72. J. Olveres, R. Nava, B. Escalante-Ramírez, E. Vallejo, J. Kybic, Left ventricle Hermite-based segmentation, *Computers in Biology and Medicine*, vol. 87, no. Supplement C, pp. 236–249, 2017.
73. J. Olveres, E. Carbajal-Degante, B. Escalante-Ramírez, E. Vallejo, C. M. García-Moreno, Deformable models for segmentation based on local analysis, *Mathematical Problems in Engineering*, vol. 2017, p. 13, 2017.
74. H. C. Assen, M. G. Danilouchkine, A. F. Frangi, S. Ordás, J. J. M. Westenberg, J. H. C. Reiber, B. P. F. Lelieveldt, SPASM: a 3D-ASM for segmentation of sparse and arbitrarily oriented cardiac MRI data, *Medical Image Analysis*, vol. 10, pp. 286–303, 2006.
75. L. Zhu, Y. Gao, V. Appia, A. Yezzi, C. Arepalli, T. Faber, A. Stillman, A. Tannenbaum, Automatic delineation of the myocardial wall from CT images via shape segmentation and variational region growing, *IEEE Transactions on Biomedical Engineering*, vol. 60, pp. 2887–2895, 2013.

76. L. Barba-J, B. Escalante-Ramírez, E. Vallejo Venegas, F. Arámbula Cosío, A 3D Hermite-based multiscale local active contour method with elliptical shape constraints for segmentation of cardiac MR and CT volumes, *Medical & Biological Engineering & Computing*, vol. 56, pp. 833–851, 2018.
77. C. Li, C. Y. Kao, J. C. Gore, Z. Ding, Minimization of region-scalable fitting energy for image segmentation, *IEEE Transactions on Image Processing*, vol. 17, pp. 1940–1949, 2008.
78. A. Andreopoulos and J. K. Tsotsos, Efficient and generalizable statistical models of shape and appearance for analysis of cardiac MRI, *Medical Image Analysis*, vol. 12, pp. 335–357, 2008.
79. H. Sliman, F. Khalifa, A. Elnakib, A. Soliman, A. El-Baz, G. M. Beache, A. Elmaghraby, G. Gimel'farb, Myocardial borders segmentation from cine MR images using bidirectional coupled parametric deformable models, *Medical Physics*, vol. 40, pp. 092302–n/a, 2013.
80. Y. Wu, Y. Wang, Y. Jia, Segmentation of the left ventricle in cardiac cine MRI using a shape-constrained snake model, *Computer Vision and Image Understanding*, vol. 117, pp. 990–1003, 2013.
81. S. Lankton and A. Tannenbaum, Localizing region-based active contours, *IEEE Transactions on Image Processing*, vol. 17, pp. 2029–2039, 2008.
82. C. Pluempitiwiriyawej, J. M. F. Moura, Y.-J. L. Wu, C. Ho, STACS: new active contour scheme for cardiac MR image segmentation, *IEEE Transactions on Medical Imaging*, vol. 24, pp. 593–603, 2005.
83. J. L. Silvan-Cardenas and B. Escalante-Ramirez, The multiscale Hermite transform for local orientation analysis, *IEEE Transactions on Image Processing*, vol. 15, pp. 1236–1253, 2006.
84. B. Escalante-Ramírez, The Hermite transform as an efficient model for local image analysis: An application to medical image fusion, *Computers and Electrical Engineering*, vol. 34, pp. 99–110, 2008.
85. A. Suinesiaputra, B. R. Cowan, J. P. Finn, C. G. Fonseca, A. H. Kadish, D. C. Lee, P. Medrano-Gracia, S. K. Warfield, W. Tao, A. A. Young, Statistical atlases and computational models of the heart. *Imaging and Modelling Challenges: Second International Workshop, STACOM 2011*, Held in Conjunction with MICCAI 2011, Toronto, ON, Canada, September 22, 2011, Revised Selected Papers, Berlin, Heidelberg: Springer Berlin Heidelberg, 2012, pp. 88–97.

Taylor & Francis
Taylor & Francis Group
http://taylorandfrancis.com

11 Cardiovascular Imaging for Early Detection of Coronary Artery Disease

Giorgos Papanastasiou[1], *George Markousis-Mavrogenis*[2], *Sophie I. Mavrogeni*[2]
[1]Clinical Research Imaging Centre, University of Edinburgh, Edinburgh, UK
[2]Onassis Cardiac Surgery Center, Athens, Greece

CONTENTS

11.1 CARDIOVASCULAR IMAGING: AN ENGINEERING PERSPECTIVE

11.1.1 Magnetic Resonance Imaging

11.1.1.1 T_1 Mapping

Over the last 10 years, myocardial T_1 mapping has been extensively implemented in cardiovascular imaging research. It is a measure of the longitudinal or spin-lattice relaxation time of the protons in the myocardial tissue. Following an excitation pulse (radiofrequency pulse used to tip the net

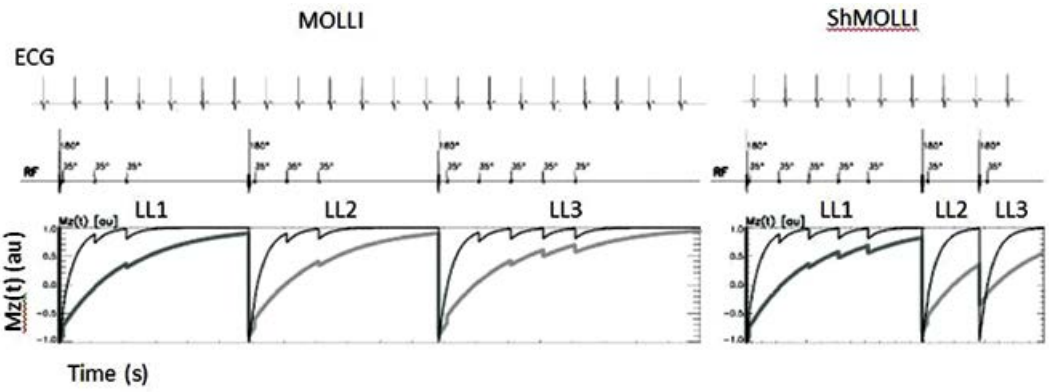

FIGURE 11.1 MOLLI and ShMOLLI pulse sequence schemes shown. The readouts are simplified to a single 35° each. For MOLLI, three sets of Look-Locker (LL) experiments are performed successively (LL1 = three images, LL2 = three images, LL3 = five images), with increasing inversion time within one breath-hold's time. To select end-diastole, images were acquired using a specific trigger delay. For T1 calculation, images are regrouped for post-processing according to their effective inversion time. Similarly, for ShMOLLI, three sets of LL experiments are performed successively (LL1 = five images, LL2 = one image, LL3 = one image). Modified from [8].

magnetization M_0 in the transverse plane), it is the time required for the z component of M_0 to return back to 63% of its original value. During T_1 relaxation, protons interact with their surrounding tissues. The absorbed energy is transferred from the excited protons (spin) to their surroundings (lattice), and the T_1 recovery time is characteristic for each tissue [1].

Look and Locker demonstrated for the first time a multi-point approach that samples the T_1 relaxation curve multiple times after an initial preparation pulse [2]. Although this was an appropriate technique for T_1 measurements of the brain [3–5], it was not possible to be implemented for cardiac applications, since cardiac motion across the cardiac cycle compromised the pixel-by-pixel T_1 mapping of the heart. In 2004, Messroghli et al. developed the Modified Look-Locker Inversion recovery (MOLLI) pulse sequence (Figure 11.1) [6]. The MOLLI approach introduces two major developments to the standard Look and Locker technique: a) uses electrocardiogram (ECG)-gated image acquisition at end-diastole and b) merges images from three consecutive inversion recovery experiments into one data set. MOLLI T_1 mapping was therefore made possible in a single breath hold, over 17 successive heartbeats. This method was fully optimized [7] and it has become the most popular approach for cardiac T_1 mapping.

The Shortened MOLLI (ShMOLLI) approach uses sequential inversion recovery measurements in a single breath hold across only nine successive heartbeats (Figure 11.1). ShMOLLI was developed to minimize MOLLI sensitivity to heart rate [8], as well as breath hold durations, which may be important particularly for patients with respiratory function compromise [9]. Other pulse sequences for T_1 mapping have been developed such as the saturation recovery single shot acquisition (SASHA) [10] and the saturation pulse prepared heart rate-independent inversion recovery (SAPPHIRE) [11], which are also emerging in the clinical setting. A T_1 method comparison study has recently demonstrated that SASHA and SAPPHIRE reached high accuracy, similar reproducibility, but less precision versus MOLLI and ShMOLLI, using phantom experiments and data from seven healthy volunteers [12].

The signal intensity equation for the MOLLI technique is:

$$M(t) = A - B \cdot \exp\left(-\frac{t}{T_1^*}\right) \tag{11.1}$$

where $A = M_o^* = M_o \cdot T_1^* / T_1$, $B = M_o + M_o^* = M_o \cdot (1 + T_1^* / T_1)$ and T_1^* is the effective relaxation time observed in the MOLLI experiment, which is smaller than T_1. A, B, and T_1^* can be obtained by a three parameter fit. T_1 can be calculated from the resulting parameters by applying Eq. 11.2 [13]:

$$T_1 = T_1^* \cdot (B / A - 1) \tag{11.2}$$

Unlike MOLLI, ShMOLLI does not have a dedicated mathematical model for T_1 quantification, which is calculated using a conditional processing algorithm [8]. This conditional data analysis method uses the MOLLI algorithm (Eqs. 11.1–11.2) [6, 7, 13], whilst considering data from the last two Look-Locker experiments only if the T_1 is short enough, so that near to complete relaxation recovery after the second and/or first Look-Locker experiment can be assumed [8].

T_1 maps acquired prior to and after gadolinium-based contrast agent injections can be used for the calculation of the extravascular-extracellular space (known as ECV or v_e) [14]. To quantify ECV through T_1 mapping, the following equation is implemented:

$$ECV = (1 - hct) \cdot \frac{\dfrac{1}{T_{1myo}(post - contrast)}}{\dfrac{1}{T_{1blood}(post - contrast)}} - \frac{\dfrac{1}{T_{1myo}(pre - contrast)}}{\dfrac{1}{T_{1blood}(pre - contrast)}} \tag{11.3}$$

where *hct*, *myo,* and *blood* refer to haematocrit, myocardial tissue, and arterial blood (note that pre-contrast T_1 is the native T_1 of the tissue). Based on this method, a range of ECV values of 25.3 ± 3.5% have been reported in healthy volunteers at 1.5T [15]. This range of values is in agreement with ECV values obtained from studies that performed kinetic modelling analysis from MR perfusion data (see subsection 1.1.4) in healthy volunteers, at 1.5T [16] and 3T [17].

Despite technical disparities between pulse sequence and analysis methods, modern T_1 mapping techniques allow the image-derived characterization of the myocardium. This step has allowed non-invasive clinical investigations that were previously possible only through invasive procedures [6–12, 18]. T_1 mapping is already implemented in the clinical setting and it is therefore considered as a valuable tool for the in vivo investigation of numerous cardiovascular diseases, including CAD [14].

11.1.1.2 T_2*-, T_2-Weighted BOLD Imaging

Myocardial ischaemia initiates when the supply of oxygen (through the blood flow) to the myocardial tissue is not adequate to meet the metabolic oxygen demands of the myocardium. This can be caused by (upstream) coronary artery stenosis that reduces blood supply [19]. To assess oxygenation levels in the myocardial tissue, an MR imaging technique has been developed to detect the so-called BOLD (Blood Oxygen Level Dependence) effect.

BOLD contrast in MRI is designed to reflect the differential deoxyhemoglobin content of blood in the myocardial tissue [19, 20]. Deoxygenated blood has higher content of deoxyhemoglobin, which is paramagnetic and causes strong field inhomogeneities that lead to evident MR signal loss in oxygenation-sensitive T_2^*-weighted and T_2-weighted images. In contrast, highly oxygenated blood is diamagnetic and causes no MR signal loss, hence increasing the signal intensity in oxygenation-sensitive T_2^*-weighted and T_2-weighted images [1]. T_2 relaxation is known as transverse or spin-spin relaxation time and is the time required for the transverse component of M_0 to decay to 37% of its initial value, due to spin interactions (at the atomic and molecular level). T_2^* relaxation is the process by which the transverse magnetiation gradually decays due to magnetic field inhomogeneities [1]. Their relationship can be expressed as:

$$\frac{1}{T_2^*} = \frac{1}{T_2} + \frac{1}{T_2'} \tag{11.4}$$

where T_2' is the relaxation rate contribution due to magnetic field inhomogeneities.

One of the first studies showing proof of concept of the BOLD effect in vivo was performed by Li et al. [21]. They demonstrated increased T_2^* signal changes when dipyridamole versus dobutamine were injected in human subjects. Dipyridamole is a coronary vasodilator that induces hyperaemia with minimum oxygen consumption. Hence, during hyperaemia, increased oxygen saturation is observed in the myocardial venous system [22]. On the other hand, dobutamine induces hyperaemia because it increases oxygen consumption in the myocardium, thus oxygen saturation in the venous system tends to remain balanced [23].

Several oxygenation-sensitive T_2^*-weighted imaging protocols have been implemented to detect reduced oxygenation levels in the presence of CAD at 1.5T, showing promising results [24, 25]. To benefit from the inherently higher signal-to-noise ratio (SNR) at 3T and therefore to increase signal intensity changes between normal and pathologic areas, T_2^*-weighted imaging protocols have been investigated at 3T [26]. Manka et al. demonstrated promising diagnostic performance for the detection of myocardial areas with reduced oxygenation through BOLD T_2^*-weighted imaging at 3T, in the presence of CAD [26]. However, image quality was compromised in a number of subjects due to susceptibility artefacts, particularly in the heart-lung interface.

To overcome systematic susceptibility artefacts that are present in T_2^* protocols, oxygenation-sensitive T_2-weighted imaging has been optimized [27]. Compared to T_2^*-weighted, sensitivity to oxygenation with T_2-weighted imaging is reduced, but it is considered to be much less prone to changes in temperature, haematocrit and susceptibility artefacts [19]. Similarly to T_2^*, Dharmakumar et al. showed that the sensitivity to detect changes in oxygenation-sensitive T_2-weighted imaging may increase at 3T, compared to 1.5T [28]. BOLD T_2-weighted imaging has been compared versus absolute values of myocardial blood flow from dynamic positron emission tomography and MR perfusion data in patients with CAD [29–31]. In these studies, BOLD demonstrated interesting clinical results and performed high diagnostic performance for the detection of obstructive CAD, against invasive reference standard measurements. It was also showed that reduced blood flow may not necessarily be associated with decreased levels of oxygenation in the presence of stenotic lesions [29, 31], which is an interesting finding that could be evaluated in larger patient cohort studies. In the context of oxygenation-sensitive T_2-weighted imaging, Tsaftaris et al. showed that signal intensity differences between systole (higher oxygenation time frame in healthy subjects) and diastole (lower oxygenation time frame compared to systole) were marginalized in the presence of ischaemia even at rest (without pharmacological stress), using canines [32].

There is still a debate whether T_2^* or T_2-weighted protocols can be used to consistently achieve efficient, free of artefacts, BOLD sensitivity. T_2^* protocols are more sensitive to detect changes but are more prone to susceptibility artefacts, which can be evident at 3T. T_2-weighted protocols at 3T are strong candidates for BOLD imaging, but careful MR shimming and protocol optimization is necessary to account for magnetic field inhomogeneities and persistent susceptibility artefacts [31]. Further work in the field will potentially lead to oxygenation-sensitive MR imaging method optimization, which could be a useful step toward establishing robust implementations of cardiac BOLD imaging in the clinical setting.

11.1.1.3 Magnetic Resonance Angiography

Magnetic resonance angiography (MRA) was developed as a potentially useful technique for the non-invasive assessment of coronary arteries and the detection of atherosclerotic plaques. However, long imaging times, lower spatial resolution (compared to computed tomography angiography, see subsection 1.2.1), and operator dependency have limited its use in the clinical setting [33].

To date, there is limited work describing the implementation of coronary MRA in the setting of non-invasive CAD assessment, whilst the majority of studies used relatively small patient cohorts [34]. A recent meta-analysis study demonstrated an overall sensitivity and specificity of 89% and 72%, respectively, across all MR sequences that have been examined [35]. There is an increasing clinical demand to develop a non-invasive, no-radiation technique to improve the assessment and

management of atherosclerotic plaque [34, 35], which has stimulated further development work in coronary MRA imaging.

Various MR imaging techniques have been developed and optimized [33, 35]. The steady state free precession (SSFP) sequences benefit from high T_2/T_1 ratio of the blood, which in turn acts as an intrinsic contrast medium in coronary MR angiography [36]. Whole-heart coronary MR angiography by using free-breathing SSFP sequences showed increased performance to image all three major epicardial arteries in a single 3D acquisition [37]. Another study, published in 2012, demonstrated that whole-heart coronary MR angiography using a 32-channel coil and a gradient echo (fast low angle shot, FLASH) sequence at 3T, reached high diagnostic performance for the detection of obstructive CAD (sensitivity 96%, specificity 89%, in per vessel analysis) [38].

Despite the aforementioned improvements, additional work needs to be done in order to evaluate coronary MRA in the clinical setting. Due to the lack of standardized protocols and the limited experience, coronary MRA imaging and analysis are both operator dependent [33, 34]. Moreover, the available MRA protocols still vary between vendors, whilst additional clinical assessments are important to examine which imaging protocols can increase the MRA diagnostic performance. Standardization of MRA protocols and appropriate training for technologists and clinicians are therefore a necessary step for the implementation of coronary MRA imaging in the setting of CAD assessments.

11.1.1.4 Dynamic Contrast Enhanced Magnetic Resonance Imaging

Dynamic contrast enhanced (DCE)-MRI has been widely used to perform myocardial perfusion imaging [39]. Cardiac DCE-MRI commonly involves the acquisition of dynamic (successive) images to rapidly track the passage of a gadolinium-based contrast agent injected through the myocardium. Mathematical modelling of cardiac DCE-MRI data can allow myocardial blood flow (MBF) estimations [39], as well as provide additional information about coronary vascularity and permeability [16, 17]. Quantitative DCE-MRI techniques have the potential to improve the diagnosis of CAD, the assessment of coronary microcirculation, as well as to evaluate perfusion changes during or after therapeutic interventions [39, 40] (Figure 11.2).

Saturation recovery pulse sequences for T_1-weighted imaging are most commonly used to perform DCE-MRI, in which the inherent short echo times involved (for T_1-weighted imaging) can minimize the effects of myocardial tissue motion and flow [39, 41]. A full coverage of the heart is required across all sequential dynamic frames (typically 45–60 dynamic frames to track the wash-in and wash-out phase of the contrast agent through the tissue), which can be achieved by using a minimum of three slices, in order to be able to extract a standardized 16-segment heart model [42]. Cardiac DCE-MRI is not yet widely used in the clinical setting, mainly due to the technical challenges in the data analysis field [39].

The following steps are required to be established in order for perfusion analysis (from DCE-MRI data) to be considered as a potential setup in the clinical environment.

a. Automatic segmentation techniques have to be developed in order to accurately outline myocardial areas in a timely manner (to avoid time-consuming, operator-dependent manual segmentations of large perfusion data sets).
b. A quantifiable, nonlinearity correction relationship between signal intensity and contrast agent concentration is needed [39, 41, 43, 44]. This step needs to be optimized based on the scanner platform characteristics, such as the MR perfusion sequence used, the contrast agent concentration, and the field strength [17, 44].
c. A quantitative analysis approach has to be standardized (which may depend on the scanner platform characteristics), and its diagnostic performance has to be assessed, against invasive reference standard measurements.

Automatic segmentation techniques based on convolutional neural network deep learning approaches have recently been developed for MR imaging data [45]. Although these techniques

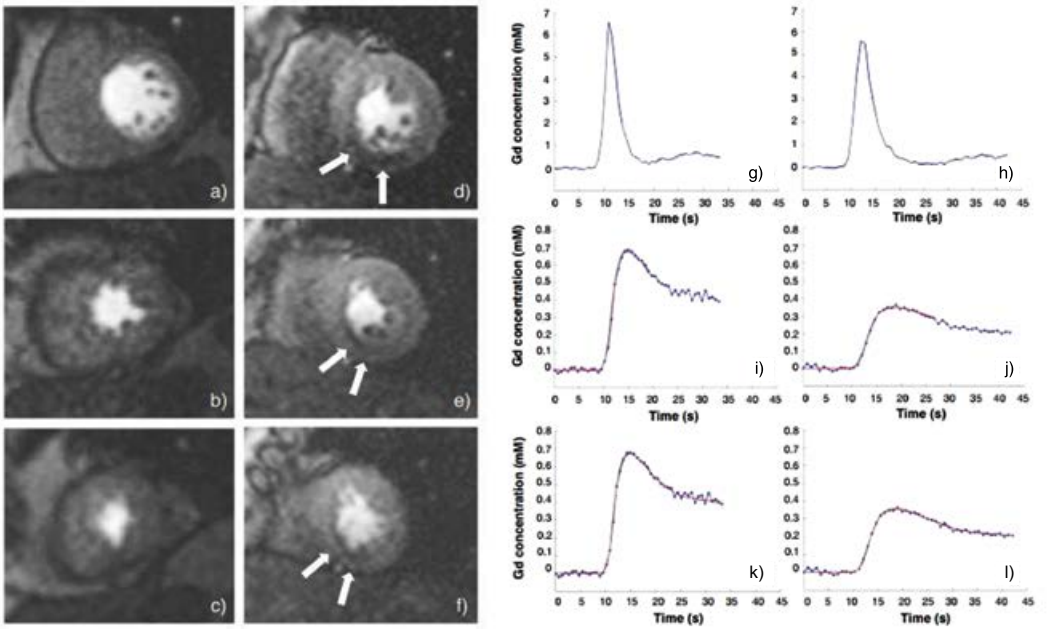

FIGURE 11.2 Cardiac DCE-MR images from a patient with minor CAD (a, b, c) and a patient with (1-vessel) coronary artery disease (d, e, f). White arrows show perfusion defect in the inferior and inferoseptal myocardial regions, across all three perfusion slices acquired. Basal (a, d), mid-ventricular (b, e) and apical slices (c, f) are illustrated. Arterial input functions and model fits on myocardial tissue curves extracted from DCE-MRI data. Perfusion curves from a patient with minor (g, i, k) and a patient with 1-vessel (h, j, l) CAD are shown. g, h, i, j, k, l show arterial input functions, Fermi modelling, and distributed parameter modeling fits, respectively. Gd: gadolinium (modified from [54]).

have demonstrated high performance, more work needs to be done in order to automatically segment epicardial regions, as well as the most apical and basal cardiac anatomies, in which inherent cardiac motion and lower SNR can compromise method accuracy [45, 46]. Oktay et al. have recently developed a new method to incorporate prior knowledge about organ shape and location into convolutional neural networks [47]. Further work on similar approaches can potentially improve further the performance of deep learning techniques in the setting of automatic cardiac segmentations and can help to optimize these algorithms for cardiac DCE-MRI data.

The nonlinear relationship between signal intensity and gadolinium concentration can be modelled by a signal equation [48]. The signal equation for a saturation recovery T_1-weighted pulse sequence can typically be:

$$S(t) = \Psi \cdot f(R_1(t), PD, n) \tag{11.6}$$

where S(t) is the equilibrium signal intensity at time t, Ψ is a calibration constant dependent on instrument conditions, PD is the pre-pulse delay, which is the time between saturation pulse and the central line of k-space, n is the number of applied pulses of flip angle α. However, signal equations do not account for signal saturation effects that may be evident in the left ventricle blood pool region (used to derive an arterial input function (AIF) for MBF quantification), where the accuracy of gadolinium concentration estimation can be compromised [17, 39, 43, 44]. Different methods have been proposed to correct signal saturation effects in the AIF, such as the dual bolus [17, 43], the dual sequence [49], or retrospective correction using calibration curves [50]. The behavior of nonlinearity correction methods may depend considerably on the protocol, field strength, and gadolinium concentrations used, and careful evaluation is needed prior to method implementation [44].

In the final step of perfusion analysis, gadolinium concentration curves derived from different myocardial tissue areas and the blood pool (AIF) are used to perform model-independent or model-constrained deconvolution analysis for MBF quantification. The convolution product of two functions is important for the analysis of such a system:

$$C_t(t) = R(\tau) \otimes C_{AIF}(t - \tau) \tag{11.7}$$

where R represents the tissue impulse response if an impulse input of contrast agent is applied at the region input, such as a Dirac-delta input function (δ(t)). C_t is the gadolinium concentration derived from a myocardial tissue region, and C_{AIF} is the AIF. MBF can then be derived by the initial amplitude of the R, as described by:

$$R(t = 0) = MBF \tag{11.8}$$

Model-independent approaches are based on imposing smoothness constraints to mathematically stabilize the numerical inversion of the deconvolution operation (for the calculation of the tissue impulse response from equation 7 and therefore of MBF estimates), with some approaches showing higher accuracy versus others [51]. Model-constrained approaches use either an empirical model known as the Fermi function [39], or models based on tracer kinetic analysis such as the distributed parameter model [16, 17] to describe and estimate R. Although more models based on tracer kinetic analysis are recently presented in the literature, the authors here focus on describing some of the modelling approaches that have recently demonstrated high diagnostic performance for obstructive CAD detection.

In the context of diagnostic investigations, quantitative DCE-MRI studies have demonstrated high diagnostic performances by either using model-independent [52], Fermi at 1.5 T [53], or distributed parameter modelling at 3T [54]. Further analysis using larger patient cohorts and/or in multicenter trials are needed to determine which might be the most accurate analysis techniques for obstructive CAD assessments. Despite all the technical challenges discussed, cardiac DCE-MRI is a promising technique that can provide important physiological and functional information and can be clinically useful for assessing blood flow and microvascular characteristic changes, during or after revascularization and/or therapy.

11.1.1.5 Cardiac Function Using SSFP Sequences

As mentioned previously, SSFP sequences are using a mixture of T_1 and T_2-weighted imaging and can provide two-, four-chamber, and short axis cardiac view images with optimum signal to noise ratio (without using contrast agent injections). For SSFP imaging, ECG gating is used to commonly acquire about 25 to 30 short axis (known as cine-images) per heartbeat, across sequential (commonly 7–12) heartbeats to acquire full cardiac coverage [28, 29]. As much as 175 to 300 cardiac views can be acquired on average (depending on the cardiac size of individual patients) with high temporal resolution (typically of about 30 ms) across different cardiac slices. Standard cine SSFP sequences are widely routinely acquired during cardiac MR protocols to assess cardiac function. Image analysis of cine images using dedicated cardiac software can derive important measurements of cardiac function such as ejection fraction, cardiac output, end diastolic, and end systolic volumes, necessary component estimations in the setting of standard cardiac assessments as well as clinical trials [28–30].

11.1.2 Computed Tomography

11.1.2.1 Computed Tomography Angiography

In clinical practice, the new generation of multidetector computed tomography (MDCT) scanners have enabled the implementation of coronary CT angiography and perfusion within one cardiac imaging protocol [55]. The main advantage of MDCT scanners is the reduction in radiation dose

and scan times, whilst they are able to detect highly defined anatomical details of coronary arteries, reducing arrhythmias and respiratory motion artefacts [55, 56]. Furthermore, the application of MDCT scanners introduced a different approach to image analysis in which the operator can reconstruct and navigate planar images through the use of dedicated software tools [56].

Using modern MDCT imaging technology, recent studies demonstrated that non-invasive CT coronary angiography (CTCA) has the potential to exclude significant CAD [57, 58] and can provide prognostic information in patients with suspected CAD [59]. CTCA can also reach excellent sensitivity in detecting significant CAD [60]. However, the specificity of these modern techniques is relatively reduced, because they tend to overestimate heavily calcified lesions [61]. Furthermore, studies have shown that CT coronary angiography is a poor predictor of reversible myocardial ischaemia [62] and that functional information is needed, particularly in patients with moderate to severe coronary artery disease [63]. To overcome the limitations of CTCA, additional information on the functional significance of coronary artery stenosis is needed from CT scanning. Cardiac CT perfusion imaging may provide additional functional information and has the potential to improve the diagnostic accuracy of CT angiography for the detection of coronary stenoses, albeit at the cost of additional ionizing radiation exposures [63].

In cardiac CT angiography imaging, the high radiation doses involved have raised serious concerns in literature, as the risks of radiation-induced malignancy are not negligible [63, 64], particularly when repetitive scans are needed to assess disease progression or response to therapy. Methods to minimize the radiation dose in cardiac CT angiography protocols have been proposed, such as using prospective ECG-triggering, with which it is possible to image only specific parts of the cardiac cycle [63, 64].

11.1.2.2 Computed Tomography (Static) Perfusion

As mentioned in the previous subsection, CT angiography alone has a limited ability to determine the functional significance of coronary stenosis, and myocardial perfusion imaging can be included in order to provide complementary functional information [62–64]. After contrast agent injection (the same bolus injection used for CT angiography), MDCT images may provide qualitative (visual estimates) or semi-quantitative information about myocardial perfusion. Short axis views of the left ventricle and myocardium can be reconstructed from the MDCT data, and the presence of a myocardial perfusion defect can be detected from a static (or snapshot) image during the arterial phase of peak contrast enhancement, using prospective ECG-triggering [63] (Figure 11.3).

CT angiography and perfusion may be performed in a single examination to acquire both anatomical and functional information on modern, advanced wide detector CT systems. Despite the introduction of some early dynamic CT perfusion protocols in animal and human studies (these will

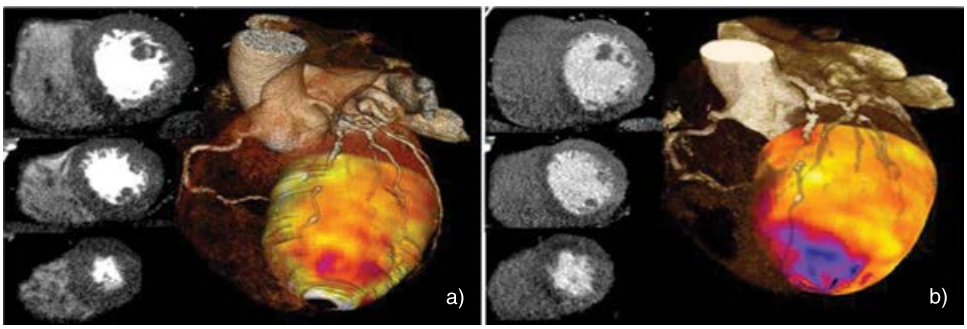

FIGURE 11.3 Short-axis basal, mid and apical images of the left ventricle a) at rest and b) during hyperaemia are illustrated, together with 3D representations of the transmural perfusion ratio as well as coronary anatomy. Hypoattenuation (represented here with blue color) is seen in myocardial areas during hyperaemia, whilst mild hypoattenuation in the RCA territory is also observed on rest imaging (adapted from [70]).

be discussed in the next subsection), the vast majority of CT perfusion imaging applications in the clinical setting is still limited to a static acquisition at the peak of contrast enhancement, in order to limit the overall radiation dose exposure (in a dynamic CT perfusion examination).

There are several studies published that have focused on evaluating myocardial perfusion using modern techniques in MDCT scanners. For example, spiral CT image acquisition involves transport of a patient at a constant speed through the gantry, whilst spiral (also known as helical) CT data are simultaneously and continuously acquired over multiple gantry rotations [65]. With the standard spiral acquisition mode of conventional (i.e., with narrower detector arrays) MDCT scanners, it is feasible to image only an early phase of first pass contrast enhancement [66]. This has allowed semi-quantification measurements of myocardial perfusion such as regional signal density ratio (i.e., myocardial signal density/left ventricular signal density) [66] and the generation of qualitative perfusion maps [67], in canines. Recent studies in human subjects using new generation wide detector MDCT scanners (such as 64-, 256-, and 320-slice systems), have shown that the diagnostic accuracy of CT angiography for the detection of significant coronary artery disease can be improved, when combined with static CT perfusion imaging [66, 68]. Static perfusion images can be acquired both under vasodilator-induced stress and at rest. These studies showed that CT perfusion imaging can detect transmural differences in myocardial perfusion, which can be quantified as the transmural perfusion ratio (i.e., subendocardial/subepicardial attenuation density) [66].

In a case study using a 320-slice MDCT scanner, perfusion defects have been accurately detected, as compared with invasive coronary angiography, with the application of a low radiation dose (snapshot) perfusion acquisition protocol [69]. Another study using CTCA/CTP from the same group showed strong correlations against ^{15}O-water PET-derived MBF (which is considered as the reference standard technique for MBF quantification) and comparable diagnostic performance to the current invasive reference standard measurements of invasive coronary angiography and fractional flow reserve [70].

11.1.2.3 Dynamic Contrast Enhanced Computed Tomography

As discussed in subsections 1.2.1 and 1.2.2, dynamic acquisition of CT perfusion images using ECG-gating is restricted due to radiation exposure limitations. Most clinical CT perfusion protocols are limited to acquire a static image at the peak of contrast enhancement both during vasodilator-induced stress and at rest. Despite this, some early dynamic CT perfusion acquisition protocols have been introduced, although with limited cardiac coverage and/or temporal resolution and/or time frame of contrast enhancement and/or SNR, and absolute myocardial blood flow quantification has been made possible.

Wide detector MDCT scanners can potentially provide improved temporal resolution together with high spatial resolution while allowing full cardiac coverage using lower radiation doses [71]. With the use of modern acquisition techniques in these new generation scanners, it is possible to dynamically visualize different phases of first pass myocardial contrast agent kinetics, which are needed for absolute myocardial blood flow measurements [71]. Using a 64-slice MDCT scanner, dynamic CT perfusion images have been acquired in canines, which allowed absolute myocardial blood flow quantification using two-compartmental modelling [72].

Dual energy MDCT imaging has also been used to generate perfusion-maps from snapshot images at the peak of contrast enhancement using relatively low radiation doses in patients with suspected coronary artery disease [73]. The operation of dual energy MDCT scanners is based on the application of two simultaneous X-ray sources with different photon energy, which can acquire two data sets with different attenuation levels. Images acquired at two different attenuation levels can then be processed with specific software applications, and differences in tissue composition can be emphasized [74]. With the implementation of dual energy MDCT scanners, the acquisition of dynamic ECG-triggered myocardial perfusion images in patients with known or suspected coronary artery disease was made possible [75, 76]. However, these dynamic perfusion protocols were still unable to cover the entire left ventricle [75]. Model-independent deconvolution analysis

of these dynamic CT perfusion data provided absolute myocardial blood flow values in the myocardial areas that were imaged [75]. The previous method has provided accurate myocardial blood flow measurements when compared with invasive coronary angiography outcomes from patients with suspected coronary artery disease. Kido et al. have reported the use of conventional 16-slice MDCT scanners for non-ECG gated dynamic perfusion image acquisition in human subjects [77]. Nevertheless, this protocol was unable to cover the entire left ventricle at each dynamic image acquisition.

Recently, low-dose dynamic CT perfusion imaging protocols have been developed, and global MBF from the myocardium (using two-compartmental modelling) was calculated [78]. In this study, regional MBF was not possible to be derived due to the noisy profile of the dynamic curves extracted (because of the low-dose, low-SNR dynamic images generated), which caused unstable model fitting. Another study performed dynamic CT perfusion imaging to derive MBF values together with CTCA measurements, although the already increased radiation exposure did not allow the implementation of dynamic imaging at rest [79]. There is an ongoing research to develop a combined protocol of dynamic CT perfusion (for MBF measurements) along with CTCA, in order to robustly extract important functional as well as anatomical information of the coronary arteries in a single CT examination.

11.1.3 Ultrasound

Echocardiography is a useful medical imaging modality due to its availability, low cost, no radiation exposure, real-time operation, and ease of use. Modern imaging approaches in ultrasounds have allowed the extraction of clinically useful parameters of myocardial function and anatomy, such as myocardial blood flow velocities and deformation measurements [80].

In conventional b-mode ultrasound imaging, the pixel brightness is determined by the amplitude of the returned echo. The detection and estimation of blood flow velocity is based on processing the scattered echo from the red blood cells. To detect and quantify blood flow velocity, the frequency shift as well as the amplitude of the returned echoes are detected and post-processed [80]. The conventional pulsed-wave Tissue Doppler Imaging (TDI) is a technique that was initially used to derive myocardial blood flow velocities and deformations (strain and strain rate analysis) [81], [82]. However, one of the main limitations of TDI for blood flow velocity assessments is that the information is obtained from a single sample volume and, therefore, it is angle dependent [82]. This is also a limitation for conventional TDI-derived strain analysis, as prior knowledge is needed with regard to the direction of motion of the myocardial tissue, in order to align the tissue beam parallel to the vector of contraction in the tissue region of interest [80–82].

The color Doppler flow imaging was developed to overcome the limitations of the conventional pulsed-wave TDI technique. It is designed to detect the high velocity/low echo amplitude profile of the moving blood [83]. In contrast, the myocardial tissue has a combination of relatively low velocity/high echo amplitude profile. In color Doppler imaging, the high velocity/low echo amplitude characteristic profile of the blood can be distinguished from the myocardial signal, through the implementation of appropriate thresholds and filters [82, 83]. The development of color Doppler imaging performs frequency shift and amplitude detection along a number of acoustic lines, which can overcome major angle dependence limitations of the conventional TDI. A 2D image depicting flow velocity is finally generated, which in turn is superimposed on the 2D grey-scale conventional real-time b-mode image [83, 84]. Although the development of color Doppler imaging improved the diagnostic assessments of blood flow velocity and myocardial tissue deformation estimates compared to the conventional Doppler technique, the main limitation of any Doppler technique is still the dependency of the measurements on the angle between the ultrasound beam and the direction of motion [82–85]. This inherent limitation of the Doppler techniques allows quantitative assessments of only the longitudinal function of the heart (see Figure 11.4b) [82].

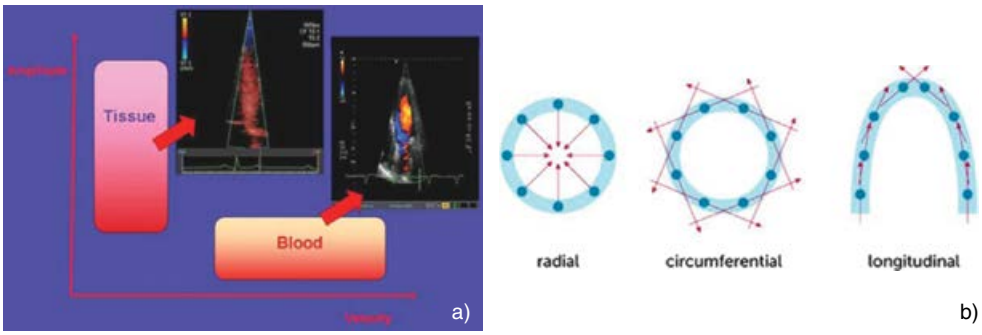

FIGURE 11.4 a) Graph demonstrating the low velocity/high echo amplitude of the myocardial tissue and high velocity/low echo amplitude of the blood. b) The three types of left ventricular wall strains that can be derived using 2D-speckle imaging and analysis (a. adapted from [82] and b. from [80]).

A modern echocardiography approach that aims to overcome limitations of previous techniques is the 2D-speckle tracking [82]. In the 2D-speckle tracking mode, the reflected echo from the tissue results from the interference of numerous reflected wavelets deriving from the inhomogeneous tissue [82, 86]. Some of the interference patterns remain constant throughout parts of the cardiac cycle and are tracked by using an algorithm that detects the most similar speckle pattern from one time frame to another [86]. Speckle tracking can provide information across the longitudinal, radial, and circumferential myocardial function. In addition, through the detection of the spatial movement of speckles, it is possible to directly derive Lagrangian strain parameters, with increased lateral resolution compared to Doppler techniques [82, 85].

The Lagrangian strain ε is defined as the change of the myocardial fiber length during stress at end-systole (l), as compared to its original length in the relaxing end-diastolic phase (l_0):

$$\varepsilon = \frac{l - l_0}{l_0} \tag{11.9}$$

Strain is expressed in (%), whilst the change of strain per unit of time can also be defined, which is referred to as strain rate. With speckle imaging, more advanced measurements to assess cardiac mechanics can be quantified, such as the left ventricle rotation, twist and torsion [87]. This means that by using speckle imaging, a combination of myocardial tissue deformation measures can be extracted and can provide complementary information of myocardial function and anatomy. Hence, 2D-speckle imaging is considered a valuable tool for assessing left ventricular systolic and diastolic function [81, 82, 87], as well as potentially different functional biomarkers that can describe cardiac mechanics.

2D-speckle imaging-derived strain analysis can potentially provide additive functional information of cardiac mechanics [81, 82]. However, clinical investigations have showed that there are differences in the threshold values used to stratify pathological from normal 2D-speckle imaging-derived strain analysis measures, across different patient groups [81–84, 87]. Thus, more extensive work is needed to further validate these measures in the clinical setting. Some of the current limitations that may affect the reproducibility and accuracy of 2D-speckle imaging-derived measurements is that they can be compromised by image quality issues, out of plane motion of speckles (that can affect strain analysis), whilst thorough technical assessments are often limited by unknown software algorithms (black box operations which may vary across vendors) used to track speckles [82]. Some of these limitations can potentially be overcome by the use of 3D-speckle imaging. Although not yet fully validated and optimized, 3D-speckle imaging could allow more advanced and less operator dependent 3D strain analysis in the clinical setting, by deriving complex strain assessments using a

single 3D data set [81, 82]. Further evaluations in the context of 2D- and 3D-speckle imaging may help to demonstrate the diagnostic credibility of echocardiography-derived measures across various applications in the clinical setting.

11.2 CARDIOVASCULAR IMAGING: A CLINICAL PERSPECTIVE

11.2.1 Ultrasonography/Echocardiography

Echocardiography (ultrasonography of the heart) is an imaging modality that utilizes ultrasound-frequency (>20 kHz) waves to generate images of the heart and great vessels. Echocardiography is the primary bedside imaging modality used for the evaluation of the cardiovascular (CV) system and has a well-established role as an inexpensive, first-line method of early CV disease (CVD) assessment. Soundwaves are produced via a transducer and are emitted inside the body of the patient being examined; these initial waves are called incident waves. As incident waves travel through body tissues, they react differently with each one. Generally, waves of sound behave similarly to those of electromagnetic waves (light). As occurs with electromagnetic waves, the wavelength of soundwaves is inversely proportional to its frequency and is determined based on the formula $\lambda = \frac{\upsilon}{f}$, where λ is the wavelength, υ is the velocity of the wave in the medium it is traversing, and f is the frequency of the wave. As a result, waves with higher frequencies (e.g., ultrasound frequencies) have smaller wavelengths. These smaller wavelengths make ultrasound waves capable of being reflected by much smaller objects than waves of lower frequencies, which affords ultrasonography a good special resolution.

Apart from reflection, other physical phenomena such as refraction and diffraction occur as soundwaves travel through the body. Diagnostically, reflection is most informative to the operator performing the examination, as reflected soundwaves (echoes) that return to the transducer are digitized and processed to create an image. Wave reflection occurs at the point where different tissues intersect. Whether no reflection, a partial reflection, a substantial reflection, or a complete reflection of the incident wave will occur, depends on the acoustic properties of the medium the wave is about to enter. Namely, depending on the difference of acoustic impedance (i.e., the difference in density and wave propagation speed) between the current medium and the one the wave is attempting to cross into is minimal, then little or no reflection will occur. Conversely, media with high difference in acoustic impedance will reflect most or all of the emitted waves, in the latter case not allowing them to traverse the body beyond them. Weaker and stronger echoes help identify different tissues in an image and are displayed in a range of colors from black to white, with the extreme of black color signifying no reflection and white color signifying complete reflection.

Ultrasonography has been successfully used to identify patients with coronary artery disease (CAD) early in the course of its development. A very well-known measurement that has been extensively used for the early identification and risk stratification of patients with CAD is the measurement of the carotid intima-media thickness (CIMT). CIMT measurement with B-Mode ultrasound is a non-invasive and sensitive technique that can be used for quantifying and CAD risk [88] [1]. CIMT has been demonstrated to be associated with increased risks for CAD and/or myocardial infarction (MI) occurrence in a review of various studies [89] [2]. CIMT can additionally reclassify patients at intermediate CVD risk and can discriminate between patients and with and without prevalent CVD [88] [1].

Echocardiography, more specifically, also has diverse applications in the evaluation of CAD. Perhaps most importantly, stress echocardiography is nowadays an established technique for evaluating CAD, where 2D echocardiography is combined with a cardiac stressor in order to evaluate cardiac function during rest and stress, as well as the differences between the two phases. Cardiac stress can be evoked by physical exercise, by administration of pharmacologic agents (e.g., dobutamine, dipyridamole, adenosine), or via transcutaneous pacing to the desired heart rate [90] [3]. The endpoint of stress echocardiography is the detection of transient changes in regional myocardial

function during stress and their comparison to resting conditions; if regional abnormalities are identified, these could be indicative of myocardial ischemia among others. Essentially, four possible patterns can be seen in stress echocardiography: normal, ischemic, viable, and necrotic [90, 91] [3], [4]. Under normal conditions, we expect the myocardium to be normokinetic at rest and hyperkinetic at stress. When ischemia is present, function worsens during stress due to the unmet metabolic demands of the myocardium. Conversely, stunned or hibernating myocardium is usually akinetic but "springs to life" when stressed, which is a typical finding for still viable tissue. Finally, segments with dysfunction present at both stress and rest are usually necrotic. The addition of coronary flow reserve (CFR) to the examination of segmental myocardial wall motion is of additional value in predicting CAD-related mortality [90] [3]. However, this is only limited to the left anterior descending artery (LAD), as other coronary arteries are more difficult to visualize. Nevertheless, a normal stress echocardiography with normal CFR in the LAD confers an annual risk of death that is <1% [92] [5].

Despite the aforementioned benefits of stress echocardiography, it is still an operator dependent technique that is primarily based on visual evaluation of wall motions, which can in turn be affected by overall cardiac displacement during contraction, or by tethering of adjacent segments that lead to mimicry of healthy movements. A potential solution for this dependency is the use of deformation imaging in the form of strain/strain rate [91] [4]. These indices are nowadays mostly derived from so-called speckle tracking methods, instead of tissue Doppler imaging that was used in previous years. Strain measurements can be segmental or global when respective functions are being investigated. Myocardial strain can be distinguished into longitudinal, radial, and circumferential types [see engineering section for more details]. Associations of decreased coronary perfusion with longitudinal strain in particular have been reported in a number of studies [91] [4]. However, evaluation of cardiac strain parameters is at the time not extensively used in the clinical setting. This is partly due to the fact that no clear normal cut-off values for strain imaging exist, as well as due to large differences between vendors and extrapolating software, which also compound the less than perfect inter-rater agreement of echocardiography. In addition, strain imaging is susceptible to poor visual window and is thus of more limited utility in patients whose heart cannot be completely visualized during the entirety of the cardiac cycle.

Here, special mention should be made regarding the right ventricle (RV). All aforementioned methods are primarily used for the assessment of the workhorse of the heart, namely the left ventricle. When the right ventricle is affected by CAD, wall motion abnormalities are the most sensitive and specific findings seen in echocardiography; these are usually localized in the inferior wall of the heart, but may also more rarely manifest in the anterior and/or lateral walls [91] [4]. Impairments in RV wall motion may affect RV systolic function indices such as tricuspid annular plane systolic excursion (TAPSE), S wave velocity and RV fractional area change [93] [6]. RV deformation analysis using speckle tracking is also a possible way of examining RV function, although again limited by visual window, vendor and software differences, and operator dependency. Next to RV dysfunction, the ventricular cavity may be enlarged, with subsequent RV diastolic dysfunction [93] [6]. This in turn leads to enlargement of the inferior vena cava (IVC) and minimization of IVC diameter differences between inspiration and expiration.

11.2.2 Computerized Tomography

Computerized tomography (CT) is a non-invasive imaging modality that utilizes X-ray wavelength photon beams to generate detailed images of human anatomy in slices. These high energy photons are produced in an X-ray tube, and as they traverse human tissues, they interact with and are attenuated by them, depending on the density of each tissue [94] [7]. More dense structures like calcium in bones and vascular calcifications absorb a greater quantity of high energy photons, while less dense materials like air in air-filled structures or blood in vessels absorb far less photons. An X-ray detector is placed at a diametrically opposite position from the X-ray photon source. This detector

is excited by photons exiting the body at the opposite side of entry. These exiting photons have less energy than when they entered the body of the patient, with the remaining energy depending on the density of tissues they passed through on their way out (and thus the degree of attenuation). The X-ray tube/detector pair rotates around the patient in a helical manner. This allows the detector to acquire data on the specific area of interest from different viewpoints, which are then sent to a computer for further processing. The computer by means of an extrapolating algorithm finally creates an image based on the available data [94] [7].

Although the role of CT is widely recognized in the evaluation of abdominal and general thoracic pathology, cardiac evaluation presented difficulties in the past, as cardiac motion led to the generation of imaging artifacts and poorer image quality [95] [8]. The introduction of multislice CT scanners (also known as multidetector CT scanners), however, has led to a solution for this issue. Multislice CT scanners, in contrast to earlier types of scanners, are equipped with multiple X-ray detectors instead of <16 detectors in previous models. This affords them the capability of generating multiple slices in one beam emission, which also makes them better suited for use in cardiovascular imaging. When combined with electrocardiogram-gating, multislice CT is even better suited for cardiovascular imaging. Cardiac CT has a much broader role in the evaluation of CAD currently than in the past. Some noteworthy applications include the assessment of coronary stenosis, the prediction of CAD outcomes, the characterization of atherosclerotic plaques, and the identification of non-stenotic plaques that are otherwise undetectable by invasive coronary angiographic procedures [95] [8].

Coronary artery calcium (CAC) is used in the risk evaluation for CAD in healthy patients, as an additional index to traditional cardiovascular risk factors. CAC is determined as the area and density of all identifiable foci of calcification in the coronary arteries, with the sum of area and density being used to generate a CAC score, which is a unit-less index of the overall burden of coronary calcification [96] [9]. Cardiac atherosclerosis is usually proportional to CAC, which is why these measurements provide incremental value to typical cardiovascular risk assessment. CAC has been demonstrated to predict CAD occurrence with incremental benefit compared to commonly used risk factors. Additionally, large studies have demonstrated that absent CAC is associated with an event-free probability of 99% per year [97] [10]. It should nevertheless be kept in mind that CAC is also related to demographics (age, race, gender) as well as the presence of other cardiac risk factors.

Coronary plaque characterization is a somewhat less validated technique. In order to characterize coronary plaques, an iodine-based vascular contrast agent is used to delineate the lumen of coronary vessels. Subsequently, the attenuation of vascular plaques can be compared to that of the contrast-enhanced lumen. Based on that comparison, coronary plaques can be categorized as non-calcified, calcified, and mixed types, as their calcium content will affect attenuation [95] [8]. This classification is in turn important for clinical prognostication, as a greater number of mixed plaques is associated with major cardiac events and obstructive coronary stenosis. Calcified plaques, on the other hand, rarely result in obstructive stenosis, which suggests that plaque composition plays a very important role in the development of adverse cardiac events than luminal stenosis by itself [95] [8].

Apart from CAC scoring and plaque evaluation, the primary application of cardiac CT is in the evaluation of patients with signs and symptoms suggestive of myocardial ischemia, by following a procedure called CT coronary angiography or simply computed tomography angiography (CTA). CTA requires the administration of intravenous iodinated contrast agents, and its principles are similar to that of invasive coronary angiography. There are however a number of limitations when considering CTA for patients. First of all, heart rate should be controlled with beta adrenoreceptor blockade before the test, except if newer dual source CT scanners are available [98] [11]. In any case, high or abnormal heart rates decrease image quality. Additionally, the patient must be able to collaborate with breath-holding instructions during imaging. Morbid obesity and high coronary artery calcium contents constitute relative contraindications, as they reduce image quality to increased attenuation [99, 100] [12], [13].

Similar to echocardiography, CT can also perform stress perfusion studies by means of pharmacologic stress (e.g., dobutamine, adenosine). In this newer approach for CT, myocardial perfusion

disturbances are determined as differences between two standardized contrast-enhanced CTAs during rest and pharmacologically induced stress, where the first-pass of the contrast agent is used for imaging. Although the method has relatively good sensitivity and specificity, it is limited by the required radiation dose, which is in the range of nuclear perfusion studies [101] [14]. Another relatively new method is the determination of myocardial fractional flow reserve (FFR); this is currently in development, but the technique holds promise in that it does not require a stress phase and can simply be extrapolated from a resting CTA [102] [15].

Cardiac CT also has a role in the prognosis of CAD. This has been performed using two distinct approaches. One approach has used the number of coronary arteries involved, namely from one to three and the left main, while another uses a segment involvement score for atherosclerosis based on the number of coronary segments with plaques present and plaque severity. Regardless of which method is finally used, more severe scores are associated with worse cardiovascular outcomes. To illustrate this further, a study of the CONFIRM registry yielded an annual risk-adjusted hazard ratio of 1.62 for non-obstructive CAD compared to normal coronary arteries. Similarly, hazard ratios were higher for one vessel-disease (2.00), two-vessel disease (2.92), and three vessel/left main disease (3.70) [103] [16].

Finally, a discussion of cardiac CT would not be complete without mentioning the effects of ionizing radiation. X-rays are known to be carcinogenic and, in general, medical practitioners are advised to avoid unnecessary CT scans. However, the benefits have to be weighed with regard to nuclear imaging modalities and invasive coronary angiography. Arguably, advances in CT technology have reduced and continue to reduce radiation doses compared to other modalities. Still, examinations such as CT stress perfusion have a relatively high radiation dose, even comparable to nuclear imaging. Furthermore, if a CT examination is not diagnostic, then radiation burden will be even greater if invasive coronary angiography or nuclear imaging also has to be performed. Therefore, specific indications have to be formulated for when such use is warranted. Additionally, in the era of multimodality imaging, the exact niches of echocardiography, CT, magnetic resonance imaging and nuclear imaging have not yet been clearly defined; this constitutes an important future goal.

11.2.3 Cardiovascular Magnetic Resonance

Cardiovascular magnetic resonance (CMR) can provide an integrated approach in the evaluation of coronary artery disease (CAD) by including coronary arteries, cardiac function and stress myocardial perfusion-fibrosis assessment [104] (1).

11.2.3.1 Evaluation of the Coronary Arteries

The clinical indications of cardiovascular magnetic resonance coronary angiography (CMRA) are at the moment limited only to the detection of abnormal origin of coronary arteries, coronary ectasia, and/or aneurysms (class I indication) and coronary bypass grafts (CABG) evaluation (class II indication). The routine application of CMRA for diagnosis of CAD is not at the moment part of clinical practice [105, 106] (2, 3).

CMRA can precisely assess the abnormal origin of coronary arteries and the location and dimensions of coronary artery aneurysms. This is facilitated by the larger caliber and the proximal location of the coronary artery aneurysms (CAA). The most important benefit of CMRA is the absence of ionizing radiation, which is of special clinical value for children and women [105, 107] (2, 4). Diseases characterized by ectatic or aneurysmatic coronary arteries are Kawasaki disease, autoimmune vasculitis, and coronary artery ectasia [108–111] (5–8).

Bypass grafts can be also assessed very well by CMRA, because they are relatively immobile and have larger diameter compared to native coronary arteries. Different imaging protocols have been already used, including spin echo [112–115] (9–12) and gradient echo techniques. The application of contrast agents for better imaging of the blood signal [116, 117] (13, 14) increased the sensitivity to 95%. However, metallic clips in grafts constitute the common limitation of coronary bypass MRA. CMRA can be used at some special centers to detect lesions in bypass grafts [107] (4).

CMRA can reliably assess the initial part of the coronary arteries in almost 100% of patients, with excellent results acquired for the left anterior descending (LAD) and the right coronary artery (RCA); the left circumflex (LCX), due to its peculiar way, is at a increased distance from the cardiac coil, and therefore its visualization is usually of inferior quality, compared to the rest of the coronary arteries. According to previous studies, the imaged length for LAD is 50 mm, for RCA is 80 mm, and for LCX is 40 mm [118–125] (15–22). An excellent agreement between the proximal parts of coronary arteries measured by CMRA and X-ray invasive angiography was assessed by previous studies [126] (23). Unfortunately, the resolution of CMRA remains lower compared with invasive coronary angiography and does not allow the evaluation of stenosis in the mid and peripheral part of coronary arteries; however, CMRA was shown to have a high sensitivity (92%) for the detection of CAD and its diagnostic performance was further improved. In a subanalysis of left main or three vessel disease, a sensitivity of 100% and a negative predictive value of 100% was documented. These findings were also supported by smaller single-center studies [118, 125–133] (15, 24–32). A meta-analysis compared coronary MRA and multislice computed tomography (CT) for assessment of significant CAD (112) (9). CT was more accurate than MRA, and therefore CT was suggested as the preferred non-invasive alternative to X-ray coronary angiography. However, the superiority of CMRA is that it can offer more data about the patient, including cardiac anatomy, function, inflammation, stress perfusion, and fibrosis evaluation. Recently, a multicenter study showed that whole heart CMRA at 1.5 T can detect significant CAD with high sensitivity (88%) and moderate specificity (72%). Additionally, a negative predictive value (NPV) of 88% indicates that this technique can effectively be used to exclude the presence of significant CAD [134] (33). We should mention that this NPV reported by this trial is identical to the NPV of the CORE-64 CTA multicenter study (135) (34). Proving the value of CMRA to rule out CAD in patients with low pre-test probability (<20%) [136] (35). Finally, in a direct comparison between CMRA and CTA no significant difference was proved for the detection of CAD between 3 T MR and 64-slice CTA [137] (36).

Additionally, there are studies documenting the potential role of coronary vessel wall imaging to detect increased vessel wall thickness in type I diabetes with abnormal renal function. It was also documented by Jansen et al. (138)(37) that non-contrast enhanced T_1-weighted MR visualized thrombus in acute myocardial infarction. Currently, new techniques using late gadolinium enhancement (LGE) allowed the direct assessment of inflamed plaques in the coronary arteries. Clinically used contrast agents showed non-specific uptake in plaques of patients with chronic angina [139] (38), acute coronary syndromes (ACS) (140)(39), and systemic lupus erythematosus [141] (40). The contrast enhancement by CMR, assessed in patients with stable angina, was associated with calcified or mixed plaques on MSCT, while in ACS it was transient, probably due to inflammatory process. New contrast agents have been already used in animals, and their accumulation in blood was associated with increased endothelial permeability and/or increased neovascularization [142] (41). Additionally, increased accumulation of iron-oxide particles (USPIO) was indicative of increased endothelial permeability and vessel wall inflammation, due to intraplaque macrophages [143, 144] (42, 43). Such molecules have been used as targets for new molecular contrast agents that allowed the assessment of inflammatory indexes, such as intercellular adhesion molecule-1 (ICAM-1), vascular adhesion molecule-1(VCAM-1) or matrix metalloproteinase (MMP) [145, 146] (44, 45). Furthermore, thrombi labeling using a fibrin-specific contrast agent [147, 148] (47, 48) and evaluation of extracellular matrix remodelling, using targeting elastin, is a new promising molecular imaging technique.

11.2.3.2 Measurement of Volumes: Ejection Fraction

CMR measures ventricular volumes and ejection fraction (EF) non-invasively and without contrast agent. Echocardiography is still the everyday, bedside tool for function evaluation, but there is a place for CMR due to its excellent reproducibility and capability to perfectly evaluate RV morphology and function, which is of special interest in rheumatic diseases [149] (88). In a direct comparison of CMR versus echocardiography, it has been shown that for an 80% power and a p value of 0.05,

the sample size required would be 505 patients for validation using 2D echo, but only 14 patients for CMR [150] (89).

11.2.3.3 Evaluation of Myocardial Perfusion-Fibrosis

11.2.3.3.1 CMR Detection of Ischemia

A. CMR detects ischemia by two different ways: Observation of wall motion abnormalities, using the stress factor dobutamine. Compared to stress echo, dobutamine stress CMR has better sensitivity (86% vs. 74%) and specificity (86% vs. 70%) [151, 152] (96, 97).
B. Observation of myocardial perfusion using the first pass of a T_1-shortening contrast agent (first-pass gadolinium) [153, 154] (98, 99). Data acquired during intravenous vasodilator-stress (most commonly with adenosine) delineate the underperfused regions, due to myocardial ischemia. The spatial resolution of CMR is 2 to 3 mm, greatly superior to nuclear techniques, so that subendocardial ischemia can be more reliably identified [153, 154] (98, 99). The interpretation is most commonly visual, but quantitative approaches are also available [155] (100) and have been validated against X-ray angiography, SPECT, and PET [153, 154] (98, 99).

11.2.3.3.2 CMR Detection of Fibrosis

CMR is the most reliable imaging technique for detecting and quantifying scar or fibrotic tissue, due to irreversible myocardial damage (viability study). Following acute ischemic injury, the myocardial distribution of gadolinium is increased, due to sarcrolemmal rupture and abnormal wash-out kinetics. Imaging within the first few minutes after contrast agent administration is the method of choice to delineate microvascular obstruction (MVO), which prevents contrast delivery to the infarct core and thus results in low signal on T1-weighted imaging [156] (105). Both acute and old infarctions without MVO retain contrast agent and appear bright (bright is dead) [156] (105). The preferred imaging time for scar detection is 10 to 20 minutes after gadolinium administration, when differences between scar, normal myocardium, and blood pool are maximal. This method is referred to as late gadolinium-enhancement (LGE) and is the gold standard for in vivo assessment of myocardial scar.

Non-invasive methods for assessing myocardial viability include PET, SPECT, and dobutamine echocardiography [157] (106). However, they can only interpret myocardial viability as an all-or-none phenomenon within a given myocardial region, and none of them assess the transmurality of viability. CMR not only detects infarction in as little as 1 cm^3 of tissue, substantially less than other in vivo methods, but has excellent agreement with histology in animal and human studies [157, 158] (106, 107) and was also proved useful in detecting small myocardial scars and diffuse subendocardial fibrosis, missed by other imaging techniques [159].

11.2.3.4 Future Perspectives of CMR in the Early Diagnosis of CAD

Our expectations for the future include:

1. **Non-contrast perfusion.** The potential to diagnose CAD, as early as possible, without the use of contrast agents is a very important query in the CAD evaluation. In this effort, there are already studies in patients with well-controlled type 2 diabetes (T2DM). These patients, even in the absence of arterial hypertension and significant CAD, exhibit blunted maximal non-contrast T1 response during adenosine vasodilatory stress, reflecting coronary microvascular dysfunction. Adenosine stress and rest T1 mapping can detect subclinical abnormalities of the coronary micro-vasculature, without the need for gadolinium contrast agents. According to these studies, CMR may identify subclinical cardiac risk markers in well-controlled T2DM, offering a great opportunity for early therapeutic intervention [160].
2. **Oxygen consumption.** Another important parameter is the oxygen consumption. This is reduced during myocardial hibernation, a condition in which contractile function is down-regulated in parallel with chronic hypoperfusion. The importance of myocardial oxygen

consumption has also been demonstrated using positron emission tomography (PET) based ^{11}C-acetate imaging [161]. Perfusion changes can be assessed based on regional signal intensity differences during first-pass infusion of gadolinium-based contrast agents. Independent of perfusion, CMR can assess myocardial oxygenation consumption via a technique termed blood oxygen level–dependent (BOLD) imaging. This technique can be performed without the use of contrast agent and is based on the differences in magnetic susceptibility between oxyhemoglobin and deoxyhemoglobin. While oxyhemoglobin is mildly diagmagnetic, deoxyhemoglobin is paramagnetic, and this latter property produces local field gradients between red blood cells and their surroundings. The shift in frequency, caused by these gradients, affects transverse (T2) relaxation times, with red blood cell deoxygenation (deoxyhemoglobin) causing a decrease to T2. Like the classic perfusion evaluation, BOLD imaging can be performed during rest and pharmacological stress to assess dynamic changes in myocardial physiology. BOLD imaging has been validated in animal models and has been shown to be feasible in human studies [162–164] (10–12). However, clinical studies about its utility in CAD are still pending.

3. **Non-invasive, non-radiating plaque characterization.** CMR can characterize atherosclerotic plaque burden and activity including noncontrast and contrast-enhanced vessel wall imaging. These approaches have shown great potential to assess various characteristics of vulnerable plaques, such as inflammation [165](12), necrotic core size [166](6), neovascularization [167](13), intraplaque hemorrhage [166](6), and positive vessel wall remodeling [168](14).

Kawasaki et al. [169](15) reported the high diagnostic accuracy of hyperintense coronary plaques (HIP) with noncontrast enhanced T1-weighted (T1W) coronary CMR (16) for the detection of complicated plaques in the coronary arteries. Given the high diagnostic value of HIP in the carotid arteries (sensitivity and specificity of 84%, negative predictive value of 70%, and positive predictive value of 93%) and the strong association of HIP with other markers specific for vulnerable plaque, noncontrast T1W coronary plaque imaging may have a great potential to assess complex coronary lesions in patients with unstable CAD. However, there are no reproducibility and follow-up imaging data as well as correlation with clinical endpoints.

In another study, it was shown that not only the presence of HIS, but also the elevated ratio between the signal intensities of coronary plaque and cardiac muscle (PMR) itself may be used as a quantitative marker of plaque vulnerability in clinical evaluation [170]. Furthermore, Magnetic Resonance (MR) defined inflammation using Ultra Small Super-Paramagnetic Iron Oxide (USPIO) particles showed that the carotid territory is more likely to take up USPIO if another vascular territory is symptomatic [171].

References

1. Brown MA, Semelka RC. *MRI: Basic Pulse Principles and Applications*, 4th ed. New York: Wiley-Blackwell, 2010.
2. Look DC, Locker DR. Time saving in measurement of NMR and EPR relaxation times. *Rev Sci Instrum*. 1970; 41:250–251.
3. Brix G, Schad LR, Deimling M, Lorenz WJ. Fast and precise T1 imaging using a TOMROP sequence. *Magn Reson Imaging* 1990; 8:351–356.
4. Freeman AJ, Gowland PA, Mansfield P. Optimization of the ultrafast Look-Locker echo-planar imaging T1 mapping sequence. *Magn Reson Imaging* 1998; 16:765–772.
5. Karlsson M, Nordell B. Phantom and in vivo study of the Look-Locher T1 mapping method. *Magn Reson Imaging* 1999; 17:1481–1488.
6. Messroghli DR, Radjenovic A, Kozerke S, Higgins DM, Sivananthan MU, Ridgway JP. Modified Look-Locker inversion recovery (MOLLI) for high resolution T1 mapping of the heart. *Magn Reson Med*. 2004; 52:141–146.

7. Messroghli DR, Greiser A, Fröhlich M, Dietz R, Schulz-Menger J. Optimization and validation of a fully-integrated pulse sequence for modified look-locker inversion-recovery (MOLLI) T1 mapping of the heart. *J Magn Reson Im* 2007; 26:1081–1086.
8. Piechnik SK, Ferreira VM, Dall' Armellina E, Cochlin LE, Greiser A, Neubauer S, Robson MD. Shortened Modified Look-Locker Inversion recovery (ShMOLLI) for clinical myocardial T1-mapping at 1.5 and 3 T within a 9 heartbeat breathhold. *J Cardiovasc Magn Reson*. 2010; 12:69.
9. Marks B, Mitchell DG, Simelaro JP. Breath-holding in healthy and pulmonary-compromised populations: effects of hyperventilation and oxygen inspiration. *J Magn Reson Imaging* 1997; 7(3):595–597.
10. Chow K, Flewitt JA, Green JD, Pagano JJ, Friedrich MG, Thompson RB. Saturation recovery single-shot acquisition (SASHA) for myocardial T1 mapping. *Magn Reson Med*. 2014; 71:2082–2095.
11. Weingärtner S, Akçakaya M, Basha T, Kissinger KV, Goddu B, Berg S, Manning WJ, Nezafat R. Combined saturation/inversion recovery sequences for improved evaluation of scar and diffuse fibrosis in patients with arrhythmia or heart rate variability. *Magn Reson Med*. 2014; 71:1024–1034.
12. Roujol S, Weingartner S, Foppa M, Chow K, Kawaji K, Ngo LH, Kellman P, Manning WJ, Thompson RB, Nezafat R. Accuracy, precision, and reproducibility of four T1 mapping sequences: a head-to-head comparison of MOLLI, ShMOLLI, SASHA, and SAPPHIRE. *Radiology* 2014; 272:683–689.
13. Deichmann R, Haase A. Quantification of T1 values by snapshot-FLASH NMR imaging. *J Magn Reson Im* 1992; 96(3):608–612.
14. Haaf P, Garg P, Messroghli DR, Broadbent RA, Greenwood JP, Plein S. Cardiac T1 mapping and extracellular volume (ECV) in clinical practice: a comprehensive review. *J Cardiovasc Magn Reson* 2016; 30:18.
15. Sado DM, Flett AS, Banypersad SM, White SK, Maestrini V, Quarta G, Lachmann RH, Murphy E, Mehta A, Hughes DA, McKenna WJ, Taylor AM, Hausenloy DJ, Hawkins PN, Elliott PM, Moon JC. Cardiovascular magnetic resonance measurement of myocardial extracellular volume in health and disease. *Heart* 2012; 98:1436–1441.
16. Broadbent DA, Biglands JD, Larghat A, Sourbron SP, Radjenovic A, Greenwood JP, Plein S, Buckley DL. Myocardial blood flow at rest and stress measured with dynamic contrast-enhanced MRI: comparison of a distributed parameter model with a Fermi function model. *Magn Reson Med* 2013; 70:1591–1597.
17. Papanastasiou G, Williams MC, Kershaw LE, Dweck MR, Alam S, Mirsadraee S, Connell M, Gray C, MacGillivray T, Newby DE, Semple SIK. Measurement of myocardial blood flow by magnetic resonance perfusion imaging: comparison of distributed parameter and Fermi models with single and dual bolus. *J Cardiov Magn Reson* 2015; 17:17.
18. Taylor AJ, Salerno M, Dharmakumar R, Jerosch-Herold M. T1 mapping: basic techniques and clinical applications. *JACC Cardiovasc Imaging* 2016; 9:67–81.
19. Zheng J. Assessment of myocardial oxygenation with MRI. *Quant Imaging Med Surg* 2013; 3(2):67–72.
20. Arnold JR, Karamitsos TD, Bhamra-Ariza P, Francis JM, Searle N, Robson MD, Howells RK, Choudhury RP, Rimoldi OE, Camici PG, Banning AP, Neubauer S, Jerosch-Herold M, Selvanayagam JB. Myocardial oxygenation in coronary artery disease: insights from blood oxygen level-dependent magnetic resonance imaging at 3 tesla. *J Am Coll Cardiol* 2012; 59:1954–1964.
21. Li D, Dhawale P, Rubin PJ, Haacke EM, Gropler RJ. Myocardial signal response to dipyridamole and dobutamine: demonstration of the BOLD effect using a double-echo gradient-echo sequence. *Magn Reson Med* 1996; 36:16–20.
22. McGuinness ME, Talbert RL. Pharmacologic stress testing: experience with dipyridamole, adenosine, and dobutamine. *Am J Hosp Pharm*. 1994; 51(3):328–346.
23. Massie BM, Schwartz GG, Garcia J, Wisneski JA, Weiner MW, Owens T. Myocardial metabolism during increased work states in the porcine left ventricle in vivo. *Circ Res* 1994; 74:64–73.
24. Friedrich MG, Niendorf T, Schulz-Menger J, Gross CM, Dietz R. Blood oxygen level-dependent magnetic resonance imaging in patients with stress-induced angina. *Circulation* 2003; 108:2219–2223.
25. Wacker CM, Hartlep AW, Pfleger S, Schad LR, Ertl G, Bauer WR. Susceptibility-sensitive magnetic resonance imaging detects human myocardium supplied by a stenotic coronary artery without a contrast agent. *J Am Coll Cardiol* 2003; 41:834–840.
26. Manka R, Paetsch I, Schnackenburg B, Gebker R, Fleck E, Jahnke C. BOLD cardiovascular magnetic resonance at 3.0 tesla in myocardial ischemia. *J Cardiovasc Magn Reson*. 2010; 12:54.
27. Dharmakumar R, Arumana JM, Larson AC, Chung Y, Wright GA, Li D. Cardiac phase-resolved blood oxygen-sensitive steady-state free precession MRI for evaluating the functional significance of coronary artery stenosis. *Invest Radiol*. 2007; 42:180–188.
28. Dharmakumar R, Arumana JM, Tang R, Harris K, Zhang Z, Li D. Assessment of regional myocardial oxygenation changes in the presence of coronary artery stenosis with balanced SSFP imaging at 3.0 T: theory and experimental evaluation in canines. *J Magn Reson Imaging*. 2008; 27:1037–1045.

29. Karamitsos TD, Leccisotti L, Arnold JR, Recio-Mayoral A, Bhamra-Ariza P, Howells RK, Searle N, Robson MD, Rimoldi OE, Camici PG, Neubauer S, Selvanayagam JB. Relationship between regional myocardial oxygenation and perfusion in patients with coronary artery disease: insights from cardiovascular magnetic resonance and positron emission tomography. *Circ Cardiovasc Imaging*. 2010; 3:32–40.
30. Jahnke C, Gebker R, Manka R, Schnackenburg B, Fleck E, Paetsch I. Navigator-gated 3D blood oxygen level-dependent CMR at 3.0-T for detection of stress-induced myocardial ischemic reactions. *JACC: Cardiovasc Img.* 2010; 3:375–384.
31. Arnold JR, Karamitsos TD, Bhamra-Ariza P, Francis JM, Searle N, Robson MD, Howells RK, Choudhury RP, Rimoldi OE, Camici PG, Banning AP, Neubauer S, Jerosch-Herold M, Selvanayagam JB. Myocardial oxygenation in coronary artery disease: insights from blood oxygen level-dependent magnetic resonance imaging at 3 tesla. *J Am Coll Cardiol*. 2012; 59:1954–1964.
32. Tsaftaris SA, Zhou X, Tang R, Li D, Dharmakumar R. Detecting myocardial ischemia at rest with cardiac phase-resolved blood oxygen level-dependent cardiovascular magnetic resonance. *Circ Cardiovasc Imaging*. 2013; 6:311–319.
33. Chiribiri A, Botnar RM, Nagel E. Magnetic resonance coronary angiography: where are we today? *Curr Cardiol Rep* 2013; 15:328.
34. Schuetz GM, Zacharopoulou NM, Schlattmann P, Dewey M. Meta-analysis: noninvasive coronary angiography using computed tomography versus magnetic resonance imaging. *Ann Intern Med* 2010; 152:167–177.
35. Di Leo G, Fisci E, Secchi F, et al. Diagnostic accuracy of magnetic resonance angiography for detection of coronary artery disease: a systematic review and meta-analysis. *Eur Radiol* 2016; 26:3706–3718.
36. McCarthy RM, Shea SM, Deshpande VS, et al. Coronary MR angiography: true FISP imaging improved by prolonging breath holds with preoxygenation in healthy volunteers. *Radiology* 2003; 227(1):283–288.
37. Sakuma H, Ichikawa Y, Suzawa N, et al. Assessment of coronary arteries with total study time of less than 30 minutes by using whole-heart coronary MR angiography. *Radiology* 2005; 237(1):316–321.
38. Yang Q, Li K, Liu X, Du X, Bi X, Huang F, Jerecic R, Liu Z, An J, Xu D, Zheng H, Fan Z, Li D. 3.0T whole-heart coronary magnetic resonance angiography performed with 32-channel cardiac coils: a single-center experience. *Circ Cardiovasc Imaging*. 2012; 5:573–579.
39. Jerosch-Herold M. Quantification of myocardial perfusion by cardiovascular magnetic resonance. *J Cardiov Magn Reson* 2010; 12:57–67.
40. Morton G, Chiribiri A, Ishida M, et al. Quantification of absolute myocardial perfusion in patients with coronary artery disease: comparison between cardiovascular magnetic resonance and positron emission tomography. *J Am Coll Cardiol* 2012; 60(16):1546–1555.
41. Kellman P, Arai AE. Imaging sequences for first-pass perfusion: a review. *J Cardiov Magn Reson* 2007; 9(3):527–537.
42. Cerqueira MD. Standardized myocardial segmentation and nomenclature for tomographic imaging of the heart: a statement for healthcare professionals from the cardiac imaging committee of the Council on Clinical Cardiology of the American Heart Association. *Circulation* 2002; 105:539–542.
43. Hsu L-Y, Rhoads KL, Holly JE, Kellman P, Aletras AH, Arai AE. Quantitative myocardial perfusion analysis with a dual-bolus contrast-enhanced first-pass MRI technique in humans. *J Magn Reson Im* 2006; 23:315–322.
44. Broadbent DA, Biglands JD, Ripley DP, Higgins DM, Greenwood JP, Plein S, Buckley DL. Sensitivity of quantitative myocardial dynamic contrast enhanced MRI to saturation pulse efficiency, noise and T1 measurement error: comparison of nonlinearity correction methods. *Magn Reson Med* 2015; 75(3):1290–1300.
45. Ronneberger O, Fischer P, Brox T. U-Net: convolutional networks for biomedical image segmentation. In: *MICCAI*. 2015; 234–241.
46. Tran PV. A fully convolutional neural network for cardiac segmentation in short-axis MRI (preprint arXiv: 1604.00494), 2016.
47. Oktay O, Ferrante E, Kamnitsas K, Heinrich M, Bai W, Caballero J, Guerrero R, Cook S, de Marvao A, Dawes T, O'Regan D, Kainz B, Glocker B, Rueckert D. Anatomically Constrained Neural Networks (ACNN): application to cardiac image enhancement and segmentation. *IEEE Trans Med Imag* 2017 (in press).
48. Larsson HBW, Fritz-Hansen T, Rostrup E, Søndergaard L, Ring P, Henriksen O. Myocardial perfusion modeling using MRI. *Magn Reson Med* 1996; 35(5):716–726.
49. Kim D, Axel L. Multislice, dual-imaging sequence for increasing the dynamic range of the contrast-enhanced blood signal and CNR of myocardial enhancement at 3T. *J Magn Reson Imaging* 2006; 23:81–86.

50. Hsu LY, Kellman P, Arai AE. Nonlinear myocardial signal intensity correction improves quantification of contrast-enhanced first-pass MR perfusion in humans. *J Magn Reson Imaging* 2008; 27:793–801.
51. Zarinabad N, Chiribiri A, Hautvast GLTF, Ishida M, Schuster A, Cvetkovic Z, Batchelor PG, Nagel E. Voxel-wise quantification of myocardial perfusion by cardiac magnetic resonance. Feasibility and methods comparison. *Magn Reson Med* 2012; 68:1994–2004.
52. Huber A, Sourbron S, Klauss V, Schaefer J, Bauner KU, Schweyer M, Reiser M, Rummeny E, Rieber J. Magnetic resonance perfusion of the myocardium: semiquantitative and quantitative evaluation in comparison with coronary angiography and fractional flow reserve. *Invest Radiol.* 2012; 47:332–338.
53. Biglands JD, Magee DR, Sourbron SP, Plein S, Greenwood JP, Radjenovic A. Comparison of the diagnostic performance of four quantitative myocardial perfusion estimation methods used in cardiac MR imaging. *Radiology* 2015; 275:393–402.
54. Papanastasiou G, Williams MC, Dweck MR, Alam S, Cooper A, Mirsadraee S, Newby DE, Semple SI. Quantitative assessment of myocardial blood flow in coronary artery disease by cardiovascular magnetic resonance: comparison of Fermi and distributed parameter modeling against invasive methods. *J Cardiovasc Magn Reson* 2016; 18(1):57.
55. Choi AD, Joly JM, Chen MY, Weigold GW. State of the Art. Physiologic evaluation of ischemia using cardiac CT: current status of CT myocardial perfusion and CT fractional flow reserve. *J Cardiovasc Comput Tomogr* 2014; 8: 272–281.
56. Pons-Llado G, Leta-Petracca R (eds). *Atlas of Noninvasive Coronary Angiography by Multidetector Computed Tomography*, 1st ed. New York: Springer, 2006.
57. Meijboom WB, Meijs MF, Schuijf JD, et al. Diagnostic accuracy of 64-slice computed tomography coronary angiography: a prospective, multicenter, multivendor study. *J Am Coll Cardiol* 2008; 52:2135–2144.
58. Miller JM, Rochitte CE, Dewey M, et al. Diagnostic performance of coronary angiography by 64-row CT. *N Engl J Med* 2008; 359:2324–2336.
59. Gopal A, Nasir K, Ahmadi N, et al. Cardiac computed tomographic angiography in an outpatient setting: an analysis of clinical outcomes over a 40-month period. *J Cardiovasc Comput Tomogr* 2009; 3:90–95.
60. Mowatt G, Cook JA, Hillis GS, Walker S, Fraser C, Jia X, Waugh N. 64-slice computed tomography angiography in the diagnosis and assessment of coronary artery disease: systematic review and meta-analysis. *Heart* 2008; 94:1386–1393.
61. Park MJ, Jung JI, Choi YS, Ann SH, Youn HJ, Jeon GN, Choi HC. Coronary CT angiography in patients with high calcium score: evaluation of plaque characteristics and diagnostic accuracy. *Int J Cardiovasc Imaging* 2011; 27(1):43–51.
62. Rispler S, Keidar Z, Ghersin E, et al. Integrated single photon emission computed tomography and computed tomography coronary angiography for the assessment of hemodynamically significant coronary artery lesions. *J Am Coll Cardiol* 2007; 49:1059–1067.
63. George RT, Arbab-Zadeh A, Miller JM, et al. Adenosine stress 64- and 256-row detector computed tomography angiography and perfusion imaging: a pilot study evaluating the transmural extent of perfusion abnormalities to predict atherosclerosis causing myocardial ischemia. *Circ Cardiovasc Imaging* 2009; 2:174–182.
64. Sun Z. Coronary CT angiography with prospective ECG-triggering: an effective alternative to invasive coronary angiography. *Cardiovasc Diagn Ther* 2012; 2(1):28–37.
65. Hu H, He DH, Foley WD, Fox SH. Four multi-detector-row helical CT: image quality and volume coverage speed. *Radiology* 2000; 215:55–62.
66. George RT, Silva C, Cordeiro MA, DiPaula A, Thompson DR, McCarthy WF, Ichihara T, Lima JA, Lardo AC. Multidetector computed tomography myocardial perfusion imaging during adenosine stress. *J Am Coll Cardiol* 2006; 48:153–160.
67. Zhang LJ, Peng J, Wu S-Y, Yeh BM, Yeh BM, Zhou CS, Lu GM. Dual source dual energy CT of acute myocardial infarction: correlation with histopathological findings in a canine model. *Invest Radiol* 2010; 45:290–297.
68. George RT, Arbab-Zadeh A, Cerci RJ, et al. Diagnostic performance of combined noninvasive coronary angiography and myocardial perfusion imaging using 320-MDCT: the CT angiography and perfusion methods of the CORE320 multicenter multinational diagnostic study. *AJR Am J Roentgenol* 2011; 197(4):829–837.
69. Williams MC, Cruden NL, Uren NG, Newby DE. Image in cardiovascular CT: a low-dose comprehensive cardiac CT protocol assessing anatomy, function, perfusion, and viability. *J Cardiovasc Comput Tomogr* 2013; 7:69–72.

70. Williams MC, Mirsadraee S, Dweck MR et al. Computed tomography myocardial perfusion vs ^{15}O-water positron emission tomography and fractional flow reserve. *Eur Radiol*. 2017; 27:1114–1124.
71. Bastarrika G, Ramos-Duran L, Rosenblum MA, Kyoung Kang D, Rowe GD, Schoepf UJ. Adenosine-stress dynamic myocardial CT perfusion imaging. Initial clinical experience. *Invest Radiol* 2010; 45:306–313.
72. George RT, Jerosch-Herold M, Silva C, Kitagawa K, Bluemke DA, Lima JA, Lardo AC. Quantification of myocardial perfusion using dynamic 64-detector computed tomography. *Invest Radiol* 2007; 42:815–822.
73. Ruzsics B, Lee H, Zwerner PL, Gabregziabher M, Costello P, Schoepf UJ. Dual-energy CT of the heart for diagnosing coronary artery stenosis and myocardial ischemia-initial experience. *Eur Radiol* 2008; 18:2414–2424.
74. Graser A, Johnson TRC, Chandarana H, Macari M. Dual energy CT: preliminary observations and potential clinical applications in the abdomen. *Eur Radiol* 2009; 19:13–23.
75. Ho KT, Chua KC, Klotz E, et al. Stress and rest dynamic myocardial perfusion imaging by evaluation of complete time attenuation curves with dual source CT. *JACC Cardiovasc Imaging* 2010; 3:811–20.
76. Nakauchi Y, Iwanaga Y, Ikuta S, et al. Quantitative myocardial perfusion analysis using multi-row detector CT in acute myocardial infarction. *Heart* 2012; 98:566–572.
77. Kido T, Kurata A, Higashino H, Inoue Y, Kanza RE, Okayama H, Higaki J, Murase K, Mochizuki T. Quantification of regional myocardial blood flow using first-pass multidetector-row computed tomography and adenosine triphosphate in coronary artery disease. *Circ J* 2008; 72:1086–1091.
78. Kikuchi Y, Oyama-Manabe N, Naya M, et al. Quantification of myocardial blood flow using dynamic 320-row multi-detector CT as compared with ^{15}O-H_2O PET. *Eur Radiol* 2014; 24:1547–1556.
79. Wang Y, Qin L, Shi X, et al. Adenosine-stress dynamic myocardial perfusion imaging with second-generation dual-source CT: comparison with conventional catheter coronary angiography and SPECT nuclear myocardial perfusion imaging. *AJR* 2012; 198:521–529.
80. Blessberger H, Binder T. Non-invasive imaging: two dimensional speckle tracking echocardiography: basic principles. *Heart* 2010; 96:716–722.
81. Biswas M, Sudhakar S, Nanda NC, Buckberg G, Pradhan M, Roomi AU, Gorissen W, Houle H. Two- and three-dimensional speckle tracking echocardiography: clinical applications and future directions. *Echocardiography* 2013; 30:88–105.
82. Pavlopoulos H, Nihoyannopoulos P. Strain and strain rate deformation parameters: from tissue Doppler to 2D speckle tracking. *Int J Cardiovasc Imaging* 2008; 24:479–491.
83. Kasai C, Namekawa K, Koyano A, Omoto R. Realtime two-dimensional blood flow imaging using an autocorrelation technique. *IEEE Trans Sonics Ultrason* 1985; 32:458–464.
84. Hangiandreou NJ. B-mode US. Basic concepts and new technology. *RadioGraphics* 2003; 23:1019–1033.
85. Yu CM, Sanderson JE, Marwick TH, Oh JK. Tissue Doppler imaging: a new prognosticator for cardiovascular disease. *J Am Coll Cardiol* 2007; 49:1903–1914.
86. Bohs LN, Trahey GE. A novel method for angle independent ultrasonic imaging of blood flow and tissue motion. *IEEE Trans Biomed Eng* 1991; 38:280–286.
87. Notomi Y, Lysyansky P, Setser RM, et al. Measurement of ventricular torsion by two-dimensional ultrasound speckle tracking imaging. *J Am Coll Cardiol* 2005; 45:2034–2041.
88. Stein JH, et al., Use of carotid ultrasound to identify subclinical vascular disease and evaluate cardiovascular disease risk: a consensus statement from the American Society of Echocardiography Carotid Intima-Media Thickness Task Force Endorsed by the Society for Vascular. *Journal of the American Society of Echocardiography* 2008; 21(2):93–111.
89. Lorenz MW, Markus HS, Bots ML, Rosvall M, Sitzer M. Prediction of clinical cardiovascular events with carotid intima-media thickness: a systematic review and meta-analysis. *Circulation* 2007; 115(4):459–467.
90. Sicari R, Cortigiani L. The clinical use of stress echocardiography in ischemic heart disease. *Cardiovasc. Ultrasound* 2017; 15(1):7.
91. Votavová R, Linhartová A, Kořínek J, Marek J, Linhart A. Echocardiography in coronary artery disease. *Cor et Vasa* 2015; 57(6):e408–e417.
92. Cortigiani L, Dodi C, Paolini EA, Bernardi D, Bruno G, and Nannini E. Prognostic value of pharmacological stress echocardiography in women with chest pain and unknown coronary artery disease. *J. Am. Coll. Cardiol.* 1998; 32(7):1975–1981.
93. DiLorenzo MP, Bhatt SM, Mercer-Rosa L. How best to assess right ventricular function by echocardiography. *Cardiol. Young* 2015; 25(8):1473–1481.
94. Duliu OG, Seletchi ED. Image processing and data analysis in computed tomography. *Rom Journ Phys* 2006; 52:667–675.

95. Sun Z. Cardiac CT imaging in coronary artery disease: current status and future directions. *Quant. Imaging Med. Surg.* 2012; 2(2):98–105.
96. Shah NR, Coulter SA. An evidence-based guide for coronary calcium scoring in asymptomatic patients without coronary heart disease. *Texas Hear. Inst. J.* 2012; 39(2):240–242.
97. Sarwar A, et al. Diagnostic and prognostic value of absence of coronary artery calcification. *JACC Cardiovasc. Imaging* 2009; 2(6):675–688.
98. Sabarudin A, Sun Z. Beta-blocker administration protocol for prospectively ECG-triggered coronary CT angiography. *World J. Cardiol.* 2013; 5(12):453–458.
99. Sun Z, Choo GH, Ng KH. Coronary CT angiography: current status and continuing challenges. *British Journal of Radiology* 2012; 85(1013):495–510.
100. Leschka S, et al. Dual source CT coronary angiography in severely obese patients. *Invest. Radiol.* 2009; 44(11):720–727.
101. Rossi A, Merkus D, Klotz E, Mollet N, de Feyter PJ, Krestin GP. Stress myocardial perfusion: imaging with multidetector CT. *Radiology* 2014; 270(1):25–46.
102. Coenen A, et al. Integrating CT myocardial perfusion and CT-FFR in the work-up of coronary artery disease. *JACC Cardiovasc. Imaging* 2017; 10(7):760–770.
103. Chow BJW et al. Incremental prognostic value of cardiac computed tomography in coronary artery disease using CONFIRM: COroNary Computed Tomography Angiography Evaluation for Clinical Outcomes: An InteRnational Multicenter Registry. *Circ. Cardiovasc. Imaging* 2011; 4(5):463–472.
104. Mavrogeni S, Markousis-Mavrogenis G, Kolovou G. Contribution of cardiovascular magnetic resonance in the evaluation of coronary arteries. *World J Cardiol* 2014; 6(10):1060–1066.
105. Hundley WG, Bluemke DA, Finn JP, Flamm SD, Fogel MA, Friedrich MG, Ho VB, Jerosch-Herold M, Kramer CM, Manning WJ, Patel M, Pohost GM, Stillman AE, White RD, Woodard PK. ACCF/ACR/AHA/NASCI/SCMR 2010 expert consensus document on cardiovascular magnetic resonance: a report of the American College of Cardiology Foundation Task Force on Expert Consensus Documents. *J Am Coll Cardiol* 2010; 55:2614–2662.
106. Chiribiri A, Ishida M, Nagel E, Botnar RM. Coronary imaging with cardiovascular magnetic resonance: current state of the art. *Prog Cardiovasc Dis* 2011; 54:240–252.
107. Chiribiri A, Ishida M, Nagel E, Botnar RM. Coronary imaging with cardiovascular magnetic resonance: current state of the art. *Prog Cardiovasc Dis* 2011; 54:240–252.
108. Mavrogeni S, Papadopoulos G, Hussain T, Chiribiri A, Botnar R, Greil GF. The emerging role of cardiovascular magnetic resonance in the evaluation of Kawasaki disease. *Int J Cardiovasc Imaging* 2013; 29:1787–1798.
109. Mavrogeni S, Papadopoulos G, Douskou M, Kaklis S, Seimenis I, Baras P, Nikolaidou P, Bakoula C, Karanasios E, Manginas A, Cokkinos DV. Magnetic resonance angiography is equivalent to X-ray coronary angiography for the evaluation of coronary arteries in Kawasaki disease. *J Am Coll Cardiol* 2004; 43:649–652.
110. Greil GF, Stuber M, Botnar RM, Kissinger KV, Geva T, Newburger JW, Manning WJ, Powell AJ. Coronary magnetic resonance angiography in adolescents and young adults with Kawasaki disease. *Circulation* 2002; 105:908–911.
111. Mavrogeni S, Manoussakis MN, Karagiorga TC, Douskou M, Panagiotakos D, Bournia V, Cokkinos DV, Moutsopoulos HM. Detection of coronary artery lesions and myocardial necrosis by magnetic resonance in systemic necrotizing vasculitides. *Arthritis Rheum* 2009; 61:1121–1129.
112. Galjee MA, van Rossum AC, Doesburg T, van Eenige MJ, Visser CA. Value of magnetic resonance imaging in assessing patency and function of coronary artery bypass grafts. An angiographically controlled study. *Circulation* 1996; 93:660–666.
113. Jenkins JP, Love HG, Foster CJ, Isherwood I, Rowlands DJ. Detection of coronary artery bypass graft patency as assessed by magnetic resonance imaging. *Br J Radiol* 1988; 61:2–4.
114. Rubinstein RI, Askenase AD, Thickman D, Feldman MS, Agarwal JB, Helfant RH. Magnetic resonance imaging to evaluate patency of aortocoronary bypass grafts. *Circulation* 1987; 76:786–791.
115. White RD, Caputo GR, Mark AS, Modin GW, Higgins CB. Coronary artery bypass graft patency: noninvasive evaluation with MR imaging. *Radiology* 1987; 164:681–686.
116. Vrachliotis TG, Bis KG, Aliabadi D, Shetty AN, Safian R, Simonetti O. Contrast-enhanced breathhold MR angiography for evaluating patency of coronary artery bypass grafts. *Am J Roentgenol* 1997; 168:1073–1080.
117. Wintersperger BJ, von Smekal A, Engelmann MG, Knez A, Penzkofer HV, Laub G, Reiser M. Contrast media enhanced magnetic resonance angiography for determining patency of a coronary bypass: a comparison with coronary angiography. *Rofo* 1997; 167:572–578.

118. Botnar RM, Stuber M, Danias PG, Kissinger KV, Manning WJ. Improved coronary artery definition with T2-weighted, free-breathing, three-dimensional coronary MRA. *Circulation* 1999; 99:3139–3148.
119. Hofman MB, Paschal CB, Li D, Haacke EM, van Rossum AC, Sprenger M. MRI of coronary arteries: 2D breath-hold vs 3D respiratory-gated acquisition. *J Comput Assist Tomogr* 1995; 19:56–62.
120. Lobbes MB, Miserus RJ, Heeneman S, Passos VL, Mutsaers PH, Debernardi N, Misselwitz B, Post M, Daemen MJ, van Engelshoven JM, Leiner T, Kooi ME. Atherosclerosis: contrast-enhanced MR imaging of vessel wall in rabbit model-comparison of gadofosveset and gadopentetate dimeglumine. *Radiology* 2009; 250:682–691.
121. Manning WJ, Li W, Boyle NG, Edelman RR. Fat-suppressed breath-hold magnetic resonance coronary angiography. *Circulation* 1993; 87:94–104.
122. Paschal CB, Haacke EM, Adler LP. Three-dimensional MR imaging of the coronary arteries: preliminary clinical experience. *J Magn Reson Imaging* 1993; 3:491–500.
123. Post JC, van Rossum AC, Hofman MB, Valk J, Visser CA. Three-dimensional respiratory-gated MR angiography of coronary arteries: comparison with conventional coronary angiography. *Am J Roentgenol* 1996; 166:1399–1404.
124. Stuber M, Botnar RM, Danias PG, Sodickson DK, Kissinger KV, Van Cauteren M, De Becker J, Manning WJ. Double oblique free-breathing high resolution three-dimensional coronary magnetic resonance angiography. *J Am Coll Cardiol* 1999; 34:524–531.
125. Scheidegger MB, Müller R, Boesiger P. Magnetic resonance angiography: methods and its applications to the coronary arteries. *Technol Health Care* 1994; 2:255–265.
126. Bogaert J, Kuzo R, Dymarkowski S, Beckers R, Piessens J, Rademakers FE. Coronary artery imaging with real-time navigator three-dimensional turbo-field-echo MR coronary angiography: initial experience. *Radiology* 2003; 226:707–716.
127. Dewey M, Teige F, Schnapauff D, Laule M, Borges AC, Rutsch W, Hamm B, Taupitz M. Combination of free-breathing and breathhold steady-state free precession magnetic resonance angiography for detection of coronary artery stenoses. *J Magn Reson Imaging* 2006; 23:674–681.
128. Jahnke C, Paetsch I, Nehrke K, Schnackenburg B, Gebker R, Fleck E, Nagel E. Rapid and complete coronary arterial tree visualization with magnetic resonance imaging: feasibility and diagnostic performance. *Eur Heart J* 2005; 26:2313–2319.
129. Jahnke C, Paetsch I, Schnackenburg B, Bornstedt A, Gebker R, Fleck E, Nagel E. Coronary MR angiography with steadystate free precession: individually adapted breath-hold technique versus free-breathing technique. *Radiology* 2004; 232:669–676.
130. Maintz D, Aepfelbacher FC, Kissinger KV, Botnar RM, Danias PG, Heindel W, Manning WJ, Stuber M. Coronary MR angiography: comparison of quantitative and qualitative data from four techniques. *Am J Roentgenol* 2004; 182:515–521.
131. Manning WJ, Li W, Edelman RR. A preliminary report comparing magnetic resonance coronary angiography with conventional angiography. *N Engl J Med* 1993; 328:828–832.
132. Ozgun M, Hoffmeier A, Kouwenhoven M, Botnar RM, Stuber M, Scheld HH, Manning WJ, Heindel W, Maintz D. Comparison of 3D segmented gradient-echo and steadystate free precession coronary MRI sequences in patients with coronary artery disease. *AJR Am J Roentgenol* 2005; 185:103–109.
133. Sakuma H, Ichikawa Y, Chino S, Hirano T, Makino K, Takeda K. Detection of coronary artery stenosis with wholeheart coronary magnetic resonance angiography. *J Am Coll Cardiol* 2006; 48:1946–1950.
134. Sakuma H, Ichikawa Y, Suzawa N, Hirano T, Makino K, Koyama N, Van Cauteren M, Takeda K. Assessment of coronary arteries with total study time of less than 30 minutes by using whole-heart coronary MR angiography. *Radiology* 2005; 237:316–321.
135. Schuetz GM, Zacharopoulou NM, Schlattmann P, Dewey M. Meta-analysis: noninvasive coronary angiography using computed tomography versus magnetic resonance imaging. *Ann Intern Med* 2010; 152:167–177.
136. Kato S, Kitagawa K, Ishida N, Ishida M, Nagata M, Ichikawa Y, Katahira K, Matsumoto Y, Seo K, Ochiai R, Kobayashi Y, Sakuma H. Assessment of coronary artery disease using magnetic resonance coronary angiography: a national multicenter trial. *J Am Coll Cardiol* 2010; 56:983–991.
137. Miller JM, Rochitte CE, Dewey M, Arbab-Zadeh A, Niinuma H, Gottlieb I, Paul N, Clouse ME, Shapiro EP, Hoe J, Lardo AC, Bush DE, de Roos A, Cox C, Brinker J, Lima JA. Diagnostic performance of coronary angiography by 64-row CT. *N Engl J Med* 2008; 359:2324–2336.
138. Nagel E. Magnetic resonance coronary angiography: the condemned live longer. *J Am Coll Cardiol* 2010; 56:992–994.
139. Hamdan A, Asbach P, Wellnhofer E, Klein C, Gebker R, Kelle S, Kilian H, Huppertz A, Fleck E. A prospective study for comparison of MR and CT imaging for detection of coronary artery stenosis. *JACC Cardiovasc Imaging* 2011; 4:50–61.

140. Jansen CH, Perera D, Makowski MR, Wiethoff AJ, Phinikaridou A, Razavi RM, Marber MS, Greil GF, Nagel E, Maintz D, Redwood S, Botnar RM. Detection of intracoronary thrombus by magnetic resonance imaging in patients with acute myocardial infarction. *Circulation* 2011; 124:416–424.
141. Yeon SB, Sabir A, Clouse M, Martinezclark PO, Peters DC, Hauser TH, Gibson CM, Nezafat R, Maintz D, Manning WJ, Botnar RM. Delayed-enhancement cardiovascular magnetic resonance coronary artery wall imaging: comparison with multislice computed tomography and quantitative coronary angiography. *J Am Coll Cardiol* 2007; 50:441–447.
142. Ibrahim T, Makowski MR, Jankauskas A, Maintz D, Karch M, Schachoff S, Manning WJ, Schömig A, Schwaiger M, Botnar RM. Serial contrast-enhanced cardiac magnetic resonance imaging demonstrates regression of hyperenhancement within the coronary artery wall in patients after acute myocardial infarction. *JACC Cardiovasc Imaging* 2009; 2:580–588.
143. Puntmann VO, D'Cruz D, Taylor PC, Hussain T, Indermuhle A, Butzbach B, Botnar R, Nagel E. Contrast enhancement imaging in coronary arteries in SLE. *JACC Cardiovasc Imaging* 2012; 5:962–964.
144. Phinikaridou A, Andia ME, Protti A, Indermuehle A, Shah A, Smith A, Warley A, Botnar RM. Noninvasive magnetic resonance imaging evaluation of endothelial permeability in murine atherosclerosis using an albumin-binding contrast agent. *Circulation* 2012; 126:707–719.
145. Kooi ME, Cappendijk VC, Cleutjens KB, Kessels AG, Kitslaar PJ, Borgers M, Frederik PM, Daemen MJ, van Engelshoven JM. Accumulation of ultrasmall superparamagnetic particles of iron oxide in human atherosclerotic plaques can be detected by in vivo magnetic resonance imaging. *Circulation* 2003; 107:2453–2458.
146. Tang TY, Howarth SP, Miller SR, Graves MJ, Patterson AJ, U-King-Im JM, Li ZY, Walsh SR, Brown AP, Kirkpatrick PJ, Warburton EA, Hayes PD, Varty K, Boyle JR, Gaunt ME, Zalewski A, Gillard JH. The ATHEROMA (Atorvastatin Therapy: Effects on Reduction of Macrophage Activity) Study. Evaluation using ultrasmall superparamagnetic iron oxide enhanced magnetic resonance imaging in carotid disease. *J Am Coll Cardiol* 2009; 53:2039–2050.
147. Makowski MR, Wiethoff AJ, Blume U, Cuello F, Warley A, Jansen CH, Nagel E, Razavi R, Onthank DC, Cesati RR, Marber MS, Schaeffter T, Smith A, Robinson SP, Botnar RM. Assessment of atherosclerotic plaque burden with an elastin specific magnetic resonance contrast agent. *Nat Med* 2011; 17:383–388.
148. von Bary C, Makowski M, Preissel A, Keithahn A, Warley A, Spuentrup E, Buecker A, Lazewatsky J, Cesati R, Onthank D, Schickl N, Schachoff S, Hausleiter J, Schφmig A, Schwaiger M, Robinson S, Botnar R. MRI of coronary wall remodelling in a swine model of coronary injury using an elastin-binding contrast agent. *Circ Cardiovasc Imaging* 2011; 4:147–155.
149. Schalla S, Nagel E, Lehmkuhl H, Klein C, Bornstedt A, Schnackenburg B, et al. Comparison of magnetic resonance real-time imaging of LV function with conventional magnetic resonance imaging and echocardiography. *Am J Cardiol* 2001; 87:95–99.
150. Bottini PB, Carr AA, Prisant M, et al. Magnetic resonance imaging compared to echo/phy to assess LV MASS in the hypertensive patient. *Am J Hypertension* 1995; 8:221–226.
151. Nagel E, Lehmkuh HB, Bocksch W, et al. Noninvasive diagnosis of ischemia-induced wall motion abnormalities with the use of high-dose dobutamine stress MRI: comparison with dobutamine stress echocardiography. *Circulation* 1999; 99:763–770.
152. Wahl A, Paetsch I, Roethemeyer S, Klein C, Fleck E, Nagel E. High-dose dobutamine-atropine stress cardiovascular magnetic resonance for follow-up after coronary revascularization procedures in patients with wall motion abnormalities at rest. *Radiology* 2004; 233:210–216.
153. Schwitter J, Nanz D, Kneifel S, Bertschinger K, Buchi M, Knusel PR, Marincek B, Luscher TF, von Schulthess GK. Assessment of myocardial perfusion in coronary artery disease by magnetic resonance: a comparison with positron emission tomography and coronary angiography. *Circulation* 2001; 103:2230–2235.
154. Greenwood JP, Maredia N, Younger JF, Brown JM, Nixon J, Everett CC, Bijsterveld P, Ridgway JP, Radjenovic A, Dickinson CJ, Ball SG, Plein S. Cardiovascular magnetic resonance and single-photon emission computed tomography for diagnosis of coronary heart disease (CE-MARC): a prospective trial. *Lancet* 2012; 379(9814):453–460.
155. Fritz-Hansen T, Hove JD, Kofoed KF, Kelbaek H, Larsson HB. Quantification of MRI measured myocardial perfusion reserve in healthy humans: a comparison with positron emission tomography. *J Magn Reson Imaging* 2008; 27:818–824.
156. Kim RJ, Chen EL, Lima JA, Judd RM. Myocardial Gd-DTPA kinetics determine MRI contrast enhancement and reflect the extent and severity of myocardial injury after acute reperfused infarction. *Circulation* 1996; 94:3318–3326.

157. Underwood R, Bax JJ, von Dahl J, Henein MY, Van Rossum AC, Schwartz E, Vanoverschelde JL, van der Wall E, Wijns W. Imaging techniques for the assessment of myocardial hibernation: report of a study group of the European Society of Cardiology. *Eur Heart J.* 2004; 25:815–836.
158. Kim RJ, Wu E, Rafael A, Chen EL, Parker MA, Simonetti O, Klocke FJ, Bonow RO, Judd RM. The use of contrast-enhanced magnetic resonance imaging to identify reversible myocardial dysfunction. *N Engl J Med* 2000; 343:1445–1453.
159. Mavrogeni SI, Sfikakis PP, Koutsogeorgopoulou L, Markousis-Mavrogenis G, Dimitroulas T, Kolovou G, Kitas GD. Cardiac tissue characterization and imaging in autoimmune rheumatic diseases. *JACC Cardiovasc Imaging* 2017; 10(11):1387–1396.
160. Levelt E, Piechnik SK, Liu A, Wijesurendra RS, Mahmod M, Ariga R, Francis JM, Greiser A, Clarke K, Neubauer S, Ferreira VM. Adenosine stress CMR T1-mapping detects early microvascular dysfunction in patients with type 2 diabetes mellitus without obstructive coronary artery disease. *Journal of Cardiovascular Magnetic Resonance* 2017; 19(1):81.
161. Weinsaft JW, Spincemaille P. BOLD new directions in myocardial ischemia imaging–myocardial oxygenation assessment by cardiac magnetic resonance. *J. Am. Coll. Cardiol.* 2012; 59(22):1965.
162. Fieno DS, Shea SM, Li Y, Harris KR, Finn JP, Li D. Myocardial perfusion imaging based on the blood oxygen level-dependent effect using T2-prepared steady-state free-precession magnetic resonance imaging. *Circulation* 2004; 110:1284–1290.
163. Friedrich MG, Niendorf T, Schulz-Menger J, Gross CM, Dietz R. Blood oxygen level-dependent magnetic resonance imaging in patients with stress-induced angina. *Circulation* 2003; 108:2219–2223.
164. Janke C, Gebker R, Manka R, Schnackenburg B, Fleck E, Paetsch I. Navigator-gated 3D blood oxygen level-dependent CMR at 3.0-T for detection of stress-induced myocardial ischemic reactions. *J Am Coll Cardiol Img* 2010; 3:375–384.
165. Ruehm SG, Corot C, Vogt P, Kolb S, Debatin JF. Magnetic resonance imaging of atherosclerotic plaque with ultrasmall superparamagnetic particles of iron oxide in hyperlipidemic rabbits. *Circulation* 2001; 103:415–422.
166. Yuan C, Mitsumori LM, Ferguson MS, et al. In vivo accuracy of multispectral magnetic resonance imaging for identifying lipid-rich necrotic cores and intraplaque hemorrhage in advanced human carotid plaques. *Circulation* 2001; 104:2051–2056.
167. Kerwin W, Hooker A, Spilker M, et al. Quantitative magnetic resonance imaging analysis of neovasculature volume in carotid atherosclerotic plaque. *Circulation* 2003; 107:851–856.
168. Kim WY, Stuber M, Bornert P, Kissinger KV, Manning WJ, Botnar RM. Three-dimensional black-blood cardiac magnetic resonance coronary vessel wall imaging detects positive arterial remodeling in patients with nonsignificant coronary artery disease. *Circulation* 2002; 106:296–299.
169. Kawasaki T, Koga S, Koga N, et al. Characterization of hyperintense plaque with noncontrast T1-weighted cardiovascular magnetic resonance coronary plaque imaging: comparison with multislice computed tomography and intravascular ultrasound. *J Am Coll Cardiol Img* 2009; 2:720–728.
170. Matsumoto K, Ehara S, Hasegawa T, Nishimura S, Shimada K. The signal intensity of coronary culprit lesions on T1-weighted magnetic resonance imaging is directly correlated with the accumulation of vulnerable morphologies. *Int J Cardiol.* 2017; 231:284–286.
171. Tang TY, Howarth SP, Miller SR, Graves MJ, U-King-Im JM, Li ZY, Walsh SR, Hayes PD, Varty K, Gillard JH. Comparison of the inflammatory burden of truly asymptomatic carotid atheroma with atherosclerotic plaques in patients with asymptomatic carotid stenosis undergoing coronary artery bypass grafting: an ultrasmall superparamagnetic iron oxide enhanced magnetic resonance study. *Eur J Vasc Endovasc Surg.* 2008; 35(4):392–398.

12 The State-of-the-Art Echocardiography and Its Viewpoint Classifications

Xiaohong W. Gao[1], Wei Li[2], Martin Loomes[1], Yu Qian[3], Qiang Lin[4], Liqin Huang[4], Lianyi Wang[5]

[1]Middlesex University
[2]Middlesex University and Fuzhou University
[3]Cortexica Vision Systems
[4]Fuzhou University
[5]Tsinghua University

CONTENTS

12.1 INTRODUCTION

Echocardiography remains one of the most important tools in cardiology for diagnosis of heart diseases and relies on ultrasonic techniques to generate both single image and image sequences of the heart, providing insights into cardiac structures, motion status, and detailed anatomical and functional information. Significantly, echocardiography (or echo) can present the moving heart in real time, revealing its health status in vivo while sustaining as a non-invasive, painless, easy to operate,

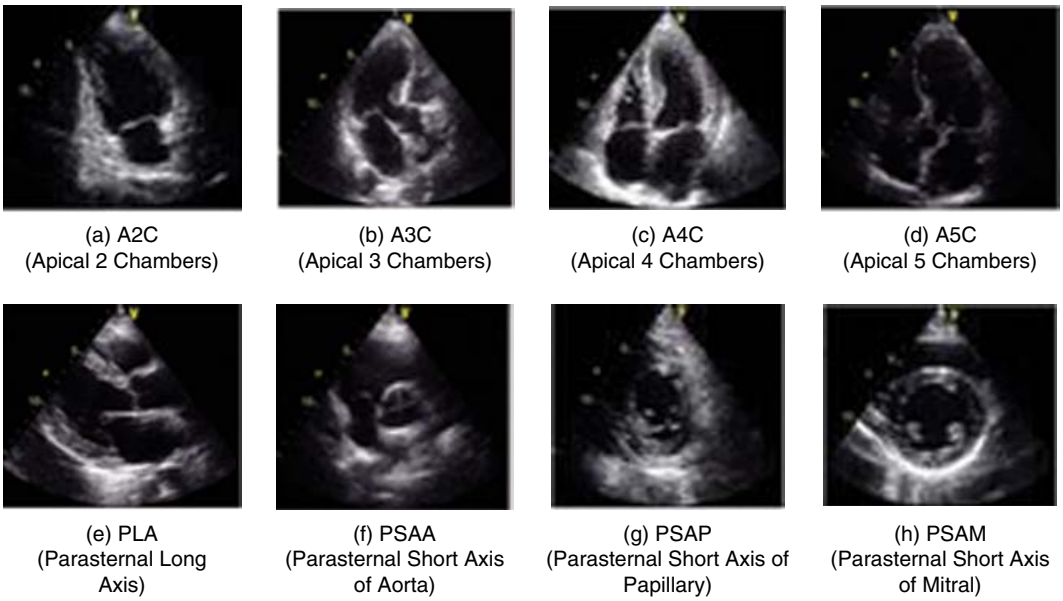

FIGURE 12.1 The illustration of the eight views of echocardiogram videos.

inexpensive, and portable imaging tool. While advanced 4D echocardiography (i.e., 3D heart moving over time) scanners are available, 3D echo imaging tools remain the most common in clinical settings. In order to depict different anatomical sections of the three-dimensional (3D) heart over time (1D), there are eight standard view positions in 3D echocardiography whereby each specific section of the moving heart with distinguished characteristics can be captured, whereas any other viewpoints can either provide complementary views or no clearer pictures at all. Figure 12.1 illustrates the exemplar frames acquired at all eight views that an echocardiography can reveal. Usually, the acquisition of echo videos is performed by sonographers who will then transfer the acquired data to clinicians to make diagnostic decisions upon them. By doing so, clinically, once each viewpoint is determined, a number of major anatomical structures, such as left ventricle, can then be manually delineated, measured, and analyzed in order to ascertain the status of the functioning heart. As presented in Figure 12.1, several images might appear similar (e.g., (g) and (h)), but 3D echo videos over time provide different viewpoints to distinguish clearer differences. These images in essence capture discriminative information from both spatial and temporal points of view. Hence, the determination and classification of the viewpoint upon which the video image under consideration is obtained constitute a crucial first step for the subsequent measurement, analysis, and diagnosis as well as the development of computer-aided diagnostic systems [1–4].

This chapter reviews the state-of-the-art echocardiography and the cutting-edge methodologies of viewpoint classifications. It is organized in the following structure. Section 2 reviews the principles of cardiology imaging tools. Section 3 entails the current approaches applied in classification of echo videos. In Section 4, elaboration of three popular approaches advanced in this research is provided. Section 5 specifies the implementation details and experimental results. To complete the chapter, Section 6 offers the conclusion and discussion.

12.2 CARDIOLOGY IMAGING

Heart disease is one of the leading causes of death in the world in both developed and developing countries. In the UK and United States, more than a quarter of deaths is caused by heart failure each year [5, 6], whereas in China, about 230 million people have cardiovascular disease. It is predicted

that this figure is set to increase by 50% between 2010 and 2030 due to population aging and growth alone in China [7]. Therefore, improving the management of cardiovascular diseases is one of the greatest challenges faced by healthcare sectors and industries in every country.

To investigate the status of the moving heart in vivo and to make a clinical decision, cardiologists mainly rely on cardiologic imaging tools. At present, there are three popular imaging modalities utilized in hospitals, which are Magnetic Resonance Imaging (MR), Computed Tomography (CT), and Echocardiography (Echo) or Ultrasound. The acquired images can be used to assess cardiac structure and function, the presence and severity of dynamic obstruction, the presence of mitral valve abnormalities, and the severity of mitral regurgitation, as well as myocardial ischemia, fibrosis, and metabolism [8].

Each imaging tool has its own advantages and disadvantages. For example, cardiovascular MR imaging is able to produce detailed pictures of the structures within the heart, which allow physicians to evaluate and determine the presence of certain diseases [9], such as regional and global functions. However, these images have to be acquired in advance rather than in real time due to the presence of the magnetic field of MR. In addition, holding breath briefly during the scanning period may pose challenges for some patients. On the other hand, to study suspected cases of aortic dissection or pulmonary embolism which may have atypical clinical features overlapping with those of acute myocardial infarction, a CT imaging of thorax is frequently required. Multi-detector CT can provide complementary imaging for MRI, offering a combined morphological and angiographic assessment. CT angiography can also be employed to assess ventricular systolic function, both globally and regionally, and myocardial perfusion. Since CT scanning has radiation, it is not suitable for a number of patients who have an allergic reaction to the contrast dye.

While MR and CT can provide valuable information of the heart, they all fall short of being portable and convenient due to their sizable tunnel-like volumes for a number of situations (e.g., not handy for screening programs in remote regions or in emergency). In addition to the economic concerns, the ability to acquire dynamic information of the moving heart in vivo makes echocardiography (echo) imaging the favorite choice of diagnosis. Applying ultrasonic technique, echo imaging, one of the most widely applied imaging technologies in medicine [10], has been routinely applied in the diagnosis, management, and follow-up of patients with any suspected or known heart diseases. It provides a wealth of useful information, including the size and shape of the heart (internal chamber size quantification), pumping capacity, and the location and extent of any tissue damage. Furthermore, an echocardiogram can also offer physicians other estimates of heart functions such as cardiac output, ejection fraction (EF), and diastolic function.

12.2.1 Echocardiography

Echocardiography is a typical application of ultrasound imaging and is the most widely used tool in clinical practice for the evaluation of cardiac function due to its nature of being easy to operate, inexpensive, non-invasive, and offering in-vivo observation of the moving heart. In addition, this echo imaging tool can be of varying sizes, from a desktop computer size to the size of a mobile phone, giving rise to its much wider applications, including in emergency and screening programs. As a mature medical technology, at present, one in four diagnostic imaging studies has been carried out applying ultrasonic imaging in the world, and the trend continues to increase.

Echocardiography works rather like sonar, whereby sound waves are applied to locate the position of an object based on the characteristics of the reflected signals, hence coining the term of *echo* [11]. To acquire a video clip, an echo transducer (or probe) of the size of a computer mouse is placed on the chest wall surface (or thorax) of the subject, from which images are taken. This procedure is a non-invasive, highly accurate, and fast assessment of the overall health status of the heart. A standard echocardiogram is also known as a transthoracic echocardiogram (TTE), or cardiac ultrasound. It has three basic modes that are used to image the heart: M-mode imaging, two-dimensional (2D) imaging, and Doppler imaging. The M-mode echo, which supplies a 1D view, is

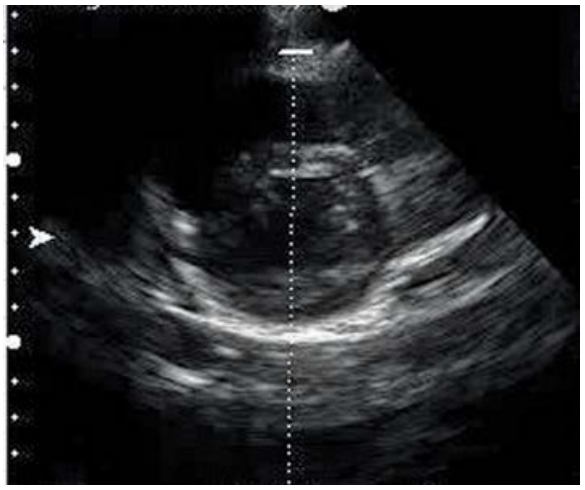

(a)

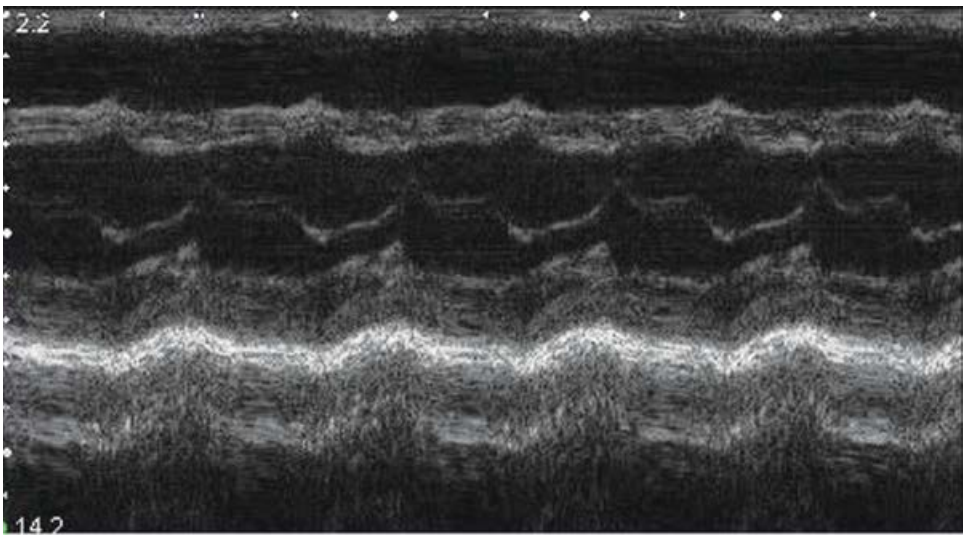

(b)

FIGURE 12.2 An example of typical 2D. (a) 2D echo frame; (b) 1D motion over the time along the line on (a).

usually employed for fine measurements. 2D mode imaging is the mainstream of echo imaging and allows structures to be viewed in vivo in real time for any cross-section of the heart. In 2D mode imaging clips, all chambers and valves of the heart as well as the adjacent proximal connections of large vessels can be depicted. In this way, the spatial relationships among normal and abnormal intra-cardiac structures can be revealed. In addition, the more advanced mode of 4D echo has been recently introduced, which in essence comprises the sequence of the 3D structural heart in motion. Similarly, 3D echo often refers to the sequence (e.g., video) of 2D frames. Figures 12.2–12.4 demonstrate examples of 1D to 4D echo frames.

Moreover, Doppler ultrasound is set to estimate the velocity of blood flow in the human heart and vasculature noninvasively [12] as illustrated in Figure 12.5 where red color indicates the flow coming in the direction towards the viewer and blue away from the viewer. Both videos of Figures 12.3 and 12.5 are from the same subject at the same viewpoint of PLA.

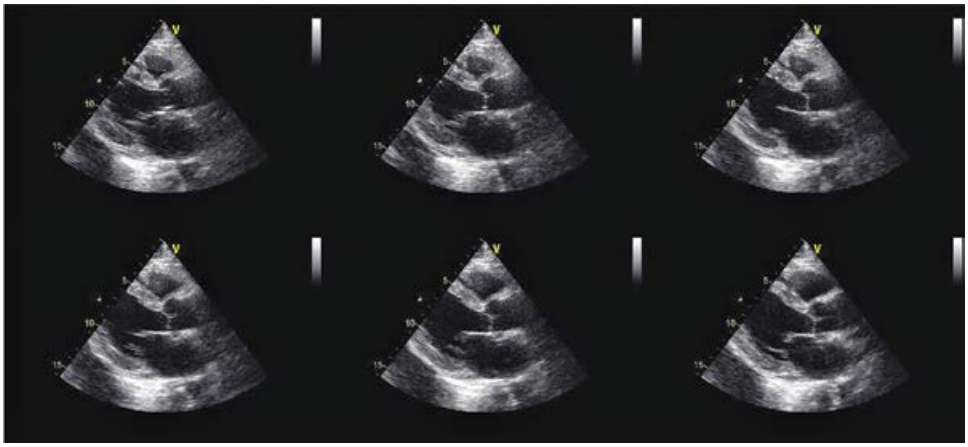

FIGURE 12.3 A sequence of 2D echo frames over time, i.e., 3D echo.

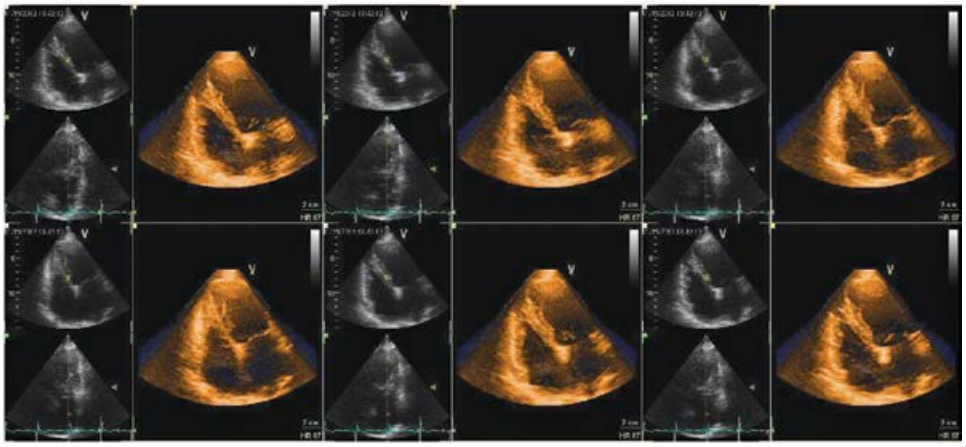

FIGURE 12.4 A sequence of 3D moving heart that can be viewed in every angle, i.e., 4D echo.

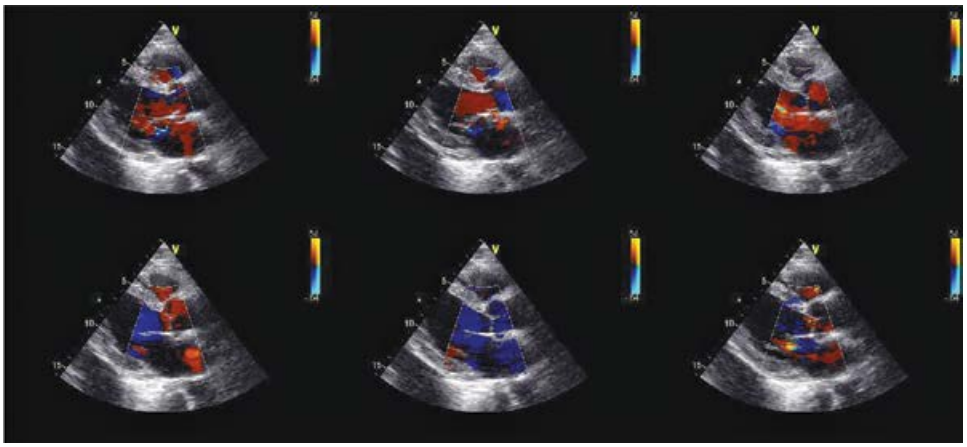

FIGURE 12.5 Color Doppler mode of Figure 12.3 illustrating blood flows where red is the flow running towards the viewer and blue away from.

12.2.2 Basic Principles of Ultrasound

Ultrasound is the term used to describe the frequencies of sound above 20,000 Hertz (Hz), beyond the range of human hearing (between 20 to 20K Hz) [13]. Most cardiac applications are performed based on frequencies from 2 million to 10 million (M) hertz, or 2 to 10 megahertz (MHz) [14]. During the examination, sound travels in mechanical waves with a speed dependent on the density and elastic properties of the medium in which they are travelling through [15]. When a sound wave, which is generated by electrical stimulation of a piezoelectric crystal in the transducer, is transmitted into heart tissues, it partially echoes back to the transducer from the layers between different cardiac tissues and partially scattered from smaller structures. Then the rest travels forward through further tissue layers. The amount of reflection depends on the variation of impedance of the two adjacent tissues, for example, myocardium and blood.

The amplitude, or strength, of the returning echo wave that is picked up by the transducer is then converted into the scale of brightness (whiteness) of an echo pixel. The bright structures are termed as hyperechoic, whereas low-amplitude waves are rendered into shades of grey-hypoechoic regions, with the structure without reflecting any waves being cast as a black dot (anechoic), constructing an echocardiogram as depicted in Figure 12.1. The vertical position of the echo pixel on the screen is based on the time delay between the emission and return of the ultrasound beam. On the assumption that velocity is constant within soft tissue, quicker returning echoes are hence regarded as superficial structures, whereas slower returning ones are the deeper structures. Horizontal position of the echo pixel on the screen is based on the receiving piezoelectric crystal's location along the transducer [16, 17].

12.2.3 View Position and Viewpoints for Acquisition of 3D Echocardiograms

The human heart is a two-stage (systolic and diastolic) electrical pump that circulates blood throughout the body through the creation of pressure. When in a systolic state, the heart is contracted, during which the blood in the chambers is forced onward. Diastole performs the opposite, by which the heart is dilated with chambers being filled with blood. As illustrated in Figure 12.6, there are four chambers (spaces) inside the heart. Two top chambers are called atriums, while the bottom ones correspond to ventricles. Each side of the heart forms its own pumping systems (i.e., a right heart and a left heart), and consists of an atrium and a ventricle. Within these systems, blood always flows in

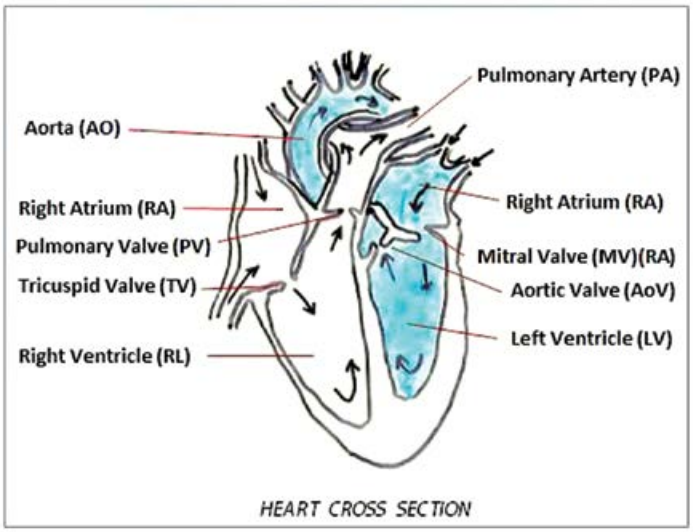

FIGURE 12.6 The structure of the heart cross-section where arrows indicating blood flow directions.

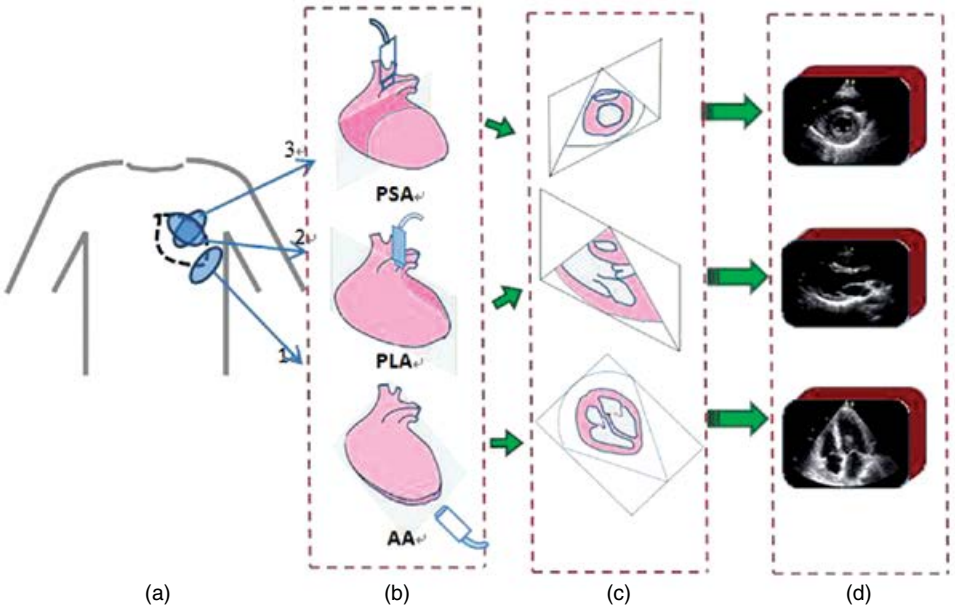

FIGURE 12.7 The procedure of acquisition of a section of the heart applying echocardiographic imaging. (a) The location of the three primary positions on the chest; (b) the planes that the echo beams scan from the transducer; (c) cross-section drawn along the echo beams; (d) the reconstructed cardiac image/video displaying in the screen.

only one direction due to the fact that the valves between atriums and ventricles open in one direction like trapdoors to let the blood pass through.

As illustrated in Figure 12.7, in order to acquire any view section of the heart, physically, an ultrasound transducer is set to posit at three primary positions on the surface of a person's chest. At each position, while rotating angles of the transducer, more sections of the heart can be brought out.

In practice, there are three primary positions that can capture the images of the heart, which are parasternal short axis (PSA), parasternal long axis (PLA), and aorta angle (AA). At each position, by varying the angles or viewpoints of the transducer, different sections of the heart can be sampled. For example, at PSA, the level of the aortic valve (PSAA), level of the mitral valve (PSAM) and papillary muscles can be acquired (PSAP). At AA, four sections of the heart can be viewed, including apical two chambers (A2C), apical three chambers (A3C), apical four chambers (A4C) and apical five chambers (A5C). Clinically, eight viewpoints, including one parasternal long axis (PLA) viewpoint, are most commonly applied. While a number of pictures can be acquired at other angle positions, they do not depict as clear a picture as at these eight viewpoints. Hence, classification of these eight viewpoints will form the focus point of this chapter. Table 12.1 shows the relationship between three view positions and the eight viewpoints.

TABLE 12.1

The list of the three primary positions and eight viewpoints.

Viewpoint Primary View	1	2	3	4	5	6	7	8
Apical Angle (AA)	A2C	A3C	A4C	A5C				
Parasternal long axis (PLA)					PLA			
Parasternal short axis (PSA)						PSAA	PSAM	PSAP

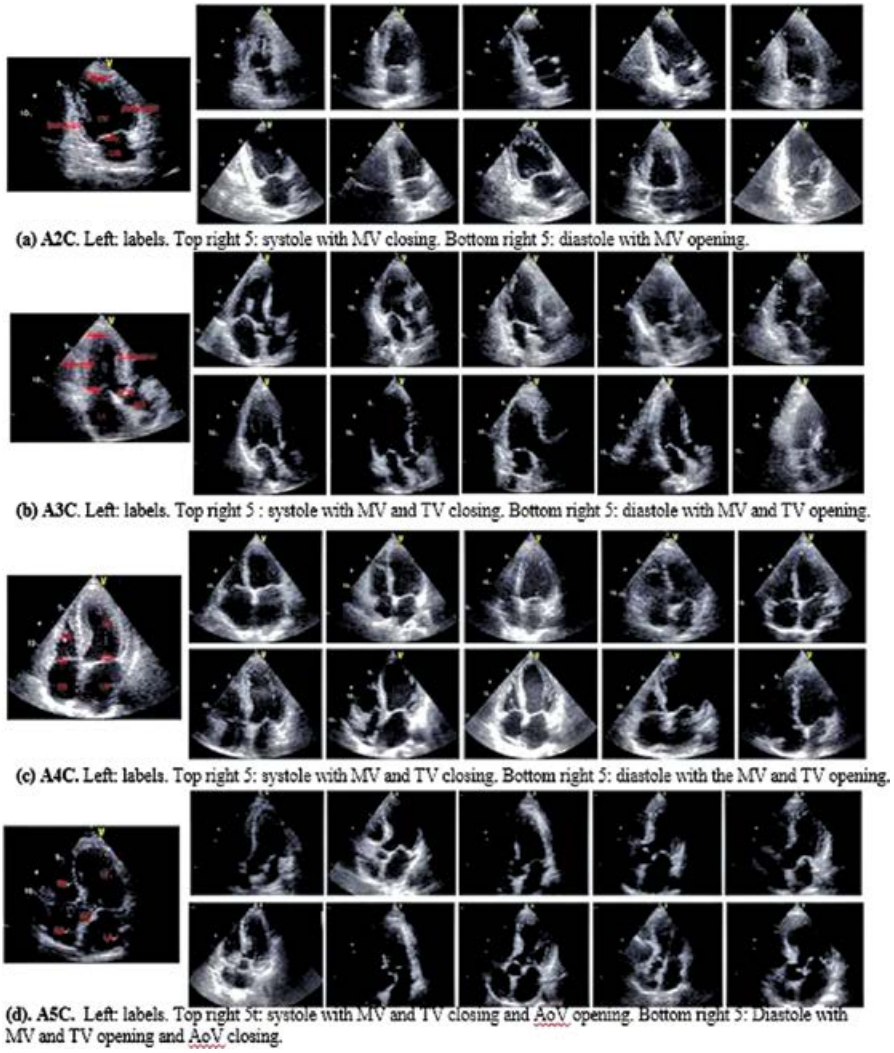

FIGURE 12.8 Video clips for four viewpoints in the primary position of AA. Left: labels. Right: sequential frames. (a) A2C; (b) A3C; (c) A4C; (d) A5C.

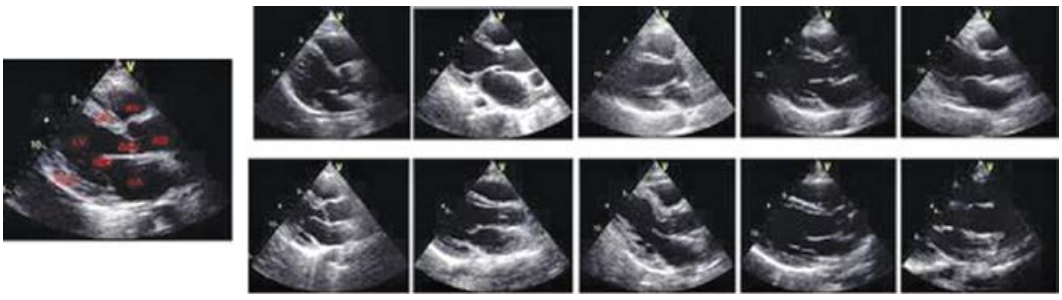

FIGURE 12.9 Video clip for PLA view position and viewpoint. Left: Labels. Top right: Systole with the MV closing, while AoV opening. Bottom right: Diastole with the MV opening while AoV closing.

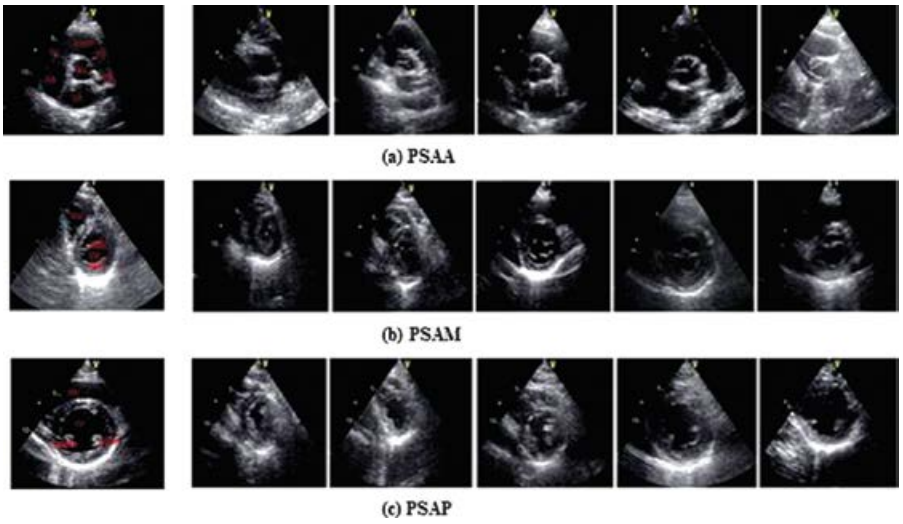

FIGURE 12.10 Sample frames from PSA view. (a) At PSAA viewpoint; (b) At PSAM viewpoint; (c) At PSAP viewpoint. Left: labels. Columns 2–3: cardiac systole. Columns 4–6: cardiac diastole.

Figures 12.8–12.10 demonstrate video clips of primary views of AA, PLA, and PSA in the states of both ventricular systole of the heart (contraction, top row) and diastole (relaxing, bottom row) together with the labels of regions that can be captured at each viewpoint (left column). The abbreviations are the same as those in Figure 12.6.

12.3 THE STATE OF THE ART OF CLASSIFICATION OF ECHOCARDIOGRAMS BASED ON VIEWPOINTS

12.3.1 Challenges in Classification of Viewpoints by Computers

The resolution of an ultrasonic image is inherently limited due to the loss of proper contact or air gaps between the transducer probe and the chest surface [18]. The presence of this kind of speckle noise severely degrades the fine details and contrast resolution of the image, bringing up a challenge in detecting small and low contrast structures of the heart [19, 20]. In addition, the quality of ultrasound imaging is also affected by human factors, including a patient's physical motion and breath motion as well as the skillfulness of an operator. Significantly, the similarities within intra- and inter-viewpoints present more difficulties in the classification task. Figure 12.11 exemplifies the similarities between frames of intra-viewpoint (Figure 12.11(a)) and inter-viewpoint (Figure 12.11(b)),

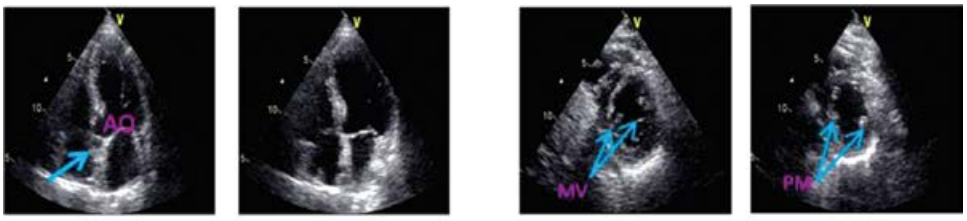

FIGURE 12.11 Cardiac structures illustrating the variation of intra-viewpoint and inter-viewpoint. (a) The aortic root (AO) structure indicated in the left frame fades away in the right one; (b) the similarity between viewpoints of PSAM and PSAP where mitral valve (MV) and papillary muscles (PM) appear similar.

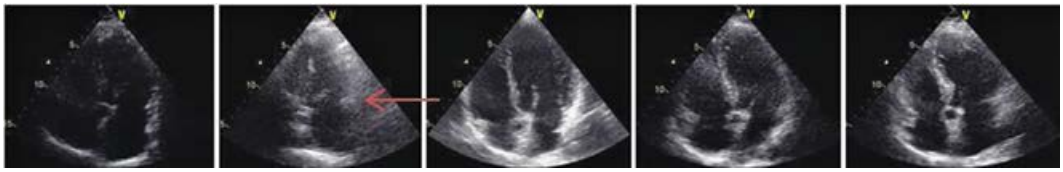

FIGURE 12.12 Sample frames from A5C viewpoint in diastole state with both MV and TV opening and AoV closing. The arrow frame demonstrates the resemblance to A4C.

where the aortic root (AO) structure presented on the left frame fades away in the following frame (Figure 12.11(a)) and the appearances of PSAM and PSAP (Figure 12.11(b)) appear similar between mitral valve (MV) and papillary muscles (PM).

Figures 12.12 and 12.13 further entail the similar intra-viewpoint by showing the sequential structure of five chambers (A5C) and four chambers (A4C) of the heart, respectively. Figure 12.12 depicts diastole state with both MV and TV opening and AoV closing, during which, as pointed by an arrow, the image bear similar features to four chambers (A4C class). On the other hand, Figure 12.13 exhibits an A4C class where the frame with an arrow on display resembles an appearance of five chambers.

Notably, in this study, the collected video images do not have ECG (electrocardiogram) data that record the rhythm and electrical activity of the heart. Therefore, the video images cannot be aligned at the same phase of the cardiac (heartbeat) cycle.

Echo videos are usually obtained by sonographers independently in advance, who endeavor to acquire as much cross-sections as possible for cardiologists to view, analyze, and diagnose. Therefore knowing where those video clips are coming from, or classification of viewpoints, plays a crucial part for both computer aided systems and clinicians. As such, a large number of work has been conducted to classify viewpoints in an automatic way. Table 12.2 summarizes most of the current studies, which will be elaborated in detail below.

Broadly speaking, the classification of echo viewpoints can be categorized into two groups, *spatial or frame based* and *spatial-temporal fusion methods,* with the former focusing on spatial relationship of the heart structures and the latter exploring spatial-temporal relations to combine both motion information of echocardiogram sequences with the spatial and contextual information on each frame.

12.3.2 Frame-Based Methods

The frame-based method processes echocardiogram images frame by frame to extract spatial information of cardiac structures such as location, gradient, energy, and other statistical characters. Approaches in this field pay attention mainly on mining and collecting spatial features or relationships between cardiac structures by representing these features into different forms in order to train and test by utilizing classification methods. Because temporal information is disregarded in these approaches, the whole echo cardiac video can be processed frame by frame, whereby features and spatial relationships are extracted from each image independently. Typical approaches include Scale

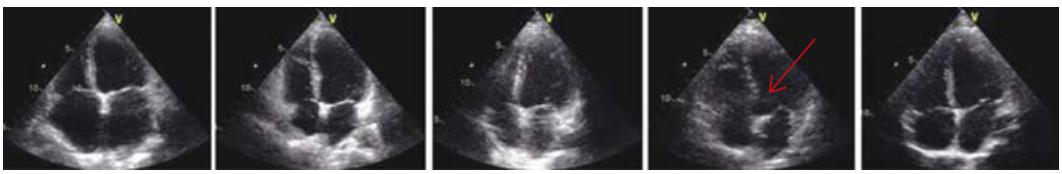

FIGURE 12.13 A sequence of frames corresponding to A4C viewpoint when in systole state with both MV and TV closing. The arrow points to the similarity to A5C class that contains five chambers.

TABLE 12.2

Summarization of most of the current classification methods in the literature. The last three marked with* refer to the work carried out by the authors of this chapter.

Method	Number of Classes	Mean Accuracy(%)
Balaji et al. (2014) [21]	3	94.56
Ebadollahi et al. (2004) [22]	4	67.8
Otey et al. (2006) [23]	4	92.7
Aschkenasy et al. (2006) [24]	4	90
Wu. et al. (2013) [25]	8-way (no A3C, A5C)	98.51
Park et al. (2007) [26]	4	96.3
Zhou et al. (2006) [27]	2	90.2
Roy et al. (2008) [28]	4	97.19
Agarwal et al. (2013) [29]	2	98
Balaji et al. (2015) [30]	4	90.7
Kumar et al. (2009) [31]	4\8	98.4\81
Beymer et al. (2008) [32]	4	87.9
*Qian et al. (2013) [33]	3\8	90\72
*Li et al. (2015) [34]	3\8	97.4\90
*Gao et al. (2017) [35]	3\8	98\92.1

Invariant Feature Transform (SIFT) [36], the Speeded Up Robust Features (SURF) [37], and KAZE features [38].

For example, in [34], KAZE features are applied to represent and thereafter to classify echo images, whereas in [24], the key points of echo images are detected and described using SURF. Towards this end, the input echo images with extracted SURF descriptors need to match those of a template image that is calculated in advance for each category. The classification results can then be obtained by minimizing the Euclidean distance between the matching points from the template and the input image. As a result, the accuracy of recognition is highly dependent on the matching degree.

The significant difference between SIFT, SURF, and KAZE is the choice of scale space. The former two make use of the Gaussian scale space through the linear diffusion or approximation of Gaussian derivatives to detect features, whilst KAZE concentrates on nonlinear diffusion of filtering [39]. In this way, more boundary and detailed information related to cardiac structures can be retained while reducing the level of noises. Figure 12.14 manifests the differences where feature points are extracted by the application of the three approaches of SIFT, SURF, and KAZE respectively. From the representation of cardiac structure (i.e., boundary) point of view, KAZE appears to perform better with more features highlighting the edge of the structure and less scattering.

In addition to these three approaches, many other approaches are also developed to highlight cardiac cavity, which are mainly applied to viewpoints of A2C, A3C, A4C, and A5C as applied in [21, 22] where the approach of Grey-Level Symmetric Axis Transform (GSAT) has been developed. This is based on the assumption that the constellation of chambers in each image is established as a relational structure with attributes of location, area, directionality, distance, and angle. The statistical variations and spatial relationships of this constellation are then encoded by using Markov Random Field (MRF) models to obtain the optimal energy. The classification is then conducted by applying support vector machine (SVM) in the energy space.

Another approach is to use the shape of a deformation map [24], whereby the standard views of echo videos are rendered as a template library by applying multi-resolution spline filters to intensity images. For each unknown sample image, the deformation map and its warped image with

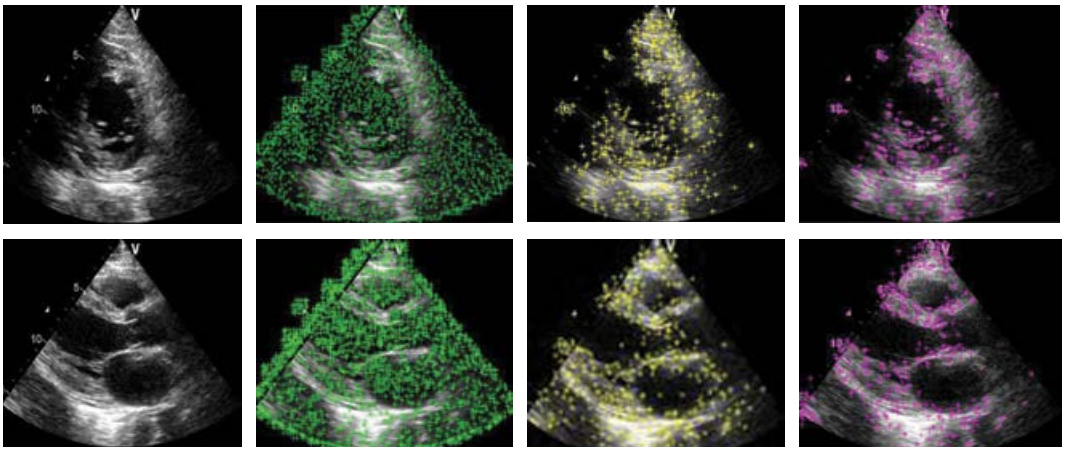

FIGURE 12.14 Manifestation of differences between SIFT, SURF, and KAZE on the extraction of feature points. From left column to right: original, SIFT (2nd), SURF (3rd), and KAZE (right).

reference to each template can be procured by matching it against the template library. To classify it, both deformation energy and the similarity between the warped image and reference templates are employed by applying a linear discriminant classifier. Apparently, the success of this approach depends very much on the amount of deformation energy (the smaller the better) and the degree of similarity (the more the better).

Similar to SIFT, generalized search tree (GIST) is a widely applied technique to extract echo image features [25]. In doing so, an echo image is divided into a set of non-overlapping image blocks. Upon each block the spectral energy is computed applying GIST features on the basis of multiple oriented Gabor filters of different scales. The global information is then represented through the concatenation of all block features and is classified by SVM.

In addition, MLBoost Learning algorithm coupled with multi-object detection can also be implemented for cardiac echo video classification [26] through the application of Haar-wavelet type local features or Haar-like local rectangle features [27], mainly for AA classes. According to a multiclass classifier, the final classification result can be determined applying the majority voting rule.

On the other hand, *Artificial Neural Network* (ANN) also remains one of the popular methods for classifications, which have been increasingly applied in medical image processing [40–43]. For example, to classify heart valve diseases, pre-process medical echocardiography images applying Gaussian and Gabor filters takes place first to combine features of intensity histogram and Gray Level Co-occurrence Matrix (GLCM). Then these global texture features are fed into an artificial neural network for automatic classification based on a back-propagation algorithm [42].

For detection of spatial features of an echo image, statistical histograms are commonly employed. For example, a number of histograms can be generated presenting the number of cavities, their orientations, and heart muscles in each viewpoint [28]. In addition, the classification of four AA viewpoints can be realized by the application of simple gray-scale (intensity) histograms of a region of interest (ROI) incorporating a neural network classifier or SVM and Back Propagation Neural Network (BPNN) [44]. The approach of *Histogram of Oriented Gradients* (HOG) is applied to depict the spatial arrangement of echo images [29] to capture local structure.

From network design point of view, a hierarchical classification strategy for viewpoint classification is implemented in [23], using hierarchical classifiers (one on the top level, two classifiers on the second level) to classify all the images by employing the rule of leave-one-out cross-validation. The top-level classifier is designed to distinguish between the apical and parasternal views, whereas on the second level, each one is applied to distinguish two or four apical chamber viewpoints and to parasternal long or short viewpoints respectively, following top-down processes.

12.3.3 Spatial-Temporal Fusion Methods

Since the heart cycles periodically, temporal or motion information also plays an important role in classification of viewpoints in comparison with image-based methods. The common fusion approaches set to distinguish location and global features between temporal and spatial information with local motion structures integrated into global dense features as depicted in most image-based methods. It is expected that local space-time features capture cardiac characteristic appearance and motion information for a local region, which provide a relatively independent representation of structures with respect to their spatial-temporal shifts and multiple motions in the scene. Such features can be extracted directly from videos.

For instance, based on the optical flow field, the edge-filtered motion maps for echo sequences can be produced whereas local spatial-temporal features can then be discerned using SIFT, which are subsequently recounted by concatenating location, motion histogram, and intensity histogram into a feature vector [31, 45].

The approach of *active shape models* (ASMs) is also exploited to capture the shape and texture information, which are then tracked across the whole video sequence to derive motion information [32]. One of the shortcomings of this approach is that the original ASM feature points need to be located manually in the training data, which can be not only time consuming, but also subjective.

Another research direction is to consolidate 2D frame with 1D time into a 3D space as implemented by Qian et al. [33]. In this method, the space-time interest points of an echo video clip are discovered by applying Cuboid detector (including the 2D spatial Gaussian smoothing kernel and 1D temporal Gabor filter) with each interest point being characterized by a 640-dimension vector using a 3D SIFT descriptor. In the training stage, a codebook of echo videos is constructed following the *Bag of Word* (BoW) paradigm. Then all 3D SIFT features corresponding to space-time interest points in each testing video are coded into a feature vector based on the trained codebook. Multiclass SVM is applied to complete an eight viewpoints classification of echocardiogram video in the final stage.

More recently, Gao et al. [35] took the lead to advance a fused deep learning architecture to categorise eight viewpoints by the application of convolutional neural network (CNN) coupled with acceleration along the motion space. As a result, their work has achieved state-of-the-art results with an accuracy rate of 92.1%.

12.4 METHODOLOGY AND MATERIALS

This section elaborates three popular spatial-temporal approaches for classification, namely, 3D SIFT, 3D KAZE, and deep learning, which are implemented in this study, together with motion feature descriptors attained in the field of acceleration.

12.4.1 SIFT Descriptor in Three Dimensions

As a fused approach, the method of 3D SIFT features [46, 33] has been applied in an attempt to include temporal information. Figure 12.15 exhibits the three stages that usually take place to treat each video as a 3D object with the third dimension being time. First, the detection of spatial-temporal interesting points is conducted using a Cuboid detector [47]. Then these points are represented by the employment of 3D SIFT descriptors. And finally the construction of a visual vocabulary dictionary is coordinated based on the approach of *Sparse Coding*.

Specifically, as shown in Figure 12.15 (a and b), a $12 \times 12 \times 12$ neighborhood volume around an interest point is selected and then divided into $2 \times 2 \times 2 = 8$ sub-volumes. For each sub-volume, the gradient magnitude and orientation of each voxel in the sub-volume are calculated by using Haar wavelet transform along x, y, and z direction, respectively, whereby the magnitude of the gradient

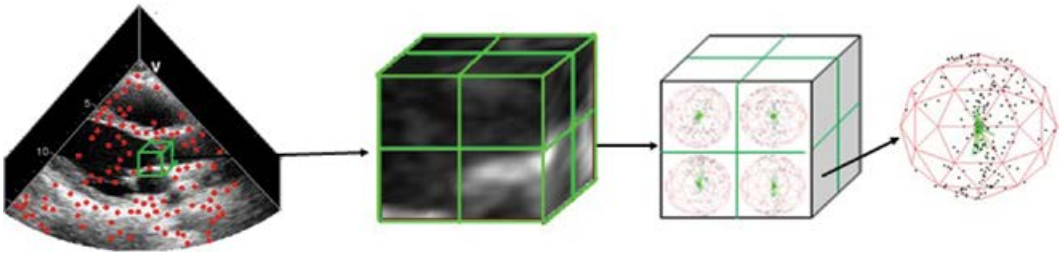

FIGURE 12.15 The process of obtaining 3D SIFT descriptors.

is subsequently accumulated to the corresponding bin of the gradient orientation. The tessellation based orientation histogram is then implemented in this study. By using the tessellation technique, each bin of 3D gradient orientation is approximated with a mesh of small piece of 3D volume seen as a triangle in Figure 12.15(d). The gradient orientations pointing to the same triangle then belong to the same bin, as marked by the black points in Figure 12.15(d). The total number of the bins is calculated as 20 × (4 ^ Tessellation level). The tessellation level decides the number of constituting triangle surfaces, that is, the number of bins of gradient orientation in 3D space. In this study, the tessellation level is set to 1, thus resulting in 80 bins. Each sub-volume is accumulated into its own sub-histogram. Subsequently, the 3D SIFT descriptor X of each interest point is of $2 \times 2 \times 2 \times 80$ (= 640) dimensions.

12.4.2 KAZE Features in 3D

Similar to Section 4.1, 3D KAZE also is formalized in this research. As exemplified in Figure 12.16 and described in [34], 2D KAZE appears to deliver better performance in the representation of feature points for echo videos. This study will extend this technique to 3D to embed temporal information. In doing so, the detection of KAZE features undergoes the processes of 3D Gaussian smoothness, calculation of conductivity, creation of nonlinear scale spaces, extraction of features, and finally coarse-to-fine suppression, as shown in Figure 12.16.

First, each echo video undertakes a pre-processing stage by the application of 3D anisotropic Gaussian kernel to de-noise video volume v. Then the calculation of conductivity equation is underway using nonlinear partial differential equations (PDEs) as formulated in Eq. (12.1).

$$\begin{cases} \dfrac{\partial u}{\partial t} = div\left(C\left(x,y,z,t\right)\cdot\nabla u\right) \\ u\,|_{t=0} = u_0 \end{cases} \tag{12.1}$$

where u_0 refers to the original volumetric image, with div and ∇ indicating the divergence and gradient operators respectively. Furthermore, the diffusion coefficient C can make the filtering adaptive to local image structure and is chosen to be able to estimate the gradient as suggested in [48], which is given in Eq. (12.2).

$$C\left(x,y,z,t\right) = g\left(\left\|\nabla G_{\sigma,\tau} * v\left(x,y,z\right)\right\|\right) \tag{12.2}$$

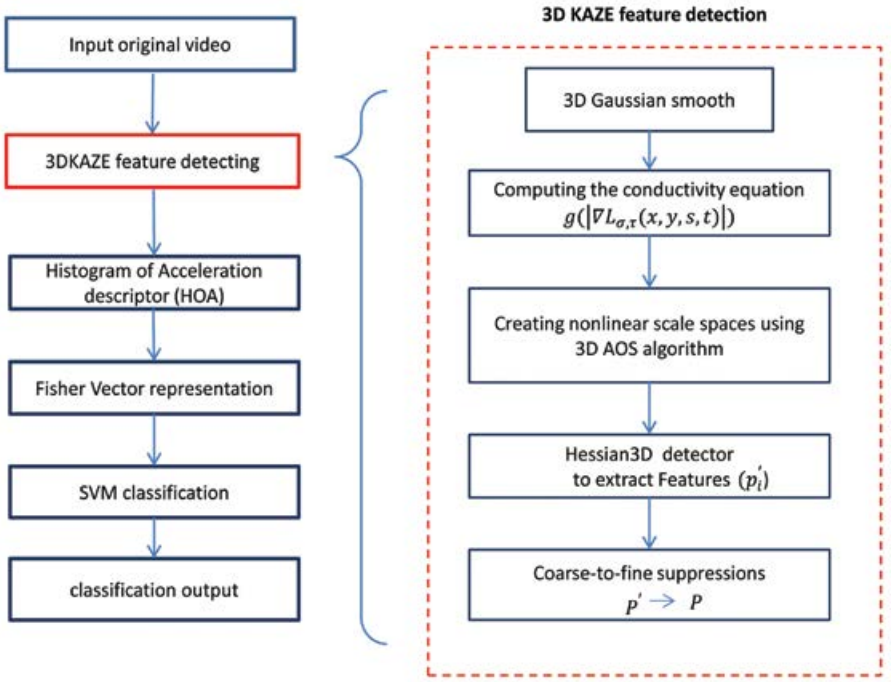

FIGURE 12.16 The flowchart of echo video classification applying 3D KAZE.

where $G_{\sigma,\tau}$ is the spatial-temporal separable Gaussian kernel. As a result, the gradient of spatial-temporal feature points can be recognized by the application of Eqs. (12.3) and (12.4) to calculate gradients at two different levels.

$$g_1\left(\left\|\nabla(x,y,z)\right\|\right) = \exp\left(-\left(\frac{\left\|\nabla(x,y,z)\right\|}{K}\right)^2\right) \tag{12.3}$$

$$g_2\left(\left\|\nabla(x,y,z)\right\|\right) = \frac{1}{1+\left(\frac{\left\|\nabla(x,y,z)\right\|}{K}\right)^2} \tag{12.4}$$

where K indicates the contrast parameter to control the smooth level, which can be determined automatically to reflect the grey level distribution of images in each video sequences; and $\|\cdot\|$ refers to absolute value.

12.4.3 Histogram of Acceleration (HoA) in Acceleration Field

Since echocardiograms are in a video form, the motion information with reference to time needs to be taken into account, which includes velocity and acceleration. To measure velocity, optical flow is widely employed using a histogram of flow (HOF) descriptor to encode motion information. For an echo video, the motion of the heart is attained from periodic systolic and diastolic functions of

myocardium and varies in different stages. In a cardiac circle, the myocardium of different structures has discriminative stress states, which accordingly is reflected as different motion states in each echo video.

Acceleration, on the other hand, representing the rate of the change of velocity, reflects the stress state of an object. Mathematically, acceleration is defined as the derivative of velocity of (v_x, v_y), which can be approximated employing discrete difference between two sequential frames in optical flow, shown as Eq. (12.5):

$$a(x,y,t) = \frac{dv}{dt} = v(x,y,t+1) - v(x,y,t) \tag{12.5}$$

Similar to velocity field, the acceleration field is composed of horizontal and vertical components (a_x, a_y), which have both magnitude and direction as formulated in Eqs. (12.6) and (12.7), respectively.

$$mag(x,y) = \sqrt{a_x^2 + a_y^2} \tag{12.6}$$

$$\theta(x,y) = tan^{-1}\left(\frac{a_y}{a_x}\right) \tag{12.7}$$

In this work, a new descriptor based on acceleration (a_x, a_y) is developed utilizing a histogram of acceleration (HoA) based on magnitude of Eq. (12.6) when implementing 3D KAZE. Figure 12.17 provides a comparison of velocity and acceleration fields sampled during a cardiac circle in a PSAP echo video, in particular in the region of blue boxes.

12.4.4 Deep Learning: Convolutional Neural Network (CNN)

One important aspect regarding the previously discussed hand-crafted approaches (e.g., 3D SIFT and 3D KAZE) is that they are image-dependent, that is, one method that performs excellent on one group of images may not work well on several other collections, which prompts the development of neural network led deep learning methods to detect salient features automatically.

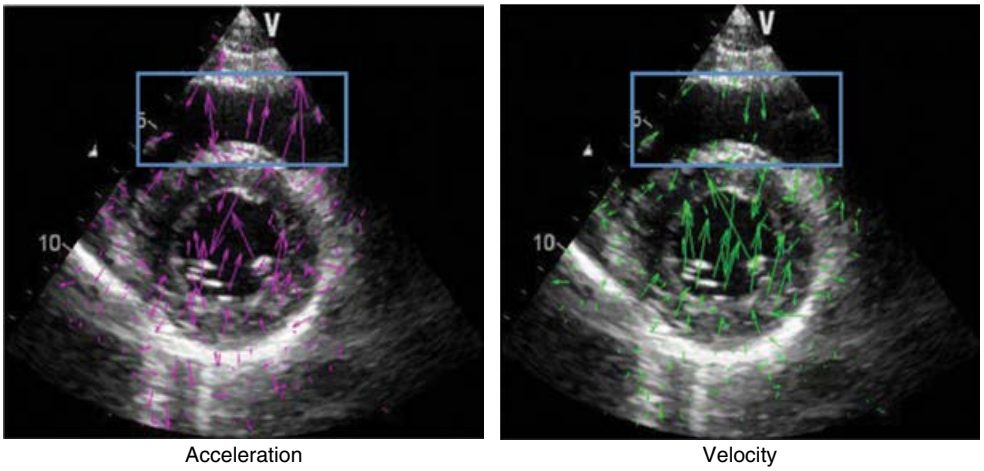

Acceleration Velocity

FIGURE 12.17 The illustration of acceleration and velocity fields in a frame during a cardiac contraction period.

Deep learning neural networks refer to a class of computing machines that can learn a hierarchy of features by establishing high-level features from low-level ones and is pioneered by Fukushima [49]. One of these models is the convolutional neural network (CNN) developed by LeCun et al. [50]. Consisting of a set of algorithms in machine learning, CNN comprises several (deep) layers of processing involving learnable operators (both linear and non-linear), and hence has the ability to learn a hierarchy of information by building high-level information from low-level data, thereby automating the process of construction of discriminative information [51]. It has demonstrated that, when trained with appropriate regularization, CNNs can deliver superior performance on the tasks of visual object recognition without relying on hand-crafted features. In addition, CNNs appear to be relatively insensitive to certain variations on the inputs due to the fact that a CNN network is designed to imitate biological vision processes and implement a feed-forward artificial neural network, simulating variations of multilayer perceptrons of the vision system where the individual neurons are tiled in such a way that they respond to overlapping regions in the visual field. As a direct result, they are widely applied for image and video recognition. Specifically, CNNs have been demonstrated as an effective class of models for understanding image content, giving state-of-the-art results on image recognition, segmentation, detection, and retrieval. In addition, recent advances of computer hardware technology (e.g., Graphics Processing Unit (GPU)) have propitiated the implementation of CNNs in representing images.

To apply a CNN, mathematically, for a training dataset $(\boldsymbol{x}^{(i)}, \boldsymbol{y}^{(i)})$, where image $\boldsymbol{x}^{(i)}$ is in three-dimension (with the third dimension being intensity color channels) and $\boldsymbol{y}^{(i)}$ the indicator vector of class of $\boldsymbol{x}^{(i)}$, the weights of feature maps of an image, namely, $w_1, \ldots, w_L$, will be learned by solving Eq. (12.8).

$$\underset{\boldsymbol{w}_1,\ldots,\boldsymbol{w}_L}{argmin} \frac{1}{n} \sum_{i=1}^{n} \ell\left(f\left(\mathbf{x}^i; \boldsymbol{w}_1, \ldots, \boldsymbol{w}_L\right), \boldsymbol{y}^i\right) \tag{12.8}$$

where ℓ refers to a suitable loss function (e.g., the hinge or log loss).

To obtain these feature maps $\boldsymbol{v}_{ij}^{xy}$ computationally, 2D convolution is performed at the convolutional layers to extract features from local neighborhood on feature maps acquired in the previous layer. Then an additive bias is applied whereby the result is passed through a sigmoid function as illustrated in Eq. (12.9) mathematically.

$$\boldsymbol{v}_{ij}^{xy} = tanh\left(\boldsymbol{b}_{ij} + \sum_{m} \sum_{p=0}^{P_i-1} \sum_{q=0}^{Q_i-1} \boldsymbol{w}_{ijm}^{pq} \boldsymbol{v}_{(i-1)m}^{(x+p)(y+q)}\right) \tag{12.9}$$

where the notations of those parameters in Eq. (12.9) are explained in Table 12.3.

TABLE 12.3

Notations of the parameters in Eq. (12.9).

Parameter	Notation
$tanh(.)$	hyperbolic tangent function
m	index over the set of feature maps in the $(i-1)th$ layer
b_{ij}	bias for the feature map f in Eq. (12.1)
w_{ijk}^{pq}	value at the position (p, q) of the kernel connected to the k_{th} feature map
(p, q)	2D position of a kernel
P_i, Q_i	height and width of the kernel

In the subsampling layers, the resolution of feature maps is reduced by pooling over a local neighborhood on the feature maps in the previous layer, thereby increasing invariance to distortions on the inputs. As a result, the CNN architecture can be constructed by stacking multiple layers of convolution and subsampling in an alternating fashion. The parameters of CNN, such as the bias b_{ij} and the kernel weight $\boldsymbol{w}_{ijk}^{pq}$, are usually trained using unsupervised approaches [52], whereby their initial values are set up randomly as explained in Table 12.3.

12.4.5 The Fused Architecture of Two Strands of Deep Learning CNN

Figure 12.18 illustrates the integrated architecture of networks implemented in the study in [35]. Specifically, two CNN networks are schemed along space and time directions respectively and executed individually, whereas the integration of both spatial and temporal information is fused upon the final classification scores obtained from both networks. The spatial CNN network works upon the original echo video images that are normalized into the size of $227 \times 227 \times 26$ frames to learn spatial information automatically. Whilst for the temporal CNN network, all the images undergo pre-processing in advance before the learning starts. Towards this direction, they are resized to $175 \times 200 \times 26$ pixels first, which is about half the video spatial size, in order to speed up subsequent processing. Then the approach of *Optical Flow* is applied twice to obtain velocity and thereafter acceleration images. Based on both networks, the final classification result is consolidated though the linear combination of the classification scores obtained from each network using the algorithm of Softmax [53], which tags a probability of belonging to each of the eight classes for each image frame in question. As for a video clip with 26 frames in the spatial network, a histogram based voting system with eight bins ranks the final score for all the frames.

In Figure 12.18, seven layers of operations are performed on each of CNN networks of CNN-1 (top graph) and CNN-2 (bottom graph).

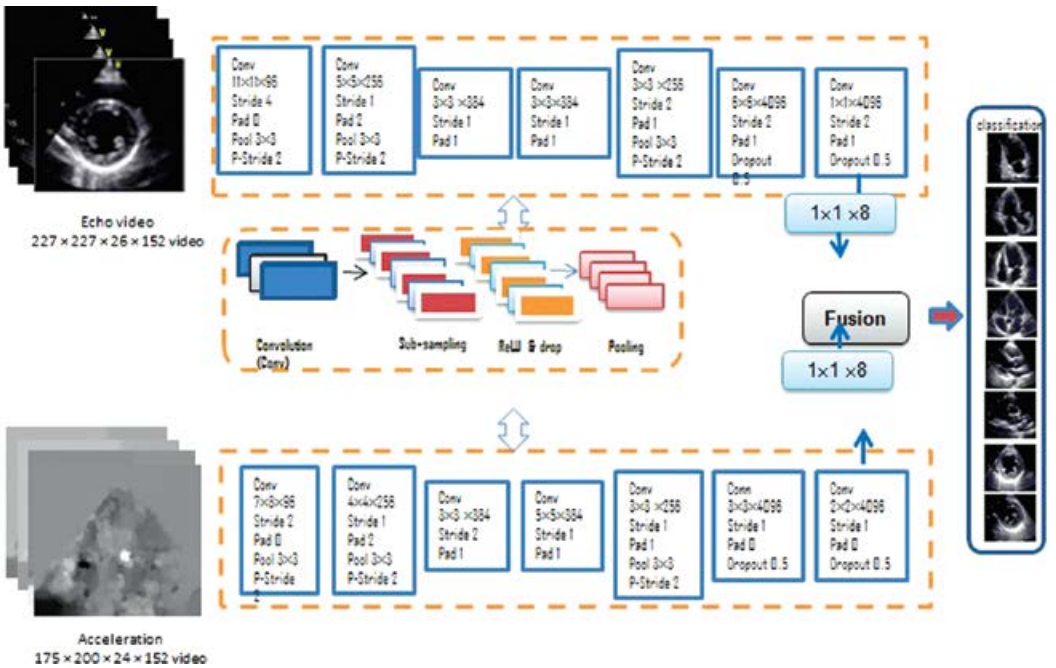

FIGURE 12.18 The fusion of deep learning networks integrating both spatial and temporal information.

In each layer, to learn jointly, both forward and backward processing are staged, composed of several operators in an end-to-end manner. As such, a forward neural network tends to be the composition of a number of functions as formulated in Eq. (12.10) [54].

$$\boldsymbol{y} = f(\boldsymbol{x}) = f_L\left(\ldots f_2\left(f_1(\boldsymbol{x};\boldsymbol{w}_1);\boldsymbol{w}_2\right)\ldots;\boldsymbol{w}_L\right) \tag{12.10}$$

Each function f_l takes a datum $\boldsymbol{x}_l$ as input that has a size of $M \times N$ pixels $\times K$ channels (default of K being 3 representing R, G, and B color channels) and a parameter vector $\boldsymbol{w}_l$, then produces an output datum $\boldsymbol{x}_{l+1}$. The very first input of $\boldsymbol{x} = \boldsymbol{x}_0$ indicates an echo frame for CNN-1 or acceleration image for CNN-2, whereas the rest of $\boldsymbol{x}_l$ ($l > 0$) are intermediate feature maps. For each convolutional layer, the initial input filter bank of $\boldsymbol{w}_i$ is randomly generated but with pre-defined filter sizes. For example, in Figure 12.18 top graph, for Conv-1, the filter size is set as $11 \times 11 \times 3$, generating 96 filter banks. The output of the convolution with this bank of filters, $\boldsymbol{y}$, is assessed in Eq. (12.11).

$$\boldsymbol{y}_{i'j'k'} = \sum_{ijk} \boldsymbol{w}_{ijkk'} \boldsymbol{x}_{i+i',j+j',k} \tag{12.11}$$

where $k' = 96$, $k = 3$, $i' = 11$, and $j' = 11$ for the first Conv layer. In other words, each convolutional operator generates K' dimensional map of $\boldsymbol{y}$ by Eq. (12.11). For example, for layer 1 where $\boldsymbol{x}_0 = (227, 227, 3)$ with the original frame size, feature map $\boldsymbol{x}_1 = (27, 27, 96)$ is generated after layer-1 convolutional operator. Since the images are in grey, the third dimension representing RGB color channels is ignored, that is, $\boldsymbol{x}_0 = (227, 227, 3)$ being replaced by $\boldsymbol{x}_0 = (227, 227)$. The calculation of the size of the feature map follows the rule set out in Eq. (12.12).

$$size\_x_{i+1} = \left(\frac{size\_x_i - \boldsymbol{F}_i + 2Pad}{Stride} + 1\right) \tag{12.12}$$

Additionally, each component or pixel of a feature map is subject to a non-linear gating process to legitimize the processed data. In this study, the simplest approach of rectified linear unit (ReLU) is conveyed in Eq. (12.13) that thresholds the data with zero.

$$\boldsymbol{y}_{ijk} = \max\left\{0, \boldsymbol{x}_{ijk}\right\} \tag{12.13}$$

This operator however does not change the size of each feature map. To downsize the feature map, pooling is employed to coalesce nearby feature values into one downsized sampling and reduce the influence of noise while operating on each individual feature channel. The most commonly used choice of pooling is max-pooling to select the largest component within a neighborhood as shown in Eq. (12.14).

$$\boldsymbol{y}_{ijk} = \max\left\{\boldsymbol{y}_{i'j'k} : i \le i' < i + p, j \le j' < j + q\right\} \tag{12.14}$$

whereas the downsize rate is controlled by pooling stride (P-Stride).

Another operator remains *Dropout* to deal with overfitting in the CNN networks. In doing so, randomly dropped-out units (along with their connections) from the neural network during the training stage are selected and discarded. The dropout rate in this study is set to be 0.5, which is half the data unit numbers.

Once each layer of forward processing is completed, backward process proceeds to ensure that the parameters of feature maps, $\boldsymbol{w} = (\boldsymbol{w}_1, \ldots, \boldsymbol{w}_L)$, are learned in such a way that the overall function of $z = f(\boldsymbol{x}, \boldsymbol{w})$ sustains a minimum loss, $\ell(z, \hat{z})$, where $z = (z_1, \ldots, z_i, \ldots)$ corresponds with the output

value of $\boldsymbol{x}_i$ and $\hat{z}_i$ the ground truth of $\boldsymbol{x}_i$ in the training datasets. Therefore the loss function can be determined in Eq. (12.15).

$$L(\boldsymbol{w}) = \frac{1}{n}\sum_{i=1}^{n} \ell\left(z_i, f\left(\boldsymbol{x}_i, \boldsymbol{w}\right)\right) \tag{12.15}$$

There exists a number of algorithms for minimizing L. In this research, the approach of *gradient descent* is employed, which quantifies the gradient of L at a current solution $\boldsymbol{w}^t$and then updates t along the direction of fastest descent of L as revealed in Eq. (12.16).

$$\boldsymbol{w}^{t+1} = \boldsymbol{w}^t - \eta_t \frac{\partial f}{\partial \boldsymbol{w}}\left(\boldsymbol{w}^t\right) \tag{12.16}$$

where η_t refers to the learning rate that is usually pre-defined and is within the range of (0, 1). In this way, parameters of $\boldsymbol{w}$ can be solved using training datasets.

Substantially, while filter sizes can be of any size within the limit of data size and are chosen manually in advance, the dimension of the output layer at the end of CNN architecture must be $1 \times 1 \times 8$, which reduces the full input image into a single vector of class scores (in our case, class number is 8), arranged along the depth dimension, and can be computed using Eq. (12.12) completed with the values of pooling stride.

In addition, in this investigation, the batch size is set to be 100 (i.e., the system takes 100 images in one go to process) whereas GPU is employed. Furthermore, the learning rate is set to be 0.01 with initial bias being 0.1. Although the filter size is defined in each layer, the initial values of each filter are randomly generated to start the deep learning process in each network. The epoch number of the cycles that the network runs is set to be 150 for both CNNs when the error rates change little as monitored in Figure 12.19 for CNN-2.

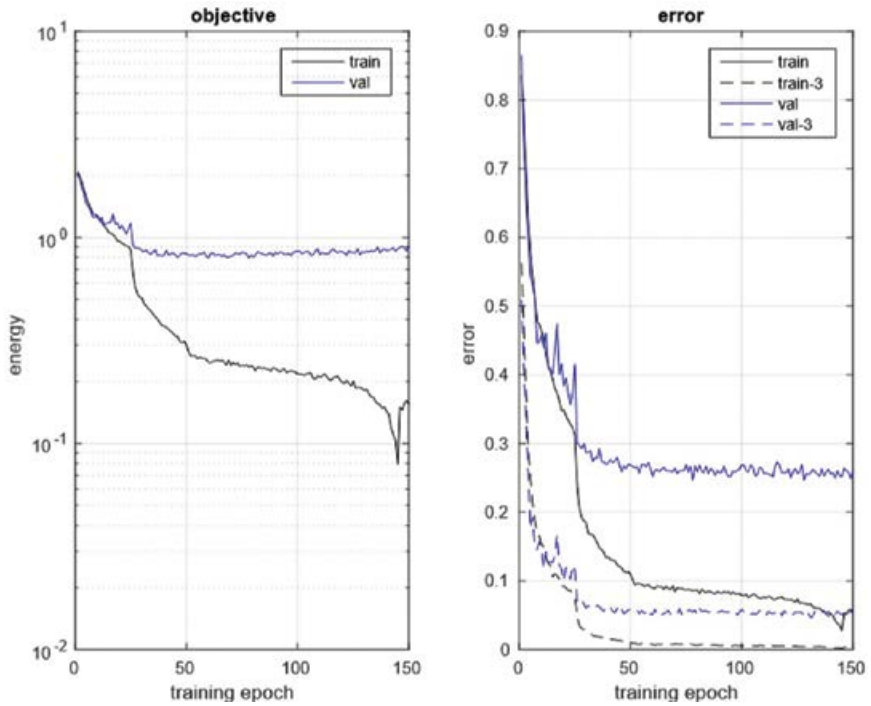

FIGURE 12.19 The training information for CNN-2.

The final classification result is realized during the fusion stage by the linear integration of both class score vectors. Individually, at each network, the classification is performed using Softmax classifier that determines a score of normalized class probabilities as mathematically defined in Eq. (12.17).

$$f_i(z) = \frac{e^{z_j}}{\sum_k e^{z_k}} \tag{12.17}$$

where the function takes a vector of arbitrary real-valued scores (in z) and compresses it to a vector of values between zero and one that sum to one. The obtaining of the class scores f involves the calculation of cross-entropy loss that is formulated in Eq. (12.18).

$$L_i = -f_{y_i} + \log \sum_j e^{f_j} \tag{12.18}$$

where the notation f_j refers to the j_{th} element of the vector of class scores f [53].

12.5 IMPLEMENTATION AND RESULTS

The implementation of a CNN-based approach takes place in this section in comparison with a number of hand-crafted methods as described in Section 4.

12.5.1 Datasets

In total, 432 video images of ultrasonic video images of the heart are collected from both Tsinghua University Hospital at Beijing and Fuzhou University Hospital at Fuzhou, China. Conforming to informed patient consent, these data contain eight view classes and are captured from 93 different patients aged between 7 and 85 years old (comprising 35 wall motion abnormalities and 58 normal cases). All videos are recorded with a duration of ~2 seconds from GE Vivid 7 or E9 and are stored in DICOM (Digital Imaging and Communications in Medicine) format with the size of either 434 *x* 636 *pixels x* 26 *frame* or 341 *x* 415 *pixels x* 26 *frames*. Each clip belongs to one of the eight different views, as detailed in Table 12.4. These ground truth data of eight different view videos are catalogued by clinicians in both hospitals in advance.

12.5.2 Results

For CNN-2 of Figure 12.18, the temporal information is learned from acceleration images along the time direction of the echo videos, which is extracted applying optical flow twice, following the work of variational optical flow [55]. Upon the application to the original echo video with n frames,

TABLE 12.4
The numbers of videos for each of eight viewpoints in the database and applied for training and testing respectively.

View	A2C	A3C	A4C	A5C	PLA	PSAA	PSAM	PSAP	Total
Videos	62	46	58	40	79	57	48	42	432
Training	40	30	38	26	51	37	32	26	280
Testing	22	16	20	14	28	20	16	16	152

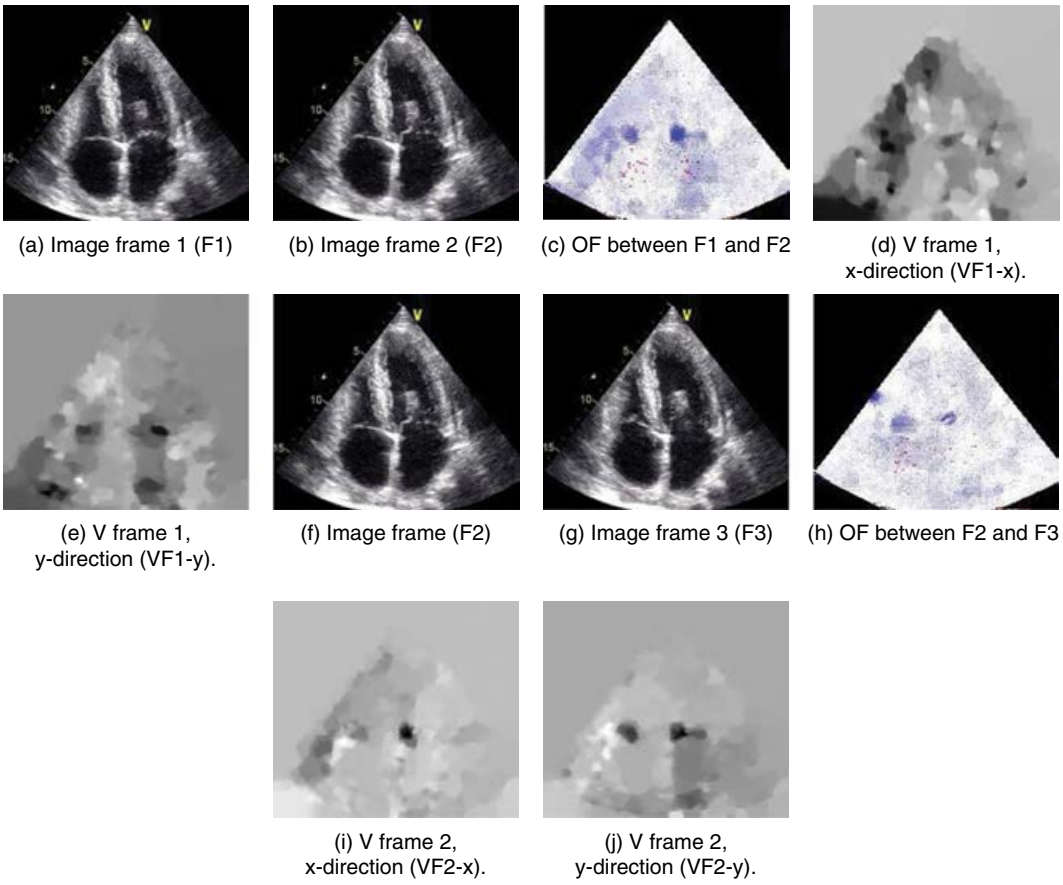

FIGURE 12.20 Image frames of 1 to 3 ((a), (b), (f), (g)) and their corresponding optical flow (OF) maps ((c), (h)) and velocity image frames 1 ((d), (e)) and 2 ((i), (j)).

the velocity video images are obtained with n-1 frames. Then the video images are obtained when optical flow (OF) is applied on the velocity video with n-2 frames. This process is conducted offline since it takes time (1 day in our case). Figure 12.20 exhibits the process of obtaining velocity (V) frames from image frames 1 (F1), 2 (F2), and 3 (F3), while Figure 12.21 portrays the acceleration (A) frame along both x and y directions.

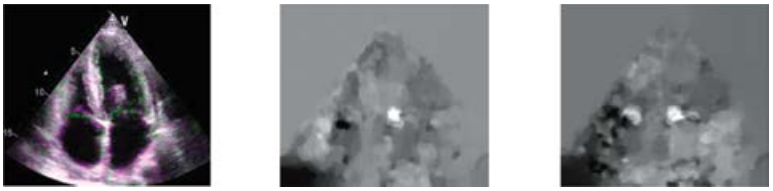

FIGURE 12.21 Acceleration created from velocity frames 1 and 2 along both x (b) and y (c) directions. (a) Superimposed figure of images F1 to F3 in Figure 12.20.

TABLE 12.5

Confusion matrix for eight echocardiogram view classification employing both two-CNN-network and one-CNN-network (i.e., without Acceleration (A)) architecture.

	A2C	A3C	A4C	A5C	PLA	PSAA	PSAM	PSAP	AR (%) 2-CNN	AR (%) 1-CNN
A2C	22								100	100
A3C		16							100	100
A4C			20						100	95
A5C		4		10					71.4	57
PLA					27		1		96.4	100
PSAA					1	19			95	90
PSAM					1	1	12	2	75	68.8
PSAP							2	14	87.5	87.5
Overall AR									92.1	89.5

All the programming work is implemented using Matlab software based on MatConvNet [54], in a computer that runs Ubuntu 64-bit operating system with 64 GByte memory and GPU facility. For each strand of CNN network in Figure 12.18, it takes about two days processing all 432 video images. In addition, the creation of acceleration frames is accomplished offline in advance to expedite the process, which takes another two days.

Table 12.5 presents the final classification results obtained in the form of confusion matrix. The second last column shows the result applying two CNN networks proposed in this study integrating both spatial and temporal information, whereas the last column supplies the outcome concerning only spatial information (i.e., using single CNN network). As a result, the averaged accuracy rate (AR) calculated applying Eq. (12.19) from two-strand network is 92.1% in comparison with 89.5% from the single CNN network.

$$AR = \frac{num\_correctly\_classified}{total\_num\_this\_class} \tag{12.19}$$

In many published works, presentation based on three primary locations is also emphasized, which is provided in Table 12.6, where the overall precision rate of the classification is 98%, which remains the same for both two-strand and single-strand CNN network architecture.

TABLE 12.6

Confusion matrix for 3 primary view locations.

	AA (Apical Angle)	PLA (Parasternal Long Axis)	PSA (Parasternal Short Axis)	Accuracy Rate (AR) (%) 2-CNN	AR without A (%) 1-CNN
AA	72			100	100
PLA		27	1	96.43	100
PSA		2	50	96.15	94.23
Overall AR				98.02	98.02

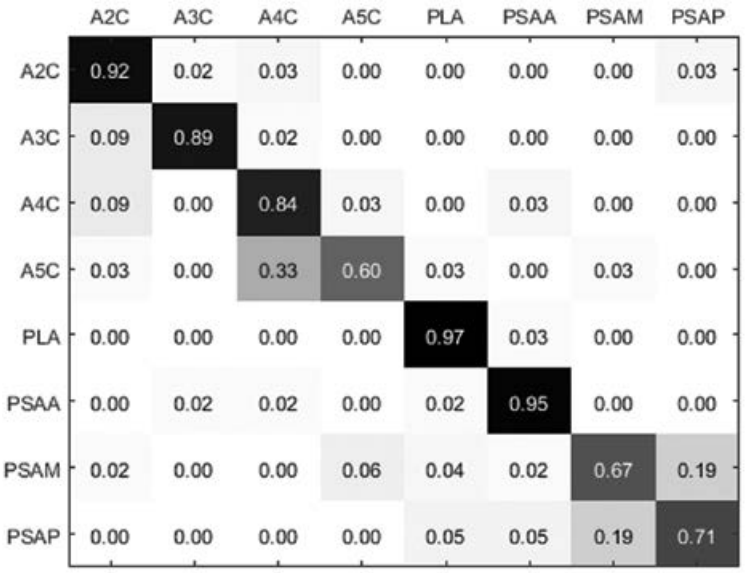

FIGURE 12.22 The confusion matrix of 2DKAZE with optical flow method. The average accuracy is about 84.3%.

In addition, comparisons with a number of well-known hand-crafted methods are performed, including 2D KAZE detector combining with the histogram of optical flow, 2D KAZE, 3D KAZE detector with HOA, dense optical flow detecting, and 3D SIFT. For encoding features, they are all represented using Fisher vector with $K = 128$. Figures 12.22–12.26 present confusion matrixes respectively with the averaged accuracy rates being 84.3%, 89.4%, 87.9%, 79.4%, and 73.8%.

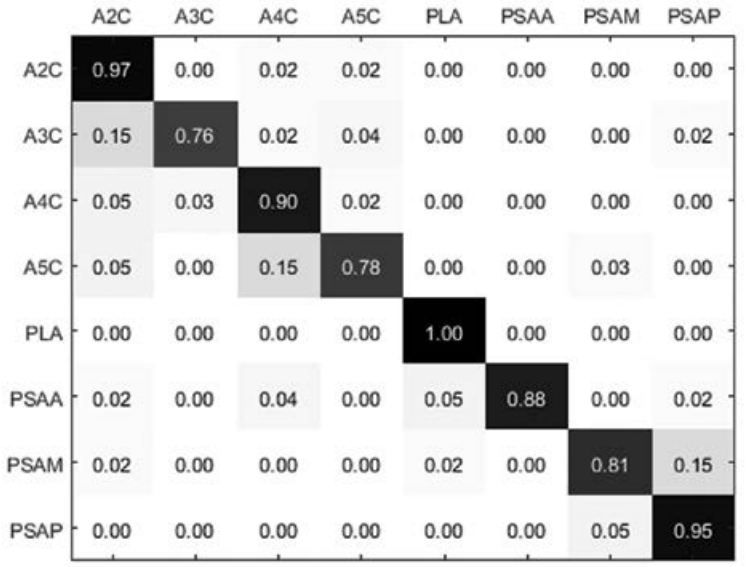

FIGURE 12.23 The confusion matrix of 2D KAZE with the average accuracy of 89.4%.

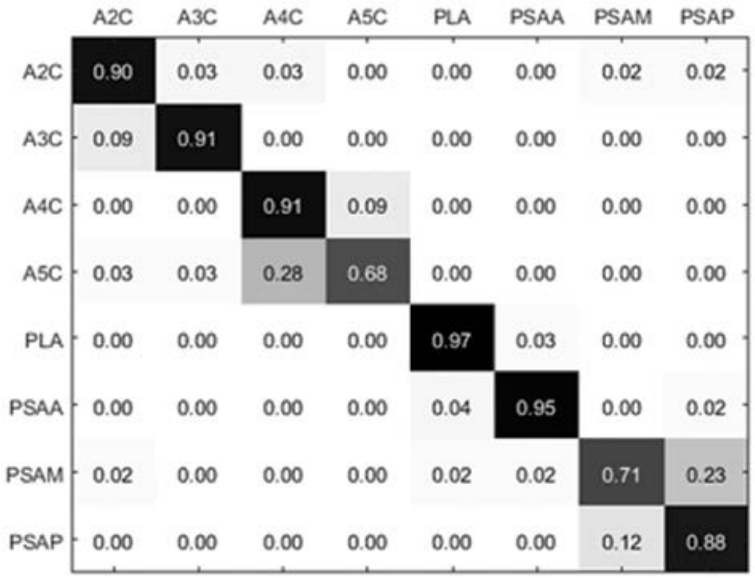

FIGURE 12.24 Confusion matrix of 3D KAZE with the average accuracy of 87.9%.

Table 12.7 summarizes the results for all the approaches implemented in this study.

As indicated in Table 12.7, the two-network CNN architecture proposed in this paper performs the best. Without the inclusion of acceleration of temporal information, CNN still outperforms all the other hand-crafted approaches with 89.5% precision rate. Among those hand-crafted approaches, 2D KAZE appears to achieve the best for this group of echo images with the overall AR maintaining 89.4%.

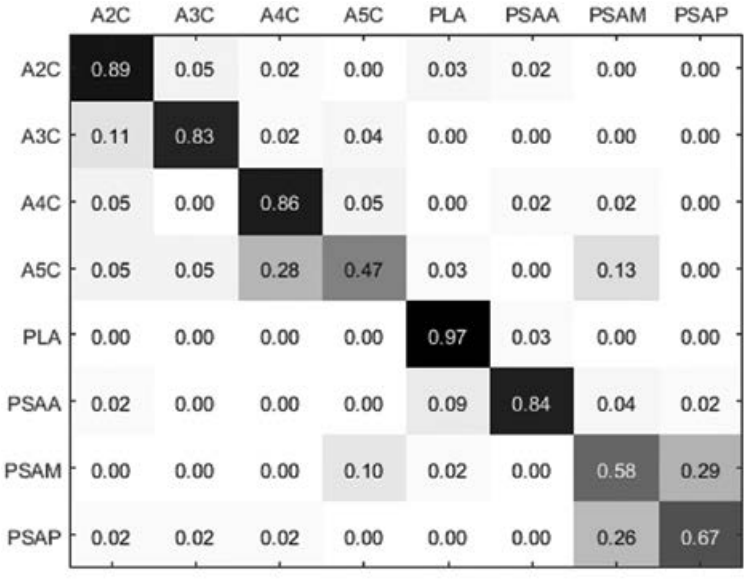

FIGURE 12.25 The confusion matrix of dense optical flow with the average accuracy of 79.4%.

FIGURE 12.26 Confusion matrix of 3D SIFT. The average accuracy is about 73.8%.

12.6 CONCLUSION AND DISCUSSION

This chapter reviews the state-of-the-art echocardiography and its viewpoint classifications. In particular, three approaches are elaborated, including 3D SIFT, 3D KAZE, and the cutting-edge deep learning technique. Specifically, a fused CNN architecture is designed featuring both automatic and selective deep learning networks for the classification of echo videos of eight viewpoint classes. Significantly, this CNN architecture with two-strand networks performs the best with classification results up to 92.1% of accuracy, the best so far in the published work. This implies that deep learning led techniques can be implemented onto medical images and have shown potential in finding discriminative features automatically for echo video images. In theory, deep learning networks accomplish better with the increase of the number of datasets. In our investigation, the

TABLE 12.7
Comparison results between hand-crafted approaches and proposed CNN network.

Methods	Average Accuracy
2D space domain	
2D KAZE	89.4%
2D SIFT	83.8%
Spatial-temporal domain	
2D KAZE + optical flow	84.3%
Optical flow	79.4%
3D SIFT	73.8%
3D KAZE + HoA	87.9%
Deep learning	
CNN	89.5%
Deep learning with two networks	
CNN + Acceleration	**92.1%**

total number of the data is just over 400 video clips, which is not significantly large in comparison with the published work built on bench mark datasets [56–58] where each class amasses more than 1 million datasets. Still, CNN outperforms all the hand-crafted approaches studied in this investigation. Specifically, with the embedding of acceleration information along temporal dimension, two-strand-networks of CNN achieve significantly better (92.1%) than the single-network of CNN without temporal information (89.5%). Interestingly, the performance of the single network of CNN is very close to that of 2D KAZE (89.4%), indicating that when the number of datasets are in a small quantity, the hand-crafted methods can achieve just as well. It should be noted that in this study both 2D hand-crafted approaches appear to function better than their 3D counterparts, namely, 2D KAZE (89.4%) vs. 3D KAZE (87.9%) and 2D SIFT (83.8%) vs. 3D SIFT (73.8%), which can be explained away by the fact that all these collected echo videos are not normalized. In other words, each video can have a different starting point at any phase of the cardiac (heartbeat) cycle. As a result, the temporal information is not aligned and may sometimes provide conflicting information depending on the features to be explored. In the future, further study will be carried out to probe if this phenomenon correlates with video length by acquiring echo clips to contain more than one cycle. Furthermore, the dimension along the temporal direction is significantly lower in comparison with spatial ones (i.e., 26 *vs* 341×415 or 434×636), which might lead to difficulties in extraction of distinguishing temporal information. Nevertheless, temporal information constitutes an inseparable part of video images and will enhance the classification results if correct features are implemented as evidenced in this study where acceleration features are employed.

Importantly, not only does the proposed method of two-strand deep-learning network outperform the state-of-the-art hand-crafted approaches, but also it applies to the datasets that are not normalized. In other words, any echo videos can be classified without the need of availability of ECG data, which will provide significant benefit when it comes to the development of computer-aided diagnostic systems.

Although the temporal information contributes significantly to the final classification results (i.e., 92.1% vs. 89.5%), temporal information alone cannot represent echo videos completely with only 79.4% accuracy rate when only optical flow is applied.

Furthermore, along the temporal direction, the technique of optical flow is employed to capture the motion features of velocity and acceleration of the moving heart, which operates on dense motion fields. In the case of an ultrasonic image, echocardiography can only generate a fan-shape view window, suggesting that each image frame may always introduce new points/objects that are not present in the previous frame, leading to a wrong match of brightness-based points to a certain extent as depicted in Figure 12.27. Hence the application of acceleration features alone to classify viewpoints

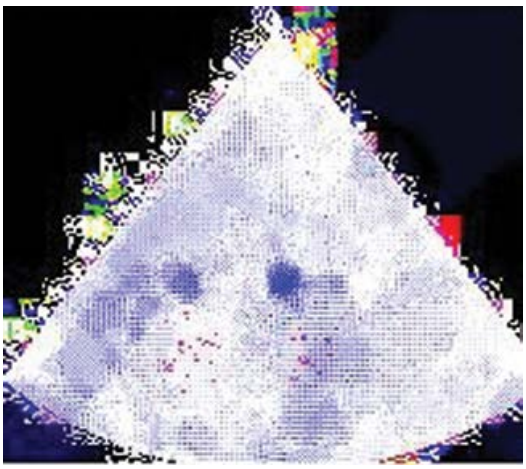

FIGURE 12.27 The optical flow image without the exclusion of edge points outside of the fan shape.

is not expected to give better performance. In this study, those points outside of the fan shapes are excluded for the subsequent processes and are replaced by the background grey level as shown in the flow maps of Figure 12.20 (middle column).

The class of A5C contains the smallest number of datasets (40) and has the worst classification rate (71.4%). Therefore, future work is to collect more data.

The output of CNN led architecture is a classification system or a model that bundles up every parameter for echocardiography. Although the initial development and training of this system may take weeks or months depending on the volume of collected data, the system/model will operate in real-time mode once the classifier or classification model is established. In other words, once a new video clip is made available and sent to the system, it takes a couple of minutes (depending on the length of the video) to give out the classification result of the video. Furthermore, similar to any other software systems, updating this classification system or model can be conducted at a regular basis whenever new dataset/information/evidence is made available.

To compare with the existing work, it appears that more data does improve the classification rate. In [33] where 3D SIFT is employed, the average accuracy rate (AAR) stands at 72% with 219 datasets, whereas 73.8% is achieved with 432 data in this study. Similarly, in [34] that applies the same 2D KAZE features, 81.09% AAR is realized based on a collection of 312 datasets, whereas in our study with 432 datasets, a significant increase of accuracy is attained amounting to 89.4%. While the accuracy rate is secured at 81% in [31] based on 113 video clips, results may not be comparable directly. In their work, their collection of video data has been subjected to a normalization stage (to align all the videos to start at the same phase of a cardiac cycle) with the addition of extra information extracted from ECG (electrocardiogram) data, whilst ours remain raw video clips. Remarkably, this fact further promotes the significance of the applied fused CNN architecture in the classification of echo videos, which competes with the best AAR so far at 92.1%.

Acknowledgments

This work is conducted in the project of WIDTH (2011–2014, Grant number: PIRSES-GA-2010-269124) that is funded by EU FP7 under Marie Curie scheme. Their financial support is gratefully acknowledged.

References

1. Syeda-Mahmood T, Wang F. Characterizing normal and abnormal cardiac echo motion patterns, *Computers in Cardiology* 2006, 33:725–728.
2. Syeda-Mahmood T, Wang F, Beymer D, London M, Reddy R. Characterizing spatial-temporal patterns for disease discrimination in cardiac echo videos, *Conference of Medical Image Computing and Computer-Assisted Intervention (MICCAI)* 2007, pp. 261–269.
3. Beymer D, Syeda-mahmood T. Cardiac disease detection in echocardiograms using spatio-temporal statistical models, *Annual Conference of IEEE Engineering in Medicine and Biology Society (EMBS)* 2008, pp. 723–730.
4. Kumar R, Wang F, Beymer D, Syeda-mahmood T. Cardiac disease detection from echocardiogram using edge filtered scale-invariant motion features, *IEEE Computer Society Workshop on Mathematical Methods in Biomedical Image Analysis (MMBIA)* 2010, pp. 162–169.
5. British Heart Foundation. CVD statistics. https://www.bhf.org.uk/research/heart-statistics. Retrieved in September 2017.
6. Centers for Disease Control and Prevention. Heart disease facts. https://www.cdc.gov/heartdisease/facts.htm. Retrieved in September 2017.
7. WHO. Cardiovascular diseases: the situation in China. http://www.wpro.who.int/china/mediacentre/factsheets/cvd/en/. Retrieved in September 2017.
8. Nagueh SF, Bierig SM, Budoff MJ, et al. American society of echocardiography clinical recommendations for multimodality cardiovascular imaging of patients with hypertrophic cardiomyopathy, *J Am Soc Echocardiography* 2011, 24:473–498.

9. Carreño-Morán P, Breeze J, Rees MR. The top ten cases in cardiac MRI and the most important differential diagnoses. In *Medical Imaging in Clinical Practice* 2013, 253–282, InTech, Croatia.
10. Chan V, Perlas A. Basics of ultrasound imaging. In *Atlas of Ultrasound-Guided Procedures in Interventional Pain Management* 2011, 13–19, Springer.
11. Ryding A. *Essential Echocardiography*, 2nd ed., 2013, Elsevier.
12. Lohr JL, Sivanandam S. Introduction to echocardiography. In Iaizzo PA (ed): *Handbook of Cardiac Anatomy, Physiology and Devices* 2009, pp. 319–330, Springer.
13. Lutz H, Meudt R. *Manual of Ultrasound*, 1984, Springer, Berlin.
14. Benzarti F, Amiri H. Speckle noise reduction in medical ultrasound images, *International Journal of Computer Science* 2012, 9(2):187–194.
15. Vermilion RP. Basic physical principles. In Snider R (ed): *Echocardiography in Pediatric Heart Disease* 1997, pp. 1–10, St. Louis.
16. Bakhru RN, Schweickert WD. Intensive care ultrasound: I. Physics, equipment, and image quality. In *Annals of the American Thoracic Society* 2013, 10(5):540–548. doi: 10.1513/AnnalsATS.201306-191OT
17. Gao X. Feature-wise representation for both still and motion 3D medical images, *2014 IEEE Southwest Symposium on Image Analysis and Interpretation (SSIAI)*, San Diego, USA, 2014, pp. 1–4.
18. Abbott JG, Thurstone FL. Acoustic speckle: theory and experimental analysis, *Ultrasonic Imaging* 1979, 1:303–324.
19. Bini AA, Bhat MS. Despeckling low SNR, low contrast ultrasound images via anisotropic level set diffusion. In *Multidim Syst Sign Process* 2014, 25:41–65. DOI 10.1007/s11045-012-0184-5.
20. Benzarti F, Amiri H. Speckle noise reduction in medical ultrasound images. In *International Journal of Computer Science* 2012, 9(2):187–194.
21. Balaji GN, Subashini TS, Suresh A. An efficient view classification of echocardiogram using morphological operations, *Journal of Theoretical and Applied Information Technology* 2014, 67(3):732–735.
22. Ebadollahi S, Chang SF, Wu H. Automatic view recognition in echocardiogram videos using Parts-based representation. *IEEE Conf. on Computer Vision and Pattern Recognition (CVPR)* 2004, pp. 2–9.
23. Otey M, Bi J, Krishna S, Rao B, Stoeckel J, Han AS, Parthasarathy S. Automatic view recognition for cardiac ultrasound images. In *MICCAI: Intl Workshop on Computer Vision for Intravascular and Intracardiac Imaging* 2006, pp. 187–194.
24. Aschkenasy S, Jansen C, Osterwalder R, Linka A, Unser M, Marsch S, Hunziker P. Unsupervised image classification of medical ultrasound data by multiresolution elastic registration, *Ultrasound in Medicine and Biology* 2006, 32(7):1047–1054.
25. Wu H, Bowers DM, Huynh TT, Souvenir R. Echocardiogram view classification using low-level features, *IEEE 10th International Symposium on Biomedical Imaging: From Nano to Macro* 2013, pp. 752–755.
26. Park J, Zhou S, Simopoulos C, Otsuki J, Comaniciu D. Automatic cardiac view classification of echocardiogram, *ICCV* 2007, pp. 1–8.
27. Zhou S, Park J, Georgescu B, Simopoulos J, Otsuki J, Comaniciu D. Image-based multiclass boosting and echocardiographic view classification, *CVPR* 2006, pp. 1559–1565.
28. Roy A, Sural S, Mukherjee J, Majumdar AK. State-based modeling and object extraction from echocardiogram video, *IEEE Transactions on Information Technology in Biomedicine* 2008, 12(3):366–376.
29. Agarwal D, Shriram KS, Subramanian N. Automatic view classification of echocardiograms using Histogram of Oriented Gradients, *IEEE 10th International Symposium on Biomedical Imaging: From Nano to Macro* 2013, pp. 1368–1371.
30. Balaji GN, Subashini TS, Chidambaram N. Cardiac view classification using speed up robust features, *Indian Journal of Science and Technology* 2015, 8(Suppl.7):1–5.
31. Kumar R, Wang F, Beymer D, Syeda-mahmood T. Echocardiogram view classification using edge filtered scale-invariant motion features, *IEEE Conf. on Computer Vision and Pattern Recognition (CVPR)* 2009.
32. Beymer D, Syeda-Mahmood T, Wang F. Exploiting spatio-temporal information for view recognition in cardiac echo videos, *IEEE Computer Society Workshop on Mathematical Methods in Biomedical Image Analysis (MMBIA)* 2008, pp. 1–8.
33. Qian Y, Wang L, Wang C, Gao X. The synergy of 3D SIFT and sparse codes for classification of viewpoints from echocardiogram videos. In Greenspan H, et al. (eds): *MCBR-CDS* 2012, *LNCS* 2013, 7723:68–79.
34. Li W, Qian Y, Loomes M, Gao X. The application of KAZE feature to the classification of echocardiogram videos, *MRMD* 2015, *LNCS* 2015, 9059:61–72.
35. Gao X, Li W, Loomes M, Wang L. A fused deep learning architecture for viewpoint classification of echocardiography, *Information Fusion* 2017, 36:103–113.

36. Lowe D. Distinctive image features from scale-invariant key points, *International Journal of Computer Vision* 2004, 60(2):91–110.
37. Bay H, Ess A, Tuytelaars T, Van Gool L. Speeded-Up robust features (SURF), *Computer Vision and Image Understanding* 2008, 110:346–359.
38. Alcantarilla PF, Bartoli A, Davison AJ. KAZE features. In Fitzgibbon A, et al. (eds): *ECCV 2012, Part VI, LNCS 7577*, pp. 214–227, Springer-Verlag Berlin Heidelberg, 2012.
39. Perona P, Malik J. Scale-space and edge detection using anisotropic diffusion, *IEEE Transactions on Pattern Analysis and Machine Intelligence* 1990, 12:629–639.
40. Uddin MS, Halder KK, Tahtali M, et al. Speckle reduction and deblurring of ultrasound images using artificial neural network. *Picture Coding Symposium (PCS)* 2015, pp. 105–108.
41. Suganya R, Rajaram S. Content based image retrieval of ultrasound liver diseases based on hybrid approach. *American Journal of Applied Sciences* 2009, 9(6):938–945.
42. Atta E, Mohamed E, Hosnia A. Artificial neural networks in medical images for diagnosis heart valve diseases. *International Journal of Computer Science Issues (IJCSI)* 2013, 10(5):83–90.
43. Sharma N, Ray AK, Sharma S, Shukla KK, Pradhan S, Aggarwal LM. Segmentation and classification of medical images using texture-primitive features: application of BAMtype artificial neural network. *Journal of Medical Physics* 2008, 33(3):119–126.
44. Rumelhart D, Hinton G, Williams R. Learning representations by back-propagating errors. *Nature* 1986, 323:533–536.
45. Grauman K, Darrell T. Approximate correspondences in high dimensions. In *NIPS* 2006.
46. Dollar P, Rabaud V, Cottrell G, Belongie S. Behavior recognition via sparse spatio-temporal features, *IEEE International Workshop on Visual Surveillance and Performance Evaluation of Tracking and Surveillance (VS-PETS)* 2005, pp. 65–72.
47. Scovanner P, Ali S, Shah M. A 3-Dimensional SIFT descriptor and its application to action recognition, *ACM Conference on Multimedia* 2007, pp. 357–360.
48. Catté F, Lions PL, Morel JM, Coll T. Image selective smoothing and edge detection by nonlinear diffusion, *SIAM J. Numer. Anal.* 1992, 29:182–193.
49. Fukushima K. Neocognitron: a self-organizing neural network model for a mechanism of pattern recognition unaffected by shift in position, *Biol. Cyb.* 1980, 36:193–202.
50. LeCun Y, Bengio Y, Hinton G. Deep learning, *Nature* 2015, 521:436–444.
51. LeCun Y, Huang FJ, Bottou L. Learning methods for generic object recognition with invariance to pose and lighting. In *CVPR'04* 2004, pp. 97–104.
52. LeCun Y. LeNet-5, convolutional neural networks, http://yann.lecun.com/exdb/lenet/. Retrieved April 2016.
53. Bishop CM. *Pattern Recognition and Machine Learning*, Springer, 2006.
54. Vedaldi A, Lenc K. MatConvNet Convolutional Neural Networks for MATLAB, *Proceedings of the 23rd ACM International Conference on Multimedia* 2015, pp. 689–692.
55. Brox T, Malik J. Large displacement optical flow: descriptor matching in variational motion estimation, *IEEE Transactions on Pattern Analysis and Machine Intelligence* 2011, 33(3):500–513.
56. Ji S, Xu W, Yang M, Yu K. 3D convolutional neural networks for human action recognition, *IEEE Transactions on Pattern Analysis and Machine Intelligence* 2013, 35(1):221–231.
57. Simonyan K, Zisserman A. *Two-Stream Convolutional Networks for Action Recognition Videos*, NIPS 2014.
58. Karpathy A, Toderici G, Shetty S, Leung T, Sukthankar R, Li F. *Large-Scale Video Classification with Convolutional Neural Networks*, CVPR, 2014.

13 Sensor-Enabled 3D Printed Tissue-Mimicking Phantoms: Application in Pre-Procedural Planning for Transcatheter Aortic Valve Replacement

Kan Wang[1], Chuck Zhang[1], Ben Wang[1], Mani A Vannan[2], Zhen Qian[3]
[1]Georgia Institute of Technology
[2]Piedmont Heart Institute
[3]Tencent America

CONTENTS

13.1 INTRODUCTION

The aortic valve is a heart valve situated between the left ventricle (LV) of the heart and the aorta. It functions like a one-way flow controller that allows blood from the LV to be pumped into the aorta but prevents the backflow of the blood. Aortic stenosis (AS), which is a narrowing of the aortic valve opening, is the most common valvular heart disease in developed countries [1]. Advanced age is a major risk factor of the development of AS. Some congenital heart defects,

such as a bicuspid aortic valve, can also cause AS. The progression of AS involves a series of deteriorations of the cardiac function, including an elevated LV systolic pressure, LV concentric hypertrophy, an elevated LV diastolic pressure, and a decreased cardiac output. If untreated, AS patients ultimately develop heart failure.

Patients with severe aortic stenosis may be asymptomatic for many years. However, once the symptoms appear and are only treated medically, the condition of the symptomatic AS patient declines quickly. Mortality rates from the onset of symptoms are approximately 25% at 1 year and 50% at 2 years. Aortic valve replacement where the diseased aortic valve is replaced with a mechanical or tissue valve during a surgical procedure, is a viable treatment option for symptomatic AS patients. Conventional aortic replacement surgery requires sternotomy, cardioplegic arrest, and cardiopulmonary bypass. For severe AS patients with inoperable conditions or who are designated as high risk for surgery, transcatheter aortic valve replacement (TAVR), also known as transcatheter aortic valve implantation (TAVI) or percutaneous aortic valve replacement (PAVR), has been established as the treatment of choice. In this procedure, an aortic valve is implanted using a transcatheter technique and the sternotomy and cardiopulmonary bypass procedures are avoided.

Paravalvular leak (PVL) is a major complication post-TAVR. Recent studies [2] have reported that 26% - 67% of all patients that received TAVR developed a mild or more severe PVL, which is higher than the probability of PVL after surgical aortic valve replacement. Multicenter studies [3], [4] have shown that moderate-to-severe PVL post-TAVR is an independent risk factor for increased short- and long-term mortality. Researchers have proposed a number of PVL predictors that are derived from pre-TAVR imaging, for example, CT or echocardiography, to estimate the occurrence and severity of PVL post-TAVR. These predictors included the presence of valve under-sizing, elliptical annulus, landing-zone calcification, etc. However, the mechanism of the occurrence of PVL is complex and multifactorial, which involves the dynamic interaction between the native aortic valve, the implanted TAVR valve, and blood flow. It is still difficult to reliably predict the occurrence and degree of PVL before the TAVR procedure, and there is no broad consensus on an optimal strategy in patient or prosthesis selection to reduce PVL. Computer-based numerical analysis, such as finite element analysis, has also been used to quantitatively simulate TAVR implantation [5]. However, it remains challenging to numerically simulate the implantation in an environment of viscous blood flows and deformable structures, such as the aortic wall and the native valve leaflets, that endure large deformation. Spatial and temporal discretization of the numerical domain has to be fine enough to ensure model stability, which, however, inevitably leads to very expensive computational costs. For instance, in finite element analysis, the large displacement of the valve leaflets makes remeshing the fluid domain prohibitively expensive to compute. Current numerical analysis approaches have to simplify the computer simulation by decoupling the fluid and the deformable structure under quasi-static conditions or by simply removing the fluid component from the simulation. Furthermore, most numerical methods have to make assumptions about the material properties of the aortic tissue and the prosthesis, as well as the contact constraint in between.

3D printing or additive manufacturing (AM) refers to the fabrication of objects layer by layer in an additive process from 3D digital models. It has been widely applied in the biomedical field, including prosthetics and orthopedic implants [6], [7], and tissue/organ printing [8]. Compared to numerical models, the 3D printed phantom provides a more intuitive hands-on experience to the physicians performing procedures. Due to the rapid growth of percutaneous treatments for aortic valve disease and the inherent complexity of the catheter-based intervention on a beating heart, TAVR has been frequently targeted for 3D printing-guided pre-procedural planning. With recent advances in additive manufacturing, it is possible to create a patient-specific aortic valve phantom with accurate anatomy and comparable mechanical properties. Such phantoms can be used as a pre-procedural planning platform for TAVR simulation and a quantitative tool for post-TAVR PVL assessment.

This chapter aims to review the materials and techniques used in fabricating sensor-enabled tissue-mimicking valve phantoms and the latest application in pre-procedural simulation of valve interventions. In the following sections, we will introduce the two major technical components of

the 3D printing-based simulation platform: a novel tissue-mimicking 3D printing technique and an in-vitro imaging-based strain quantification technique. To demonstrate the clinical potential of this technology, we will also present the framework of 3D printing-based TAVR pre-procedural planning.

13.2 TISSUE-MIMICKING PHANTOMS AND 3D PRINTING TECHNIQUES

13.2.1 Tissue-Mimicking Phantoms Before 3D Printing

Tissue mimicking phantoms were first used for characterization and calibration of medical imaging technologies in 1972, when Robinson and Kossoff used water to substitute tissue in medical ultrasound measurements and calibrations [9]. Since then, phantoms have been used to compare the performance of medical imaging systems, train radiology technicians, validate computer models, and assist in the development of new medical imaging techniques. The tissue-mimicking phantoms for medical imaging have well-defined attenuation or acoustic impedance, dimensions and internal features, thereby simplifying and standardizing the imaging experiments. Before 3D printing was broadly used in studying heart valves, many research groups [10]–[13] presented non-patient-specific phantoms that mimic the imaging properties of human valves. In these studies, the valve phantoms were molded to idealized valve shapes with silicone, agarose, gelatin, PVA cryogel, etc. The phantoms were kept stationary in most simulations.

Generic phantoms that mimic the imaging properties of biological tissues have played an important role in in-vitro imaging studies, such as X-ray, MRI, and ultrasound. In 1982, Madsen and Fullerton proposed an ultrasonically tissue-mimicking material for use in NMR imaging phantoms. The material is essentially water-based proteinaceous gels with glycerol and graphite particle additives for temporal stability and high melting temperature. It was reported that the NMR T_1 of this material depends primarily on the concentration of glycerol and the NMR T_2 depends primarily on the graphite particle concentration. In addition, the ranges of T_1 and T_2 can be tuned with gelatin concentration. With these properties, effective contrast-resolution phantoms with stable T_1 and T_2 distributions can be produced. Bush and Hill later reported a soft tissue substitute using gelatin and alginate, with calcium chloride added to improve thermal stability [14].

This gelatin-alginate phantom was further improved by Bamber and Bush in 1996 to enable representation of distinct inner structure [15].

Agarose-based phantom is one of the most widely used substitutes for soft tissues due to its well-characterized performance and simple fabrication process. Mitchell et al. reported their study of agarose as a phantom material for NMR imaging in 1986 [12]. Agarose is derived from agar, a hydrophilic colloid that is extracted from algae. In this recipe, dry agarose is dissolved in a mixture of water and propanol. In later versions, other additives, such as evaporated milk [16] or glass beads [17] were added to tune attenuation or scattering properties. In 2001, Ramnarine et al. incorporated the agar-based technique into vascular phantoms in a European commission project [18]. In this material, water and glycerol were mixed with a high-strength agar. Other gradients were also used. Benzalkonium chloride was added to control microbial invasion. Al_2O_3 powder was added to control attenuation. SiC powder was added to tune backscatter. The high-strength agar was reported to provide superior structural rigidity compared with standard agarose-based materials and was well suited for vascular flow tests.

Polyvinyl alcohol (PVA)–based materials have been used to make basic vascular phantoms. Nadkarni et al. reported that a combination of 10% PVA with 0.75% enamel paint followed by two freeze-thaw cycles has properties similar to human vascular tissue [19]. The mechanical properties of the phantoms can be tuned by changing the concentrations of PVA.

Latex rubber is another popular material for vascular phantoms. Zhang and Greenleaf fabricated a femoral artery phantom using latex rubber tubing and mounted tubing within a gelatin filled frame to mimic the adjacent soft tissue [20]. Kawase et al. used a rubber ring with wires attached to the outer surface to provide fiducial markers [21].

Before the introduction of 3D printing, tissue-mimicking phantoms had been extensively studied and used in medical imaging. Other than the materials mentioned previously, additional materials have been explored, such as polyurethane [22], polyacrylamide gels [23], open cell foam [24, 25], and silicone [26]. Those phantom materials often provide a few composition or processing parameters as tuning factors for various properties. By changing those factors, researchers can tune the imaging properties or mechanical properties of phantoms to mimic the native tissues under different circumstances. With the increasing need of biomedical research, other applications of tissue-mimicking phantoms have also been demonstrated, such as the simulation of electromagnetic properties of tissues [27], mechanical property mimicking [28], and focused ultrasound ablation [29]. In these applications, phantoms were fabricated as population-averaged idealized models and the individual differences among patients were overlooked. In individual cases, the information that the population-averaged phantoms can provide is very limited since specific information of each patient, such as age, sex, race and medical history, may heavily affect the tissue properties [30]–[32].

13.2.2 3D Printed Patient-Specific Phantoms

Additive manufacturing technologies provide an opportunity towards development of more complex, patient-specific phantoms for medical device testing and surgical planning. 3D printing can transform any digital 3D model into a real-world 3D object, while medical imaging can provide the digital 3D model of the patient's tissue. Imaging techniques have evolved dramatically in the past few decades. Multi-detector-row computed tomography (MDCT) and magnetic resonance imaging (MRI) can provide high resolution 3D data of the human body. 3D printing technologies have provided a rapid and low-cost method to generate patient-specific tissue-mimicking phantoms from the imaging data. A 3D printed patient-specific phantom has an accurate geometry of the target human organ and also could contain the desired patient-specific pathophysiologic information. It has enormous potential in many biomedical applications and clinical practices, such as computational model validation, medical device testing, surgery planning, medical education, and doctor-patient interaction.

3D printing features a high ability for customization, high geometrical complexity, and cost effectiveness in manufacturing cases with low production volume, which is perfectly suited for biomedical applications like prosthetics implants [33], orthopedic implants [7], [34], [35], and tissue/organ printing [8], [36], [37]. Bose et al. did a comprehensive review of cases where additive manufacturing technologies were applied in bone tissue engineering [38]. In some of those cases, multiple types of materials, including ceramics and polymers, were used to tune the mechanical properties of the printed scaffolds. Biglino et al. demonstrated the fabrication of compliant arterial phantoms with PolyJet technology, an additive manufacturing technique that deposits liquid photopolymer layer by layer through orifice jetting and then solidifies by UV exposure [39]. A rubber-like material named TangoPlus (Stratasys Ltd) was used in this study because its mechanical properties are similar to the real tissue. Cloonan et al. did a comparative study on common tissue-mimicking materials and 3D printing materials including TangoPlus with the abdominal aortic aneurysm phantoms [40]. Their results suggested that TangoPlus was a suitable material for modeling arteries in terms of dispensability and it outperformed poly (dimethylsiloxane) (PDMS) Sylgard elastomers that were commonly used in the investment casting process in terms of uniaxial tensile properties.

The integration of modern medical imaging techniques and additive manufacturing has enabled the production of anatomically accurate medical phantoms. Compliant 3D printing materials are the cornerstone of the manufacturing of lifelike 3D printed medical phantoms. However, it is still challenging to find materials that perfectly match the mechanical properties of biologic tissues. The most commonly used 3D printable biological materials include thermoplastic polymers and photopolymers. The mechanical properties of these 3D printable materials are usually tunable with content composition, additives, or degrees of polymerization. However, due to the fundamental difference between polymeric materials and natural tissues, the dynamic response of a 3D printed phantom is usually different from its native counterpart in large strain ranges.

The post-printing cleaning process of support material is another challenge to the 3D printed patient-specific phantoms. The removal of support material usually employs mechanical handling methods with tools or water jets. This process can damage the phantom, especially when the phantom has delicate structures such as thin walls (less than 2mm). Some printable material may also experience permanent deformation during the cleaning process, which compromises the geometrical accuracy.

Another limitation of 3D printed phantoms is the feature resolution, which is determined by the choice of technique. With current 3D printing technologies, the smallest feature size achievable is around 20 micrometers in the layer direction and 100 micrometers in plane. If the desired feature is smaller than the feature resolution of 3D printing, other techniques, such as nanoimprint, must be used.

13.3 DEVELOPMENT OF BIOMECHANICALLY ACCURATE PHANTOMS

13.3.1 Design of Metamaterial Phantoms

Although the uniaxial tensile properties of 3D printed materials can be close to biological soft tissues at small strain (<3%) range, the creep tendency, an inherent characteristic of polymers, makes them behave quite differently than the soft tissues under larger deformation. For tissue-mimicking phantoms, the strain range-of-interest is normally the working strain range of the biological tissue. As illustrated in Figure 13.1, soft tissues typically exhibit a strain-stiffening behavior initially, which is represented by a convex stress-strain curve in the initial setting. As the strain increases, the curve changes from convex to concave, which indicates yielding of the material [41]. In contrast, the stress-strain curve of a polymer material is usually concave from the beginning, indicating a strain-softening feature. Even though the initial Young's modulus of a polymeric phantom can be designed to match the Young's modulus of the real tissue, the mechanical behavior of the phantom will deviate from the real tissue at higher strain levels. Such difference prevents the use of polymeric phantoms in many biomedical studies that employ simulated working environment of soft tissues. For example, current 3D printed aorta models have limitations in pre-operative assessments of TAVR. In order to achieve optimal clinical outcomes, an individualized assessment of the interactions between the native aortic tissue, the prosthesis, and the blood flow is critical. The peak strain of human aortic tissues is typically larger than 10%, where the mechanical responses of the aortic tissue and the 3D printable polymer differ significantly.

Since creep is an intrinsic property of polymeric materials, single-material polymer 3D printing is fundamentally not capable of generating phantoms that are mechanically accurate in the

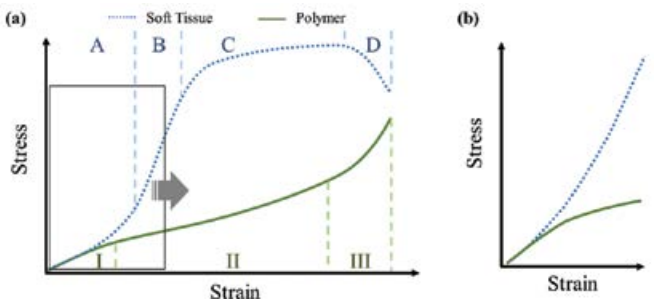

FIGURE 13.1 Comparison of mechanical behaviors of soft tissue and polymer. (a) Typical stress-strain curves of a soft tissue (dotted line) and a polymer (solid line). Soft tissue: A - toe region, B - elastic region, C - plastic region, D - failure region. Polymer: I - primary creep, II - secondary creep, III - tertiary creep; and (b) zoomed view of the curves in the strain range-of-interest for most tissue-mimicking phantoms.

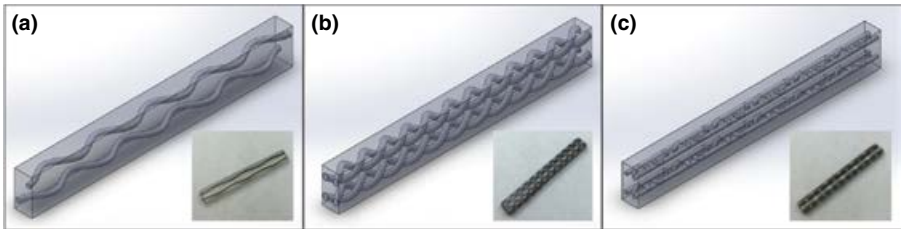

FIGURE 13.2 CAD models and printed samples of three metamaterials: (a) sinusoidal wave design, (b) double helix design, and (c) interlocking chain design.

strain range-of-interest. Recent advances in 3D printed metamaterials provide new insight into this challenge. Metamaterials were first introduced as novel electromagnetic (EM) materials, and their characteristic structural length is one or more orders smaller than the EM wavelengths [42], [43]. Since then, the concept of metamaterials has been extended to include any materials whose effective properties are delivered by its structure rather than the bulk behavior of the materials it is composed with [44]. With multi-material 3D printing technologies, the feasibility of designing the mechanical properties of metamaterials has been proven [45]. Similarly, if a micro-structured material is embedded into a soft polymer, the mechanical properties of the combined material should be tunable by adjusting the structural parameters. With this principle in mind, dual-material 3D printed metamaterials with micro-structured reinforcement embedded in a soft polymeric matrix were developed to mimic the convex stress-strain curve of soft tissues [46].

The passive biomechanical properties of human soft tissues were determined by the microstructure of the tissues at the cellular level. For instance, the nonlinear behavior of human vessels comes from the wavy collagen fibers in the proteoglycan matrix being straightened under tensile loading [47], [48]. This observation can be imitated by embedding wavy stiff structures into soft polymeric matrix. During elongation, the stiff structures will straighten up and compensate for the creep of the matrix polymer. The computer-aided design (CAD) models and pictures of printed samples of three such designs are demonstrated in Figure 13.2. The sinusoidal wave (SW) design has often been used as an assumption for theoretical analysis or numerical simulation of natural wavy fibrous systems. The DH design resembles the microstructure of filament actin (F-actin) strands. The IC design was a representative non-continuous fiber structure. Each design is assembled from a soft matrix part file and a stiff reinforcing microstructure.

13.3.2 Tuning of Metamaterial Phantoms

The strain-stiffening behavior of soft tissues comes from the interaction between elastin and collagen [49]. Soft tissues in the human body work like fiber reinforced composite structures, where elastin and proteoglycans are the matrix and collagen fibrils are the reinforcements. Elastin is a protein that forms the major constituent of the extracellular matrix of soft tissues. It is usually in the form of thin strands that are long and flexible. Elastin molecules build up a 3D rubber-like network, which may be stretched to about 250% of the unloaded length. Its mechanical behavior is essentially linear elastic with marginal relaxation effects [50]. Collagen is a macromolecular protein with a length of about 280nm. Collagen molecules are linked to each other by strong covalent bonds to form collagen fibrils that are much stiffer than the elastin. Depending on the primary function of the tissue and its requirement of strength, the diameter of collagen fibrils varies around 1.5nm [51]. The strain-stiffening effect can be explained by the self-aligning and straightening of collagen fibrils [47], [48], [52]. Initially, collagen fibrils are randomly oriented, wavy, and in a relaxed condition when the deformation is small. Since the elastin is mainly responsible for load carrying at this stage, the stress-strain relation is approximately linear and the modulus is close to that of elastin (0.1–2 MPa).

As the deformation increases, collagen fibers start to align with the direction of tension and carry loads. The wavy collagen fibers gradually elongate, and this results in an increasing modulus, hence the convex stress-strain curve. After collagen fibers are entirely straightened along the load direction, the modulus of soft tissue reaches its maximum level and the stress-strain curve becomes almost linear again with a slight concave that is caused by relaxation.

Even though it is impossible to print nanoscale fibrils, the self-aligning and straightening process of stiff fibers can be imitated at a larger scale by embedding wavy, stiff microstructures into the soft polymeric matrix. Theoretically, the stiff structures would straighten up during elongation and compensate for the creep of the matrix polymer, or even outweigh the effect of creep, resulting in an increasing slope on the stress-strain curve. Indeed, strain-stiffening behaviors at certain degrees were observed in some of those designs, for example, the SW design. The degree of this strain-stiffening behavior, and the tensile properties in general, can be tuned by the parameters of the design. For the SW design, these tuning parameters can be: the wavelength λ; the amplitude, A, of the sinusoidal wave; and the radius of fibers r_f. To characterize a typical stress-strain curve with a stress-stiffening effect within the 0–20% strain range, the initial modulus (E_0), the modulus at 20% strain ($E_{0.2}$), the maximum modulus (E_i), and the strain at the inflection point (ε_i) can serve as the key specifications.

Wang et al. conducted a series of experiments to investigate the effects of each tuning parameter of the SW design on the stress-strain curve [53]. In their study, a Connex350 Polyjet printer (Stratasys, Eden Prairie, MN) was used to fabricate variants of dual-material metamaterial coupons. The materials were commercially available. The base materials used for the stiff fiber and elastic matrix are VeroBlackPlus® (RGD875) and TangoPlus® (FullCure 930), respectively. These two materials represent the two extremes of printable materials with VeroBlackPlus being the stiffest and TangoPlus the most elastic. The Connex350 can also mix the two base materials at a certain ratio and print them simultaneously to form digital materials that have mechanical properties between the base materials. In the present study, only the base materials were used to prepare the samples. It should be noted that the material choice could also serve as a tuning factor. The stress-strain curves of the single materials are shown in Figure 13.3. Both materials exhibited strain-softening as expected.

The results of tensile tests for the λ-variants of the SW design are presented in Figure 13.4. When other design parameters are fixed, as the wavelength increases, the fiber became more aligned with the direction of the load. As the stiff fibers with a higher degree of alignment carried

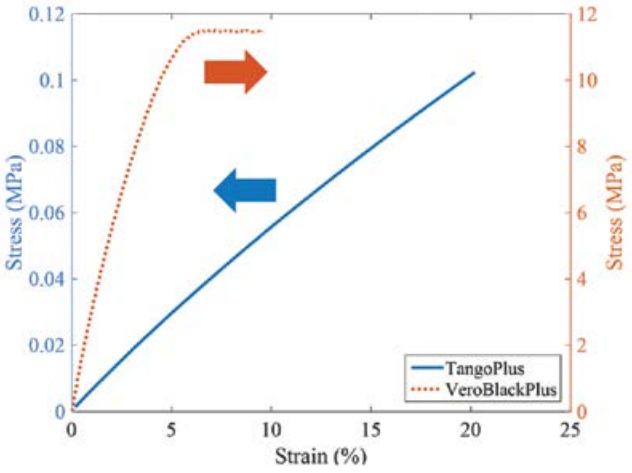

FIGURE 13.3 Stress-strain curves of pure TangoPlus sample (solid, left y-axis) and VeroBlackPlus sample (dotted, right y-axis).

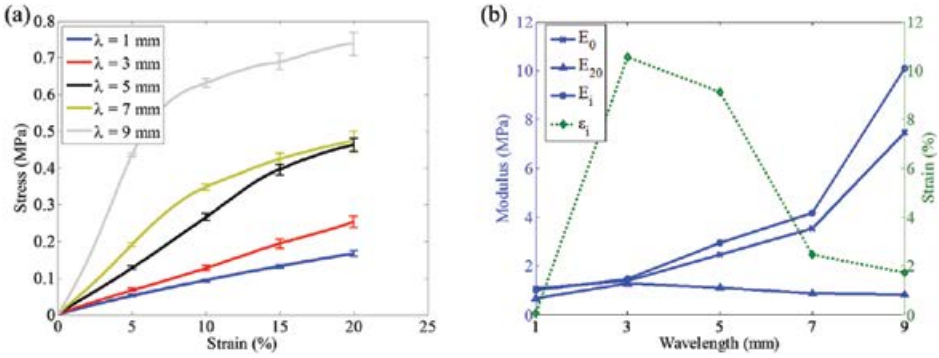

FIGURE 13.4 (a) The stress-strain curves of the SW design with different wavelengths; (b) the effect of the wavelength on curve specifications.

more load, the initial modulus, E_0, increased with the wavelength. We noticed that the moduli at 20% strain for all five variants were about the same. The reason is that at this strain level, the fiber structures in the variants were stretched to their limits where the degree of alignment was about 100%. Just like the stretching mechanism of soft tissues, the mechanical behavior became linear at 5–15% strain, depending on the initial waviness of the fibers. The five variants entered the "linear stage" before the 20% strain, therefore they all had similar E_{20}. Obviously, fibers with larger λ/A ratio will reach the straightened state faster. Therefore, variants with a larger wavelength have the inflection points at smaller strain levels. During the tensile test, it was observed that the samples were distorted after the fibers were straightened. This is because the stiff fibers had to push the soft material aside to become straight. The degree of distortion was positively correlated to the deformation of the fibers from their initial state to the straightened state. Hence, the larger E_i of metamaterials with a larger fiber wavelength can be explained by the fact that the distortion in those samples was smaller.

The results of the tensile tests for the *A*-variants of the SW design are presented in Figure 13.5. With the wavelength fixed, changing the amplitude allowed us to investigate the other portion of the λ/A spectrum. Similar to the λ-variants, higher initial modulus and higher maximum modulus were observed in variants with larger λ/A ratio, that is, smaller *A*. The location of the inflection point also followed the same trend. When the λ/A is very large (>20), the fibers are almost straight at the

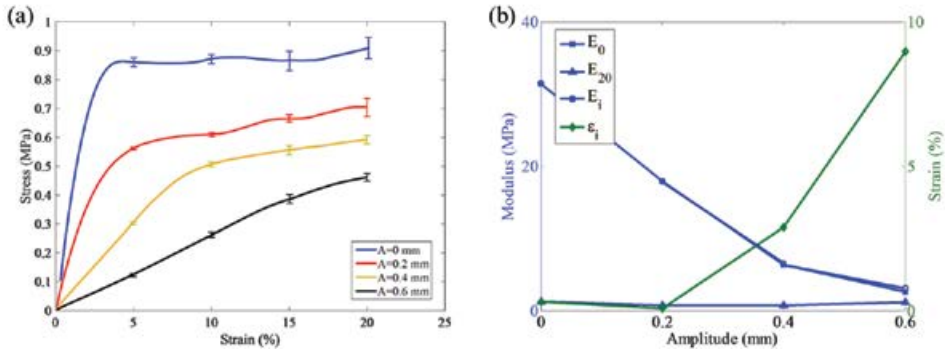

FIGURE 13.5 (a) The stress-strain curves of the SW design with different amplitudes; (b) the effect of the amplitude on curve specifications.

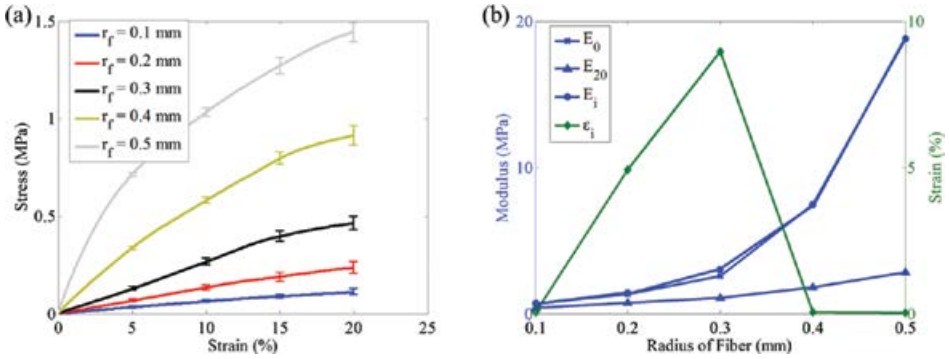

FIGURE 13.6 (a) The stress-strain curves of the SW design with different radii of the fiber; (b) the effect of the radius of the fiber on curve specifications.

initial state. No strain-stiffening effect was seen since the fibers carried most of the load from the beginning of the tensile tests. Also, the variants with straight or near straight fibers yielded around 4–5%, which is about the same as the strain of yield for VeroBlackPlus.

The results of tensile tests for the r_f-variants of the SW design are presented in Figure 13.6. Unlike the wavelength and the amplitude, changing the radius of fiber did not change the λ/A ratio. It changed the volume fraction of fiber. As expected, increasing values for the initial modulus, maximum modulus, and the modulus at 20% strain were observed as the radius of fiber increased. The existence of a "working window" for the radius of the fiber was also noticed. We observed that if r_f is too small or too large, the soft TangoPlus or the stiff VeroBlackPlus dominated the mechanical behavior of the metamaterial. In either case, the metamaterial did not give the desired strain stiffening. In this design, the lower limit of this window was between 0.1mm and 0.2mm; the upper limit was between 0.3mm and 0.4mm.

As shown in the results, the correlation between the specifications of the stress-strain curve and the design parameters is nonlinear and demands further investigation. Nevertheless, there are a few general design guidelines observed during the experiments that are summarized below:

1. The volume fraction of stiff fibers needs to be in a moderate range to prevent the mechanical behavior from being dominated by either material;
2. The "aspect ratio" a, i.e., λ/A for the SW design, can potentially be a good indicator for the strain-stiffening effect. E_0 and E_i are positively correlated to a, and ε_i is negatively correlated to a;
3. The radius of the fiber, r_f, can be used as a tuning parameter for the overall stiffness of the metamaterial.

Although the design space is currently limited by the material options and 3D printing technologies, this dual-material metamaterial design provides a potential method to bridge the inherent difference in mechanical behaviors of soft tissues and polymers. On the other hand, the strain-stiffening effects exhibited in the proposed designs were much weaker than what human tissues have. Great effort needs to be made to simulate real tissue with 3D printed phantoms. With evolving additive manufacturing technologies, it will be possible to fabricate "plastic tissues" with accurate mechanical properties that are associated with gender, age, ethnicity, and other physiological/pathological characteristics of a patient. Being able to represent the biomechanical responses, the mechanically accurate, patient-specific, tissue-mimicking phantoms would find more applications than the conventional geometric phantoms.

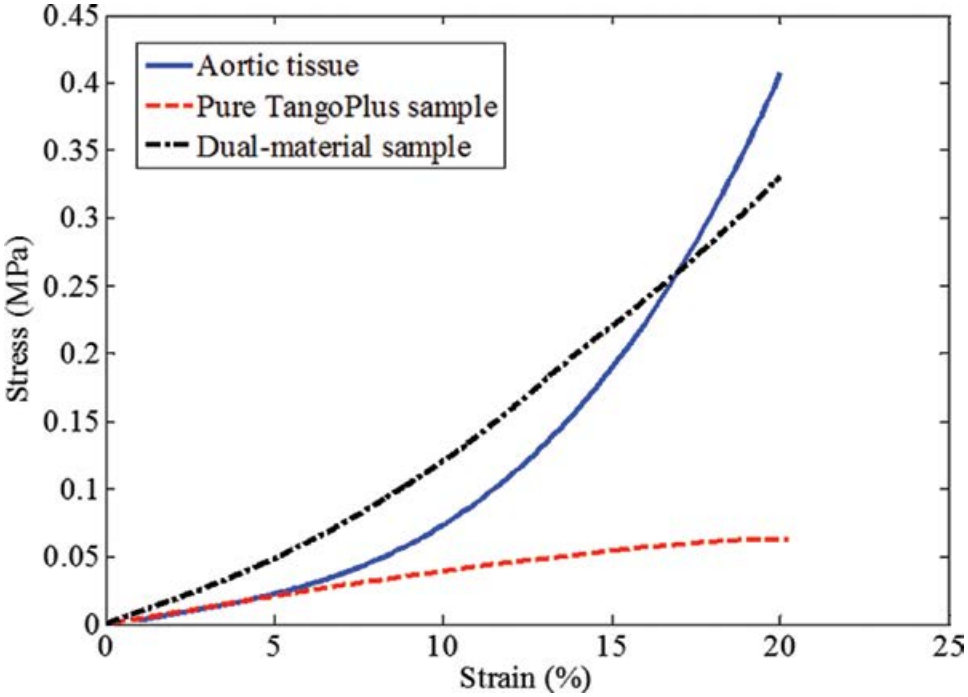

FIGURE 13.7 The comparison of stress-strain curves of a typical aortic tissue, a pure TangoPlus sample, and a dual-material sample. The dual-material sample used the SW design with $\lambda = 0.8mm$, $A = 0.65mm$, and $r_f = 0.1mm$.

13.3.3 Patient-Specific Aortic Valve Phantom

With the help of CAD and finite element analysis (FEA) tools, it is possible to approximate the mechanical properties of any soft tissue. As an example, an SW design with $\lambda = 0.8mm$, $A = 0.65mm$, and $r_f = 0.1mm$ was used to approximate aortic tissue. The comparison of the real aortic tissue, a pure TangoPlus sample, and the metamaterial sample is shown in Figure 13.7. Although the mechanical properties of the metamaterial are still different from those of real tissues, the stress-strain curve of the metamaterial followed the trend better than the pure TangoPlus sample did because the fibers straightened in the metamaterials, which compensated for the creep of the matrix. The dual-material 3D printing provided a way to tweak the mechanical behavior of the printed metamaterials.

This metamaterial approach can be integrated into the procedure of fabricating patient-specific aortic valve phantoms, during which a pre-procedural contrast-enhanced CT scan can be used to generate the 3D model of the aortic valve. The sinusoidal fibers are then embedded into the 3D model of the aortic wall to achieve strain-stiffening properties that are comparable to human aortic tissues. Finally, the 3D model is converted to the Stereolithography (STL) format and exported to a multi-material 3D printer for printing.

13.3.4 Pre-TAVR CT Imaging

Pre-TAVR contrast-enhanced CT scans are preferable for the 3D modeling of the aortic root. As shown in Figure 13.8, such scans are routinely performed on a modern multi-detector-row CT scanner using a standard TAVR CT protocol, which typically consists of a prospectively ECG-gated full R-R acquisition from the subclavian to the diaphragm, and an immediately following non-ECG-gated acquisition of the abdomen and pelvis. The tube voltage is typically set to 100–135 kVp

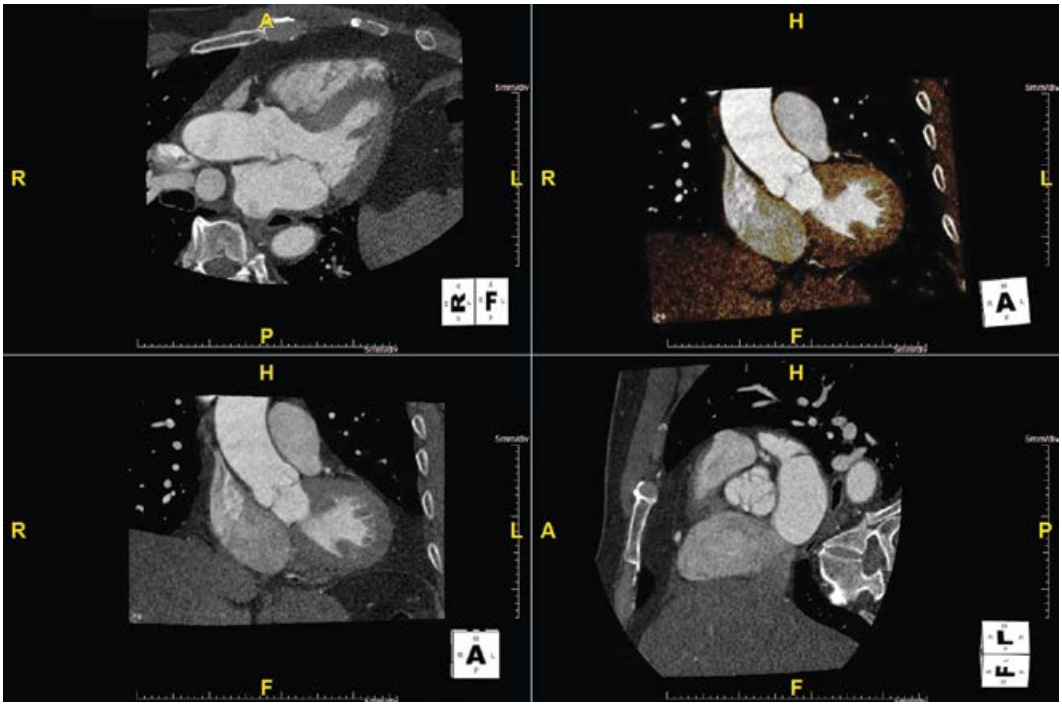

FIGURE 13.8 An example of the 3D contrast-enhanced pre-TAVR CT volume that covers the cardiac region (cardiac phase: 37% R-R).

depending on the patient's size. The tube current could be automatically selected by a modern scanner. The detector width of the scanner should be ≤0.65 mm. The gantry rotation time should be ≤350 ms. Cardiac CT images can be reconstructed with 10% increments starting at 0% of the R-R interval using a 0.5 mm slice thickness. The volume of iodinated contrast should be adapted to the patient's size (typical dosage: 80–125 ml) at a flow rate of 4.0–5.0 ml/s.

13.3.5 CT Image Analysis and 3D Modeling

The 3D model of the aortic valve should be reconstructed at a late systolic cardiac phase, in which the aortic valve has the maximum annular diameter. Therefore, the pre-TAVR CT images at peak aortic valve opening are identified and used to produce the 3D model of the aortic root. A research software (CT Auto Valve, Siemens Corporate Technology, Princeton, NJ) is used to semi-automatically segment the images and produce a single-layer 3D model of the aortic root, which consists of the arterial wall and the valvular leaflets, as shown in Figure 13.9. Proprietary in-house software has been further developed to refine the 3D model by extending the model into the ascending aorta and the left ventricular outflow tract (LVOT). The lowest level of the model was empirically set to 10 mm below the aortic valve annulus. In addition, our software empirically adds a 2.0-mm wall thickness to the aortic root and a 0.5-mm thickness to the leaflets.

Aortic valve calcification is a common condition in AS patients, in which calcium deposits form on the aortic valve, mainly due to aging and inflammation. Valvular calcification is a regulated process resembling the osteogenic process (bone formation). Calcified lesions on the aortic valve exhibit a rigid material property, which could be reproduced by 3D printing using a rigid printing material. To generate the 3D models of the calcium deposits on the aortic valve, as shown in Figure 13.9, the calcified lesions are segmented in 3D using a thresholding method, in which the

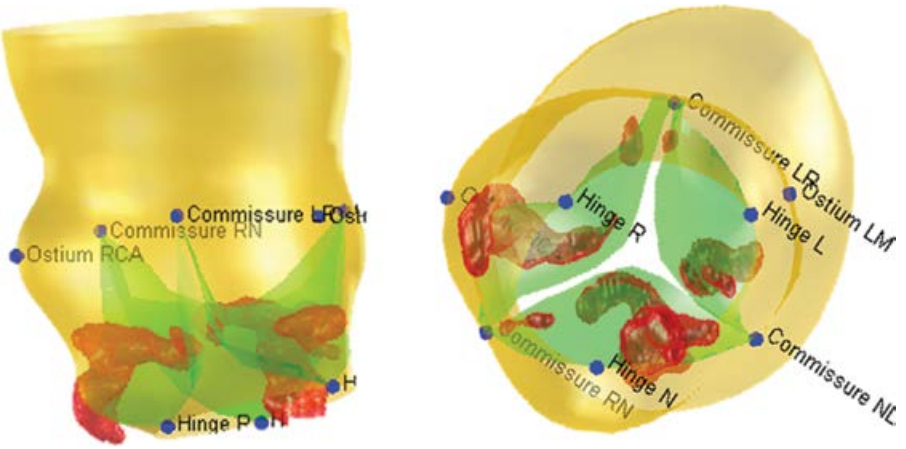

FIGURE 13.9 The aortic valve model viewing from the side and the LVOT. The aortic wall is depicted in yellow. The aortic leaflets are depicted in green. The calcified lesions are depicted in red. Anatomic landmarks are depicted in blue.

cut-off is set to the mean plus three standard deviations of the luman attenuation in the aortic root. The 3D meshes of the calcified lesions are generated using a marching cubes meshing method [54].

Based on the metamaterial configurations described in the previous section, sinusoidal fibers can be created and embedded in the 3D model of the aortic wall to achieve strain-stiffening properties that were comparable to human aortic tissues. Briefly, the amplitude, radius, and wavelength of the fibers are set to 0.4 mm, 0.5 mm, and 7.0 mm, respectively. As shown in Figure 13.10, the principal orientations of the fibers are aligned circumferentially to the aortic root model, while the sinusoidal is aligned radially. The fibers are designed to be semi-evenly distributed and adaptive to the model's local curvature, with the spacing approximately set to 2.0 mm. Finally, the 3D models of the aortic root, the leaflets, the calcified lesions, and the fibers are converted into the Stereolithography (STL) format, and exported to a 3D printer for printing.

13.3.6 3D Printing of the Aortic Valve Phantom

The 3D printing of the metamaterial phantom needs to be performed on a multi-material jetting printer, such as a PolyJet 3D printer (Objet 350, Stratasys, Israel). PolyJet 3D printing materials, TangoPlus, VeroWhitePlus, and a digital material RGD8525, which is a mix of TangoPlus and VeroWhitePlus, are used to print the aortic root soft tissues, the calcified lesions, and the embedded fibers, respectively. The 3D printer is able to read in STL files from up to 10 patient data sets in one batch, and it takes a total of 9 to 10 hours to print these 10 3D phantoms simultaneously. Post-print processing, such as removing the support materials, takes about 15 minutes for each phantom. The cost of the printing materials in each phantom is approximately $100 in December 2017.

13.4 DEVELOPMENT OF THE SENSOR-ENABLED 3D PRINTED PHANTOMS

The advantage of using the tissue-mimicking metamaterial technique is that it has greatly improved the fidelity of the procedural simulation on the 3D printed phantoms. In Qian et al.'s study [55], the same type and size of TAVR valves as in clinical use could be deployed in the tissue-mimicking phantoms. During the simulation process, the deployment depth and angle could be easily adjusted, and different deployment techniques could be tested. The deformation and interactions of the self-expanding prosthesis and the passively dilating aortic root could be closely monitored using sensor-enabled phantoms.

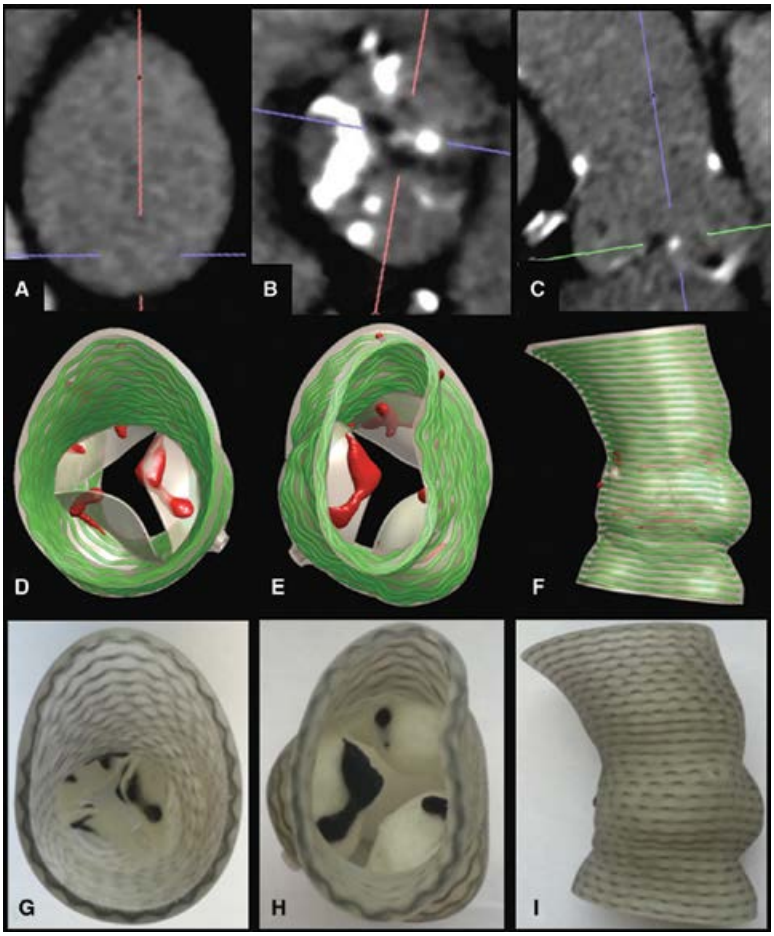

FIGURE 13.10 Computed tomography (CT) cross-sectional views show the ascending aorta (A), the Valsalva (B), and the longitudinal view (C). Three-dimensional (3D) computational model viewing shows the ascending aorta (D), the left ventricular outflow tract (E), and the side (F). The calcifications were drawn in red. The embedded fibers were drawn in green. (G to I) Images show the 3D-printed phantom. The calcifications and the fibers were printed with VeroBlackPlus for better illustration.

There are actually a variety of sensors that we could add to the 3D printed phantom for quantitative assessment of the relevant pathophysiological parameters. For example, as shown in Figure 13.11, flexible sensors could be directly written or attached onto the surface of the 3D printed phantom. They can be used to assess the pressure, temperature, flow velocity, and tissue strain.

Printed electronics by direct-write technologies show promise for use in a wide range of applications, such as thin film transistors, solar cells, RFIDs, antennas, sensors, and displays [56]–[60]. They are affordable, efficient, flexible, and environmentally friendly compared to conventional photolithographic, electroplating, and etching techniques [61]. The Aerosol Jet Printing (AJP) process developed by Optomec (Albuquerque, NM) uses aerodynamic focusing to deposit aerosolized materials onto planar or non-planar substrates and is capable of fabricating electronic features with sizes as small as 10 μm. It provides a viable solution to high resolution conformal printing. Generally, the AJP process consists of three stages: ink atomization, aerosol deposition, and post-processing. It has been proven to be applicable to print strain sensors directly on the surface of common 3D printed parts. A novel silver-carbon nanotube (Ag-CNT) hybrid ink has been developed to achieve high flexibility and a large strain sensing capability, as shown in Figure 13.11.

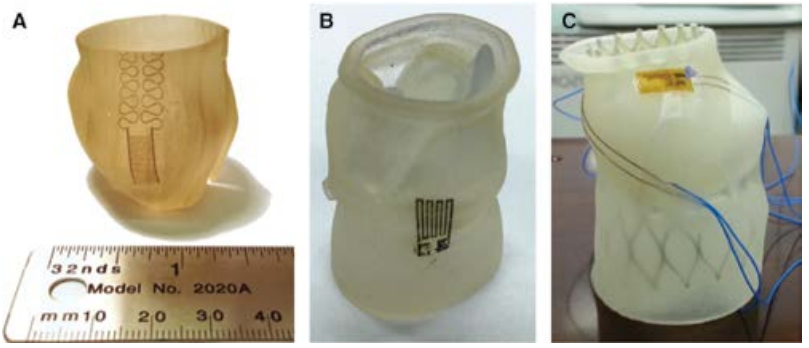

FIGURE 13.11 Examples of the sensor-enabled 3D printed phantoms. (A, B) The sensors are designed in-house and directly written onto the surface of the 3D printed phantoms using the AJP process. (C) The sensor is a commercial sensor attached to the surface of the phantom.

In addition, imaging landmarks can be attached to the 3D printed phantoms to work with ultrasound/CT/MRI to track tissue deformation and assess tissue strain. These measurements can be potentially applied to various clinical scenarios in cardiovascular medicine.

Qian et al. developed a CT-based strain quantification technique to quantify the post-TAVR aortic root strain distribution [55]. In this study, radiopaque beads were attached to the surface of the phantom circumferentially at the levels of the LVOT, the annulus, the center of the sinus of valsalva, the sinotubular junction, and the ascending aorta, as shown in Figure 13.12.

Because of its high spatial resolution and ease of use, CT imaging has been used to quantify the strain in vitro. The sensor-enabled phantom underwent two CT scans before and after the installation of the prosthetic valve in vitro. A modified CT calcium scoring protocol was used to measure the displacement of the radiopaque landmarks on the 3D printed phantoms before and after the deployment of the prosthesis. The CT images were acquired on a 320-detector row CT scanner (Aquilion ONE, Toshiba Medical Systems, Otawara, Japan) using the volumetric acquisition mode. The tube voltage was 120 kVp. The tube current was 250 mA. The detector width was 0.5 mm. The number of the detectors was 320. The reconstruction slice thickness was 0.5 mm. The threshold for detecting the radiopaque landmarks was 5000 HU.

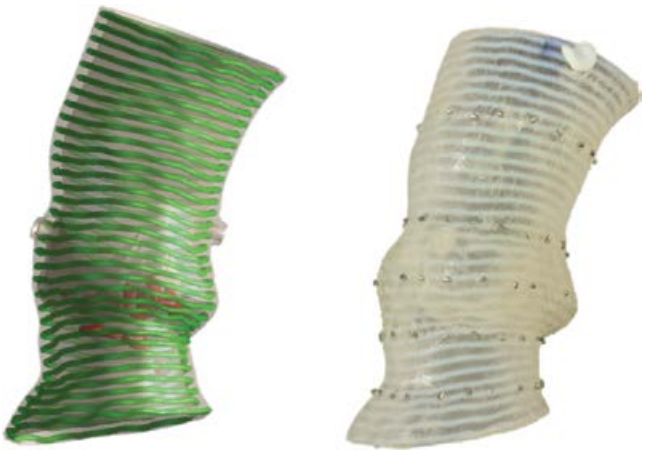

FIGURE 13.12 The 3D phantom was printed based on the 3D computer model. Then, radiopaque beads were manually attached to the surface of the 3D printed phantom to serve as strain landmarks.

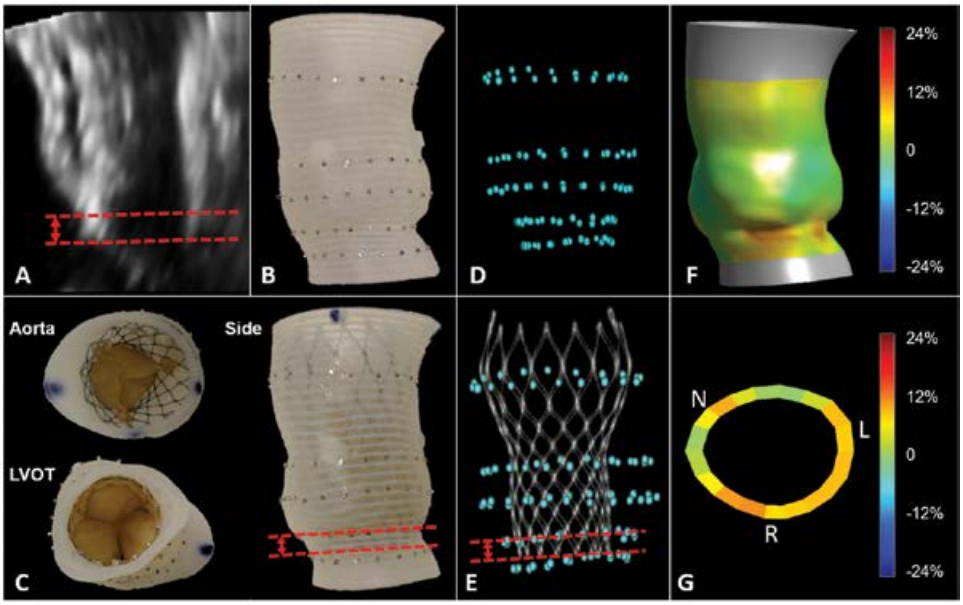

FIGURE 13.13 (A) The clinical intraprocedural transesophageal echocardiography is shown. Prosthesis deployment depth was measured as the distance between the annulus and the ventricular end of the prosthesis (red lines). (B) The three-dimensional-printed phantom with the radiopaque landmarks is shown. (C) The phantom implanted with the prosthesis, viewed from the aorta, the left ventricular outflow tract (LVOT), and the side. (D and E) These images are the three-dimensional reconstructions of the computed tomography scans of (B) and (C), respectively. As shown in (C) and (E), the prosthetic valve was implanted to the same depth as in (A). The strain distributions of the aortic root (F) and the annulus (G) are shown. L = left coronary cusp; N = noncoronary cusp; R = right coronary cusp.

The locations of the landmarks were extracted from the CT scans and the two sets of landmarks before and after the valve deployment were co-registered. The circumferential strains in the aortic root phantom were calculated by projecting the derivatives of the landmarks' displacements to the circumferential direction. As shown in Figure 13.13 (D-G), circumferential strains were quantified at the five levels, and the whole aortic root strain distribution could be obtained via interpolation based on the geodesic distance on the 3D model.

13.5 APPLICATION: PREDICTIONS OF POST-TAVR PVL

13.5.1 Background

In 2017, Qian et al. reported a study that aimed to develop a procedure simulation platform for TAVR using 3D printed patient-specific aortic valve phantoms [55]. It was a retrospective, single-center, observational study approved by the Institutional Review Board of Piedmont Healthcare. This study included 18 patients who underwent clinically indicated TAVR with a CoreValve system (self-expanding valve) (Medtronic, Minneapolis, Minnesota) between April 2014 and September 2015. The patients were selected using stratified random sampling, in which seven to eight patients were randomly selected in the none, trace-to-mild, and moderate-to-severe groups that constituted a representative spectrum of different degrees of post-TAVR PVL. Before the TAVR procedure, all patients received a contrast-enhanced cardiac CT scan. Prosthesis size was determined by the CT-derived annular diameter as per standard recommendation [62]. During the TAVR procedure, valve implantation was performed under the guidance of fluoroscopy and transesophageal echocardiography (TEE). Even though the initial positioning and anchoring of the self-expanding valve system was optimal

and successful in all 18 patients, TEE revealed that seven patients had moderate-to-severe PVL after the initial valve deployment, which required post-deployment balloon dilation in an attempt to reduce PVL. TEE post-balloon dilation showed the PVL in three of these patients was reduced to trace or mild, and in the other four, the PVL degrees remained unchanged.

13.5.2 Methods

Patient-specific 3D printed tissue-mimicking aortic valve phantoms of the 18 patients were fabricated with the procedure as previously described. For each patient, according to the size and model used in the clinical procedure, the same self-expanding valve prosthesis was selected and manually implanted in the 3D printed phantom in vitro. The prosthetic valve was carefully deployed to the same depth as in the clinical procedure and manually adjusted to ensure optimal orientation and apposition in the phantom, as shown in Figure 13.13 (C). Because the self-expanding valve is a shape memory device made of nitinol, the phantom and the implanted prosthesis were submerged in 37°C water to ensure the full expansion of the valve as in the in vivo environment.

The post-TAVR aortic root strain distribution was quantified in the 3D-printed phantom as described in the previous section. As shown in Figure 13.14, a bulge detector was designed to detect the low-high-low strain pattern along the phantom's annulus after the in vitro implantation. It was formulated to be a Mexican hat wavelet [6], which is a digital filter that has a shape similar to a Mexican hat. It is usually used to detect the low-high-low pattern in a series of numbers. It can be derived by taking the negative normalized second derivative of a Gaussian function. Based on the design of the CoreValve prosthesis, which had 12 or 15 struts at the ventricular end (the CoreValve 23mm has 12 struts, and all the other sized valves have 15 struts), the width of the detector's positive peak was set to equal the circular angle between two adjacent struts at the ventricular end of the self-expanding valve. The bulge index was calculated by convolving the annular strain with the bulge detector, and in each phantom, the maximum bulge index was reported.

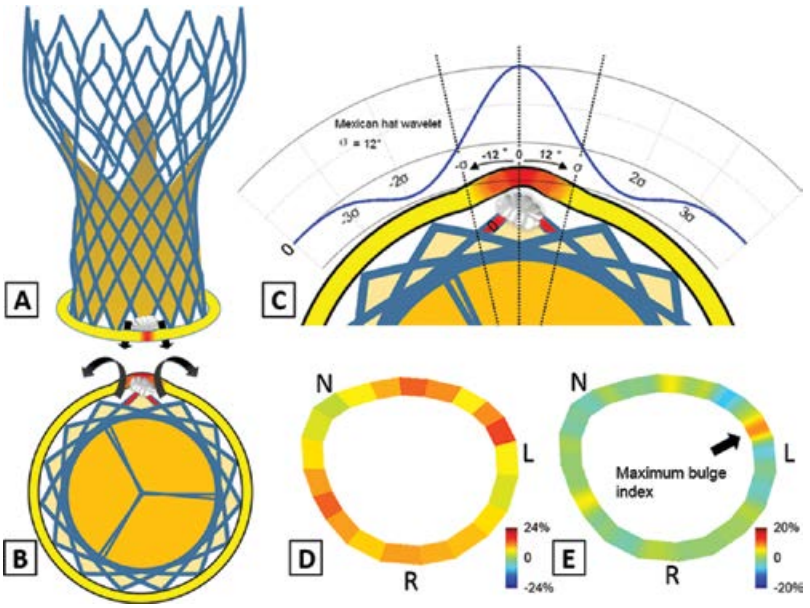

FIGURE 13.14 (A and B) Illustrations of the hypothesis of the paravalvular leak mechanism. Focal strain unevenness could be caused by annular anomalies, such as annular calcification. When the scale of the low-high-low strain pattern was similar to the interstrut circular angle, paravalvular leaking tended to occur. (C) The design of the bulge detector is shown. The results are shown as annular strain (D) and bulge index (E) maps.

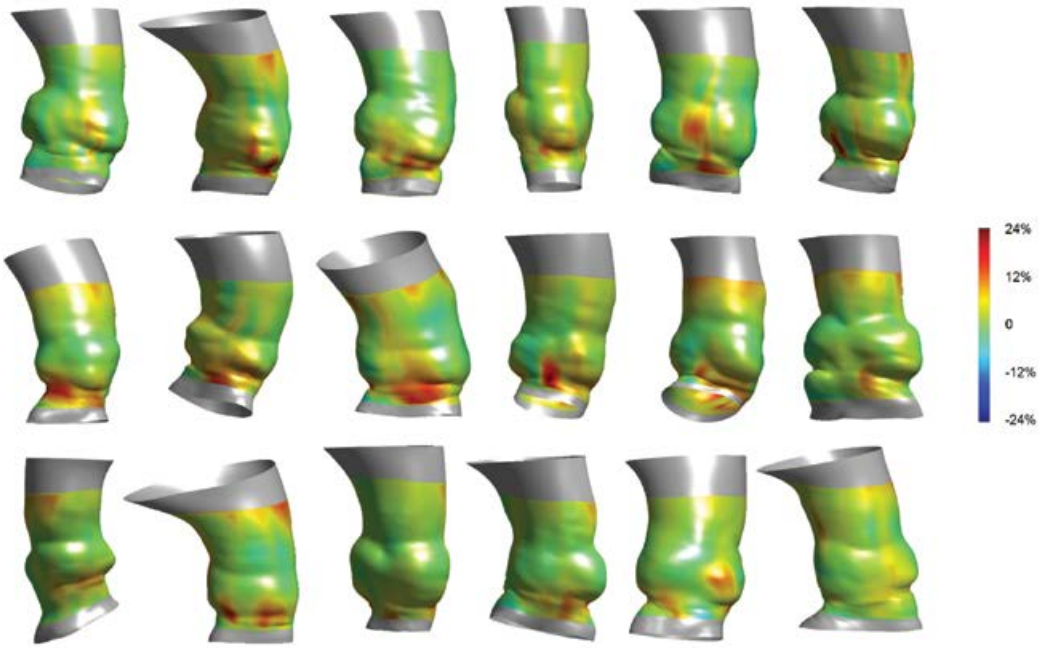

FIGURE 13.15 Illustrations of the aortic root strain distributions in the 18 patients.

13.5.3 Results and Discussion

As shown in Figure 13.15, each phantom's strain distribution showed a distinctive pattern. At the annular level, the maximum, mean, and minimum circumferential strain was 15.7% ± 4.3%, 8.1% ± 3.6%, 1.3% ± 4.1%, respectively. As shown in Table 13.1, the maximum annular bulge index was significantly different among the three PVL subgroups ($p = 0.047$) immediately after valve deployment, with higher bulge index being associated with the higher degree of PVL. Balloon expansion was done after initial deployment for >mild PVL in seven patients. Three of these patients were reassigned to the trace-mild subgroup. Similar to pre-balloon dilation, the maximum annular bulge index was significantly different among the three reclassified subgroups ($p = 0.001$). But, pairwise comparison showed that the bulge index in the moderate-severe PVL group was now significantly higher than in the other two subgroups.

Figure 13.16 compared the predictions of the PVL locations using bulge index and the actual PVL locations from TEE for 12 patients who had any degree of post-TAVR PVL. The bulge index predicted the locations of the dominant PVL in nine patients (accuracy = 75%). In patients #1 and #5, who had multiple PVL sites, the second largest bulge index position predicted the dominant PVL location, whereas the maximum bulge index predicted a minor PVL site. In patient #6, the annular strain distribution showed multiple high bulges (indicated by the warm color) besides the maximum bulge site, and only 1 of them predicted PVL.

Table 13.2 compared the power of prediction by the Annular Bulge Index with other known predictors. It indicated that Annular Calcification was the best predictor of moderate-to-severe PVL (ROC AUC = 83%; 95% confidence interval [CI]: 58% to 96%; $p < 0.001$) after initial deployment. Bulge index was a significant but less accurate predictor (AUC = 77%; 95% CI: 51% to 93%; $p = 0.04$). However, no other variables were predictive of PVL. Post-balloon expansion annular calcium lost its predictive power. Instead, bulge index became the only significant predictor of moderate-to-severe PVL (AUC = 95%; 95% CI: 73% to 99.9%; $p < 0.0001$), and it achieved a net reclassification improvement of 25% over annular calcium.

TABLE 13.1

Annular bulge index compared with other known predictors of PVL.

ANOVA analysis was performed to test if the variables were significantly different in the three PVL subgroups defined as before or after the post-deployment balloon dilation.* indicates that the Levene's test was positive, and the Kruskal-Wallis test was performed.

	Immediately after valve deployment and before post-TAVR dilation				
	No PVL	Trace to mild PVL	Moderate to severe PVL	ANOVA p value	Total
Annular Bulge Index	3.7% ± 1.2%	5.4% ± 1.7%	7.2% ± 3.2%	**0.047**	5.6% ± 2.7%
Aortic Calcium Volume* (mm^3)	670 ± 653	572 ± 383	707 ± 199	0.79*	657 ± 421
Annular Calcium Volume (mm^3)	59 ± 60	74 ± 78	156 ± 69	**0.048**	101 ± 79
LVOT Calcium Volume* (mm^3)	2 ± 3	8 ± 9	37 ± 40	0.13*	17 ± 29
Annular Ellipticity	1.31 ± 0.18	1.27 ± 0.14	1.31 ± 0.07	0.87	1.30 ± 0.09
Prosthesis Diameter to Annular Diameter Ratio	1.14 ± 0.08	1.17 ± 0.08	1.17 ± 0.05	0.66	1.16 ± 0.07
	After post-TAVR balloon dilation				
	No PVL	Trace to mild PVL	Moderate to severe PVL	ANOVA p value	Total
Annular Bulge Index	3.7% ± 1.2%	5.2% ± 1.8%	9.1% ± 2.5%	**0.001**	5.6% ± 2.7%
Aortic Calcium Volume* (mm^3)	670 ± 653	645 ± 347	661 ± 109	0.96*	657 ± 421
Annular Calcium Volume (mm^3)	59 ± 60	108 ± 85	149 ± 78	0.20	101 ± 79
LVOT Calcium Volume* (mm^3)	2 ± 3	8 ± 10	58 ± 42	0.07*	17 ± 29
Annular Ellipticity	1.31 ± 0.18	1.30 ± 0.12	1.27 ± 0.06	0.90	1.30 ± 0.09
Prosthesis Diameter to Annular Diameter Ratio	1.14 ± 0.08	1.17 ± 0.07	1.18 ± 0.02	0.62	1.16 ± 0.07

The comparison showed that the annular bulge index outperformed the other morphologic variables in predicting PVL post-balloon dilation. A possible explanation for this is that the bulge index is a mechanical descriptor of the strain / stress mismatch in the post-TAVR annulus, and therefore it is more directly associated with PVL than morphological descriptors, such as the annular calcium volume. In addition, balloon dilation likely worked as a fine-tuning tool that smoothed the strain mismatch caused by calcium and adjusted the contact between the prosthesis and the aortic root, and thus improved the sealing of the annulus.

Furthermore, we found that a bulge detector scale that equaled the inter-strut angle of the CoreValve at the ventricular end (24° for valve sizes ≥26mm, and 30° for 23mm valve size) performed the best with regard to the prediction of ≥moderate PVL (Figure 13.17) before and after balloon dilation. On the contrary, smaller and larger scale bulge detectors were not as good for predicting significant PVL. Perhaps the random distribution of the severity and location of annular calcium, which creates various scales of strain unevenness, results in imperfect annular sealing and significant PVL. Balloon dilation likely smoothed out these areas of large annular unevenness in a global fashion. However, it may not as effectively fix focal PVL that is caused by small scale of strain unevenness that extends between two adjacent struts. Thus, annular calcium volume was superior to the bulge detector pre-balloon to predict significant PVL. However, if the bulge persists between two consecutive struts even after balloon dilation, then there is likely to be significant residual PVL. This hypothesis is exemplified by Patient #5 in Figure 13.16 where the pre-balloon PVL was located at 12 o'clock within an area of large annular strain but with an angular extent that was larger than 24° and, hence, was not seen as a hot area in the bulge index map. This PVL

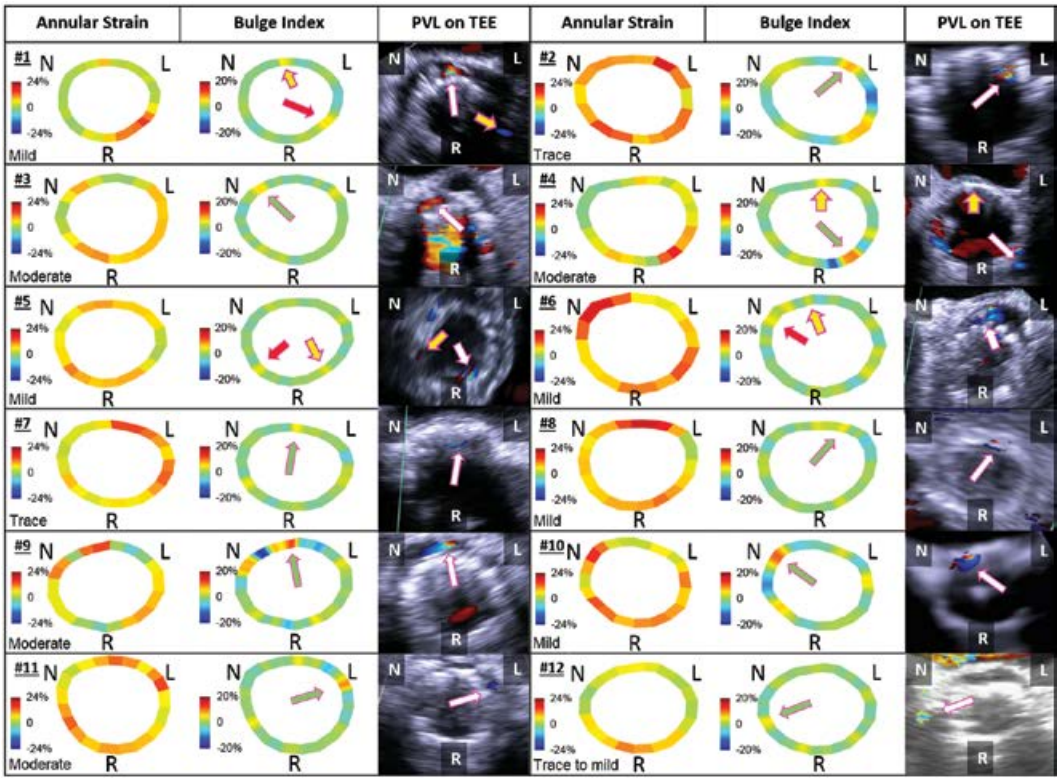

FIGURE 13.16 In the bulge index images, green arrows indicate correct predictions of the dominant PVL sites; red arrows indicate that the maximum bulge index did not predict the dominant PVL site; yellow arrows indicate that a submaximal high bulge index corresponded to the dominant PVL site. In the transesophageal echocardiography (TEE) images, white arrows indicate the dominant PVL sites, and yellow arrows indicate minor PVL sites.

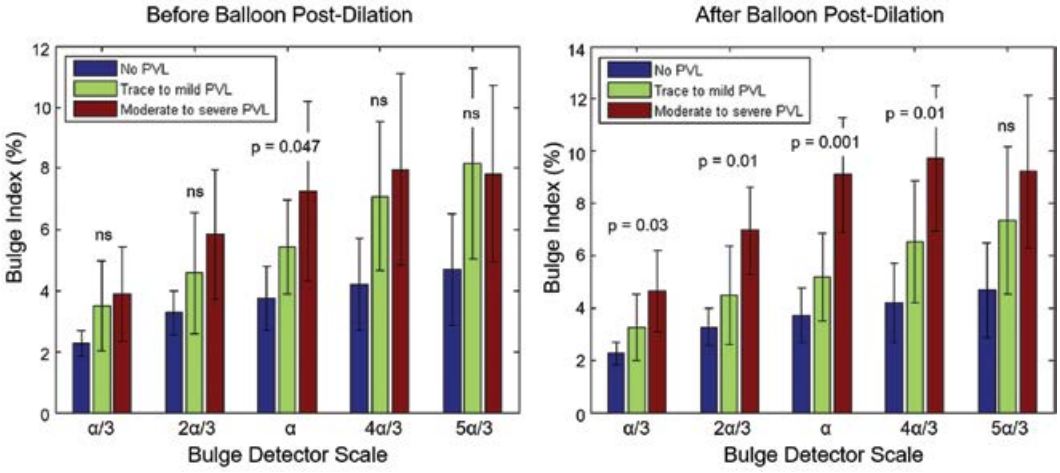

FIGURE 13.17 Comparison of the discernibility of PVL subgroups using ANOVA based on the bulge indices calculated with variant detector scales. Detector scale is defined as the circular angle of the detector's positive portion. α is the inter-strut angle of the CoreValve ($\alpha = 24°$ for valve sizes $\geq$ 26mm, and 30° for CoreValve 23mm). For each detector scale, ANOVA significant p value or non-significant (ns) is reported.

TABLE 13.2

MWW-test and ROC analysis of the annular bulge index in predicting dichotomized PVL, compared with other known predictors.

	Immediately after valve deployment and before post-TAVR dilation							
	<Moderate PVL	**≥Moderate PVL**	**MWW-test p value**	**ROC AUC**	**ROC p value**	**ROC cutoff**	**Sensitivity**	**Specificity**
Annular Bulge Index	4.5% ± 1.6%	7.2% ± 3.2%	0.06	**76.6%**	**0.04**	0.056	71.43	81.82
Aortic Calcium Volume	626 ± 524	707 ± 199	0.50	59.7%	0.50	356	100	45.45
Annular Calcium Volume	59 ± 60	156 ± 69	**0.02**	**83.1%**	**0.0007**	83	85.71	72.73
LVOT Calcium Volume	2 ± 3	37 ± 40	0.11	72.7%	0.11	8.6	57.14	90.91
Annular Ellipticity	1.29 ± 0.15	1.31 ± 0.07	0.62	57.1%	0.62	1.25	85.71	54.55
Prosthesis Diameter to Annular Diameter Ratio	1.16 ± 0.08	1.17 ± 0.05	0.22	55.8%	0.69	1.14	85.71	54.55
	After post-TAVR balloon dilation							
	<Moderate PVL	**≥Moderate PVL**	**MWW-test p value**	**ROC AUC**	**ROC p value**	**ROC cutoff**	**Sensitivity**	**Specificity**
Annular Bulge Index	4.6% ± 1.7%	9.1% ± 2.5%	**0.008**	**94.6%**	**<0.0001**	0.056	100	78.57
Aortic Calcium Volume	656 ± 479	661 ± 109	0.92	51.8%	0.90	441	100	50
Annular Calcium Volume	87 ± 77	149 ± 78	0.14	75%	0.07	151	75	78.57
LVOT Calcium Volume	5 ± 8	58 ± 42	0.07	80.4%	0.12	24	75	100
Annular Ellipticity	1.31 ± 0.14	1.27 ± 0.06	0.67	57.1%	0.63	1.33	100	42.86
Prosthesis Diameter to Annular Diameter Ratio	1.16 ± 0.08	1.18 ± 0.02	0.92	60.7%	0.42	1.15	100	7.14

disappeared post-balloon as we would expect from the hypothesis that the balloon dilation evens out large bulge areas. Additionally, the final residual mild PVL was now located at 5 and 7 o'clock positions at the sites of the bulges with angular extents close to 24°.

The annular bulge index in this study was designed to be a novel indicator of the post-TAVR annular strain unevenness. It can be quantified by in vitro TAVR simulation on a 3D printed patient-specific phantom, using unique tissue-mimicking metamaterials. This bulge index outperformed established variables and achieved a high degree of accuracy in predicting the occurrence, severity, and location of post-TAVR PVL. Thus, it may be feasible to perform procedural simulations on a 3D printed phantom for pre-TAVR planning, especially in those who are at high-risk for post-TAVR PVL. This may refine the current approach for the selection of valve type/size and potentially reduce the rate of post-TAVR PVL.

13.5.4 A Case Review

Patient #5 was an 84-year-old female. She received a CoreValve Evolut R 29 mm prosthetic valve via the subclavian approach. She had moderate PVL after the initial valve deployment, which was reduced to the mild level after balloon post-dilation. As shown in Figure 13.18, patient #5 had two large calcified lesions on the annulus in the proximity of the non and left aortic valve leaflets (A), which caused two areas of relatively high annular strain values between them. The warm-colored area between 11 and 2 o'clock (B) had a large patch of high strain between them, where a moderate PVL was seen before the balloon dilation (D). However, because of the angular extent of this area that was greater than 24°, it was not detected in the bulge index map (C). This PVL disappeared

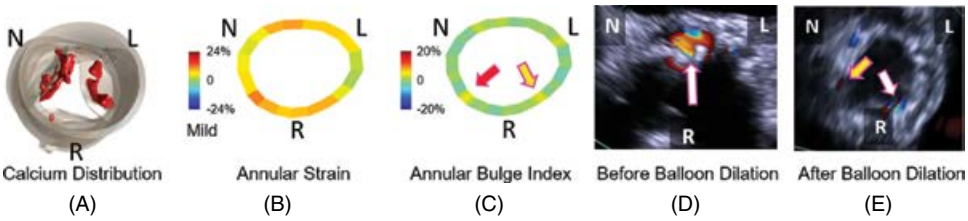

FIGURE 13.18 **A** shows the patient's aortic calcium distribution. Calcium was depicted in red. **B** and **C** show the in vitro derived annular strain and annular bulge index, respectively. **D** and **E** show the PVL on echocardiographs before and after the balloon dilation, respectively.

post-balloon (E) as we would expect from the hypothesis that the balloon dilation evens out large bulge areas. On the other hand, the warm-colored area between 5 and 7 o'clock had high strain values in B, which included two small-scale bulges that were detected at the 5 and 7 o'clock positions in the bulge index map (C, arrows). The final residual mild PVL was seen at the 5 and 7 o'clock positions, which agreed with the bulge index map. However, the position of the highest bulge index (5 o'clock) corresponded to a minor PVL location, and the position of the second highest bulge index (7 o'clock) corresponded to the major PVL location (E).

13.6 CONCLUSION

In conclusion, 3D printed patient-specific tissue-mimicking phantoms have the potential to play a more important role than conventional medical phantoms do in pre-operative assessment. In this chapter, their applications in the prediction of PVL post-TAVR have been explored extensively. The 3D printed phantom potentially provides a practical way to quantitatively assess the distribution of post-TAVR annular strain in vitro, which has proven to be closely associated with the occurrence and severity of PVL. This may lead to a better understanding of the role of the annular calcification in the genesis of PVL, and may be extendable to other transcatheter valve therapies. However, the 3D tissue-mimicking technique described in this chapter is still limited by the material printability and the resolution of 3D printing technologies. Great effort needs to be made to improve the mechanical or even the bio-fidelity of the tissue-mimicking 3D printed phantoms. Combining with the current trend of attachable/printable sensors, such as the flexible electronics, the multifunctional "smart phantoms," which are equipped with tissue-mimicking, sensing, and actuation capabilities, might become a trend that may eventually shift the paradigm of future healthcare.

References

1. K. Maganti, V. H. Rigolin, M. E. Sarano, and R. O. Bonow, "Valvular heart disease: diagnosis and management," *Mayo Clin. Proc.*, vol. 85, no. 5, pp. 483–500, May 2010.
2. R. A. Siemieniuk *et al.*, "Transcatheter versus surgical aortic valve replacement in patients with severe aortic stenosis at low and intermediate risk: systematic review and meta-analysis," *BMJ*, vol. 354, p. i5130, Sep. 2016.
3. S. K. Kodali *et al.*, "Two-year outcomes after transcatheter or surgical aortic-valve replacement," *N. Engl. J. Med.*, vol. 366, no. 18, pp. 1686–1695, May 2012.
4. P. Généreux *et al.*, "Paravalvular leak after transcatheter aortic valve replacement: the new Achilles' heel? A comprehensive review of the literature," *J. Am. Coll. Cardiol.*, vol. 61, no. 11, pp. 1125–1136, Mar. 2013.
5. Q. Wang, C. Primiano, R. McKay, S. Kodali, and W. Sun, "CT image-based engineering analysis of transcatheter aortic valve replacement," *JACC Cardiovasc. Imaging*, vol. 7, no. 5, pp. 526–528, May 2014.
6. J. W. J. Hosken, "Ricker wavelets in their various guises," *First Break*, vol. 6, no. 1203, 1988.

7. A. Curodeau, E. Sachs, and S. Caldarise, "Design and fabrication of cast orthopedic implants with freeform surface textures from 3-D printed ceramic shell," *J. Biomed. Mater. Res.*, vol. 53, no. 5, pp. 525–535, 2000.
8. S. V. Murphy and A. Atala, "3D bioprinting of tissues and organs," *Nat. Biotechnol.*, vol. 32, no. 8, pp. 773–785, 2014.
9. D. E. Robinson and G. Kossoff, "Performance tests of ultrasonic echoscopes for medical diagnosis," *Radiology*, vol. 104, no. 1, pp. 123–132, 1972.
10. E. L. Madsen and G. D. Fullerton, "Prospective tissue-mimicking materials for use in NMR imaging phantoms," *Magn. Reson. Imaging*, vol. 1, no. 3, pp. 135–141, 1982.
11. D. C. Goldstein, H. L. Kundel, M. E. Daube-Witherspoon, L. E. Thibault, and E. J. Goldstein, "A silicone gel phantom suitable for multimodality imaging," *Invest. Radiol.*, vol. 22, no. 2, pp. 153–157, 1987.
12. M. D. Mitchell, H. L. Kundel, L. Axel, and P. M. Joseph, "Agarose as a tissue equivalent phantom material for NMR imaging," *Magn. Reson. Imaging*, vol. 4, no. 3, pp. 263–266, 1986.
13. M. W. Groch, J. A. Urbon, W. D. Erwin, and S. Al-Doohan, "An MRI tissue equivalent lesion phantom using a novel polysaccharide material," *Magn. Reson. Imaging*, vol. 9, no. 3, pp. 417–421, 1991.
14. N. L. Bush and C. R. Hill, "Gelatine-alginate complex gel: A new acoustically tissue-equivalent material," *Ultrasound Med. Biol.*, vol. 9, no. 5, pp. 479–484, 1983.
15. J. C. Bamber and N. L. Bush, "Freehand elasticity imaging using speckle decorrelation rate," in *Acoustical Imaging*, 1996, pp. 285–292.
16. E. L. Madsen, G. R. Frank, and F. Dong, "Liquid or solid ultrasonically tissue-mimicking materials with very low scatter," *Ultrasound Med. Biol.*, vol. 24, no. 4, pp. 535–542, May 1998.
17. W. D. D'Souza, E. L. Madsen, O. Unal, K. K. Vigen, G. R. Frank, and B. R. Thomadsen, "Tissue mimicking materials for a multi-imaging modality prostate phantom," *Med. Phys.*, vol. 28, no. 4, pp. 688–700, Apr. 2001.
18. K. V. Ramnarine, P. R. Hoskins, H. F. Routh, and F. Davidson, "Doppler backscatter properties of a blood-mimicking fluid for Doppler performance assessment," *Ultrasound Med. Biol.*, vol. 25, no. 1, pp. 105–110, Jan. 1999.
19. S. K. Nadkarni, H. Austin, G. Mills, D. Boughner, and A. Fenster, "A pulsating coronary vessel phantom for two- and three-dimensional intravascular ultrasound studies," *Ultrasound Med. Biol.*, vol. 29, no. 4, pp. 621–628, 2003.
20. X. Zhang and J. F. Greenleaf, "Measurement of wave velocity in arterial walls with ultrasound transducers," *Ultrasound Med. Biol.*, vol. 32, no. 11, pp. 1655–1660, 2006.
21. Y. Kawase *et al*., "Comparison of nonuniform rotational distortion between mechanical IVUS and OCT using a phantom model," *Ultrasound Med. Biol.*, vol. 33, no. 1, pp. 67–73, Jan. 2007.
22. Kondo, Toshio, Mituyoshi Kitatuji, and H. Kanda, "New tissue mimicking materials for ultrasound phantoms," *Ultrasonics Symposium*, 2005 IEEE. Vol. 3. IEEE, 2005.
23. K. Zell *et al*., "Acoustical properties of selected tissue phantom materials for ultrasound imaging," *Physics in Medicine and Biology*, vol. 52, no. 20, p. N475, 2007.
24. J. Ophir, "Ultrasound phantom material," *The British Journal of Radiology*, vol. 57, no. 684, p. 1161, 1984.
25. R. A. Lerski, T. C. Duggan, and J. Christie, "A simple tissue-like ultrasound phantom material," *The British Journal of Radiology*, vol. 55, no. 650, pp. 156–157, 1982.
26. J. Robertson *et al*., "Flow measurement using duplex Doppler ultrasound: haemodynamic changes in patients with colorectal liver metastases," *Clinical Physics and Physiological Measurement*, vol. 13, no. 4, p. 299, 1992.
27. M. Lazebnik, E. L. Madsen, G. R. Frank, and S. C. Hagness, "Tissue-mimicking phantom materials for narrowband and ultrawideband microwave applications," *Phys. Med. Biol.*, vol. 50, no. 18, pp. 4245–4258, 2005.
28. R. K. Wang, Z. Ma, and S. J. Kirkpatrick, "Tissue Doppler optical coherence elastography for real time strain rate and strain mapping of soft tissue," *Appl. Phys. Lett.*, vol. 89, no. 14, p. 144103, 2006.
29. M.-K. Sun *et al*., "Reusable tissue-mimicking hydrogel phantoms for focused ultrasound ablation," *Ultrason. Sonochem.*, vol. 23, pp. 399–405, Mar. 2015.
30. O. Lund *et al*., "Primary aortic valve replacement with allografts over twenty-five years: Valve-related and procedure-related determinants of outcome," *J. Thorac. Cardiovasc. Surg.*, vol. 117, no. 1, pp. 77–91, 1999.
31. J. M. Brown, S. M. O'Brien, C. Wu, J. A. H. Sikora, B. P. Griffith, and J. S. Gammie, "Isolated aortic valve replacement in North America comprising 108,687 patients in 10 years: changes in risks, valve types, and outcomes in the Society of Thoracic Surgeons National Database," *J. Thorac. Cardiovasc. Surg.*, vol. 137, no. 1, pp. 82–90, Jan. 2009.

32. A. Tsamis, J. T. Krawiec, and D. A. Vorp, "Elastin and collagen fibre microstructure of the human aorta in ageing and disease: a review," *J. R. Soc. Interface*, vol. 10, no. 83, p. 20121004, Jun. 2013.
33. A. Sulaiman *et al*., "In vitro non-rigid life-size model of aortic arch aneurysm for endovascular prosthesis assessment," *Eur. J. Cardiothorac. Surg.*, vol. 33, no. 1, pp. 53–57, Jan. 2008.
34. D. W. Hutmacher, "Scaffolds in tissue engineering bone and cartilage," in *The Biomaterials: Silver Jubilee Compendium*, 2000, pp. 175–189.
35. D. W. Hutmacher, M. Sittinger, and M. V. Risbud, "Scaffold-based tissue engineering: rationale for computer-aided design and solid free-form fabrication systems," *Trends Biotechnol.*, vol. 22, no. 7, pp. 354–362, Jul. 2004.
36. F. P. W. Melchels, M. A. N. Domingos, T. J. Klein, J. Malda, P. J. Bartolo, and D. W. Hutmacher, "Additive manufacturing of tissues and organs," *Prog. Polym. Sci.*, vol. 37, no. 8, pp. 1079–1104, 2012.
37. D. Seliktar, D. Dikovsky, and E. Napadensky, "Bioprinting and tissue engineering: recent advances and future perspectives," *Isr. J. Chem.*, vol. 53, no. 9–10, pp. 795–804, Oct. 2013.
38. S. Bose, S. Vahabzadeh, and A. Bandyopadhyay, "Bone tissue engineering using 3D printing," *Mater. Today*, vol. 16, no. 12, pp. 496–504, 2013.
39. G. Biglino, P. Verschueren, R. Zegels, A. M. Taylor, and S. Schievano, "Rapid prototyping compliant arterial phantoms for in-vitro studies and device testing," *J. Cardiovasc. Magn. Reson.*, vol. 15, no. 1, p. 2, 2013.
40. A. J. Cloonan, D. Shahmirzadi, R. X. Li, B. J. Doyle, E. E. Konofagou, and T. M. McGloughlin, "3D-printed tissue-mimicking phantoms for medical imaging and computational validation applications," *3D Print Addit Manuf*, vol. 1, no. 1, pp. 14–23, Mar. 2014.
41. M. L. Raghavan, M. W. Webster, and D. A. Vorp, "Ex vivo biomechanical behavior of abdominal aortic aneurysm: Assessment using a new mathematical model," *Ann. Biomed. Eng.*, vol. 24, no. 5, pp. 573–582, 1996.
42. J. B. Pendry, A. J. Holden, W. J. Stewart, and I. Youngs, "Extremely low frequency plasmons in metallic mesostructures," *Phys. Rev. Lett.*, vol. 76, no. 25, pp. 4773–4776, 1996.
43. J. B. Pendry, A. J. Holden, D. J. Robbins, and W. J. Stewart, "Magnetism from conductors and enhanced nonlinear phenomena," *IEEE Trans. Microw. Theory Tech.*, vol. 47, no. 11, pp. 2075–2084, Nov. 1999.
44. J.-H. Lee, J. P. Singer, and E. L. Thomas, "Micro-/nanostructured mechanical metamaterials," *Adv. Mater.*, vol. 24, no. 36, pp. 4782–4810, Sep. 2012.
45. K. Wang, Y.-H. Chang, Y. Chen, C. Zhang, and B. Wang, "Designable dual-material auxetic metamaterials using three-dimensional printing," *Mater. Des.*, vol. 67, pp. 159–164, Feb. 2015.
46. K. Wang, C. Wu, Z. Qian, C. Zhang, B. Wang, and M. A. Vannan, "Dual-material 3D printed metamaterials with tunable mechanical properties for patient-specific tissue-mimicking phantoms," *Additive Manufacturing*, vol. 12, pp. 31–37, Oct. 2016.
47. Y.-C. Fung, *Biomechanics*. New York, NY: Springer New York, 1993.
48. G. A. Holzapfel and R. W. Ogden, *Biomechanics of Soft Tissue in Cardiovascular Systems*. Springer Science & Business Media, 2003.
49. A. A. H. J. Sauren, M. C. van Hout, A. A. van Steenhoven, F. E. Veldpaus, and J. D. Janssen, "The mechanical properties of porcine aortic valve tissues," *J. Biomech.*, vol. 16, no. 5, pp. 327–337, 1983.
50. C. A. J. Hoeve and P. J. Flory, "The elastic properties of Elastin 1, 2," *J. Am. Chem. Soc.*, vol. 80, no. 24, pp. 6523–6526, Dec. 1958.
51. M. Nimni, "The molecular biology of collagen and structural glycoproteins," in *The Comparative Molecular Biology of Extracellular Matrices*, 1972, pp. 297–385.
52. F. H. Silver, J. W. Freeman, and G. P. Seehra, "Collagen self-assembly and the development of tendon mechanical properties," *J. Biomech.*, vol. 36, no. 10, pp. 1529–1553, 2003.
53. K. Wang *et al*., "Controlling the mechanical behavior of dual-material 3D printed meta-materials for patient-specific tissue-mimicking phantoms," *Mater. Des.*, vol. 90, pp. 704–712, Jan. 2016.
54. W. E. Lorensen and H. E. Cline, "Marching cubes: A high resolution 3D surface construction algorithm," *SIGGRAPH Comput. Graph.*, vol. 21, no. 4, pp. 163–169, Aug. 1987.
55. Z. Qian *et al*., "Quantitative prediction of paravalvular leak in transcatheter aortic valve replacement based on tissue-mimicking 3D printing," *JACC Cardiovasc. Imaging*, vol. 10, no. 7, pp. 719–731, Jul. 2017.
56. S. M. Bidoki, D. M. Lewis, M. Clark, A. Vakorov, P. A. Millner, and D. McGorman, "Ink-jet fabrication of electronic components," *J. Micromech. Microeng.*, vol. 17, no. 5, pp. 967–974, 2007.
57. C. S. Jones, X. Lu, M. Renn, M. Stroder, and W.-S. Shih, "Aerosol-jet-printed, high-speed, flexible thin-film transistor made using single-walled carbon nanotube solution," *Microelectron. Eng.*, vol. 87, no. 3, pp. 434–437, Mar. 2010.

58. M. Maiwald, C. Werner, V. Zoellmer, and M. Busse, "INKtelligent printed strain gauges," *Sens. Actuators A Phys.*, vol. 162, no. 2, pp. 198–201, Aug. 2010.
59. V. Wood *et al.*, "Electroluminescence from nanoscale materials via field-driven ionization," *Nano Lett.*, vol. 11, no. 7, pp. 2927–2932, Jul. 2011.
60. L. Yang, A. Rida, R. Vyas, and M. M. Tentzeris, "RFID tag and RF structures on a paper substrate using inkjet-printing technology," *IEEE Trans. Microw. Theory Tech.*, vol. 55, no. 12, pp. 2894–2901, 2007.
61. K. J. Lee, B. H. Jun, J. Choi, Y. I. Lee, J. Joung, and Y. S. Oh, "Environmentally friendly synthesis of organic-soluble silver nanoparticles for printed electronics," *Nanotechnology*, vol. 18, no. 33, p. 335601, 2007.
62. A. M. Kasel *et al.*, "Standardized imaging for aortic annular sizing: implications for transcatheter valve selection," *JACC Cardiovasc. Imaging*, vol. 6, no. 2, pp. 249–262, Feb. 2013.

14 Cardiac Fiber Imaging with 3D Ultrasound and MR Diffusion Tensor Imaging

Xulei Qin[1], *Baowei Fei*[2]
[1]Stanford University School of Medicine
[2]University of Texas Southwestern Medical Center and University of Texas at Dallas

CONTENTS

14.1 INTRODUCTION

14.1.1 Cardiac Microstructures for Physiological Functions

Cardiac fiber is a bundle formed by several cardiomyocytes that functions as a basic structural, mechanical, and electrophysiological unit for a beating heart to maintain its diastolic and systolic functions [1, 2]. As myocardial mechanical contraction and electrical propagation are mainly along fiber directions, cardiac fiber orientations play an important role in determining stress distributions within myocardium and determining electrical activation spreading among ventricles. Therefore, to efficiently pump blood from ventricles into circulation, cardiac fibers are aligned into a complex architecture to achieve optimal electromechanical functions that allow for more than 2 billion heartbeats in a healthy person's lifetime. This myocardial architecture consists of helical arrangements of cardiac fibers in which their orientations continuously change from the epicardium to the endocardium [3]. These transmural changes typically range from −60° at the epicardium to 60° at endocardium. Thus, the overall arrangement of fiber orientations can be summarized as: the epicardial region has left-handed helical orientations, the middle myocardial region has horizontal ones, and the endocardial region has right-handed helical ones. This helical arrangement of cardiac

fiber orientations is crucial for cardiac functions. It has been theoretically proved to be energetically efficient and mechanically uniform for cardiac contraction and relaxation [4, 5]. Moreover, the anisotropic cardiac fiber orientations also coordinate the activation and repolarization patterns of the heart to keep it rhythmically beating [6, 7].

14.1.2 Microstructural Abnormality in Cardiac Diseases

As cardiac fiber orientations are crucial to determine the electromechanical function of the heart, their abnormality directly relates to cardiac dysfunctions (i.e., decreased contractility or arrhythmia) that may result in heart failure or even sudden death [1, 8]. For instance, studies have shown that cardiac fiber orientations play a key role in the generation and maintenance of reentrant arrhythmia [9]. Thus the abnormal fiber orientations could directly decide the activation patterns during the electrical induction of ventricular fibrillation. More importantly, significant abnormality of cardiac fiber orientations usually occurs in ischemic heart disease, the leading cause of death worldwide. This disease causes permanent damage to the heart muscles, thus resulting in severe disarray of cardiac fibers in the infarcted myocardium. In vivo imaging showed that after injury, the death of cardiomyocytes led to increased dispersion and significant reorientation of cardiac fiber architecture in the infarct region [10, 11]. The redistribution of fiber orientations decreased the contractility of the heart and increased the risk of lethal ventricular tachycardia. Besides acute diseases, the progression of abnormal cardiac fiber orientations can also be found in chronic ventricular remodeling. In the dilated heart failure, an altered transmural fiber gradient accompanies a geometry change of local wall thinning in the septum. Hypertrophic cardiomyopathy also induces abnormal myocardial laminar orientations compared to the healthy group [12]. Specifically, right ventricular hypertrophy induced by pressure loading was found not only to increase ventricular weight and myocardium thickness but also to change intramyocardial fiber orientations [13], including decreased transmural changes of cardiac fiber orientations in the failing right ventricle [14]. Recently, considering the importance of cardiac fiber orientations, researchers have started to employ them in treatment plans to guide cardiac resynchronization therapy (CRT) [15].

14.2 CURRENT APPROACHES FOR ESTIMATING CARDIAC FIBER ORIENTATIONS

Although cardiac fiber orientations are important for researchers to understand both heart physiology and pathology, the determination of cardiac fiber orientations is still challenging due to the difficulty of measuring fiber orientations from heart [16]. To this end, different measurement strategies have been proposed.

14.2.1 Direct Measurement Approaches

The initial work is a straightforward approach to directly measure cardiac fiber orientations from histological slides of ex vivo hearts [17, 18]. These efforts have been made since 1960s, and they conclude that cardiac fibers are arranged helically encircling the ventricles. Among them, an impressive work was completed by Nielsen et al [19]. Using customized histological equipment, they measured cardiac fiber orientations at a large amount of sites of myocardium and completed the relationship between ventricular geometry and fiber orientation. They found that cardiac fiber orientations transmurally changed from epicardial to endocardial surfaces with opposite base–apex directions and rotated to a circumferential direction in the middle myocardium. However, this histological measurement has its limitations. The accuracy of the ex vivo results could be affected by the histological procedure with tissue fixation and cutting deformation. Additionally, these histological procedures require manual operations and significant time consumption.

Recently, magnetic resonance (MR) diffusion tensor imaging (DTI) has been used in measuring fiber structures because it can image the diffusion tensors of the water in biological tissues to

indicate the orientations of the fiber structures [20]. Thus, DTI was introduced to measure fiber orientations of the heart ex vivo [3, 21–25]. Ex vivo DTI has the advantages of three-dimensional (3D) volumetric imaging and high spatial resolutions (100–1000 μm), but also needs a long acquisition time of several hours. In spite of recent progress in MR sequences [10, 26, 27], applying DTI for cardiac imaging in vivo still faces severe artifacts due to the fast heart beating and respiration motions. It also requires high short duration pulses supported by high-performance gradients to achieve enough diffusion sensitization. Consequently, these issues limit the application of DTI in clinics, especially for those patients with pacemakers or irregular heart rates. To address the problem faced by DTI, Lee et al. recently introduced an alternative approach of ultrasound shear wave imaging to measure cardiac fiber orientations. They quantified cardiac fiber orientations from in vivo hearts and proved that these measured fiber orientations were consistent with both histological and DTI results [28, 29]. However, this is a newly developed procedure and still needs more effort to improve their accuracy of 3D fiber orientations in the whole heart.

14.2.2 Geometry-Based Estimation Approaches

Considering current limitations of those direct measurement methods, alternative approaches are also developed to estimate fiber orientations from cardiac geometries based on their corresponding relationship. First, according to prior knowledge of histological measurements, rule-based methods were developed to parameterize helical fiber orientations that were transmurally through different layers of ventricular walls [30, 31]. This fiber architecture was defined in the whole ventricular geometry that was measured from cardiac imaging. However, the rule-based method faces the problem of oversimplifying regional differences of fiber orientations, especially when regional heterogeneous abnormality occurs during ventricular remodeling. Thus, an approach that can comprehensively represent these heterogeneous fiber orientations of the whole ventricle is still needed.

To this end, a new pipeline has been proposed similarly based on the relationship between fiber orientations and geometry of the heart. But different from the rule-based methods, it uses cardiac fiber atlas of ex vivo DTI as the template to provide patient-specific cardiac fiber orientations [25] and has been applied in cardiac diagnosis and therapies [32]. Generally, this approach estimates cardiac fiber orientations from the template DTI based on geometric similarity between both target and template hearts. This similarity is mostly measured by registering both volumetric geometries. Following this approach, Helm et al. proposed an algorithm of large deformation diffeomorphic metric mapping (LDDMM) to map cardiac fiber orientations from ex vivo DTI data to the target heart. After mapping, they further validated the results by comparing with their histological findings [33]. Later, a new registration approach of elastic registration was proposed to map the DTI template onto a patient-specific heart [34]. Similarly, using Demons registration, Zhang et al. provided an atlas-based geometry pipeline that could deform DTI data to patient-specific cardiac geometries for constructing three-dimensional cubic Hermite finite element meshes of the whole human heart [15]. Moreover, to validate the accuracy of this geometry-based approach for electrophysiological simulations, Vadakkumpadan et al. used LDDMM to register the MRI geometry of an ex vivo heart atlas to the CT geometry of an in vivo target heart and then deformed the diffusion tensors of the atlas as the estimated fiber orientations of the patient [25]. Their simulation results demonstrated that the estimated fiber orientations through this approach only slightly affected the electrophysiological properties of the target heart.

14.3 Ultrasound Geometry-Based Estimation of Cardiac Fibers

14.3.1 Ultrasound Imaging in Cardiology

Cardiac ultrasound, one of the most widely used diagnostic tests in clinics, is routinely used in the diagnosis, management, and follow-up of suspected or known heart diseases. It is a noninvasive, safe, and cost-efficient imaging modality and can provide real-time images and comprehensive

clinical information. Thus, only from 2007 through 2011, there were approximately 34 million cardiac ultrasound procedures performed on Medicare beneficiaries. This service cost 11% of Medicare that were spent on imaging services, spending approximately $1.2 billion. Compared to cardiac ultrasound, cardiac MRI only accounts for a small portion of the total expenditures for cardiac imaging, which is less than 5%. However, its cost for Medicare average was much higher than cardiac ultrasound [35]. Thus, to facilitate clinical practice and relieve the current healthcare burden, advancing current cardiac ultrasound technology will significantly benefit the patients from cardiac examinations, especially for those with severe arrhythmia or pacemakers. It will also directly help the early detection of cardiac diseases when performing routine cardiac ultrasound for screening.

Unfortunately, although cardiac ultrasound is a crucial imaging modality for the diagnosis of cardiac diseases, previous work of estimating personalized cardiac fiber orientations mainly focused on cardiac MRI or CT modalities. Only a few efforts were made on investigating the effects of myocardium anisotropy on the characteristics of cardiac ultrasound. To meet this need, our recent work employed ex vivo DTI atlas to estimate fiber orientation from cardiac ultrasound, especially from 3D image volumes. It estimated the cardiac fiber orientations of the target heart by deforming the fiber orientations of the template heart. This deformation used the deformation field generated by registering the MRI geometry of the template heart to the ultrasound geometry of the target heart [36]. The work will not only extend current ultrasound applications in cardiology but also benefit the diagnosis and therapy of heart diseases.

14.3.2 Ultrasound Geometry-Based Estimation Approach

In the proposed approach, the volumetric geometry of the target heart is measured from ultrasound images of the target heart whereas the fiber orientations and volumetric geometry of the template heart are derived from DTI and T1-weighted MR images, respectively. Both target and template hearts are from different subjects. The MRI of template heart can achieve high spatial resolutions (~100 μm) through ex vivo imaging. After image processing, ventricular geometries of both hearts are reconstructed with the segmentation of ultrasound and T1-MRI images, respectively. There are two steps to map cardiac fiber orientations from the template heart to the target heart, as shown in Figure 14.1.

The first step is to register the geometry of the template heart to the geometry of the target heart measured from ultrasound images. This registration includes both affine and deformable registrations. The template geometry is first registered to the target geometry by supervised affine transformations (translation, rotation, shear, and scaling) to roughly align both geometries. Then a deformable registration is used to perform fine registrations. In this step, diffeomorphic transformation is needed to deform ventricular geometries while the invertible transformation matrix is also needed for the following reorientation of template fibers. Here, the diffeomorphic Demons (DD) is preferred for the deformable registration because it is diffeomorphic for deformable registration and computationally efficient [37]. Both affine and deformable registrations generate deformation field between both geometries. Based on this deformation field, the second step is to relocate and

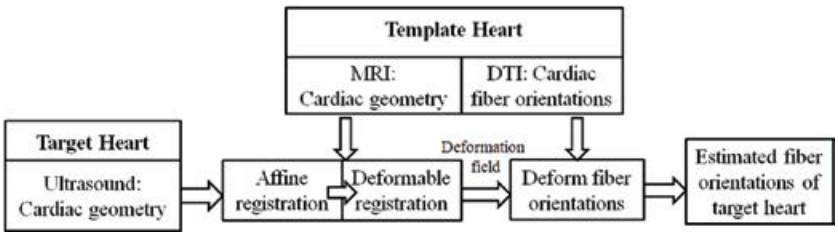

FIGURE 14.1 Approach of estimating cardiac fiber orientations from ultrasound geometry based on the geometric registrations between target ultrasound and template MRI.

reorient the DTI fiber orientations of the template heart as the estimated fiber orientations of the target heart. Following the registration-generated deformation field, each voxel containing fiber orientation of the template heart is first relocated to the geometry of the target heart. Then, based on the same deformation field, the fiber orientation of each relocated voxel is reoriented with a method named preservation of principal directions (PPD) [38]. The reoriented results are the estimated fiber orientations of the target heart.

14.3.3 Evaluation Parameters

After estimating cardiac fiber orientations for the target heart, their accuracies are evaluated by comparing with the gold standard that is measured from the DTI of the target heart ex vivo. To fully estimate the accuracy of the proposed approach, four different evaluation parameters are presented as illustrated in Figure 14.2.

The first parameter is to quantitatively evaluate the accuracy of geometric registrations by comparing the registered geometry from the template heart with the corresponding geometry of the target heart. The Dice similarity coefficient (DSC) is employed here to assess the similarity score between both geometries. Its computational equation is described as follows:

$$DSC(R,S) = \frac{2Volum(R \cap S)}{Volum(R) + Volum(S)} \tag{14.1}$$

Here R and S represent the voxels of both registered geometry and the corresponding target geometry, respectively.

The second parameter to evaluate the accuracy of the geometry registrations is called target registration error (TRE). It is calculated by measuring the distance between corresponding markers

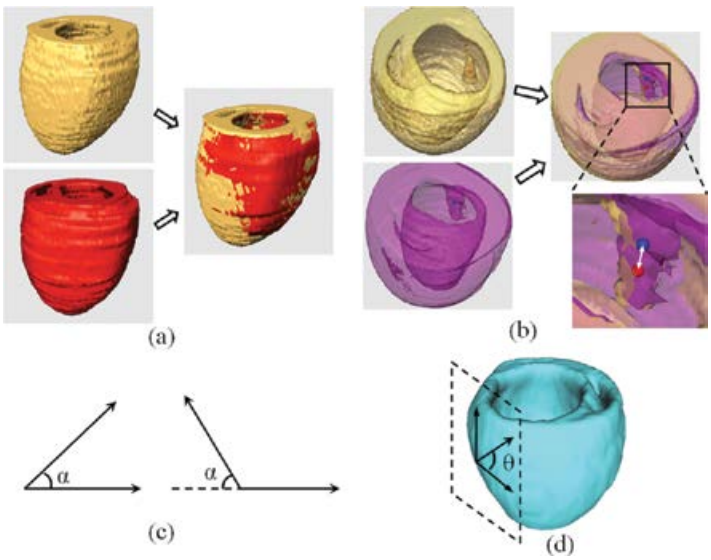

FIGURE 14.2 Evaluation parameters for the accuracy of both geometry and fiber orientation deformations. (a) Dice similarity coefficient: 3D geometric overlap ratio between the target (red) and template (yellow) hearts. (b) Target registration error: Distance between the corresponding papillary muscle centers of the template (red dot) and target (blue dot) hearts, the distance of the white double-head arrow in the amplified image. (c) Acute angle α: between both imaged and estimated fiber directions. (d) Inclination angle θ: between the tangential directions of the epicardial contour in the short axis plane and the fiber direction projected in the epicardial tangential surface.

of both registered and target geometries. In this approach, the papillary muscles inside the hearts are used as the anatomic markers. Thus the distance between both mass centers of the markers is considered as the target error.

More importantly, besides the evaluation of geometric registration, the estimated cardiac fiber orientations following the proposed approach are needed to be evaluated. The parameter of acute angle error (AAE) is used to measure the angular differences between both estimated and ground-truth orientations of the same fiber. It calculates the absolute of their dot product into an angle between 0° and 90° [34, 38]. But this parameter is insufficient for the evaluation of cardiac fiber orientations because it is more important to measure the arrangement of cardiac fibers in myocardium.

Hence, the other parameter called inclination angle error (IAE), typical range between 0° and 180°, is used for this evaluation [39]. There are three steps to calculate this parameter. First, the orientation of a cardiac fiber is projected onto its nearest tangential plane of epicardium. Then, the inclination angle of each voxel is measured as the angle between the projected vector and the tangential vector of the epicardial contour in the short axis view. Finally, the absolute difference between both inclination angles of estimated and ground-truth fiber orientations is calculated as the IAE.

14.3.4 Validation on Animal Hearts

After setting up the proposed approach, several experiments were performed to validate its feasibility of estimating cardiac fiber orientations from ultrasound geometries on animal hearts.

First, the accuracy of this approach was validated on rat hearts ex vivo. Three excised rat hearts were arrested at diastole. Then they were fixed using 4% phosphate-buffered paraformaldehyde (PFA) solution for 14 hours. After that, they were embedded into agarose and imaged by cardiac ultrasound with Vevo 2100 ultrasound system (FUJIFILM VisualSonics, Inc., Toronto, Canada) and a 30 MHz transducer. 3D ultrasound images of the whole were imaged in B-mode short-axis view from apex to base. After ultrasound imaging, these hearts were imaged by a high-field Biospec 7 T MRI system (Bruker Corporation, Massachusetts, USA) with an RF coil of 30 mm inner diameter. Then the cardiac geometries were imaged by T1-weighted anatomical images at a high spatial resolution. After that, the cardiac fiber orientations were imaged in 30 directions by the spin echo sequences with an isotropic resolution. They were imaged slice by slice in the short-axis view from the apex to the base. After DTI data acquisitions, both T1-weighted MRI and ultrasound images were segmented by closed splines interpolated from the semi-automatically placed landmark points on both endocardium and epicardium. The 3D geometric volumes of all hearts were reconstructed from both modalities, respectively. Using the segmented cardiac masks, cardiac fiber orientations were reconstructed from DTI data by tensor decomposition. Their visualization was tracked following a determinative method of fractional anisotropy [40] and performed in 3D by the DSI studio [41]. The accuracies of the cardiac fiber orientations estimated from the ultrasound geometries of three rats were all evaluated based on the four evaluation parameters. Following the procedure in Table 14.1, the estimation of fiber orientations from ultrasound geometry of each target heart used the MRI data of the other two hearts, respectively. The accuracies of both registered cardiac geometry and estimated fiber orientations for each heart were compared with its corresponding ground truth measured from its own MRI data. The final results showed that the average DSC of geometric registrations for the three hearts was 95.4%, and their average angle errors were 21.0° in AAE and 19.4° in IAE, respectively [36]. Although there were estimation errors in cardiac fiber orientations, previous studies in cardiac electrophysiological modeling proved that there were no significant differences at a clinically observable level when the IAE less than 20° between both estimated and acquired fiber orientations [25].

Second, the accuracy of this approach was further validated on large animals of pig hearts ex vivo. Four healthy pig hearts were used for this study, where two were in the diastolic phase and two were in the systolic phase. All hearts were fixed by neutral buffered 10% formalin. After fixation, they were rinsed with PBS and then embedded into a 2% agar gel phantom. Post preprocessing, these hearts were imaged by the 7T Bruker Biospec system with an isotropic resolution of 1mm for T1-weighted

TABLE 14.1

Geometry and fiber orientation errors of rat hearts estimated from cardiac ultrasound.

Target		Template	DSC (%)			
Geometry	Rat No.	(Rat No.)	Affine	DD	AAE (degree)	IAE (degree)
US	1	3	85.3	96.2	20.2	18.4
US	2	1	82.4	96.9	21.7	20.7
US	3	2	80.1	93.2	21.1	19.2
T1-MRI	1	3	86.5	96.9	17.3	16.7
T1-MRI	2	1	80.9	95.9	20.2	19.1
T1-MRI	3	2	81.5	95.4	19.4	18.5

* US: ultrasound; DD: diffeomorphic Demons; DSC: Dice similarity coefficient; AA: acute angle error; IAE: inclination angle error.

MRI and 1.5 mm for 30 directions of DTI. Their ultrasound volumes were imaged with a series of short-axis slices by a BK Flex Focus 400 ultrasound system (Analogic Corp., MA). These ultrasound images were acquired with a step size of 0.2 mm. Similarly, these images were semi-manually segmented and reconstructed into both geometry and fiber orientations for each heart. As shown in Table 14.2, the proposed approach was applied to these four pig hearts that were with maximal ventricular diameters of 10 cm and in two different cardiac phases. The average DSC evaluation on the geometric registrations between ultrasound and registered geometries were 0.819 ± 0.05 [42]. Cardiac fiber orientations for each heart were also estimated. For the registrations between two diastolic hearts, the average AAE was $19.96° \pm 1.23°$ whereas the average AAE was $29.92° \pm 1.00°$ for two systolic hearts. When registering diastolic hearts to systolic ones and vice versa, the average AAE was $25.91° \pm 5.08°$. These errors were partially due to the errors derived from segmentation and registration.

Moreover, the feasibility of this approach was also demonstrated on rat heart in vivo. In an in vivo experiment of 3D ultrasound imaging, the beating heart of a rat was imaged in vivo by the Vevo 2100 ultrasound imaging system with a 21 MHz transducer. Serial B-mode ultrasound images of the heart in short-axis view were imaged from base to apex with slice thickness of a 0.2 mm.

TABLE 14.2

Dice similarity coefficients (DSC) for the geometric registration of pig hearts and acute angle error (AAE) for the estimated cardiac fiber orientations.

Template	Target	DSC (%)	AAE (degree)
Pig 1	Pig 2	79.7	25.92
Pig 1	Pig 3	83.4	19.89
Pig 1	Pig 4	79.9	18.73
Pig 2	Pig 1	82.0	33.65
Pig 2	Pig 3	86.9	28.92
Pig 2	Pig 4	82.3	29.77
Pig 3	Pig 1	83.1	28.24
Pig 3	Pig 2	85.3	30.92
Pig 3	Pig 4	86.1	29.87
Pig 4	Pig 1	87.9	21.19
Pig 4	Pig 2	71.1	21.34
Pig 4	Pig 3	74.7	18.61

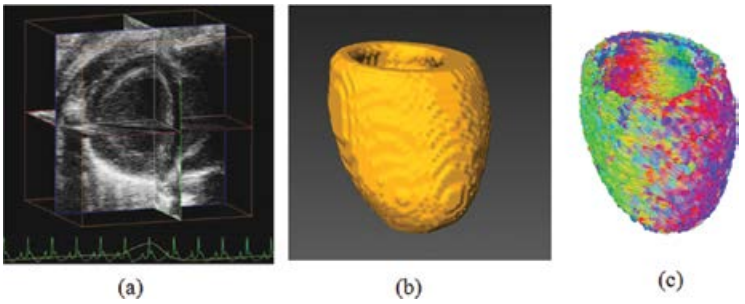

FIGURE 14.3 3D ultrasound-based estimation of cardiac fiber orientations for a rat heart in vivo. (a) 3D ultrasound volume in vivo. (b) Reconstructed cardiac geometry. (c) Estimated cardiac fiber orientations from the geometry.

The spatial resolution of the B-mode image was 0.06 mm. In each slice position, dynamic image serial was acquired during several beating cycles. Meanwhile, both ECG and respiration signals were also recorded. Based on the cardiorespiratory signals, 3D ultrasound volume in the diastole phase was selected and reconstructed. Finally, following the proposed approach, the fiber orientations of the in vivo heart were estimated by using the DTI data of another ex vivo heart as the template. The result in Figure 14.3 demonstrated the feasibility of using the proposed approach to estimate cardiac fiber orientations from 3D cardiac ultrasound in vivo.

14.3.5 Potential Applications

Measuring cardiac fiber orientations has many applications for cardiac research and clinics. Using the mapped cardiac fiber orientations, we have explored their potential applications in the electrical simulations and cardiac ultrasound properties.

After mapping both ultrasound geometry and fiber orientations of the heart, we could predict cardiac electricity interventions by assisting the electrophysiological modeling of the cardiac electrical propagations [43]. Electrophysiological simulation and prediction are an important issue in clinical diagnosis and therapies of arrhythmia [44]. Thus, we mapped the estimated cardiac fiber orientations to evaluate the electrical abnormality caused by myocardial infarction and then predict the 3D electrophysiological properties post CRT intervention. For this purpose, both reconstructed cardiac meshes from 3D ultrasound geometry and the mapped cardiac fiber orientations were integrated into an electrophysiological model, where the geometric meshes were generated with software of iso2mesh [45] and the cardiac electricity was simulated with a toolbox of Chaste [46]. Figure 14.4 demonstrated the electrical differences between a normal and an infarcted heart. When an end of a pacemaker electrode was internally connected to the myocardium of the heart apex, the cardiac electricity distributions around the 3D geometry were corrected. Figure 14.5 showed that after the impulse of the pacemaker, the action potentials at different time points evenly propagated among both ventricles.

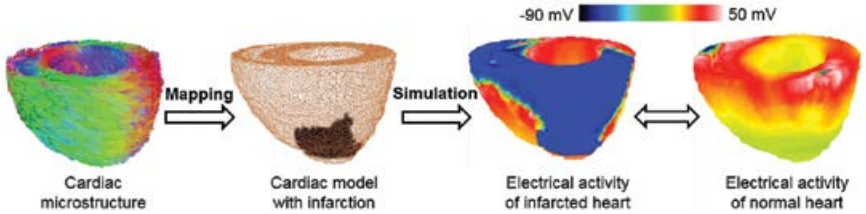

FIGURE 14.4 Cardiac modeling to measure the difference of electrical activities between both infarcted and normal hearts. This modeling uses imaging-based geometry and microstructure of the heart.

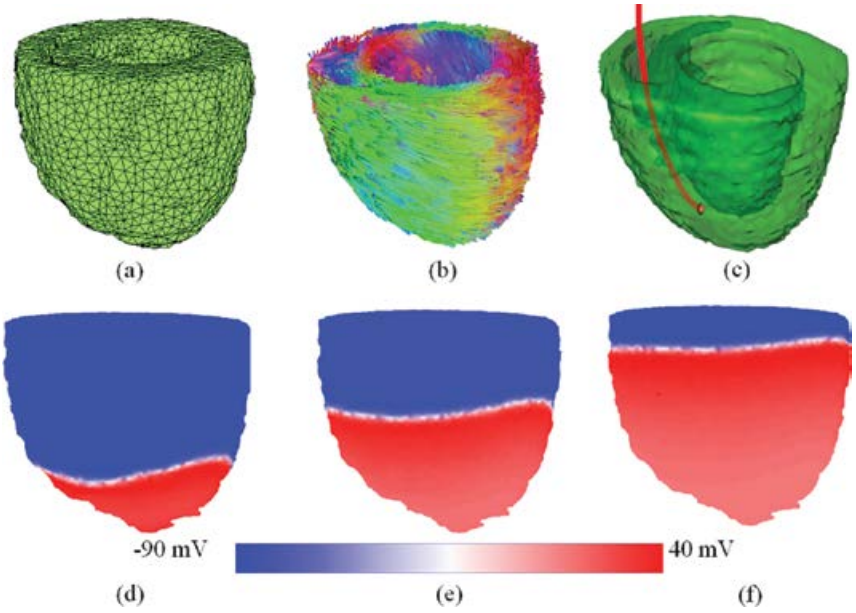

FIGURE 14.5 Predicting cardiac electricity distributions during cardiac resynchronization therapy based on the mapped ultrasound geometry and fiber orientations. (a) The reconstructed mesh volume of ultrasound. (b) The mapped cardiac fiber orientations. (c) The cardiac resynchronization therapy (CRT) conducted by an internal electrode (red line) from a pacemaker. (d-f) The simulation results of the action potentials at three different time points (15 ms, 30 ms, and 45 ms) after the impulse of the pacemaker. The colors indicate the action potentials from –90 mV to 40 mV.

In addition, as cardiac fiber orientations directly affect the inhomogeneity of ultrasound intensities, measuring cardiac fiber orientations can also help investigate the properties of cardiac ultrasound. We proposed a method to quantify these ultrasound imaging properties by mapping cardiac fiber orientations to the cardiac geometry [47]. Using 3D architectures of both cardiac geometry and fiber orientations, this method could simulate the B-mode ultrasound images. These images not only maintained the accuracy of cardiac geometry and ultrasound speckle patterns but also generated the anisotropic intensity distributions that were presented in normal cardiac ultrasound images. Specifically, these results were able to represent the abnormal ultrasound images, such as right ventricle heart failure with pulmonary artery hypertension (Figure 14.6). It may reveal the pathological remodeling during disease progression.

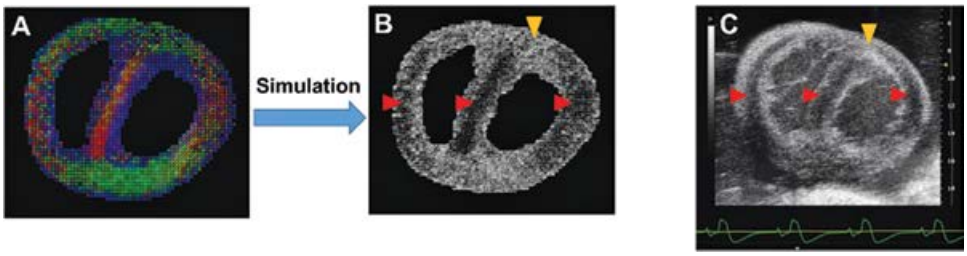

FIGURE 14.6 Using mapped cardiac fiber orientations to generate ultrasound image for a diseased rat heart with pulmonary artery hypertension. (a) Mapped cardiac fiber orientations. (b) Simulated ultrasound image based on both measured geometry and fiber orientations of the heart. (c) Acquired ultrasound image in vivo. The red arrows indicate the lower intensity regions of myocardium and the yellow ones indicate the higher intensity regions, which are affected by different fiber orientations.

14.4 SUMMARY

Cardiac fiber orientations play important roles in determining both electrical and mechanical functions of the heart. Their abnormality causes cardiac dysfunction that may results in heart failure or sudden death. Thus, the estimation of fiber orientations will be valuable for the clinical diagnosis of cardiac diseases. Considering the wide application of ultrasound in cardiology, ultrasound-derived cardiac fiber orientations would provide useful information for the diagnosis of cardiac abnormality. In addition, when the fiber information is combined with electrophysiological modeling it might also play a key role in both surgical plans and ablation guidance for the treatment of ventricular tachycardia and ventricular arrhythmia. Thus, our proposed method and its future improvements will contribute to better understanding of cardiac physiology and also provide a tool for diagnosis of heart diseases and prediction of their treatments.

However, the current approach for the estimation of cardiac fiber orientations also has its limitations. Specifically, the estimated accuracy of the current procedure highly relies on the accurate myocardium segmentations on ultrasound images, a challenge in current clinical practice. Comparing with the geometry-based registration, an intensity-based registration (e.g., mutual information) between both MRI and ultrasound images may provide more accurate and robust registrations. Especially, the inhomogeneous backscatter intensity of cardiac ultrasound has been found quantitatively related to the fiber orientations from both in vivo and ex vivo data. It could be an additional indicator for the fiber variations between both the template and the target hearts rather than only using geometric deformations. Hence, several attempts used the absolute value of the anisotropic intensities in ultrasound images to directly estimate cardiac fiber orientations. They directly estimated cardiac fiber orientations from the B-mode intensities of short-axis ultrasound images [48, 49]. Similarly, fiber orientations were estimated from ultrasound intensities for ultrasound simulation purposes [50]. Unfortunately, these results were sensitive to the image noises and hardly acquired the complicated 3D architectures. Thus, the integration of both geometry registration and intensity quantification may provide an ideal approach to accurately estimate cardiac fiber orientations from cardiac ultrasound. This might provide valuable information for the diseased hearts with large ventricular remodelings, such as hypertension-induced heart remodeling or myocardial hypertrophy, when estimating fiber orientations from a normal heart template.

Acknowledgments

This publication was supported in part by research grants from the American Heart Association 17SDG33460212, NIH grants (CA176684, CA156775, and CA204254), and a pilot grant from the Children's Heart Research and Outcomes Center of Children's Healthcare of Atlanta.

References

1. P. P. Sengupta, J. Korinek, M. Belohlavek, J. Narula, M. A. Vannan, A. Jahangir, *et al.*, "Left ventricular structure and function: basic science for cardiac imaging," *J Am Coll Cardiol*, vol. 48, pp. 1988–2001, Nov 21 2006.
2. G. Buckberg, J. I. E. Hoffman, A. Mahajan, S. Saleh, and C. Coghlan, "Cardiac mechanics revisited the relationship of cardiac architecture to ventricular function," *Circulation*, vol. 118, pp. 2571–2587, Dec 9 2008.
3. H. Lombaert, J. M. Peyrat, P. Croisille, S. Rapacchi, L. Fanton, F. Cheriet, *et al.*, "Human atlas of the cardiac fiber architecture: study on a healthy population," *IEEE Trans Med Imaging*, vol. 31, pp. 1436–1447, Jul 2012.
4. M. Vendelin, P. H. Bovendeerd, J. Engelbrecht, and T. Arts, "Optimizing ventricular fibers: uniform strain or stress, but not ATP consumption, leads to high efficiency," *Am J Physiol Heart Circ Physiol*, vol. 283, pp. H1072–H1081, Sep 2002.

5. P. Savadjiev, G. J. Strijkers, A. J. Bakermans, E. Piuze, S. W. Zucker, and K. Siddiqi, "Heart wall myofibers are arranged in minimal surfaces to optimize organ function," *Proc Natl Acad Sci USA*, vol. 109, pp. 9248–9253, Jun 12 2012.
6. B. Taccardi, E. Macchi, R. L. Lux, P. R. Ershler, S. Spaggiari, S. Baruffi, *et al.*, "Effect of myocardial fiber direction on epicardial potentials," *Circulation*, vol. 90, pp. 3076–3090, Dec 1994.
7. A. Kanai and G. Salama, "Optical mapping reveals that repolarization spreads anisotropically and is guided by fiber orientation in guinea-pig hearts," *Circ Res*, vol. 77, pp. 784–802, Oct 1995.
8. P. P. Sengupta, V. K. Krishnamoorthy, J. Korinek, J. Narula, M. A. Vannan, S. J. Lester, *et al.*, "Left ventricular form and function revisited: applied translational science to cardiovascular ultrasound imaging," *J Am Soc Echocardiogr*, vol. 20, pp. 539–551, May 2007.
9. P. S. Chen, Y. M. Cha, B. B. Peters, and L. S. Chen, "Effects of myocardial fiber orientation on the electrical induction of ventricular fibrillation," *Am J Physiol*, vol. 264, pp. H1760–H1773, Jun 1993.
10. D. E. Sosnovik, C. Mekkaoui, S. Huang, H. H. Chen, G. Dai, C. T. Stoeck, *et al.*, "Microstructural impact of ischemia and bone marrow-derived cell therapy revealed with diffusion tensor magnetic resonance imaging tractography of the heart in vivo," *Circulation*, vol. 129, pp. 1731–1741, Apr 29 2014.
11. M. T. Wu, W. Y. Tseng, M. Y. Su, C. P. Liu, K. R. Chiou, V. J. Wedeen, *et al.*, "Diffusion tensor magnetic resonance imaging mapping the fiber architecture remodeling in human myocardium after infarction: correlation with viability and wall motion," *Circulation*, vol. 114, pp. 1036–1045, Sep 5 2006.
12. P. F. Ferreira, P. J. Kilner, L. A. McGill, S. Nielles-Vallespin, A. D. Scott, S. Y. Ho, *et al.*, "In vivo cardiovascular magnetic resonance diffusion tensor imaging shows evidence of abnormal myocardial laminar orientations and mobility in hypertrophic cardiomyopathy," *J Cardiovasc Magn Reson*, vol. 16, p. 87, 2014.
13. F. Tezuka, W. Hort, P. E. Lange, and J. H. Nurnberg, "Muscle fiber orientation in the development and regression of right ventricular hypertrophy in pigs," *Acta Pathol Jpn*, vol. 40, pp. 402–407, Jun 1990.
14. D. Benoist, R. Stones, A. P. Benson, E. D. Fowler, M. J. Drinkhill, M. E. Hardy, *et al.*, "Systems approach to the study of stretch and arrhythmias in right ventricular failure induced in rats by monocrotaline," *Prog Biophys Mol Biol*, Jul 9 2014.
15. M. Sermesant, R. Chabiniok, P. Chinchapatnam, T. Mansi, F. Billet, P. Moireau, *et al.*, "Patient-specific electromechanical models of the heart for the prediction of pacing acute effects in CRT: a preliminary clinical validation," *Med Image Anal*, vol. 16, pp. 201–215, Jan 2012.
16. G. Buckberg, A. Mahajan, S. Saleh, J. I. Hoffman, and C. Coghlan, "Structure and function relationships of the helical ventricular myocardial band," *J Thorac Cardiovasc Surg*, vol. 136, pp. 578–589, 589 e1–11, Sep 2008.
17. M. McLean and J. Prothero, "Myofiber orientation in the weanling mouse heart," *Am J Anat*, vol. 192, pp. 425–441, Dec 1991.
18. E. K. Theofilogiannakos, G. K. Theofilogiannakos, A. Anogelanaki, P. G. Danias, H. Zairi, T. Zaraboukas, *et al.*, "A fiber orientation model of the human heart using classical histological methods, magnetic resonance imaging and interpolation techniques," *Comput Cardiol 2008*, *Vols 1 and 2*, pp. 307–310, 2008.
19. P. M. Nielsen, I. J. Le Grice, B. H. Smaill, and P. J. Hunter, "Mathematical model of geometry and fibrous structure of the heart," *Am J Physiol*, vol. 260, pp. H1365–H1378, Apr 1991.
20. H. Johansen-Berg and M. F. S. Rushworth, "Using diffusion imaging to study human connectional anatomy," *Annu Rev Neurosci*, vol. 32, pp. 75–94, 2009.
21. L. Geerts-Ossevoort, P. Bovendeerd, F. Prinzen, T. Arts, and K. Nicolay, "Myofiber orientation in the normal and infarcted heart, assessed with MR-diffusion tensor imaging," *Comput Cardiol 2001*, *Vol.* 28, pp. 621–624, 2001.
22. L. Geerts, P. Bovendeerd, K. Nicolay, and T. Arts, "Characterization of the normal cardiac myofiber field in goat measured with MR-diffusion tensor imaging," *Am J Physiol Heart Circ Physiol*, vol. 283, pp. H139–H145, Jul 2002.
23. M. T. Wu, W. Y. I. Tseng, M. Y. M. Su, C. P. Liu, K. R. Chiou, V. J. Wedeen, *et al.*, "Diffusion tensor magnetic resonance imaging mapping the fiber architecture remodeling in human myocardium after infarction - correlation with viability and wall motion," *Circulation*, vol. 114, pp. 1036–1045, Sep 5 2006.
24. P. Savadjiev, G. J. Strijkers, A. J. Bakermans, E. Piuze, S. W. Zucker, and K. Siddiqi, "Heart wall myofibers are arranged in minimal surfaces to optimize organ function," *Proc Natl Acad Sci USA*, vol. 109, pp. 9248–9253, Jun 12 2012.

25. F. Vadakkumpadan, H. Arevalo, C. Ceritoglu, M. Miller, and N. Trayanova, "Image-based estimation of ventricular fiber orientations for personalized modeling of cardiac electrophysiology," *IEEE Trans Med Imaging*, vol. 31, pp. 1051–1060, May 2012.
26. U. Gamper, P. Boesiger, and S. Kozerke, "Diffusion imaging of the in vivo heart using spin echoes-considerations on bulk motion sensitivity," *Magn Reson Med*, vol. 57, pp. 331–337, Feb 2007.
27. C. Nguyen, Z. Fan, B. Sharif, Y. He, R. Dharmakumar, D. S. Berman, *et al.*, "In vivo three-dimensional high resolution cardiac diffusion-weighted MRI: a motion compensated diffusion-prepared balanced steady-state free precession approach," *Magn Reson Med*, vol. 72, pp. 1257–1267, Nov 2014.
28. W. N. Lee, B. Larrat, M. Pernot, and M. Tanter, "Ultrasound elastic tensor imaging: comparison with MR diffusion tensor imaging in the myocardium," *Phys Med Biol*, vol. 57, Aug 21 2012.
29. W. N. Lee, M. Pernot, M. Couade, E. Messas, P. Bruneval, A. Bel, *et al.*, "Mapping myocardial fiber orientation using echocardiography-based shear wave imaging," *IEEE Trans Med Imag*, vol. 31, pp. 554–562, Mar 2012.
30. M. Potse, B. Dube, J. Richer, A. Vinet, and R. M. Gulrajani, "A comparison of monodomain and bidomain reaction-diffusion models for action potential propagation in the human heart," *IEEE Trans Biomed Eng*, vol. 53, pp. 2425–2435, Dec 2006.
31. M. J. Bishop, P. Hales, G. Plank, D. J. Gavaghan, J. Scheider, and V. Grau, "Comparison of rule-based and DTMRI-derived fibre architecture in a whole rat ventricular computational model," *Functional Imaging and Modeling of the Heart, Proceedings*, vol. 5528, pp. 87–96, 2009.
32. M. Sermesant, F. Billet, R. Chabiniok, T. Mansi, P. Chinchapatnam, P. Moireau, *et al.*, "Personalised electromechanical model of the heart for the prediction of the acute effects of cardiac resynchronisation therapy," *Functional Imaging and Modeling of the Heart, Proceedings*, vol. 5528, pp. 239–248, 2009.
33. P. Helm, M. F. Beg, M. I. Miller, and R. L. Winslow, "Measuring and mapping cardiac fiber and laminar architecture using diffusion tensor MR imaging," *Communicative Cardiac Cell*, vol. 1047, pp. 296–307, 2005.
34. S. Hari Sundar, D. G. Shen, G. Biros, H. Litt, and C. Davatzikos, "Estimating myocardial fiber orientations by template warping," *2006 3rd IEEE International Symposium on Biomedical Imaging: Macro to Nano*, *Vols. 1–3*, pp. 73–76, 2006.
35. S. A. Francis, C. Daly, B. Heydari, S. Abbasi, R. V. Shah, and R. Y. Kwong, "Cost-effectiveness analysis for imaging techniques with a focus on cardiovascular magnetic resonance," *J Cardiovasc Magn Reson*, vol. 15, Jun 14 2013.
36. X. Qin and B. Fei, "DTI template-based estimation of cardiac fiber orientations from 3D ultrasound," *Med Phys*, vol. 42, pp. 2915–2924, 2015.
37. T. Vercauteren, X. Pennec, A. Perchant, and N. Ayache, "Diffeomorphic demons: efficient non-parametric image registration," *Neuroimage*, vol. 45, pp. S61–S72, Mar 2009.
38. D. C. Alexander, C. Pierpaoli, P. J. Basser, and J. C. Gee, "Spatial transformations of diffusion tensor magnetic resonance images," *IEEE Trans Med Imag*, vol. 20, pp. 1131–1139, Nov 2001.
39. D. F. Scollan, A. Holmes, R. Winslow, and J. Forder, "Histological validation of myocardial microstructure obtained from diffusion tensor magnetic resonance imaging," *Am J Physiol Heart Circ Physiol*, vol. 275, pp. H2308–H2318, Dec 1998.
40. P. Mukherjee, S. Chung, J. Berman, C. Hess, and R. Henry, "Diffusion tensor MR imaging and fiber tractography: technical considerations," *Am J Neuroradiol*, vol. 29, pp. 843–852, 2008.
41. F. C. Yeh, V. Wedeen, and W. Y. I. Tseng, "Estimation of fiber orientation and spin density distribution by diffusion deconvolution," *Neuroimage*, vol. 55, pp. 1054–1062, Apr 1 2011.
42. J. D. Dormer, Y. G. Meng, X. D. Zhang, R. Jiang, M. B. Wagner, and B. W. Fei, "Estimating cardiac fiber orientations in pig hearts using registered ultrasound and MR image volumes," *Medical Imaging 2017: Ultrasonic Imaging and Tomography*, vol. 10139, 2017.
43. Y. Zhang, X. Liang, J. Ma, Y. Jing, M. J. Gonzales, C. Villongco, *et al.*, "An atlas-based geometry pipeline for cardiac Hermite model construction and diffusion tensor reorientation," *Med Image Anal*, vol. 16, pp. 1130–1141, Aug 2012.
44. X. Qin, S. Wang, and M. Wan, "Improving reliability and accuracy of vibration parameters of vocal folds based on high-speed video and electroglottography," *IEEE Trans Biomed Eng*, vol. 56, pp. 1744–1754, Jun 2009.
45. Q. Q. Fang and D. A. Boas, "Tetrahedral mesh generation from volumetric binary and gray-scale images," *2009 IEEE International Symposium on Biomedical Imaging: From Nano to Macro*, *Vols 1 and 2*, pp. 1142–1145, 2009.

46. G. R. Mirams, C. J. Arthurs, M. O. Bernabeu, R. Bordas, J. Cooper, A. Corrias, *et al*., "Chaste: an open source c plus plus library for computational physiology and biology," *PLOS Comput Biol*, vol. 9, Mar 2013.
47. X. Qin, S. Wang, M. Shen, G. Lu, X. Zhang, M. B. Wagner, *et al*., "Simulating cardiac ultrasound image based on MR diffusion tensor imaging," *Med Phys*, vol. 42, pp. 5144–5156, Sep 2015.
48. M. L. Milne, G. K. Singh, J. G. Miller, and M. R. Holland, "Feasibility of echocardiographic-based assessment of myocardial fiber structure in individual hearts," *2011 IEEE International Ultrasonics Symposium*, pp. 2009–2012, 2012.
49. M. L. Milne, G. K. Singh, J. G. Miller, and M. R. Holland, "Echocardiographic-based assessment of myocardial fiber structure in individual, excised hearts," *Ultrasonic Imaging*, vol. 34, pp. 129–141, Jul 2012.
50. J. Crosby, T. Hergum, E. W. Remme, and H. Torp, "The effect of including myocardial anisotropy in simulated ultrasound images of the heart," *IEEE Trans Ultrason Ferroelectr Freq Control*, vol. 56, pp. 326–333, Feb 2009.

Taylor & Francis
Taylor & Francis Group
http://taylorandfrancis.com

15 Technical Advances and Clinical Perspectives in Coronary MR Imaging

Giulia Ginami, Imran Rashid, René M. Botnar, Claudia Prieto
King's College London

CONTENTS

15.1 INTRODUCTION

Coronary artery disease (CAD) remains the leading cause of death in industrialized countries [1], despite continuous progress in its prevention, diagnosis, and treatment. Invasive X-ray coronary angiography, via the radial or femoral artery, is the current reference standard for assessment of coronary stenosis. Invasive coronary angiography allows 2D visualization of coronary obstructions with high spatial and temporal resolution, with the advantage of potential for therapeutic intervention (such as coronary angioplasty) at the time of the imaging procedure. However, about 30% of patients who are currently referred for X-ray angiography for CAD assessment are found to have negative stenosis findings [2, 3]; nevertheless, these subjects still experience an invasive, potentially risky [4] and costly procedure to achieve a clinical diagnosis [5, 6]. Furthermore, the presence of severe luminal narrowing represents a late stage of CAD; in fact, CAD is an extremely heterogeneous disease that is characterized by the gradual accumulation of lipid and fibrotic elements in the vessel intima causing thickening, stiffening, and loss of elasticity of the coronary wall [7]. As CAD progresses, different manifestations of the pathology can be observed (Figure 15.1). The initial marker of CAD—arising before any structural change at the level of both the coronary lumen and wall become visible—is coronary endothelial dysfunction [8–11]. Endothelial dysfunction manifests itself as a loss in the capability of maintaining homeostasis as well as in the capability of regulating cardiovascular tone in response to vasoactive factors, hormones, and neurotransmitters [12].

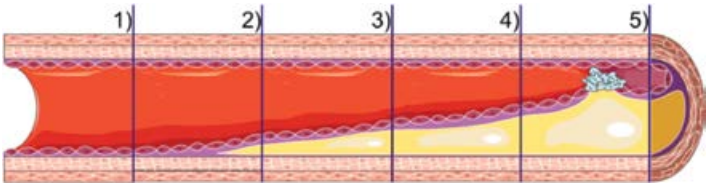

FIGURE 15.1 Schematic of CAD progression. 1) Normal and healthy coronary artery. 2) Early stages of CAD may involve coronary endothelial dysfunction without important structural changes at the level of both the coronary lumen and the coronary vessel wall. Initiation of the plaque deposition progress can cause positive remodelling of the coronary vessel wall, consisting on the outward growth of the vessel wall itself without any actual luminal narrowing. 3–5) Progressive luminal narrowing occurs with the development of the pathology. During these stages, intraplaque haemorrhage may occur within the atherosclerotic plaque; the plaque can therefore become at risk and prone to rupture. Progressive luminal narrowing as well as sudden plaque rupture can cause intraluminal thrombosis, one of the main manifestations of acute CAD.

In addition, endothelial dysfunction leads to an increase in vascular permeability that gives rise to the accumulation of blood-born macromolecules (e.g., LDL) in the vessel wall causing a chronic inflammatory response. Endothelial dysfunction is typically followed by the so-called "positive vessel wall remodeling" [13], consisting of outward growth of atherosclerotic plaque within the coronary vessel wall with preserved lumen size. Ongoing inflammation results in progressive accumulation of inflammatory cells (e.g., macrophages), lipid and matrix proteins that augment lesion size. This results in actual narrowing of the coronary lumen that can lead to reduced perfusion of the myocardium and predispose to subsequent myocardial infarction. During this pathological evolution, the fibrotic cap of the plaque becomes weaker and, as a consequence, can become unstable. At these advanced stages, the coronary plaque also may develop intraplaque hemorrhage (IPH), thus enhancing its degree of instability [14–16]. Plaque rupture may lead to obstructive intraluminal coronary thrombosis; additionally, embolic material following coronary plaque rupture and thrombosis can result in microvascular obstruction of the distal vessels (e.g., at the level of the carotid arteries, thus causing cerebral stroke) [7]. The presence of CAD can remain unnoticed for a prolonged period of time, and often will reveal itself only at advanced stages of disease. Therefore, and due to the inhomogeneous nature of CAD manifestation, a non-invasive imaging modality for monitoring the progression of CAD would be highly desirable. While X-ray angiography and multidetector computed tomography (CT) can image the coronary lumen at high resolution, ICA is invasive and both modalities involve the exposure to ionizing radiation, with assessment of atherosclerotic plaque characteristics limited to patterns of either calcification or low X-ray attenuation (a marker of lipid content within the necrotic core). Recently, coronary magnetic resonance imaging (MRI) has emerged as a promising non-invasive imaging modality for the diagnosis of CAD. Even though coronary MRI does not currently achieve the sub-millimeter spatial resolution, it can generate different imaging contrasts that hold promise for both the detection and characterization of plaque and monitoring of multiple stages of CAD. This chapter reviews the most prominent technical challenges as well as the latest developments aimed at addressing those challenges. MRI strategies for the assessment of different CAD stages will be described and reviewed; furthermore, a brief overview on coronary vein MRI—currently gaining relevance in the field of interventional cardiac procedures—will be provided.

15.2 TECHNICAL CHALLENGES IN CORONARY MRI

The unique nature of the coronary arteries challenges MRI acquisition strategies in comparison to similar sized vessels elsewhere in the body, as coronary arteries exhibit near-constant motion due

to both respiration and cardiac contraction. Furthermore, and in addition to their particularly small diameter (typically ranging from 3 to 5 mm in the proximal segments and 1 to 2 mm in more distal segments), the coronary arteries exhibit complex geometry and follow tortuous paths. Therefore, there is the need for both high resolution and adequate volumetric coverage. The acquisition of large and high-resolution MR volumetric datasets, however, far exceeds the duration of the typical cardiac cycle; therefore, data acquisition is typically performed over multiple consecutive cardiac cycles under the assumption that cardiac motion is the same (or nearly the same) between heartbeats. Moreover, normal breathing during the scan leads to a shift and deformation of the heart that differ strongly between different subjects. As such, effective motion suppression strategies are required to minimize cardiac and respiratory motion artefacts—image blurring and ghosting—that can affect the diagnostic accuracy of the acquired images. In order to avoid the risk of excessively prolonged examination times that would be required to achieve high resolution and volumetric coverage, strategies for accelerated data acquisition are currently under investigation. Furthermore, and in order to avoid high-signal contribution from the tissues surrounding the coronaries (e.g., myocardium and epicardial fat), specific preparatory radiofrequency (RF) pulses are conventionally utilized. Hereafter, current strategies for compensating cardiac and respiratory motion, reducing examination times, and enhancing the signal from the coronary arteries are presented.

15.2.1 Cardiac Motion

The heart muscle contracts during systole, while myocardial relaxation occurs in diastole. The continuous and repetitive polarization and de-polarization of the myocardial tissue induces a small voltage that can be detected by using an MR compatible electrocardiogram (ECG) device, in order to extrapolate an indirect measurement of the cardiac motion. However, vector ECG approaches [17] are preferred since the ECG signal in the main magnetic field is distorted by both the magnetohydrodynamic effect and by the rapidly switching gradient waveforms. To minimize motion within the cardiac cycle, the acquisition of MR data is targeted to periods with minimal cardiac motion [18]. It has been shown that minimal motion of both the left ventricle and coronaries typically occurs during late-systole or mid-diastole [20–22]. The mid-diastolic rest period is usually preferred due to the higher blood flow and longer resting period (~100 ms in comparison to ~50 ms for late-systole). The end-systolic rest period is usually preferred in subjects with high heart rates (thus shortened mid-diastolic rest periods), pediatric patients, or in cases of highly variable heart rates. The time window of minimal cardiac contraction is subject dependent, and this is conventionally identified from a two-dimensional (2D) high-temporal resolution cine MR image acquired prior to the acquisition of a high-resolution coronary MR image. Coronary MRI data are then collected during such time window with minimal cardiac motion over multiple cardiac cycles, by setting a specific trigger delay (time lapsed from the R-wave of the ECG to the beginning of data acquisition) (Figure 15.2). These conventional ECG-triggered acquisitions provide a static visualization of the heart (either in end-systole or in mid-diastole). Recently, approaches that image the heart at different cardiac phases have been developed, thus allowing for the simultaneous assessment of functional information and of the coronary anatomy. Dual-phase coronary MRI [24, 25] has been proposed to acquire two different three-dimensional (3D) whole-heart volumes in both systole and diastole in a single free-breathing examination; this enables quantification of right- and left-ventricular volumes along with the visualization of the coronary arteries (Figure 15.3). More recently, so-called free-running acquisitions [19, 20] have been introduced to image the heart and coronary anatomy at different points of the cardiac cycle. With these approaches, data acquisition is performed continuously throughout the entire cardiac cycle and retrospective ECG-gating is used to assign the data to different cardiac phases. These free-running acquisitions allow for the quantification of functional endpoints along with the visualization of the coronary anatomy. A non-rigid motion compensation algorithm has been proposed to align the different cardiac phases of a free-running acquisition to a reference phase, leading to a single, motion-free, 3D whole-heart volume for the visualization of

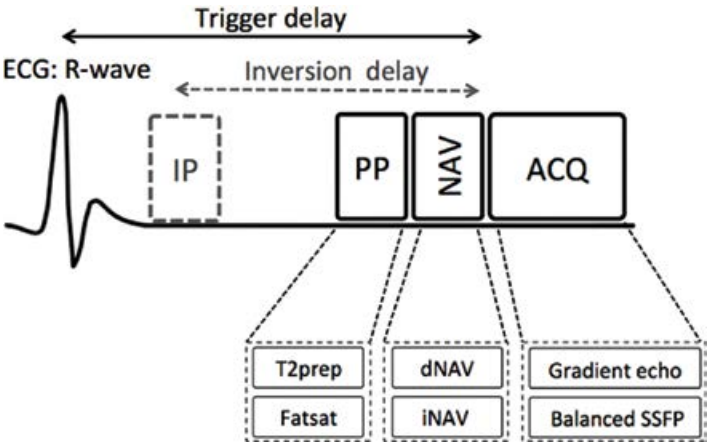

FIGURE 15.2 Schematic of a typical coronary MRI acquisition sequence. Data acquisition (ACQ) is performed following a subject-specific time delay from the R-wave (trigger delay) in order to minimize cardiac motion. Preparatory pulses (PP), such as T_2 preparation (T2Prep) and fat saturation (Fatsat), can be exploited in order to improve the contrast between the coronary arteries and the surrounding tissues. The use of an inversion pulse (IP) can be exploited to generate black-blood contrast; in this case, data acquisition is performed after a pre-determined inversion delay to null the signal from the blood. Motion compensation techniques (NAV) are employed to compensate for respiratory motion.

the coronary anatomy [21]; this improves signal and sharpness of the 3D whole-heart volume that will be used for coronary assessment, while functional endpoints can be computed from the original cardiac-resolved reconstruction.

15.2.2 Respiratory Motion

The tidal movement of respiratory structures such as the diaphragm and the chest wall causes a respiratory-induced motion of the thoracic and abdominal organs. The respiratory-induced displacement of the heart mostly happens along the superior-inferior (SI) direction but also leads to additional 3D affine and non-linear motion components that differ strongly between different

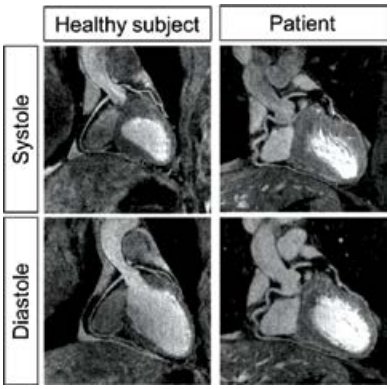

FIGURE 15.3 Results from a whole-heart dual-phase acquisition in a healthy subject (first column) and in a patient with total occlusion of the left coronary artery (second column). Images are displayed for systole (first row) and diastole (second row) acquired in the same sequence.

subjects [22]. A simple approach to minimize respiratory motion is to perform the acquisition under one or multiple breath-holds of about 15 seconds. However, this approach is incompatible with clinically preferred high-resolution 3D targeted or 3D whole-heart coronary MRI due to the long scan time required to satisfy signal-to-noise and spatial resolution requirements. Respiratory motion monitoring can be used in free breathing 3D coronary MRI to combine data from multiple breathing cycles acquired at a similar respiratory position. The widely employed solution in the clinical setting for respiratory motion compensation in 3D whole-heart coronary MRI is the use of one-dimensional (1D) diaphragmatic navigator echoes (Figure 15.4). With this approach, the respiratory motion of the dome of the diaphragm is monitored by acquiring a fast pre-pulse right before or after data acquisition [23–25]. The high contrast between the lung-liver interface enables the continuous monitoring of the diaphragmatic SI translation. This signal is used to gate the acquisition, that is, data are accepted/acquired only when the respiratory signal is within a predefined narrow acceptance window (3–5 mm) of the breathing cycle (typically end-expiration) with all other data being rejected. Conversely, data falling outside the acceptance window are rejected and need to be re-acquired at subsequent cardiac cycles. Diaphragmatic navigators can be also used to correct for residual motion within the gating window, usually referred to as tracking [30]. This method assumes that the heart motion is dominated by translation in the SI direction, and that this displacement is proportional to that of the diaphragm [22]. The proportional scaling factor between the diaphragmatic and cardiac SI displacements is known as the tracking factor and is commonly fixed to the value 0.6 [26]. 1D diaphragmatic navigator approaches have shown to considerably reduce motion artefacts when small gating windows are employed, however they lead to prolonged scan times since only a portion of the data (typically 30–50%) is accepted for reconstruction (referred to as scan efficiency). In addition, as respiratory

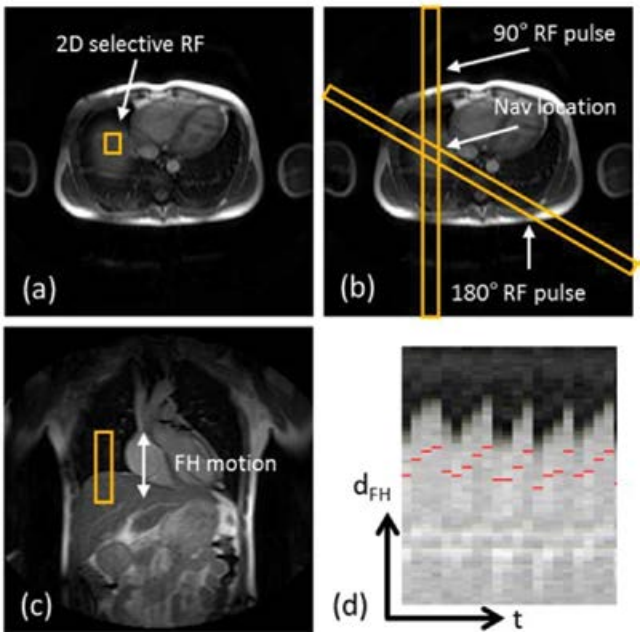

FIGURE 15.4 Planning of a 1D navigator-gated coronary MRI acquisition. A "pencil-beam excitation" (a) or a two obliquely aligned excitation (90° RF pulse) and refocusing (180° RF pulse) pulses can be used. This allows the tracking of the lung-liver interface along the superior-inferior direction (c). The resulting navigator signal allows us to indirectly estimate the respiratory displacement of the heart (d_{FH}) over time (t) (d). Image reprinted with permission from Henningsson and Botnar [136].

irregularities in the breathing pattern of the subject may occur, the examination time is unpredictable and unknown a priori [27]. Moreover, the diaphragmatic navigator method is limited because it infers (rather than measures) the motion of the heart, does not account for the multidimensional non-linear motion of the heart or hysteresis effects between inspiration and expiration [20, 35]. Several technical developments have been proposed to overcome some of these drawbacks and achieve 100% scan efficiency (thus shorter scan times) with none or minimal data rejection. Self-navigation (SN) methods have been proposed to derivate the respiratory-induced motion of the heart from the acquired data itself without the need of either a 1D diaphragmatic navigator or a heart-diaphragm tracking factor. Respiratory-induced displacements of the heart can be directly estimated from the repetitive acquisition of the central k-space point [28] or the central k-space line [29–31], corresponding to zero-dimensional or one-dimensional projections of the field of view along the SI direction. SI translational respiratory motion compensation, typically to end-expiration, is performed directly in k-space by applying a linear phase shift before image reconstruction. More recently it has been shown that iteratively identifying the most frequently occurring respiratory phase as reference for motion compensation can lead to improved coronary sharpness [40]. Moreover, multi-dimensional SN approaches, involving the acquisition of 1D multiple projections oriented along the right-left (RL) and anterior-posterior (AP) direction, in addition to SI direction, have been also proposed to improve the accuracy of motion correction [29, 32]. However, respiratory SN techniques account for translational motion only and inaccuracies in motion estimation can be introduced from the contribution of the static tissues (such as the chest wall) present in the zero- or one-dimensional projection of the entire imaging volume. In order to address this hurdle, the so-called image navigator (iNAV) methods [33–35] have been proposed (Figure 15.5). Such approaches aim at spatially isolating the moving heart from the surrounding tissues by acquiring a low resolution 2D image [33] or 3D volume [35–37] prior to data collection or as part of the acquired data itself. This improves the quality of motion

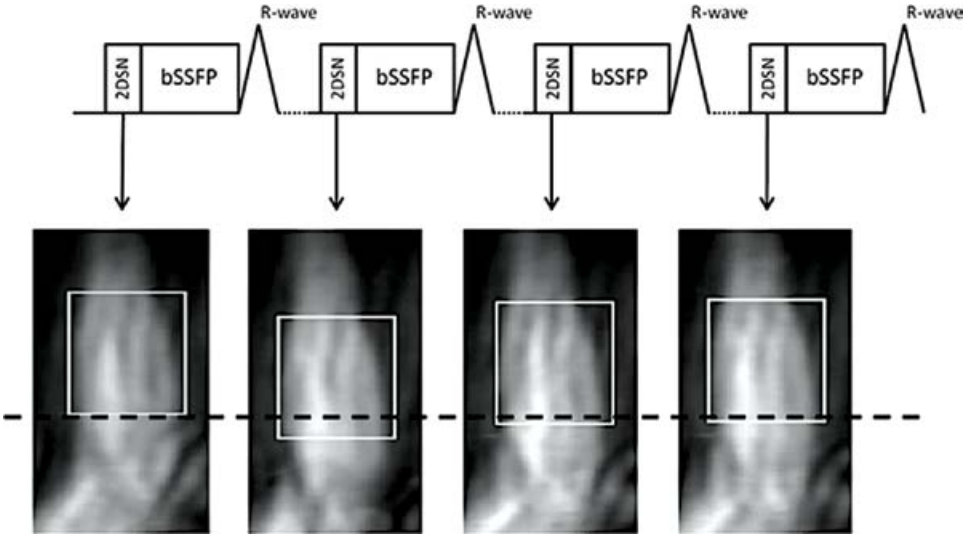

FIGURE 15.5 Image-based navigation for coronary MRI. In this approach, a low-resolution image of the heart is acquired encoding the start-up pulses of a balance steady state free precession (bSSFP) sequence. Such low-resolution images, referred to as image navigators, allows for the detection of the respiratory displacement of the heart along both the superior-inferior and right-left direction (in this case). Acquired data are corrected to the same respiratory position prior to image reconstruction. The approach enables data acquisition at 100% scan efficiency, while examination time is known a priori. Figure reprinted with permission from Henningsson *et al.* [33].

detection not only by eliminating the contribution from the chest wall, but also by enabling multiple degrees of freedom for motion correction. iNAVs have been used to extract information on the translational motion of the heart in 2D (SI and right left, or RL, directions) [33] and 3D (SI, RL, and anterior posterior, or AP, directions) [35–40]. In several approaches, the SI translational respiratory motion of the heart—estimated either via SN or iNAV strategies—is used to bin the imaging data at different respiratory stages or bins [41–47]. Such bin images can be used for the estimation of inter-bin non-rigid motion fields, thus allowing for the reconstruction of a single, non-rigid motion-corrected, 3D whole-heart volume composed of all the acquired k-space data [48] (Figure 15.6). Additionally, the image quality of each individual bin can be augmented by exploiting sparsity along the respiratory dimension, obtaining respiratory motion-resolved images [49]. These approaches were originally proposed for radial imaging acquisitions, that are less sensitive to motion. In order to enable their extension to Cartesian imaging, approaches have been introduced that incorporate translational motion information derived from the iNAVs to increase the sparsity along the respiratory direction, and thus improve the motion-resolved reconstructed images [50] (Figure 15.7). Recently, approaches aimed at resolving the motion of the heart along both the respiratory and the cardiac dimensions have been introduced, allowing for respiratory-resolved images of the heart throughout the entire cardiac cycle for the simultaneous respiratory motion-resolved visualization of the coronary anatomy and quantification of cardiac function [51]. These novel technical developments are currently mainly in the proof-of-concept state and clinical validation is awaited to establish their efficacy.

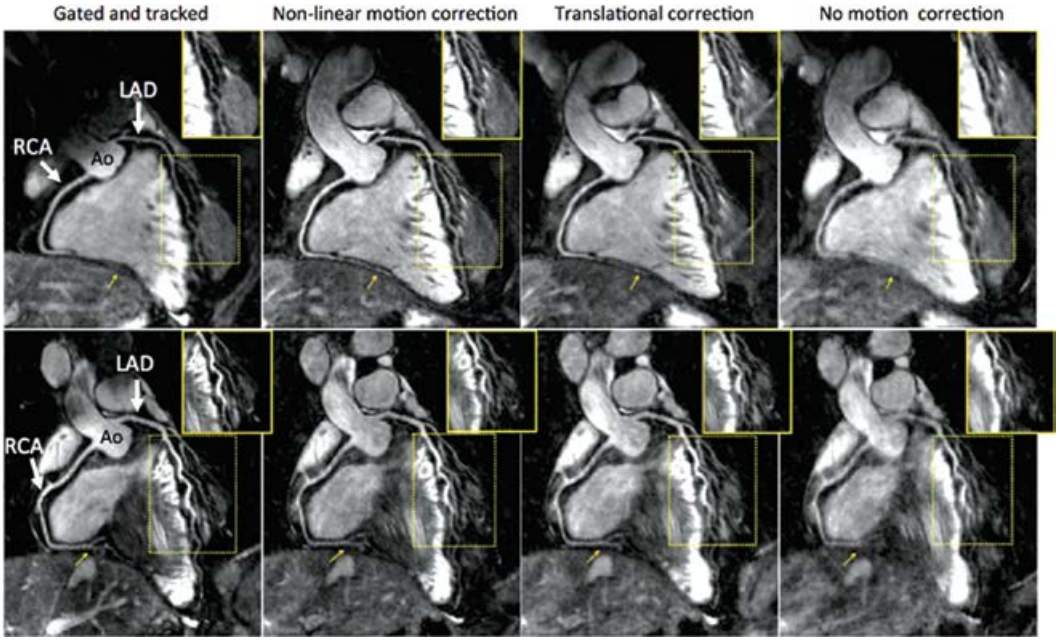

FIGURE 15.6 Comparison of different respiratory motion correction strategies for 3D whole-heart coronary MR angiography. Reformatted images are shown for conventional diaphragmatic navigator gated and tracked acquisition, non-linear motion correction, translation correction only and no motion correction in two healthy subjects. Blurring present in the no motion correction images is reduced with translation correction and sharpness further increased with the non-linear motion correction approach (boxes), particularly in the distal part of both the right (RCA) and the left (LAD) coronaries (arrows). The non-linear motion correction approach has similar image quality to the conventional navigator gated acquisition, while ensuring reduced acquisition time. RCA: right coronary artery, LAD: left anterior descending coronary artery, Ao: aorta.

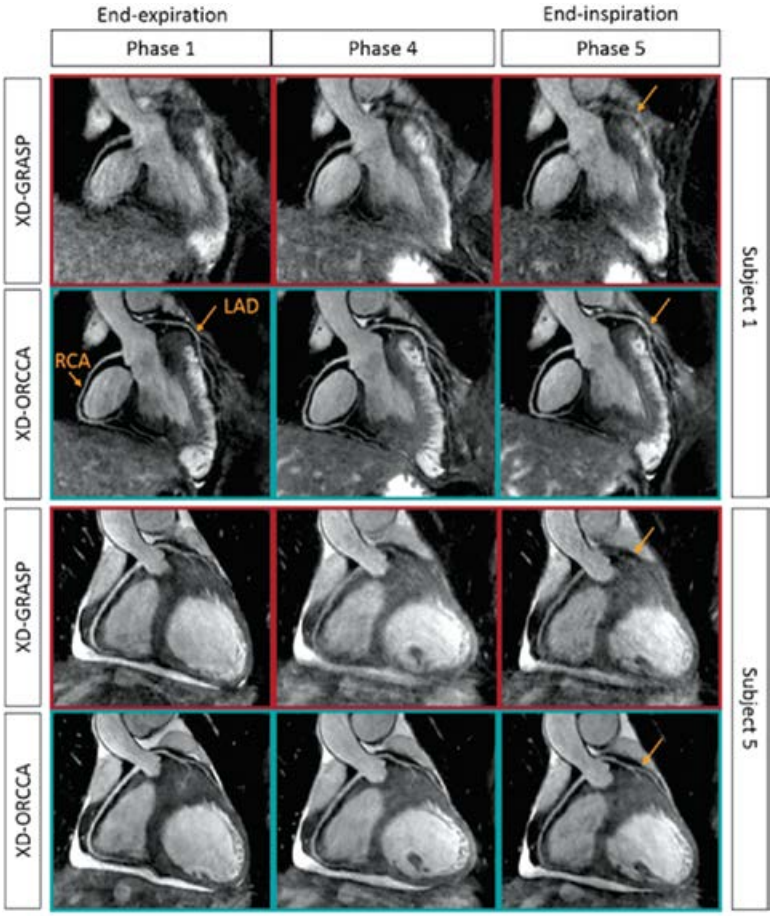

FIGURE 15.7 Respiratory-resolved reconstructions obtained in two healthy subjects using a Cartesian trajectory integrated with image-based navigation and respiratory-resolved reconstruction. Here, beat-to-beat translational motion information derived from the iNAVs are integrated in the respiratory-resolved reconstruction in order to increase the sparsity in the respiratory dimension. This approach (referred to as XD-ORCCA) provides improved right (RCA) and left (LAD) coronary sharpness in comparison to approaches that do not account for such information (XD-GRASP). Images are shown for three different respiratory phases, moving from end-expiration (right) to end-inspiration (left).

15.2.3 Coronary Signal Enhancement

In order to adequately enhance the signal from the coronary lumen and coronary wall with respect to that of the surrounding epicardial fat and myocardial tissue, specific imaging strategies need to be adopted (Figure 15.2). As epicardial fat exhibits a lower T1 in comparison to luminal blood, frequency selective excitation pulses can be exploited to saturate the signal from the epicardial fat, thus enabling the visualization of the underlying coronary arteries [52–54] (Figure 15.8). In order to improve blood to myocardium contrast, T2 preparatory pulses are typically used [55–57]. T2 preparation is a convenient choice for imaging the coronary arteries, as it suppresses contribution from both the myocardium and the venous blood. Furthermore, T2 preparatory pulses are typically less energy consuming and therefore more widely used. Recently, spatially selective T2 preparation pulses have been developed in order to suppress the signal from the static tissues outside the heart [58, 59]. The use of gadolinium-based MRI contrast agents can be also exploited to improve the contrast between myocardium and blood. Depending on the clinical information

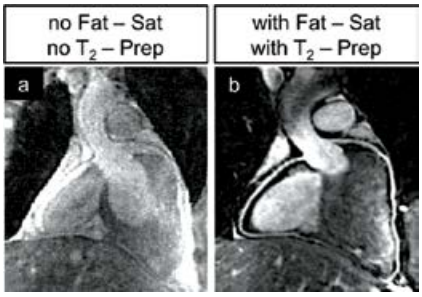

FIGURE 15.8 Impact of imaging preparation pulses in a 3D whole-heart coronary MRI acquisition. When imaging preparation is not used (a), the coronary lumen appears undistinguishable from the surrounding myocardium and epicardial fat. The use of both T_2 preparation (T_2-Prep) and fat saturation (Fat-Sat) enables the depiction of the coronary vessels for their entire extension (b).

requested, extracellular, blood-pool, or albumin-binding contrast agents can be chosen [60–63]. The prolonged retention time and the higher relaxivities of albumin-binding contrast agents, for instance, makes them an appealing option for combined imaging of coronary arteries and infarcts. Prior clinical indication of contrast-enhanced acquisitions, the presence of nephrogenic systemic fibrosis in patients with co-existent renal dysfunction needs to be considered [64].

15.2.4 Volumetric Coverage and Acquisition Speed

The major coronary arteries, consisting of the right coronary artery (RCA) and the left main (LM) coronary artery which branches into the left anterior descending (LAD) artery and the left circumflex (LCX) artery, have a proximal normal diameter of 3–5 mm and 1–2 mm in more distal segments. Moreover, the coronaries exhibit a complex geometry and follow tortuous paths. Therefore, large volumetric coverage with isotropic high spatial resolution, ideally below 1 mm, is needed to correctly visualize and characterize the coronaries. The first approaches to address this requirement for high-resolution volumetric imaging of coronary arteries utilized either a targeted approach [65] or a three-point scan tool [66] (Figure 15.9, a and b) based on a preliminary low-resolution image. These techniques are highly operator dependent, and several acquisitions are needed to image the different coronary segments, thus prolonging the overall scan time. 3D whole-heart acquisition approaches have been introduced [67] to allow for the complete volumetric coverage of the heart with less operator dependent scans (Figure 15.9c). Multiplanar reformatting to visualize the different coronary segments can be obtained from the 3D whole-heart images using dedicated software tools,

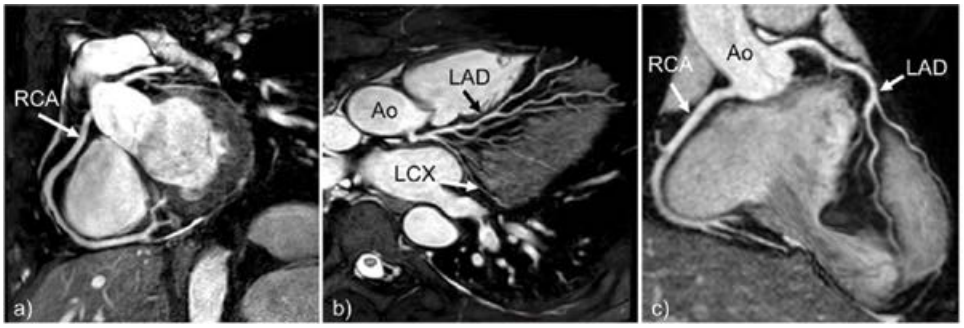

FIGURE 15.9 Visualization of the right (RCA) and the left (LAD) coronary arteries in targeted acquisitions (a, b) and in a 3D whole-heart acquisition (c). LCX: left circumflex, AO: aorta.

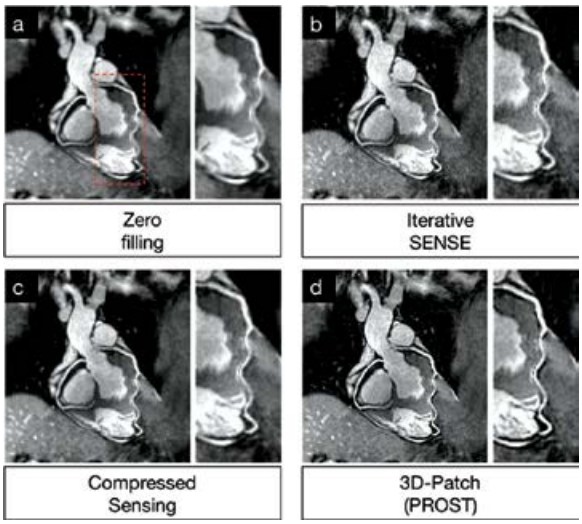

FIGURE 15.10 3D whole-heart coronary MR angiography acquired in a healthy subject using a variable density Cartesian trajectory with a 4-fold acceleration factor. The direct zero-filling reconstruction exhibits image blurring due to the undersampling. Sharpness is improved with the conventional parallel image reconstruction (It-SENSE), but a higher level of noise can be observed. Conversely, the noise level decreases in the Compressed Sensing reconstruction. The use of a patch-based reconstruction (3D-PROST) eliminated the background noise while improving coronary sharpness.

such as the one described in [68]. However, high-resolution whole-heart coronary MRI still requires long acquisition times. Several approaches have been proposed to accelerate the acquisition speed of coronary MRI including fast trajectories [38, 69, 70], undersampling reconstruction techniques, and respiratory motion correction approaches with 100% scan efficiency (described in section 2.2). Parallel imaging reconstruction techniques such as SENSE or GRAPPA [73, 74], which exploits the sensitivity of phased array coils, have become the standard to reduce the acquisition time in coronary MRI by 2 to 3 times while maintaining high image quality. Further acceleration may be achieved by combining parallel imaging with compressed sensing (CS) approaches [76, 77] that exploit the sparsity of the reconstructed image in a specific transform domain, although the efficacy of these approaches in clinical practice has yet to be established. Recent improvements in these types of techniques include taking advantage of structural patch-based similarities within the coronary arteries [78, 79]. These techniques have been recently combined with motion correction approaches with 100% scan efficiency [137] and promise to enable sub-millimeter isotropic resolution (0.9 mm) coronary MRI in clinically feasible scan times (Figure 15.10).

15.3 THE ROLE OF MRI TO ASSESS CORONARY ARTERY DISEASE PROGRESSION

15.3.1 Coronary Endothelial Dysfunction Assessment

Coronary endothelial dysfunction has proved to be associated with processes of inflammation as well as with clinical events; and it is considered a very early marker of CAD. Detection of coronary endothelial dysfunction is challenging as it does not cause any visible structural change at the coronary vessel itself. Coronary vasomotor response has been evaluated in previous studies, where the discrimination between normal and abnormal coronary endothelial function could provide an early diagnosis of CAD [9, 10, 12, 71]. In a clinical setting, endothelial function may be currently assessed by invasive X-ray angiography in combination with Doppler flow measurements. These

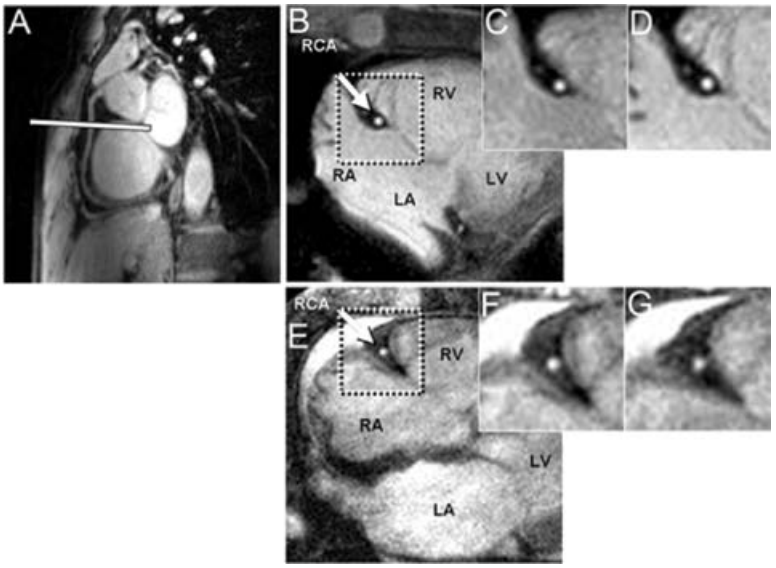

FIGURE 15.11 MRI-measured response at isometric handgrip exercise in terms of dilation of the right coronary artery (RCA) in healthy subjects and patients. In this study, a preliminary scout scan was acquired (A) in order to prescribe the following 2D acquisitions (B, E) in correspondence to the RCA cross-sectional area. In healthy subjects, a physiological dilation in the RCA can be appreciated during exercise (D) in comparison to rest (C). Differently, in patients the cross-sectional RCA area slightly decreases with stress (G) in comparison to rest (F). Figure reprinted with permission from Hays *et al*. [72].

measurements are associated with an increased radiation exposure, as measurements have to be performed prior to and following the administration of pharmacological vasodilation. Recently, the feasibility of MRI to detect anomalies in coronary endothelial function has been shown [72–77]. In these studies, MR images of the cross-sectional area of the coronary artery were acquired while the subjects were performing isometric handgrip exercise, a factor of physical and endothelial dependent stress. When images were compared to those acquired at rest, it has been shown that isometric exercise causes significant coronary dilation in healthy subjects, while, in the case of CAD patients, there was a significant reduction in luminal area change (Figure 15.11). In a smaller cohort of subjects, nitroglycerine was administered and showed to cause an endothelial-independent relative coronary area change in both healthy subjects and CAD patients [72], and thus could not be used to distinguish the two populations. One of the main challenges in coronary endothelial function MRI is that acquiring data while the subject is under physical stress could have a detrimental effect on the quality of the recorded ECG, thus on the quality of cardiac motion compensation and on the final image sharpness. Therefore, technical advances in this field aim at the development of strategies enabling the estimation of myocardial contraction from the imaging data itself, without the need of an external ECG [78, 79]. In addition, and as MRI measurements of cross-sectional coronary area are currently limited to 2D acquisitions performed under breath-hold, future studies will reasonably aim at the extension of such techniques to achieve higher volumetric coverage under free-breathing.

15.3.2 Imaging of Positive Vessel Wall Remodeling

Positive vessel wall remodeling occurs before any luminal narrowing is detectable. Therefore, the presence of positive remodeling cannot be assessed with luminography techniques such as invasive X-ray angiography. The rupture of unobstructive plaque (with positive remodeling) can lead to acute coronary syndromes in the absence of prior symptoms. Positive vessel wall remodeling can be quantified with the assessment of atherosclerotic plaque burden, by measuring the vessel wall

thickness (or area) at different locations along the vessel [80]. In a study by Stone et al. [81], performed in 697 patients with coronary syndromes, coronary plaque burden (equal to 70% or greater) has shown to be an independent predictor of subsequent coronary events.

Additionally, it has been shown that lipid-lowering therapies using statins result in a reduction of the local progression of coronary atherosclerosis quantified by the plaque burden [82]. Intravascular ultrasound (IVUS) and optical coherence tomography (OCT) provide high-resolution images of coronary plaque, but they are invasive and thus not suitable for screening or follow-up. Black-blood coronary MRI [83, 84] allows for high contrast visualization of the coronary vessel wall; this is achieved by suppressing the signal from the flowing blood and by enhancing that of the static tissues. As such, black-blood coronary MRI is a potential candidate for non-invasive investigation of the atherosclerotic processes occurring in the vessel wall and for the assessment of coronary plaque burden. The first in vivo studies on plaque characterization were performed by exploiting the double inversion recovery (DIR) technique [85, 86]; DIR is a flow-dependent technique that utilizes two separate inversion pulses to (1) non-selectively invert the signal from static tissues and blood within the imaging volume and (2) selectively re-invert the signal of static tissues within a target 2D slice. At the moment of data collection, and within the target slice, static tissues will have re-inverted positive magnetization while in-flowing blood will have approximately nulled magnetization (Figures 15.12 and 15.13). Initial clinical studies assessed the presence of plaques in carotid arteries [87–89]. Imaging the coronary vessel wall is more challenging since, as anticipated, the coronaries are small in diameter, exhibit a complex geometry, and are subject to cardiac and respiratory motion. DIR for coronary vessel wall MRI has been performed under breath-hold [86] or during free-breathing [85] in combination with diaphragmatic navigator; ECG-triggering has been used to address the presence of cardiac motion. As mentioned, DIR acquisitions are typically performed in 2D, however the use of local inversion pulses together with 3D imaging can enable larger anatomical coverage that allows for the visualization of the coronary wall along extensive portions of the vessel [90]. In one of the initial non-contrast enhanced coronary MRI vessel wall studies, the presence of positive remodeling in patients with subclinical coronary atherosclerosis was shown [91] (Figure 15.12). In a subsequent multiethnic study, increased coronary vascular remodeling was observed in subjects without prior history of CAD [92, 93]. Similarly, a different study showed increased positive remodeling of the coronary vessel wall in asymptomatic subjects [94]. Therefore, coronary vessel wall MRI holds promise as a screening tool in asymptomatic subjects for detection and quantification of positive remodeling and plaque burden. One of the main disadvantages of DIR, however, consists in the fact that it requires sophisticated acquisition planning, as data has to be collected during the period of optimal blood signal nulling and of minimal cardiac contraction. For these reasons, the reported failure rate of DIR acquisitions in clinical studies is particularly high (about 30%) [18, 86, 95].

To address some of these shortcomings, time-resolved techniques have been proposed in order to improve the robustness of DIR [96, 97] (Figure 15.14). These techniques enable the retrospective

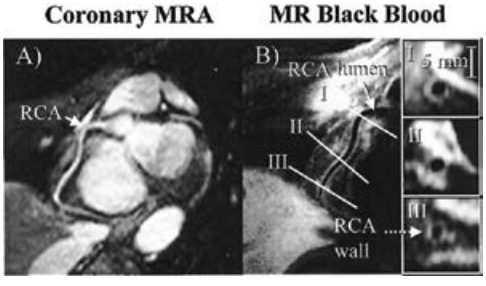

FIGURE 15.12 Reformatted 3D coronary MRA (A) and a double-inversion recovery acquisition (B) of the right coronary artery (RCA) in one subject. Cross-sectional views are shown at three different levels (I, II, III). Figure reprinted with permission from Kim *et al.* [91].

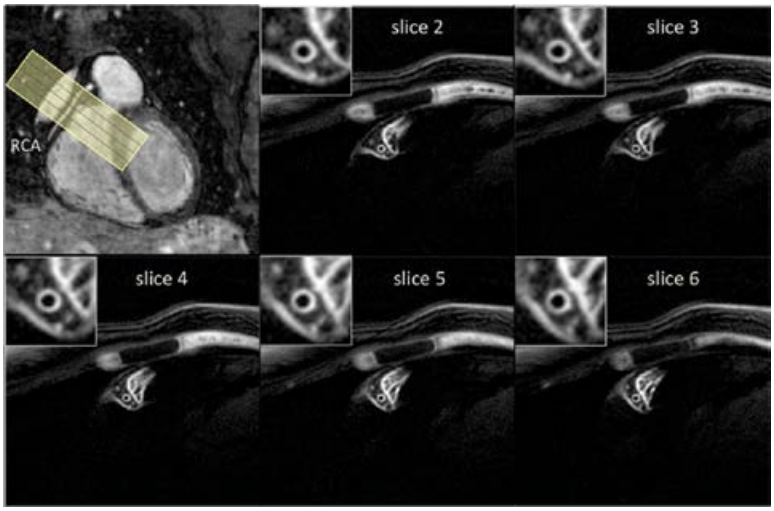

FIGURE 15.13 3D cross-sectional coronary vessel wall imaging obtained using a local inversion pre-pulse and a stack of spiral trajectory (in-plane spatial resolution of 0.6mm × 0.6mm, slice thickness of 3mm). The 3D imaging volume was positioned perpendicular to a relatively linear portion of the proximal-mid right coronary artery. Image adapted with permission from Peel *et al.* [138].

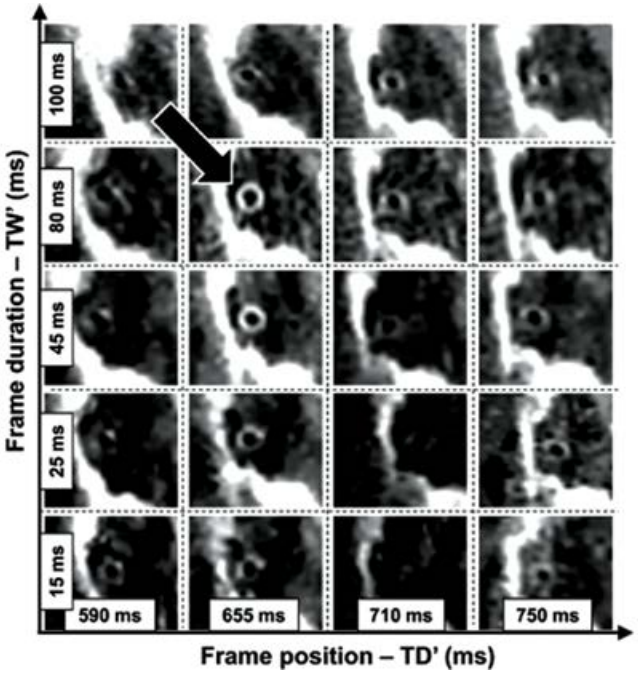

FIGURE 15.14 Coronary vessel wall images reconstructed at different time-points (TD') within the cardiac cycle and with different temporal duration (TW'). This allows to retrospectively identify the image that provided the most improved vessel wall delineation. Figure reprinted with permission from Ginami *et al.* [97].

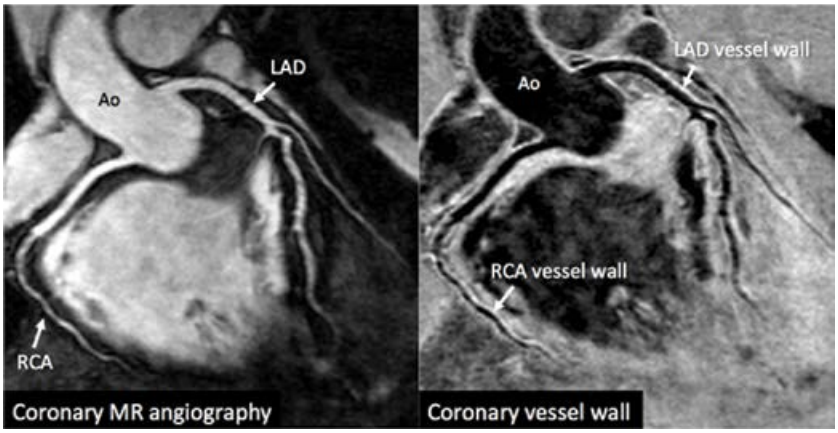

FIGURE 15.15 3D whole-heart acquisition obtained using interleaved T_2 preparation for simultaneous coronary lumen and vessel wall visualization. Interleaved acquisition and subtraction between two datasets acquired with and without T_2 preparation allows for blood signal nulling while maintaining the signal from the myocardium and the vessel wall (right). Data with T_2 preparation provide the visualization of the coronary lumen. RCA: right coronary artery, LAD: left anterior descending coronary artery, Ao: aorta.

selection of the cine frame providing the most optimized blood signal suppression and the most adequate cardiac motion minimization. A major limitation of all the DIR implementations is their intrinsic sensitivity to flow and, as a consequence, its robustness may be compromised by slow flowing blood, and whole-heart volumetric coverage is difficult to achieve. For this reason, a flow-independent 3D whole-heart coronary vessel wall MRI technique has been introduced [98] (Figure 15.15); this approach is based on the weighted subtraction of two differently T2-weighted 3D volumes to achieve blood signal nulling, thus providing high contrast between the suppressed blood signal and the vessel walls. This technique was initially implemented in combination with diaphragmatic navigator; more recently, the same approach has been integrated with iNAV and non-rigid respiratory motion correction [44], thus enabling whole-heart coverage in a predictable examination time. The use of elastin-specific MRI contrast agents (ESMA) may further improve plaque burden quantification. In fact, the high-signal provided by ESMA allows for imaging at particularly high spatial resolution [99, 100].

15.3.3 Imaging of Plaque Inflammation, Thrombus, and Intraplaque Hemorrhage

Vascular inflammation during CAD progression can compromise the structural integrity of plaque and promote instability by suppressing collagen generation and promoting matrix degradation [101, 102]. In this scenario, the plaque becomes unstable and at risk of rupture, which may lead to myocardial infarction and stroke [14, 103]. Therefore, imaging plaque inflammation could potentially be used to facilitate the detection of high-risk plaques and guide administration of therapies. However, MR imaging of inflammation at the level of the coronary arteries remains challenging due to the previously mentioned technical challenges.

Another factor promoting plaque destabilization is the presence of intraplaque hemorrhage (IPH). IPH can originate from the rupture of the fibrotic cap and subsequent penetration of blood from the coronary lumen [104], as well as from extravasation of blood from the immature vasculature within the coronary plaque [105, 106]. Most of the cases of acute coronary syndrome have shown to be caused by sudden plaque rupture, that can lead to the formation of intracoronary thrombus, causing partial or total occlusion of the vessel [107, 108]. Therefore, an imaging modality for the rapid assessment of intraluminal thrombosis in such patients is highly desirable. The administration

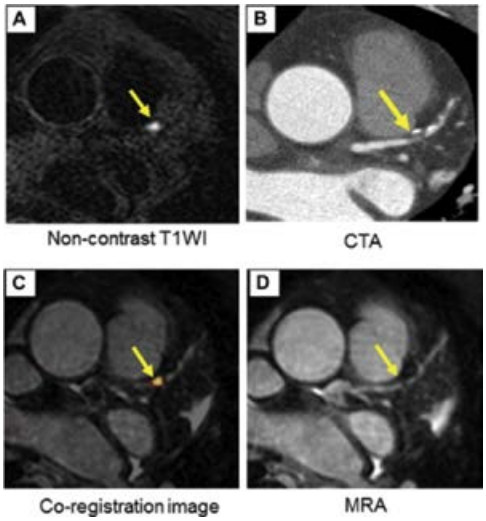

FIGURE 15.16 High intensity signal on a T1-weighted coronary MRI acquisition (A) positively correlates with to the coronary plaque identified by computed tomography angiography (CTA, B). The co-registration (C) of the T1-weighted acquisition (A) with a separate bright-blood coronary MRI acquisition allows to anatomically locate the plaque along the coronary vessel. Figure reprinted with permission from Noguchi *et al.* [117].

of gadolinium (Gd)-based contrast agents can lead to an hyperenhancement of the atherosclerotic plaque [109]. In preclinical studies, the presence of contrast enhancement in MR images has been shown to correlate with the presence of inflammation in the coronary vessel wall [110, 111]. The presence of IPH and coronary thrombus can be assessed with non-contrast MRI using T1-weighted sequences [112–117]; such approaches rely on the short T1 relaxation time of methemoglobin, a component of both acute thrombus and IPH. As such, T1-weighted sequences aim at suppressing the signal from both the static tissues and the flowing blood, while providing an enhanced signal in the location of IPH and thrombus. These approaches typically acquire a first T1-weighted black-blood image for hyperenhancement detection and, subsequently, a bright-blood reference image. The two images are then co-registered to localize the region of hyperenhancement along the coronary tree (Figures 15.16 and 15.17). As the black-blood T1-weighted and the reference acquisitions

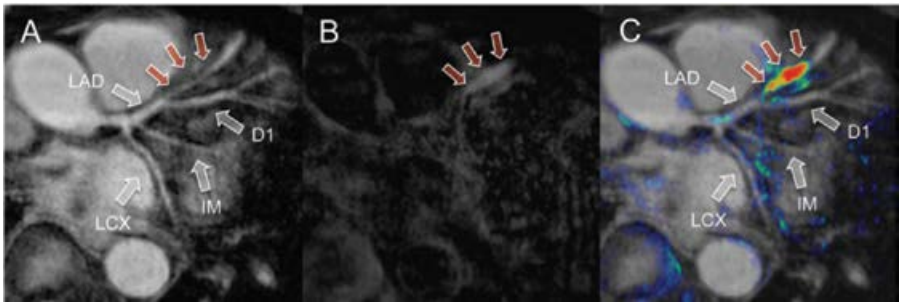

FIGURE 15.17 MRI visualization of coronary thrombus in a 64-year-old man with anterior myocardial infarction. Coronary MRI of the lumen (A) shows a reduced vessel lumen size of the LAD (red arrows). T1-weighted black-blood imaging (B) shows a region of hyperenhancement at the corresponding location. Morphological location of the region of hyperenhancement is better depicted after the fusion of the two images in A and B (C). LAD: left anterior descending coronary artery, LCX: left circumflex, IM: ramus intermedium, D1: diagonal branch. Figure reprinted with permission from Jansen *et al.* [115].

are typically performed in free-breathing, diaphragmatic navigators are used to compensate for respiratory motion. Therefore, such approaches entail prolonged and unpredictable examination times, while there is the risk of misregistration errors between the black- and the bright-blood datasets. To overcome these drawbacks, a 3D whole-heart and respiratory self-navigated sequence, called CATCH, has been introduced to acquire a black-blood T1-weighted volume and a bright-blood reference image in an alternated fashion [118]. An extension of this approach, called BOOST, has been recently proposed [119] to acquire two differently weighted bright-blood datasets in an interleaved fashion, that are combined in a PSIR reconstruction [120] in post-processing to obtain a complementary and fully co-registered black-blood dataset.

15.3.4 Imaging of Luminal Narrowing

Initial studies for imaging the coronary lumen with MRI were performed in the late 1980s and early 1990s. However, at that stage the technique was not mature enough to allow for the visualization of actual luminal narrowing. These pioneering studies raised interest in the scientific community that started to focus on the technical developments needed to address the challenges associated with imaging the coronary lumen. In a study by Jahnke et al. [121], free-breathing coronary MR angiography (CMRA) acquired with diaphragmatic navigator showed improved accuracy for stenosis detection when compared to previously introduced breath-hold acquisition. A prospective comparison between free-breathing CMRA and X-ray angiography has been performed using a single-vendor technology [55, 66], and in a multicenter study [122], where eight international centers were involved. In this study, CMRA showed high sensitivity for CAD detection; however, the specificity remained low (about 40%), and about 25% of the acquired images provided poor image quality. Nevertheless, CMRA showed a specificity and sensitivity of 100% for the detection of stenosis along the left main (LM) and for the detection of triple vessel disease. These studies were performed using a volume targeting approach. Subsequently, studies exploiting 3D whole-heart acquisitions were carried out. A seven center trial in Japan [123] reported a value of specificity of almost 90% for coronary MRI, and a sensitivity value of 72%, while the amount of diagnostically interpretable images was of about 92%. CMRA has been compared with computed tomography acquisitions as well [124], and it showed lower sensitivity and specificity, but comparable predictive value. Studies have shown that coronary MRI can provide reliable depiction of the proximal part of the coronary arteries, including the entire left main (LM), the first 80 mm of the RCA, and the first 40 mm of the LCX [25, 55]. Therefore, CMRA is nowadays considered a reliable imaging modality for excluding the presence of CAD, especially in subjects with low CAD likelihood. More recently, initial clinical studies investigating the feasibility of the latest respiratory motion compensation techniques, such as SN and iNAV (section 2.2), have been performed. 1D respiratory SN has been performed in 78 patients on a 1.5 Tesla system [125] and on 39 patients on 3 Tesla scanner [130], showing adequate diagnostic quality for the main and proximal coronary segments in 92.3% and 92.7% of all the acquired images. Sensitivity and specificity in these studies in comparison to X-ray angiography amounted to 65% and 85% (1.5 Tesla) and 78.2% and 75% (3 Tesla). A clinical feasibility study of iNAV approaches for the detection of coronary stenosis was also carried out on a 1.5 Tesla system [126]. The reported diagnostic quality was of 98%, 94%, and 91% for proximal, mid, and distal segments, respectively, with a sensitivity and specificity of 86% and 83% in comparison to X-ray angiography. Sensitivity and specificity values of both SN and iNAV methods are approaching those reported in previous multicenter studies based on diaphragmatic navigator acquisitions. However, further work, not yet clinically validated, is ongoing, including non-rigid motion compensation and acceleration techniques.

The use of coronary MRI for imaging the coronary lumen has shown promise not only for the detection of luminal narrowing, but also for acquisitions in patients with aneurysms (such as those caused by Kawasaki disease) [127–129] and for imaging coronary bypass grafts [130, 131].

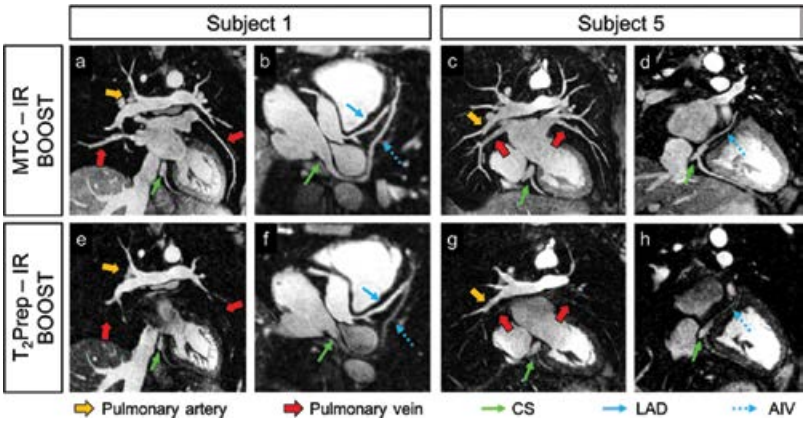

FIGURE 15.18 Bright-blood visualization of the cardiac anatomy using a simultaneous bright and black blood framework incorporating MTC. With this approach, a bright-blood volume (MTC-IR BOOST) is generated and ensures the visualization of both the arterial and the venous system with high signal and contrast (a–d). Conversely, a T_2-prepared configuration of such approach sinus. LAD: left anterior descending coronary artery, AIV: anterior interventricular vein.

15.4 IMAGING OF THE CORONARY VEINS

MRI has been commonly used for the visualization of the coronary artery circulation. Imaging the coronary vein circulation is currently gaining interest, especially in the context of resynchronization therapies. In fact, in this context, the cannulation of the coronary sinus (CS) is performed in order to gain access to the left atrial and the left ventricular epicardium. However, more traditional sequences exploiting T2-preparation to improve the contrast between arterial blood and myocardium are not directly applicable in this scenario. In fact, de-oxygenated venous blood is characterized by a very short T2 relaxation time in comparison to arterial blood (35 ms versus 250 ms, respectively) [132], and therefore it appears suppressed when such preparatory pulses are used. As an alternative to T2-preparation, imaging of the coronary veins can be obtained using an intravascular contrast agent [132]. Alternatively, magnetization transfer contrast (MTC) has been exploited for non-contrast imaging the coronary veins [133–135]. Such sequences have been proposed as volume-targeted acquisitions [133], or as whole-heart approaches [134], in combination with diaphragmatic navigators. With the increasing interest in coronary vein imaging, there is the need of combining whole-heart MT-prepared sequences with respiratory SN or iNAV for improved scan efficiency, facilitating clinical translation. In this regard, a novel multi-contrast sequence integrating MTC within a PSIR framework enables the depiction of the heart anatomy, with equal signal and contrast when comparing the arterial and the venous system. The sequence is integrated with image-based navigation and non-rigid respiratory motion correction. With respect to T2-prepared acquisitions, the use of MTC ensures preserved signal of the venous vessels (Figure 15.18).

15.5 CONCLUSION

Coronary MRI is a promising and non-invasive technique for imaging the progression of CAD. With its ability of generating different imaging contrasts, MRI has shown capability of detecting coronary endothelial dysfunction, positive coronary vessel wall remodeling, IPH, inflammation, and intraluminal thrombosis. Currently, the largest validation of MRI has been carried out for the detection of luminal stenosis. Ongoing research efforts aim at addressing the most important challenges currently preventing a broader adoption of coronary MRI in the clinical practice.

Specifically, there is the need to improve the spatial resolution of coronary MRI, while being able to perform data acquisition with sufficiently large volumetric coverage and within a reasonable acquisition time. Furthermore, the presence of motion remains a major challenge in coronary MRI and a topic of ongoing investigation.

References

1. A. S. Go *et al.*, "Heart disease and stroke statistics—2014 update: a report from the American Heart Association," *Circulation*, vol. 129, no. 3, pp. e28–e292, Jan 21 2014.
2. B. J. Chow *et al.*, "Diagnostic accuracy and impact of computed tomographic coronary angiography on utilization of invasive coronary angiography," *Circ Cardiovasc Imaging*, vol. 2, no. 1, pp. 16–23, Jan 2009.
3. J. M. Miller *et al.*, "Diagnostic performance of coronary angiography by 64-row CT," *N Engl J Med*, vol. 359, no. 22, pp. 2324–2336, Nov 27 2008.
4. M. Tavakol, S. Ashraf, and S. J. Brener, "Risks and complications of coronary angiography: a comprehensive review," *Glob J Health Sci*, vol. 4, no. 1, pp. 65–93, Jan 1 2012.
5. M. Hamon, J. C. Baron, F. Viader, and M. Hamon, "Periprocedural stroke and cardiac catheterization," *Circulation*, vol. 118, no. 6, pp. 678–683, Aug 5 2008.
6. S. Dukkipati *et al.*, "Characteristics of cerebrovascular accidents after percutaneous coronary interventions," *J Am Coll Cardiol*, vol. 43, no. 7, pp. 1161–1167, Apr 7 2004.
7. P. Libby, U. Schoenbeck, F. Mach, A. P. Selwyn, and P. Ganz, "Current concepts in cardiovascular pathology: the role of LDL cholesterol in plaque rupture and stabilization," *Am J Med*, vol. 104, no. 2A, pp. 14S-18S, Feb 23 1998.
8. V. Schachinger, M. B. Britten, and A. M. Zeiher, "Prognostic impact of coronary vasodilator dysfunction on adverse long-term outcome of coronary heart disease," *Circulation*, vol. 101, no. 16, pp. 1899–1906, Apr 25 2000.
9. J. P. Halcox *et al.*, "Prognostic value of coronary vascular endothelial dysfunction," *Circulation*, vol. 106, no. 6, pp. 653–658, Aug 6 2002.
10. T. H. Schindler *et al.*, "Prognostic value of abnormal vasoreactivity of epicardial coronary arteries to sympathetic stimulation in patients with normal coronary angiograms," *Arterioscler Thromb Vasc Biol*, vol. 23, no. 3, pp. 495–501, Mar 1 2003.
11. J. Davignon and P. Ganz, "Role of endothelial dysfunction in atherosclerosis," *Circulation*, vol. 109, no. 23 Suppl 1, pp. III27–III32, Jun 15 2004.
12. A. Sandoo, J. J. van Zanten, G. S. Metsios, D. Carroll, and G. D. Kitas, "The endothelium and its role in regulating vascular tone," *Open Cardiovasc Med J*, vol. 4, pp. 302–312, Dec 23 2010.
13. S. Glagov, E. Weisenberg, C. K. Zarins, R. Stankunavicius, and G. J. Kolettis, "Compensatory enlargement of human atherosclerotic coronary arteries," *N Engl J Med*, vol. 316, no. 22, pp. 1371–1375, May 28 1987.
14. P. Libby, P. M. Ridker, and A. Maseri, "Inflammation and atherosclerosis," *Circulation*, vol. 105, no. 9, pp. 1135–1143, Mar 5 2002.
15. K. Sakakura, M. Nakano, F. Otsuka, E. Ladich, F. D. Kolodgie, and R. Virmani, "Pathophysiology of atherosclerosis plaque progression," *Heart Lung Circ*, vol. 22, no. 6, pp. 399–411, Jun 2013.
16. M. Aikawa *et al.*, "Lipid lowering reduces oxidative stress and endothelial cell activation in rabbit atheroma," *Circulation*, vol. 106, no. 11, pp. 1390–1396, Sep 10 2002.
17. S. E. Fischer, S. A. Wickline, and C. H. Lorenz, "Novel real-time R-wave detection algorithm based on the vectorcardiogram for accurate gated magnetic resonance acquisitions," *Magn Reson Med*, vol. 42, no. 2, pp. 361–370, Aug 1999.
18. W. Y. Kim, M. Stuber, K. V. Kissinger, N. T. Andersen, W. J. Manning, and R. M. Botnar, "Impact of bulk cardiac motion on right coronary MR angiography and vessel wall imaging," *J Magn Reson Imaging*, vol. 14, no. 4, pp. 383–390, Oct 2001.
19. J. Pang *et al.*, "ECG and navigator-free four-dimensional whole-heart coronary MRA for simultaneous visualization of cardiac anatomy and function," *Magn Reson Med*, vol. 72, no. 5, pp. 1208–1217, Nov 2014.
20. S. Coppo *et al.*, "Free-running 4D whole-heart self-navigated golden angle MRI: initial results," *Magn Reson Med*, vol. 74, no. 5, pp. 1306–1316, Nov 2015.
21. J. Pang *et al.*, "High efficiency coronary MR angiography with nonrigid cardiac motion correction," *Magn Reson Med*, vol. 76, no. 5, pp. 1345–1353, Nov 2016.

22. D. Manke, K. Nehrke, P. Bornert, P. Rosch, and O. Dossel, "Respiratory motion in coronary magnetic resonance angiography: a comparison of different motion models," *J Magn Reson Imaging*, vol. 15, no. 6, pp. 661–671, Jun 2002.
23. R. L. Ehman and J. P. Felmlee, "Adaptive technique for high-definition MR imaging of moving structures," *Radiology*, vol. 173, no. 1, pp. 255–263, Oct 1989.
24. D. Li *et al.*, "Coronary arteries: three-dimensional MR imaging with retrospective respiratory gating," *Radiology*, vol. 201, no. 3, pp. 857–863, Dec 1996.
25. J. N. Oshinski, L. Hofland, S. Mukundan, Jr., W. T. Dixon, W. J. Parks, and R. I. Pettigrew, "Two-dimensional coronary MR angiography without breath holding," *Radiology*, vol. 201, no. 3, pp. 737–743, Dec 1996.
26. Y. Wang, S. J. Riederer, and R. L. Ehman, "Respiratory motion of the heart: kinematics and the implications for the spatial resolution in coronary imaging," *Magn Reson Med*, vol. 33, no. 5, pp. 713–719, May 1995.
27. A. M. Taylor, P. Jhooti, D. N. Firmin, and D. J. Pennell, "Automated monitoring of diaphragm end-expiratory position for real-time navigator echo MR coronary angiography," *J Magn Reson Imaging*, vol. 9, no. 3, pp. 395–401, Mar 1999.
28. M. Buehrer, J. Curcic, P. Boesiger, and S. Kozerke, "Prospective self-gating for simultaneous compensation of cardiac and respiratory motion," *Magn Reson Med*, vol. 60, no. 3, pp. 683–690, Sep 2008.
29. P. Lai, X. Bi, R. Jerecic, and D. Li, "A respiratory self-gating technique with 3D-translation compensation for free-breathing whole-heart coronary MRA," *Magn Reson Med*, vol. 62, no. 3, pp. 731–738, Sep 2009.
30. C. Stehning, P. Bornert, K. Nehrke, H. Eggers, and M. Stuber, "Free-breathing whole-heart coronary MRA with 3D radial SSFP and self-navigated image reconstruction," *Magn Reson Med*, vol. 54, no. 2, pp. 476–480, Aug 2005.
31. D. Piccini, A. Littmann, S. Nielles-Vallespin, and M. O. Zenge, "Respiratory self-navigation for whole-heart bright-blood coronary MRI: methods for robust isolation and automatic segmentation of the blood pool," *Magn Reson Med*, vol. 68, no. 2, pp. 571–579, Aug 2012.
32. P. Lai, A. C. Larson, X. Bi, R. Jerecic, and D. Li, "A dual-projection respiratory self-gating technique for whole-heart coronary MRA," *J Magn Reson Imaging*, vol. 28, no. 3, pp. 612–620, Sep 2008.
33. M. Henningsson, P. Koken, C. Stehning, R. Razavi, C. Prieto, and R. M. Botnar, "Whole-heart coronary MR angiography with 2D self-navigated image reconstruction," *Magn Reson Med*, vol. 67, no. 2, pp. 437–445, Feb 2012.
34. M. Henningsson, J. Smink, R. Razavi, and R. M. Botnar, "Prospective respiratory motion correction for coronary MR angiography using a 2D image navigator," *Magn Reson Med*, vol. 69, no. 2, pp. 486–494, Feb 2013.
35. A. D. Scott, J. Keegan, and D. N. Firmin, "Beat-to-beat respiratory motion correction with near 100% efficiency: a quantitative assessment using high-resolution coronary artery imaging," *Magn Reson Imaging*, vol. 29, no. 4, pp. 568–578, May 2011.
36. M. Henningsson, C. Prieto, A. Chiribiri, G. Vaillant, R. Razavi, and R. M. Botnar, "Whole-heart coronary MRA with 3D affine motion correction using 3D image-based navigation," *Magn Reson Med*, vol. 71, no. 1, pp. 173–181, Jan 2014.
37. H. H. Wu, P. T. Gurney, B. S. Hu, D. G. Nishimura, and M. V. McConnell, "Free-breathing multiphase whole-heart coronary MR angiography using image-based navigators and three-dimensional cones imaging," *Magn Reson Med*, vol. 69, no. 4, pp. 1083–1093, Apr 2013.
38. N. O. Addy, R. R. Ingle, H. H. Wu, B. S. Hu, and D. G. Nishimura, "High-resolution variable-density 3D cones coronary MRA," *Magn Reson Med*, vol. 74, no. 3, pp. 614–621, Sep 2015.
39. J. Luo *et al.*, "Nonrigid Motion Correction With 3D Image-Based Navigators for Coronary MR Angiography," *Magn Reson Med*, vol. 77, no. 5, pp. 1884–1893, May 2017.
40. R. R. Ingle *et al.*, "Nonrigid autofocus motion correction for coronary MR angiography with a 3D cones trajectory," *Magn Reson Med*, vol. 72, no. 2, pp. 347–361, Aug 2014.
41. A. P. Aitken, M. Henningsson, R. M. Botnar, T. Schaeffter, and C. Prieto, "100% Efficient three-dimensional coronary MR angiography with two-dimensional beat-to-beat translational and bin-to-bin affine motion correction," *Magn Reson Med*, vol. 74, no. 3, pp. 756–764, Sep 2015.
42. C. Prieto *et al.*, "Highly efficient respiratory motion compensated free-breathing coronary MRA using golden-step Cartesian acquisition," *J Magn Reson Imaging*, vol. 41, no. 3, pp. 738–746, Mar 2015.
43. C. Munoz *et al.*, "Motion-corrected simultaneous cardiac positron emission tomography and coronary MR angiography with high acquisition efficiency," *Magn Reson Med*, vol. 79, no. 1, pp. 339–350, Jan 2018.

44. G. Cruz, D. Atkinson, M. Henningsson, R. M. Botnar, and C. Prieto, "Highly efficient nonrigid motion-corrected 3D whole-heart coronary vessel wall imaging," *Magn Reson Med*, vol. 77, no. 5, pp. 1894–1908, May 2017.
45. J. Pang *et al.*, "Whole-heart coronary MRA with 100% respiratory gating efficiency: self-navigated three-dimensional retrospective image-based motion correction (TRIM)," *Magn Reson Med*, vol. 71, no. 1, pp. 67–74, Jan 2014.
46. H. Bhat, L. Ge, S. Nielles-Vallespin, S. Zuehlsdorff, and D. Li, "3D radial sampling and 3D affine transform-based respiratory motion correction technique for free-breathing whole-heart coronary MRA with 100% imaging efficiency," *Magn Reson Med*, vol. 65, no. 5, pp. 1269–1277, May 2011.
47. G. Bonanno, G. Puy, Y. Wiaux, R. B. van Heeswijk, D. Piccini, and M. Stuber, "Self-navigation with compressed sensing for 2D translational motion correction in free-breathing coronary MRI: a feasibility study," *PLoS One*, vol. 9, no. 8, p. e105523, 2014.
48. G. Cruz, D. Atkinson, M. Henningsson, R. M. Botnar, and C. Prieto, "Highly efficient nonrigid motion-corrected 3D whole-heart coronary vessel wall imaging," *Magn Reson Med*, May 25 2016.
49. D. Piccini *et al.*, "Four-dimensional respiratory motion-resolved whole heart coronary MR angiography," *Magn Reson Med*, Mar 28 2016.
50. T. Correia *et al.*, "Optimized respiratory-resolved motion-compensated 3D Cartesian coronary MR angiography," *Magn Reson Med*, Apr 22 2018.
51. L. Feng *et al.*, "5D whole-heart sparse MRI," *Magn Reson Med*, vol. 79, no. 2, pp. 826–838, Feb 2018.
52. R. R. Edelman, W. J. Manning, D. Burstein, and S. Paulin, "Coronary arteries: breath-hold MR angiography," *Radiology*, vol. 181, no. 3, pp. 641–643, Dec 1991.
53. D. Li, C. B. Paschal, E. M. Haacke, and L. P. Adler, "Coronary arteries: three-dimensional MR imaging with fat saturation and magnetization transfer contrast," *Radiology*, vol. 187, no. 2, pp. 401–406, May 1993.
54. J. Park, A. C. Larson, Q. Zhang, O. Simonetti, and D. Li, "4D radial coronary artery imaging within a single breath-hold: cine angiography with phase-sensitive fat suppression (CAPS)," *Magn Reson Med*, vol. 54, no. 4, pp. 833–840, Oct 2005.
55. R. M. Botnar, M. Stuber, P. G. Danias, K. V. Kissinger, and W. J. Manning, "Improved coronary artery definition with T2-weighted, free-breathing, three-dimensional coronary MRA," *Circulation*, vol. 99, no. 24, pp. 3139–3148, Jun 22 1999.
56. J. H. Brittain, B. S. Hu, G. A. Wright, C. H. Meyer, A. Macovski, and D. G. Nishimura, "Coronary angiography with magnetization-prepared T2 contrast," *Magn Reson Med*, vol. 33, no. 5, pp. 689–696, May 1995.
57. S. M. Shea, V. S. Deshpande, Y. C. Chung, and D. Li, "Three-dimensional true-FISP imaging of the coronary arteries: improved contrast with T2-preparation," *J Magn Reson Imaging*, vol. 15, no. 5, pp. 597–602, May 2002.
58. A. J. Coristine, R. B. van Heeswijk, and M. Stuber, "Combined T2-preparation and two-dimensional pencil-beam inner volume selection," *Magn Reson Med*, vol. 74, no. 2, pp. 529–536, Aug 2015.
59. J. Luo *et al.*, "Combined outer volume suppression and T2 preparation sequence for coronary angiography," *Magn Reson Med*, vol. 74, no. 6, pp. 1632–1639, Dec 2015.
60. M. E. Huber *et al.*, "Performance of a new gadolinium-based intravascular contrast agent in free-breathing inversion-recovery 3D coronary MRA," *Magn Reson Med*, vol. 49, no. 1, pp. 115–121, Jan 2003.
61. D. Li, R. P. Dolan, R. C. Walovitch, and R. B. Lauffer, "Three-dimensional MRI of coronary arteries using an intravascular contrast agent," *Magn Reson Med*, vol. 39, no. 6, pp. 1014–1018, Jun 1998.
62. K. Nassenstein, F. Breuckmann, P. Hunold, J. Barkhausen, and T. Schlosser, "Magnetic resonance coronary angiography: comparison between a Gd-BOPTA- and a Gd-DTPA-enhanced spoiled gradient-echo sequence and a non-contrast-enhanced steady-state free-precession sequence," *Acta Radiol*, vol. 50, no. 4, pp. 406–411, May 2009.
63. L. Tang *et al.*, "Volume-targeted and whole-heart coronary magnetic resonance angiography using an intravascular contrast agent," *J Magn Reson Imaging*, vol. 30, no. 5, pp. 1191–1196, Nov 2009.
64. B. Wagner, V. Drel, and Y. Gorin, "Pathophysiology of gadolinium-associated systemic fibrosis," *Am J Physiol Renal Physiol*, vol. 311, no. 1, pp. F1–F11, Jul 1 2016.
65. P. A. Wielopolski, R. J. van Geuns, P. J. de Feyter, and M. Oudkerk, "Breath-hold coronary MR angiography with volume-targeted imaging," *Radiology*, vol. 209, no. 1, pp. 209–219, Oct 1998.
66. M. Stuber *et al.*, "Double-oblique free-breathing high resolution three-dimensional coronary magnetic resonance angiography," *J Am Coll Cardiol*, vol. 34, no. 2, pp. 524–531, Aug 1999.
67. O. M. Weber, A. J. Martin, and C. B. Higgins, "Whole-heart steady-state free precession coronary artery magnetic resonance angiography," *Magn Reson Med*, vol. 50, no. 6, pp. 1223–1228, Dec 2003.

68. A. Etienne, R. M. Botnar, A. M. Van Muiswinkel, P. Boesiger, W. J. Manning, and M. Stuber, ""Soap-Bubble" visualization and quantitative analysis of 3D coronary magnetic resonance angiograms," *Magn Reson Med*, vol. 48, no. 4, pp. 658–666, Oct 2002.
69. D. Piccini, A. Littmann, S. Nielles-Vallespin, and M. O. Zenge, "Spiral phyllotaxis: the natural way to construct a 3D radial trajectory in MRI," *Magn Reson Med*, vol. 66, no. 4, pp. 1049–1056, Oct 2011.
70. M. H. Moghari, M. Uecker, S. Roujol, M. Sabbagh, T. Geva, and A. J. Powell, "Accelerated whole-heart MR angiography using a variable-density poisson-disc undersampling pattern and compressed sensing reconstruction," *Magn Reson Med*, vol. 79, no. 2, pp. 761–769, Feb 2018.
71. J. E. Deanfield, J. P. Halcox, and T. J. Rabelink, "Endothelial function and dysfunction: testing and clinical relevance," *Circulation*, vol. 115, no. 10, pp. 1285–1295, Mar 13 2007.
72. A. G. Hays, G. A. Hirsch, S. Kelle, G. Gerstenblith, R. G. Weiss, and M. Stuber, "Noninvasive visualization of coronary artery endothelial function in healthy subjects and in patients with coronary artery disease," *J Am Coll Cardiol*, vol. 56, no. 20, pp. 1657–1665, Nov 9 2010.
73. A. G. Hays *et al.*, "Regional coronary endothelial function is closely related to local early coronary atherosclerosis in patients with mild coronary artery disease: pilot study," *Circ Cardiovasc Imaging*, vol. 5, no. 3, pp. 341–348, May 1 2012.
74. A. G. Hays *et al.*, "Coronary vasomotor responses to isometric handgrip exercise are primarily mediated by nitric oxide: a noninvasive MRI test of coronary endothelial function," *Am J Physiol Heart Circ Physiol*, vol. 308, no. 11, pp. H1343–H1350, Jun 1 2015.
75. A. G. Hays *et al.*, "Local coronary wall eccentricity and endothelial function are closely related in patients with atherosclerotic coronary artery disease," *J Cardiovasc Magn Reson*, vol. 19, no. 1, p. 51, Jul 6 2017.
76. S. Kelle *et al.*, "Coronary artery distensibility assessed by 3.0 Tesla coronary magnetic resonance imaging in subjects with and without coronary artery disease," *Am J Cardiol*, vol. 108, no. 4, pp. 491–497, Aug 15 2011.
77. M. Terashima *et al.*, "Noninvasive assessment of coronary vasodilation using magnetic resonance angiography," *J Am Coll Cardiol*, vol. 45, no. 1, pp. 104–110, Jan 4 2005.
78. J. Yerly *et al.*, "Coronary endothelial function assessment using self-gated cardiac cine MRI and k-t sparse SENSE," *Magn Reson Med*, vol. 76, no. 5, pp. 1443–1454, Nov 2016.
79. G. Bonanno, A. G. Hays, R. G. Weiss, and M. Schar, "Self-gated golden angle spiral cine MRI for coronary endothelial function assessment," *Magn Reson Med*, Dec 27 2017.
80. T. Saam *et al.*, "Predictors of carotid atherosclerotic plaque progression as measured by noninvasive magnetic resonance imaging," *Atherosclerosis*, vol. 194, no. 2, pp. e34–e42, Oct 2007.
81. G. W. Stone *et al.*, "A prospective natural-history study of coronary atherosclerosis," *N Engl J Med*, vol. 364, no. 3, pp. 226–235, Jan 20 2011.
82. S. E. Nissen *et al.*, "Effect of antihypertensive agents on cardiovascular events in patients with coronary disease and normal blood pressure: the CAMELOT study: a randomized controlled trial," *JAMA*, vol. 292, no. 18, pp. 2217–2225, Nov 10 2004.
83. R. R. Edelman, D. Chien, and D. Kim, "Fast selective black blood MR imaging," *Radiology*, vol. 181, no. 3, pp. 655–660, Dec 1991.
84. R. R. Edelman *et al.*, "Extracranial carotid arteries: evaluation with "black blood" MR angiography," *Radiology*, vol. 177, no. 1, pp. 45–50, Oct 1990.
85. R. M. Botnar, M. Stuber, K. V. Kissinger, W. Y. Kim, E. Spuentrup, and W. J. Manning, "Noninvasive coronary vessel wall and plaque imaging with magnetic resonance imaging," *Circulation*, vol. 102, no. 21, pp. 2582–2587, Nov 21 2000.
86. Z. A. Fayad *et al.*, "Noninvasive in vivo human coronary artery lumen and wall imaging using black-blood magnetic resonance imaging," *Circulation*, vol. 102, no. 5, pp. 506–510, Aug 1 2000.
87. J. F. Toussaint, G. M. LaMuraglia, J. F. Southern, V. Fuster, and H. L. Kantor, "Magnetic resonance images lipid, fibrous, calcified, hemorrhagic, and thrombotic components of human atherosclerosis in vivo," *Circulation*, vol. 94, no. 5, pp. 932–938, Sep 1 1996.
88. C. Yuan, K. W. Beach, L. H. Smith, Jr., and T. S. Hatsukami, "Measurement of atherosclerotic carotid plaque size in vivo using high resolution magnetic resonance imaging," *Circulation*, vol. 98, no. 24, pp. 2666–2671, Dec 15 1998.
89. S. E. Clarke, R. R. Hammond, J. R. Mitchell, and B. K. Rutt, "Quantitative assessment of carotid plaque composition using multicontrast MRI and registered histology," *Magn Reson Med*, vol. 50, no. 6, pp. 1199–1208, Dec 2003.
90. R. M. Botnar, W. Y. Kim, P. Bornert, M. Stuber, E. Spuentrup, and W. J. Manning, "3D coronary vessel wall imaging utilizing a local inversion technique with spiral image acquisition," *Magn Reson Med*, vol. 46, no. 5, pp. 848–854, Nov 2001.

91. W. Y. Kim, M. Stuber, P. Bornert, K. V. Kissinger, W. J. Manning, and R. M. Botnar, "Three-dimensional black-blood cardiac magnetic resonance coronary vessel wall imaging detects positive arterial remodeling in patients with nonsignificant coronary artery disease," *Circulation*, vol. 106, no. 3, pp. 296–299, Jul 16 2002.
92. C. Miao *et al.*, "Positive remodeling of the coronary arteries detected by magnetic resonance imaging in an asymptomatic population: MESA (Multi-Ethnic Study of Atherosclerosis)," *J Am Coll Cardiol*, vol. 53, no. 18, pp. 1708–1715, May 5 2009.
93. A. A. Malayeri *et al.*, "Coronary vessel wall evaluation by magnetic resonance imaging in the multi-ethnic study of atherosclerosis: determinants of image quality," *J Comput Assist Tomogr*, vol. 33, no. 1, pp. 1–7, Jan-Feb 2009.
94. S. C. Gerretsen *et al.*, "Visualization of coronary wall atherosclerosis in asymptomatic subjects and patients with coronary artery disease using magnetic resonance imaging," *PLoS One*, vol. 5, no. 9, Sep 29 2010.
95. M. Terashima *et al.*, "Right coronary wall CMR in the older asymptomatic advance cohort: positive remodeling and associations with type 2 diabetes and coronary calcium," *J Cardiovasc Magn Reson*, vol. 12, p. 75, Dec 30 2010.
96. K. Z. Abd-Elmoniem, R. G. Weiss, and M. Stuber, "Phase-sensitive black-blood coronary vessel wall imaging," *Magn Reson Med*, vol. 63, no. 4, pp. 1021–1030, Apr 2010.
97. G. Ginami, J. Yerly, P. G. Masci, and M. Stuber, "Golden angle dual-inversion recovery acquisition coupled with a flexible time-resolved sparse reconstruction facilitates sequence timing in high-resolution coronary vessel wall MRI at 3 T," *Magn Reson Med*, vol. 77, no. 3, pp. 961–969, Mar 2017.
98. M. E. Andia *et al.*, "Flow-independent 3D whole-heart vessel wall imaging using an interleaved T2-preparation acquisition," *Magn Reson Med*, vol. 69, no. 1, pp. 150–157, Jan 2013.
99. M. R. Makowski *et al.*, "In vivo assessment of intraplaque and endothelial fibrin in ApoE(-/-) mice by molecular MRI," *Atherosclerosis*, vol. 222, no. 1, pp. 43–49, May 2012.
100. R. M. Botnar *et al.*, "In vivo assessment of aortic aneurysm wall integrity using elastin-specific molecular magnetic resonance imaging," *Circ Cardiovasc Imaging*, vol. 7, no. 4, pp. 679–689, Jul 2014.
101. R. Virmani *et al.*, "Atherosclerotic plaque progression and vulnerability to rupture: angiogenesis as a source of intraplaque hemorrhage," *Arterioscler Thromb Vasc Biol*, vol. 25, no. 10, pp. 2054–2061, Oct 2005.
102. S. T. Nikkari *et al.*, "Interstitial collagenase (MMP-1) expression in human carotid atherosclerosis," *Circulation*, vol. 92, no. 6, pp. 1393–1398, Sep 15 1995.
103. A. C. Newby, "Metalloproteinases and vulnerable atherosclerotic plaques," *Trends Cardiovasc Med*, vol. 17, no. 8, pp. 253–258, Nov 2007.
104. M. J. Davies and A. C. Thomas, "Plaque fissuring: the cause of acute myocardial infarction, sudden ischaemic death, and crescendo angina," *Br Heart J*, vol. 53, no. 4, pp. 363–373, Apr 1985.
105. T. Saam *et al.*, "The vulnerable, or high-risk, atherosclerotic plaque: noninvasive MR imaging for characterization and assessment," *Radiology*, vol. 244, no. 1, pp. 64–77, Jul 2007.
106. J. B. Michel *et al.*, "From intraplaque haemorrhages to plaque vulnerability: biological consequences of intraplaque haemorrhages," *J Cardiovasc Med (Hagerstown)*, vol. 13, no. 10, pp. 628–634, Oct 2012.
107. M. J. Davies and A. Thomas, "Thrombosis and acute coronary-artery lesions in sudden cardiac ischemic death," *N Engl J Med*, vol. 310, no. 18, pp. 1137–1140, May 3 1984.
108. E. Falk, "Pathogenesis of atherosclerosis," *J Am Coll Cardiol*, vol. 47, no. 8 Suppl, pp. C7–C12, Apr 18 2006.
109. C. R. Weiss *et al.*, "Arterial wall MRI characteristics are associated with elevated serum markers of inflammation in humans," *J Magn Reson Imaging*, vol. 14, no. 6, pp. 698–704, Dec 2001.
110. A. Phinikaridou *et al.*, "In vivo detection of vulnerable atherosclerotic plaque by MRI in a rabbit model," *Circ Cardiovasc Imaging*, vol. 3, no. 3, pp. 323–332, May 2010.
111. O. G. Abela *et al.*, "Plaque Rupture and Thrombosis: the Value of the Atherosclerotic Rabbit Model in Defining the Mechanism," *Curr Atheroscler Rep*, vol. 18, no. 6, p. 29, Jun 2016.
112. A. R. Moody *et al.*, "Characterization of complicated carotid plaque with magnetic resonance direct thrombus imaging in patients with cerebral ischemia," *Circulation*, vol. 107, no. 24, pp. 3047–3052, Jun 24 2003.
113. T. Kawasaki *et al.*, "Characterization of hyperintense plaque with noncontrast T(1)-weighted cardiac magnetic resonance coronary plaque imaging: comparison with multislice computed tomography and intravascular ultrasound," *JACC Cardiovasc Imaging*, vol. 2, no. 6, pp. 720–728, Jun 2009.

114. M. L. Oei *et al.*, "T1-weighted MRI for the detection of coronary artery plaque haemorrhage," *Eur Radiol*, vol. 20, no. 12, pp. 2817–2823, Dec 2010.
115. C. H. Jansen *et al.*, "Detection of intracoronary thrombus by magnetic resonance imaging in patients with acute myocardial infarction," *Circulation*, vol. 124, no. 4, pp. 416–424, Jul 26 2011.
116. T. Noguchi *et al.*, "Effect of Intensive Statin Therapy on Coronary High-Intensity Plaques Detected by Noncontrast T1-Weighted Imaging: The AQUAMARINE Pilot Study," *J Am Coll Cardiol*, vol. 66, no. 3, pp. 245–256, Jul 21 2015.
117. T. Noguchi *et al.*, "High-intensity signals in coronary plaques on noncontrast T1-weighted magnetic resonance imaging as a novel determinant of coronary events," *J Am Coll Cardiol*, vol. 63, no. 10, pp. 989–999, Mar 18 2014.
118. Y. Xie *et al.*, "Coronary Atherosclerosis T1-Weighed Characterization With Integrated Anatomical Reference: Comparison With High-Risk Plaque Features Detected by Invasive Coronary Imaging," *JACC Cardiovasc Imaging*, Oct 06 2016.
119. G. Ginami, R. Neji, A. Phinikaridou, J. Whitaker, R. M. Botnar, and C. Prieto, "Simultaneous bright- and black-blood whole-heart MRI for noncontrast enhanced coronary lumen and thrombus visualization," *Magn Reson Med*, Jul 19 2017.
120. P. Kellman, A. E. Arai, E. R. McVeigh, and A. H. Aletras, "Phase-sensitive inversion recovery for detecting myocardial infarction using gadolinium-delayed hyperenhancement," *Magn Reson Med*, vol. 47, no. 2, pp. 372–383, Feb 2002.
121. C. Jahnke *et al.*, "Rapid and complete coronary arterial tree visualization with magnetic resonance imaging: feasibility and diagnostic performance," *Eur Heart J*, vol. 26, no. 21, pp. 2313–2319, Nov 2005.
122. W. Y. Kim *et al.*, "Coronary magnetic resonance angiography for the detection of coronary stenoses," *N Engl J Med*, vol. 345, no. 26, pp. 1863–1869, Dec 27 2001.
123. S. Kato *et al.*, "Assessment of coronary artery disease using magnetic resonance coronary angiography: a national multicenter trial," *J Am Coll Cardiol*, vol. 56, no. 12, pp. 983–991, Sep 14 2010.
124. M. J. Budoff *et al.*, "Diagnostic performance of 64-multidetector row coronary computed tomographic angiography for evaluation of coronary artery stenosis in individuals without known coronary artery disease: results from the prospective multicenter ACCURACY (Assessment by Coronary Computed Tomographic Angiography of Individuals Undergoing Invasive Coronary Angiography) trial," *J Am Coll Cardiol*, vol. 52, no. 21, pp. 1724–1732, Nov 18 2008.
125. D. Piccini *et al.*, "Respiratory self-navigated postcontrast whole-heart coronary MR angiography: initial experience in patients," *Radiology*, vol. 270, no. 2, pp. 378–386, Feb 2014.
126. M. Henningsson, J. Shome, K. Bratis, M. S. Vieira, E. Nagel, and R. M. Botnar, "Diagnostic performance of image navigated coronary CMR angiography in patients with coronary artery disease," *J Cardiovasc Magn Reson*, vol. 19, no. 1, p. 68, Sep 11 2017.
127. C. Boffano, A. Chiribiri, and F. Cesarani, "Native whole-heart coronary imaging for the identification of anomalous origin of the coronary arteries," *Int J Cardiol*, vol. 137, no. 1, pp. e27–e28, Sep 11 2009.
128. G. F. Greil *et al.*, "Coronary magnetic resonance angiography and vessel wall imaging in children with Kawasaki disease," *Pediatr Radiol*, vol. 37, no. 7, pp. 666–673, Jul 2007.
129. G. F. Greil *et al.*, "Coronary magnetic resonance angiography in adolescents and young adults with kawasaki disease," *Circulation*, vol. 105, no. 8, pp. 908–911, Feb 26 2002.
130. J. P. Jenkins, H. G. Love, C. J. Foster, I. Isherwood, and D. J. Rowlands, "Detection of coronary artery bypass graft patency as assessed by magnetic resonance imaging," *Br J Radiol*, vol. 61, no. 721, pp. 2–4, Jan 1988.
131. R. I. Rubinstein, A. D. Askenase, D. Thickman, M. S. Feldman, J. B. Agarwal, and R. H. Helfant, "Magnetic resonance imaging to evaluate patency of aortocoronary bypass grafts," *Circulation*, vol. 76, no. 4, pp. 786–791, Oct 1987.
132. V. Rasche *et al.*, "Whole-heart coronary vein imaging: a comparison between non-contrast-agent- and contrast-agent-enhanced visualization of the coronary venous system," *Magn Reson Med*, vol. 57, no. 6, pp. 1019–1026, Jun 2007.
133. R. Nezafat *et al.*, "Coronary magnetic resonance vein imaging: imaging contrast, sequence, and timing," *Magn Reson Med*, vol. 58, no. 6, pp. 1196–1206, Dec 2007.
134. C. T. Stoeck *et al.*, "Whole heart magnetization-prepared steady-state free precession coronary vein MRI," *J Magn Reson Imaging*, vol. 29, no. 6, pp. 1293–1299, Jun 2009.
135. C. T. Stoeck *et al.*, "Optimization of on-resonant magnetization transfer contrast in coronary vein MRI," *Magn Reson Med*, vol. 64, no. 6, pp. 1849–1854, Dec 2010.

136. M. Henningsson and R. M. Botnar, "Advanced Respiratory Motion Compensation for Coronary MR Angiography," *Sensors*, vol. 13, no. 6, pp. 6882–6899, Jun 2013.
137. A. Bustin *et al.*, "Five-minute whole-heart coronary MRA with sub-millimeter isotropic resolution, 100% respiratory scan efficiency, and 3D-PROST reconstruction," *Magn Reson Med*, Jul 2018. https://doi.org/10.1002/mrm.27354
138. S. A. Peel *et al.*, "Cross-sectional and in-plane coronary vessel wall imaging using a local inversion prepulse and spiral read-out: a comparison between 1.5 and 3 Tesla," *J Magn Reson Imaging*, vol. 35, no. 4, pp. 969–975, Apr 2012.

16 Hypertension and Correlation to Cerebrovascular Change: A Brief Overview

Heba Kandil[1], Dawn Sosnin[1], Ali Mahmoud[1], Ahmed Shalaby[1], Ahmed Soliman[1], Adel Elmaghraby[1], Jasjit S. Suri[2], Guruprasad Giridharan[1], Ayman El-Baz[1]

[1]University of Louisville

[2]AtheroPoint, LLC

CONTENTS

16.1 INTRODUCTION

High blood pressure (hypertension) is a clinical condition in which the pressure and force of the blood against the arterial walls is elevated. Blood pressure is often reported as systolic and diastolic blood pressures in millimeters of mercury (mmHg), which correspond to the peak aortic pressure during ventricular ejection (systolic) and the lowest pressure in the aorta during ventricular relaxation (diastolic). The mean arterial pressure (MAP) is the average aortic blood pressure during the entire cardiac cycle. A normal blood pressure reading is a systolic measurement of less than 120 mmHg, a diastolic measurement of less than 80 mmHg, and a MAP of approximately 95 mmHg (Table 16.1). Hypertension was traditionally defined as systolic blood pressure >160 mmHg, diastolic blood pressure >100 mmHg, or MAP >120 mmHg.

Hypertension can be classified as primary (or essential or idiopathic), secondary, accelerated, hypertension urgency, or as malignant hypertension. Essential hypertension develops over years, even decades, with no single identified lifestyle or genetic cause. Approximately 90–95% of patients

TABLE 16.1

Blood pressure measurements definitions. [4]

Blood Pressure Measurements	Definition
Systolic Blood Pressure (SBP)	First Korotkoff sound[1]
Diastolic Blood Pressure (DBP)	Fifth Korotkoff sound
Pulse Pressure	(SBP – DBP)
Mean Arterial Pressure (MAP)	DBP plus one-third pulse pressure (or) (SBP + 2*DBP)/3
Mid-Blood Pressure	(SBP + DBP)/2

[1] Korotkoff sounds are the sound that medical specialists hear when they are measuring blood pressure noninvasively.

diagnosed with hypertension are classified as primary hypertension [1]. Secondary hypertension is a secondary disease which can develop due to conditions including adrenal and thyroid problems, obstructive sleep apnea, drugs and medications, chronic alcohol abuse, etc. [2]. An example of secondary hypertension is renal (or renovascular) hypertension, where hormones released by the kidneys increase blood pressure throughout the systemic circulation in response to narrowing of the arteries that supply blood to the kidneys. Accelerated hypertension (recent significant increase) and malignant hypertension are hypertensive emergencies, defined as high blood pressure (typically ≥180/≥120) with acute impairment of one or more organ systems. Diagnosis of malignant hypertension requires the presence of papilledema, or in the absence of stage III or IV retinopathy, damage to a minimum of three target organs [3]. Hypertensive urgency is severely elevated blood pressure with no organ damage.

Hypertension can be a localized condition, such as portal vein hypertension (PVH) or pulmonary hypertension (PH). PVH is elevated pressure in the hepatic (liver) portal system caused by problems such as cirrhosis (most commonly) or venous thrombosis (a blood clot) in the liver. PH is elevated blood pressures in the pulmonary circulation. Discussion for this chapter will focus on systemic (or body) hypertension that affects the entire circulatory system and is referred to hereafter as hypertension. There are variabilities in blood pressure throughout the day due to the circadian (sleep-wake) cycle, hormonal changes, activities, meals, etc. [5], which are extraneous to this discussion. This chapter will focus on the condition of persistent systemic primary hypertension.

Typically, hypertension is the medical term used to refer to the chronic condition of having persistent elevated blood pressure. In the advanced stages of the disease, some people may experience symptoms (e.g., shortness of breath, dizziness, visual changes, flushing, etc.) [6]. However, hypertension is often referred to as a "silent killer" because many people will experience no apparent symptoms.

The guideline for diagnosing primary hypertension was recently updated. Previously, hypertension was diagnosed when a patient had a sustained blood pressure measurement ≥140/90 mmHg. The Joint National Committee is a panel of specialists, such as cardiologists, nephrologists, etc., from across the United States who determine what guidelines and regulations should be in place for diagnosing and treating hypertension. In the 2017 guideline, an update of the 2003 Seventh Report of the Joint National Committee on Prevention, Detection, Evaluation and Treatment of High Blood Pressure (JNC7), categorization for hypertension based upon blood pressure measurements was changed to the following recommendations: normal (<120/<80 mmHg), elevated or pre-hypertension (120–129/<80 mmHg), hypertension stage 1 (130–139 mmHg systolic or 80–89 diastolic mmHg), and hypertension stage 2 (≥140 mmHg systolic or ≥90 diastolic mmHg) [5], [4], (Table 16.2). These new guidelines are intended to help patients and physicians address high blood pressure sooner, which has been demonstrated to help prevent or slow the rate of organ damage. The reduction of blood pressure for the diagnosis of clinical hypertension, and the more precise categorization of hypertension diagnoses, is in response to the mounting evidence of the importance of early intervention for improved patient outcomes and reduction of hypertension-related morbidity and mortality.

TABLE 16.2
Categories of blood pressure in adults.

Category	Systolic Blood Pressure	Diastolic Blood Pressure
Normal	<120 mmHg	And <80 mmHg
Elevated	120–129 mmHg	And <80 mmHg
Hypertension-Stage I	130–139 mmHg	Or 80–89 mmHg
Hypertension-Stage II	≥140 mmHg	Or ≥90 mmHg

The rest of this chapter is organized as follows: Section 16.2 will discuss the importance of studying hypertension as one of the risk factors threatening humans' health nowadays. Section 16.3 will present current techniques used in measuring blood pressure invasively and noninvasively. Section 16.4 will discuss current imaging modalities used to help clinicians to quantify symptoms preceding the onset of hypertension and how this would help in preventing or reducing further disease complications. Sections 16.5 and 16.6 will give a discussion of the current and the emerging trends in quantifying and measuring high blood pressure. The conclusion is then given in section 16.7.

16.2 IMPORTANCE AND RELEVANCE

Elevated blood pressure is associated with increase in cardiovascular disease risk [4]. Table 16.3 presents the cardiovascular disease risk factors that are common in hypertensive patients. In addition, hypertension damages small and large blood vessels, including those in the brain. Conditions such as vascular dementia (sometimes called vascular neurocognitive disorder) and Alzheimer's disease have been correlated to hypertension induced changes in the cerebral blood vessels. These cerebrovascular changes develop long before symptoms appear, and thus significant vascular damage precedes diagnosis of hypertension. Functional reorganization (neuroplasticity) occurs early in the disease course, with compensatory changes including the use of more cerebral regions to complete tasks [7]. A recent study found that hypertension increases the risk for developing vascular dementia by 62% for patients between the ages of 30 and 50 and increases the vascular dementia risk by 26% for patients in the age range of 51 to 70 years old. The risk for vascular dementia is still reduced when blood pressure is lowered in older patients [8]. The risk for cognitive decline in patients with elevated systolic and diastolic blood pressures was reduced by 38% with antihypertensive therapy [9].

TABLE 16.3
Risk factors of CVD related to hypertensive patients. [4]

Modifiable[1]	Relatively Fixed[2]
Current cigarette smoking, secondhand smoking	Chronic kidney disease
Diabetes mellitus	Family history
Dyslipidemia/hypercholesterolemia	Increased age
Overweight/obesity	Low socioeconomic/educational status
Physical inactivity/low fitness	Male sex
Unhealthy diet	Obstructive sleep apnea
	Psychosocial stress

[1] Modifiable factors are those that could be changed, and if so, could reduce the CVD risks.
[2] Relatively Fixed factors are those that are difficult to change.

16.3 CURRENT TECHNOLOGIES FOR DIAGNOSING PRIMARY HYPERTENSION

The invasive and noninvasive techniques used for measuring blood pressure are presented in the following sections.

16.3.1 Noninvasive Blood Pressure (NIBP) Measurement Techniques

Hypertension can be diagnosed by a clinician through different tests. The most common screening method for hypertension is use of the sphygmomanometer, also known as a blood pressure monitor or blood pressure meter. This measurement is typically taken by a nurse or clinician at a medical care provider's office or at a hospital. It is noninvasive, inexpensive, and portable. While generally accurate as a screening tool, it should be noted that measurements taken with this method could include variability due to cuff size as matched—or mismatched—to patient arm circumference, machine calibration, patient resting time just prior to taking the reading, etc. Some patients also experience anxiety while at a physician's office which can cause a temporary elevation in blood pressure, sometimes referred to as "white coat hypertension." Therefore, it is recommended that the first elevated reading identified at an initial screening be considered as an indication for further monitoring, not as a conclusive result for a diagnosis.

Currently, the treating physician obtains additional measurements or ambulatory blood pressure monitoring over a 24-hour period to confirm hypertension diagnosis. The patient may be asked to return to the medical care provider up to two times, with the visits timed to be at least two days apart, for additional pressure measurements. The pressure measurements from the two visits are then averaged to obtain the patient's blood pressure measurement [5]. In a recent study, average variability of at least 5 mmHg was found between automated office blood pressure and daytime ambulatory blood pressure monitoring (ABPM) in 90% of participating patients, with a greater degree of underestimation among hypertensive patients [10]. ABPM can be conducted with the use of an automated system. A radial pulse wave acquisition device is worn on the wrist and captures and records data wirelessly. Measurements are taken automatically, typically every 15 minutes and enables the capture of circadian variation of blood pressure. Arm cuff and finger monitors are also options for ABPM. The patient returns to the clinician's office the following day, and the information is downloaded for evaluation and diagnosis. Patient self-measurement is sometimes a suitable and practical alternative and can in some cases provide a better picture of blood pressure fluctuations in patients who smoke.

Doppler ultrasound, which is usually used for flow measurements, can also be used to measure blood pressure. A recent comparative study found that arterial tonometry does not provide accuracy similar to that of arterial cannulation, especially during movement [11]. However, it was also reported that radial artery applanation tonometry (measuring pressure required to keep artery flattened) can be used to determine the shape of the aortic waveform to measure the central pulse pressure [12].

Lab tests are also an important tool in making or supporting a diagnosis of hypertension. Tests that could be related to hypertension include the following: measurement of serum potassium and creatinine levels (or estimated glomerular filtration rate), which is an indication of how well the patient's kidneys are functioning; blood glucose and hematocrit; cholesterol profiles and triglycerides. An increase in serum calcium due to increased activity of the parathyroid glands can be associated with hypertension. Urine samples can be tested for albumin (microalbumin), a protein, and blood urea nitrogen (BUN). Hypertensive retinopathy, diagnosed by fundoscopic examination, is an ophthalmologic symptom of chronic hypertension or other cardiovascular diseases [5], [13]. Direct ophthalmoscopy, photography, and angiography can also reveal hypertensive choroidopathy and hypertensive optic neuropathy. A 12-lead electrocardiogram can detect signs of myocardial damage due to hypertension. An echocardiogram can be performed to identify conditions such as atherosclerosis, left ventricular hypertrophy, etc., which provide important information that may

support the diagnosis of hypertension. The JNC 7 on High Blood Pressure lists high-sensitivity C-reactive protein (HS-CRP), homocysteine, and elevated heart rate as "emerging risk factors" [5].

16.3.2 Invasive Blood Pressure Measurement Techniques

Noninvasive manual aneroid, auscultatory (being phased-out), and oscillometric (transducer and sphygmomanometer) blood pressure measurement methods are not as reliable as intra-arterial pressure readings [14], [15]. There is some variability of measurement readings (estimations generated by each company's algorithm) between oscillometric blood pressure measurement devices [16]. Sources of error include improper arm cuff fit or placement, inadequate or infrequent device calibration, not waiting for the recommended 5 minutes to have patients in a resting seated position prior to taking a measurement, etc. [17], [18], [19].

An intra-arterial catheter is an invasive technique that provides direct, real-time continuous monitoring, typically in a hospital setting, and is considered the reference standard for blood pressure measurement. An arterial line is a thin catheter with a pressure transducer that is inserted into an artery (femoral, brachial, radial, etc.). A pressurized saline slow infusion system in the tubing allows a continuous slow flush through the catheter tip into the bloodstream. Distortion or deformation of a dome diaphragm on the pressure transducer varies with the changes in pressure of the saline column, which varies with arterial pressure pulsation. The diaphragm distortion causes changes in resistance in the transducer electrical circuit [20].

Invasive blood pressure monitoring also offers beat to beat visual display of the arterial waveform, which measures the rapid changes in pressure over the measurement epochs. The waveform display provides information such as steepness and narrowness of systolic stroke, dicrotic notch, and wave reflections. Pulse pressure is the difference between the peak arterial pressure measurement and the diastolic pressure at the trough. MAP is the area under the curve divided by the width of a single cardiac cycle. MAP provides a measurement that is less affected by wave reflection than the systolic and diastolic readings [14], [21].

Typical risks associated with invasive blood pressure measurement techniques are thrombosis and infection. An arterial line is only typically indicated for critical care patients (intra-operatively, with use of vasoactive drugs, for intensive care monitoring, etc.), patients with severe extremity burns, frequent blood gas sampling, etc.

16.4 CURRENT IMAGING TECHNOLOGIES

Medical imaging techniques enable physicians to capture noninvasive images of structures inside the body (e.g., blood vessels, tissue, bones) as well as their function (egg, brain activity). Imaging techniques may require the use of contrast agents to highlight or enhance the imaging resolution of tissues. These agents can be administered intravenously, orally, rectally, or through inhalation. The kidneys and liver filter and excrete these agents from the body.

This section will be a brief overview of current imaging technologies available to physicians, clinicians, specialists, and researchers with a greater focus on technologies used for imaging blood vessels to evaluate vascular function.

16.4.1 CT and CTA

Tomography is a technique for creating a three-dimensional image using cross-sectional X-ray images. X-rays are high-energy short-wavelength electromagnetic waves (high-energy radiation) that pass through the body. X-rays readily pass through soft tissues (grey matter), while denser anatomical structures (e.g., bones) block X-rays. The X-ray attenuation due to structures in the body can be captured using sensors. Computed tomography (CT) or computed axial tomography (CAT) scans use cross-sectional X-rays taken from multiple angles to form medical images of the body.

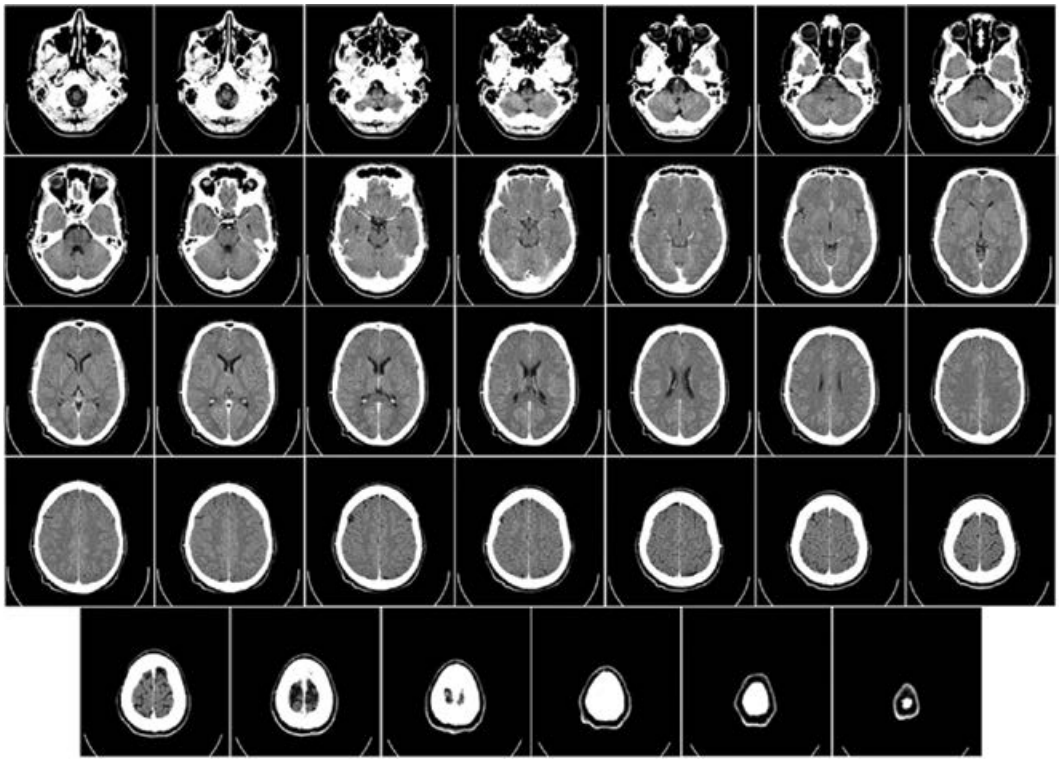

FIGURE 16.1 Computed Tomography (CT) of human brain from base of the skull to top [24].

The CT scans are typically focused on one area of interest such as the head (Figure 16.1) or the chest. CT has been used to detect pulmonary hypertension and mean pulmonary artery pressure by measuring and analyzing diameters of pulmonary arteries noninvasively [22]. Electron beam CT (Ultrafast CT) has been used to detect coronary artery disease by detecting calcium deposits in coronary arteries [23]. Although CT images provide 3-D anatomical information and preserve topology, they cause radiation exposure.

Computed tomography angiography (CTA) is an imaging technique that uses an intravenously administered iodine-rich contrast agent to capture X-ray images of blood and vasculature. A sample of a CTA image is shown in Figure 16.2. It can be used to assess arterial sizes, evaluate blood flows to diagnose vascular conditions such as stenosis (narrowing of the blood vessel), embolism (blockage), atherosclerosis, etc. Ley et al. used CTA of pulmonary arteries to diagnose patients with chronic thromboembolic pulmonary hypertension [25]. CT perfusion imaging enables evaluation of cerebral blood flow and perfusion. Multi-detector computed tomography (MDCT) utilizes a two-dimensional array of detector elements instead of a linear array of detector elements used in typical and helical CT scanners [26], which allows for high imaging acquisition speed, high spatial resolution, and more coverage of the patient [27]. Flat panel CT (FPCT) offers z-axis imaging in one rotation, which offers high spatial resolution images of entire organ systems (e.g., the cerebrovasculature) [28], [29].

16.4.2 Nuclear

Nuclear imaging is used to capture physiologic processes such as metabolic rates or blood flow. Positron emission tomography (PET) is a nuclear medicine imaging technique that captures gamma photons emitted in different directions by a positron-emitting radionucleotide (called a radiotracer), which is administered intravenously, orally, or by inhalation [30]. Figure 16.3 shows a schema of

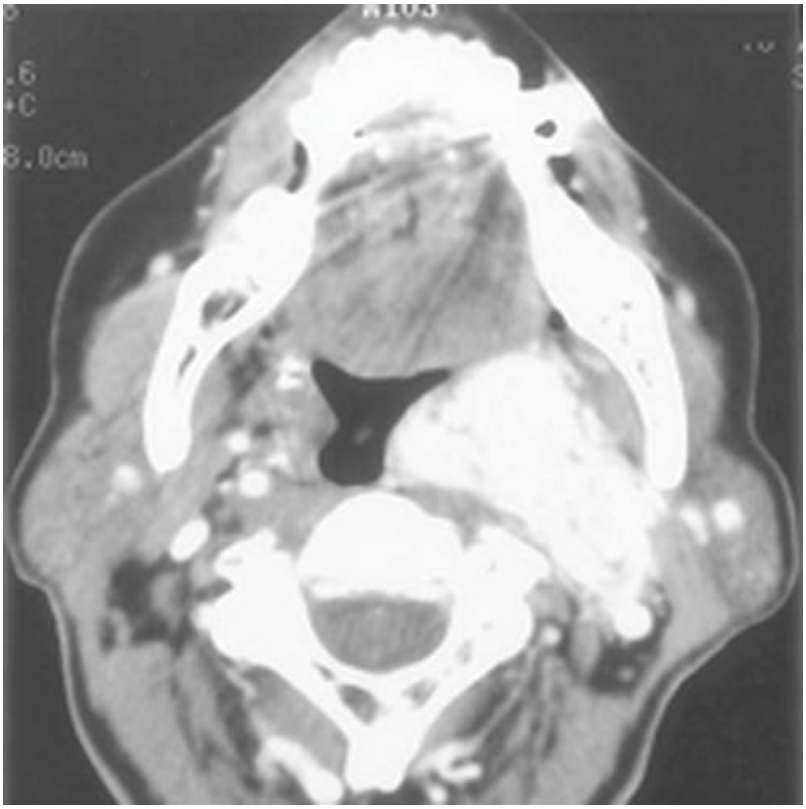

FIGURE 16.2 A sample of CTA image.

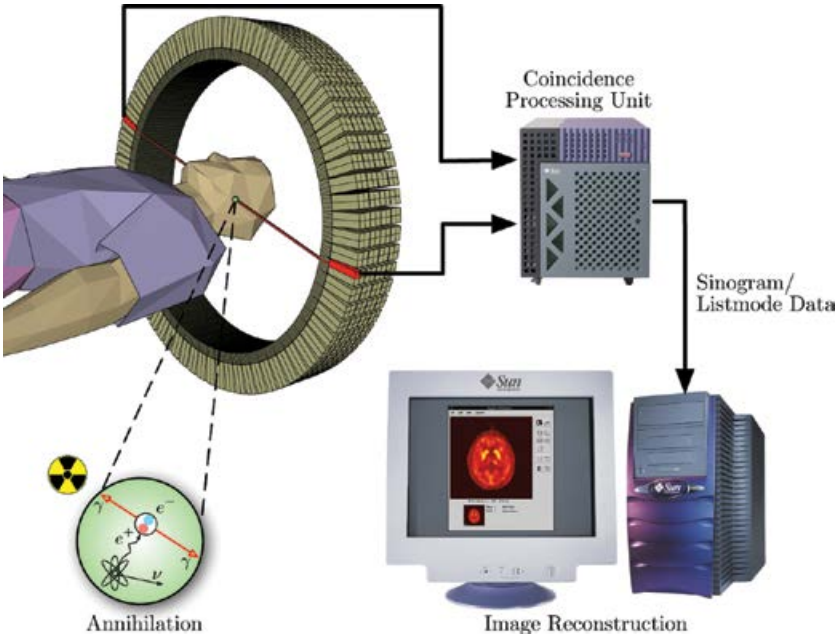

FIGURE 16.3 Schema of PET acquisition process [32].

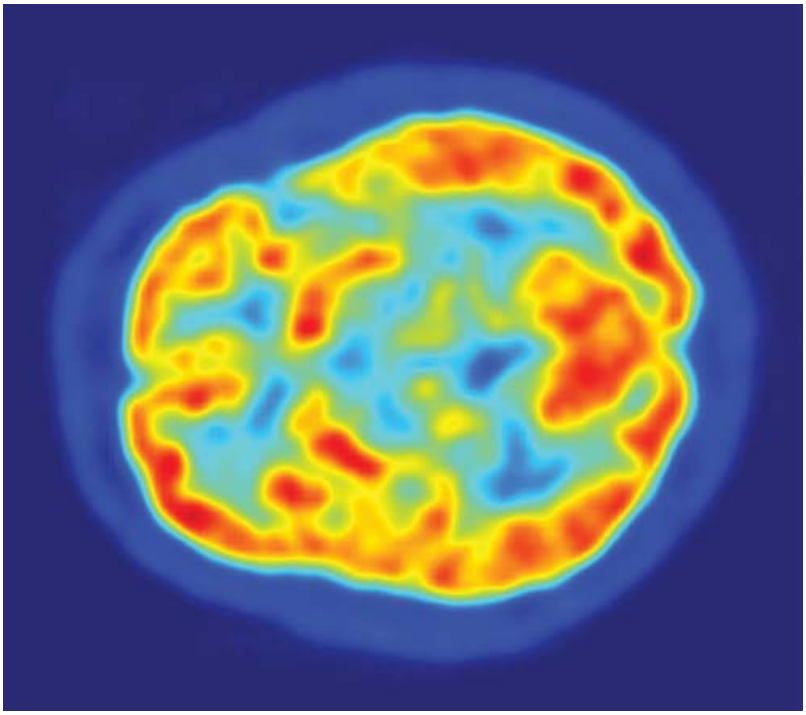

FIGURE 16.4 PET scan of the human brain [32].

the acquisition process of PET, and Figure 16.4 shows a sample image of it. Single photon emission computed tomography (SPECT) directly measures gamma radiation from a (typically injected) radiotracer or radiopharmaceutical, and can be used in bone imaging to measure blood flow, determine organ function such as cardiac efficiency, functional brain imaging (e.g., effects of dementia), etc. [30]. SPECT was used to measure cerebral blood flow in a study that was conducted to determine whether hypertensive patients with acute ischemic strokes should be treated using antihypertensive medication in the immediate post-stroke period [31].

16.4.3 MRI, fMRI, and MRA

Magnetic resonance imaging (MRI) uses powerful magnets and radio waves as opposed to the ionizing radiation used for X-ray imaging. The MRI machine generates a strong magnetic field that aligns the spins of protons in the water molecules within the body. A radio frequency generates a varying magnetic field whose energy flips the protons' spins (opposite direction). They return to their normal spin (precession, which happens at different rates for different tissues) when the magnetic field is turned off, and the scanner captures the radio signal produced during this process to produce an image (Figure 16.5).

MRI images capture skeletal structures as well as soft tissues as 2-D cross-section images. Because a single image cannot capture the entire brain—which is a 3-D structure—it takes multiple axial cross-section images (from a perspective looking down at the top of the patient's head) put together to get a complete 3-D image of the entire brain. A brain MRI volume is made of over 100 2-D images (image volume). MRI is considered the best modality to scan soft tissues such as brain tissues and does not have any associated radiation exposure. However, MRI imaging is slow and less accurate for bone scanning.

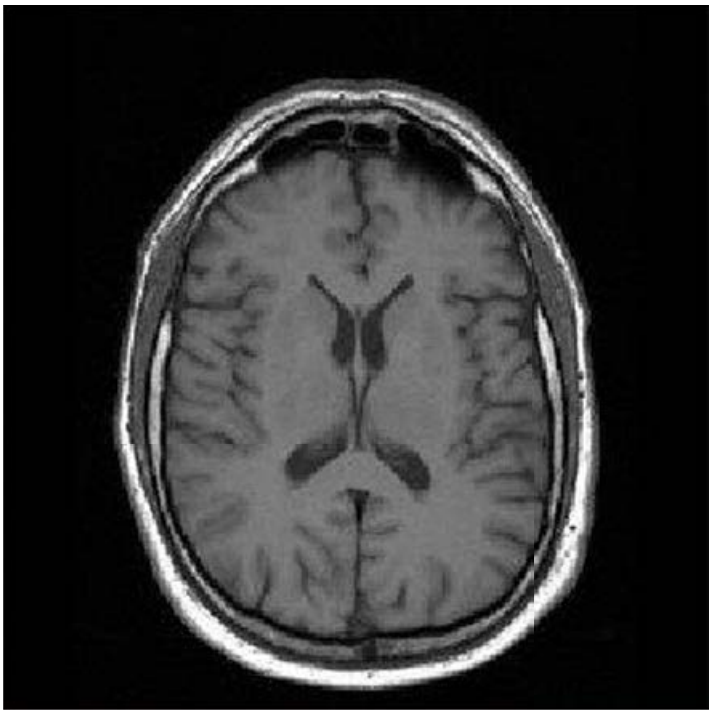

FIGURE 16.5 A sample of MRI data.

Cardiovascular magnetic resonance (CMR) is used to assess or measure cardiac structure and physiology (e.g., biventricular function and volumes, vascular pathology, etc.). CMR has been used to measure left ventricular mass, wall thickness, and function. CMR is the preferred technique for assessing left ventricular hypertrophy, and provides enough clarity to discern the differences between hypertrophic cardiomyopathy and LVH [33].

Patients' blood and vascular tissues, including cerebrovascular structures (blood vessels in the brain), can be best captured using magnetic resonance angiograms (MRAs). An MRA sample image is shown in Figure 16.6. MRA images are captured using MRI scanners. MRA is used to image arteries and arterial blood flow, while magnetic resonance venography (MRV) is used to assess blood flow in veins (e.g., detect deep vein thrombosis). MRA has been used to visualize intracranial circulation and extracranial carotid vessels, screening for renovascular hypertension, depiction of peripheral arterial occlusive disease, abdominal tumor stating, and the evaluation of abnormalities of the central veins of the body [34]. However, detection of cerebrovascular structural changes and correlating them to blood pressure using MRA analysis has not been accomplished due to the lack of accurate segmentation algorithms that can delineate the smaller blood vessels in the brain from the surrounding soft tissue. In contrast enhanced MRA (CE-MRA), a contrast agent is administered intravenously. It can be used to image vasculature (including aneurysm, esp. for follow-up), luminal surfaces, and arterial plaques and atherosclerosis [28]. There are several MRA techniques that do not require the use of a contrast agent. Time-of-flight (TOF) MRA (Figure 16.7) uses the inflow-enhancement effect, which is an increased signal from the inflow of spins of fully magnetized blood flowing into an area of tissues that are less magnetized (saturated) due to repeated exposure to radio frequency pulses. Researchers continue to work toward improved options for MRI and MRA diagnostic efficacy in the early stages of cerebrovascular-related diseases such as hypertension, dementia, Parkinson's disease, etc. [35].

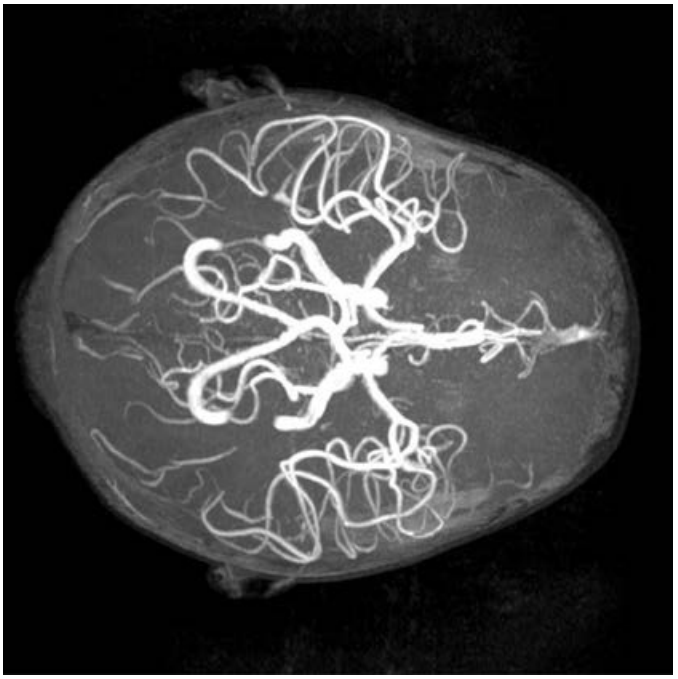

FIGURE 16.6 A sample of MRA data.

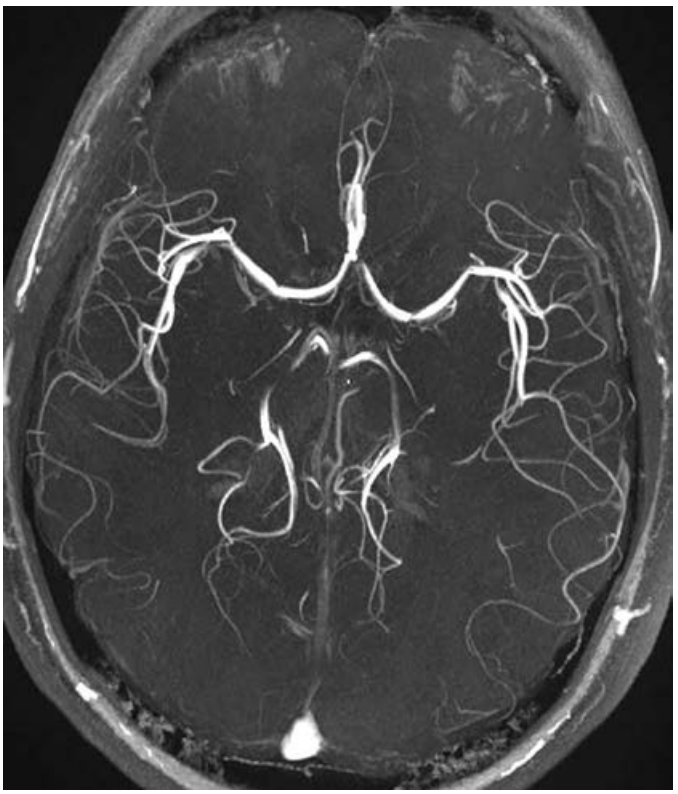

FIGURE 16.7 A sample of TOF-MRA data.

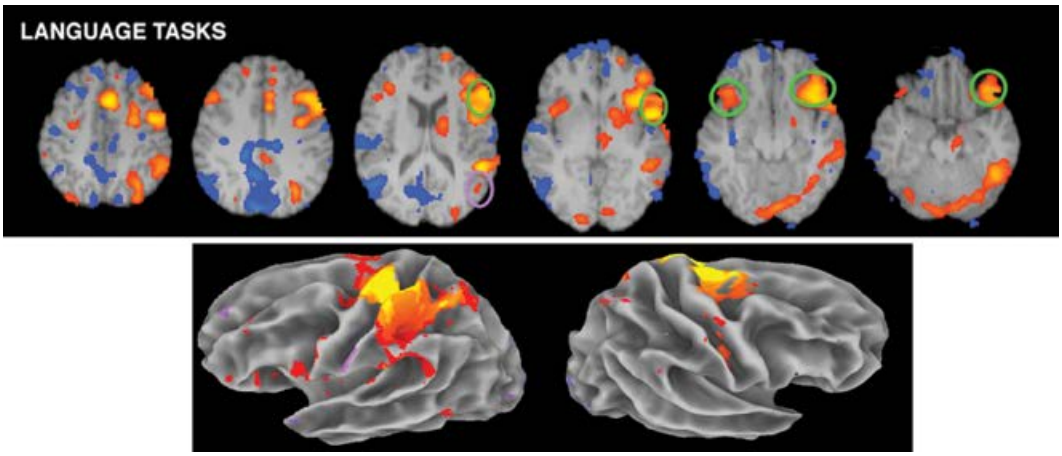

FIGURE 16.8 A sample of fMRI data.

Phase contrast MRA (PC-MRA) can be used to image moving fluids such as cerebrospinal fluid and blood (e.g., MRV, measuring pulmonary artery (PA) flow velocities and pressures, etc.) [21], [36], [37]. Velocity data obtained from PC-MRA also allows for determination of shear stresses against the inner vessel wall, flow volume, and pressure gradients. Four images are used to measure 3-D flow, and cardiac gating is used with this procedure [38]. Because blood flows throughout the body, conditions in one area of the body can affect other areas, and MRA can provide important information regarding both localized and systemic conditions. PC-MRA has been used to quantify intracranial venous resistance to drainage [39]. PC-MRA has been utilized to study the effect of elevated blood pressures to study cerebrovascular changes (tortuosity) [40]. PC-MRA has also been used in conjunction with other medical procedures such as intraoperative catheterization to improve flow measurement accuracy [41]. Renovascular hypertension can be evaluated using 3-D gadolinium-enhanced magnetic resonance angiography (MRA) [33].

Arterial spin labeling (ASL) MRI uses pulse inversion to differentiate tissues moving into the imaging field from other tissues, which are subtracted (requires acquisition of two images) or uses background suppression single-shot ASL [42], [43]. ASL-MRI can be used to quantify blood flow using changes in magnetization of blood water to tissues. Functional MRI (fMRI) measures changes in blood flow and can be used to identify active areas in the brain. For many years, fMRI has been used to investigate correlations between hypertension and cognitive and related functions (e.g., working memory) [44]. fMRI is useful in the study of cerebral function and arteriopathies (e.g., Lewis bodies, cerebral amyloid angiopathy) to Alzheimer's, vascular dementia, etc. [45], [46]. Blood oxygen level dependent (BOLD) contrast imaging is used in fMRI to observe the active areas in the brain and other organs by measurement changes in oxyhemoglobin and deoxyhemoglobin (oxygen changes) [35]. Figure 16.8 presents a sample of fMRI data.

16.4.4 Ultrasound

Doppler ultrasonography (handheld, Duplex, Color, and Power) uses high-frequency sound waves generated by a transducer to measure blood flow using the Doppler Effect and blood pressure [47]. The transducer is pressed externally against the patient's skin, with gel between the transducer head and the patient's skin to act as a coupler and eliminate air and to reduce static. This painless noninvasive procedure is generally performed in a hospital radiology department by a sonographer. Intravascular ultrasound is a noninvasive, clean, safe, and inexpensive modality that offers detailed imaging of cardiac arteries [48]. However, it is noisy and cannot image gas-filled and bony structures because they absorb ultrasound waves.

Recent research suggests that left ventricular diastolic dysfunction may be an early development of left ventricular remodeling due to hypertension, and an evaluation can be done using 2-D, 3-D, and Doppler ultrasound echocardiography. Blood flow velocities and wall thicknesses can be measured using these imaging modalities [49].

16.4.5 Hybrid Imaging Techniques

Hybrid imaging techniques use two or more imaging techniques, to provide better detection, resolution, spatial and functional information, etc. compared to a single imaging technique.

PET-CT scanners can be used to observe metabolic processes and capture 3-D images, and have been used to detect cancer, determine blood flow to the heart, evaluate normal and abnormal brain structures and function, etc., [30]. SPECT can be used in conjunction with a CT scanner (SPECT-CT) to acquire anatomical and functional data, which can correct for errors due to abnormal uptake of the radiotracer [30], [50].

Often, specific radiopharmaceuticals are used with hybrid imaging techniques for specific applications, such as the use of 18F-FDG-PET-CT (2-deoxy-2-[fluorine-18]fluoro-D-glucose is moved into cells and detected by the use of PET with CT scanning) for detecting various cancers and the extent of metastasis, infective endocarditis [51], [52], [53], [54].

Gating (or triggering) is the use of an electrocardiograph signal (cardiac), peripheral pulse or level of inspiration (respiratory) to select a particular point in the cardiac or respiratory cycle, which reduces cardiorespiratory movement artifacts and improves resolution in image acquisition. In retrospective gating, the ECG, pulse, or respiratory levels are recorded during continuous imaging, and correlation is performed during post-processing. Two gating methods (e.g., respiratory and cardiac) can be used to further improve image quality. Gating can be used to evaluate cardiac and pulmonary structures, such as coronary artery calcification (atherosclerosis) [55], [56]. An example of a specific diagnostic application was the recently proposed non-gated CTA method for differentiating between pulmonary hypertension (affecting the arteries in the lungs) due to heart failure with preserved ejection fraction (volume of blood ejected by the heart) and idiopathic pulmonary arterial hypertension [57]. Fast spin echo (FSE) MRA uses cardiac gating to capture images during systole, when both arteries and veins have high signal values, and during diastole, when arterial signal strength falls. Images of the arteries are created by subtracting the systole images from those taken during diastole. Another example of the critical importance of gating in acquiring images that are extremely sensitive to motion is the application of pulse triggering with diffusion weighted MRI (DW-MRI) of the brain (Brownian motion of water molecules) [58].

Consistency and accuracy of imaging data are improved when calculations and measurements are performed by automated systems, either online or offline. Parameters important for diagnosis and assessment of hypertension and related conditions are blood pressure, blood flow velocities, arterial and cardiac wall thicknesses, stenosis and occlusion identification, heart valve function, etc. Color Doppler ultrasound can provide important information such as blood flow velocity and direction.

16.5 DISCUSSION

Cerebrovascular health and physiological changes, such as vascular remodeling, can provide important information about the risk for developing diseases like hypertension and dementia. It is estimated that roughly one-third of dementia cases could be prevented by treating the underlying cause [59], [60], which is often hypertension. Chronic systemic hypertension can cause temporary or permanent disability, especially when left untreated. Hypertension causes damage especially to smaller blood vessels, and significantly increases the risk for end-organ damage, with greatest concern focused mainly on the heart (e.g., heart failure, LVH), kidneys (e.g., renal failure), eyes (visual impairment), brain (e.g., dementia, stroke), and the lungs (pulmonary hypertension). It also

contributes to early mortality. The Centers for Disease Control and Prevention (CDC) reports that in 2014, hypertension directly or indirectly affected the cause of death for over 400,000 people in the U.S. [61].

There are currently invasive and noninvasive methods for diagnosing hypertension and assessing its pathophysiological effects. The early stages of hypertension can cause left ventricular wall thickening and cerebrovascular remodeling [62], even while noninvasive blood pressure measurements are still within the normal range. However, these cerebrovascular changes are not easily detectible as current software programs are only capable of segmenting larger cerebrovascular structures in MRAs. A technique has recently been developed that will detect and segment the smaller cerebrovascular structures, with extraction and analysis of three relevant features: inner vessel diameter, bifurcations, and tortuosity. Cerebrovascular structural changes in blood vessel diameters have been reported to be an early indication of vascular dysfunction from in vivo and clinical observations [63]. Bifurcations are points where venous and arterial vessels divide into two branches. Tortuosity is a term referring to how twisted (or tortuous) the curves and turns of the blood vessels are. It is a measure of how sharply a vessel is turning as it is traversing. Increased vascular tortuosity has been previously linked to hypertension, genetic defects, aging, atherosclerosis, and diabetes mellitus [64]. These cerebrovascular changes can be bellwethers for the development or progression of problems such as cognitive impairment or memory loss. Early detection and quantification of cerebral blood vessel changes (diameters and/or tortuosity) may enable early-stage diagnosis and treatment of hypertension prior to disease onset and identify patients at risk of adverse events.

Hypertension is a progressive disease that may take a decade or two before it is discovered or diagnosed. Reported correlations between changes in smaller cerebrovascular vessels and hypertension may be used to diagnose hypertension in its early stages, 10 to 15 years before the appearance of symptoms such as cognitive impairment and memory loss. This diagnostic procedure may identify and analyze relevant cerebrovascular features related to these changes and track disease progression and treatment efficacy. Screening for other problems, such as intracranial hypertension (increased pressure inside the skull), could also be accomplished using MRA taken for this procedure since the original image will remain unaltered. Progression of dementia and Alzheimer's is currently measured with diagnostic tools such as the global deterioration scale (GDS), which can include error due to differences in interpretation, perspective, and experience between different clinicians. Computer aided diagnostic (CAD) systems that utilize MRA to quantify cerebrovascular changes by calculating alterations in cerebral vessel features (diameter and tortuosity) [63, 65] may enable proactive monitoring and management of hypertension. However, MRA screening for hypertension is expensive and thus patients deemed to be at high risk of developing hypertension due to family or medical history would need to be identified by their healthcare providers as candidates for this diagnostic procedure.

Screening tests may help physicians open a dialogue regarding the medical consequences of resisting a diagnosis and subsequently strengthen the opportunity and commitment for patients to engage in their health. Some people do not feel any effects of hypertension, even in more advanced stages. It is not uncommon for patients to dismiss high blood pressure readings with rationalizations such as the high readings being the result of being nervous or stressed. They often do not want to accept the diagnosis, nor want to be medicated for hypertension. Because they are often asymptomatic, even when prescribed medication patients often do not take the medication properly as prescribed. Having quantitative measurements provides physicians with scientific data that helps validate a diagnosis and provides patients with numeric information that can be communicated to them easily and in a way that it is hoped will help them have better insight and understanding of their condition and the need to take action. Proactive and preventive lifestyle changes, especially in the very early stages, 10 to 15 years before the symptomatic development of hypertension, will often slow the progression of the disease.

Timely information regarding vascular health could improve prognosis and quality of life for patients and their families and help to reduce healthcare costs. The Lewy Body Dementia

Association reports that costs associated with long-term care (75–84% of total costs of care) for patients with dementia account for most of the $157–$215 billion annual cost associated with this disease. Many people cannot afford long-term care in a facility, which increases the burden on families and friends to provide care and supervision. This can interfere with family members' jobs, income, and stress levels. Caring for a family member who has a dementia-related disease can adversely affect caregivers' health.

The risks must be weighed and discussed between patients and their healthcare providers. Aggressive preventive treatment may include prescription medication (e.g., calcium or beta blockers typically used to reduce hypertension). False positive results could prompt healthcare providers to prescribe medications to treat hypertension. These medications could not only cause the adverse effects associated with that medication, but also they could cause imbalance within the body by treating for a condition that does not exist. Jaul and Meiron point out that irregular presentation of symptoms could lead to misdiagnosis and subsequent treatment (e.g., prescription of antispasmodic medication to treat bladder urgency) which could accelerate or allow progression of the patient's underlying hypertensive condition, resulting in the progression of vascular related diseases such as dementia, Alzheimer's, cognitive deterioration, etc. [66]. False negative results would be detrimental by allowing the condition to progress without proper observation or treatment.

Many of the tests used by mainstream medicine are excellent at detecting disease and are very useful for identifying specific disease processes. However, most of them identify disease processes at later stages where most of the damage might not be reversed [9]. While antihypertensive treatment can slow the progression of the disease and its effects, detection and efforts to slow or halt its development earlier in the disease course are desired to reduce risk and improve patient quality of life [9], [67], [68]. Thus, there is a need for automatic computerized systems that are capable of providing accurate screening and diagnoses for early detection of prehypertension for prolonging life and improving patients' quality of life. These automatic systems may help identify hypertension many years before its onset compared to current testing methods. Screening and early diagnosis gives patients, families, and providers the opportunity to take steps to prevent or delay the onset of the disease process, or to limit the severity of symptoms and sequelae, improving patient-oriented outcomes.

16.6 EMERGING TECHNIQUES AND TRENDS

16.6.1 Measuring Blood Pressure

Blood pressure measurement devices continue to be improved and developed. Waveform analysis acquired by noninvasive means is becoming increasingly reliable. Studies show that brachial waveform measured with a volume-clamp method is a reliable method for continuous blood pressure monitoring [20], [69], [70], [71]. Nitzan et al. proposed a photoplethysmography-based systolic blood pressure measurement (segmental pressure) technique, which uses an arm pressure cuff in conjunction with a photoplethysmographic (PPG) fingertip probe [15]. This device and technique is investigational as of July 2017. A giant magneto resistance (GMR) based plethysmograph measures a time delay between two sensors placed on the arm to measure pulse wave velocity, which can be used to estimate blood pressure. It is sensitive to arterial flow in the magnetic field and does not require a wrist cuff or arm band. It can also measure heart rate and respiration rate [72]. While the study conducted on this method reported a MAP error as high as ±9 mmHg, it is an example of devices pushing for utilization of more technological advances to become more comfortable and even less invasive (e.g., cuffless). Researchers continue to work toward reliable noninvasive continuous blood pressure measurement techniques that can replace invasive methods due to its inherent risks. And as patients become engaged in their health, development of devices that make reliable home monitoring and communication with care providers easier will continue to advance technologies that already can take accurate measurements with no artifacts from movement and work with mobile apps.

Currently, intra- and central arterial blood pressure monitoring remain the most reliable measurement methods. As noninvasive technologies (and methodologies related to them) continue to improve, it is being questioned whether intra-arterial monitoring can be delayed for some less critically ill patients and for less critical intra-operative monitoring in favor of continuous noninvasive monitoring techniques [18], [73], [74], [75].

16.6.2 Imaging

Continuing research and innovations will expand noninvasive evaluation methods and enable correlation of these findings to new and emerging diseases and conditions. This will increase options for and improve diagnostic techniques, allowing for early detection of developing conditions and preventive treatments. For example, research into the temporal and medicated versus unmedicated functional connectivity and changes in resting state (task-free) fMRI using BOLD holds promise in diagnosing early stage development of Parkinson's and other brain diseases [35]. Another example is the recent work on a PC-MRA optimization method for measuring cerebral blood flow within the entire brain [76].

A recent research project applied calibrated (using ASL and BOLD) fMRI to estimate levels of cerebral metabolic rate of oxygen (CMRO2) and correlate these quantifications to early detection of Alzheimer's and other conditions such as Parkinson's disease [77]. Another study found that ASL MRI was less accurate than PDG-PET in diagnosing dementia, but it was noted that research with a larger subject group that included use of anatomical MRI had results comparable to FDG-PET diagnostic accuracies [78]. Continued research will improve methods using this technology and provide expanded applications and better diagnostic capabilities. This includes the need for minimizing variability between manufacturers' machines, techniques, and procedures such as registration, image reconstruction, etc. [79].

Spectral CT, which was approved by the FDA just a few years ago, uses a single-source multilayer detector that can provide both high and low MonoEnergetic images. It can display iodine (a contrast agent) as a different color than calcium, which enables quantification of arterial plaques. This differentiation can also provide higher resolution of tumor contours. As techniques with this modality continue to be researched, vascular-related applications will surely be developed that expand upon current imaging capabilities.

Contrast enhanced ultrasound (CEUS) uses microbubble-based contrast agents, and current technology offers a sensitivity that can identify a single bubble [80]. Injected microbubbles improve the echogenicity of blood. This technique captures the vascular lumen (vessel interior) and vascular wall, which improves vascular related diagnostics in the brain as well as other organs. Continuing research includes targeted microbubbles with use of ligands [81]. Currently, this technology offers visibility in parenchymal microcirculation, which allows characterization of lesions, and research has included its use in left ventricular pressure quantification [82]. Some imaging modalities, such as CE-MRA, can be used to measure shear stress against the inner vessel walls. Low shear stress increases the risk for development of atherosclerotic plaques. In the future, measurement of this cerebrovascular condition may also be researched as a correlating marker (esp. in conjunction with measurements of tortuosity) in the risk for developing hypertension or vascular dementia.

16.7 CONCLUSION

This chapter presented an overview of hypertension, its causes and effects, and current technologies used to measure and predict it. Cerebrovascular changes including blood vessel diameters and tortuosity occur before the onset of hypertension. Current approaches to use and analyze imaging modalities to predict the potential of hypertension are promising. These modalities will help in better management of handling pre-hypertension and hypertension patients and reducing or preventing any adverse events.

References

1. O. A. Carretero and S. Oparil, "Essential hypertension," *Circulation*, vol. 101, no. 3, pp. 329–335, 2000.
2. T. H. K. Puar, Y. Mok, R. Debajyoti, J. Khoo, C. H. How, and A. K. H. Ng, "Secondary hypertension in adults," *Singapore Medical Journal*, vol. 57, no. 5, p. 228, 2016.
3. A. Cremer *et al*., "From malignant hypertension to hypertension-MOD: a modern definition for an old but still dangerous emergency," *Journal of Human Hypertension*, vol. 30, no. 8, pp. 463–466, 2016.
4. P. K. Whelton *et al*., "2017 ACC/AHA/AAPA/ABC/ACPM/AGS/APhA/ASH/ASPC/NMA/PCNA guideline for the prevention, detection, evaluation, and management of high blood pressure in adults: a report of the American College of Cardiology/American Heart Association Task Force on Clinical Practice Guidelines," *Journal of the American College of Cardiology*, p. 24430, 2017.
5. A. V. Chobanian *et al*., "The seventh report of the joint national committee on prevention, detection, evaluation, and treatment of high blood pressure: the JNC 7 report," *JAMA*, vol. 289, no. 19, pp. 2560–2571, 2003.
6. National Heart and Blood Institute. (01/26/2018). *High Blood Pressure*.
7. P. Naumczyk *et al*., "Compensatory functional reorganization may precede hypertension-related brain damage and cognitive decline: a functional magnetic resonance imaging study," *Journal of Hypertension*, vol. 35, no. 6, p. 1252, 2017.
8. C. A. Emdin *et al*., "Blood pressure and risk of vascular dementia," *Stroke*, vol. 47, no. 6, pp. 1429–1435, 2016.
9. H. M. School. (2009, 01/25/2018). *Blood Pressure and Your Brain*.
10. J. S. Ringrose, J. Cena, S. Ip, F. Morales, P. Hamilton, and R. Padwal, "Comparability of automated office blood pressure to daytime 24-hour ambulatory blood pressure," *Canadian Journal of Cardiology*, vol. 34, no. 1, pp. 61–65, 2018.
11. J. Harju *et al*., "Comparison of non-invasive blood pressure monitoring using modified arterial applanation tonometry with intra-arterial measurement," *Journal of Clinical Monitoring and Computing*, vol. 32, no. 1, pp. 13–22, 2018.
12. M. R. Nelson, J. Stepanek, M. Cevette, M. Covalciuc, R. T. Hurst, and A. J. Tajik, "Noninvasive measurement of central vascular pressures with arterial tonometry: clinical revival of the pulse pressure waveform?" in *Mayo Clinic Proceedings*, vol. 85, no. 5, pp. 460–472, 2010.
13. U. T. Nguyen *et al*., "Automated quantification of retinal arteriovenous nicking from colour fundus images," in *Engineering in Medicine and Biology Society (EMBC), 2013 35th Annual International Conference of the IEEE*, 2013, pp. 5865–5868.
14. S. Ribezzo, E. Spina, S. Di Bartolomeo, and G. Sanson, "Noninvasive techniques for blood pressure measurement are not a reliable alternative to direct measurement: a randomized crossover trial in ICU," *The Scientific World Journal*, vol. 2014, 2014.
15. M. Nitzan, I. Slotki, and L. Shavit, "More accurate systolic blood pressure measurement is required for improved hypertension management: a perspective," *Medical Devices (Auckland, NZ)*, vol. 10, p. 157, 2017.
16. B. S. Alpert, D. Quinn, and D. Gallick, "Oscillometric blood pressure: a review for clinicians," *Journal of the American Society of Hypertension*, vol. 8, no. 12, pp. 930–938, 2014.
17. M. K. Rakotz *et al*., "Medical students and measuring blood pressure: results from the American Medical Association Blood Pressure Check Challenge," *The Journal of Clinical Hypertension*, 2017.
18. Y. Ostchega, C. Dillon, R. Prineas, M. McDowell, and M. Carroll, "Tables for the selection of correct blood pressure cuff size based on self-reported height and weight and estimating equations for mid-arm circumference: data from the US National Health and Nutrition Examination Survey," *Journal of Human Hypertension*, vol. 20, no. 1, pp. 15–22, 2006.
19. M. G. U. Garcia, E. Ang, N. M. Ahmad, and C. C. Lim, "Correct placement of blood pressure cuff during blood pressure measurement," *International Journal of Evidence-Based Healthcare*, vol. 10, no. 3, pp. 191–196, 2012.
20. S. A. Esper and M. R. Pinsky, "Arterial waveform analysis," *Best Practice & Research Clinical Anaesthesiology*, vol. 28, no. 4, pp. 363–380, 2014.
21. B. H. McGhee and E. J. Bridges, "Monitoring arterial blood pressure: what you may not know," *Critical Care Nurse*, vol. 22, no. 2, pp. 60–79, 2002.
22. K. Kuriyama, G. Gamsu, R. G. Stern, C. E. Cann, R. J. Herfkens, and B. H. Brundage, "CT-determined pulmonary artery diameters in predicting pulmonary hypertension," *Investigative Radiology*, vol. 19, no. 1, pp. 16–22, 1984.
23. C. R. Becker *et al*., "Coronary artery calcium measurement: agreement of multirow detector and electron beam CT," *American Journal of Roentgenology*, vol. 176, no. 5, pp. 1295–1298, 2001.

24. "CT Scan," https://en.wikipedia.org/wiki/CT_scan.
25. S. Ley *et al.*, "Value of contrast-enhanced MR angiography and helical CT angiography in chronic thromboembolic pulmonary hypertension," *European Radiology*, vol. 13, no. 10, pp. 2365–2371, 2003.
26. "Medical definition of multidetector computed tomography," https://www.medicinenet.com/script/main/art.asp?articlekey=40639.
27. J. Burrill, Z. Dabbagh, F. Gollub, and M. Hamady, "Multidetector computed tomographic angiography of the cardiovascular system," *Postgraduate Medical Journal*, vol. 83, no. 985, pp. 698–704, 2007.
28. Z. A. Hage, A. Alaraj, G. D. Arnone, and F. T. Charbel, "Novel imaging approaches to cerebrovascular disease," *Translational Research*, vol. 175, pp. 54–75, 2016.
29. R. Gupta *et al.*, "Flat-panel volume CT: fundamental principles, technology, and applications," *Radiographics*, vol. 28, no. 7, pp. 2009–2022, 2008.
30. W. Heindel, R. Gübitz, V. Vieth, M. Weckesser, O. Schober, and M. Schäfers, "The diagnostic imaging of bone metastases," *Deutsches Ärzteblatt International*, vol. 111, no. 44, p. 741, 2014.
31. D. R. Lisk *et al.*, "Should hypertension be treated after acute stroke? A randomized controlled trial using single photon emission computed tomography," *Archives of Neurology*, vol. 50, no. 8, pp. 855–862, 1993.
32. "Positron emission tomography," https://en.wikipedia.org/wiki/Positron_emission_tomography.
33. A. M. Maceira and R. H. Mohiaddin, "Cardiovascular magnetic resonance in systemic hypertension," *Journal of Cardiovascular Magnetic Resonance*, vol. 14, no. 1, p. 28, 2012.
34. M. M. Almi'ani and B. D. Barkana, "Automatic segmentation algorithm for brain MRA images," in *Systems, Applications and Technology Conference (LISAT), 2012 IEEE Long Island*, 2012, pp. 1–5.
35. P. Tuite, "Brain Magnetic Resonance Imaging (MRI) as a potential biomarker for Parkinson's Disease (PD)," *Brain Sciences*, vol. 7, no. 6, p. 68, 2017.
36. L. Nocetti, A. Mantovani, S. Vallone, T. Costi, P. Carpeggiani, and G. Pinna, "Phase contrast MR as non-invasive tool in the diagnosis of benign intracranial hypertension," *The Neuroradiology Journal*, vol. 24, no. 2, pp. 271–272, 2011.
37. B. Battal, M. Kocaoglu, N. Bulakbasi, G. Husmen, H. Tuba Sanal, and C. Tayfun, "Cerebrospinal fluid flow imaging by using phase-contrast MR technique," *The British Journal of Radiology*, vol. 84, no. 1004, pp. 758–765, 2011.
38. P. Turski *et al.*, "Neurovascular 4DFlow MRI (phase contrast MRA): emerging clinical applications," *Neurovascular Imaging*, vol. 2, no. 1, p. 8, 2016.
39. S. Fall, G. Pagé, J. Bettoni, R. Bouzerar, and O. Balédent, "Use of phase-contrast MRA to assess intracranial venous sinus resistance to drainage in healthy individuals," *American Journal of Neuroradiology*, vol. 38, no. 2, pp. 281–287, 2017.
40. S. Neumann *et al.*, "Non-invasive wave intensity analysis in the aorta and internal carotid using phase-contrast MR angiography: the effect of hypertension," *Artery Research*, vol. 20, p. 51, 2017.
41. M. Schäfer *et al.*, "Measuring flow hemodynamic indices and oxygen consumption in children with pulmonary hypertension: a comparison of catheterization and phase-contrast MRI," *Pediatric Cardiology*, pp. 1–7, 2017.
42. S. Petcharunpaisan, J. Ramalho, and M. Castillo, "Arterial spin labeling in neuroimaging," *World Journal of Radiology*, vol. 2, no. 10, p. 384, 2010.
43. Q. Shen and T. Q. Duong, "Background suppression in arterial spin labeling MRI with a separate neck labeling coil," *NMR in Biomedicine*, vol. 24, no. 9, pp. 1111–1118, 2011.
44. A. P. Haley, J. Gunstad, R. A. Cohen, B. A. Jerskey, R. C. Mulligan, and L. H. Sweet, "Neural correlates of visuospatial working memory in healthy young adults at risk for hypertension," *Brain Imaging and Behavior*, vol. 2, no. 3, pp. 192–199, 2008.
45. B. C. Dickerson and R. A. Sperling, "Functional abnormalities of the medial temporal lobe memory system in mild cognitive impairment and Alzheimer's disease: insights from functional MRI studies," *Neuropsychologia*, vol. 46, no. 6, pp. 1624–1635, 2008.
46. J. Tian, J. Shi, and D. Mann, "Cerebral amyloid angiopathy and dementia," *Panminerva Medica*, vol. 46, no. 4, pp. 253–264, 2004.
47. B. W. Beulen, N. Bijnens, G. G. Koutsouridis, P. J. Brands, M. C. Rutten, and F. N. van de Vosse, "Toward noninvasive blood pressure assessment in arteries by using ultrasound," *Ultrasound in Medicine & Biology*, vol. 37, no. 5, pp. 788–797, 2011.
48. S. Nissan and P. Yuck, "Intravascular ultrasound: novel pathophysiological insights and current clinical application," *Circulation*, vol. 103, no. 4, pp. 604–611, 2001.
49. J. P. Sun *et al.*, "Early diastolic dyssynchrony in relation to left ventricular remodeling and function in hypertension," *International Journal of Cardiology*, vol. 179, pp. 195–200, 2015.

50. B. Bybel, R. C. Brunken, F. P. DiFilippo, D. R. Neumann, G. Wu, and M. D. Cerqueira, "SPECT/CT imaging: clinical utility of an emerging technology," *Radiographics*, vol. 28, no. 4, pp. 1097–1113, 2008.
51. A. Almuhaideb, N. Papathanasiou, and J. Bomanji, "18F-FDG PET/CT imaging in oncology," *Annals of Saudi Medicine*, vol. 31, no. 1, p. 3, 2011.
52. K. Leung, "[18F] Fluoro-2-deoxy-2-D-glucose," 2005.
53. M. N. Pizzi *et al.*, "18F-FDG-PET/CT angiography in the diagnosis of infective endocarditis and cardiac device infection in adult patients with congenital heart disease and prosthetic material," *International Journal of Cardiology*, vol. 248, pp. 396–402, 2017.
54. T. S. Aukema *et al.*, "Utility of preoperative 18F-FDG PET/CT and brain MRI in melanoma patients with palpable lymph node metastases," *Annals of Surgical Oncology*, vol. 17, no. 10, pp. 2773–2778, 2010.
55. B. Desjardins and E. A. Kazerooni, "ECG-gated cardiac CT," *American Journal of Roentgenology*, vol. 182, no. 4, pp. 993–1010, 2004.
56. R. E. Kanza, C. Allard, and M. Berube, "Cardiac findings on non-gated chest computed tomography: a clinical and pictorial review," *European Journal of Radiology*, vol. 85, no. 2, pp. 435–451, 2016.
57. A. E. H. Veld *et al.*, "CTA-derived left to right atrial size ratio distinguishes between pulmonary hypertension due to heart failure and idiopathic pulmonary arterial hypertension," *International Journal of Cardiology*, vol. 223, pp. 723–728, 2016.
58. O. Dietrich, S. Heiland, T. Benner, and K. Sartor, "Reducing motion artefacts in diffusion-weighted MRI of the brain: efficacy of navigator echo correction and pulse triggering," *Neuroradiology*, vol. 42, no. 2, pp. 85–91, 2000.
59. I. Skoog *et al.*, "15-year longitudinal study of blood pressure and dementia," *The Lancet*, vol. 347, no. 9009, pp. 1141–1145, 1996.
60. G. Livingston *et al.*, "Dementia prevention, intervention, and care," *The Lancet*, vol. 390, no. 10113, pp. 2673–2734, 2017.
61. T. Nwankwo, S. Yoon, V. Burt, and Q. Gu, "Hypertension among adults in the US: National Health and Nutrition Examination Survey, 2011–2012. NCHS data brief, no. 133," *National Center for Health Statistics, Centers for Disease Control and Prevention, Hyattsville, MD, US Dept of Health and Human Services Ref Type: Report*, 2013.
62. N. F. Renna, N. de las Heras, and R. M. Miatello, "Pathophysiology of vascular remodeling in hypertension," *International Journal of Hypertension*, vol. 2013, 2013.
63. Y. A. Gebru, "A novel MRA-based framework for the detection of changes in cerebrovascular blood pressure," 2017.
64. H.-C. Han, "Twisted blood vessels: symptoms, etiology and biomechanical mechanisms," *Journal of Vascular Research*, vol. 49, no. 3, pp. 185–197, 2012.
65. H. K. *et al.*, "A novel MRA framework based on integrated global and local analysis for accurate segmentation of the cerebral vascular system," 2018.
66. E. Jaul and O. Meiron, "Systemic and disease-specific risk factors in vascular dementia: diagnosis and prevention," *Frontiers in Aging Neuroscience*, vol. 9, p. 333, 2017.
67. C. Tzourio, "Hypertension, cognitive decline, and dementia: an epidemiological perspective," *Dialogues in Clinical Neuroscience*, vol. 9, no. 1, p. 61, 2007.
68. C. Sierra, A. De La Sierra, M. Salamero, J. Sobrino, E. Gómez-Angelats, and A. Coca, "Silent cerebral white matter lesions and cognitive function in middle-aged essential hypertensive patients," *American Journal of Hypertension*, vol. 17, no. 6, pp. 529–534, 2004.
69. D. W. Eeftinck Schattenkerk *et al.*, "Nexfin noninvasive continuous blood pressure validated against Riva-Rocci/Korotkoff," *American Journal of Hypertension*, vol. 22, no. 4, pp. 378–383, 2009.
70. J. R. Martina *et al.*, "Noninvasive blood pressure measurement by the Nexfin monitor during reduced arterial pulsatility: a feasibility study," *ASAIO Journal*, vol. 56, no. 3, pp. 221–227, 2010.
71. G. Chen, L. Meng, B. Alexander, N. P. Tran, Z. N. Kain, and M. Cannesson, "Comparison of noninvasive cardiac output measurements using the Nexfin monitoring device and the esophageal Doppler," *Journal of Clinical Anesthesia*, vol. 24, no. 4, pp. 275–283, 2012.
72. V. K. Chugh, K. Kalyan, C. Anoop, A. Patra, and S. Negi, "Analysis of a GMR-based plethysmograph transducer and its utility for real-time blood pressure measurement," in *Engineering in Medicine and Biology Society (EMBC), 2017 39th Annual International Conference of the IEEE*, 2017, pp. 1704–1707.
73. F. Liang, Z. Yin, Y. Fan, K. Chen, and C. Wang, "In vivo validation of an oscillometric method for estimating central aortic pressure," *International Journal of Cardiology*, vol. 199, pp. 439–441, 2015.

74. G. B. Papini, P. Fonseca, X. L. Aubert, S. Overeem, J. W. Bergmans, and R. Vullings, "Photoplethysmography beat detection and pulse morphology quality assessment for signal reliability estimation," in *Engineering in Medicine and Biology Society (EMBC), 2017 39th Annual International Conference of the IEEE*, 2017, pp. 117–120.
75. K. Lakhal, S. Ehrmann, and T. Boulain, "Non-invasive blood pressure monitoring in the critically ill: time to abandon the intra-arterial catheter?" *Chest*, 2017.
76. S. L. Peng *et al.*, "Optimization of phase-contrast MRI for the quantification of whole-brain cerebral blood flow," *Journal of Magnetic Resonance Imaging*, vol. 42, no. 4, pp. 1126–1133, 2015.
77. I. Lajoie *et al.*, "Application of calibrated fMRI in Alzheimer's disease," *NeuroImage: Clinical*, vol. 15, pp. 348–358, 2017.
78. U. C. Anazodo *et al.*, "Using simultaneous PET/MRI to compare the accuracy of diagnosing frontotemporal dementia by arterial spin labelling MRI and FDG-PET," *NeuroImage: Clinical*, vol. 17, pp. 405–414, 2018.
79. H. J. Mutsaerts *et al.*, "Comparison of arterial spin labeling registration strategies in the multi-center GENetic frontotemporal dementia initiative (GENFI)," *Journal of Magnetic Resonance Imaging*, vol. 47, no. 1, pp. 131–140, 2018.
80. J.-B. Liu, G. Wansaicheong, D. A. Merton, F. Forsberg, and B. B. Goldberg, "Contrast-enhanced ultrasound imaging: state of the art," *Journal of Medical Ultrasound*, vol. 13, no. 3, pp. 109–126, 2005.
81. A. L. Klibanov, "Targeted delivery of gas-filled microspheres, contrast agents for ultrasound imaging," *Advanced Drug Delivery Reviews*, vol. 37, no. 1, pp. 139–157, 1999.
82. J. K. Dave *et al.*, "Noninvasive LV pressure estimation using subharmonic emissions from microbubbles," *JACC: Cardiovascular Imaging*, vol. 5, no. 1, pp. 87–92, 2012.

Taylor & Francis
Taylor & Francis Group
http://taylorandfrancis.com

17 Predicting the Biomechanics of the Aorta Using Ultrasound

Mansour AlOmran, Alexander Emmott, Richard L. Leask, Kevin Lachapelle
McGill University

CONTENTS

17.1 INTRODUCTION

Thoracic aortic disease continues to be associated with a significant burden of morbidity and mortality in the general population. Disease of the thoracic aorta is due to aneurysm and/or dissection. An aneurysm is by definition an aortic diameter twice the normal size. This can lead to frank rupture or dissection then rupture. A dissection is a tearing of the inner lumen of the aorta such that the layers of the media separate and blood flows into a false lumen as well as the true lumen. An aortic rupture and an ascending aortic dissection (Type A) are considered surgical emergencies. The mortality is high and generally over 50% are dead without surgical treatment within two weeks. Despite improvement in diagnostics and advanced surgical techniques, mortality rates following surgery for acute aortic syndromes such as a rupture or type A aortic dissection continue to be associated with an overall mortality of 20–25% and significant morbidity such as stroke [1–5]. This high mortality following acute life-saving surgery is contrasted by the much lower risk of mortality (1.5–2.5%) when the ascending aortic aneurysm is repaired electively [3, 4, 6, 7]. This comparison illustrates the critical importance of early detection of individuals at risk for acute aortic syndromes such as dissection and rupture. Currently, most aortic aneurysms are detected incidentally when undergoing imaging for an unrelated issue, as aortic disease is generally asymptomatic until a first presentation of catastrophic dissection or even sudden death [9].

At the present time, aortic size above a certain cut-off is generally the most widely accepted indication for elective aortic repair to prevent acute aortic syndromes. The latest guidelines published by the American Heart Association and affiliates in 2010 recommends that asymptomatic patients with a degenerative thoracic aortic aneurysm with an ascending thoracic aorta or aortic sinus diameter of 5.5 cm or greater should be evaluated for surgical repair [10]. This is based on epidemiological studies of the natural history of aortic aneurysms that illustrated a sharp “hinge point” at 6 cm at which the probability of complications from the ascending aortic aneurysm increase dramatically

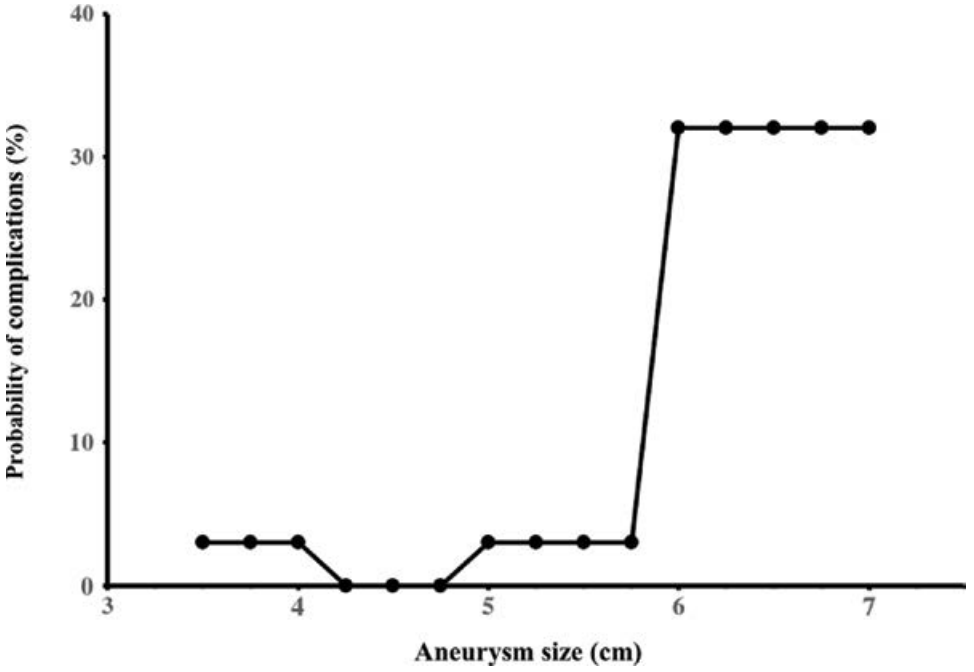

FIGURE 17.1 Increased risk of complications with increasing ascending aorta size with "hinge point" at 6 cm (from Coady *et al.*, *The Journal of Thoracic Cardiovascular Surgery* 1997) [11].

(Figure 17.1) [11]. In addition, follow-up studies did demonstrate very high wall tension in enlarged aortas (more than 6 cm) during episodes of moderate hypertension [12].

While the current recommendations provide an easy to follow and readily obtainable cut-off, aortic size by itself fails to address a few important points: 1) Size per se does not necessarily provide information on the integrity of the aortic wall. Although wall tension increases with diameter according to Laplace's Law, rupture and dissection occur probably related to an imbalance between the wall tension, blood pressure, and the histopathologic function of the aortic wall. Essentially, it is the biomechanics of the aortic wall that will determine the risk for each patient. 2). Although size is associated with risk, not all large aneurysms will rupture but many smaller aortas will dissect. It has been shown in the International Registry of Acute Aortic Dissections that the majority of patients with acute type A dissection had an ascending aorta diameter smaller than 5.5 cm. Nearly 60% of aortic dissection would not be prevented by current guidelines employed today. However, simply decreasing the cut-off for intervention and employing more aggressive criteria, for example less than 5 cm, would fail to prevent 40% of ascending aortic dissections (Figure 17.2) [1], and potentially expose a segment of patients to surgical harm needlessly. Additionally, aortic wall dilatation is only one of many consequences of the various etiologies that cause aortic wall disease. Considering how imprecise size is in predicting risk, there is a need for a methodology that provides better risk assessment.

The capacity to assess the biomechanics of the aorta in vivo prior to surgery has become a focus of active research and study. Cardiovascular imaging, particularly using echocardiography and ultrasound (US), provides a non-invasive approach and has shown promise in evaluating the biomechanics of the aorta. This chapter will review the use of ultrasound and its capacity to help clinicians understand the nature of aortic disease and more importantly, provide information regarding the timing of surgery.

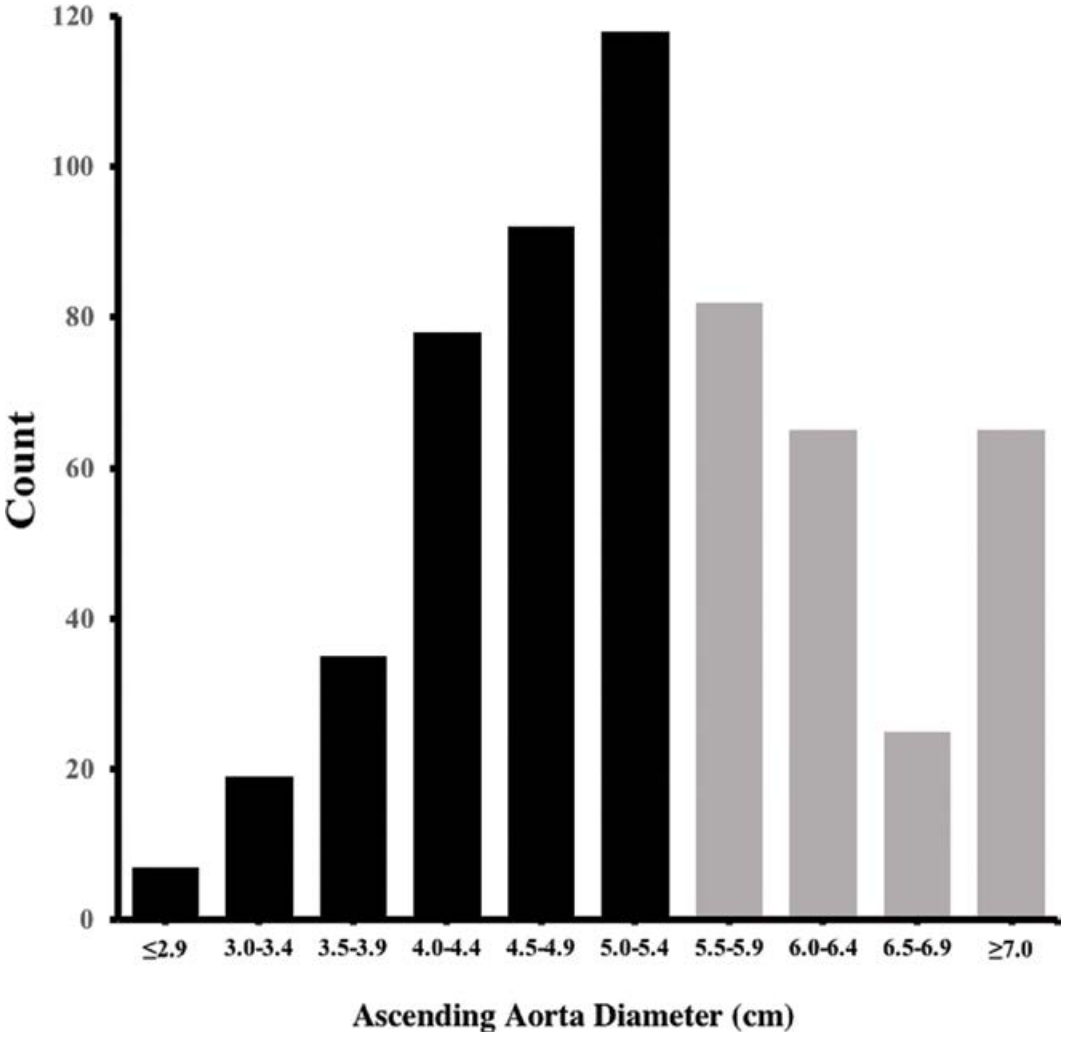

FIGURE 17.2 Distribution of aortic size at time of presentation with acute type A aortic dissection. Bars in *black* indicate individuals with diameter less than 5.5 cm (adapted from Pape et al., *Circulation* 2007) [1]).

17.2 STRUCTURAL PROPERTIES OF THE AORTA

The aortic wall is composed of three layers: the intima, media, and adventitia. These layers serve different biochemical and biomechanical functions. These functions dictate the size and structure of each layer. The intima is essentially a monolayer of endothelial cells adherent to a basement membrane [13], which serves as a barrier between the circulating blood and the thrombogenic media [14]. In the ascending aorta, intimal thickening is minimal but does present in atherosclerotic lesions. The biological structure of the media is critically important to the mechanical function of the aortic wall and progression of aneurysms, which will be discussed further in the following. Lastly, the adventitia is composed of thick bundles of collagen fibrils, vasa vasorum, and loose connective tissues. It provides the aorta with stiffness and support at higher levels of mechanical stress [15].

The media is the layer that contributes the most to the mechanical properties of elastic arteries [14]. It contains a complex network of bundles of collagen, elastin, and smooth muscle cells [14, 16]. In the media of the aorta, these components are organized into lamellar units about 10 micrometers thick on average [17].

17.3 EXTRACELLULAR MATRIX AND PROTEINS, AND VASCULAR SMOOTH MUSCLE CELLS

Collagen is the most abundant protein in mammals, and it is essential for most mechanically functional tissues in the human body such as bones, muscles, ligaments, and blood vessels [18]. Collagen bundles in arteries are generally aligned in a circumferential pattern, which facilitates increased circumferential strain resistance [19]. Collagen bundles are anisotropic, and have low extensibility (about 13%). It has a stiffness modulus approximately 1000 times greater than that of elastin. Collagen bundles are only engaged mechanically at moderate to high levels of strain to prevent vessel failure [19–21].

Various changes to collagen's quantity and structure take place during the aging process. The increased content of collagen in the aging aortic wall has been well-established [22–25]. Faber and Moller-Hou found that collagen content (as percentage of dry weight of aortic tissue) increases from 20% at the age of 20 to 30.5% at the age of 70 years [26].

Elastin is the functional protein of biological elastic fibers [27], which are the dominant component of the aortic wall extra-cellular matrix at 42% of its dry weight [28]. It exhibits reversible deformation with very high resilience, with maximal extension of more than 100%. Elastin also has low stiffness but high strain. These mechanical properties make elastin an efficient elastic-energy storage component [20]. These same properties are essential to the role of elastic fibers in initial compliance at lower and mid-level strain in elastic blood vessels [19, 21]. These elastic fibers are anisotropic [19] and organized into circumferential lamellae [22].

Elastin's concentration in the human ascending thoracic aorta decreases by 33% (of tissue dry weight) between the second and ninth decades of life [29]. However, the total content remained unchanged [30]. This is likely due to an increase in other components, especially collagen [22–25].

Vascular smooth muscle cells (VSMCs) are specialized cells that carry out multiple functions in the aortic wall, performed by distinct differentiated phenotypes, namely contractile and synthetic [31]. In healthy vessels, they're predominantly located in the media [32], with thin layers of fibers interposed between the cells [33, 34]. VSMCs are also generally circumferentially oriented [16], which adds to vessels' anisotropy passively [19].

The quantity of VSMCs decreases in aging vessels and in individuals with hypertension [22–25, 35]. However, human and animal studies have shown that the phenotypic transition of VSMCs from contractile to synthetic could be of greater importance than their absolute quantity; as synthetic VSMCs production of metalloproteinases could tip the balance of the extracellular matrix into a proteolytic state [36, 37].

17.4 MECHANICAL FUNCTION OF THE NORMAL AORTIC WALL

The mechanical function of the aorta is largely defined by extracellular components of the medial layer. A normal aorta is defined by alternating concentric layers of elastic sheets and smooth muscle cells with little dispersed collagen [38]. A mechanically normal aorta serves as an elastic capacitor, storing energy during systolic expansion and releasing energy in diastolic recoil. This property is known as the *Windkessel* function and is central in maintaining systemic circulation during diastole as well as a healthy pulse pressure [39].

It is the multi-component nature of the vessel wall that defines the elastic properties of the aorta. Mechanically, the aorta is characterized by a *hyperelastic* and *viscoelastic* stress-strain relation. Notably, *stress* (σ) is the amount of force in a given area of tissue (i.e., Force/Area) and,

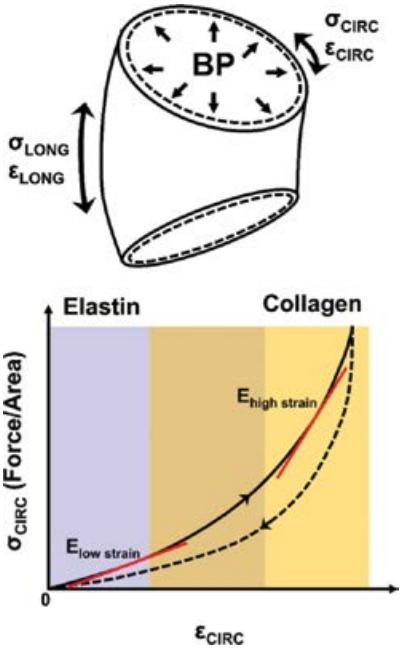

FIGURE 17.3 Mechanical behavior of the aorta. Schematic of an ascending aortic segment and the corresponding principle axes of stress (σ) and strain (ε). Typical hyperelastic circumferential aortic stress-strain curve. Elastin contributes to low-strain stiffness (slope of red line), while collagen contributes to high-strain stiffness. Hysteresis caused by tissue viscoelasticity is apparent by distinct loading (→) and unloading (←) paths. Note, CIRC-circumferential, LONG-longitudinal, BP-blood pressure.

physiologically, is generated by blood flow, residual tissue strain, and the motion of the heart. *Strain* (ε) is the relative deformation of the aortic wall, $\varepsilon = L/L_0$, where L_0 is a segment length in a reference position (typically the zero-stress state) and L is the current segment length. The stress-strain relationship around (circumferential) and along (longitudinal) the aorta determines its Windkessel function.

Hyperelasticity is defined by increased compliance at low strain and increased stiffness at high strain and therefore results in a nonlinear J-shaped stress-strain relation (Figure 17.3). This is attributed to the relative differences in stiffness of elastic fibers and collagen fibrils, respectively, as they become mechanically engaged at different levels of tissue strain [19]. Several tensile parameters can be used to describe the material properties of vascular tissues. The first, stiffness, is the tissue's resistance to deformation and is defined as the slope of a line tangent to the stress-strain curve. As the stress-strain curve is nonlinear, it must be defined at a fixed strain (or stress) value; in this context, is called the incremental (or apparent) elastic modulus. The second parameter, tensile strength, is the absolute value of stress the tissue can withstand before tearing and can only be determined by destructive testing.

Viscoelasticity is a characteristic of materials that exhibit both elastic and viscous properties. A purely elastic material can recover all stored elastic energy when it is relaxed. Conversely, viscoelastic materials dissipate a fraction of the elastic energy through viscous shearing (i.e., internal friction). This dampening results in hysteresis in the stress-strain relation where the curve follows two distinct paths between loading (increasing tension) and unloading (decreasing tension) (Figure 17.4). The energy loss parameter is a measure of the relative degree of hysteresis over a testing cycle and has been used to describe aortic tissues [40].

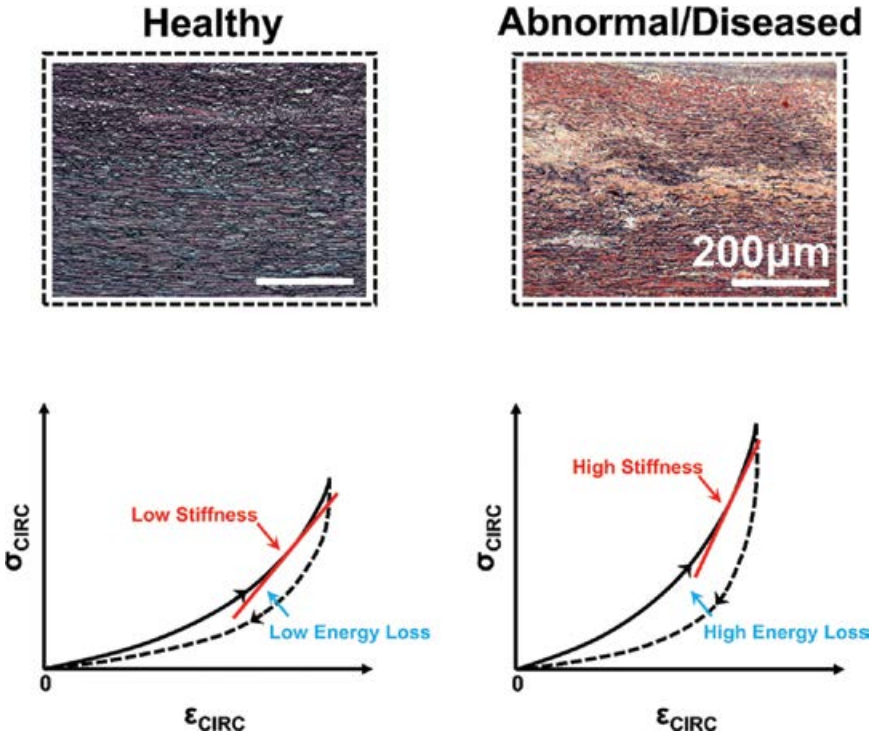

FIGURE 17.4 Representative medial histological sections and stress-strain curves from normal (left) and diseased (right) ascending aorta. Elastin is stained in *black*, collagen in *yellow,* and smooth muscle cells in *red* in Movat-stained histological sections. Stress-strain curves represent relative differences in stiffness by the apparent elastic modulus and energy loss by differences in hysteresis. The modulus in both graphs is measured at the same strain.

17.5 MECHANICAL FUNCTION OF THE DISEASED AORTIC WALL

In the formation of aortic aneurysms with various etiologies such as aging, hypertension, connective tissue disorders, and atherosclerosis, the organization and relative quantities of the aortic wall's structural components are disturbed. A shared endpoint of these etiologies is exaggerated extracellular matrix degradation leading to progressive aortic dilatation and eventual dissection or rupture [41, 42]. Features of medial disruption include the fragmentation of the elastic structure, excessive deposition of collagen and, occasionally, pooling of glycosaminoglycans [13] (Figure 17.4). Severe pathological medial remodeling can also include smooth muscle cell dropout [13]. Generally, aortic aneurysms are the result of an unproductive tissue remodeling that degenerates the medial layer structure. As the aneurysm grows, degradation of the ECM occurs and new tissue is synthesized, helping the vessel wall to maintain its thickness as the diameter grows [38].

The material properties of the aorta in persons with aortopathy and/or advanced age are markedly different from those measured in healthy individuals. For instance, ex vivo studies on resected ascending aortic tissue from patients receiving corrective aortic replacement have revealed that aneurysmal tissue is stiffer [43, 44], and has greater energy loss [40, 45] and lower tensile strength [43] than in persons with non-dilated ascending aortas. The magnitude of these parameters have been directly correlated with the medial expression of collagen and elastin [46, 47]. A more exhaustive comparison between diseased and normal aortas from ex vivo mechanical testing is reviewed in Emmott et al. [38]. Figure 17.4 presents the typical histological profile and stress-strain behavior

of normal and diseased ascending aorta. In this figure, differences in stiffness and energy loss are observed by the apparent modulus (slope of red tangent line) and increase in the hysteresis area, respectively.

In a clinical context, without access to a tissue biopsy, mechanical assessment is confined to an in situ analysis of the passive vessel deformation in response to the blood pressure waveform of the cardiac cycle. Tensile strength and other yielding properties cannot be measured under these conditions, and therefore stiffness, or its approximation, has been used as the surrogate measure of the mechanical properties of the vessel wall. As we explore, medical imaging modalities including ultrasound can be adapted for these in situ measurements on the aorta.

17.6 ULTRASOUND IMAGING

Ultrasound imaging utilizes the principle that sonic energy travels uniformly in a homogeneous medium, but when met with a structural interface with a different acoustic impedance a portion of that sonic energy is reflected back. This reflected energy is used to construct an image after processing the materials' density and distance [48]. Echocardiography is the application of ultrasound imaging to the heart and great vessels, including the thoracic aorta. Depending on the plane-of-view required by the clinician, the sonographer images through the chest (transthoracic, TTE) or the esophagus (transesophageal, TEE). TTE is non-invasive and is frequently used to capture a parasternal long-axis view of the heart or vessels and is often used to assess left ventricle function. TEE, in contrast, places the probe closer to the imaging plane by insertion within the esophagus and, in some cases, into the stomach. As a result, patients require sedation or, if used peri-operatively, a general anaesthetic.

Owing to the required focal depth of each modality (TEE, *low depth*, proximal; TTE, *high depth*, distal), TTE uses low ultrasonic frequency transducers of 2–5 MHz, while TEE uses high frequency transducers of 3.5–7 MHz. Physically, this is described by the attenuation ($A = af[2x]$), which is the product of the pulse frequency (f), the distance from the transducer to the image plane (x), and the attenuation coefficient (a) of the transmitting material (soft tissue, blood, bone, etc.) [49, 50]. As a result, the attenuation per unit depth is proportional to the transducer frequency. Because TEE is performed proximal to the thoracic aorta, one can compromise on increased signal attenuation for superior axial (parallel to the beam) and lateral resolution (orthogonal to the beam) as both increase with transducer frequency.

Ultrasound is emerging as a valuable instrument for the measurement of aortic in vivo stiffness (Table 17.1). It is readily available at the majority of hospitals and research centers. It is also portable, does not employ ionizing radiation, and is not as time-consuming as other comparable instruments (e.g., MRI). Furthermore, ultrasound assessment of biomechanics requires no assumption of models of circulation (Windkessel, propagative), as ultrasound-obtained measurements are used to assess local vascular stiffness directly from the change in volume driven by the change in pressure [51]. These measurements are taken from two standard ultrasound imaging modes. The first, M-mode (motion mode), is used to capture a single dimension (1D) ultrasound image, for instance the aortic cross-section showing opposite walls, over a period of time with very high temporal resolution. The second, B-mode (brightness mode), is used to capture a two-dimensional (2D) ultrasound image along the beam's axial and lateral axes. These images can be acquired in a cine loop to create a real-time moving image of the aortic cross-section or longitudinal structure.

However, the quality of the images obtained are patient and operator dependent [51]. Ultrasound images inherently provide poor lateral spatial resolution, and limited precision, as it's based on video-image analysis, that is, high-quality images involving the whole structure of interest are required for accurate assessment [51–53]. Additionally, most of the analysis is performed on two-dimensional images, which might present some limitations in fully assessing a three-dimensional structure. Another inherent limitation is that blind spots cause local anatomic constraints, such as structures behind ribs, the aortic arch, and the distal ascending aorta [54]. However, the use of

TABLE 17.1

2D STE: Two-dimensional speckle-tracking echocardiography. 2D VVI: Two-dimensional velocity vector imaging. β1: Stiffness index obtained via M-Mode. β2: Stiffness index obtained via speckle-tracking. LVEF: Left ventricular ejection fraction. Z_{va}: Valvulo-Arterial Impedance. SVR: Systemic vascular resistance. CCPM: Cardiac Cycle Pressure Modulus. CCSM: Cardiac Cycle Stress Modulus.

Author	Year	Region of Interest	Vascular Indices (Methodology)	Findings
Oishi *et al.*[57]	2008	Abdominal Aorta	β1 (M-Mode) β2 (2D STE) Peak Circumferential Strain (2D STE) Peak Circumferential Strain Rate (2D STE) Time to Peak Strain (2D STE)	• First study to use 2D STE to measure aortic biomechanics • β1 and β2 were correlated with age, especially β2 • Peak circumferential strain, strain rate, and time to peak strain were correlated negatively with age-correlation of strain and strain rate was closer than β1's correlation
Kim *et al.*[72]	2009	Descending Thoracic Aorta	Peak Circumferential Strain (VVI) Fractional Shortening (M-Mode) Fractional Area Change (M-Mode, VVI)	• Fractional Shortening (FS) and Fractional Area Change (FAC) (VVI) were significantly associated/negatively correlated with heart-femoral/brachial ankle PWV • Peak Circumferential Strain (PCS) and FAC by VVI were significantly negatively correlated with aging
Petrini *et al.*[97]	2010	Descending Thoracic Aorta	Stiffness Index (β1, β2) (M-Mode, VVI) Distensibility (M-Mode, VVI) Peak Circumferential Strain (VVI)	• Patients with Aortic Regurgitation (RA) had higher VVI strain than patients with Aortic Stenosis (AS) • Patients with AS were older and had higher aortic stiffness (VVI and M-Mode) compared with those with AR • VVI-derived strain, distensibility, and stiffness had strong correlation with the corresponding M-mode–derived parameters (despite systematic differences: VVI stiffness higher, VVI distensibility lower) • No significant difference in VVI strain between the proximal and distal levels of descending aorta
Oishi *et al.*[98]	2011	Abdominal Aorta	β1 (M-Mode) β2 (2D STE)	• Significant positive correlation β1, β2 with age (especially β2) in clinically normal individuals and individuals with cardiovascular risk factors without clinical disease • β1, β2 were similar between males and females • β1, β2 was significantly greater (abrupt and non-linear increase) in individuals over age 50 year than those less than 50 year

Oishi *et al.*[99]	2013	Abdominal Aorta (AA), Common Carotid Artery (CCA)	Peak Circumferential Strain AA (2D STE) Peak Circumferential Strain CCA (2D STE) β2 AA (2D STE) β2 CCA (2D STE)	• Mean CCA and AA strains were significantly greater in individuals less than 50 year compared with individuals 50 years and over • CCA and AA strains decreased with age with a more negative slope in individuals aged less than 50 years • Mean CCA strain in lower than AA strain at all ages • Mean CCA stiffness is greater than of AA stiffness at all ages • Mean CCA and AA stiffness were significantly increased non-linearly with age • AA and CCA stiffness steeply increased after the age of 50 years (especially AA)
Oishi *et al.*[73]	2013	Abdominal Aorta	β2 (2D STE)	• An increase in aortic stiffness was associated with increased LA stiffness and impaired LV relaxation in individuals with cardiovascular risk factors
Teixeira *et al.*[100]	2013	Ascending Thoracic Aorta	β1 (M-Mode) β2 (2D STE) Circumferential Ascending Aortic Stain (CAAS) (2D STE)	• Global CAAS predicted low flow more accurately than LVEF, Z_{va}, and SVR • β2 was significantly associated with a higher pulse pressure and lower stroke volume index
Gregory *et al.*[74]	2013	Ascending Thoracic Aorta	Aortic Compliance (2D STE)	• Aortic compliance is associated with diastolic function; as much as 25% of the variation of myocardial diastolic velocity being attributed to aortic compliance
Petrini *et al.*[101]	2014	Descending Thoracic Aorta	Stiffness index (β1, β2) (M-Mode, VVI) Aortic Distensibility (M-Mode, VVI) Peak Circumferential Strain (VVI)	• In AR: Bicuspid Aortic Valve (BAV) morphology is associated with lower regional strain and distensibility • In AS: Only distensibility was related to valve morphology • BAV was not associated with altered stiffness of the descending aorta in patient with severe AR or As
Teixeira *et al.*[75]	2015	Ascending Thoracic Aorta	β1 (M-Mode) Global Circumferential Ascending Aortic Strain Rate (CAASR) (2D STE)	• Stiffness index was independently associated associated with CAASR • CAASR was noted to be long-term prognostic marker
Leite *et al.*[76]	2016	Ascending Thoracic Aorta	CAASR (2D STE) CAAS (2D STE) β1 (M-Mode) β2 (2D STE)	• CAASR was significantly lower in patients with severe AR as opposed to moderate AR • Lower CAAS, Corrected CAAS and CAASR noted in patients with AS (Age and gender matched) • Lower values of global CAAS, Corrected CAAS, and Global CAASR was signigicantly associated with higher global mortality and cardiovascular death

(*Continued*)

TABLE 17.1 (Continued)

Author	Year	Region of Interest	Vascular Indices (Methodology)	Findings
Longobardo *et al.*[102]	2017	Ascending Thoracic Aorta	β1 (M-Mode) Aortic Strain (M-Mode) Longitudinal Strain (LS) (2D STE)	• Significant reduction of LS of the ascending arorta of BAV patients • Patients with heterozygous elastin polymorphism have increased aortic stiffness and decreased LS. And homozygous patients have more reduced strain than heterozygous patients • In BAV patients; those with a dilated ascending aorta had significantly decreased LS and greater stiffness when compared with BAV patients without dilatation
Teixeira *et al.*[103]	2017	Descending Thoracic Aorta	β1 (M-Mode) CAAS (2D STE) CAASR (2D STE)	• Evaluation of aortic mechanics using speckle-tracking in patients with non-valvular AF was feasible • Patients with history of stroke had aortas with significantly reduced strain and strain rate values • Higher risk of stroke (as per CHA_2DS_2-VASc) was associated with reduced values of strain and strain rate of the descending aorta
Bieseviciene *et al.*[104]	2017	Ascending Thoracic Aorta	Peak Longitudinal Strain (2D STE) Longitudinal Velocity (VL) (2D STE) Longitudinal Displacement (LD) (2D STE) Transverse displacement (2D STE) Distensibility (2D STE) Elastic modulus (2D STE) β2 (2D STE)	• The most marked biomechanics parameters (increased stiffness, decreased elasticity) were seen in patients with an ascending aorta diameter >45 mm. • Longitudinal wall mechanics (LD and VL) was most prominently impaired in patient with aortas >45 mm
Alreshidan *et al.*[77]	2017	Ascending Thoracic Aorta	β2 (2D STE) Apparent Stiffness (*ex vivo*)	• Compared *ex vivo* measured stiffness to *in vivo* calculated stiffness of the same aortic tissue • Mean steffness values obtained *in vivo* were similar to those measured *ex vivo* • *In vivo* stiffness index showed a significant difference between anterior, inner curvature, and posterior wall; ex vivo calculations showed a similar but non-significant trend.
Emmott *et al.*[78]	2018	Ascending Thoracic Aorta	CCPM (2D STE) CCSM (2D STE) Apparent Stiffness (*ex vivo*)	• Both CCPM and CCSM were predictive of the *ex vivo* Mechanical properties (CCSM had stronger correlation) • Both the CCSM and CCPM correlated strongly with the collagen/elastin ration of the ascending aorta

transesophageal echocardiography to complement transthoracic echocardiography alleviates most of the aforementioned anatomical limitations with the added risk (albeit low) of sedation and the invasive probe introduction [55, 56].

Ultrasound imaging's primary use in the field of vascular biomechanics is the determination of the local stiffness of a segment of a vessel [51]. This is carried out by measuring the change in volume (*strain*) driven by the change in local pressure (*contributing to wall stress*) between systole and diastole [51]. The measurement of the changes in volume are performed on the two-dimensional images obtained of a longitudinal or cross-section view of the vessel of interest. These measurements can be obtained directly from the M-mode images taken or using speckle-tracking imaging employing post-processing software [8].

Lastly, Doppler ultrasound technology has also been employed to assess tissue strain. Traditionally, Doppler ultrasound is used to determine the velocity and direction of blood flow by measuring changes in frequency of sound wave reflection off of red blood cells [48]. This same principle was applied to cardiac tissue; most commonly to assess ventricular function by measuring the velocity of the mitral annulus by analyzing the sound waves reflected off of the annulus itself [48]. More recently, aortic wall tissue mechanics were studied using Doppler technology to measure its velocity and direction to estimate the aortic systolic radial strain [57]. Doppler ultrasound technology is highly angle dependent [48], which limits its use only to specific areas of the arterial tree.

17.7 SPECKLE TRACKING ECHOCARDIOGRAPHY

Two-dimensional (2D) speckle-tracking echocardiography (STE) is an imaging modality that exploits the presence of natural acoustic markers (i.e., "speckles") from standard B-mode (brightness mode) ultrasound images. Speckles are both stable and evenly distributed within the area of the imaged tissue [58]. As a result, speckles can be tracked within a time-series of B-mode images allowing for the measurement of tissue velocity (Figure 17.5). Strain (ε) can be obtained from STE by measuring the deformation between adjacent speckles: $\varepsilon = \delta / L_0$, where L_0 is the original length between the two speckles, and δ is the change in length (i.e., $\delta = L - L_0$) [59]. This process can be scaled and applied to larger segmentations of a tissue; for instance, a quadrant of the circumference of the aortic wall. And unlike Doppler technology, it uses 2D grayscale images and thus is angle independent (i.e., it is not necessary for the main motion vector to be parallel to the ultrasound beam vector, which also renders it independent from cardiac translational movement) [53, 60–63].

Depending on the angle at which the beam intersects the tissue, different planes-of-view corresponding to different axes of strain can be imaged for various cardiovascular structures.

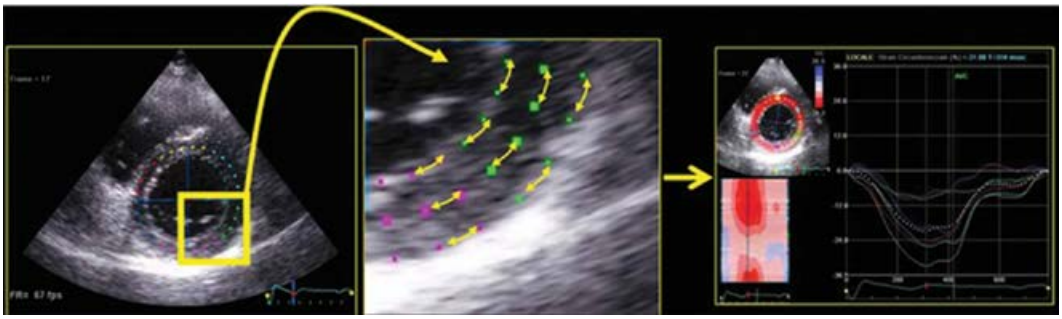

FIGURE 17.5 Speckle-Tracking Echocardiography for myocardial circumferential strain analysis post-processing views. Left: the area of interest delineated in a dotted colored line. Middle: Graphical representation of the speckles being analyzed. Right: The resultant strain curves. (Adapted from Mondillo et al., *Journal of Ultrasound in Medicine* 2011 [60]).

For the ascending aorta, two standard TEE views are available with the probe at the level of the mid-esophagus. The first is the short-axis (SAX) view that captures a transverse cross-section of the ascending aorta. A SAX view allows for the measurement of circumferential (ε_{CIRC}) and radial strain (ε_{RAD}). The second is the long-axis (LAX) view that captures a longitudinal view of the inner and outer curvature of the aorta. A LAX view allows for the measurement of longitudinal strain (ε_{LONG}) as well as radial strain and 2D diameter change, although both are limited to the intersecting plane.

In the last decade 2D STE gained exponential increase in interest in the literature [60]. 2D STE is traditionally used to assess left ventricular function and mechanics [60, 61]. It is a relatively new technology in the field of echocardiography that provides objective and quantitative global and regional myocardial function evaluation [60]. This type of tissue analysis was only feasible using MRI before the emergence of this technology; and cardiac magnetic resonance imaging (CMRI) is still the reference for this field of study. However, high expense, limited access, relative complexity of image acquisition, and the time-consuming nature of image analysis make CMRI less attractive than 2D STE for clinical application [60, 64, 65].

After image acquisition, image analysis is often carried out offline on a dedicated workstation equipped with the appropriate software suite. This is a semi-automated process that provides good inter- and intra-observer reliability [66]. The major manufacturers have proprietary software and non-standardized routines. With the GE Vivid™ EchoPAC™ software the internal surface of the tissue segment of interest is traced manually in a point and click fashion. Then the external surface tracing is automatically generated to create the area (myocardium, vessel wall) to be analyzed. This can be manually tweaked and adjusted. The software then divides the traced area into six segments and scores the tracking quality; with the possibility of further adjustment. Regions with sub-optimal scores will be rejected by the software and excluded from the analysis. Afterwards, strain curves are generated for each of the segments, and peak and time to peak strain values can be calculated. From these values, the function and mechanics of the segment could be inferred [60, 61].

In terms of validation, longitudinal strain of the left ventricle has been noted to correlate well with left ventricular ejection fraction (LVEF) [67, 68], and it also allowed for early detection of systolic dysfunction in patients with preserved LVEF (by assessing different myocardial regions quantitatively) [69]. Global longitudinal strain was also noted to be a superior outcome predictor when compared to LVEF and wall motion score index [70].

The study by Oishi et al. was the first to demonstrate the feasibility of studying aortic biomechanics using 2D STE in a clinical setting. Oishi et al. were able to demonstrate that speckle-tracking-derived strain parameters of the abdominal aorta were significantly negatively correlated with age, and both conventional M-mode-derived stiffness index and 2D STE-derived stiffness index were associated with age (Figure 17.6) [8]. Interestingly, the 2D STE-derived parameters had stronger correlation with age. Another study aiming to validate that speckle-tracking-derived strain parameters of the aorta was carried out by Kim et al., in which these parameters correlated significantly with pulse-wave velocity, which is considered the gold standard of in vivo stiffness assessment [71].

A follow-up study by Oishi et al. demonstrated the association between the increased 2D STE-derived aortic stiffness, increased left atrial stiffness, and impaired left ventricular relaxation [72]. Another related study revealed the correlation between aortic compliance and left ventricular diastolic function [73]. Both of these studies hint at the interaction between the left heart chambers and aortic biomechanics, or a related underlying disease process. Moreover, the two studies by Teixeira et al. [74] and Leite et al. [75] demonstrated the prognostic potential of 2D STE-derived ascending aorta strain parameters.

More recently, two studies revealed a significant correlation between in vivo stiffness parameters measured using 2D STE and ex vivo measured parameters [76, 77]. And in addition to that, the latest study by Emmott et al. showed an additional significant correlation between 2D STE-derived parameters and histopathology of patients undergoing ascending thoracic aortic aneurysm replacement [77].

Two-dimensional speckle-tracking echocardiography is not without its limitations. Assessment of individuals with non-sinus heart rhythm can be challenging (early aorta biomechanics

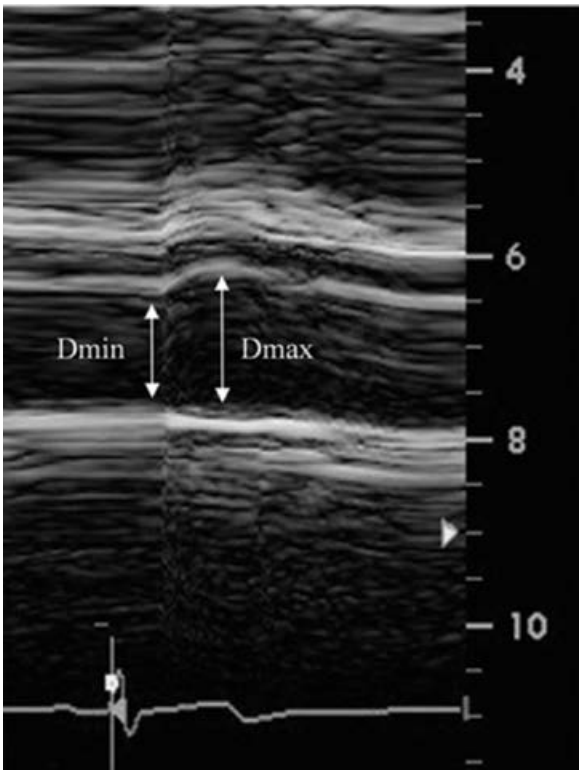

FIGURE 17.6 Assessment of aortic biomechanics of the abdominal aorta using M-mode ultrasonography. D_{min} = minimal aortic diameter. D_{max} = maximal aortic diameter. (Adapted from Oishi et al., *Echocardiography* 2008) [8]

speckle-tracking studies excluded patients with atrial fibrillation [8, 72]). Furthermore, high-quality images including the area of interest wholly (the whole ventricle or vessel) for correct border delineation are necessary for accurate assessment [60]. It is also affected by the frame rate of the image loop, and comparatively poor lateral resolution might cause lateral dropout [53]. Lastly, the measurements depend on the specific make of the ultrasound machine, as they're not interchangeable between manufacturers [60].

17.8 IN VIVO MECHANICAL INDICES

In a clinical context, without access to a tissue biopsy, mechanical assessment is confined to an in situ analysis of the passive vessel deformation in response to the blood pressure waveform of the cardiac cycle. Tensile strength and other yielding properties cannot be measured under these conditions and therefore stiffness, or its approximation, has been used as the surrogate measure of the mechanical properties of the vessel wall. Several stiffness parameters have been developed previously that use one or more of the blood pressure waveform, the systolic (P_S) and diastolic (P_D) pressures, and the vessel geometry by echo-measured deformation:

1. The Stiffness Index (β) [52, 78]: $\beta = \ln(P_S/P_D)/([D_{max} - D_{min}]/D_{min})$, unitless
   Where D_{min} and D_{max} correspond to the minimum and maximum vessel diameters, respectively.

The stiffness index of the aorta has been shown to have a strong positive correlation with a multitude of cardiovascular conditions. It was found to be positively associated with age and as a marker of vascular degeneration [8].

2. Elastic Modulus (E) [52, 78]: $E = (P_S - P_D) \times D_{min} / (D_{max} - D_{min})$, units of force/area

   The elastic modulus is the pressure change required for a theoretic 100% stretching of a material from resting diameter [78, 79].

3. Pulse Wave Velocity (PWV) [52, 78]: $PWV = d_{P1-P2} / \Delta t_{P1-P2}$, units of length/time

   Where d_{P1-P2} is the arterial distance between two measurement points along an arterial branch and Δt_{P1-P2} is the time for the pressure wave to travel between these points. According to the Moens-Korteweg equation, PWV is proportional to $\sqrt{E_Y}$, where E_Y is the Young's modulus of the vessel wall.

   In other words, PWV is the speed of the pulse generated by the ventricular systolic stroke along an arterial segment (based on the propagative model of circulation), or the distance between two points in the travel of the pulse divided by the delay between those two points [78].

   The waveforms of the pulse are typically acquired transcutaneously (using tonometry, mechanotransducers or ultrasound) at two pre-determined points on the body, then the transit time (time delay) is calculated between the two wave feet (foot-to-foot method). Afterwards the distance between the two surface sites of wave acquisition is used in the calculation as a surrogate distance [51]. PWV can be measured over various points in the body, with the carotid-femoral PWV being one of the more commonly used. It stands for the aortic trunk stiffness [78]. And being based on the propagative wave model, stiffer vessels convey a faster PWV [51].

   PWV is considered the gold standard of stiffness assessment [51, 57]. This is because PWV is simple, non-invasive, and reproducible [51], and has been shown as a predictor of clinical outcomes in a plethora of studies [80–90].

4. Cardiac Cycle Moduli (CCPM/CCSM): Units of Force/Area

   Slope of a linear fit through the blood pressure-strain (CCPM) or stress-strain (CCSM) loops. CCPM uses blood pressure and global circumferential strain values obtained from an invasive pressure catheter and the strain imaging of the aortic short axis, respectively.

   CCSM is a correction of the CCPM by the formula $CCSM = CCPM \times D/(2\tau)$, where D is the maximum aortic diameter and τ is the aortic wall thickness. This definition uses a Laplace Law approximation between pressure (P) and circumferential stress (i.e., $\sigma_{CIRC} = P \times D/(2\tau)$).

   In a recent study by Emmott et al. [77], the CCPM and CCSM measured on the ascending aorta at the time of surgery were correlated with the ex vivo stiffness and energy loss measured on the resected aortic tissue. Both CCPM and CCSM were predictive of the ex vivo mechanical properties. However, the CCSM had stronger correlations, likely owing to the effect of tissue thickness on calculating stiffness. Similar to the approach used by Pagani et al. [91] and Lang et al. [92], the CCPM and CCSM are stiffness calculations that account for the full blood pressure and strain profile over a cardiac cycle and not simply a two-point measure like the β stiffness index and peak strain. Furthermore, it was demonstrated that both the CCPM and CCSM were more predictive of ex vivo mechanical indices (higher coefficient of variance, R^2) than both the aortic diameter and the β stiffness index. Since aortic diameter is used as the standard to evaluate whether or not a surgical intervention is necessary, adding biomechanics-based criteria may provide crucial information when identifying at-risk patients who don't meet size criteria.

5. Strain and Strain Rate

   Strain is the deformation of a material in response to applied stress [93]. Interest in these parameters in the field of aortic biomechanics has seen a significant increase in the last 10 years (Table 17.1). This is possibly spurred on by the innovative application of

speckle-tracking imaging to measure vascular biomechanics, which rendered obtaining these parameters accessible and reliable for various vascular segments (e.g. ascending, descending, and abdominal aorta, common carotid arteries).

It has been shown that these parameters have significant correlation with multiple disease states [57], such as the correlation between the common carotid arteries circumferential strain and strain rate with coronary artery disease [94].

Each of these parameters has its advantages and limitations. The advantage of parameters 1–3 is the availability and simplicity of the measured inputs. However, their primary limitation is that there is no accounting for the tissue thickness. As a result, this simplification requires a substitution of pressure, acting normal to the vessel wall, for stresses within the wall.

When full-cycle measurements of blood pressure and strain are obtained for the aorta (e.g. CCPM), they are temporally related to each other by end-diastolic gating using the patient's electrocardiogram. Due to procedural restrictions/conventions, it is not always possible to place the pressure catheter at the site of imaging. In fact, it's common to obtain the blood pressure trace from an invasive catheter in a peripheral artery (e.g., radial artery). As a result of a temporal shift in pressure between central and peripheral arteries, the pressure waveform needs to be corrected to temporally align with the change in aortic strain. In addition, due to wave reflection there is an increase in systolic pressure in peripheral arteries compared to the aorta. However, this difference becomes attenuated with increasing age [52].

For the parameters that rely on diameter changes (stiffness index, elastic modulus, CCPM, CCSM, strain and strain rate), the diameter being studied is assumed to be uniform around the circumference of that vessel, which is also a simplification of the non-uniform geometry of that vessel. It is worth noting that obtaining strain and strain rate curves, CCPM, and CCSM is relatively time consuming and requires specialized software for image post-processing [57, 77].

Traditionally, PWV has only been used over longer arterial segments, as its accuracy deteriorates over shorter segments [52]. PWV also requires high-fidelity instruments for accurate, precise readings of the waveforms [51]. Other caveats to consider are that the femoral waveform is difficult to record in obese individuals, and in the presence of peripheral vascular disease or tortuous vessels [79, 95]. Also, the presence of central obesity or a large chest size could complicate distance measurement [95]. Additionally, investigators studying central inaccessible vessels might be forced to compromise by using the nearest superficial artery to measure a surrogate waveform [52].

All the above parameters do not account for the local anatomy (e.g., trachea, spine) supporting certain segments of the aortic wall. These global parameters also do not account for heterogeneity within the aortic wall. They provide obtainable estimates of in vivo biomechanical function, but cannot identify local tissue failure that occurs with dissection and rupture.

17.9 FUTURE CONSIDERATIONS

It is clear that measurements of aortic biomechanics using non-invasive imaging modalities will prove to be a valuable tool to aid clinical decision making. However, significant challenges still remain to be tackled. Heterogeneity of the data remains an issue; different investigators use different protocols to collect data using different scales and units. This makes comparing data complicated and difficult, which limits the progression of the field. Multiple bodies are attempting to tackle this issue by releasing consensus documents to unify the language, methodology, and units used [51, 93].

Currently, aortic aneurysm size is the main criterion used in guidelines that aid clinicians in deciding when to intervene to prevent dissection or rupture. But as discussed in this chapter, using size alone as a guide would fail to prevent 60% of aortic dissections. Hence the need for more robust parameters to inform intervention guidelines in addition to aneurysm size.

A fundamental requirement to advance biomechanical aortic wall studies from research discourse into clinical application lies in linking population-based ex vivo mechanics to clinical

imaging modalities to distinguish between stable and unstable aortic disease. With this in mind, we believe that image-based in vivo strain assessment, when well validated with histopathologic and ex vivo mechanical data, will help in stratification of patients for thoracic aortic intervention [38].

References

1. L. A. Pape *et al.,* "Aortic diameter >or = 5.5 cm is not a good predictor of type A aortic dissection: observations from the International Registry of Acute Aortic Dissection (IRAD)," *Circulation*, vol. 116, no. 10, pp. 1120–1127, Sep 4 2007.
2. J. F. Sabik, B. W. Lytle, E. H. Blackstone, P. M. McCarthy, F. D. Loop, and D. M. Cosgrove, "Long-term effectiveness of operations for ascending aortic dissections," *J Thorac Cardiovasc Surg*, vol. 119, no. 5, pp. 946–962, May 2000.
3. B. Chiappini *et al.,* "Early and late outcomes of acute type A aortic dissection: analysis of risk factors in 487 consecutive patients," *Eur Heart J*, vol. 26, no. 2, pp. 180–186, Jan 2005.
4. S. Trimarchi *et al.,* "Contemporary results of surgery in acute type A aortic dissection: The International Registry of Acute Aortic Dissection experience," *J Thorac Cardiovasc Surg*, vol. 129, no. 1, pp. 112–122, Jan 2005.
5. J. B. Williams *et al.,* "Contemporary results for proximal aortic replacement in North America," *J Am Coll Cardiol*, vol. 60, no. 13, pp. 1156–1162, Sep 25 2012.
6. K. J. Zehr *et al.,* "Surgery for aneurysms of the aortic root: a 30-year experience," *Circulation*, vol. 110, no. 11, pp. 1364–1371, Sep 14 2004.
7. R. R. Davies *et al.,* "Yearly rupture or dissection rates for thoracic aortic aneurysms: simple prediction based on size," *Ann Thorac Surg*, vol. 73, no. 1, pp. 17–27; discussion 27–28, Jan 2002.
8. Y. Oishi, Y. Mizuguchi, H. Miyoshi, A. Iuchi, N. Nagase, and T. Oki, "A novel approach to assess aortic stiffness related to changes in aging using a two-dimensional strain imaging," *Echocardiography*, vol. 25, no. 9, pp. 941–945, Oct 2008.
9. G. A. Kuzmik, A. X. Sang, and J. A. Elefteriades, "Natural history of thoracic aortic aneurysms," *J Vasc Surg*, vol. 56, no. 2, pp. 565–571, Aug 2012.
10. L. F. Hiratzka *et al.,* "2010 ACCF/AHA/AATS/ACR/ASA/SCA/SCAI/SIR/STS/SVM guidelines for the diagnosis and management of patients with Thoracic Aortic Disease: a report of the American College of Cardiology Foundation/American Heart Association Task Force on Practice Guidelines, American Association for Thoracic Surgery, American College of Radiology, American Stroke Association, Society of Cardiovascular Anesthesiologists, Society for Cardiovascular Angiography and Interventions, Society of Interventional Radiology, Society of Thoracic Surgeons, and Society for Vascular Medicine," *Circulation*, vol. 121, no. 13, pp. e266–e269, Apr 6 2010.
11. M. A. Coady *et al.,* "What is the appropriate size criterion for resection of thoracic aortic aneurysms?," *J Thorac Cardiovasc Surg*, vol. 113, no. 3, pp. 476–491; discussion 489–491, Mar 1997.
12. G. Koullias, R. Modak, M. Tranquilli, D. P. Korkolis, P. Barash, and J. A. Elefteriades, "Mechanical deterioration underlies malignant behavior of aneurysmal human ascending aorta," *J Thorac Cardiovasc Surg*, vol. 130, no. 3, pp. 677–683, Sep 2005.
13. J. D. Humphrey, "Possible mechanical roles of glycosaminoglycans in thoracic aortic dissection and associations with dysregulated transforming growth factor-beta," *J Vasc Res*, vol. 50, no. 1, pp. 1–10, 2013.
14. G. A. Holzapfel, "Collagen in Arterial Walls: Biomechanical Aspects," in *Collagen: structure and mechanics*, P. Fratzl, Ed. New York: Springer, 2008, pp. 287–288.
15. C. A. Schulze-Bauer, P. Regitnig, and G. A. Holzapfel, "Mechanics of the human femoral adventitia including the high-pressure response," *Am J Physiol Heart Circ Physiol*, vol. 282, no. 6, pp. H2427–H2440, Jun 2002.
16. J. M. Clark and S. Glagov, "Structural integration of the arterial wall. I. Relationships and attachments of medial smooth muscle cells in normally distended and hyperdistended aortas," *Lab Invest*, vol. 40, no. 5, pp. 587–602, May 1979.
17. J. A. G. Rhodin, "Architecture of the vessel wall," in *Handbook of Physiology, The Cardiovascular System*, vol. 2, D. F. Bohr, Somlyo, A. D., and Sparks, H. V., Ed. Bethesda, Maryland: American Physiologial Society, 1980, pp. 1–31.
18. P. Fratzl, "Collagen: Structure and Mechanics, an Introduction," in *Collagen: Structure and Mechanics*, P. Fratzl, Ed. New York: Springer, 2008, pp. 1–2.

19. H. Weisbecker, C. Viertler, D. M. Pierce, and G. A. Holzapfel, "The role of elastin and collagen in the softening behavior of the human thoracic aortic media," *J Biomech*, vol. 46, no. 11, pp. 1859–1865, Jul 26 2013.
20. J. Gosline, M. Lillie, E. Carrington, P. Guerette, C. Ortlepp, and K. Savage, "Elastic proteins: biological roles and mechanical properties," *Philos Trans R Soc Lond B Biol Sci*, vol. 357, no. 1418, pp. 121–132, Feb 28 2002.
21. M. R. Roach and A. C. Burton, "The reason for the shape of the distensibility curves of arteries," *Can J Biochem Physiol*, vol. 35, no. 8, pp. 681–690, Aug 1957.
22. A. Tsamis, J. T. Krawiec, and D. A. Vorp, "Elastin and collagen fibre microstructure of the human aorta in ageing and disease: a review," *J R Soc Interface*, vol. 10, no. 83, p. 20121004, Jun 6 2013.
23. M. Sans and A. Moragas, "Mathematical morphologic analysis of the aortic medial structure. Biomechanical implications," *Anal Quant Cytol Histol*, vol. 15, no. 2, pp. 93–100, Apr 1993.
24. S. R. Greenberg, "The association of medial collagenous tissue with atheroma formation in the aging human aorta as revealed by a special technique," *Histol Histopathol*, vol. 1, no. 4, pp. 323–326, Oct 1986.
25. T. J. Schlatmann and A. E. Becker, "Histologic changes in the normal aging aorta: implications for dissecting aortic aneurysm," *Am J Cardiol*, vol. 39, no. 1, pp. 13–20, Jan 1977.
26. M. Faber and G. Moller-Hou, "The human aorta. V. Collagen and elastin in the normal and hypertensive aorta," *Acta Pathol Microbiol Scand*, vol. 31, no. 3, pp. 377–382, 1952.
27. L. B. Sandberg, N. T. Soskel, and J. G. Leslie, "Elastin structure, biosynthesis, and relation to disease states," *N Engl J Med*, vol. 304, no. 10, pp. 566–579, Mar 5 1981.
28. S. Bertelsen, in *Atherosclerosis and its origin*, M. Sandler and G. F. Bourne, Eds. New York: Academic Press, 1963, pp. 119–165.
29. Y. Hosoda, K. Kawano, F. Yamasawa, T. Ishii, T. Shibata, and S. Inayama, "Age-dependent changes of collagen and elastin content in human aorta and pulmonary artery," *Angiology*, vol. 35, no. 10, pp. 615–621, Oct 1984.
30. L. Andreotti *et al.,* "Aortic connective tissue in ageing–a biochemical study," *Angiology*, vol. 36, no. 12, pp. 872–879, Dec 1985.
31. M. R. Alexander and G. K. Owens, "Epigenetic control of smooth muscle cell differentiation and phenotypic switching in vascular development and disease," *Annu Rev Physiol*, vol. 74, pp. 13–40, 2012.
32. P. Lacolley, V. Regnault, A. Nicoletti, Z. Li, and J. B. Michel, "The vascular smooth muscle cell in arterial pathology: a cell that can take on multiple roles," *Cardiovasc Res*, vol. 95, no. 2, pp. 194–204, Jul 15 2012.
33. E. W. Raines and R. Ross, "Smooth muscle cells and the pathogenesis of the lesions of atherosclerosis," *Br Heart J*, vol. 69, no. 1 Suppl, pp. S30–S37, Jan 1993.
34. I. El-Hamamsy and M. H. Yacoub, "Cellular and molecular mechanisms of thoracic aortic aneurysms," *Nat Rev Cardiol*, vol. 6, no. 12, pp. 771–786, Dec 2009.
35. T. Toda, N. Tsuda, I. Nishimori, D. E. Leszczynski, and F. A. Kummerow, "Morphometrical analysis of the aging process in human arteries and aorta," *Acta Anat (Basel)*, vol. 106, no. 1, pp. 35–44, 1980.
36. V. Lesauskaite *et al.,* "Smooth muscle cells of the media in the dilatative pathology of ascending thoracic aorta: morphology, immunoreactivity for osteopontin, matrix metalloproteinases, and their inhibitors," *Hum Pathol*, vol. 32, no. 9, pp. 1003–1011, Sep 2001.
37. G. Ailawadi *et al.,* "Smooth muscle phenotypic modulation is an early event in aortic aneurysms," *J Thorac Cardiovasc Surg*, vol. 138, no. 6, pp. 1392–1399, Dec 2009.
38. A. Emmott *et al.,* "Biomechanics of the Ascending Thoracic Aorta: A Clinical Perspective on Engineering Data," *Can J Cardiol*, vol. 32, no. 1, pp. 35–47, Jan 2016.
39. G. G. Belz, "Elastic properties and Windkessel function of the human aorta," *Cardiovasc Drugs Ther*, vol. 9, no. 1, pp. 73–83, Feb 1995.
40. J. Chung *et al.,* "Energy loss, a novel biomechanical parameter, correlates with aortic aneurysm size and histopathologic findings," *J Thorac Cardiovasc Surg*, vol. 148, no. 3, pp. 1082–1088; discussion 1088–1089, Sep 2014.
41. H. Ince and C. A. Nienaber, "Etiology, pathogenesis and management of thoracic aortic aneurysm," *Nat Clin Pract Cardiovasc Med*, vol. 4, no. 8, pp. 418–427, Aug 2007.
42. I. Sinha *et al.,* "A biologic basis for asymmetric growth in descending thoracic aortic aneurysms: a role for matrix metalloproteinase 9 and 2," *J Vasc Surg*, vol. 43, no. 2, pp. 342–348, Feb 2006.
43. D. A. Vorp, B. J. Schiro, M. P. Ehrlich, T. S. Juvonen, M. A. Ergin, and B. P. Griffith, "Effect of aneurysm on the tensile strength and biomechanical behavior of the ascending thoracic aorta," *Ann Thorac Surg*, vol. 75, no. 4, pp. 1210–1214, Apr 2003.

44. N. Choudhury *et al.,* "Local mechanical and structural properties of healthy and diseased human ascending aorta tissue," *Cardiovasc Pathol*, vol. 18, no. 2, pp. 83–91, Mar-Apr 2009.
45. J. Chung, K. Lachapelle, R. Cartier, R. Mongrain, and R. L. Leask, "Loss of mechanical directional dependency of the ascending aorta with severe medial degeneration," *Cardiovasc Pathol*, vol. 26, pp. 45–50, Jan - Feb 2017.
46. N. Shahmansouri *et al.,* "Evaluating ascending aortic aneurysm tissue toughness: Dependence on collagen and elastin contents," *J Mech Behav Biomed Mater*, vol. 64, pp. 262–271, Dec 2016.
47. J. E. Pichamuthu *et al.,* "Differential tensile strength and collagen composition in ascending aortic aneurysms by aortic valve phenotype," *Ann Thorac Surg*, vol. 96, no. 6, pp. 2147–2154, Dec 2013.
48. T. H. Marwick, A. N. DeMaria, D. G. Blanchard, and W. A. Zoghbi, "Chapter 15: Echocardiography," in *Hurst's The Heart*, V. Fuster, R. A. Harrington, J. Narula, and Z. J. Eapen, Eds. 14 ed.: McGraw-Hill Education, 2017.
49. A. Ng and J. Swanevelder, "Resolution in ultrasound imaging," *Continuing Education in Anaesthesia Critical Care & Pain*, vol. 11, no. 5, pp. 186–192, 2011.
50. J. E. Aldrich, "Basic physics of ultrasound imaging," *Critical Care Medicine*, vol. 35, no. 5, pp. S131–S137, 2007.
51. S. Laurent *et al.,* "Expert consensus document on arterial stiffness: methodological issues and clinical applications," *Eur Heart J*, vol. 27, no. 21, pp. 2588–2605, Nov 2006.
52. I. S. Mackenzie, I. B. Wilkinson, and J. R. Cockcroft, "Assessment of arterial stiffness in clinical practice," *QJM*, vol. 95, no. 2, pp. 67–74, Feb 2002.
53. H. Geyer *et al.,* "Assessment of myocardial mechanics using speckle tracking echocardiography: fundamentals and clinical applications," *J Am Soc Echocardiogr*, vol. 23, no. 4, pp. 351–369; quiz 453–455, Apr 2010.
54. S. Pasta *et al.,* "In Vivo Strain Analysis of Dilated Ascending Thoracic Aorta by ECG-Gated CT Angiographic Imaging," *Ann Biomed Eng*, vol. 45, no. 12, pp. 2911–2920, Dec 2017.
55. J. K. Min *et al.,* "Clinical features of complications from transesophageal echocardiography: a single-center case series of 10,000 consecutive examinations," *J Am Soc Echocardiogr*, vol. 18, no. 9, pp. 925–929, Sep 2005.
56. W. G. Daniel *et al.,* "Safety of transesophageal echocardiography. A multicenter survey of 10,419 examinations," *Circulation*, vol. 83, no. 3, pp. 817–821, Mar 1991.
57. R. Teixeira, M. J. Vieira, A. Goncalves, N. Cardim, and L. Goncalves, "Ultrasonographic vascular mechanics to assess arterial stiffness: a review," *Eur Heart J Cardiovasc Imaging*, vol. 17, no. 3, pp. 233–246, Mar 2016.
58. M. Leitman *et al.,* "Two-dimensional strain-a novel software for real-time quantitative echocardiographic assessment of myocardial function," (in eng), *J Am Soc Echocardiogr*, vol. 17, no. 10, pp. 1021–1029, Oct 2004.
59. J. U. Voigt *et al.,* "Definitions for a common standard for 2D speckle tracking echocardiography: consensus document of the EACVI/ASE/Industry Task Force to standardize deformation imaging," (in eng), *J Am Soc Echocardiogr*, vol. 28, no. 2, pp. 183–193, Feb 2015.
60. S. Mondillo *et al.,* "Speckle-tracking echocardiography: a new technique for assessing myocardial function," *J Ultrasound Med*, vol. 30, no. 1, pp. 71–83, Jan 2011.
61. G. Perk, P. A. Tunick, and I. Kronzon, "Non-Doppler two-dimensional strain imaging by echocardiography–from technical considerations to clinical applications," *J Am Soc Echocardiogr*, vol. 20, no. 3, pp. 234–243, Mar 2007.
62. M. Dandel, H. Lehmkuhl, C. Knosalla, N. Suramelashvili, and R. Hetzer, "Strain and strain rate imaging by echocardiography - basic concepts and clinical applicability," *Curr Cardiol Rev*, vol. 5, no. 2, pp. 133–148, May 2009.
63. H. Blessberger and T. Binder, "NON-invasive imaging: Two dimensional speckle tracking echocardiography: basic principles," *Heart*, vol. 96, no. 9, pp. 716–722, May 2010.
64. M. B. Buchalter *et al.,* "Noninvasive quantification of left ventricular rotational deformation in normal humans using magnetic resonance imaging myocardial tagging," *Circulation*, vol. 81, no. 4, pp. 1236–1244, Apr 1990.
65. S. M. Shaw, D. J. Fox, and S. G. Williams, "The development of left ventricular torsion and its clinical relevance," *Int J Cardiol*, vol. 130, no. 3, pp. 319–325, Nov 28 2008.
66. B. M. van Dalen *et al.,* "Feasibility and reproducibility of left ventricular rotation parameters measured by speckle tracking echocardiography," *Eur J Echocardiogr*, vol. 10, no. 5, pp. 669–676, Jul 2009.
67. J. Brown, C. Jenkins, and T. H. Marwick, "Use of myocardial strain to assess global left ventricular function: a comparison with cardiac magnetic resonance and 3-dimensional echocardiography," *Am Heart J*, vol. 157, no. 1, pp. 102 e1–e5, Jan 2009.

68. J. O. Choi *et al.,* "Effect of preload on left ventricular longitudinal strain by 2D speckle tracking," *Echocardiography*, vol. 25, no. 8, pp. 873–879, Sep 2008.
69. T. Edvardsen, T. Helle-Valle, and O. A. Smiseth, "Systolic dysfunction in heart failure with normal ejection fraction: speckle-tracking echocardiography," *Prog Cardiovasc Dis*, vol. 49, no. 3, pp. 207–214, Nov-Dec 2006.
70. T. Stanton, R. Leano, and T. H. Marwick, "Prediction of all-cause mortality from global longitudinal speckle strain: comparison with ejection fraction and wall motion scoring," *Circ Cardiovasc Imaging*, vol. 2, no. 5, pp. 356–364, Sep 2009.
71. K. H. Kim *et al.,* "Usefulness of aortic strain analysis by velocity vector imaging as a new echocardiographic measure of arterial stiffness," *J Am Soc Echocardiogr*, vol. 22, no. 12, pp. 1382–1388, Dec 2009.
72. Y. Oishi, H. Miyoshi, A. Iuchi, N. Nagase, N. Ara, and T. Oki, "Negative impact of cardiovascular risk factors on left atrial and left ventricular function related to aortic stiffness–new application of 2-dimensional speckle-tracking echocardiography," *Circ J*, vol. 77, no. 6, pp. 1490–1498, 2013.
73. A. J. Gregory and G. Dobson, "Proximal aortic compliance and diastolic function assessed by speckle tracking imaging," *Can J Anaesth*, vol. 60, no. 7, pp. 667–674, Jul 2013.
74. R. Teixeira *et al.,* "Circumferential vascular strain rate to estimate vascular load in aortic stenosis: a speckle tracking echocardiography study," *Int J Cardiovasc Imaging*, vol. 31, no. 4, pp. 681–689, Apr 2015.
75. L. Leite *et al.,* "Aortic Valve Disease and Vascular Mechanics: Two-Dimensional Speckle Tracking Echocardiographic Analysis," *Echocardiography*, vol. 33, no. 8, pp. 1121–1130, Aug 2016.
76. M. Alreshidan *et al.,* "Obtaining the biomechanical behavior of ascending aortic aneurysm via the use of novel speckle tracking echocardiography," *J Thorac Cardiovasc Surg*, vol. 153, no. 4, pp. 781–788, Apr 2017.
77. A. Emmott, H. Alzahrani, M. Alreishidan, J. Therrien, R. L. Leask, and K. Lachapelle, "Transesophageal echocardiographic strain imaging predicts aortic biomechanics: Beyond diameter," *The Journal of Thoracic and Cardiovascular Surgery*, 2018.
78. M. F. O'Rourke, J. A. Staessen, C. Vlachopoulos, D. Duprez, and G. E. Plante, "Clinical applications of arterial stiffness; definitions and reference values," *Am J Hypertens*, vol. 15, no. 5, pp. 426–444, May 2002.
79. J. J. Oliver and D. J. Webb, "Noninvasive assessment of arterial stiffness and risk of atherosclerotic events," *Arterioscler Thromb Vasc Biol*, vol. 23, no. 4, pp. 554–566, Apr 1 2003.
80. J. Blacher, A. P. Guerin, B. Pannier, S. J. Marchais, M. E. Safar, and G. M. London, "Impact of aortic stiffness on survival in end-stage renal disease," *Circulation*, vol. 99, no. 18, pp. 2434–2439, May 11 1999.
81. P. Boutouyrie *et al.,* "Aortic stiffness is an independent predictor of primary coronary events in hypertensive patients: a longitudinal study," *Hypertension*, vol. 39, no. 1, pp. 10–15, Jan 2002.
82. K. Cruickshank, L. Riste, S. G. Anderson, J. S. Wright, G. Dunn, and R. G. Gosling, "Aortic pulse-wave velocity and its relationship to mortality in diabetes and glucose intolerance: an integrated index of vascular function?," *Circulation*, vol. 106, no. 16, pp. 2085–2090, Oct 15 2002.
83. S. Laurent *et al.,* "Aortic stiffness is an independent predictor of all-cause and cardiovascular mortality in hypertensive patients," *Hypertension*, vol. 37, no. 5, pp. 1236–1241, May 2001.
84. S. Laurent *et al.,* "Aortic stiffness is an independent predictor of fatal stroke in essential hypertension," *Stroke*, vol. 34, no. 5, pp. 1203–1206, May 2003.
85. F. U. Mattace-Raso *et al.,* "Arterial stiffness and risk of coronary heart disease and stroke: the Rotterdam Study," *Circulation*, vol. 113, no. 5, pp. 657–663, Feb 7 2006.
86. S. Meaume, A. Benetos, O. F. Henry, A. Rudnichi, and M. E. Safar, "Aortic pulse wave velocity predicts cardiovascular mortality in subjects >70 years of age," *Arterioscler Thromb Vasc Biol*, vol. 21, no. 12, pp. 2046–2050, Dec 2001.
87. T. Shoji *et al.,* "Diabetes mellitus, aortic stiffness, and cardiovascular mortality in end-stage renal disease," *J Am Soc Nephrol*, vol. 12, no. 10, pp. 2117–2124, Oct 2001.
88. T. Shokawa *et al.,* "Pulse wave velocity predicts cardiovascular mortality: findings from the Hawaii-Los Angeles-Hiroshima study," *Circ J*, vol. 69, no. 3, pp. 259–264, Mar 2005.
89. K. Sutton-Tyrrell *et al.,* "Elevated aortic pulse wave velocity, a marker of arterial stiffness, predicts cardiovascular events in well-functioning older adults," *Circulation*, vol. 111, no. 25, pp. 3384–3390, Jun 28 2005.
90. T. Willum-Hansen *et al.,* "Prognostic value of aortic pulse wave velocity as index of arterial stiffness in the general population," *Circulation*, vol. 113, no. 5, pp. 664–670, Feb 7 2006.

91. M. Pagani, I. Mirsky, H. Baig, W. T. Manders, P. Kerkhof, and S. F. Vatner, "Effects of age on aortic pressure-diameter and elastic stiffness-stress relationships in unanesthetized sheep," *Circ Res*, vol. 44, no. 3, pp. 420–429, Mar 1979.
92. R. M. Lang, B. P. Cholley, C. Korcarz, R. H. Marcus, and S. G. Shroff, "Measurement of regional elastic properties of the human aorta. A new application of transesophageal echocardiography with automated border detection and calibrated subclavian pulse tracings," *Circulation*, vol. 90, no. 4, pp. 1875–1882, Oct 1994.
93. R. R. Townsend *et al.,* "Recommendations for Improving and Standardizing Vascular Research on Arterial Stiffness: A Scientific Statement From the American Heart Association," *Hypertension*, vol. 66, no. 3, pp. 698–722, Sep 2015.
94. S. A. Kim *et al.,* "The relationship between mechanical properties of carotid artery and coronary artery disease," *Eur Heart J Cardiovasc Imaging*, vol. 13, no. 7, pp. 568–573, Jul 2012.
95. L. M. Van Bortel *et al.,* "Clinical applications of arterial stiffness, Task Force III: recommendations for user procedures," *Am J Hypertens*, vol. 15, no. 5, pp. 445–452, May 2002.
96. J. Petrini *et al.,* "The feasibility of velocity vector imaging by transesophageal echocardiography for assessment of elastic properties of the descending aorta in aortic valve disease," *J Am Soc Echocardiogr*, vol. 23, no. 9, pp. 985–992, Sep 2010.
97. Y. Oishi, H. Miyoshi, Y. Mizuguchi, A. Iuchi, N. Nagase, and T. Oki, "Aortic stiffness is strikingly increased with age >/= 50 years in clinically normal individuals and preclinical patients with cardiovascular risk factors: assessment by the new technique of 2D strain echocardiography," *J Cardiol*, vol. 57, no. 3, pp. 354–359, May 2011.
98. Y. Oishi, H. Miyoshi, A. Iuchi, N. Nagase, N. Ara, and T. Oki, "Vascular aging of common carotid artery and abdominal aorta in clinically normal individuals and preclinical patients with cardiovascular risk factors: diagnostic value of two-dimensional speckle-tracking echocardiography," *Heart Vessels*, vol. 28, no. 2, pp. 222–228, Mar 2013.
99. R. Teixeira *et al.,* "Circumferential ascending aortic strain and aortic stenosis," *Eur Heart J Cardiovasc Imaging*, vol. 14, no. 7, pp. 631–641, Jul 2013.
100. J. Petrini *et al.,* "Elastic properties of the descending aorta in patients with a bicuspid or tricuspid aortic valve and aortic valvular disease," *J Am Soc Echocardiogr*, vol. 27, no. 4, pp. 393–404, Apr 2014.
101. L. Longobardo *et al.,* "Impairment of elastic properties of the aorta in bicuspid aortic valve: relationship between biomolecular and aortic strain patterns," *Eur Heart J Cardiovasc Imaging*, Sep 23 2017.
102. R. Teixeira *et al.,* "Descending aortic mechanics and atrial fibrillation: a two-dimensional speckle tracking transesophageal echocardiography study," *Int J Cardiovasc Imaging*, vol. 33, no. 4, pp. 509–519, Apr 2017.
103. M. Bieseviciene, J. J. Vaskelyte, V. Mizariene, R. Karaliute, V. Lesauskaite, and R. Verseckaite, "Two-dimensional speckle-tracking echocardiography for evaluation of dilative ascending aorta biomechanics," *BMC Cardiovasc Disord*, vol. 17, no. 1, p. 27, Jan 13 2017.

18 Deep Convolutional Networks for Automated Volumetric Cardiovascular Image Segmentation: From a Design Perspective

Xin Yang, Lequan Yu, Qi Dou, Jing Qin, Pheng-Ann Heng
Chinese University of Hong Kong and Hong Kong Polytechnic University

CONTENTS

18.1 INTRODUCTION

Automatic segmentation of the whole heart from cardiovascular volumes, such as CT and MR, is an indispensable technique in interpreting the morphological and pathological information of the heart and therefore in facilitating plenty of associated applications [1], [2], such as the visualization of 3D cardiac anatomy, finite element method (FEM) based functionality simulation, quantitative analysis of blood ejection fraction, atrial fibrillation ablation [3], and cardiovascular surgical planning for congenital heart disease. However, manually delineating the boundary for the whole volume data is expert-dependent, time-consuming, and with low reproducibility [4].

Developing automatic cardiac image segmentation methods presents to be a challenging task [5], not only because of the large variations in heart scale, shape, and pose across different subjects, the varying spatial relationship between substructures, but also the boundary ambiguity caused by low contrast of anatomy against surroundings and the deficient boundary caused by shadow and noise. Depending on rough boundary and gradient information in image, early automatic segmentation solutions resort to active contours [6], [7] and level sets promoted variants [8] to fit the boundary. To reduce unreasonable boundary prediction, statistical shape models [9]–[11] and appearance models [12] incorporating explicit 2D or 3D shape and texture prior knowledge of heart and vessels become the frequent choices for cardiac image segmentation. Conveying appearance and shape constraints, atlas based segmentation is another popular stream, which propagates the class labels of annotated cardiac atlas images to unseen cases utilizing image registration and label fusion techniques [13], [14]. However, the carefully handcrafted local descriptors for boundary description and sensitivities to initializations set performance bottlenecks on aforementioned attempts. Machine learning based segmentation methods rapidly emerge as viable alternatives in the field. For quantitative functional analysis of the heart, Zheng et al. explores marginal space learning to localize key anatomical landmarks, which consequently guides a 3D shape model to delineate the boundary of multiple chambers [15]. Based on learned compact features, [16] proposes to establish a direct regression relationship between image appearance and four-chamber volume segmentation.

Recently, the resurgance of deep neural networks (DNNs) profoundly promotes the image segmentation performance over traditional machine learning based methods. Interleaving convolution layer, pooling layer, and nonlinearity layer in a bionic connection fashion, DNNs discard traditional handcrafted features and seamlessly learn the hierarchical features of an image with the training of the classifier. As popular variants of DNNs for image segmentation, convolutional neural networks (CNNs) [17], especially the fully convolutional networks (FCNs) [18], are remarkable for left ventricle (LV) and right ventricle (RV) image segmentation [19], [20]. We refer readers to [21] for a comprehensive review of deep learning based medical image analysis. Whereas, as shown in Figure 18.1, general designs of deep neural networks will be degraded when we come to the task of whole heart segmentation and the more complicated multiple substructure segmentation. In this chapter, we will introduce our recent

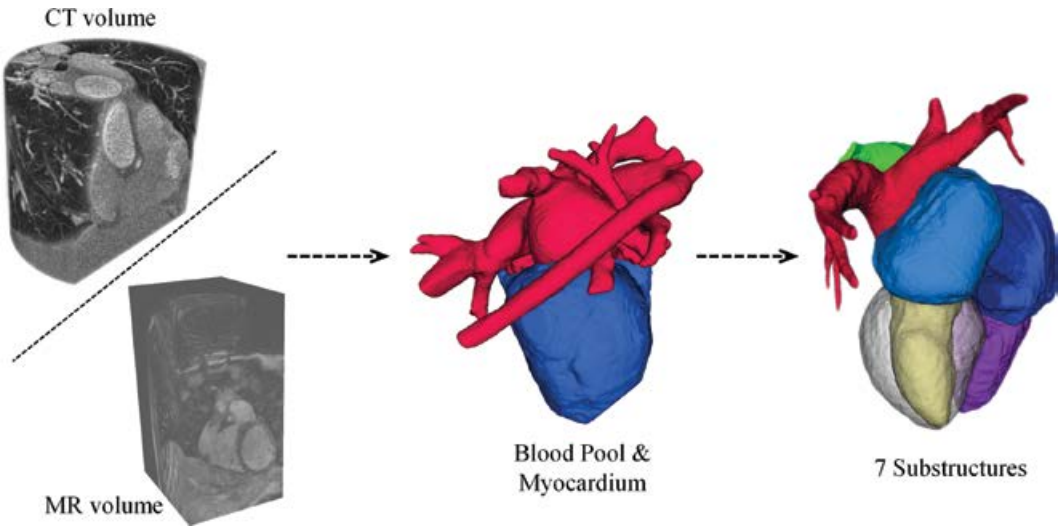

FIGURE 18.1 From left to right: cardiovascular volumetric scanning, including MR and CT, segmentation of blood pool and myocardium, segmentation of seven substructures of the heart.

efforts in modifying the design of DNNs, especially FCNs, for the whole heart segmentation. We concentrate on five problems that prove to be closely related to the network performance.

- **3D Convolution.** How to digest the volumetric input can fundamentally affect the segmentation performance. With our work, we prove that DNNs can benefit more from the spatial information that is inherently contained in the volume by upgrading all the 2D operators in DNNs with the more intuitive 3D format. However, since 3D DNNs have orders of magnitude parameters than the 2D version, 3D DNNs are potentially suffering from low training efficacy and low computation efficiency. We will introduce associated strategies to further solve these problems. (Refer to Sections II and III.)
- **Stratified Deep Supervision.** The learning process of DNNs depends on the gradient based update. However, gradient vanishing or explosion often corrupts the learning. This problem becomes more severe in 3D DNNs where more parameters need to be tuned. Enhancing the gradient flow and exposing shallow layers to the composite supervision of multiple loss signals from different semantic levels, denoted as deep supervision, is adopted in our work. Deep supervision mechanism is straightforward and proves to be effective in greatly promoting the training procedure. (Refer to Section II.)
- **Modified Layout.** Classic DNN architectures are originally designed with plain and straight layer connections to tackle classification or segmentation problems for images with plausible visual quality, such as natural and handwritten images. We need to modify these designs to fit the need in cardiovascular volumes. In Section III, we will introduce a multi-scale, fractal connection fashion that is suitable for branchy and details-required segmentation, such as the great vessel and touching boundary. We further adopt a dense connection scheme to reuse feature maps in previous layers and blend information from multi-scales, and therefore alleviate the heavy computation burden in 3D DNNs.
- **Transfer Learning for 3D DNNs.** Proper initialization and training data in large scale are critical for the training of DNNs. Transfer learning, which transfers the generic knowledge from well-trained models to task-specific DNNs, proves to be a valuable strategy in simultaneously combating the improper initialization and the absence of abundant training data. However, the prevailing well-trained models are designed for 2D applications and thus

cannot be used for 3D application. In Section IV-D, we will introduce the details of how to transfer the spatial-temporal knowledge from the model trained on videos to initialize our 3D DNNs for volumetric segmentation.

- **Class-balanced Loss Function.** Training DNNs is mainly realized by minimizing the pre-defined loss function. Thus, the inherent properties, including preference, of loss function can potentially affect the training. We find that this impact will be magnified in simultaneously segmenting seven substructures where obvious class imbalance in topology and volume size is inevitable. In Section IV-E, to leverage the strengths and suppress the bias of different loss functions, we propose a hybrid loss function to address the class imbalance and generate segmentation results, which preserves abundant branchy details while correctly differentiating the substructures in a compact format.

Figure 18.1 defines the tasks covered by this chapter. Our modified designs are firstly dedicated to the whole heart segmentation tasks across different modalities, including CT and MR. The superiority of our proposed designs are not only verified in segmenting the blood pool and myocardium of heart, but also on the more challenging task as simultaneously partitioning the whole heart into seven fine-grained substructures. We will first elaborate the details about 3D convolution and stratified deep supervision in Section II with the improvement on whole heart segmentation in MR scannings. In Section III, fractal and dense connection designs are adopted to promote the performance and efficiency of DNNs. Transfer learning for 3D DNNs and class-balanced hybrid loss function are proposed and verified for multiple substructures segmentation in Section IV-E for both CT and MR modalities. To contribute to the field, all the implementations and models are online and available with the link in each section.

18.2 VOLUMETRIC FASHION AND DEEP SUPERVISION

In this section, we will first go through the design of 3D operator based convolutional network. Then, we will further introduce the stratified deep supervision mechanism to combat the potential gradient vanishing problem.

18.2.1 3D Convolutional Network

Considering that extracting representations across three-dimensional anatomical context is vitally important for volumetric medical image segmentation, we first implement a 3D CNN. Compared with its 2D counterparts, the 3D CNN is capable of encoding representations from volumetric receptive fields, and therefore extracting more discriminative features via richer 3D spatial information. The main components of the 3D CNN are the 3D convolutional layers and 3D sub-sampling (i.e., max-pooling) layers, which are successively stacked as a hierarchical architecture.

To generate a new feature volume in a convolutional layer, we establish a set of 3D kernels sweeping over the inputs, sum up the activations from these kernels, add a bias term, and finally apply a non-linear activation function. The neurons have sparse interactions, and the kernel weights are spatially shared, which can greatly reduce the number of parameters and hence alleviate the computational workload of the model. 3D kernels are learned via the stochastic gradient descent in a data-driven manner, which is the key advancement of convolutional networks compared with traditional pre-defining transformations of hand-crafted features.

In a sub-sampling layer, the output responses from a convolutional layer are further modified by computing the summary statistic of nearby neurons. In our 3D max-pooling function, the maximum response within a small cubic neighborhood is selected out and proceeded to subsequent computations. After the pooling operation, the resolution of feature volumes are reduced corresponding to the pooling kernel size. Theoretically, the pooling contributes to make the learned features become invariant to local translations in 3D space, which is a very useful characteristic for image processing [22].

18.2.2 3D End-to-End Learning for Volumetric Segmentation

We cast the fully connected layer at the end of CNN into convolutional layer by reorganizing the parameter weight matrix into high-dimensional convolution kernels [18]. In this case, the entire network forms a fully convolutional network (FCN), where all layers are either convolutional or pooling, and both have no restriction on fixed-sized input. In other words, the network is able to input volumetric images with arbitrary sizes, and output spatially arranged classification probability volumes for the entire input images. Therefore, the fully convolutional network successfully eliminates the redundant computations due to overlappings in the patch-based methods.

While the fully convolutional architecture can predict score volumes for arbitrary-sized inputs, the outputs are usually quite coarse with reduced dimensions compared with the original input image due to successive pooling layers. In this case, the image voxels receive predictions at a stride corresponding to the setting of pooling layers in the network. However, the segmentation tasks require very dense predictions where each single voxel should obtain a class label. One straightforward way to achieve this is to interpolate the coarse score volumes into full-sized segmentation masks. But an obvious disadvantage of this approach is that it is difficult to determine the interpolation weights and inappropriate weights would introduce imprecise results, especially for the boundary regions.

We alternatively solve this problem using an effective and efficient method. We develop 3D deconvolutional layers to transform the coarse feature volumes into the dense probability predictions. Specifically, we iteratively conduct a series of $3\times3\times3$ convolutions with a backward strided output (e.g., stride of 2 for double size up-scaling). This deconvolution operation can be regarded as a reverse procedure of the convolutions in the forward pass with a corresponding stride. This strategy is quite effective to reconstruct representations from nearby neighborhoods and to up-scale feature volumes to the resolution of original input volumes. Furthermore, these deconvolutional kernels are built in-network and also trainable during the learning process.

18.2.3 3D Deep Supervision Mechanism

To segment the organ or structures from the complicated anatomical environments in volumetric cardiovascular images, we usually need relatively deep models to encode highly representative features. However, training a deep network is broadly recognized as a difficult task. One notorious problem is the presence of gradients vanishing or exploding, which would make the loss back-propagation ineffective and hamper the convergence of the training process [23]. Particularly, [24] found that the back-propagated gradients would become smaller as they move from the output layer towards the input layer during the training. This would make different layers in the network receive gradients with very different magnitudes, leading to ill-conditioning and slower training. The training challenges could be more severe in our volumetric cardiovascular image segmentation task due to the low inter-class voxel variations, the larger amount of parameters in 3D networks compared with 2D counterparts, and the limited annotated training volumes.

In order to counteract the adverse effects of unstable gradients changes, we propose to exploit explicit supervision to the training of hidden layers in our 3D fully convolutional network. Specifically, we first up-scale some lower-level and middle-level feature volumes using additional deconvolutional layers. Then, we employ the softmax function on these full-sized feature volumes and obtain extra dense predictions. For these branched prediction results, we calculate their classification errors (i.e., negative log-likelihood) with regard to the ground truth segmentation masks. These auxiliary losses together with the loss from the last output layer are integrated to energize the back-propagation of gradients for more effective parameter updating in each iteration.

We call the layers whose feature volumes are directly path-connected to the last output layer as the *mainstream network*. Let w^l be the weights in the lth ($l=1,2,\ldots,L$) layer of the mainstream network. We denote the set of weights in the mainstream network by $W=(w^1,w^2,\ldots,w^L)$.

With $p(t_i|x_i;W)$ representing the probability prediction of a voxel x_i after the softmax function in the last output layer, the negative-log likelihood loss can be formulated as:

$$\mathcal{L}(\mathcal{X};W)=\sum_{x_i\in\mathcal{X}}-\log p\left(t_i|x_i;W\right), \tag{18.1}$$

where $\mathcal{X}$ represents the training database, and t_i is the target class label corresponding to the voxel $x_i\in\mathcal{X}$.

On the other hand, we call the layers that produce auxiliary dense predictions as the *branch networks*. The deep supervision is exactly introduced via these branch networks. To introduce deep supervision from the d th hidden layer, we denote the weights of the first d layers in the mainstream network by $W_d=(w^1,w^2,\ldots,w^d)$ and use $\hat{w}_d$ to represent the weights that bridge the dth layer feature volumes to dense predictions, and then the auxiliary loss for deep supervision can be formulated as:

$$\mathcal{L}_d(\mathcal{X};W_d,\hat{w}_d)=\sum_{x_i\in\mathcal{X}}-\log p\left(t_i|x_i;W_d,\hat{w}_d\right). \tag{18.2}$$

Finally, we learn the weights W and all $\hat{w}_d$ using the back-propagation algorithm [25] by minimizing the following overall objective function:

$$\mathcal{L}=\mathcal{L}(\mathcal{X};W)+\sum_{d\in\mathcal{D}}\eta_d\mathcal{L}_d\left(\mathcal{X};W_d,\hat{w}_d\right)+\lambda\left(\|W\|^2+\sum_{d\in\mathcal{D}}\|\hat{w}_d\|^2\right), \tag{18.3}$$

where η_d is the balancing weight of $\mathcal{L}_d$, which is decayed during learning, and $\mathcal{D}$ is the set of indexes of all the hidden layers that are equipped with the deep supervision. The first term corresponds to the output predictions in the last output layer. The second term is from the deep supervision. The third term is the weight decay regularizations, and λ is the trade-off hyperparameter. In each training iteration, the inputs to the network are large volumetric data, and the error back-propagations from these different loss components are simultaneously conducted.

The effectiveness of the proposed deep supervision mechanism can be justified from the following two complementary perspectives. First, according to [26], who first proposed to improve the convergence rate and discrimination capability of CNNs for image classification by supervising the training of hidden layers, the deep supervision can directly drive the low- and mid-level hidden layers to favor highly discriminative features towards explicit predictions. In addition, decomposed from these hidden layer features, representations in upper layers can more easily gain superior determinativeness and therefore further boost its generalization capability. Second, introducing such a deep supervision mechanism into a CNN can be considered as adding a kind of shortcut connections [27], [28] established from the loss to the weights in hidden layers to a CNN, viewing the deconvolutional layers as transformations. Such shortcut connections can improve the prorogation of gradient flows within the network so that the gradient vanishing problem can be greatly alleviated, and therefore obviously enhance the discrimination capability of the networks [29]–[31].

18.2.4 Contour Refinement with Conditional Random Field

For segmentation, the contour of ambiguous regions can sometimes be imprecise if we only utilize probability thresholding on the score volumes obtained from the 3D deeply supervised FCN. To improve the accuracy of the segmentation results at these regions, we propose to employ a conditional random field (CRF) model [32] to refine the segmentation masks. The model solves the energy function $E(y)=\Sigma_i-\log\hat{p}(y_i|x_i)+\Sigma_{i,j}f(y_i,y_j)\phi(x_i,x_j)$, where the first term is the unary

potential indicating the distribution over label assignment y_i at a voxel x_i. To aggregate multi-scale information, the $\hat{p}(y_i|x_i)$ is initialized as the linear combination of the last output layer and the branch network predictions obtained from the 3D deeply supervised FCN:

$$\hat{p}(y_i|x_i) = \left(1 - \sum_{d\in\mathcal{D}} \tau_d\right) p(y_i|x_i;W) + \sum_{d\in\mathcal{D}} \tau_d\, p(y_i|x_i;W_d,\hat{w}_d). \tag{18.4}$$

The second term in $E(y)$ is the pairwise potential, where $f(y_i,y_j)=1$ if $y_i \neq y_j$, and 0 otherwise; the $\phi(x_i,x_j)$ incorporates the local appearance and smoothness by employing the gray-scale value I_i and I_j and bilateral position s_i and s_j of the voxel x_i and x_j, as follows:

$$\phi(x_i,x_j) = \mu_1 \exp\left(-\frac{\|s_i - s_j\|^2}{2\theta_\alpha^2} - \frac{\|I_i - I_j\|^2}{2\theta_\beta^2}\right) + \mu_2 \exp\left(-\frac{\|s_i - s_j\|^2)}{2\theta_\gamma^2}\right). \tag{18.5}$$

The constant weights τ_d in the unary potential and parameters μ_1, μ_2, θ_α, θ_β, θ_γ in the pairwise potential were optimized using a grid search on the training set.

18.2.5 Experiments

18.2.5.1 Heart Segmentation Dataset

To validate our proposed design for whole heart segmentation, we employed the dataset of MICCAI 2016 Challenge on *Whole-Heart and Great Vessel Segmentation from 3D Cardiovascular MRI in Congenital Heart Disease*, for short, the HVSMR Challenge. The dataset overall consisted of 20 axial, cropped images with 10 training and 10 testing. The cardiovascular MR images were acquired in an axial view on a 1.5T scanner without contrast agent using a steady-state free precession pulse sequence. The image dimension and spacing varied across subjects with an average of $390\times390\times165$ and $0.90\times0.90\times0.85\,mm$, respectively. All the MR images were normalized to have zero mean and unit variance. We utilized data augmentations including random rotations of [90°,180°,270°] and flipping along the axial plane. Some subjects had congenital heart defects, and some had undergone interventions. The task of the challenge was to segment the blood pool and myocardium from the cardiovascular MR volume. The blood pool class included the left and right atria, left and right ventricles, aorta, pulmonary veins, pulmonary arteries, and the superior and inferior vena cava. Vessels (except the aorta) were extended only a few centimeters past their origin. The segmentations of the blood pool and ventricular myocardium were manually delineated by a trained rater, and validated by two clinical experts. The ground truths of the training set were released to competitors, and those of the testing are held out by the challenge organizers for independent evaluation.

18.2.5.2 Network Architecture and Training Settings

Specifically, we constructed a 14-layer fully convolutional network, stacking 7 convolutional layers, 3 max-pooling layers, 3 deconvolutional layers, and one softmax output layer in the mainstream network. The detailed down-sampling path was input-conv1a-pool1-conv2a-conv2b-pool2-conv3a-conv3b-pool3-conv4a-conv4b.

All the convolutional layers employed small kernels of $3\times3\times3$, considering the small structures of myocardium. For the number of feature volumes, conv1a had 32 kernels; conv2a and conv2b had 64 kernels; conv3a and conv3b had 128 kernels; conv4a and conv4b had 256 kernels. In order to form a competent receptive field for the blood pool, we utilized 3 max-pooling layers with a down-sampling stride of 2. In the upsampling path, we employed 3 deconvolutional layers to learn the dense predictions. To perform 3D deep supervision, we connected the layers of conv2b and conv3b to auxiliary classifiers.

The network was trained from scratch with weights initialized from Gaussian distribution ($\mu = 0$, $\sigma = 0.01$). Considering the large variance of the heart segmentation dataset, we utilized batch normalization ([33]) to reduce the internal covariance shift within the network's hidden neurons. The learning rate was initialized as 0.01 and decayed using the "poly" learning rate policy [34]. The deep supervision balancing weights were initialized as 0.2 and 0.4 and decayed during training procedure. We cropped patches of size $64 \times 64 \times 64$ as input to the network, considering consumption of the GPU memory, and the training was stopped when the validation accuracy did not increase anymore. Code for the implementation is publicly available now.[1]

18.2.5.3 Segmentation Evaluation Metrics

The HVSMR Challenge adopted seven evaluation criteria including the Dice coefficient (Dice), Jaccard coefficient (Jac), positive predictive value (PPV), sensitivity (Sens), specificity (Spec), average distance of boundaries (Adb[mm]) and Hausdorff distance of boundaries (Hdb[mm]), which are calculated for the structures of blood pool and myocardium, respectively. Specifically, the Dice, Jaccard, average distance of boundaries, and Hausdorff distance of boundaries are defined as follows:

$$Dice(S,G) = \frac{2|S \cap G|}{|S| + |G|}, \tag{18.6}$$

$$Jac(S,G) = \frac{|S \cap G|}{|S \cup G|}, \tag{18.7}$$

$$Adb(S,G) = \frac{1}{2}\left(\frac{\sum_{v_i \in e_G} min_{v_j \in e_S} dist\left(v_i, v_j\right)}{|G|} + \frac{\sum_{v_j \in e_S} min_{v_i \in e_G} dist\left(v_j, v_i\right)}{|S|} \right) \tag{18.8}$$

$$\begin{aligned} Hdb(S,G) &= max\left(H\left(e_G, e_S\right), H\left(e_S, e_G\right)\right) \\ H\left(e_G, e_S\right) &= max_{v_i \in e_G}\left\{min_{v_j \in e_S} dist\left(v_i, v_j\right)\right\} \\ H\left(e_S, e_G\right) &= max_{v_j \in e_S}\left\{min_{v_i \in e_G} dist\left(v_j, v_i\right)\right\}. \end{aligned} \tag{18.9}$$

where S and G are algorithm segmentation and ground truth, respectively. $|\cdot|$ is the volume counter. e_G is the surface of ground truth segmentation, v_i is the vertex on the surface, $dist(v_i, v_j)$ is the Euclidean distance between vertex v_i and v_j. Larger values of the Dice and Jaccard coefficients indicate higher segmentation accuracy. In addition, three more ratios (i.e., PPV, Sens, and Spec) also belong to the volume based measurements. The PPV is the ratio of true positives to true positives plus false positives. The sensitivity represents the ratio of true positives to true positives plus false negatives. The specificity denotes the ratio of true negatives to true negatives plus false positives. For these three ratios, higher values indicate better segmentation performance.

As shown in Eqs. 18.8 and 18.9, the measure Adb[mm] symmetrically calculates the average surface distance of segmentation results and ground truth surfaces. The measure Hdb[mm] counts the maximum distance between the results and ground truth surfaces. For both Adb[mm] and Hdb[mm], the lower the distance values, the better the segmentation performance.

[1] https://github.com/yulequan/HeartSeg

18.2.6 Segmentation Results

Table 18.1 presents the heart segmentation results on the MICCAI 2016 HVSMR testing dataset. The top part lists results of the blood pool segmentation, and the bottom part shows the results of the myocardium segmentation. We compared our method with representative approaches from other participating teams in the challenge, which employed either traditional segmentation methods or machine learning based methods. Specifically, [35] developed an automated algorithm by combining multi-atlases and level-sets; [37] utilized a 3D Markov random field model combined with substructures tracking. The other two belong to machine learning based methods with [38] leveraging random forest variants and the [36] utilizing 2D dilated convolutional networks [40]. In addition, we conducted comparison experiments using the 3D U-Net [39], which also employs the 3D fully convolutional network. Specifically, we implemented the 3D U-Net architecture and obtained optimal segmentation results by carefully tuning the model on our HVSMR dataset. We submitted the results to the Challenge evaluation system to get the scores listed in Table 18.1.

In the blood pool segmentation task, our method achieved Dice of 0.928 and Jaccard of 0.865, outperforming the other participating teams. The average distance of boundaries and Hausdorff distance of our method were also quite competitive, approaching the highest performance from the [36]. For the results of myocardium segmentation, our method presented the best performance on positive predictive value and specificity, with promising performance on average distance and Hausdorff distance of boundaries. When comparing with 3D U-Net, our proposed method achieved a higher performance on segmentation of both the myocardium and blood pool. Nevertheless, the 3D U-Net results of the blood pool are quite close to ours, while better than most of other baseline approaches. This observation can validate the effectiveness of 3D FCN on volumetric medical image segmentations. For time performance, our method takes around 1 minute to handle a MR volume.

Figure 18.2 presents some typical heart segmentation results on the testing dataset, from top to down are views from the sagittal plane, transverse plane, and coronal plane, respectively. For each subject, the left column are raw image data and the right are our segmentation results. We can observe that our method successfully delineated the anatomical structures of myocardium and blood pool. Note that there exists a large variation in the testing dataset. For example, the case of Figure 18.2 (c) comes with an inverse orientation from other cases. Under this challenging

TABLE 18.1

Comparison with different approaches on whole heart segmentation task. The evaluations of blood pool and myocardium are listed in top and bottom, respectively.

Methods	Dice	Jac	PPV	Sens	Spec	Adb [mm]	Hdb [mm]
[35]	0.885±0.028	0.795±0.044	0.907±0.052	0.867±0.046	0.984±0.008	1.553±0.376	9.408±3.059
[36]	0.926±0.018	0.863±0.030	0.951±0.024	0.905±0.047	**0.992±0.004**	**0.885±0.223**	**7.069±2.857**
[37]	0.867±0.047	0.768±0.068	0.861±0.062	0.889±0.108	0.972±0.014	2.157±0.503	19.723±4.078
[38]	0.794±0.053	0.661±0.071	**0.964±0.035**	0.680±0.081	0.996±0.004	2.550±0.996	14.634±8.200
3D U-Net ([39])	0.926±0.016	0.863±0.028	0.940±0.028	0.916±0.048	0.989±0.005	0.940±0.193	8.628±3.390
Ours	**0.928±0.014**	**0.865±0.023**	0.934±0.024	**0.924±0.039**	0.988±0.003	1.017±0.181	7.704±2.892
[35]	0.747±0.075	0.602±0.094	0.767±0.054	0.734±0.108	0.989±0.004	1.099±0.204	**5.091±1.658**
[36]	**0.802±0.060**	**0.673±0.084**	0.802±0.065	**0.805±0.076**	0.990±0.004	**0.957±0.302**	6.126±3.565
[37]	0.612±0.153	0.457±0.149	0.666±0.164	0.571±0.150	0.985±0.008	2.041±1.022	13.199±6.025
[38]	0.495±0.126	0.338±0.110	0.546±0.134	0.462±0.142	0.980±0.007	2.596±1.358	12.796±4.435
3D U-Net ([39])	0.694±0.076	0.536±0.089	0.798±0.076	0.618±0.092	0.992±0.004	1.461±0.397	10.221±4.339
Ours	0.739±0.072	0.591±0.090	**0.856±0.054**	0.653±0.089	**0.994±0.002**	1.035±0.240	5.248±1.332

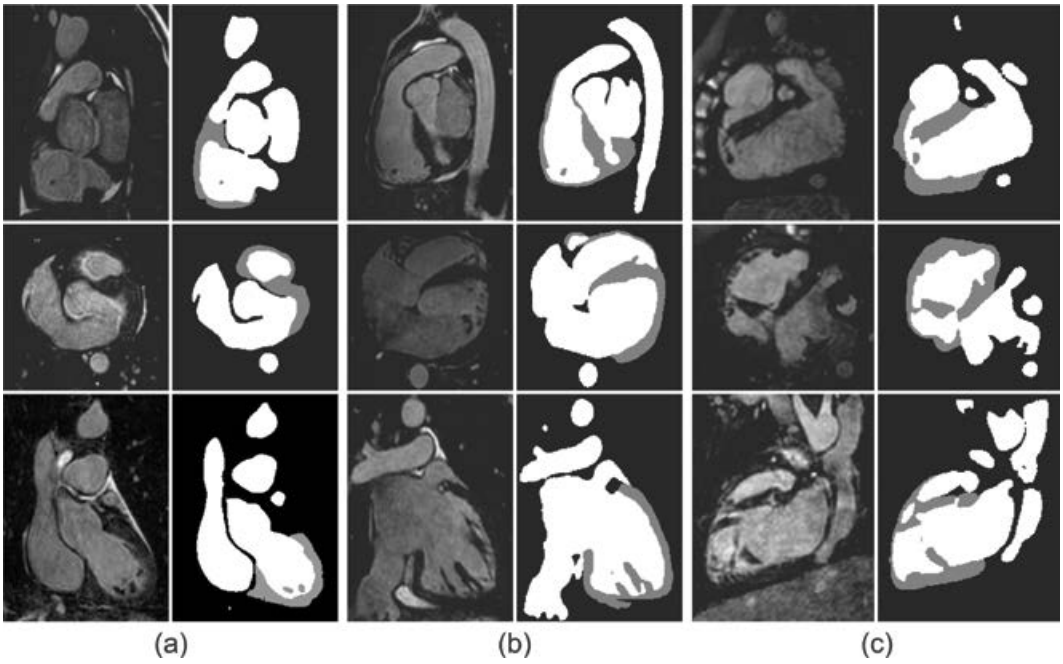

FIGURE 18.2 Typical heart segmentation results using our method. We present three view directions, with sagittal, transverse, and coronal planes listed from top to down. The white and gray regions denote segmentations for blood pool and myocardium, respectively.

situation, our method can still discriminate the characteristics of both anatomical structures and produce accurate segmentation masks, with blood pool Dice of 0.903 and myocardium Dice of 0.646. Meanwhile, as reported in Table 18.1, the standard deviations of our method are usually smaller than those of other approaches, somehow demonstrating the stability and generalization capability of our model.

18.2.7 Qualitative Comparison of Heart Segmentation Results

Finally, we qualitatively evaluate the efficacy of the 3D deep supervision mechanism on the heart segmentation task. Figure 18.3 visually compares the segmentation results obtained from the 3D deeply supervised FCN and pure end-to-end 3D CNN. The first three rows present results from three view directions (sagittal plane, transverse plane, and coronal plane from top to down); and the last row presents 3D reconstructions of the volumetric results. The first column is the raw cardiac MR image; the second and third columns are results from 3D CNN and 3D deeply supervised FCN, respectively; the fourth column shows the ground truth segmentation mask. It is observed that the 3D CNN is able to produce acceptable results which can already delineate general boundaries for the great vessels of the heart, indicating the effectiveness of the 3D fully convolutional architecture. By leveraging deep supervision, the 3D deeply supervised FCN can generate more precise boundaries for the blood pool (see the yellow arrows in Figure 18.3). In addition, the 3D deeply supervised FCN demonstrates sensible superior performance when segmenting the myocardium regions, which is the most challenging element in this application. For example, observing the first column, the contours of 3D deeply supervised FCN results (blue lines) are much closer to the ground truth (magenta lines) than contours of the pure 3D CNN results (cyan lines). In addition, viewing the 3D reconstruction results, the 3D deeply supervised FCN presents more accurate segmentations for

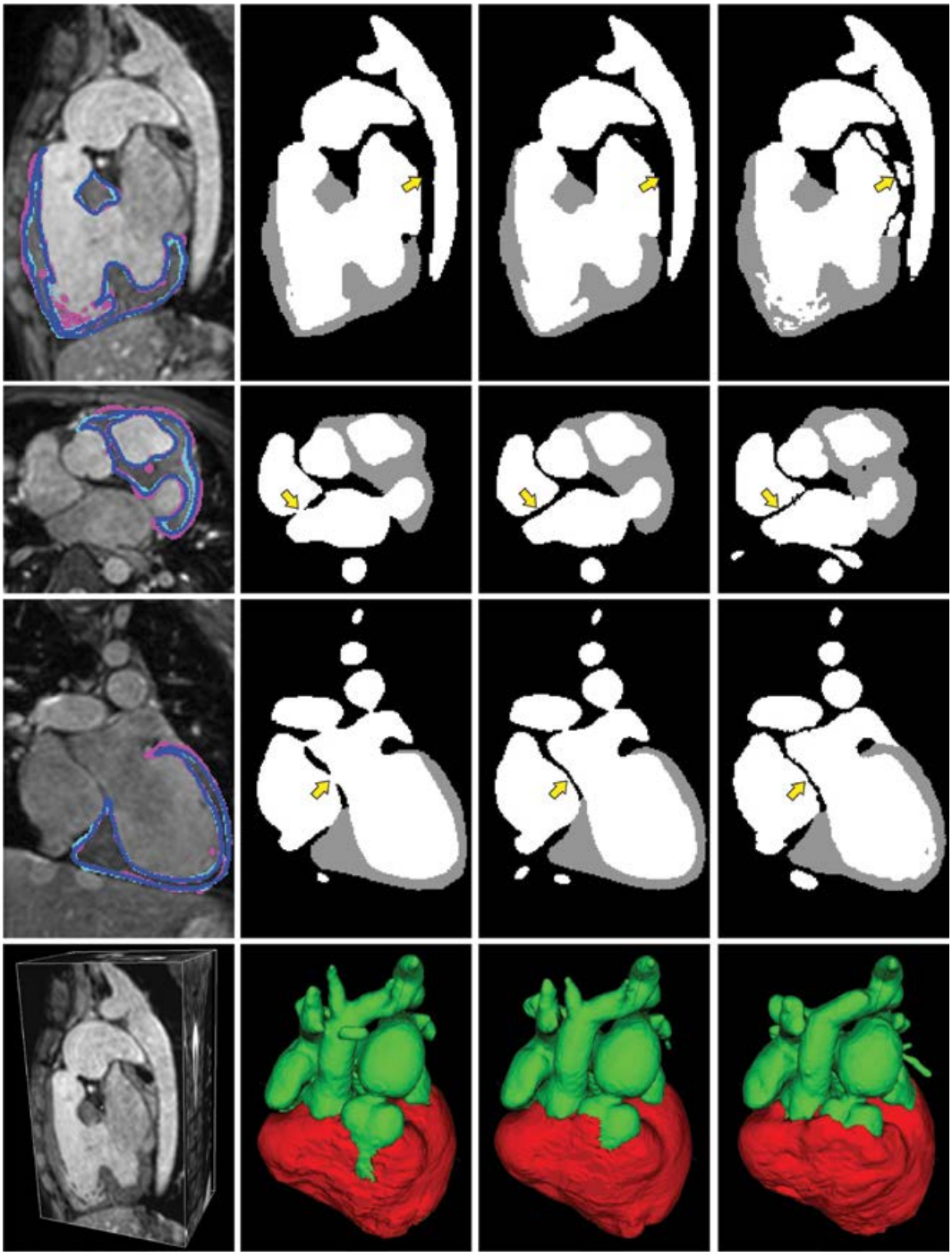

FIGURE 18.3 Qualitative comparison of heart segmentation results with and without 3D deep supervision. Columns from left to right are the raw MR images, pure 3D CNN results, 3D deeply supervised FCN results, and the ground truth masks. The white and gray regions denote structures of the blood pool and myocardium, respectively. In the first column, we overlay the contours of myocardium with the pure 3D CNN results, 3D deeply supervised FCN results, and the ground truth masks indicated in cyan, blue, and magenta colors, respectively. The last row presents 3D reconstructions of the data and segmentations with red for blood pool and green for myocardium.

the myocardium, which coincide well with the ground truth, whereas the pure 3D CNN misclassify some myocardium tissues as blood pool or background.

18.3 REFINED NETWORK STRUCTURE DESIGN

With the powerful hierarchical feature learning capability, the above 3D deeply supervised FCN can achieve decent performance in automatic whole heart and great vessel segmentation task via capturing 3D spatial contextual information of the input volumes. However, 3D FCNs are still difficult to train with the limited annotated cardiovascular images. In this section, we present two refined convolutional network (ConvNet) structures: 3D fractal network (*3D FractalNet*) and densely connected volumetric convolutional network (*DenseVoxNet*) for better performance and computation efficiency.

18.3.1 3D FractalNet

One of the refined architectures is the deeply supervised 3D fractal network (3D FractalNet) [41]. Based on fully convolutional architecture, the 3D FractalNet can efficiently map a whole volumetric data to its volume-wise label directly within a single forward process. Notably, multi-paths with various receptive fields in the network are organized in a self-similar fractal scheme to capture the multiscale hierarchical features of myocardium and vessels. Additionally, the 3D FractalNet also utilizes the deep supervision strategy proposed in Section II to attack the vanishing gradient problem of training process and thus boost the training efficiency. Figure 18.4 demonstrates the architecture of the proposed deeply supervised 3D FractalNet for dense volumetric whole heart and great vessel segmentation. It adopts 3D fully convolutional architecture and is organized in a self-similar fractal scheme. In this section, we first elaborate the formulation of fractal network, and then we will present the network architecture of 3D FractalNet. Finally, we will introduce the details of deep supervision strategy used to tackle potential optimization difficulties in training 3D FractalNet.

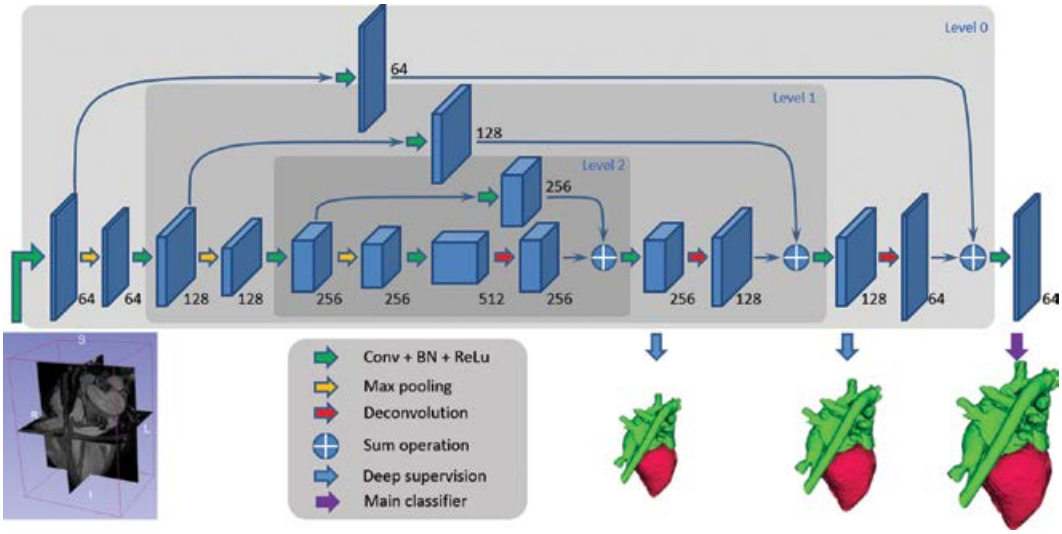

FIGURE 18.4 Illustration of our proposed deeply supervised 3D FractalNet architecture. Digits represent the number of feature volumes in each layer.

18.3.1.1 Fractal Networks

Fractal networks are constructed by repeatedly applying an expansion rule from a base case [42]. Let C denote the index of a truncated fractal $f_C(\cdot)$ (i.e., the network's structure, connections, and layer types) and the base case of a truncated fractal (Figure 18.5(a)) is a single convolutional layer:

$$f_1(z) = \text{conv}(z). \tag{18.10}$$

Then the successive fractals (Figure 18.5(b)) can be defined recursively according to the expansion rule:

$$\begin{aligned} z' &= \text{conv}(z), \\ f_{C+1}(z) &= \text{conv}[\text{conv}(z') \oplus f_C(z')] \end{aligned} \tag{18.11}$$

where $\oplus$ is a join operation and conv$(\cdot)$ is a convolution operator by a single convolutional layer. The join operation $\oplus$ merges two blobs, which are the extracted feature volumes (i.e., 4D matrices if the input are 3D volumetric data) resulting from convolutional layers and fractal operator $f_C(\cdot)$ respectively. Because these two blobs contain features from different visual levels, joining them can enhance the discrimination capability of networks. Generally, the join operator can be summation, maximization, and concatenation.

In order to further harness multi-scale features, we add down-sampling and up-sampling operators in the above expansion rule, as shown in Figure 18.5(c). Specifically, we add a max-pooling layer (with a stride 2) before the fractal $f_C(\cdot)$ and a deconvolutional layer (with stride 2) after the fractal $f_C(\cdot)$. The receptive field of a fractal thus becomes broader after the down-sample operation. When combining different receptive fields through the join operation, the network can harness multi-scale visual cues and promote itself in discriminating.

18.3.1.2 3D FractalNet

After recursively expanding the base case with the above expansion rule for three times, we obtained the 3D FractalNet used in this study, as shown in Figure 18.4. The join operation of fractal expansion in our 3D FractalNet is summation, computing the element-wise sum of two blobs. Same as introduced in Section II, the building blocks of our network, such as the convolutional, max-pooling, and deconvolutional layers, are all implemented with a 3D manner, thus the network can fully

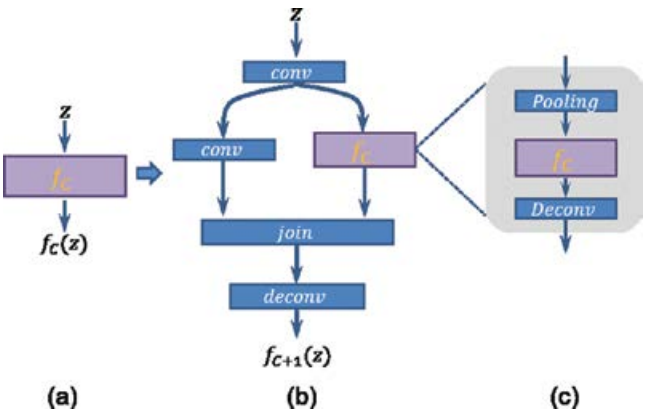

FIGURE 18.5 An illustration of the expansion rule in our fractal architecture. We add down-sampling and up-sampling operators in the expansion rule to further utilize multi-scale feature and avoid computation bottlenecks.

preserve and exploit the 3D spatial information of the input volumetric data. Note that our network adopts the fully convolutional architecture, and hence can take arbitrary-sized volumetric data as input and output corresponding sized predictions within a single forward process, which is very efficient in handling large MRI dataset.

Previous studies [43] have shown that small convolutional kernels are more efficient in network design. The effective receptive field size of stacked small kernels is equivalent to that of one large kernel (the effective receptive field of three $3\times3\times3$ kernels is the same as one $7\times7\times7$ kernel), while giving lower computation cost. Therefore, we adopt small convolution kernels with size of $3\times3\times3$ in convolutional layers. Each convolutional layer is followed by a rectified linear unit (ReLU) as the activation function. Note that we also employ batch normalization layer (BN) before each ReLU layer to accelerate the training process. At the end of the network, we add a $1\times1\times1$ convolutional layer as a main classifier to generate the segmentation results and further get the segmentation probability map after passing the softmax layer.

18.3.1.3 Deeply Supervised 3D FractalNet

Similar to in discussion in Section II, directly training such a deep 3D fractal network is also challenging due to the issue of vanishing gradients [23], which makes the back-propagation ineffective for early layers. Following previous studies on training deep neural networks with deep supervision [44], [45], we proposed the customized deeply supervised 3D FractalNet by injecting direct supervision into the hidden layers of the network. Specifically, we added M auxiliary classifiers (convolutional layers with size of $1\times1\times1$) following some hidden layers of the network, and employed deconvolutional layers to upsample the output of auxiliary classifiers. This scheme can effectively alleviate the vanishing gradients problem and assist the training process with direct supervision on the hidden layers.

Specifically, let W be the weights of main network and $w=(w^1,w^2,\ldots,w^M)$ be the weights of auxiliary classifiers. Then the cross-entropy loss function of the main classifier is

$$\mathcal{L}(\mathcal{X};W)=\sum_{x_i\in\mathcal{X}}-\log p\left(y_i=\ell\left(x_i\right)\middle|x_i;W\right), \tag{18.12}$$

where $\mathcal{X}$ represents the training samples and $p(y_i=\ell(x_i)|x_i;W)$ is the probability of target class label $\ell(x_i)$ corresponding to sample $x_i\in\mathcal{X}$. Similarly, the loss function of the m^{th} auxiliary classifier is

$$\mathcal{L}_m\left(\mathcal{X};W,w^m\right)=\sum_{x_i\in\mathcal{X}}-\log p\left(y_i=\ell\left(x_i\right)\middle|x_i;W,w^m\right). \tag{18.13}$$

Therefore, the total loss function of our deeply supervised 3D FractalNet is:

$$\mathcal{L}(\mathcal{X};W,w)=\mathcal{L}(\mathcal{X};W)+\sum_{m=1}^{M}\alpha_m\mathcal{L}_m\left(\mathcal{X};W,w^m\right)+\lambda\psi(W), \tag{18.14}$$

where the first two terms are the classifier loss, and the last part is the regularization term (L_2 norm in our experiments); α_m is the weight of different auxiliary classifiers.

18.3.1.4 Training Procedure

The proposed method was implemented with C++ and Matlab under the open source deep learning library of Caffe [46], using a standard PC with a 2.60GHz Intel(R) Xeon(R) E5-2650 CPU and a NVIDIA TITAN X GPU. The weights of networks were initialized from the Gaussian distribution

($\mu = 0, \sigma = 0.01$) and updated using stochastic gradient descend (SGD) method (batch size = 4, momentum = 0.9, weight decay = 0.0005). The learning rate was set as 0.002 initially and divided by 10 every 3000 iterations. The network was trained for up to 10000 iterations. We added two auxiliary classifiers, and the weights α_m are 0.33 and 0.67, respectively. We randomly cropped a $64 \times 64 \times 64$ sub-volume from each sample in every iteration for the input when training our network, and therefore we totally extracted 40000 patches in training. We used an overlap-tiling strategy to generate the whole volume probability map by stitching sub-volume predictions. We also employed some morphology operations including removing small isolated components and filling holes to process the prediction. Generally, it took about 12 seconds to process one volume with size of $200 \times 140 \times 120$ using the above configuration.

18.3.2 DenseVoxNet

The previous network architectures and other 3D ConvNets (e.g., 3D U-Net [47], VoxResNet [48]) usually generate a large number of feature channels in each layer, and they have plenty of parameters to be tuned during training. Although these networks introduce different skip connections to ease the training, the training of an effective model with the limited MR images for heart segmentation is still very challenging. In order to ease the training of 3D ConvNets with limited data and thus improve the segmentation performance, we propose a novel densely connected volumetric convolutional network, namely *DenseVoxNet* [49], to segment the cardiac and vascular structures in cardiac MR images. The DenseVoxNet adopts 3D fully convolutional architecture, and thus can fully incorporate the 3D image and geometric cues for effective volume-to-volume prediction. More importantly, the DenseVoxNet incorporates the concept of dense connectivity [50] and enjoys two advantages from the learning perspective:

- It implements direct connections from a layer to all its subsequent layers. Each layer can thus receive additional supervision from the loss function through the shorter skip connections, and thus make the network much easier to train.
- The DenseVoxNet has fewer parameters than the other 3D ConvNets. Since layers can access feature maps from all of its preceding layers, the learning of redundant feature maps can be possibly avoided. Therefore, the DenseVoxNet has fewer feature maps in each layer, which is essential in training convolutional networks with limited images as it has less chance to encounter the overfitting problem.

18.3.2.1 Dense Connection

In a convolutional network, we denote x_ℓ as the output of the ℓ^{th} layer, x_ℓ can be computed by a transformation $H_l(\mathrm{x})$ from the output of the previous layer, $\mathrm{x}_{\ell-1}$ as:

$$\mathrm{x}_\ell = H_\ell\left(\mathrm{x}_{\ell-1}\right), \tag{18.15}$$

where $H_\ell(\mathrm{x})$ can be a composite of operations such as convolution (Conv), pooling, batch normalization (BN) or rectified linear unit (ReLU), etc. To boost the training against the vanishing gradients, ResNet [29] introduces a kind of skip connection, which integrates the response of $H_\ell(\mathrm{x})$ with the identity mapping of the features from the previous layer to augment the information propagation as:

$$\mathrm{x}_\ell = H_\ell\left(\mathrm{x}_{\ell-1}\right) + \mathrm{x}_{\ell-1}. \tag{18.16}$$

However, the identity function and the output of H_ℓ are combined by summation, which may impede the information flow in the network.

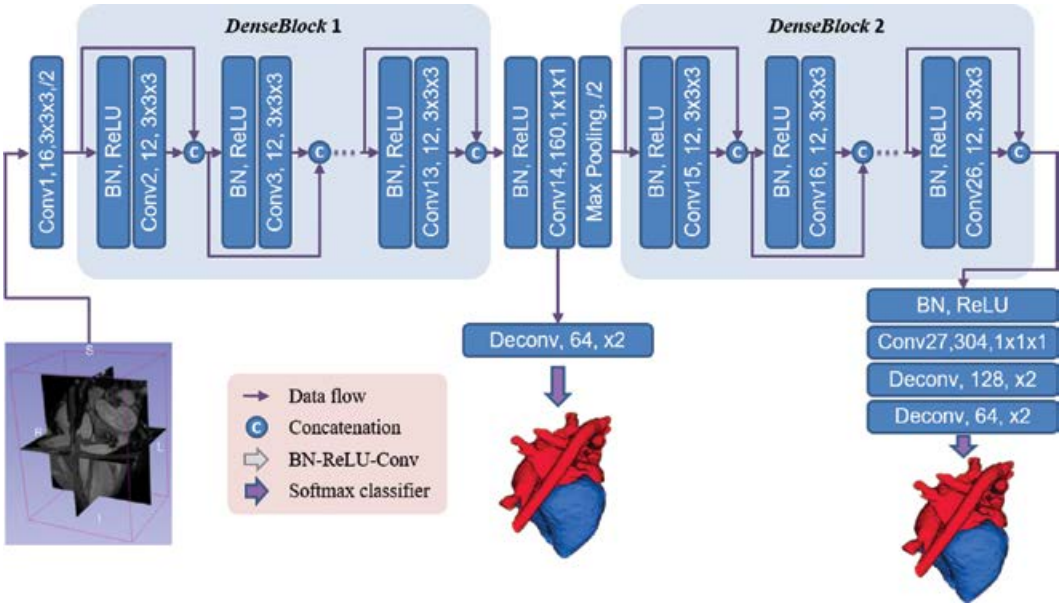

FIGURE 18.6 The architecture of our DenseVoxNet. It consists of two *DenseBlocks,* and all operations are implemented in a 3D manner.

To further improve the information flow within the network, the dense connectivity [50] exercises the idea of skip connections to the extreme by implementing the connections from a layer to all its subsequent layers. Specifically, the x_ℓ is defined as:

$$\mathrm{x}_\ell = H_\ell\left(\left[\mathrm{x}_0, \mathrm{x}_1, \ldots, \mathrm{x}_{\ell-1}\right]\right), \tag{18.17}$$

where [...] refers to the concatenation operation. The dense connectivity, as illustrated in Figure 18.7, makes all layers receive direct supervision signal. More importantly, such a mechanism can encourage the reuse of features among all these connected layers. Suppose that if the output of each layer has k feature maps, then the k, referred as *growth rate*, can be set to a small number to reduce the number of parameters as there is no need to re-learn redundant feature maps. This characteristic is

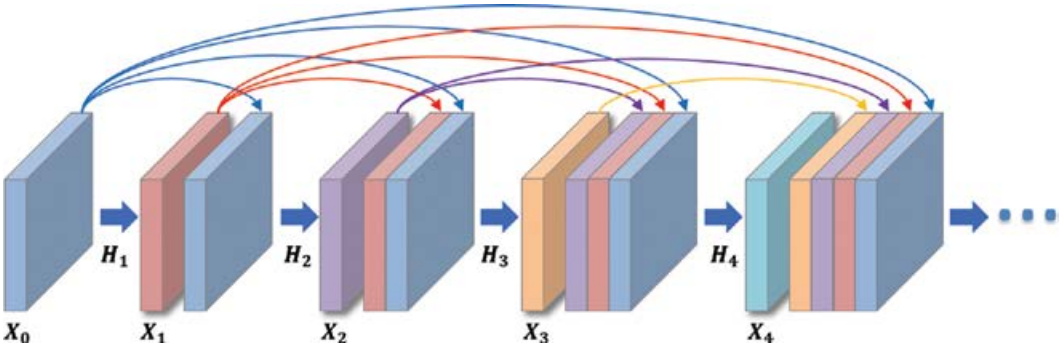

FIGURE 18.7 Illustration of the dense connectivity scheme taking a five-layer *DenseBlock* as an example.

quite compelling to medical image analysis tasks, where it is usually difficult to train an effective network with a lot of parameters with limited training data.

18.3.2.2 The Architecture of DenseVoxNet

Figure 18.6 illustrates the architecture of our proposed DenseVoxNet. It adopts the 3D fully convolutional network architecture [44], [47], [48] and has the down- and up-sampling components to achieve end-to-end training. Note that Eq. 18.17 is not applicable when the feature maps have different sizes; on the other hand, we need to reduce the feature map size for better efficiency of memory space and increase the receptive field to enclose more information when prediction. We, therefore, divide the down-sampling components into two densely connected blocks, referred as *DenseBlock*, and each *DenseBlock* is comprised of 12 transformation layers with dense connections (only draw three layers in the figure for simplicity). Each transformation layer is sequentially composed of a BN, a ReLU, and a $3\times3\times3$ Conv and the growth rate, k, of our DenseVoxNet is 12. The first *DenseBlock* is prefixed with a Conv with 16 output channels and stride of 2 to learn primitive features. In-between the two *DenseBlocks* is the transition block, which consists of a BN, a ReLU, a $1\times1\times1$ Conv, and a $2\times2\times2$ max pooling layers.

The up-sampling component is composed of a BN, a ReLU, a $1\times1\times1$ Conv, and two $2\times2\times2$ deconvolutional (Deconv) layers to ensure the sizes of segmentation prediction map consistent with the size of input images. The serial layers of BN, ReLU, and Conv perform the nonlinear reasoning, whereas the two Deconv layers aim to restore the original image dimensionality. The up-sampling component is then followed with a $1\times1\times1$ Conv layer and softmax layer to generate the final label map of the segmentation. To equip the DenseVoxNet with the robustness against the overfitting problem, the dropout layer is implemented following each Conv layer with the dropout rate of 0.2.

To further boost the information flow within the network, we implement a kind of long skip connection to connect the transition layer to the output layer with a $2\times2\times2$ Deconv layer. This skip connection shares the similar idea of deep supervision [44], as introduced in Section II, to strengthen the gradient propagation and stabilize the learning process. In addition, this long skip connection may further tap the potential of the limited training data to learn more discriminative features. Our DenseVoxNet has about 1.8M parameters in total, which is much fewer than other 3D ConvNets, for example, 3D U-Net [47] with 19.0M parameters and VoxResNet [48] with 4.0M parameters.

18.3.2.3 Training Procedure

The proposed network is implemented with Caffe [46]. The network weights were randomly initialized with a Gaussian distribution ($\mu = 0$, $\sigma = 0.01$). The optimization is realized with the stochastic gradient descend algorithm (batch size = 3, weight decay = 0.0005, momentum = 0.9). The initial learning rate was set to 0.05. We use the "poly" learning rate policy (i.e., the learning rate is multiplied by $(1-\frac{iter}{max\_iter})^{power}$) for the decay of learning rate along the training iteration. The power variable was set to 0.9, and maximum iteration number (max_iter) was set as 15000. To fit the limited GPU memory, the input of our DenseVoxNet are sub-volumes with size of $64\times64\times64$ voxels, which were randomly cropped from the training images. The final segmentation results were obtained with the major voting strategy [51] from the predictions of the overlapped sub-volumes.

18.3.3 Experiments

We also use the MICCAI 2016 HVSMR dataset to validate the efficiency of our proposed 3D FractalNet and DenseVoxNet. We report the experiment results of 3D FractalNet and DenseVoxNet on phase 2 (cropped axial images) of the Challenge dataset. As for the 3D FractalNet, we also report

the experimental results on phase 3 (cropped short-axial images). Note that we adopted the same pre-processing and data augmentation operations as Section II.

18.3.3.1 Qualitative Results

To explicitly visualize the difference between the 3D FractalNet segmentation results and the ground truth, we illustrate six surface-to-surface comparison examples of training dataset using cross-validation in Figure 18.8. We can observe that our segmentation results coincide well with ground truth. Benefiting from the multi-scale features, our network can tackle the large variation of blood pool and myocardium and effectively separate the touching boundaries of vessel. Also, the proposed method can even present more complete vessel segmentation comparing to the ground truth.

To better show the detailed difference between segmentation results and annotated ground truth, we demonstrate four typical DenseVoxNet segmentation results on training slices (the first two samples, via cross-validation) and testing slices (the last two samples) in Figure 18.8. The four slices are from different subjects but with the same coronal plane view. The blue and purple color denotes our segmentation results for blood pool and myocardium, respectively, and segmentation ground truth is also presented in white and gray regions in the first two samples. As can be observed, there exists large variation of cardiac structures among different subjects in both training and testing images. Our method can still successfully demarcate myocardium and blood pool from the low-intensity contrast cardiac MR images, demonstrating the effectiveness of the proposed DenseVoxNet.

18.3.3.2 Quantitative Results of 3D FractalNet

The main evaluation criteria in the Challenge include Dice coefficient (Dice), Hausdorff Distance of Boundaries (Hdb[mm]) and Average Distance of Boundaries (Adb[mm]) (please refer to II-E3 for detailed formulation of these criteria). Auxiliary metrics, such as Jaccard index, Cohen's Kappa, Sensitivity, and Specificity are also considered. For distance related metrics, lower values indicate better performance. We report two types of result: testing dataset result and leave-one-out

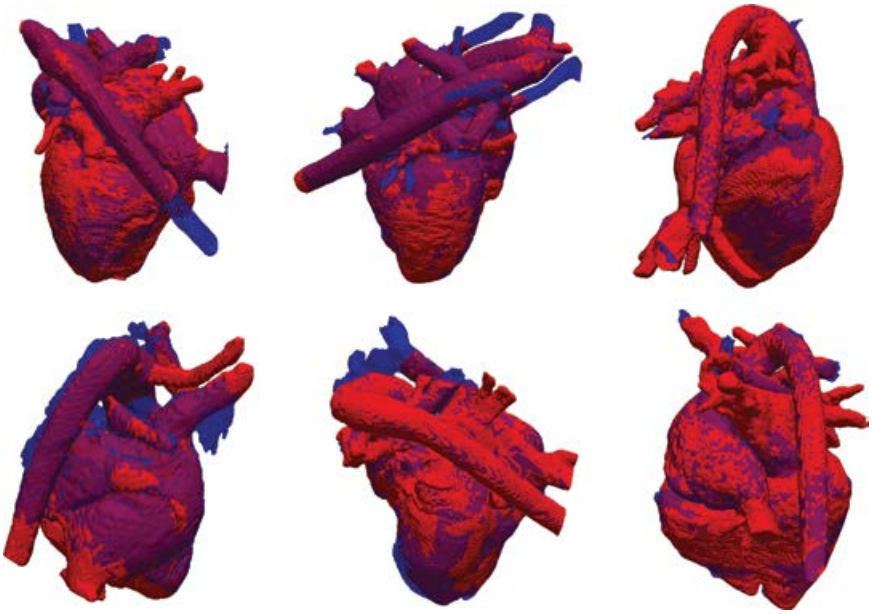

FIGURE 18.8 Explicit surface-to-surface comparison of our segmentation results (blue) with ground truth (red).

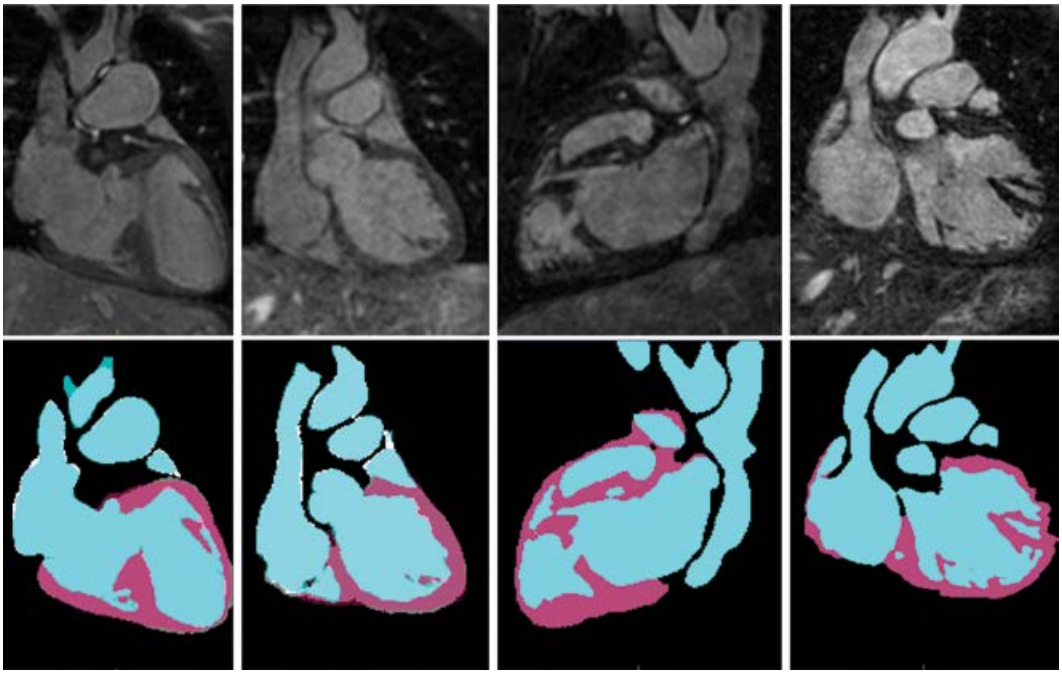

FIGURE 18.9 Segmentation results on training images (the first two) and testing images (the last two). The blue and purple color denotes our segmentation results for blood pool and myocardium, respectively, and segmentation ground truth is also presented in white and gray regions in the first two samples.

cross-validation result of training dataset on phase 2 and 3. On the Challenge website, these results are reported from our teams CUMED2 (cross-validation) and CUMED1 (testing).[2] Tables 18.2 and 18.3 illustrate the automated segmentation results under the main metrics on testing dataset and cross-validation of training dataset, respectively.

TABLE 18.2
Quantitative evaluation results on testing dataset

Sample	Phase 2						Phase 3					
	Adb1	Adb2	Dice1	Dice2	Hdb1	Hdb2	Adb1	Adb2	Dice1	Dice2	Hdb1	Hdb2
volume 10	1.120	0.843	0.727	0.939	7.640	6.508	1.228	0.643	0.671	0.948	5.820	3.713
volume 11	1.010	1.137	0.831	0.921	8.842	8.553	2.518	1.040	0.719	0.929	30.204	13.579
volume 12	0.784	0.682	0.848	0.940	5.701	7.318	0.590	0.810	0.862	0.940	2.840	9.245
volume 13	0.971	0.980	0.836	0.936	6.467	10.860	0.949	0.854	0.824	0.940	4.275	8.677
volume 14	0.872	0.916	0.762	0.926	3.951	3.877	1.043	0.983	0.690	0.920	5.372	4.292
volume 15	1.705	0.842	0.648	0.915	9.675	4.229	1.111	1.022	0.664	0.896	6.563	6.399
volume 16	0.639	1.224	0.796	0.899	3.877	12.903	0.746	0.731	0.717	0.913	3.622	7.230
volume 17	0.950	0.555	0.803	0.954	6.528	3.408	0.847	0.697	0.789	0.948	4.516	7.874
volume 18	0.504	0.588	0.851	0.948	2.032	3.771	0.513	0.695	0.819	0.937	2.089	4.100
volume 19	1.410	0.914	0.762	0.935	9.474	8.703	1.296	0.814	0.700	0.939	8.064	5.141
Average	0.997	0.868	0.786	0.931	6.419	7.013	1.084	0.829	0.746	0.931	7.336	7.025

Note: class 1: myocardium; class 2: blood pool.

[2] http://segchd.csail.mit.edu/

TABLE 18.3
Quantitative evaluation results of cross-validation on training dataset

Sample	Phase 2						Phase 3					
	Adb1	Adb2	Dice1	Dice2	Hdb1	Hdb2	Adb1	Adb2	Dice1	Dice2	Hdb1	Hdb2
volume 0	0.420	0.641	0.888	0.950	1.982	2.938	0.353	0.502	0.898	0.952	1.536	1.255
volume 1	0.681	0.636	0.868	0.943	5.388	4.324	0.992	0.555	0.858	0.947	8.577	4.314
volume 2	0.758	0.725	0.825	0.940	3.198	4.162	0.695	0.642	0.844	0.944	2.813	4.058
volume 3	0.669	0.650	0.849	0.940	2.570	4.297	0.600	0.531	0.857	0.942	3.625	2.562
volume 4	0.399	0.682	0.898	0.909	1.979	5.002	0.697	0.749	0.838	0.900	4.717	5.015
volume 5	0.485	0.544	0.876	0.921	3.053	4.016	0.304	0.729	0.920	0.903	1.674	6.544
volume 6	0.938	0.927	0.762	0.902	4.559	6.266	0.849	0.740	0.790	0.915	3.969	5.977
volume 7	1.331	0.418	0.818	0.954	13.752	1.635	0.734	0.397	0.822	0.954	5.942	2.312
volume 8	0.317	0.847	0.888	0.926	1.536	6.271	0.485	0.651	0.852	0.941	2.662	5.681
volume 9	0.748	0.866	0.844	0.917	4.776	7.515	0.549	0.651	0.861	0.934	3.192	4.609
Average	0.675	0.694	0.852	0.930	4.279	4.643	0.626	0.615	0.854	0.933	3.871	4.233

18.3.3.3 Comparison with Other Methods

The quantitative comparison between 3D FractalNet, DenseVoxNet, and four other approaches from the participating teams in this challenge is shown in Table 18.4. According to the rules of the Challenge, methods were ranked based on Dice coefficient (Dice). Meanwhile, other ancillary measures like average distance of boundary (Adb[mm]) and symmetric Hausdorff distance of boundary (Hdb[mm]) are also computed for reference. Higher Dice values suggest a higher agreement between segmentation results and ground truth, while lower Adb and Hdb values indicate higher boundary similarity. Three of the six approaches employed traditional methods based on handcrafted features, including Random Forest [52], 3D Markov Random Field and substructure tracking [53] and level-set method driven by multiple atlases [54]. The other three methods, including ours, are based on convolutional network. Wolterink et al. [55] employed 2D dilated convolutional network to segment the myocardium and blood pool, while our 3D FractalNet and DenseVoxNet utilized 3D ConvNets.

Table 18.4 reports the results of different methods. It can be observed that the ConvNet-based methods (the last three rows) can generally achieve better performance than the other methods do, suggesting that ConvNets can generate more discriminative features in a data-driven manner to better tackle the large anatomical variability of patients. Regarding the segmentation of

TABLE 18.4
Comparison with different approaches on HVSMR2016 dataset

Method	Myocardium			Blood Pool		
	Dice	Adb [mm]	Hdb [mm]	Dice	Adb [mm]	Hdb [mm]
Mukhopadhyay [52]	0.495±0.126	2.596±1.358	12.796±4.435	0.794±0.053	2.550±0.996	14.634±8.200
Tziritas [53]	0.612±0.153	2.041±1.022	13.199±6.025	0.867±0.047	2.157±0.503	19.723±4.078
Shahzad et al. [54]	0.747±0.075	1.099±0.204	**5.091±1.658**	0.885±0.028	1.553±0.376	9.408±3.059
Wolterink et al. [55]	0.802±0.060	**0.957±0.302**	6.126±3.565	0.926±0.018	0.885±0.223	7.069±2.857
D FractalNet [41]	0.786±0.064	0.997±0.353	6.419±2.574	0.931±0.016	**0.868±0.218**	**7.013±3.269**
DenseVoxNet	**0.821±0.041**	0.964±0.292	7.294±3.340	**0.931±0.011**	0.938±0.224	9.533±4.194

TABLE 18.5
Quantitative analysis of our network

		Myocardium			Blood Pool		
Method	**Parameters**	**Dice**	**Adb [mm]**	**Hdb [mm]**	**Dice**	**Adb [mm]**	**Hdb [mm]**
3D U-Net [47]	19.0M	0.694±0.076	1.461±0.397	10.221±4.339	0.926±0.016	0.940±0.192	**8.628±3.390**
VoxResNet [48]	4.0M	0.774±0.067	1.026±0.400	**6.572±3.551**	0.929±0.013	0.981±0.186	9.966±3.021
DenseVoxNet-A	1.7M	0.787±0.042	1.811±0.752	17.534±7.838	0.917±0.018	1.451±0.537	15.892±6.772
DenseVoxNet	1.8M	**0.821±0.041**	**0.964±0.292**	7.294±3.340	**0.931±0.011**	**0.938±0.224**	9.533±4.194

myocardium, DenseVoxNet achieves the best performance with the Dice, that is, the ranking metric in the Challenge, of 0.821 ± 0.041 and outperforms the second one by around 2%. For the segmentation of blood pool, DenseVoxNet and 3D FractalNet achieve the best Dice score of 0.931 ± 0.011 0.931 ± 0.018. The 3D FractalNet achieves the best Adb and Hdb scores, suggesting the efficiency of fractal scheme. It is worth noting that the dice scores of myocardium in all methods are lower than the Dice scores of blood pool, suggesting that the segmentation of myocardium is relatively more challenging due to the ambiguous borders of the myocardium in the low-resolution MR images. While the other two ConvNet-based approaches achieve quite close Dice scores to our DenseVoxNet in blood pool segmentation, DenseVoxNet is obviously better than these two methods in the Dice scores of the myocardium, demonstrating our densely connected network with auxiliary long side paths has the capability to tackle the hard myocardium segmentation problem.

We further implement two other state-of-the-art 3D ConvNets—3D U-Net [47] and VoxResNet [48]—for comparison. We also perform an ablation experiment to compare the performance of the proposed DenseVoxNet with and without auxiliary side paths. We follow the same training procedure for all networks. The quantitative comparison can be found in Table 18.5, where "DenseVoxNet-A" denotes the DenseVoxNet without the auxiliary side paths. As can be observed, our DenseVoxNet achieves much better performance than the other two 3D ConvNets in both myocardium and blood pool segmentation. It suggests that our DenseVoxNet can benefit from the improved information flow throughout the network with the dense connections. In addition, our method achieves better performance with much fewer parameters than our competitors, corroborating the effectiveness of the feature map reusing mechanism encoded in the densely connected architecture, which is quite important to enhance the capability of ConvNet models under limited training data. It is also observed that the auxiliary side path can further improve the segmentation performance, especially for the myocardium.

18.4 IMPROVED INITIALIZATION AND LOSS FUNCTION

18.4.1 Background

The designs introduced in Sections II and III are general for blood pool and ventricular structures segmentation in volumetric images. However, the scenario becomes more challenging for network design when we come to consider further differentiating the whole heart into multiple fine-grained substructures, as shown in Figure 18.10, extracting the whole heart from volumetric scanning and simultaneously partitioning it into seven substructures, including the myocardium of the left ventricle (MLV), left atrium blood cavity (LABC), left ventricle blood cavity (LVBC), right atrium blood cavity (RABC), right ventricle blood cavity (RVBC), ascending aorta (ASA), and pulmonary artery (PUA) [56].

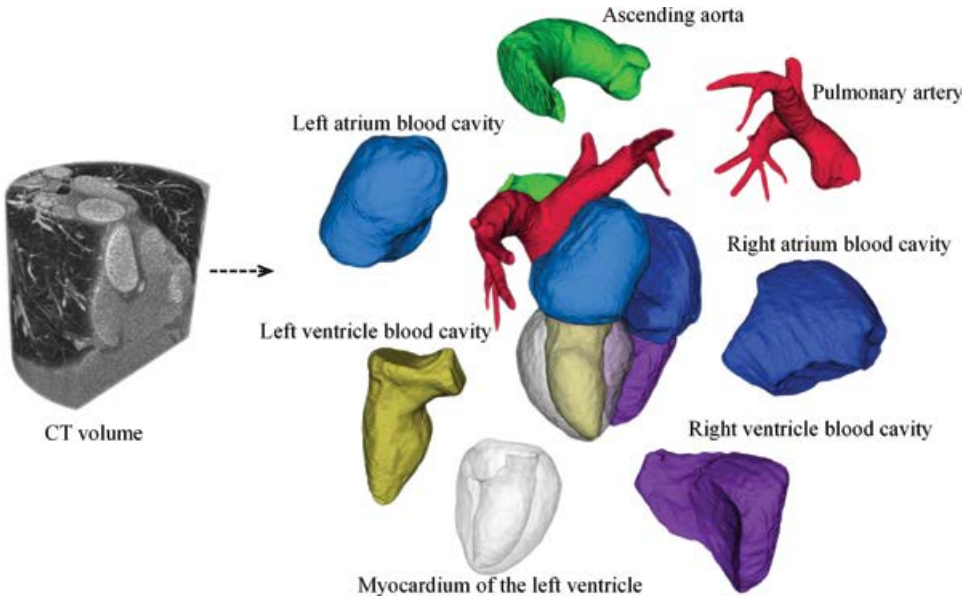

FIGURE 18.10 Illustration of the seven substructures of whole heart. Obvious topological difference in anatomy can be observed.

Parsing the whole heart into the well-defined substructures opens great opportunities for radiologists to analyze the functionalities of the heart in a more precise manner. The geometry information, such as landmarks, represented by segmentation can significantly facilitate the image registration. Detailed segmentation can also provide subtle and accurate guidance for computer aided intervention, such as surgical planning for congenital heart disease and radio-frequency ablation. When combined with real-time analysis, the extracted volumes can be applied to quantify the functional indices of the heart, such as the ejection fraction and myocardial mass [1]–[3].

Compared to the 2-class segmentation tasks in Section II and III, simultaneously differentiating seven classes intensifies two problems which should be tackled more seriously. The first is the network initialization. Deep neural networks need proper initialization to avoid being trapped in local minima when fitting the more complicated latent loss function in learning to recognize more classes. Also, good initialization can help the network to learn to collect contextual information from neighboring classes to support the local classification. Pre-training, or transfer learning, is a popular strategy to provide proper initialization, and we will elaborate our specialized transfer learning for 3D convolutional networks in Section IV-D. Another problem is the class imbalance, which can potentially bias the networks to sacrifice some minor classes or abundant details. As illustrated in Figure 18.10, the class imbalance mainly concerns the difference in topology (branchy versus compact) and volume size between different classes. We will explain the class imbalance in detail in Section IV-E and propose to alleviate it by introducing a novel, hybrid loss function to guide the training of deep networks [57].

18.4.2 Method

Figure 18.11 is the schematic illustration of our proposed framework. Following the spirit of utilizing 3D convolutions to fully explore the volumetric contextual information, all the operators in our network are also in 3D fashion. Without any auxiliary heart localization module, our system takes the original whole volume as the raw input. There is a preprocessing module

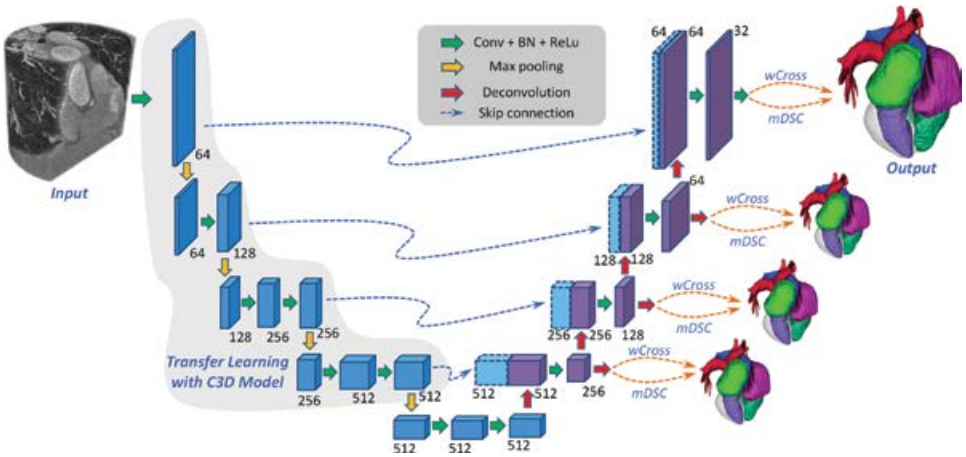

FIGURE 18.11 Schematic view of our proposed framework. Digits represent the number of feature volumes in each layer. Blue volume with dotted line is for concatenation.

to conduct intensity calibration. Our tailored 3D fully convolutional network originates from the famous U-net [58] design. Long skip connections bridging down-sampling and up-sampling path are critical for our network to recognize possible boundary details in volumes. The down-sampling path benefits from *transfer learning* strategy. The proposed *hybrid loss functions* are adopted in a stratified deep supervision manner. Limited by GPU memory, the actual input to our network are cropped sub-volumes. All the training samples are normalized as zero mean and unit variance. The output of our framework is the volume-wise labeling result for seven substructures of the heart. The detailed parameter configuration for our network are shown in Table 18.6.

TABLE 18.6

Configuration of our customized 3D fully convolutional network. Layers in bold are initialized with transfer learning. Stars denote layers where the deep supervision with auxiliary loss functions inject.

Layer	Kernel Size	Output Size	Layer	Kernel Size	Output Size
Conv 1:	$3\times3\times3$	$64\times64\times64\times64$	DeConv 1:	$4\times4\times4$	$8\times8\times8\times512$
Pooling 1:	$2\times2\times2$	$32\times32\times32\times64$	Concat 1:	–	$8\times8\times8\times1024$
Conv 2:	$3\times3\times3$	$32\times32\times32\times128$	*Conv 6:	$3\times3\times3$	$8\times8\times8\times256$
Pooling 2:	$2\times2\times2$	$16\times16\times16\times128$	DeConv 2:	$4\times4\times4$	$16\times16\times16\times256$
Conv 3a:	$3\times3\times3$	$16\times16\times16\times256$	Concat 2:	–	$16\times16\times16\times512$
Conv 3b:	$3\times3\times3$	$16\times16\times16\times256$	*Conv 7:	$3\times3\times3$	$16\times16\times16\times128$
Pooling 3:	$2\times2\times2$	$8\times8\times8\times256$	DeConv 3:	$4\times4\times4$	$32\times32\times32\times128$
Conv 4a:	$3\times3\times3$	$8\times8\times8\times512$	Concat 3:	–	$32\times32\times32\times256$
Conv 4b:	$3\times3\times3$	$8\times8\times8\times512$	*Conv 8:	$3\times3\times3$	$32\times32\times32\times64$
Pooling 3:	$2\times2\times2$	$4\times4\times4\times512$	DeConv 4:	$4\times4\times4$	$64\times64\times64\times64$
Conv 5a:	$3\times3\times3$	$4\times4\times4\times512$	Concat 4:	–	$64\times64\times64\times128$
Conv 5b:	$3\times3\times3$	$4\times4\times4\times512$	Conv 9:	$3\times3\times3$	$64\times64\times64\times32$
–	–	–	Conv 10:	$3\times3\times3$	$64\times64\times64\times7$

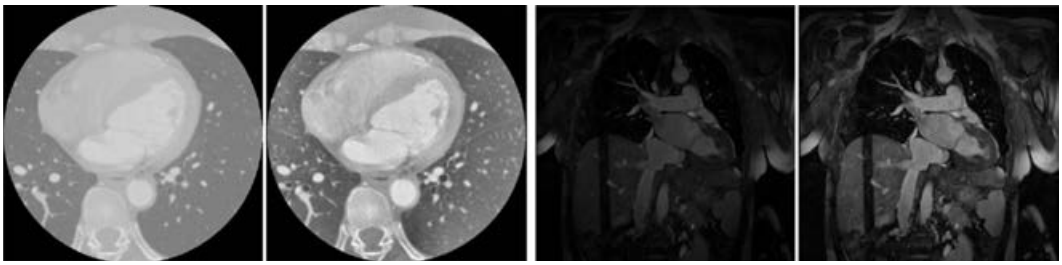

(a) (b)

FIGURE 18.12 Intensity calibration with CLAHE. (a) CT slice before and after CLAHE, (b) MR slice before and after CLAHE.

18.4.3 Datasets and Preprocessing

In this work, we are using the MM-WHS 2017 (Multi-Modality Whole Heart Segmentation) Challenge dataset,[3] which is the most recent and largest dataset in the field and mainly contributed by Fudan University and Imperial College London. It contains two modalities, CT and MR. For each modality, there are 20 training volumes and 40 testing volumes with high-quality annotations. The ground truth for the testing data are held by the Challenge organizers. Each team can only submit one time to get their testing evaluation result. The volumes are with varying dimensions and spacings. Because the Challenge datasets are collected from different subjects in different sites, the image quality vary greatly subject to imaging parameters and machines. Low contrast and inhomogeneity are common around the volumes. So, we adopt the Contrast Limited Adaptive Histogram Equalization (CLAHE) technique [59] to enhance the local contrast and reduce the inhomogeneity. Specifically, we apply CLAHE with a slice-wise manner and set the block size as 8×8. As shown in Figure 18.12, slices in CT and MR get significant visual quality improvement after applying the CLAHE.

18.4.4 Transfer Learning from Video Recognition

Proper initialization is important for the training of deep neural networks, especially in facing the limited training data and the complex scenario containing multiple classes. Equipped with 3D operators, our 3D FCN contains orders of magnitude parameters than 2D networks, which further increases the risk and asks for more tricky initialization. For vision tasks, the features learned by shallow layers in deep neural networks can be generic across different tasks. Sharing parameters, or knowledge, with models that are well-trained on large-scale datasets, denoted as *transfer learning*, proves to be beneficial in avoiding improper initialization and combating overfitting for better generalization ability, even the pre-trained model is generated in a different domain [60]. However, some popular models, like ImageNet [61] and VGG16 [43], are originally designed to interpret 2D spatial information, and thus are unable to be transferred to 3D applications.

Recently, the *C3D* architecture introduced in [62] sheds light on the transfer learning for 3D deep neural networks. Trained on large-scale video datasets, *C3D* discards 2D convolutions and directly utilizes 3D convolutions to simultaneously extract spatial and temporal abstract across consecutive frames and achieves high performance on video action recognition. By adapting spatial-temporal 3D convolutions to volumetric data, *C3D* model can be transferred to initialize our network and thus promote the volumetric segmentation tasks. Specifically, we initialize the shallow layers *conv1*, *conv2*, *conv3a*, *conv3b*, *conv4a,* and *conv4b* in our down-sampling path with the layers from the *C3D* model (denoted in Figure 18.11 and Table 18.6). During fine-tuning, we set small learning rates

[3] http://www.sdspeople.fudan.edu.cn/zhuangxiahai/0/mmwhs/index.html

for these transferred layers to avoid being overtuned. Configuration of our up-sampling path is symmetric with the down-sampling path, but initialized from uniform distribution.

18.4.5 Hybrid Loss Guided Class-Balanced Segmentation

Loss function defines the latent mapping and the functionality that deep neural network needs to fit and can finally achieve. Therefore, the choice of loss function is vital in guiding the training of deep networks. Considering the feasibility in differentiable optimization for training, the popular choice for loss function is the classical cross-entropy, which has the basic formulation as shown in Eq. 18.18. $\mathcal{X}$ represents the training samples, and $p(y_i = \ell(x_i)|x_i; W)$ is the probability of target class label $\ell(x_i)$ corresponding to sample $x_i \in \mathcal{X}$. However, cross-entropy is not perfect in classification or segmentation occasions where classes present inevitable class imbalance [45]. This problem becomes more obvious in whole heart partition. First, different substructures present disparate topologies, like the branchy pulmonary artery, tube-like ascending aorta, and sphere-like left atrium blood cavity. Second, different structures often have different volume sizes. As illustrated in Figure 18.13, as one kind of the point-wise loss functions, cross-entropy counters each voxel equally and summarizes the prediction error on each voxel without counting the significance of each class, which will lead the network to oversee minor classes and only focus on major ones. The situation gets worse when the network only takes cropped sub-volume as input in which the difference in volume size are magnified. Motivated by [45], [63], in this work, we conduct an investigation on different loss functions in balancing different classes and preserving segmentation details, and finally propose a hybrid loss function as a decent choice [57].

18.4.5.1 Volume Size Weighted Cross-Entropy

As proposed in [45] for rare edge extraction, weighting the cross-entropy loss for different classes is helpful in addressing the class imbalance. In this work, we extend the formulation in [45], and propose a volume-size weighted cross-entropy (denoted as *wCross*). Mathematically, the formulation of *wCross* is shown as Eq. 18.19. $\left|\mathcal{X}^{\ell(x_i)}\right|$ is the volume size of class $\ell(x_i)$ in patch $\mathcal{X}$ derived from the annotation patch. With the formulation, classes with smaller volume sizes can get larger weight with $\eta_{\ell(x_i)}$ and avoid being ignored by taking larger proportions in $\mathcal{L}_{wCross}$.

$$\mathcal{L}_{wCross}(\mathcal{X}; W) = \sum_{x_i \in \mathcal{X}} \log p\left(y_i = \ell\left(x_i\right)|x_i; W\right) \tag{18.18}$$

$$\mathcal{L}_{wCross}(\mathcal{X}; W) = \sum_{x_i \in \mathcal{X}} -\eta_{\ell(x_i)} \log p\left(y_i = \ell\left(x_i\right)|x_i; W\right), \eta_{\ell(x_i)} = 1 - \frac{\left|\mathcal{X}^{\ell(x_i)}\right|}{|\mathcal{X}|} \tag{18.19}$$

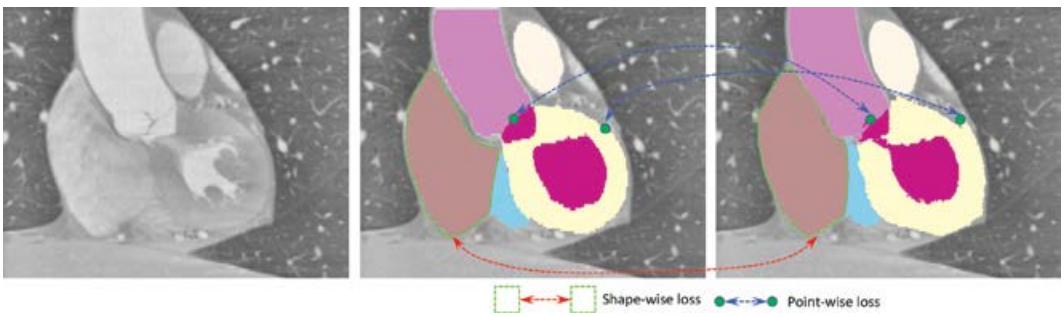

FIGURE 18.13 From left to right: a slice from CT volume, segmentation ground truth provided by experts and algorithm segmentation. Point-wise loss functions focus on comparing the labeling difference on each voxel (denoted with blue dotted line), while the shape-wise loss function focuses on comparing the global shape similarity (denoted with red dotted line).

18.4.5.2 Multi-Class Dice Similarity Coefficient

Dice similarity coefficient (DSC) based loss function is another novel attempt to alleviate class imbalance [63]. DSC is originally a metric designed to evaluate the conformity between two shapes [64], as shown in Eq. 18.20, where S is the area or volume of an object:

$$DSC = 2(S_A \cap S_B) / (S_A + S_B) \tag{18.20}$$

As illustrated in Figure 18.13, different from the point-wise loss, DSC based loss function focuses on the global shape similarity. Thus the cost for each class is volume size-independent and self-normalized before being equally counted into the total loss. We extend the loss in [63] and propose a differentiable multi-class Dice similarity coefficient (*mDSC*) based loss function to balance the training for multiple classes. Given the segmentation ground truth $G^{w\times h\times d}$, we first encode it into a one-hot format for C classes $\mathcal{G}^{C\times w\times h\times d}$, $C = 7$ for our task. With probability volumes $\mathcal{P}^{C\times w\times h\times d}$, our proposed *mDSC* can be written as:

$$\mathcal{L}_{mDSC} = -\sum_{c\in C} \frac{\frac{2}{N}\sum_{i}^{N} \mathcal{G}_c^i \mathcal{P}_c^i}{\sum_{i}^{N} \mathcal{G}_c^i \mathcal{G}_c^i + \sum_{i}^{N} \mathcal{P}_c^i \mathcal{P}_c^i}, \tag{18.21}$$

where $N = w\times h\times d$, $\mathcal{G}_c^i$ and $\mathcal{P}_c^i$ are the i^{th} voxel of c^{th} volume in $\mathcal{G}$ and $\mathcal{P}$. The $1/N$ in denominator is empirically introduced to suppress prediction noise. Improvement caused by *mDSC* is illustrated in Section IV-G. As illustrated in Section IV-G, both *wCross* and *mDSC* can reduce class imbalance. *wCross* often guides networks to preserve complex details of branchy structures but brings about many false alarms, while *mDSC* tends to generate more compact and clear predictions, but runs at the sacrifice of losing extending details. Therefore, we propose to blend these two kinds of complementary loss functions as a hybrid, shown as Eq. 18.22, so as to get segmentation results in a compact but detail-enhanced format. Because mDSC loss is no larger than 1.0 and much smaller than the *wCross* loss, we adopt a coefficient α, and we empirically set the α to 100.0 to balance the conflict between *mDSC* and *wCross* loss functions.

$$\mathcal{L}_{hybrid} = \mathcal{L}_{wCross} + \alpha\mathcal{L}_{mDSC} \tag{18.22}$$

18.4.6 Implementation Details

Based on the cropped training samples, we further augment the training dataset with 30% rotated samples to combat the pose variation of the heart. We trained two networks to segment the CT and MR volumes independently. We implemented our 3D FCN in *Tensorflow*, using two NVIDIA GeForce GTX TITAN X GPUs. The code is publicly available now.[4] Given the limited memory of one GPU, we assign the down- and up-sampling paths to different GPUs. We update the weights of network with a Adam optimizer (batch size = 1, initial learning rate is set to 0.001). With 30000 training epochs, it takes hours to train our network. Following the stratified deep supervision mechanism, we totally attached three side-paths to the up-sampling branch and set $\beta_0 = 0.2, \beta_1 = 0.4, \beta_2 = 0.8$ for feature volumes from coarse to fine scales. Randomly cropped $96\times96\times96$ sub-volumes serve as input to train our network. To avoid shallow layers being over-tuned during fine-tuning, we set

[4] https://github.com/xy0806/miccai17-mmwhs-hybrid

smaller initial learning rate for *conv1, conv2, conv3a, conv3b, conv4a,* and *conv4b* as *1e-6, 1e-6, 1e-5, 1e-5, 1e-4*, and *1e-4*. We adopt the sliding window with high overlapping ratio and overlap-tiling stitching strategies introduced in [51] to generate predictions for the whole volume, and further remove the small and unreasonable isolated connected components in the final labeling result. The testing time for one volume is about 2 minutes.

18.4.7 Quantitative and Qualitative Analysis

We use three metrics to evaluate the proposed framework on segmentation, including DSC, Jaccard, and Average Distance of Boundaries (Adb). Transfer learning (TL) and deep supervision (DS) are configured for both compared methods. We conduct experiments to compare the model driven by classical cross-entropy (denoted as *DS+TL+Cross*), *mDSC* (denoted as *DS+TL+mDSC*), and hybrid loss function (denoted as *DS+TL+hybrid*). Because the ground truth of testing dataset is held out by the organizer for independent evaluation, we get our current evaluation results by taking 10 volumes from training dataset to train and another 10 volumes as testing.

In Figure 18.14, we show the improvement of probability maps for CT segmentation when we change from cross-entropy based loss function to *mDSC* and hybrid loss functions. For each row, the warmer the color, the higher the prediction probability. As we can observe, the prediction maps obtained from cross-entropy and weighted cross-entropy are more noisy than that obtained from mDSC, but this also means more possible details are preserved. When we compare the cross-entropy and weighted cross-entropy, we can see that the probability maps from the latter present higher contrast between the foreground and background. mDSC drives the network to output much more compact and clean predictions and thus enlarges the intra-class gaps. As a combination of weighted cross-entropy and mDSC, we can see that the prediction maps from hybrid loss function get higher foreground-background contrast and preserve necessary details.

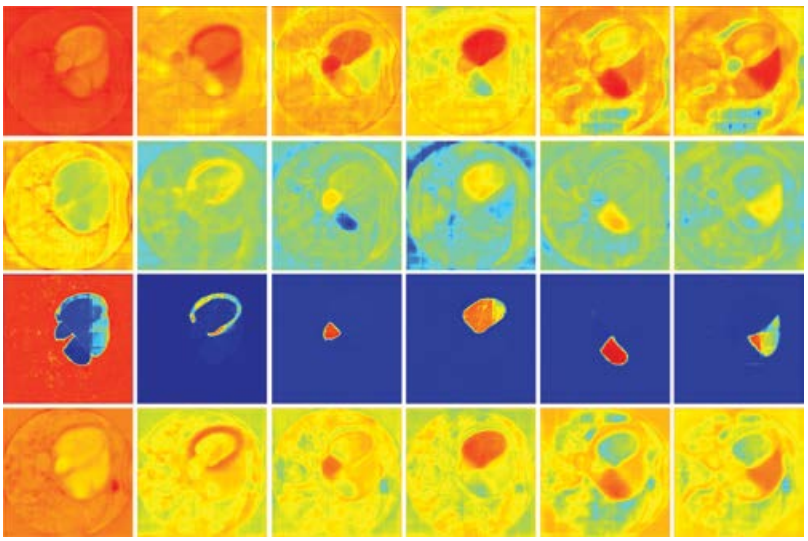

FIGURE 18.14 From left to right: probability map of background, myocardium of the left ventricle, left atrium blood cavity, left ventricle blood cavity, right atrium blood cavity, and right ventricle blood cavity. From top to bottom: training with classical cross-entropy, weighted cross-entropy, mDSC and hybrid loss functions.

TABLE 18.7
Quantitative evaluation for whole heart segmentation in CT volumes

Method	Metric	Substructures of Heart							
		MLV	LABC	LVBC	RABC	RVBC	ASA	PUA	***mean***
DS+TL+Cross	*DSC[%]*	81.31	79.07	90.86	85.39	81.61	71.71	76.38	80.90
	Jaccard[%]	69.58	71.02	83.50	75.10	70.03	62.45	63.03	70.67
	Adb[voxel]	2.954	29.01	3.345	6.178	7.371	3.509	5.378	8.249
DS+TL+mDSC	*DSC[%]*	68.97	90.00	83.42	84.36	62.50	91.51	80.84	80.22
	Jaccard[%]	55.67	82.19	73.33	74.05	49.31	85.03	68.87	69.78
	Adb[voxel]	3.185	5.415	5.666	5.875	8.245	2.692	3.875	**4.993**
DS+TL+hybrid	*DSC[%]*	81.86	84.54	87.76	81.53	77.80	94.12	82.62	**84.32**
	Jaccard[%]	69.93	76.12	78.66	70.28	65.90	89.20	71.13	**74.46**
	Adb[voxel]	2.987	22.67	4.609	6.502	8.609	2.237	5.086	7.529

Quantitative evaluation results are shown in Tables 18.7 and 18.8. We can observe that both *DS+TL+Cross* and *DS+TL+mDSC* cannot get satisfying results for all substructures and emphasize the different structures. There can be about 14% difference between LVBC and PUA in DSC metric in *DS+TL+Cross*, while *DS+TL+mDSC* slightly alleviates the problem and gets obvious improvement on ADB metric. With the hybrid loss function, for both CT and MR, our proposed method *DS+TL+hybrid* significantly balances all classes with evenly distributed performance and gets superior improvement on DSC and Jaccard metrics, especially in classes which *DS+TL+mDSC* fails. These quantitative results verifies the impact of loss functions and the efficacy of our proposed hybrid loss function.

In Figure 18.15, we visualize the segmentation results in CT and MR volumes. Our proposed method conquers complex variance of the heart and achieves promising performance in two modalities. There are more rich details in the segmentation from CT volumes, since the structural information are clearer in CT volumes than in MR, while CT is more radiation-intensive than MR. In Figure 18.16, with the segmentation results from the same CT volumes, we provide explicit proof about how the *wCross* based model can preserve more branchy details, and how the *hybrid* based model gets the compromise. *wCross* can guide the network to preserve more branchy details (denoted with green circle) because *wCross* focuses on each voxel, while it also brings about severe false alarms (denoted with blue circle). The *hybrid* loss function then drives the network to get a

TABLE 18.8
Quantitative evaluation for whole heart segmentation in MR volumes

Method	Metric	Substructures of Heart							
		MLV	LABC	LVBC	RABC	RVBC	ASA	PUA	***mean***
DS+TL+Cross	*DSC[%]*	71.98	76.96	87.05	78.60	73.38	63.50	70.85	74.62
	Jaccard[%]	58.06	65.98	78.34	68.44	62.94	50.20	58.92	63.27
	Adb[voxel])	1.323	1.679	1.587	2.062	5.901	2.075	1.781	2.344
DS+TL+mDSC	*DSC[%]*	66.54	74.62	86.80	86.16	71.43	71.24	70.19	75.28
	Jaccard[%]	52.07	64.23	77.71	75.97	60.59	58.13	57.88	63.80
	Adb[voxel]	1.509	1.761	1.646	1.773	3.300	1.560	1.587	**1.864**
DS+TL+hybrid	*DSC[%]*	74.17	78.66	85.83	81.99	81.91	72.60	69.83	**77.86**
	Jaccard[%]	60.27	67.53	76.59	71.89	71.27	58.43	55.17	**65.88**
	Adb[voxel]	1.404	1.950	2.045	2.733	4.483	3.346	4.367	2.904

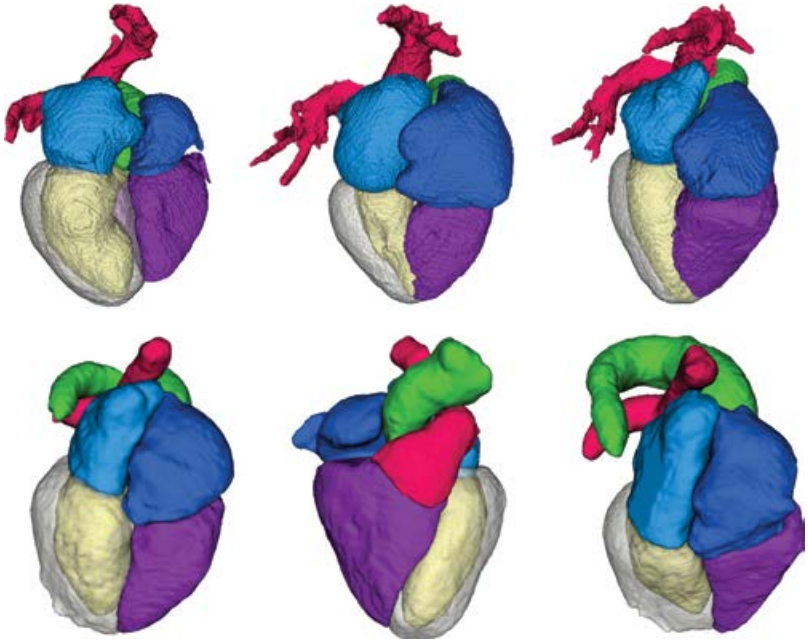

FIGURE 18.15 Visualization of segmentation results generated by hybrid loss guided models. From top to bottom: segmentation results from CT volumes and MR volumes. The color reference can be found in Figure 18.10.

proper balance. In Figure 18.17, we show an example of the Hausdorff distance (the unit is [mm]) between the substructure segmentations obtained from *DS+TL+hybrid* and the ground truth. It can be observed that our segmentation results are accurate with small Hausdorff distances for most voxels. Large displacement often happens around the branchy locations.

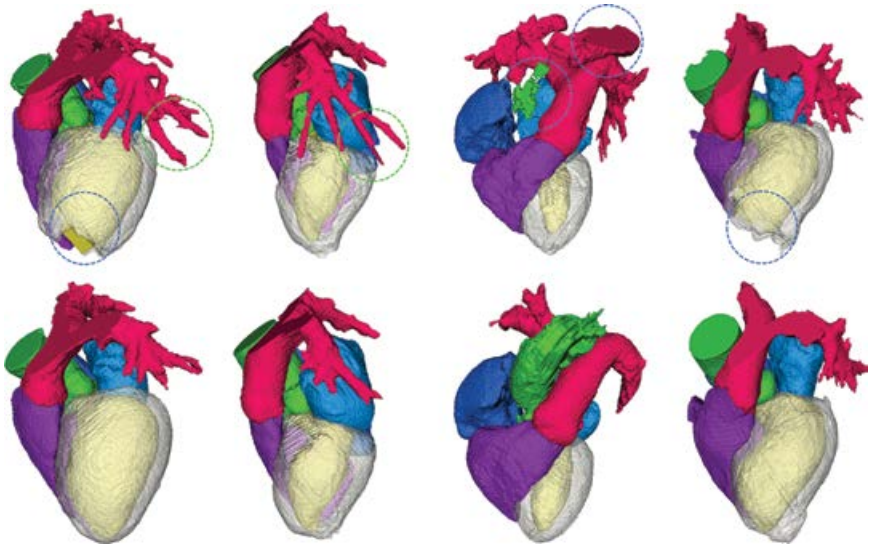

FIGURE 18.16 Compare substructure segmentation results. From top to bottom: segmentation results of the same CT volumes generated by *wCross* based model and hybrid loss based model. Green circles denote the branchy details enhanced by *wCross*, while blue circles denote the flaws caused by *wCross*.

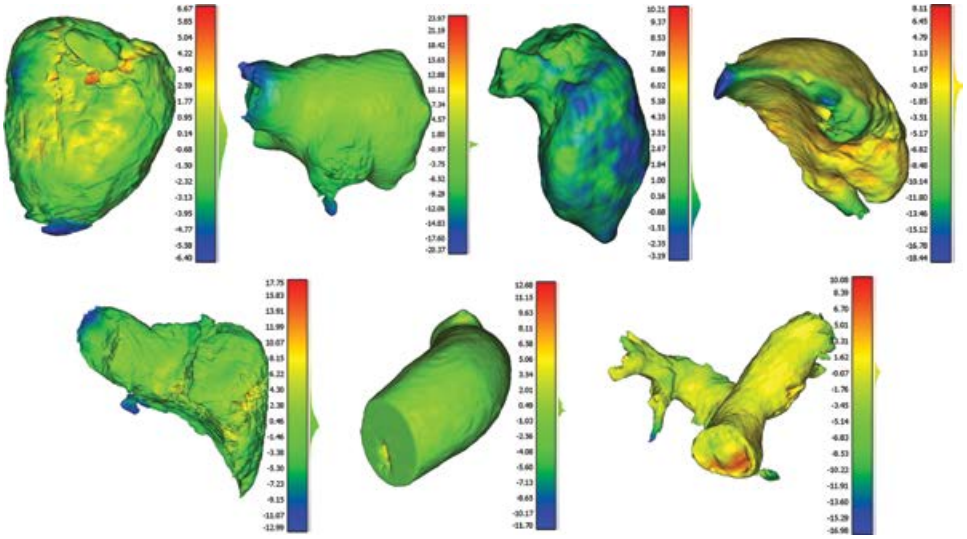

FIGURE 18.17 Illustration of the Hausdorff distance between the segmentation surface and the ground truth.

18.5 DISCUSSION AND CONCLUSION

With this chapter, we present our investigation about network designs to improve the performance for whole heart segmentation. Upgrading key operators in convolutional network into 3D version promotes the capability of deep network to fully exploit spatial context for volumetric segmentation. The stratified deep supervision with auxiliary loss functions is beneficial in boosting the training efficacy. To promote the segmentation for branchy details and reduce computation burden from a network design perspective, fractal connection and dense connection are independently explored. Transfer learning customized for 3D deep network is adopted for better initialization and generalization ability. Hybrid loss function to leverage the strengths of different loss functions is proposed to combat class imbalance. All these modified designs stem from the practical needs in the cardiovascular volume segmentation, and can be general for many other segmentation tasks.

Although the automated segmentation performance presented in this chapter is promising, there still exist many challenging problems for cardiovascular volume segmentation. First, from the varying image quality of HVSMR 2016 and MM-WHS 2017 Challenges, we can see that the image quality of CT scanning is much better than that in MR, which consequently results in better segmentation performance (see Tables 18.7 and 18.8). However, CT is more radiation-intensive than MR. So, in the future, improving the segmentation performance for MR modality is the main challenge. Leveraging the multi-modality image transformation to transform the MR image into a CT-like image to improve segmentation is a possible research direction [65]. Second, although the deep learning based method is becoming more and more popular in image processing, it still has limited capacity in encoding global shape constraints, which will hamper the segmentation in boundary-ambiguous areas. So, incorporating the shape prior represented by classic shape model with the superior nonlinear mapping capability of DNNs will be an interesting research direction. Third, as pointed out in Section III, currently 3D DNNs implementation are computationally expensive. Given the limited GPU memory, reducing the footprint of network is beneficial for network to receive input with larger size, which in turn increases the chance of network to collect more context information for better segmentation.

Acknowledgments

The work in this chapter was supported by the grants from Hong Kong Research Grants Council (Project no. CUHK 14203115 and PolyU 152035/17E), a grant from Shenzhen Science and Technology Program (No. JCYJ20160429190300857) and a grant from Guangdong Province Science and Technology Plan Project (No. 2016A020220013).

References

1. A. F. Frangi, W. J. Niessen, and M. A. Viergever, "Three-dimensional modeling for functional analysis of cardiac images, a review," *IEEE Transactions on Medical Imaging*, vol. 20, no. 1, pp. 2–5, 2001.
2. V. Y. Wang, H. Lam, D. B. Ennis, B. R. Cowan, A. A. Young, and M. P. Nash, "Modelling passive diastolic mechanics with quantitative MRI of cardiac structure and function," *Medical Image Analysis*, vol. 13, no. 5, pp. 773–784, 2009.
3. C. Tobon-Gomez, A. J. Geers, J. Peters, J. Weese, K. Pinto, R. Karim, M. Ammar, A. Daoudi, J. Margeta, Z. Sandoval *et al.*, "Benchmark for algorithms segmenting the left atrium from 3d CT and MRI datasets," *IEEE Transactions on Medical Imaging*, vol. 34, no. 7, pp. 1460–1473, 2015.
4. D. F. Pace, A. V. Dalca, T. Geva, A. J. Powell, M. H. Moghari, and P. Golland, "Interactive whole-heart segmentation in congenital heart disease," in *International Conference on Medical Image Computing and Computer-Assisted Intervention*. Springer, 2015, pp. 80–88.
5. C. Petitjean and J.-N. Dacher, "A review of segmentation methods in short axis cardiac MR images," *Medical Image Analysis*, vol. 15, no. 2, pp. 169–184, 2011.
6. M.-P. Jolly, N. Duta, and G. Funka-Lea, "Segmentation of the left ventricle in cardiac MR images," in *Computer Vision, 2001. ICCV 2001. Proceedings. Eighth IEEE International Conference on*, vol. 1. IEEE, 2001, pp. 501–508.
7. M. R. Kaus, J. von Berg, J. Weese, W. Niessen, and V. Pekar, "Automated segmentation of the left ventricle in cardiac MRI," *Medical Image Analysis*, vol. 8, no. 3, pp. 245–254, 2004.
8. K. D. Fritscher, R. Pilgram, and R. Schubert, "Automatic cardiac 4d segmentation using level sets," in *International Workshop on Functional Imaging and Modeling of the Heart*. Springer, 2005, pp. 113–122.
9. H. C. Van Assen, M. G. Danilouchkine, A. F. Frangi, S. Ordás, J. J. Westenberg, J. H. Reiber, and B. P. Lelieveldt, "Spasm: a 3d-ASM for segmentation of sparse and arbitrarily oriented cardiac MRI data," *Medical Image Analysis*, vol. 10, no. 2, pp. 286–303, 2006.
10. J. Koikkalainen, T. Tolli, K. Lauerma, K. Antila, E. Mattila, M. Lilja, and J. Lotjonen, "Methods of artificial enlargement of the training set for statistical shape models," *IEEE Transactions on Medical Imaging*, vol. 27, no. 11, pp. 1643–1654, 2008.
11. J. Peters, O. Ecabert, C. Meyer, R. Kneser, and J. Weese, "Optimizing boundary detection via simulated search with applications to multi-modal heart segmentation," *Medical Image Analysis*, vol. 14, no. 1, pp. 70–84, 2010.
12. S. C. Mitchell, B. P. Lelieveldt, R. J. Van Der Geest, H. G. Bosch, J. Reiver, and M. Sonka, "Multistage hybrid active appearance model matching: segmentation of left and right ventricles in cardiac MR images," *IEEE Transactions on Medical Imaging*, vol. 20, no. 5, pp. 415–423, 2001.
13. D. Rueckert, M. Lorenzo-Valdes, R. Chandrashekara, G. Sanchez-Ortiz, and R. Mohiaddin, "Non-rigid registration of cardiac MR: application to motion modelling and atlas-based segmentation," in *Biomedical Imaging, 2002. Proceedings. 2002 IEEE International Symposium on*. IEEE, 2002, pp. 481–484.
14. X. Zhuang and *et al.*, "A registration-based propagation framework for automatic whole heart segmentation of cardiac MRI," *IEEE TMI*, vol. 29, no. 9, pp. 1612–1625, 2010.
15. Y. Zheng, A. Barbu, B. Georgescu, M. Scheuering, and D. Comaniciu, "Four-chamber heart modeling and automatic segmentation for 3-d cardiac CT volumes using marginal space learning and steerable features," *IEEE Transactions on Medical Imaging*, vol. 27, no. 11, pp. 1668–1681, 2008.
16. X. Zhen, H. Zhang, A. Islam, M. Bhaduri, I. Chan, and S. Li, "Direct and simultaneous estimation of cardiac four chamber volumes by multioutput sparse regression," *Medical Image Analysis*, 2016.
17. Y. LeCun, L. Bottou, Y. Bengio, and P. Haffner, "Gradient-based learning applied to document recognition," *Proceedings of the IEEE*, vol. 86, no. 11, pp. 2278–2324, 1998.
18. J. Long, E. Shelhamer, and T. Darrell, "Fully convolutional networks for semantic segmentation," in *CVPR*, 2015, pp. 3431–3440.

19. P. V. Tran, "A fully convolutional neural network for cardiac segmentation in short-axis MRI," arXiv preprint arXiv:1604.00494, 2016.
20. M. Avendi, A. Kheradvar, and H. Jafarkhani, "A combined deep-learning and deformable-model approach to fully automatic segmentation of the left ventricle in cardiac MRI," *Medical Image Analysis*, vol. 30, pp. 108–119, 2016.
21. D. Shen, G. Wu, and H.-I. Suk, "Deep learning in medical image analysis," *Annual Review of Biomedical Engineering*, no. 0, 2017.
22. I. Goodfellow, Y. Bengio, and A. Courville, *Deep Learning*. MIT Press, 2016, http://www.deeplearningbook.org.
23. X. Glorot and Y. Bengio, "Understanding the difficulty of training deep feedforward neural networks." in *Aistats*, vol. 9, 2010, pp. 249–256.
24. D. M. Bradley, "Learning in modular systems," DTIC Document, Tech. Rep., 2010.
25. Y. LeCun, B. Boser, J. S. Denker, D. Henderson, R. E. Howard, W. Hubbard, and L. D. Jackel, "Backpropagation applied to handwritten zip code recognition," *Neural Computation*, vol. 1, no. 4, pp. 541–551, 1989.
26. C.-Y. Lee, S. Xie, P. Gallagher, Z. Zhang, and Z. Tu, "Deeply-supervised nets," arXiv preprint arXiv:1409.5185, 2014.
27. C. M. Bishop, *Neural Networks for Pattern Recognition*. Oxford University Press, 1995.
28. W. N. Venables and B. D. Ripley, *Modern Applied Statistics with S-PLUS*. Springer Science & Business Media, 2013.
29. K. He, X. Zhang, S. Ren, and J. Sun, "Deep residual learning for image recognition," arXiv preprint arXiv:1512.03385, 2015.
30. R. K. Srivastava, K. Greff, and J. Schmidhuber, "Highway networks," vol. abs/1505.00387, 2015.
31. C. Szegedy, W. Liu, Y. Jia, P. Sermanet, S. Reed, D. Anguelov, D. Erhan, V. Vanhoucke, and A. Rabinovich, "Going deeper with convolutions," in *Proceedings of the IEEE Conference on Computer Vision and Pattern Recognition*, 2015, pp. 1–9.
32. P. Krähenbühl and V. Koltun, "Efficient inference in fully connected CRFS with Gaussian edge potentials," arXiv preprint arXiv:1210.5644, 2012.
33. S. Ioffe and C. Szegedy, "Batch normalization: accelerating deep network training by reducing internal covariate shift," arXiv preprint arXiv:1502.03167, 2015.
34. W. Liu, A. Rabinovich, and A. C. Berg, "Parsenet: looking wider to see better," arXiv preprint arXiv:1506.04579, 2015.
35. R. Shahzad, S. Gao, Q. Tao, O. Dzyubachyk, and R. van der Geest, "Automated cardiovascular segmentation in patients with congenital heart disease from 3d CMR scans: combining multi-atlases and level-sets," in *HVSMR 2016: MICCAI Workshop on Whole-Heart and Great Vessel Segmentation from 3D Cardiovascular MRI in Congenital Heart Disease*, October 2016.
36. J. Wolterink, T. Leiner, M. Viergever, and I. Isgum, "Dilated convolutional neural networks for cardiovascular MR segmentation in congenital heart disease," in *HVSMR 2016: MICCAI Workshop on Whole-Heart and Great Vessel Segmentation from 3D Cardiovascular MRI in Congenital Heart Disease*, October 2016.
37. G. Tziritas, "Fast fully-automatic segmentation of cardiac images using 3-d MRF model optimization and substructures tracking," in *HVSMR 2016: MICCAI Workshop on Whole-Heart and Great Vessel Segmentation from 3D Cardiovascular MRI in Congenital Heart Disease*, October 2016.
38. A. Mukhopadhyay, "Total variation random forest: fully automatic MRI segmentation in congenital heart disease," in *HVSMR 2016: MICCAI Workshop on Whole-Heart and Great Vessel Segmentation from 3D Cardiovascular MRI in Congenital Heart Disease*, October 2016.
39. Ö. Çiçek, A. Abdulkadir, S. S. Lienkamp, T. Brox, and O. Ronneberger, *3D U-Net: Learning Dense Volumetric Segmentation from Sparse Annotation*. Cham: Springer International Publishing, 2016, pp. 424–432.
40. F. Yu and V. Koltun, "Multi-scale context aggregation by dilated convolutions," in *ICLR*, 2016.
41. L. Yu, X. Yang, J. Qin, and P.-A. Heng, "3D FractalNet: dense volumetric segmentation for cardiovascular MRI volumes," in *Reconstruction, Segmentation, and Analysis of Medical Images: First International Workshops, RAMBO 2016 and HVSMR 2016*, ser. LNCS, vol. 10129, 2017, pp. 103–110.
42. G. Larsson, M. Maire, and G. Shakhnarovich, "Fractalnet: ultra-deep neural networks without residuals," arXiv preprint arXiv:1605.07648, 2016.
43. K. Simonyan and A. Zisserman, "Very deep convolutional networks for large-scale image recognition," arXiv preprint arXiv:1409.1556, 2014.

44. Q. Dou, H. Chen, Y. Jin, L. Yu, J. Qin, and P.-A. Heng, "3d deeply supervised network for automatic liver segmentation from CT volumes," in *International Conference on Medical Image Computing and Computer-Assisted Intervention*. Springer, 2016, pp. 149–157.
45. S. Xie and Z. Tu, "Holistically-nested edge detection," in *Proceedings of the IEEE International Conference on Computer Vision*, 2015, pp. 1395–1403.
46. Y. Jia, E. Shelhamer, J. Donahue, S. Karayev, J. Long, R. Girshick, S. Guadarrama, and T. Darrell, "Caffe: convolutional architecture for fast feature embedding," arXiv preprint arXiv:1408.5093, 2014.
47. Ö. Çiçek, A. Abdulkadir, and *et al.*, "3d u-net: learning dense volumetric segmentation from sparse annotation," arXiv preprint arXiv:1606.06650, 2016.
48. H. Chen, Q. Dou, L. Yu, and P.-A. Heng, "Voxresnet: deep voxelwise residual networks for volumetric brain segmentation," arXiv preprint arXiv:1608.05895, 2016.
49. L. Yu, J.-Z. Cheng, Q. Dou, X. Yang, H. Chen, J. Qin, and P.-A. Heng, "Automatic 3d cardiovascular MR segmentation with densely-connected volumetric convnets," in *International Conference on Medical Image Computing and Computer-Assisted Intervention*. Springer, 2017, pp. 287–295.
50. G. Huang, Z. Liu, K. Q. Weinberger, and L. van der Maaten, "Densely connected convolutional networks," arXiv preprint arXiv:1608.06993, 2016.
51. P. Kontschieder, S. R. Bulo, H. Bischof, and M. Pelillo, "Structured class-labels in random forests for semantic image labelling," in *Computer Vision (ICCV), 2011 IEEE International Conference on*. IEEE, 2011, pp. 2190–2197.
52. A. Mukhopadhyay, "Total variation random forest: fully automatic MRI segmentation in congenital heart diseases," in *Reconstruction, Segmentation, and Analysis of Medical Images: First International Workshops, RAMBO 2016 and HVSMR 2016*, ser. LNCS, vol. 10129, 2017, pp. 165–171.
53. G. Tziritas, "Fully-automatic segmentation of cardiac images using 3-d MRF model optimization and substructures tracking," in *Reconstruction, Segmentation, and Analysis of Medical Images: First International Workshops, RAMBO 2016 and HVSMR 2016*, ser. LNCS, vol. 10129, 2017, pp. 129–136.
54. R. Shahzad, S. Gao, Q. Tao, O. Dzyubachyk, and R. vander Geest, "Automated cardiovascular segmentation in patients with congenital heart disease from 3d CMR scans: combining multi-atlases and level-sets," in *Reconstruction, Segmentation, and Analysis of Medical Images: First International Workshops, RAMBO 2016 and HVSMR 2016*, ser. LNCS, vol. 10129, 2017, pp. 147–155.
55. J. Wolterink, T. Leiner, M. Viergever, and I. Isgum, "Dilated convolutional neural networks for cardiovascular MR segmentation in congenital heart disease," in *Reconstruction, Segmentation, and Analysis of Medical Images: First International Workshops, RAMBO 2016 and HVSMR 2016*, ser. LNCS, vol. 10129, 2017, pp. 95–102.
56. X. Zhuang, "Challenges and methodologies of fully automatic whole heart segmentation: a review," *Journal of Healthcare Engineering*, vol. 4, no. 3, pp. 371–408, 2013.
57. X. Yang, C. Bian, L. Yu, D. Ni, and P.-A. Heng, "Hybrid loss guided convolutional networks for whole heart parsing," in *International Workshop on Statistical Atlases and Computational Models of the Heart*, Springer, 2017, pp. 215–223.
58. O. Ronneberger, P. Fischer, and T. Brox, "U-net: convolutional networks for biomedical image segmentation," in *International Conference on Medical Image Computing and Computer-Assisted Intervention*. Springer, 2015, pp. 234–241.
59. S. M. Pizer, E. P. Amburn, and *et al.*, "Adaptive histogram equalization and its variations," *Computer Vision, Graphics, and Image Processing*, vol. 39, no. 3, pp. 355–368, 1987.
60. H. Chen, D. Ni, J. Qin, and *et al.*, "Standard plane localization in fetal ultrasound via domain transferred deep neural networks," *IEEE JBHI*, vol. 19, no. 5, pp. 1627–1636, 2015.
61. A. Krizhevsky, I. Sutskever, and G. E. Hinton, "Imagenet classification with deep convolutional neural networks," in *Advances in Neural Information Processing Systems*, 2012, pp. 1097–1105.
62. D. Tran, L. Bourdev, R. Fergus, L. Torresani, and M. Paluri, "Learning spatiotemporal features with 3d convolutional networks," in *ICCV*, 2015, pp. 4489–4497.
63. F. Milletari, N. Navab, and S.-A. Ahmadi, "V-net: fully convolutional neural networks for volumetric medical image segmentation," in *3D Vision (3DV), 2016 Fourth International Conference on*. IEEE, 2016, pp. 565–571.
64. H.-H. Chang, A. H. Zhuang, D. J. Valentino, and W.-C. Chu, "Performance measure characterization for evaluating neuroimage segmentation algorithms," *Neuroimage*, vol. 47, no. 1, pp. 122–135, 2009.
65. X. Cao, J. Yang, Y. Gao, Y. Guo, G. Wu, and D. Shen, "Dual-core steered non-rigid registration for multi-modal images via bi-directional image synthesis," *Medical Image Analysis*, 2017.

Taylor & Francis
Taylor & Francis Group
http://taylorandfrancis.com

Index

Note: Tables are indicated by bold page references; figures, photos and/or illustrations are indicated by an italicized number.

A

B

C

E

H

I

M

N

O

P

T